Proceedings of The 8th International Conference on Analysis of Discontinuous Deformation

Fundamentals & Applications to Mining & Civil Engineering

ICADD-8

August 14-19, 2007

Beijing P. R. China

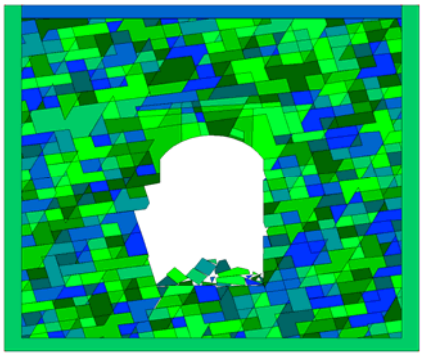

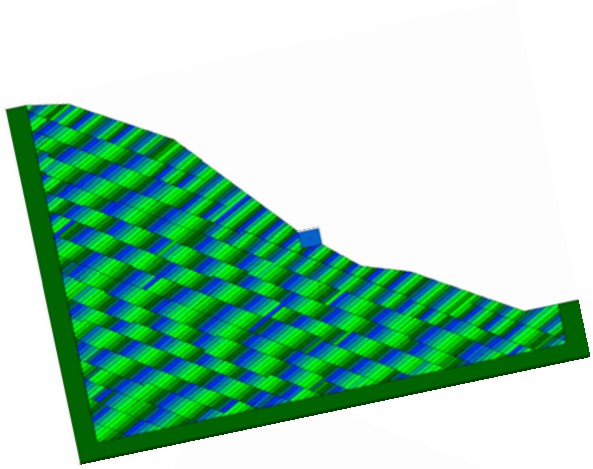

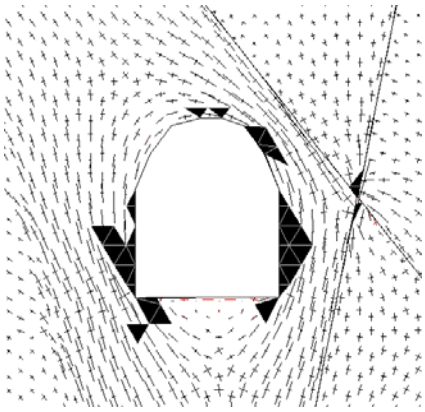

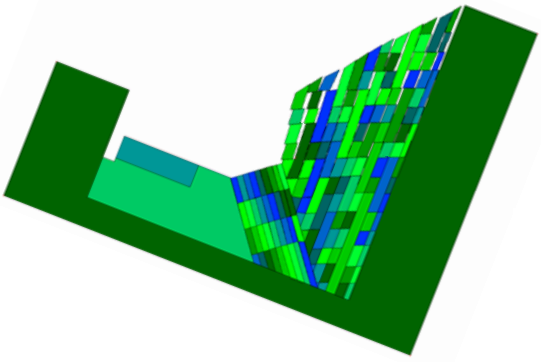

Edited by:

Yang Ju, *China University of Mining and Technology, CUMTB, P. R. CHINA*

Xisheng Fang, *Computer Science Department, Ohlone College, USA*

Haiying Bian, *China University of Mining and Technology, CUMTB, P. R. CHINA*

ICADD-8 International Organizing Committee

The organizing committee would like to express appreciation to *China University of Mining & Technology, Beijing (CUMTB), Beijing Institute of Technology (BIT), National Basic Research Project of China (2002CB412700), Graduate University of Chinese Academy of Sciences (GUCAS), K. C. Wong Education Foundation, Hong Kong, Chinese Society for Rock Mechanics & Engineering (CSRME) and American Rock Mechanics Association (ARMA)* for their supports.

The figures shown on the front cover may be found in the following papers:
Applications of discontinuous deformation analysis (DDA) to rock stability analysis by Dr. Genhua Shi
Recent insights of analyses using discontinuous methods in rock engineering in Japan by Y. Ohinshi

The conference was held August 14-19, 2007, hosting by State Key Laboratory of Coal Resources & Safe Mining, China University of Mining & Technology, and Beijing Institute of Technology, in Beijing, China.

Preface

The past few decades have witnessed a boom in the development of rock engineering in China, most notably in large-scale efforts such as the Three-Gorges Dam, the South-to-North Water Transfer project, and the Jin Ping Hydroelectric Station. Although such projects have boosted the studies and development of rock mechanics and rock engineering, they also presented great challenges in the analyses of rock masses. One such challenge is how to deal with the deformation and mechanical responses along the discontinuities in rock masses.

The idea of Discontinuous Deformation Analysis (DDA) presented by Dr. Shi's innovation in 1988 led us to a new method of treating the deformation of discontinuous media. Since then, DDA has been adopted to solve a wide range of complicated engineering problems and spread throughout the fields of rock mechanics and engineering. As the papers in these proceedings show, these DDA methods have been further developed by my Chinese colleagues to analyze some very challenging problems that arose in rock engineering in China. As a result, ICADD-7 in Hawaii in 2005 decided to move the 8th conference to China to incorporate these recent achievements in DDA theory and applications. These proceedings reflect the latest development of analysis of discontinuous deformation and engineering applications in the fields of mining and civil engineering.

This conference would not be possible without the untiring efforts of Dr. Gen-hua Shi, Dr. Yang Ju, Dr. Xi-sheng Fang, Dr. Jun Yang and all members of the local organizing committee. Their hard work in planning and organizing helped to ensure this conference was a success. We thank Dr. Mary Maclaughlin, Dr. Man-chu Ronald Yeung and Dr. Yuzo Ohnishi for volunteering to instruct a three-day DDA short course that is sure to benefit conference attendees. We would like to extend our gratitude to all sponsors for their support, including the Chinese State Key Laboratory of Coal Resources and Safe Mining, China University of Mining & Technology, Beijing Institute of Technology, National Basic Research Project of China (2002CB412700), Graduate University of Chinese Academy of Sciences, K. C. Wong Education Foundation Hong Kong, Chinese Society for Rock Mechanics and Engineering and American Rock Mechanics Association. Finally, we would like to thank the authors of the papers for their contributions and participation.

Heping Xie
Chairman, Conference International Advisory Board and Technical Committee
Academician, Chinese Academy of Engineering
President, Sichuan University, P. R. China
August 2007

Table of Contents

Keynote Speech

Section1: Algorithm & Computational Implementation of DDA

Section2: Dynamic Analyses & Discontinuous Deformation

Section3: Discontinuous Analysis & Applications

Section4: Numerical Manifold Method & Key Block Analysis

Applications of Discontinuous Deformation Analysis (DDA) to rock stability analysis

GEN-HUA SHI

DDA Company, 1746 Terrace Drive, Belmont, CA 94002, USA

Limit equilibrium is still the fundamental method for global stability analysis. Reaching limit equilibrium requires large displacements, discontinuous contacts, precise friction law, multi-step computation and stabilized time-step dynamic computation. Therefore three convergences are unavoidable: convergence of equilibrium equations, convergence of open-close iterations for contacts and convergence of the contact forces of dynamic computations. This paper focuses mainly on applications of two dimensional DDA. The applications show DDA has the ability to reach limit equilibrium of block systems. For slope stability analysis, this paper works on rock block toppling and loosening, where the block rotation is the main issue. For foundation stability analysis, this paper presents dam foundation damage computation, where the block sliding is a main issue.

Keywords: DDA; Discontinuous deformation analysis; Contacts; Limit equilibrium; Toppling; Stability analysis

1. Discontinuous Deformation Analysis (DDA)

The computation method used in this paper is mainly two dimensional discontinuous deformation analysis or 2d-DDA. DDA works on block systems. Each block has linear displacements and constant stresses and strains.

The current version of 2d-DDA bas 6 unknowns per block:

x direction movement d_x,

y direction movement d_y,

rotation r_{xy},

x direction strain ε_x,

y direction strain ε_y,

Shear strain τ_{xy}.

DDA uses multi-time steps. Both static and dynamic cases use dynamic computation. Static computation is the stabilized dynamic computation in the natural way. Therefore DDA can perform discontinuous and large deformation computation for both static and dynamic cases.

For each time steps, DDA usually has several open-close iterations. DDA readjust open, close or sliding modes until every contact position has the same contact mode before and after the equation solving then going to next time step. Here, for each open-close iteration of each time step, DDA solves global equilibrium equations. The friction law is ensured in DDA computation. The friction law is the principle law of stability which is inequality equations in mathematics.

Every single block of 2-d DDA can be a generally shaped convex or concave two dimensional polygon. Each block can have any number of edges. Based on simplex integration, the stiffness matrices, the inertia matrices and all other matrices of DDA are analytical solutions.

DDA has complete linear contact modes. If the time step is small enough and the total step number is large enough, DDA can simulate any possible complex movements of block systems.

DDA serves as a bridge between FEM and limit equilibrium method. DDA has strict equilibrium at each time step. After some time steps, the DDA reaches dynamic or static limit equilibrium for whole simply deformable block systems.

DDA also served as implicit version of DEM method. DDA has all advantages of dynamic relaxation yet the convergence is strict and the result is accurate.

More important, DDA is a very well examined method by analytical solutions, physical model tests and large engineering projects. For toppling computation DDA results are consistent with Prof. Goodman's analytical formulae.

2. Toppling of slopes: foliation planes have 40 degrees dip angle

The average dip angle of the slope is 43 degrees. The physical data of rock mass for this slope are shown in Table 1. The ground water surfaces are always input. The following table2 includes the geometric data and physical data of the joint sets.

Location	Unit Wight PSF	Elastic Modulus PSF	Poisson's Ratio
Regular Rocks	167	720000000	0.35
Weak Zone	167	72000000	0.35

Table 1 Physical data of rock mass

Table 2 Geometric and physical data of joint sets

Joint Set	1 (Foliation)	2
Dip Angle Degree	40	40
Average Spacing Ft	7	30
Average Length Ft	2000	200
Cohesion PSF	0	0
Friction Angle Degree	10	30

Computation of two dimensional DDA uses 10000 time steps, 0.002 second per step. The dynamic ratio is 0.99. It means the next time step inherent 0.99 of the velocity from the previous time step.
Figure 1 shows the result of the slope, the dip angle of the foliation planes is 40 degrees.

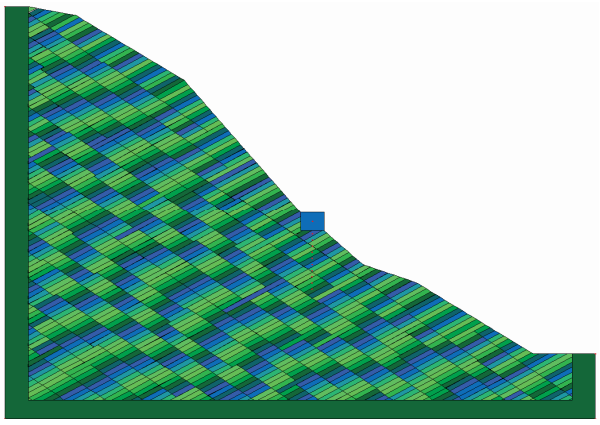

Figure 1: Toppling of the slope where the dip angle of foliation plane is 40 degrees

Figure 2 is the time depending movements of the measured points under the anchor block of the slope for the previous case of Figure 1.Under the 40 degrees dip angle of the foliation planes, the toppling is very small and almost invisible. The slope and the anchor block are stable under the 40 degrees dip angle of the foliation planes.

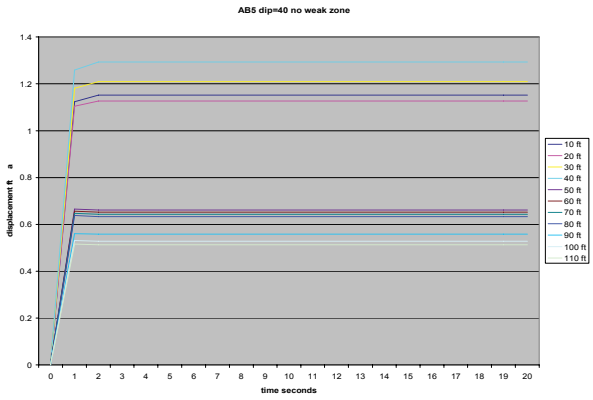

Figure 2: Displacements of points under the slope where the dip angle of foliation planes is 40 degrees

3. Toppling of slopes: foliation planes have 50 degrees dip angle

The dip angle of foliation planes is 50 degrees for the slope. The ground water surfaces are always input. The geometric data and physical data of the joint sets are same as Table2 except the dip angle of foliation planes is 50 degrees.
Computation of two dimensional DDA uses 10000 time steps, 0.002 second per step. The dynamic ratio is 0.99. It means the next time step inherent 0.99 of the velocity from the previous time step.

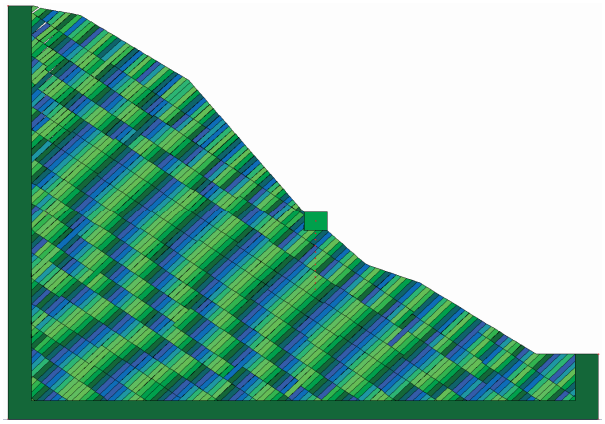

Figure 3: Toppling of the slope where the dip angle of foliation plane is 50 degrees

Figure 3 shows the result of the slope, the dip angle of the foliation planes is 50 degrees.
From Figure 3 it can be seen that rock blocks of the upper left corner have visible gapes. This means slight toppling on the upper left corner takes place. The opening gapes only appear on this very small local area.

Still the opening gapes can not be found in other locations.

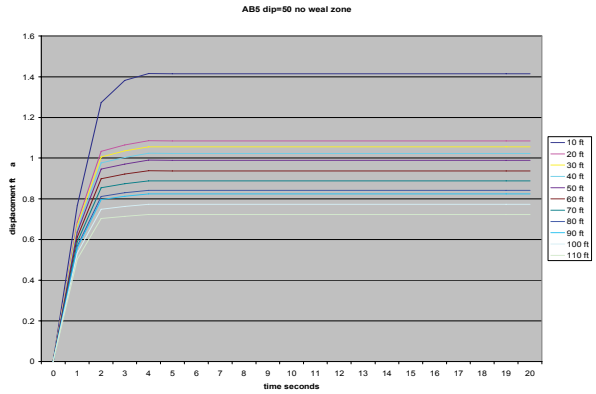

Figure 4: Displacements of points under the slope

Figure 4 is the time depending movements of the measured points under the anchor block of the slope for the previous case of Figure 3. Under the 50 degrees dip angle of the foliation planes, the toppling is still small and almost invisible. However displacements are larger than the combination 1 where the dip angle of foliation planes is 40 degrees.

4. Toppling of slopes: foliation planes have 60 degrees dip angle

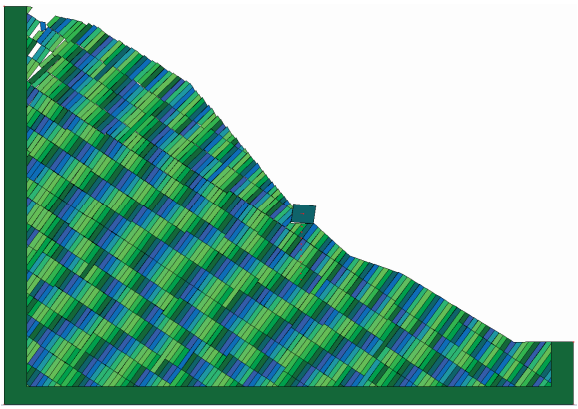

Figure 5: Toppling of the slope where the dip angle of foliation plane is 60 degrees

In this section, the dip angle of foliation planes is 60 degrees for the slope. The ground water surfaces are always input. The geometric data and physical data of the joint sets are same as Table2 except the dip angle of foliation planes is 60 degrees.
Computation of two dimensional DDA uses 30000 time steps, 0.002 second per step. The dynamic ratio is 0.99. It means the next time step inherent 0.99 of the velocity from the previous time step.
Figure 5 shows the result of the slope, the dip angle of the foliation planes is 60 degrees.

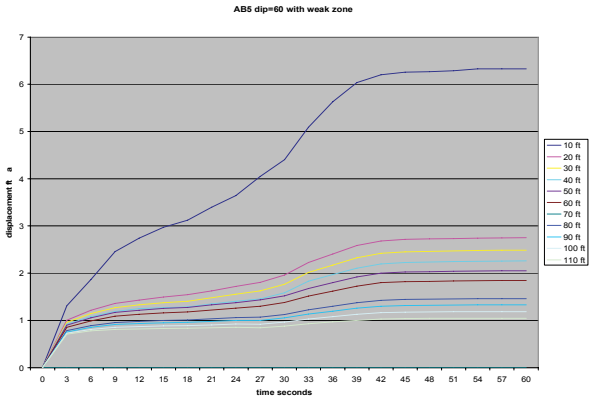

Figure 6: Displacements of points under the slope where the dip angle of foliation planes is 60 degrees

Figure 6 is the time depending movements of the measured points under the anchor block of the slope for the previous case of Figure 5. Under the 60 degrees dip angle of the foliation planes, the toppling of the slope is in large scale. It can be seen, the slope is a convex slope which gives more room for block rotation or toppling.

5. Toppling of slopes: foliation planes have 70 degrees dip angle

From the drilling data, the original dip angle of the foliation planes is about 70 degrees. If after toppling, the second joint set has 40 degrees dip angle, the original dip angle of the second joint set is about 20 degrees. The following Table 3 includes the geometric data and physical data of the joint sets and rock masses.

Table 3 Geometric and physical data of joint sets

Joint Set	1 (Foliation)	2
Dip Angle Degree	70	20
Average Spacing Ft	7	30
Average Length Ft	2000	30
Cohesion PSF	0	0
Friction Angle Degree	10	30

The following computation is to simulate or back calculate the past toppling of the slope.
Figure 7 shows the result of the slope, the dip angle of the foliation planes is 70 degrees.
Figure 8 is the time depending movements of the measured points under the anchor block of the slope for the previous case of Figure 7.

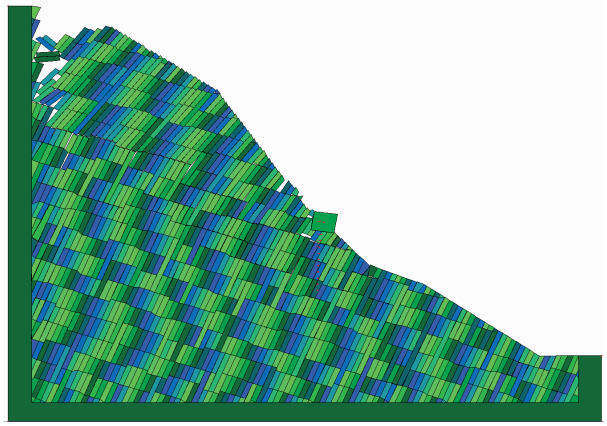

Figure 7: Toppling of the slope where the dip angle of foliation plane is 70 degrees

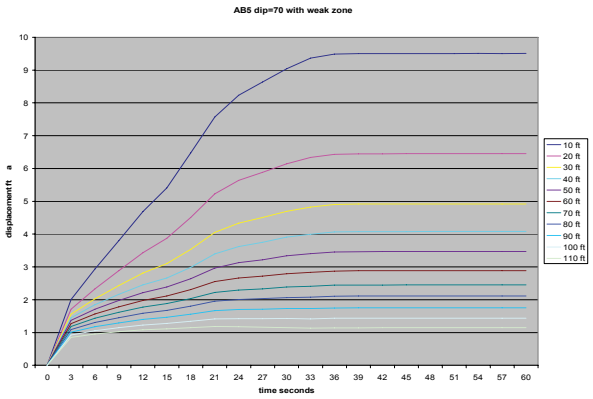

Figure 8: Displacements of points under the slope where the dip angle of foliation planes is 70 degrees

Computation of two dimensional DDA uses 30000 time steps, 0.002 second per step. The dynamic ratio is 0.99. It means the next time step inherent 0.99 of the velocity from the previous time step. Under the 70 degrees dip angle of the foliation planes, the toppling of the slope is very large. It can be seen, the slope is a convex slope which gives more room for block rotation or toppling.

6. Bolting computation of toppling slopes

In this section, three cases of bolting computations are made. The three cases are the slope with longer second set joints, the slope with shorter second set joints and the slope where the second set joints are shorter and have 20 degree flat dip angle. The dip angle of foliation planes is 60 degrees for all of these three cases. The ground water surfaces are always input.
The following table 4 includes the geometric data and physical data of the joint sets and rock masses.
Computation of two dimensional DDA uses 30000 time steps, 0.002 second per step. The dynamic ratio is 1.00.

Table 4 Geometric and physical data of joint sets

Joint Set	1 (Foliation)	2
Dip Angle Degree	60	20-40
Average Spacing Ft	7	30
Average Length Ft	2000	30-200
Cohesion PSF	0	0
Friction Angle Degree	20	30

It means the next time step inherent all of the velocity from the previous time step. The affection of earth quake can be presented from this pure dynamic computation.
Figure 9 shows the bolting result of the slope: the dip angle of the foliation planes is 60 degrees.

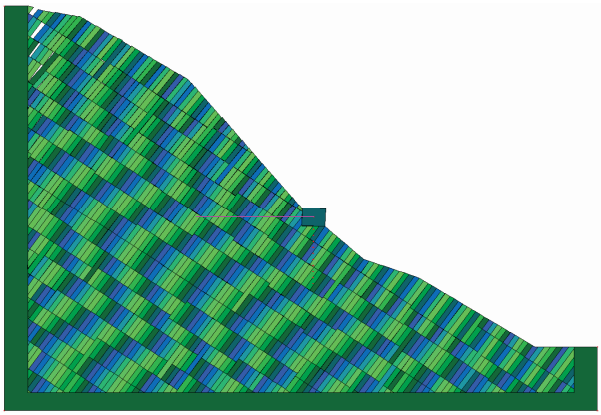

Figure 9: Bolting of toppling slope where the dip angle of foliation plane is 60 degrees

Figure 10 is the time depending forces of the bolt of the previous cases of Figure 9. It can be seen from the results; the bolts made differences here. Under the 60 degrees dip angle of the foliation planes, the maximum required bolting force is 14 Kips per foot for the whole slope section. Therefore, different kinds of reinforcements are feasible.
Since the foliation planes are very dense and the rock blocks are very thing, large numbers of blocks are needed for this DDA computation. Still there are no enough previous experiences for toppling analysis. This computation has to cover all possible cases and combinations.
Here, time depending movements are involved. Each computation has to reach static state from dynamic state. As the time is long enough, no more displacement or bolting force change can be seen from the charts.

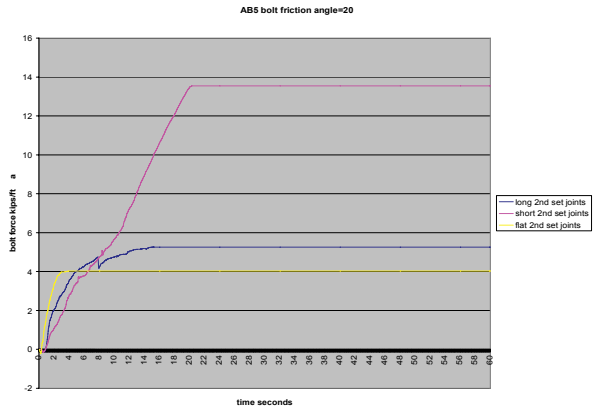

Figure 10: bolt forces of the slope where the dip angle of foliation planes is 60 degrees

7. Computation of rock block loosening

In the next 2d-DDA computation, the input data are shown by Table 5 which is the real physical data of the rock mass.

Table 5 Physical data of rock mass with original friction angle

Location	Ultra Mafics	Shear Zone Weathered	Shear Zone Fresh
Unit Wight PCF	167	130	130
Elastic Modulus PSF	720000000	150000	500000
Poisson's Ratio	0.35	0.25	0.25
Friction Angle Degree	40	35	35
Cohesion PSF	0	0	0

Computation of two dimensional DDA uses 5000 time steps, 0.002 second per step. . The dynamic ratio is 1.00. It means the next time step inherent all of the velocity from the previous time step.
Figure 11 shows the result under the normal loads. No distinct movements or damages can be seen.
Figure 12 shows the result under reduced friction angle by 5 degrees. Still no distinct movements or damages can be seen.
Figure 13 shows the result under reduced friction angle by 10 degrees. Partly loosening can be seen with unstable large displacements.
Figure 14 shows the result under reduced friction angle by 15 degrees. Global loosening of the whole block system can be seen with unstable large displacements. The Following figure 15 shows the displacements of the given point under different friction angles.
The real friction angle is α_r = 40 degrees. The failure friction angle α_f = 35 degrees. The factor of safety is tan α_r /tan α_f = 1.2

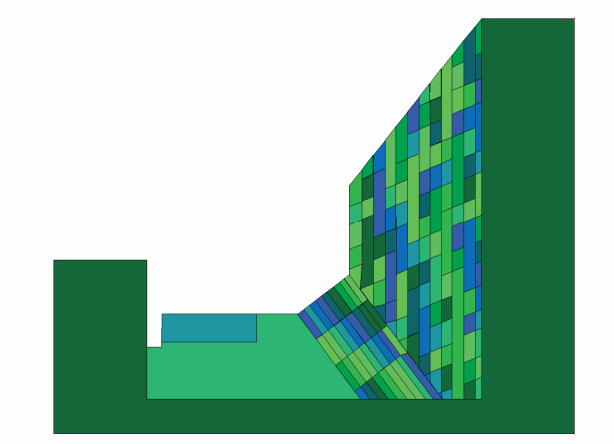

Figure 11: Case of original friction angle

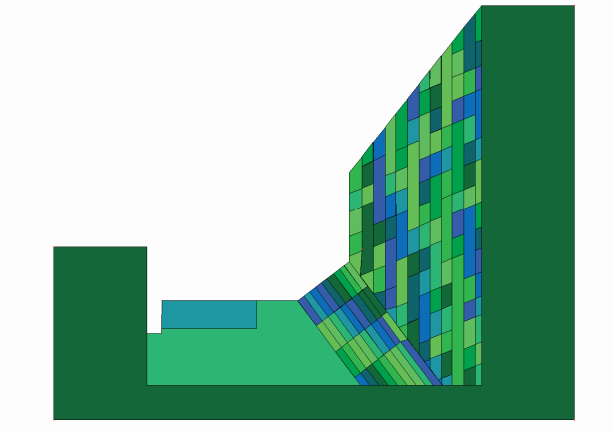

Figure 12: Case with reduced friction angle by 5 degrees

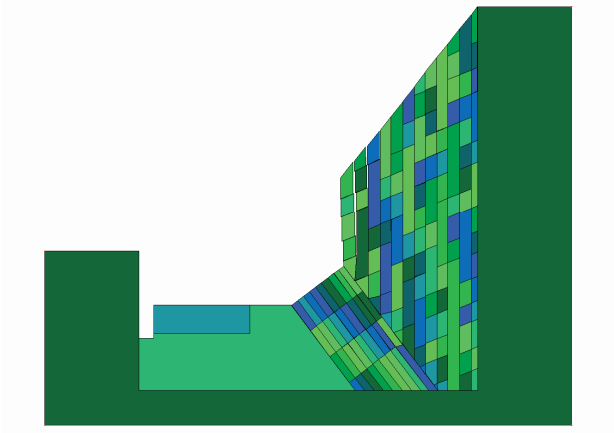

Figure 13: Case with reduced friction angle by 10 degrees

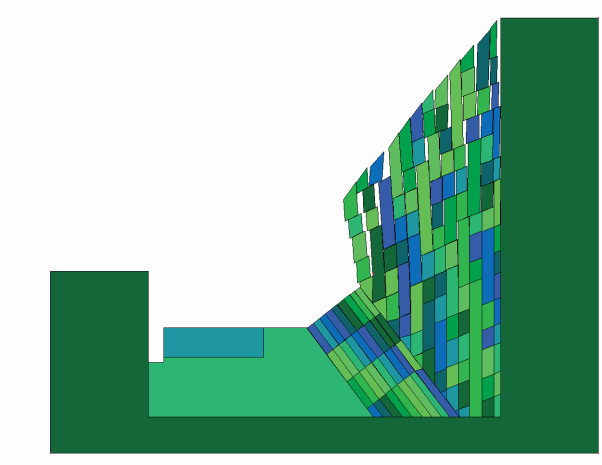

Figure 14: Case with reduced friction angle by 15 degrees

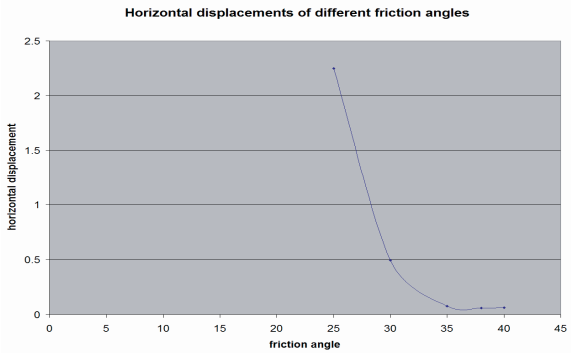

Figure 15: Horizontal displacements of a point under different friction angles

8. Dynamic earth quake load on bolts

The following dynamic earth quake acceleration curves are scaled from recorded earth quake curves of San Francisco area. The frequency of this earth quake is relatively low. Therefore it is easier to make damage than the earth quake of higher frequency. Considering the eigenvalues of the same area are unchanged, it is logical to scale the intensity of the acceleration.
Figure 16 shows the X and Y components of time-depending acceleration vectors.
Figure 17 shows the Z components and the resultant of time-depending acceleration vectors.

Table 6 Earth quake data information

Item	
Total number of steps	2000
Time interval of a step	0.05 Second
G value as unit	32.2 ft/s²
Dimension	3

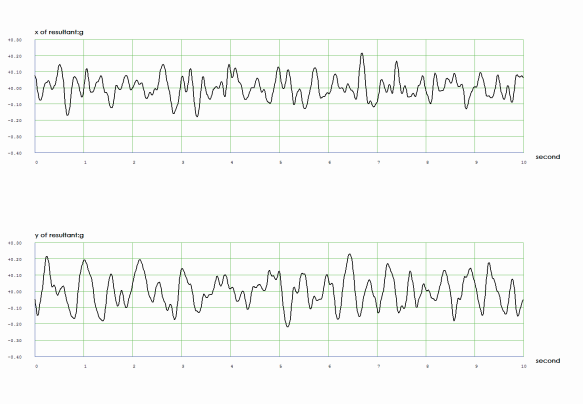

Figure 16: X and Y components of 0.3g earth quake

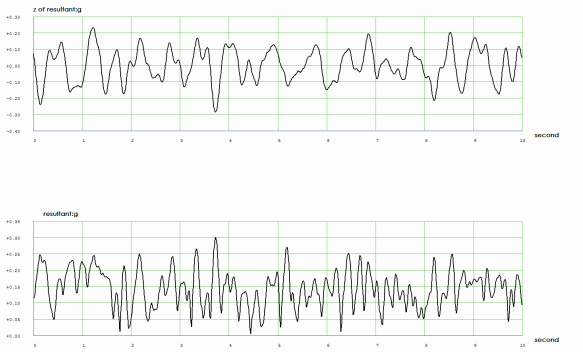

Figure 17: Z component and resultant of 0.3g earth quake

In the next 2-d DDA computation, water pressure is applied. The 0.3g dynamic earth quake is applied too.

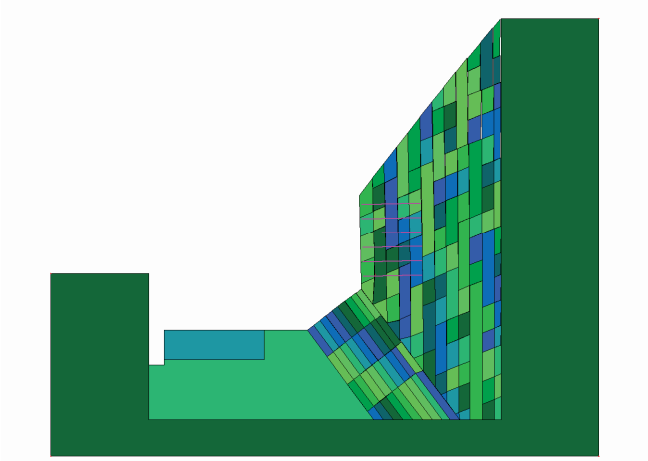

Figure 18: Bolting under 0.3g dynamic earth quake

There are 6 bolts on this slope section. The input data are shown also by Table 6 of previous section.
Computation of two dimensional DDA uses 5000 time steps, 0.002 second per step. The dynamic ratio is 1.00. It means the next time step inherent all of the velocity from the previous time step. The affection of earth

quake can be presented from this pure dynamic computation.

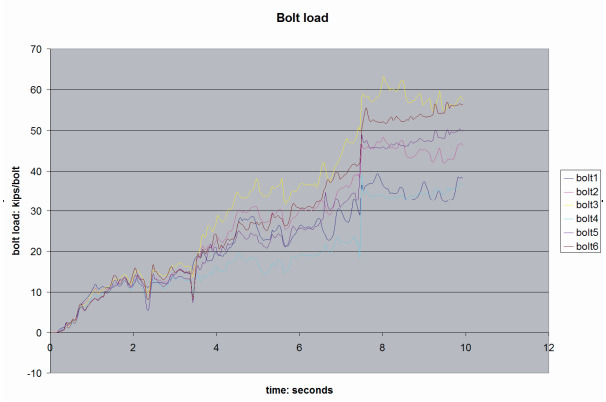

Figure 19: Time-depending bolt loads

Figure 18 shows the bolts hold the rock blocks. Figure 19 shows the time depending load of each bolt. The maximum load of all bolts and for all the time is 64 kips per bolt.

9. Gravity dam foundation stability analysis

The dam foundation computation (Figure 20) of two dimensional DDA uses 1000 time steps, 0.05 second per step. The dynamic ratio is 0.95. It means the next time step inherent 95% of the velocity from the previous time step.

Table 7 Physical data of concrete and rock mass of gravity dam foundation

Location	Concrete	Rock Mass
Unit Wight Ton/Cubic Meter	2.5	2.8
Elastic Modulus Ton/Square Meter	2400000	2600000
Poisson's Ratio	0.17	0.30
Friction Angle Degree	47	26
Cohesion Ton/Square Meter	0	0

The computations of Figure 20 reaches constant factor of safety 2.603528 and relative maximum displacements 0.0000000 in 300 time steps. This means the block system reaches limit equilibrium after 300 times steps in a very high standard.

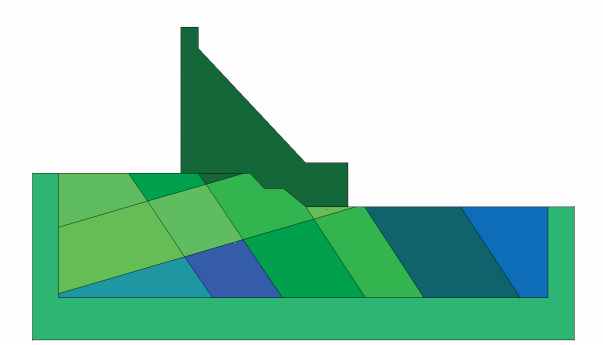

Figure 20: Dam under normal loading

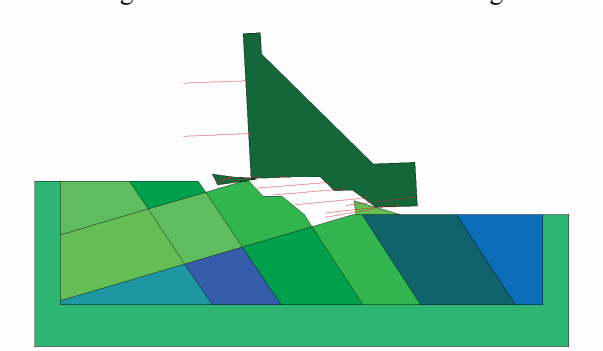

Figure 21: Dam with doubled water pressure and reduced friction angle

In order to find the mode of failure, the computation of Figure 21 uses double water pressure and reduced rock friction angle which is 15 degrees.
The computation of Figure 21 uses 3000 time steps, 0.02 second per step. The dynamic ratio is 1.00. It means the next time step inherent all of the velocity from the previous time step.
Figure 21 shows the damage which is large movements of only three blocks including the dam itself.

10. Arch dam foundation stability analysis

The thin arch dam (Figure 22) is computed by two dimensional DDA. 1000 time steps are used, 0.01 second per step. The dynamic ratio is 0.95. It means the next time step inherent 95% of the velocity from the previous time step.

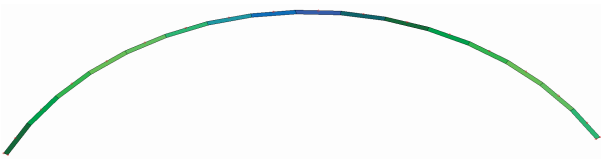

Figure 22: Thin arch Dam with five times water pressure

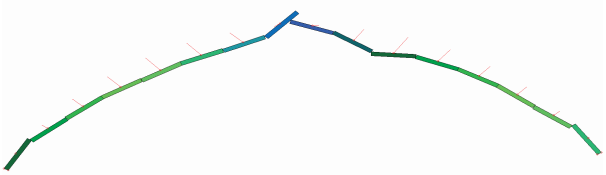

Figure 23: Thin arch dam with moving abutment and water pressure

The physical data of the arch dam of Figure 22 are shown on Table 8. The computation of Figure 22 reaches relative maximum displacements 0.0000000 in 400 time steps. This means the block system reaches limit equilibrium after 400 time steps in a very high standard.

Table 8 Physical data of concrete arch

Location	Concrete
Unit Wight Ton/Cubic Meter	2.4
Elastic Modulus Ton/Square Meter	2400000
Poisson's Ratio	0.17
Friction Angle Degree	10
Cohesion Ton/Square Meter	0

The failure of thin arch dam (Figure 23) is computed by two dimensional DDA. 4000 time steps are used, 0.01 second per step. The movement of dam abutment is applied to cause the failure.
The physical data of the thin arch dam of Figure 23 are shown on Table 8.

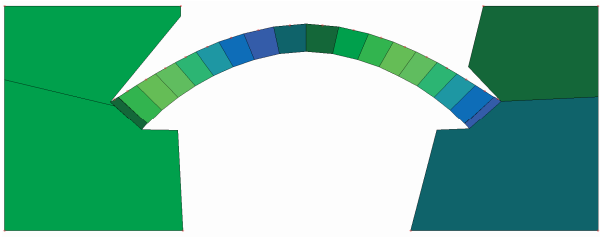

Figure 24: Arch dam and rock foundation with five times water pressure

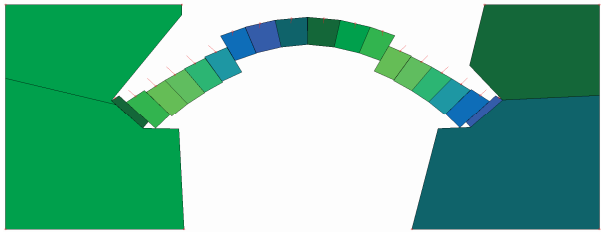

Figure 25: Arch dam and rock foundation with five times water pressure and reduced friction angle

The arch dam (Figure 24) is computed by two dimensional DDA. Five times of water pressure are applied. 1000 time steps are used, 0.01 second per step. The dynamic ratio is 0.90. It means the next time step inherent 90% of the velocity from the previous time step.
The physical data of the arch dam of Figure 24 are shown on Table 9. The computation of Figure 24 reaches relative maximum displacements 0.0000000 in 250 time steps. This means the block system reaches limit equilibrium after 250 time steps in a very high standard.

Table 9 Physical data of concrete and rock mass of arch dam foundation

Location	Concrete & Rock
Unit Wight Ton/Cubic Meter	2.4
Elastic Modulus Ton/Square Meter	2400000
Poisson's Ratio	0.17
Friction Angle Degree	25
Cohesion Ton/Square Meter	0

The failure of arch dam (Figure 25) is computed by two dimensional DDA. Five times of water pressure are applied. The friction angle is reduced to 5 degrees from the data of Table 9. Also 0.85g earth quake is applied. 4000 time steps are used, 0.01 second per step. The physical data of the arch dam of Figure 25 are shown on Table 9.

11. Buttress dam foundation stability analysis

The dam foundation computation (Figure 26) of two dimensional DDA uses 400 time steps. The time

interval was automatic chosen and controlled by maximum displacement ratio 0.001. The maximum displacement ratio is the allowed maximum step displacement divided by the half height of the whole mesh. The average time interval is 0.06 second per step. The dynamic ratio is 0.0. It means the next time step start with zero velocity.
The physical data of the dam of Figure 26 are shown on Table 10. The computation of Figure 26 reaches relative maximum displacements 0.0000000 in 200 time steps. This means the block system reaches limit equilibrium after 200 time steps in a very high standard.

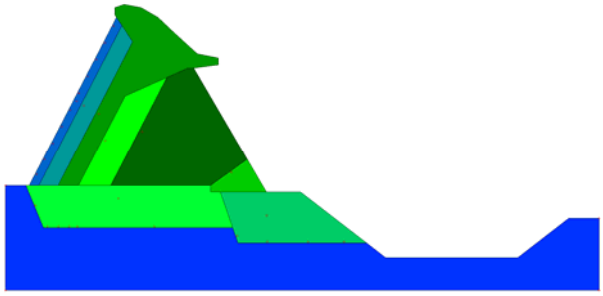

Figure 26: Buttress dam with water pressure

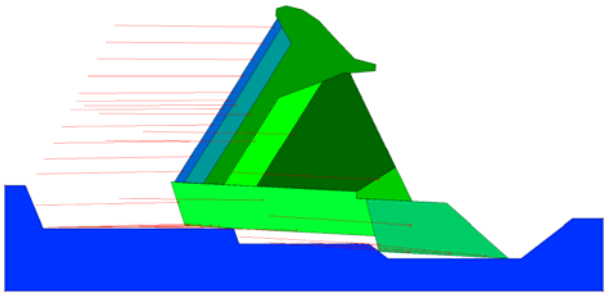

Figure 27: Buttress dam with water pressure and reduced friction angle

Failure computation (Figure 27) of dam foundation uses two dimensional DDA. The total time steps are 5000. The time interval was automatic chosen and controlled by maximum displacement ratio 0.001. The maximum displacement ratio is the allowed maximum step displacement divided by the half height of the whole mesh. The average time interval is 0.08 second per step. The dynamic ratio is 0.0. It means the next time step start with zero velocity. The physical data of the dam of Figure 27 are shown on Table 10. In order to reach failure state, the friction angle of horizontal joints reduced from 28 degrees to 17 degrees.

Table 10 Physical data of concrete and rock mass of buttress dam foundation

Location	Concrete	Rock Mass
Unit Wight Kpound/Cubic Foot	0.150	0.135
Elastic Modulus Kpound/Square Foot	432000	160000
Poisson's Ratio	0.20	0.24
Friction Angle Degree	28 (of horizontal joints)	29 (of other joints)
Cohesion Kpound/Square Foot	0	0

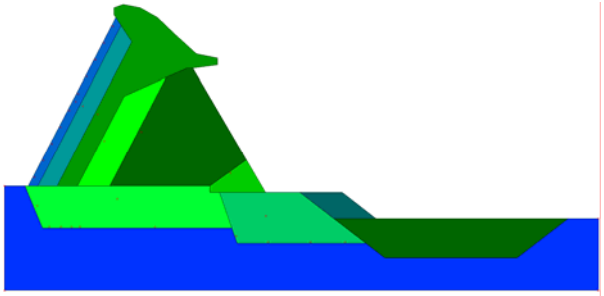

Figure 28: Buttress dam reinforced by resist block and loaded by water pressure

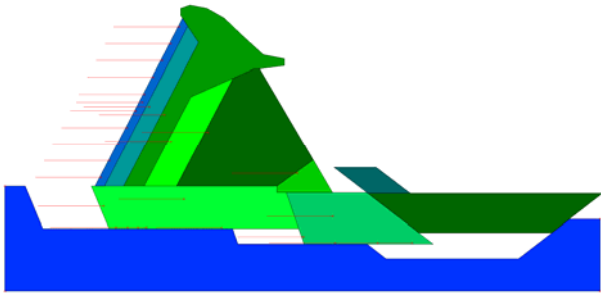

Figure 29: Buttress dam reinforced by resist block, loaded by water pressure and computed under very small friction angle

The reinforced dam foundation computation (Figure 28) of two dimensional DDA uses 500 time steps. The time interval was automatic chosen and controlled by maximum displacement ratio 0.0007. The maximum displacement ratio is the allowed maximum step displacement divided by the half height of the whole mesh. The average time interval is 0.044 second per step. The dynamic ratio is 0.0. It means the next time step start with zero velocity.

The physical data of the buttress dam of Figure 28 are shown on Table 10. The differences are the friction angles of horizontal joints and other joints are 17 degrees and 45 degrees respectively. The computation of Figure 28 reaches relative maximum displacements 0.0000000 in 200 time steps. This means the block system reaches limit equilibrium after 200 time steps in a very high standard.

The failure computation of reinforced dam foundation (Figure 29) uses two dimensional DDA. Total 5000 time steps are used. The time interval was automatic chosen and controlled by maximum displacement ratio 0.001. The maximum displacement ratio is the allowed maximum step displacement divided by the half height of the whole mesh. The average time interval is 0.06 second per step. The dynamic ratio is 0.0. It means the next time step start with zero velocity.
The physical data of the arch dam of Figure 29 are shown on Table 10. The differences are the friction angles of horizontal joints and other joints are 17 degrees and 0 degrees respectively. The 0 degrees of friction angle of non-horizontal joints cause the failure.

12. Rock falling and bolt reinforcements of underground power chambers

The rock falling computation of underground chamber (Figure 30) uses two dimensional DDA. Total 3000 time steps are used. The time interval was automatic chosen and controlled by maximum displacement ratio 0.001. The maximum displacement ratio is the allowed maximum step displacement divided by the half height of the whole mesh. The dynamic ratio is 1.0. It means in the beginning of the next time step 100% of velocity is inherited from the present time step. Therefore rock falling computation is fully dynamic without damping.
The physical data of the rock mass of Figure 30 are shown on Table 11.
The rock bolting computation of underground chamber (Figure 31) uses two dimensional DDA. Total 3000 time steps are used. The time interval was not controlled by maximum displacement ratio which is 0.0005. The step time interval is 0.001 seconds. The dynamic ratio is 0.97. It means in the beginning of the next time step 97% of velocity is inherited from the present time step.
The physical data of the rock mass of Figure 31 are shown on Table 11. To obtain the forces of bolts initial stresses are entered.

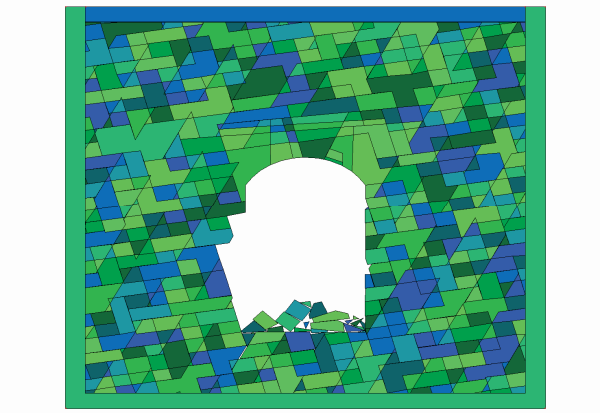

Figure 30: Rock fall computation of underground chamber by 2d DDA

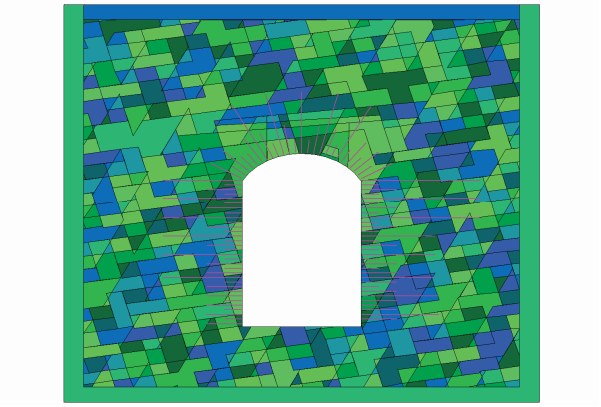

Figure 31: Rock fall and reinforcement computation of underground chamber by 2d DDA

Table 11 Physical data of underground chamber rock mass

Location	Rock Mass
Unit Wight Ton/Cubic Meter	2.7
Elastic Modulus Ton/Square Meter	3000000
Poisson's Ratio	0.25
Friction Angle Degree	20
Cohesion Ton/Square Meter	0

13. Rock falling and bolt reinforcements of tunnels

In the following, five tunnel sections are analyzed by two dimensional DDA. Each tunnel section has two cases: without bolt support and with bolt support. All five sections and ten cases are based on the same geometric data of joint sets shown by Table 12. Figure 32 to Figure 41 show the very different rock fall in the same rock and with different tunnel directions.

Table 12 Geometric data of joint sets of tunnels

Joint Set	1	2	3
Dip Angle Degree	40	70	65
Dip Direction Degree	295	105	150
Average Spacing Meter	0.75	0.45	1.5
Average Length Meter	30	7	10
Average Bridge Meter	0.1	3.0	7.5
Degree of Random 0.0–1.0	0.5	0.5	0.5

Table 13 Physical data of tunnel rock mass

Location	Rock Mass
Unit Wight Ton/Cubic Meter	2.7
Elastic Modulus Ton/Square Meter	3000000
Poisson's Ratio	0.25
Friction Angle Degree	25
Cohesion Ton/Square Meter	0

The physical data of tunnel rock mass of all ten cases (Figure 32 to Figure 41) are also the same and shown by Table 13.

All cases (Figure 32 to Figure 41) are two dimensional DDA computations. All ten cases except Figure 35 use 2000 time steps. Figure 35 uses 6000 time steps. The time interval was automatic chosen and controlled by maximum displacement ratio 0.001 for all ten cases. The maximum displacement ratio is the allowed maximum step displacement divided by the half height of the whole mesh.

Figure 32, Figure 34, Figure 36, Figure 38 and Figure 40 are rock falling cases which use dynamic ratio 1.00. It means the next time step inherent 100% of the velocity from the present time step. The maximum dynamic damage can be estimated by using this fully dynamic computation.

Figure 33, Figure 35, Figure 37, Figure 39 and Figure 41 are rock reinforcement cases which use dynamic ratio 0.98. It means the next time step inherent 98% of the velocity from the present time step. The stabilized bolt forces can be estimated by using this slight damping.

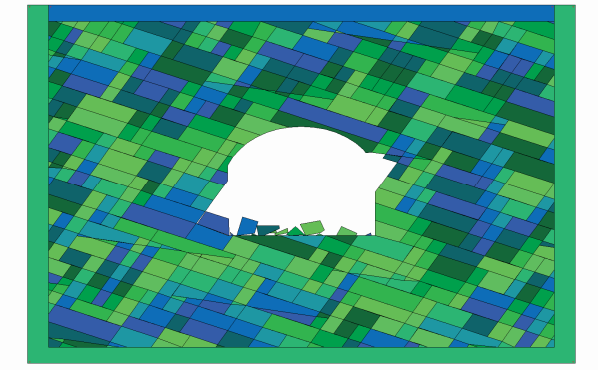

Figure 32: Rock fall computation of a tunnel with horizontal axis pointing NW 35 degrees

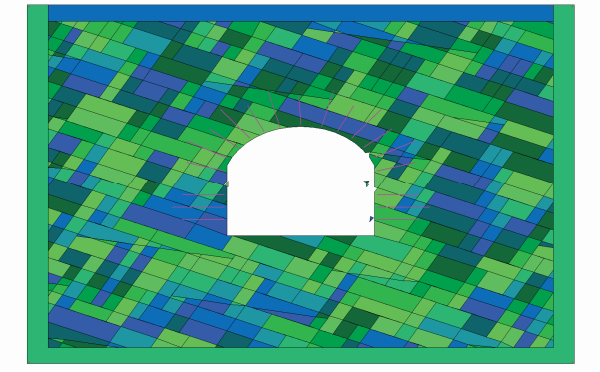

Figure 33: Rock fall and bolting computation of a tunnel with horizontal axis pointing NW 35 degrees

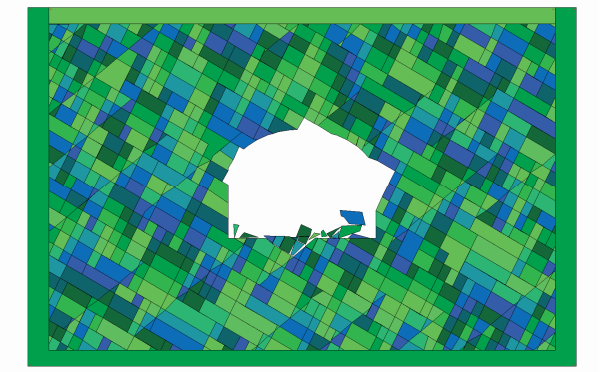

Figure 34: Rock fall computation of a tunnel with horizontal axis pointing NE 0 degrees

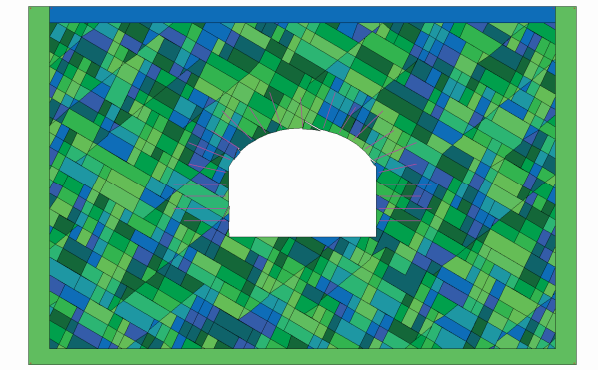

Figure 35: Rock fall and bolting computation of a tunnel with horizontal axis pointing NE 0 degrees

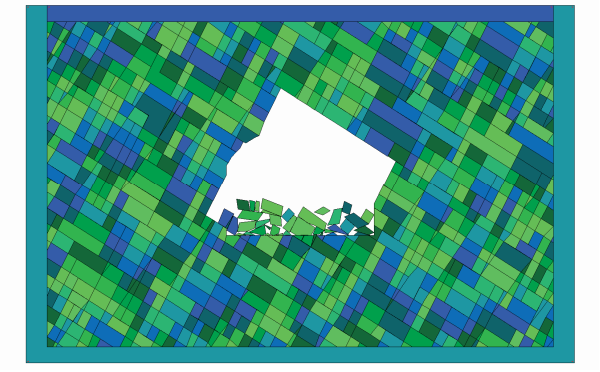

Figure 36: Rock fall computation of a tunnel with horizontal axis pointing NE 36 degrees

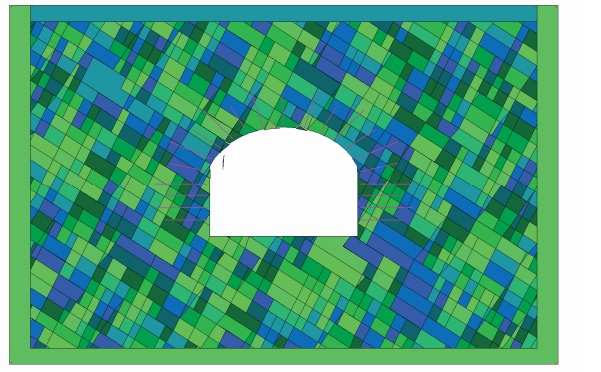

Figure 37: Rock fall and bolting computation of a tunnel with horizontal axis pointing NE 36 degrees

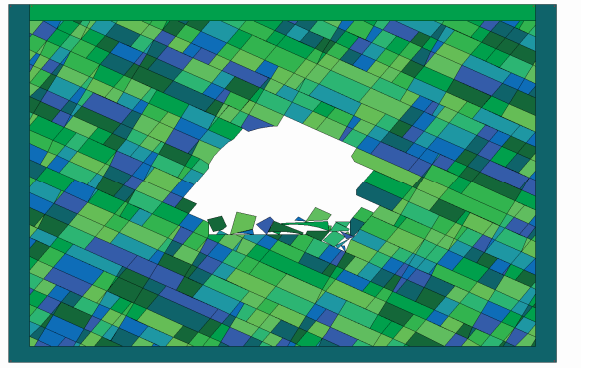

Figure 38: Rock fall computation of a tunnel with horizontal axis pointing NE 71.5 degrees

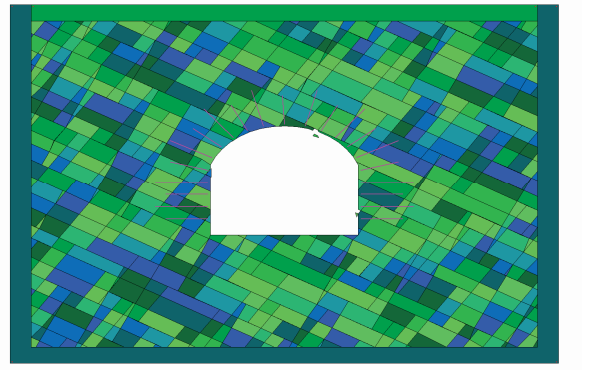

Figure 39: Rock fall and bolting computation of a tunnel with horizontal axis pointing NE 71.5 degrees

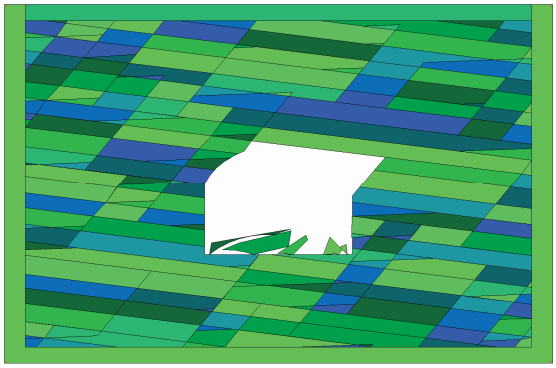

Figure 40: Rock fall computation of a tunnel with horizontal axis pointing SE 76 degrees

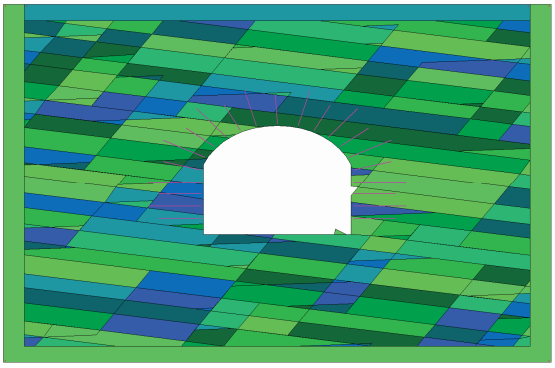

Figure 41: Rock fall and bolting computation of a tunnel with horizontal axis pointing SE 76 degrees

References

Shi, Gen-hua. Single and multiple block limit equilibrium of key block method and discontinuous deformation analysis. *Stability of Rock Structures, ICADD-5,* 3-46. Beer Sheva, Israel. 2002.

Shi, Gen-hua. Applications of discontinuous deformation analysis (DDA) and manifold method. *The Third International Conference on Analysis of Discontinuous Deformation, ICADD-3,* 3-15. Vail, Colorado. 1999.

Shi, Gen-hua. Block system modeling by discontinuous deformation analysis. *Computational Mechanics Publications,* Southampton, UK and Boston, USA. 1993.

Recent insights of analyses using discontinuous methods in rock engineering in Japan

Y. OHNISHI and S. NISHIYAMA

School of Urban & Environment Engineering, Kyoto University, Kyoto, 615-8540, JAPAN

The Japanese research group has been working on studies of discontinuous numerical analysis, such as Discontinuous Deformation Method (DDA) and Manifold method (MM). Numerous locations in Japan are potentially prone to rock slope failure and rock falls because of the commonly found precipitous terrains formed by diastrophism, most of which are weakened by alteration, as well as the frequent typhoons and earthquakes or heavy snowfalls. To deal with rock slope failure and rock falls, it is crucial to develop failure prevention methods by evaluating slope stability and predicting the failure risk, as well as minimizing damage in the event of any failure. In this paper, we introduce some applications of discontinuous numerical methods to actual engineering problems, for example, in natural disaster prevention measures.

Keywords: DDA; MM; Rock engineering; Actual engineering problem

1. Introduction

The Japanese research group tries to make database management of application examples of DDA and MM to some actual engineering problems. The reason we try to analyze actual engineering problems using DDA and MM is that these analytical methods have been proved useful for predicting the failure risk and minimizing damage in the event of any rock failure. In order to spread DDA and MM in the field of engineering, we think that it is necessary to make clear how to make analytical models and how to input the analytical parameters. In this paper, some applications of DDA and MM in landslide, rock falling and excavation of underground cavern are presented with the analytical techniques.

2. Application to landslide

Ishikawa et al. examine the applicability of DDA to numerical simulation of slope failure which occurs at fragmental rock slope in cold regions. At the fragmental volcanic soil ground in the north cold area of Japan, the degradation in strength of volcanic coarse-grained soils caused by heavy rain-fall and cyclic freeze-thaw action often makes the natural disaster such as slope failure at embankment and cut slope or landslide at a subsurface layer worse. However, the synthetic research on disaster preventive measures is behind in examining how various factors such as freeze-thaw history, rainfall, rise in ground water level at thaw season and earthquake have an influence on the mechanism of slope failure and landslide at fragmental volcanic soil ground individually. They simulate slope failure of volcanic soil ground in order to examine the effect of element mesh type and input parameters on the slope stability. Moreover, the validity of DDA simulations for simulating input parameters is examined by comparing numerical results with experimental results. The schematic section of a DDA model is shown in Fig. 1. Then, this study employs several DDA models which differ in slope angle (θ) and element mesh type. Fig.2 shows four kinds of element meshes used in this study.

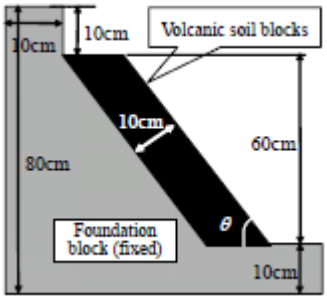

Fig.1 Simulation model of slope

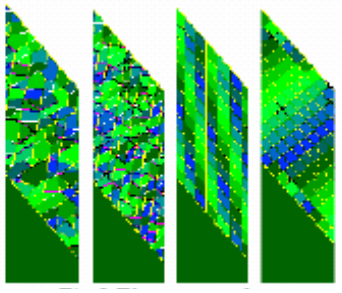

Fig.2 Outline of element mesh for simulation

Furthermore, friction angle(φ_μ) between blocks regards as a parameters ranging from 0° to 40°. Simulation results shows that slip surface can be roughly identified by displacement vectors of each DDA block, and that DDA simulation is similar in the shape and location of slope failure surface to the model test although there is

a difference in volume change of volcanic soil ground before and after slope failure as shown in Fig. 3. These results indicate the method for modeling a slope composed of crushable volcanic coarse-grained soils.

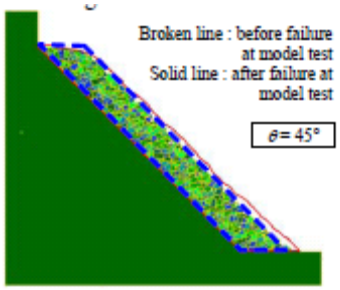

Fig.3 Result of DDA simulation and model test

Hamasaki et al. apply DDA analysis to examination of the factors which cause a landslide in the natural dam. When a landslide situated on a valley side slope slides downward, the valley is filled up with the debris. As a result, the lake which is created by the natural dam appears in the upper area of the dam. If the natural dam collapses, a debris flow occurs in the downstream and damages the downstream area. Therefore, the countermeasure to the landslide along a river is very important in order to maintain a river system. Numerical analysis about the activity conditions of the landslide is significant to draw up the plan of the countermeasure to the landslide. On the analysis, the landslide block was divided using Voronoi-diagram, because the analyzed landslide block consists of the disordered blocks of rock. As the parameters which the landslide begins to slide and the top of the landslide debris reaches to the road height (ca. 15 m height) on the opposite shore, it became clear that the cohesion of the landslide block is 5 kpa or less and the internal friction angle is 15 degrees or less shown in Fig. 4.

Dong & Osada also try to simulate landslide problems. When sliding occurs, frictional resistance falls from static friction coefficient, μ_s to a lower dynamic friction coefficient, μ_d. The magnitude of this effect depends on the displacement and velocity of displacement. The current DDA program detects the sliding condition at the contact edge by the Mohr-Coulomb criteria, but the coefficient of friction is treated as a constant value. DDA controls the calculation by time steps, and according to the shear displacement as well as velocity after each time of the open-close calculation, the coefficient of friction can be updated. They examine the validation of DDA program by verifying the displacement of a block induced by a sinusoidal motion.

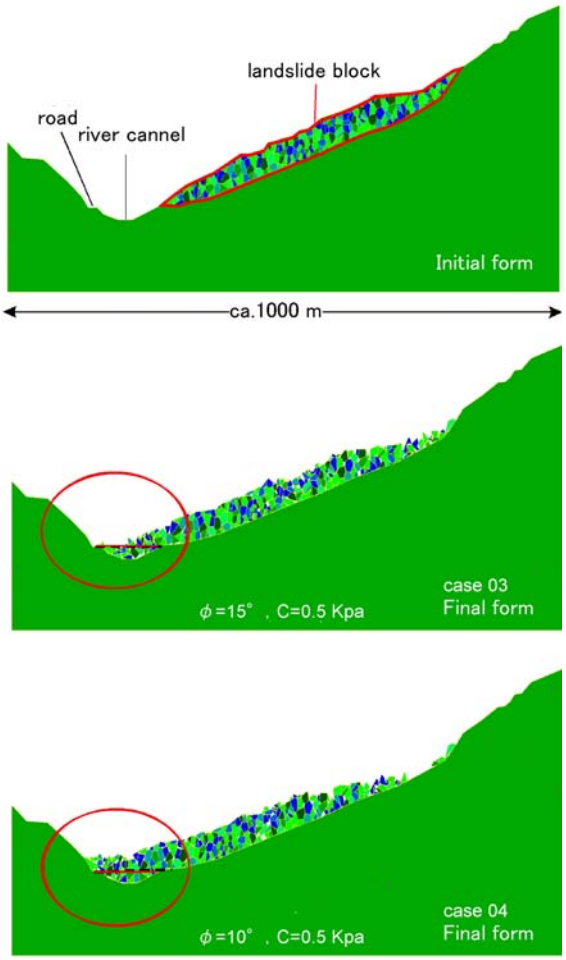

Fig.4 Result of DDA simulation using Voronoi-diagram

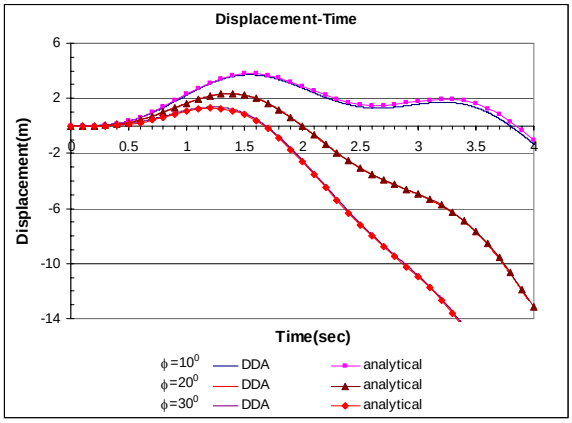

Fig.5a Displacement of block with changing of friction when amplitude of acceleration a_0 =9.81 m, f = 0.5 Hz, friction

An agreement between DDA program and analytical solution with changing in friction and frequencies of motion ensures the confidence of DDA program shown

in Fig.5a and 5b. The next step, as a simple case, a drop of static friction to the dynamic friction at the initial slip stage (at the surface contact) was assumed shown in Fig.6. The displacement of a block is accumulated after each step and this result causes the difference as an increase of time. The above analysis shows that the effect of dynamic friction is significantly influenced in case that displacement is large. This weakening of sliding resistance may, depending on the stiffness of the system, result in a dynamic instability, and the friction-displacement behaviour. Research on dynamic friction will implement in DDA and a possible approach to this effect is the constitutive friction laws of dynamics friction, in which provides a connection between friction and velocity, time dependence.

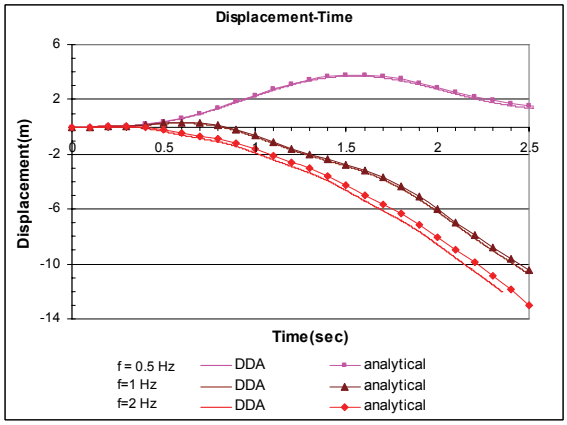

Fig.5b Effect of frequencies with a_0 =9.81 m, $\Phi=10^0$

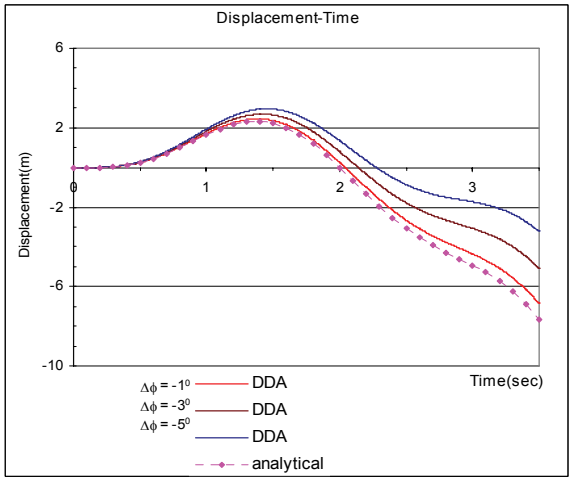

Fig.6 The displacement of overlaying block with changing into dynamic friction when a_0 = 9.81 m, f = 0.5 Hz, Φ_s =20^0.

Ma et al. try to foresee collapse of rock slope by DDA simulation. They use the actual data which was the representative case of our field monitoring studies, 13 sites in Japan. Fig.7 shows the actual rock slope which can be approximated with 4 jointed blocks, the fixed blocks (B and D), a large block (A3) and a small block (C) at the foot of A3. To investigate the physical parameters of the rock mass and joints, several samples were obtained from the field. In the laboratory, uniaxial compression tests, Brazilian tests, and direct shear tests with the natural joints were conducted to study the uniaxial compression and tensile strength of the rock mass, and the cohesion and frictional angle of the joints. Fig.8 shows the modeling of jointed rock mass by DDA. In this Figure, (a) was the side view of jointed rock mass before collapse, (b) was the Sketch, (c) was the numerical model by DDA. Fig.9 shows the image of actual collapse and the result calculated by DDA.

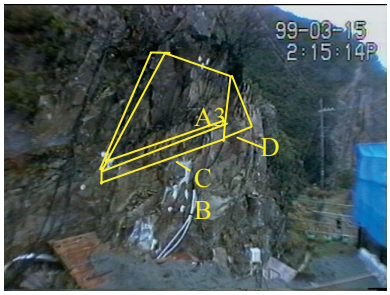

Fig.7 Rock slope that consists of 4 jointed blocks

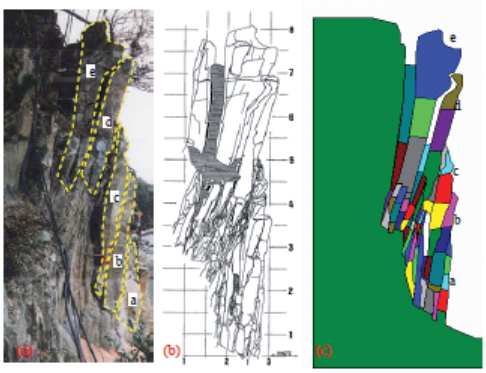

Fig.8 Simulation model for DDA analysis

Fig.9 Simulation results of rock slope failure

3. Application to rock falling

Hagiwara et al. applied a force of viscosity to the effect of vegetation on a falling rock. In the DDA method, a simulating object is considered to be a set of polygonal elements, and the motions of the elements are expressed as follows based on the principle of minimized potential energy.

$$M\ddot{u} + C\dot{u} + Ku = F \quad (1)$$

$$C = \eta M \quad (2)$$

where M is mass matrix; C is attenuation matrix; K is stiffness matrix; F is force matrix; $\ddot{u}$ is acceleration matrix; $\dot{u}$ is velocity matrix; u is displacement matrix; and η is coefficient matrix of the viscosity at the element center. In Eq. (1), linear and rotational motions are considered, and a spring based on a penalty method is assumed between elements in contact. The force of viscosity represents the resistance force operating in aerial positions and is proportional to the velocity of the elements. Fig.10 shows the trajectory sketch of a real rockfall at a plan view and a cross section along the trajectory. The rockfall incident occurred after an earthquake, and the rock stopped as it crashed against a house. The trajectory was surveyed two days after the incident by tracing contact marks on the slope surface and trees.

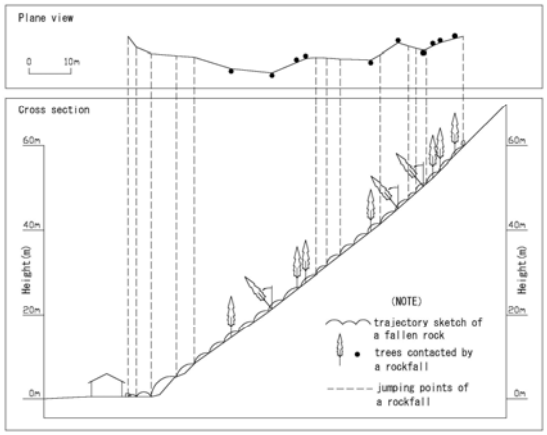

Fig.10 Trajectory sketch of a fallen rock based on the field survey

Fig. 11 shows the geometries of simulating object with some trajectory examples from the simulation. In order to examine the calculation technique, the rockfall behavior during the incident was simulated while varying the viscosity coefficient in Eq. (2). In the simulation, the physical and geomechanical properties of the objects were determined from their field characteristics in consideration of experimental data. The energy ratio in bouncing, which is defined as the energy ratio between ejection and injection in a bouncing phase, was determined from the experimental data. The object of simulation consisted of two elements, with their geometries determined from the field data. The viscosity coefficient was varied from 0.0 to 0.2, and the rotational position of the falling rock at the initial point was varied in ten ways in each case to investigate the sensitivity of calculation to the geometry. In the simulation results, the modes of rockfall motions consisted of rolling and bouncing in agreement with the field data related to the incident. Differences in the trajectory forms, such as the maximum height of bouncing, were not distinct throughout all cases, but the kinetic energy of the falling rock varied in proportion to the viscosity. Fig.12 shows the kinetic energy in each case at the lower edge of the slope. When the viscosity coefficient is low, the kinetic energy tends to be high and widely scattered. Although the rotational behavior in the rockfall incident is unknown, the kinetic energy of the rockfall at the bottom is estimated to be 141 to 281kNm on the assumption that the mass is 2371kg and the ratio of the rotation energy to the linear-motion energy is 10%. When the viscosity coefficient is 0.1, the result of the simulation agrees well with the rockfall behavior estimated from the field data shown in Fig.12.

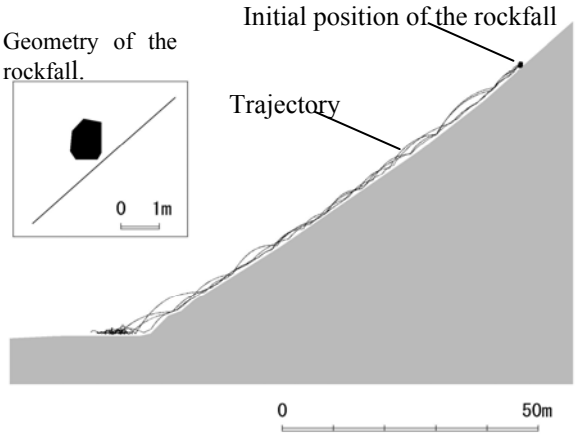

Fig.11 Some trajectory examples from the simulation.

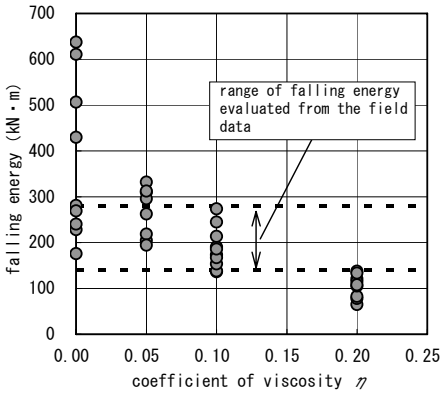

Fig.12. Kinetic energies at the lower edge of the slope from the rockfall simulations.

Shimauchi et al. investigated characteristics of input parameters through the observations of the motion of rockfall and to verify the input parameters by DDA in comparison with the observations. The motion of rockfall at bounce is shown in schematic diagram as Fig. 13. In this figure, velocity energy ratio (γ), normal and tangential restitution coefficient (Rn, Rt, respectively) are defined.

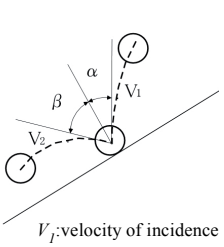

Velocity energy ratio: γ

$$\gamma = \frac{1/2\, mV_2^2}{1/2\, mV_1^2} = \frac{V_2^2}{V_1^2}$$

Normal restitution coefficient: Rn

$$Rn = \frac{V_2 \cos\beta}{V_1 \cos\alpha}$$

V_1:velocity of incidence
V_2:velocity of reflection
α :angle of incidence
β :angle of reflection

Tangential restitution coefficient: Rt

$$Rt = \frac{V_2 \sin\beta}{V_1 \sin\alpha}$$

Fig.13. Properties of bouncing motion

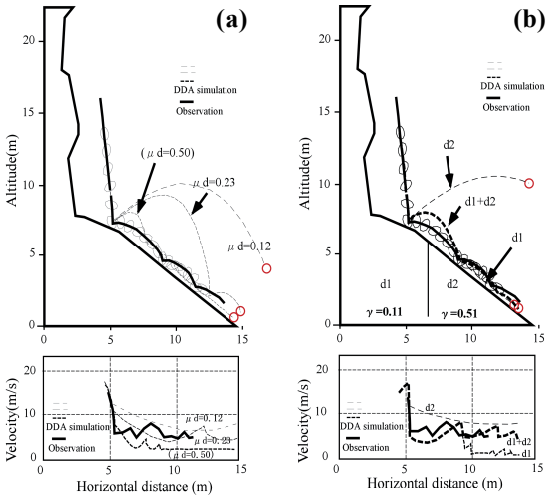

Fig.14 Examples of rockfall simulation by DDA
(a) velocity energy ratio (b) viscosity coefficient

Fig.14 shows that if numerical slope model has a significant change of gradient on center of slope around, rockfall simulation by DDA is inconsistent with the observations by means of the viscosity coefficient and velocity energy ratio obtained from the assumption of a constant gradient of model slope. It is thus necessary to apply to calculations of DDA for their coefficients considering impact angle. In conclusion, this provides a useful method to decide the design work with slope cut. In the near future, if it is to consider the influence of the rockfall in size, the velocity of incidence and the shape of rockfall, the rockfall simulation by DDA is carried out with accuracy.

4. Application to dynamic loading

Friction along the interface between the blocks is modeled according to the Mohr-Coulomb failure criterion. In DDA the kinematic equations are based on Hamilton's principle expressed by:

$$M\ddot{u} + C\dot{u} + Ku = F \qquad (3)$$

where, M : mass matrix, C : viscosity matrix, K : stiffness matrix, F : external force vector, u : displacement, $\dot{u}$: velocity, and $\ddot{u}$: acceleration of the centroid of a block. The kinematic equation (3) is solved by Newmark's β method and the equation for the increase of displacement is solved each time increment by the following three equations:

$$\tilde{K} \cdot \Delta u = \tilde{F}, \tilde{K} = \frac{2}{\Delta t^2} M + \frac{2\eta}{\Delta t} + K_e + K_f,$$
$$\tilde{F} = \frac{2}{\Delta t} M\dot{u} + (\Delta F - f) \qquad (4)$$

where, Δt : time increment, Δu : incremental displacement, K_e : elastic matrix, K_f : displacement constraint and contact matrix and so on, f : initial stress vector, ΔF : body force and point road vector, *etc*. Vibration is expressed by inputting the displacement time history to displacement constraint point as forced displacement.

Akao et al. examine the applicability of DDA to vibration analysis and its characteristics by simulating vibration response of the laminated blocks in the shaking table tests. Fig.15 shows the behavior of blocks at 5Hz-700gal vibration, the horizontal displacement of blocks gradually increased with sliding and rotation (locking).

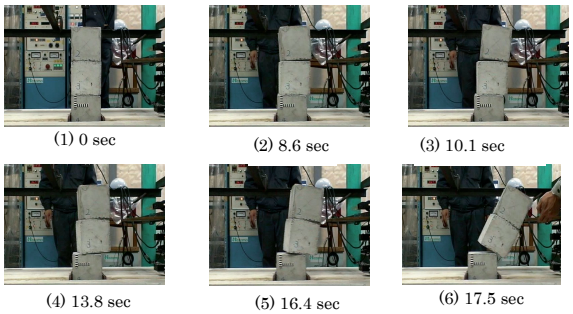

Fig.15 Behaviors of blocks on shaking table

They report that the error between DDA results and analytical solution of displacement of the block is very large and frictional force doesn't work appropriately, if contact spring stiffness is larger than hundredth of the Young's modulus of the blocks (kn=2*10^5, 2*10^6, 2*10^{7}kN/m^2). On the contrary, if contact spring stiffness is lower than thousandth part of the Young's modulus (kn=2*10^3, 2*10^{4}kN/m^2), the error is small. And when contact spring stiffness is equal to shear spring stiffness (kn/ks=1), DDA results and analytical solution are approximately the same value. Generally it is suggested that contact springs have stiffness larger than the Young's Modulus of rock masses. However, applying DDA to vibration analysis, soft springs is needed to be applied so as to make contact force (mainly frictional force) work accurately. By using soft springs whose stiffness was lower than thousandth part of the Young's Modulus of blocks, DDA can simulate well vibration response of the blocks in the experiments shown in Fig 16.

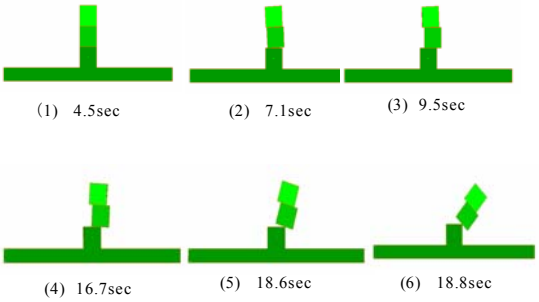

Fig.16 Simulation results of behaviors of blocks shown in Fig.15

Sasaki et al. introduce the potential energy of the penetration between blocks considering contact viscous damping into DDA shown in Figure 17. The governing equation of the potential energy Π^{sys} for large deformations of continuous and discontinuous elastic bodies:

$$\Pi^{sys} = \sum_{i=1}^{n} \Pi^{(block)i} = \sum_{i=1}^{n} \left(\Pi^{i} + \sum_{j=1}^{m} \Pi_{PL}^{ij} \right) \qquad (5)$$

The first term on the right side of Eq. (1) is the potential energy of the continuum part, and the second term is the potential energy of the contact between blocks. They try to obtain the relations between the natural frequencies of elastic block structures and applied harmonic accelerations to prepare for the shaking table experiments under the centrifugal force of complex block structures. In ordered to obtain the influence of collisions between the horizontal direction's blocks, they studied five layered staggered model in Fig.18. An input acceleration is 2Hz sinusoidal wave and Fig.19 shows the acceleration response of the base, the middle and the top block.

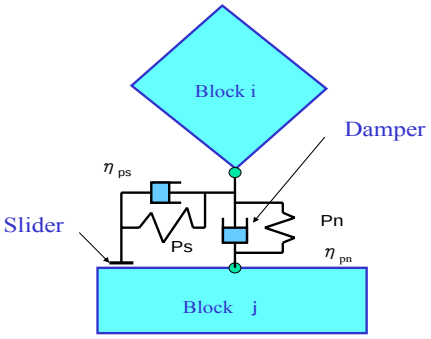

$$\Pi_{p\eta} = f_t d = \frac{1}{2}(p + \frac{\eta_p}{\Delta t}) d^2$$

Fig.17 Viscose damping on contact system in DDA simulation

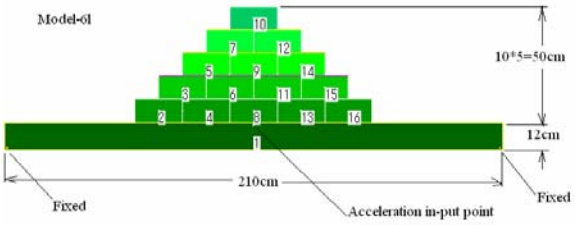

Fig.18 Simulation model

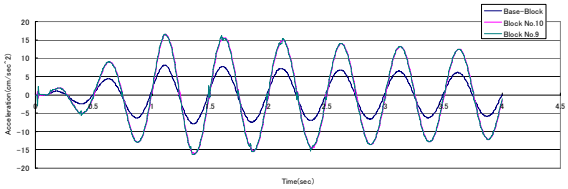

Fig.19 Acceleration response of the base, the middle and the top block.

In order to avoid a letter of stitch at the change points of accelerations directions, acceleration responses are calculated by differentiate velocities directly. Fig.20 shows velocities and displacements response of the base, the middle and the top blocks. The amplification ratios are same tendencies of the case of accelerations and there are no influences of collisions by side blocks. The influence of the collisions of the side blocks are appeared of a letter of stitch. The amplification ratios are same tendencies of the case of accelerations and there are no influences of collisions by the side blocks.

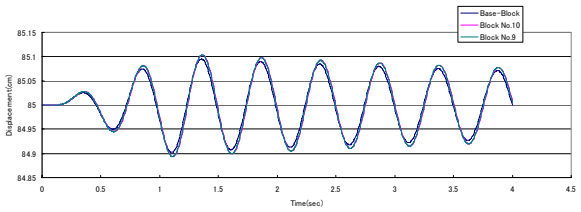

Fig.20 Displacements response of the base, the middle and the top blocks.

Fig.21 shows shaking table experiments of piled twenty layers and forty columns. Fig.22 shows acceleration of actuator input at base block. The acceleration was applied 60Hz and 30gal at first step, 80gal at second step, 100gal at third step, 200gal at forth step and 300gal at fifth step. Fig.23 shows acceleration of actuator input at base block. In this case, the base block amplification of acceleration ratio is about thirteen times of the input acceleration. Fig. 24 shows the acceleration of point No.6 as seven layers from the base block. The rate of amplitude is decreases 1/15 of base block. Fig. 25 shows the acceleration response of point No.8. The shape of acceleration mode of the base block is disappeared and the most response of accelerations is caused by collisions between blocks as pulse shapes.

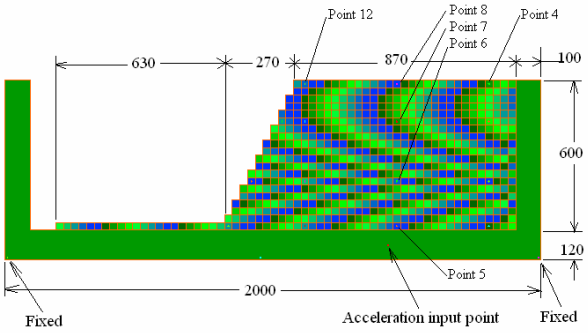

Fig.21 Shaking table experiments model

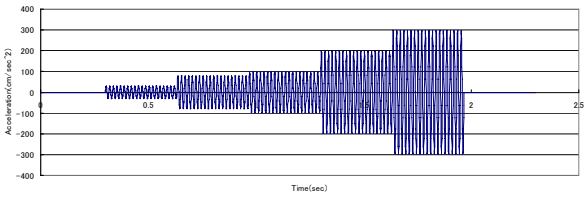

Fig.22 Acceleration of input point

The collisions by contacts between blocks are influenced multi columned model in the response of accelerations extremely. The unnatural stitch accelerations are occurred by collision between blocks of the multi columned models of accelerations response in small time intervals. This phenomenon can be improved to determine differentiate displacement results directly by controls time interval.

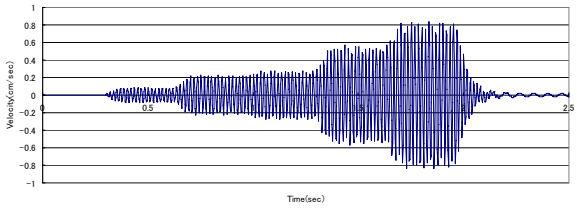

Fig.23 Acceleration response of the base block

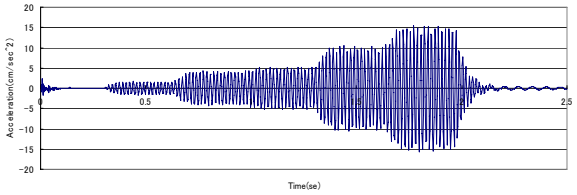

Fig.24 Acceleration response of point No. 6

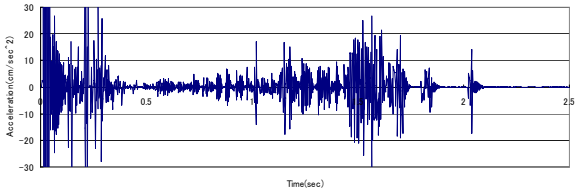

Fig.25 Acceleration response of point No. 8

5. Application to excavation of underground excavation

Miki et al. report that the MM is fitted for practical use, and the MM will enable geotechnical engineers to perform a step-by-step analysis along the construction processes. Fig.26 shows a concept of the excavation in MM simulation. The excavation areas are bounded by the joints, and the excavation areas are modeled as a block in advance. After the excavation, excavated blocks can move independently of mother block, and excavated surfaces act as free surfaces. Hence, contacts and separations between mother block and another block are enabled again. Fig.27 shows the underground cavern model with 4 joints and 1 material boundary. The model geometry was a square 300m long and wide, and the dimensions of the cavern, which was located at a center of the model, were 50m long and 40m wide. In the model, lateral displacements of both sides were constrained, and lateral and longitudinal displacements were constrained along the bottom line. The excavation area was bounded by the joint. The elastic-plastic constitutive law based on Drucker-Prager's yield criteria for an element. In the analysis, the calculation was processed by two stages. Fig.28 shows stress distribution and displacements around the cavern. The plastic regions appeared along the left and right walls, and at the crown. From the right wall to the crown, remarkable displacements were calculated. It was

considered that the plastic regions and larger displacements along right wall were closely related to the existence of the two joints. These results agree with the physical phenomenon in rock masses.

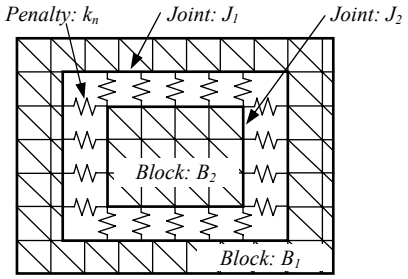

(a) Before excavation

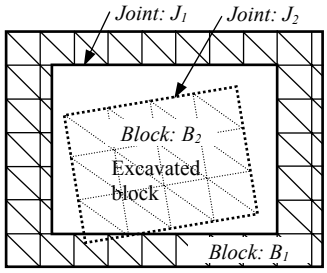

(b) After excavation

Fig.26 Concept of the excavation in MM analysis

They conclude that the material boundary is formulated as a boundary between the elements, which share common cover mesh and the excavation is realized by releasing the contacts between surrounding area and excavation area which area bounded by joints.

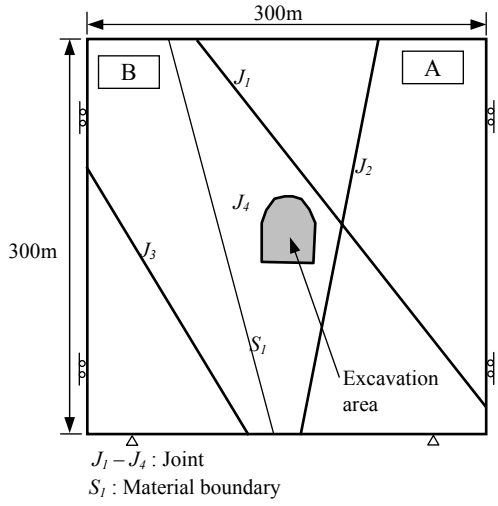

Fig.27 Underground cavern model

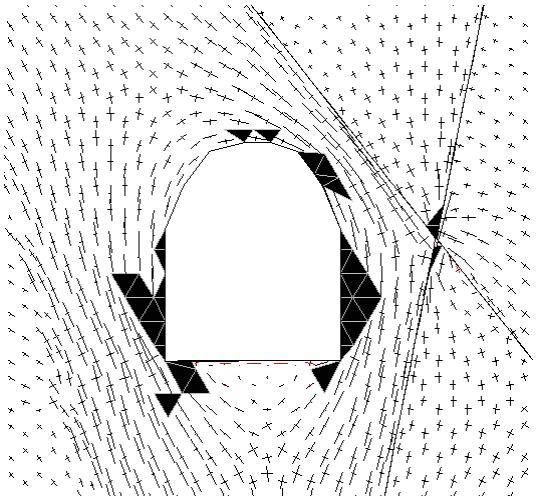

(a) Stress distribution and plastic regions after excavation

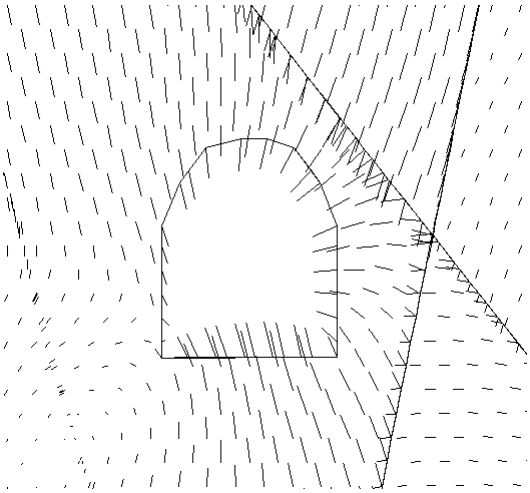

(b) Displacement vectors of the nodes after excavation (multiplied by 200)

Fig. 28 Stresses and displacements around the cavern

6. Discussion & Conclusions

Some results of studies on the DDA and MM method in Japan are shown in this paper. We introduce the aim from now on in term of the application of DDA and MM to actual engineering problems in this section.

Discontinuous analytical methods can handle and compute the contact forces when blocks contact each other. In DDA and MM method, some specific parameters, such as “reference length”, “displacement allowed ratio”, “maximum time increment”, and “stiffness of normal contact spring” and so on are employed to consider the convergence speed for each time step and the good performance of contact behaviors simultaneously. It is difficult to obtain the unknown specific parameters in the in-situ problems. The problems with lots of blocks and complicated contacts can be very sensitive to these parameters and

parameter selected badly can cause poor computation results. Our studies will focus on explaining the meaning of these parameters and discussing the setting of these parameters and we will make a database of these specific parameters in order to apply them to actual rock engineering problems. We discuss some important parameters that remains unsolved.

If the deformation process is slow enough, the effect of inertia forces can be neglected. We then have a static problem, which demands the solution of a simultaneous equation system. DDA is made to analyze quasi-static problems by using the so-called dynamic relaxation method. DDA introduces the damping effects to the analysis by discounting block velocities for each time step. Mathematically it can be shown as the following equation:

$$V_i^{(n+1)} = k01 \cdot V_f^{(n)}$$

Where, "$V_i^{(n+1)}$" is the initial velocity at time step n+1. "k01" is the type of Analysis parameter, and "$V_f^{(n)}$" indicates the final velocity at time step n. In the dynamic analysis, the initial velocities of blocks at time step n+1 accede from the final velocities of step n. In DDA, a value of 1 is entered to k01 for a full dynamic analysis and a value of 0 for static analysis. The value corresponds to different degrees of damping or energy dissipation. Some researchers introduced 0.8 as a k01 value to get better results for dynamic analysis.
We think it is necessary to get lots of examples in dynamic loading problems.

Next, the contact computations are very important but difficult in discontinuous analysis although they can be represented by inequality formula in mathematics. The contact forces should be considered when two blocks get close and contact each other, but the contact forces should be deleted when blocks separate. To explain the contacts, the vertex of Block 1 and the edge of Block 2 that make a contact pair can be simplified as point and edge showed in Fig.29. The circle presents the vertex of Block 1. The hollow circle indicates that the contact pair is separating to each other. Hence, no real contact happens to the contact pair, and this situation is called "Open". However, solid circle has opposite physical meaning and is named "Close".

Line (1) is the boundary of Close to Open which means the real contact occurs at the beginning of time step n, but judged as "Open" at the end of time step n. Line (2) is the boundary of the Block 2. Line (3) shows the boundary of Open to Close, which means judging no contact (Open) at the beginning of time step n and contact (Close) at end of time step n. Line (4) is the boundary of the deepest contact can occur to the edge. If the vertex locates deeper than Line (4), the contact happens at another edge. When the vertex of Block 1 gets close to the edge of Block 2 (Line 2) with "Open" at the beginning of time step n, the judgment can be "Close" if the vertex penetrates Line (3) at the end of time step n shown in Case 1 and Case 2 as Open-Close. However, if the vertex still locates above Line (3) at the end of time step n, the judgment can be Open-Open shown in Case 5-7. If it is "Close" at the beginning of time step n, and the vertex moves above Line (1) at the end of time step n, the Close-Open judgments are made as Case 3 and Case 4. However, if the vertex still locates below Line (1) at the end of time step n, the Close-Close judgments shown in Case 8-10 is made. To solve contact problems with accurate contact forces and fast convergence, some contact related parameters are necessary in the computations used in DDA that are Reference Length**,** Displacement Allowed Ratio, Maximum Time Increment and Stiffness of Contact Spring. The stiffness of the contact spring is most important parameter that is usually unknown when solving many problems because we use open-close criteria as the judgment of contact between two blocks.

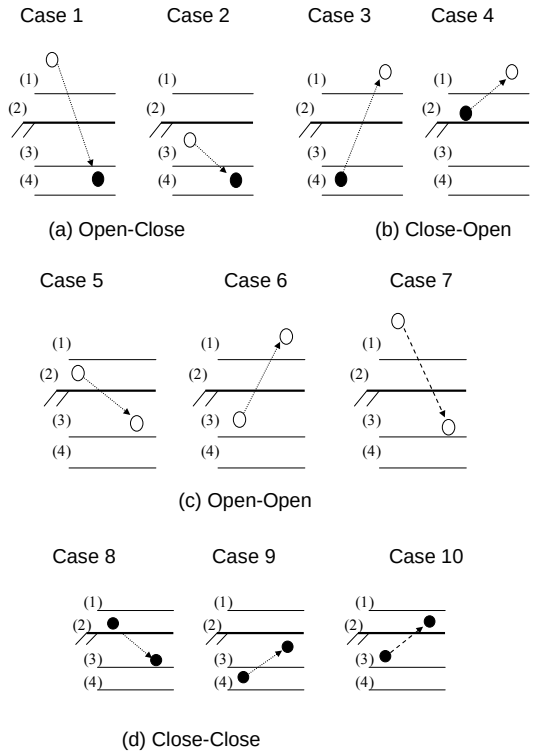

Fig. 29 Open-Close criteria

The stiffness of a contact spring increases the influence of the contact forces in the block system. Too large contact forces can be generated by stiff spring. It needs more open-close iterations to find the proper contact spring arrangements in block system and makes the computations hard to converge. In this case, the softer normal contact spring has to be applied to the computations. On the contrary, soft contact spring can not generate enough contact forces to separate contact pairs, and the large penetration distances can happen.
Moreover, it is necessary to consider the open-close criteria with the contact spring. The gaps between Line

(2)- Line (1), and Line (2)- Line (3) are criteria of opening and open-close shown in Fig.29. The gap between Line (1) and Line (3) relates to the convergence speed of contact computations. With the larger gap between Line (1) and Line (3), the computations can satisfy the criterion of no-penetration, no-tension easily. However, the tensile forces are generated when the vertex locates between Line (1) and Line (2). In addition, if the gap between Line (2) and Line (3) is large with a stiff contact spring, the contact forces can be too large and can cause unreal contact behaviors. The influence is obvious to the small blocks compared to the span of the analysis problem.

To solve this problem, the stiffer normal contact spring should be introduced to avoid the penetration with too large value. About the selection of normal contact stiffness, the value is generally selected up to 10 to 1000 times of block Young's modulus in order to guarantee the very small penetration distances among blocks compare to the deformations of blocks. Chen & Ohnishi proposed the following equation to estimate normal contact stiffness.

$$k_n = \alpha E$$

where, α is the coefficient of contact distance. E is the Young's Modulus of the block. When the shear force is smaller than the shear strength of a discontinuity, a shear contact spring is added to prevent relative displacements along the displacement. Chen & Ohnishi proposed the following equation to estimate shear spring stiffness.

$$k_s = \alpha G$$

where, α is the coefficient of contact distance. G is the shear modulus.

$$G = \frac{E}{2(1+\upsilon)}$$

Wu et al. proposed the normal contact stiffness is determined by the Young's Modulus of the block and the coefficient of penetration. The upper limit of the normal contact spring stiffness is considered as the Young's Modulus of the block. The shear spring stiffness is determined with the same coefficient of penetration used for the normal contact spring.

We introduce the study of Wu et al. as a good example about specific parameters. They study the stress distributions of discrete blocks in a box. Fig.30 shows simulation geometric model. The stress of each block comes only from the overburden. The physical parameters used in the simulations are shown in Table 1. The proper contact spring stiffness is studied to obtain correct stress distributions. In this case, external forces come from the overburden and contacts among blocks. The vertical stress changes of block 32 and 83 at each time step are used as an index to check proper contact spring stiffness for the analysis. Fig. 31 presents the results with contact spring stiffness up to 2 times of block Young's modulus. From the results, we discuss the choice of contact spring stiffness in DDA.

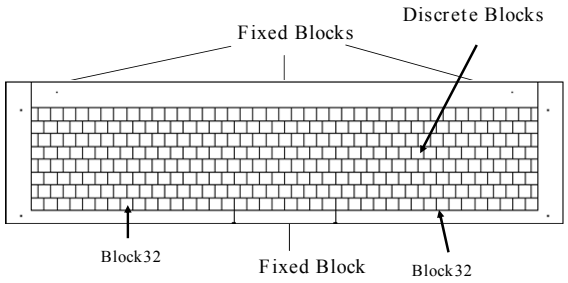

Fig. 30 Geometric models for discrete blocks

Table 1. Parameters for the DDA

Item		Value
DDA Analysis Parameters	Displacement Allowed Ratio	0.01
	Maximum Time Increment (sec)	0.001
Blocks	Unit Weight (kN/m^3)	26.4
	Poisson's Ratio	0.2
	Young's Modulus (MPa)	62
Discontinuity	Frictional Angle (°)	20.0
	Cohesion (MPa)	0.0
	Tensile Strength (MPa)	0.0

In the results, blocks' vertical stresses vibrate between 50 to –160 kPa ("-" indicates compression stress). The vibration does not converge even after 500 time steps. According to the analytical solutions, the vertical stresses of block 32 and 83 are -5kPa, however, DDA simulation results can be up to -160 kPa. It is considered that exceeding contact forces are generated in the analysis to cause high block stress. The vibrations of blocks during computations are considered as the effects of gravity turn-on. The sudden turn-on of gravity at the beginning of the first time step produces displacements due to elastic deformation of the blocks and "seating" of the contacts. Although these displacements are very small, they lead to propagation of initial block velocities and accelerations and affect the generations of initial stress distributions. The static analysis is introduced before 100 time steps. The analysis returns to full dynamic one after 100 time steps. With this method, it is considered that the vibrations of stresses in the blocks can be neglected. Fig. 32 shows the efficiency of static analysis within 100 time steps. However, the stresses of blocks still vibrate after 100 time steps although the value is smaller than Fig.31.

Fig.33 shows the DDA results by using the static analysis, k01=0. The results show that although the stress vibration is diminished, the precise stress distribution can be also obtained hardly with stiff contact spring.

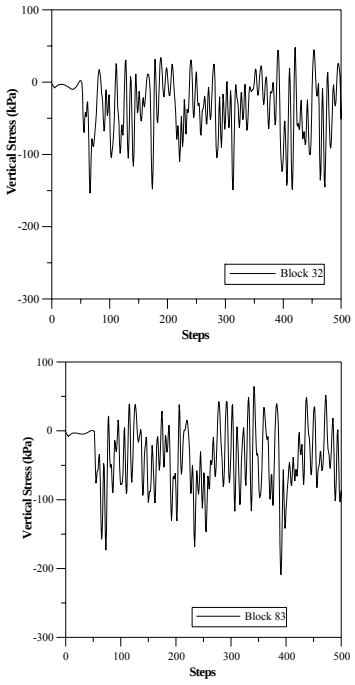

Fig. 31 Simulation results with high contact spring stiffness

To obtain the stable stress distributions of the discrete blocks, it is necessary to investigate the reason to cause stress vibrations during calculations. It is found that the discrete block is relative small compared to the span of the model. The contact computations and the model span are related. Fig.34 illustrates the reason to cause the stress vibrations shown in Fig.31. Supposing the locations of Block 1, Block 2, and Block 3 are shown in Fig. 34(a). Block 2 and Block 3 are fixed. Block 1 with weight "w" moves downward due to the gravity. When Block 1 penetrates an edge of Block 2 but locates above the boundary of open to close, Line $3_{(2)}$. The symbol "(2)" means Block 2. It is still considered as "Open". No contact spring is added to the computations, and Block 1 moves downward continuously as shown in Fig. 34(b). When Block 1 penetrates Line $3_{(2)}$ presented in Fig. 34(c), the normal contact springs with length "d" are employed to generate contact forces, fc, upward. When the gap between Line $(2)_{(2)}$ and Line $(3)_{(2)}$ is large and the contact spring is stiff, the contact forces between Block 1 and Block 2 can be very large. The contact forces are larger than the weight of discrete block and drive it moving upward if Block 1 is small or light. When the vertex moves upward to the position between Line $(1)_{(2)}$ and Line $(2)_{(2)}$, the tension can be produced to Block 1 shown in Fig. 34(d). After Bock 1 moves above Line $(1)_{(2)}$, the contact is judged as "Open", and the contact spring is deleted. When Block 1 moves upward continuously and hits Block 3. The contact sequence mentioned above repeats that causes the block stresses vibrate as shown in Fig. 31 and Fig.32.

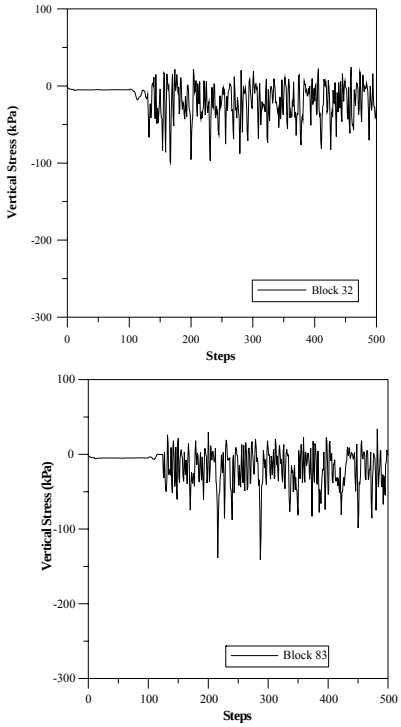

Fig. 32 Simulation results with diminishing gravity turn-On effects

To diminish exceeding contact forces and unwanted stress vibrations, lower contact spring stiffness, 620 kN/m (about 1/100 of block Young's modulus) is introduced. With softer contact spring, Block 1 does not rebound after it contact to Block 2. Fig. 35 presents that block stresses converge to a constant in the analysis, however, some unwanted vibrations are still observed. To neglect the effects of unwanted vibrations and make it converge faster, the damping effect is introduced to the analysis. The damping can be achieved by the analysis type index, k01, as 0.99. With these new parameters, the stresses tend to converge to -5 kPa(Fig.36), which is the analytical solution for these blocks within 200 time steps. Fig. 37 illustrates the stresses change accompany to depth calculated by DDA, and the analytical solutions. The results present that DDA simulation results have good agreement to analytical solutions by introducing appropriate contact spring stiffness and damping to the analysis.

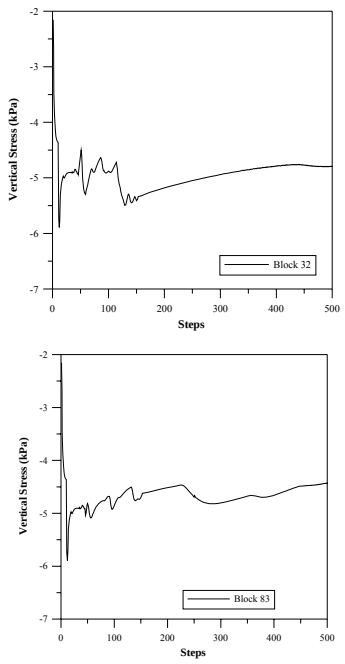

Fig. 33 Simulation results with static analysis

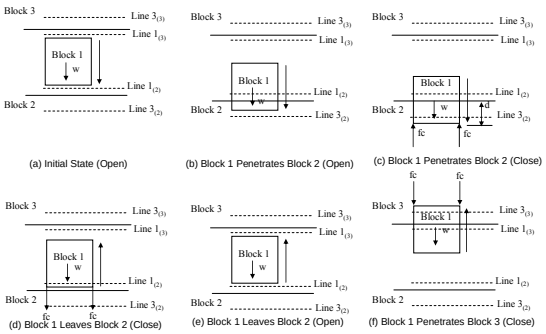

Fig. 34 The reason to cause stress vibration

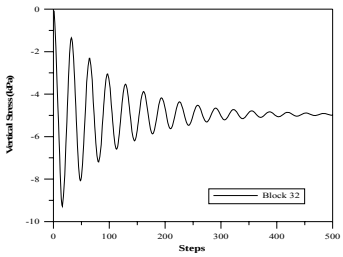

Fig. 35 Simulation results with lower contact spring stiffness

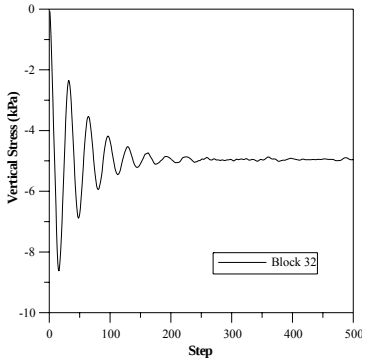

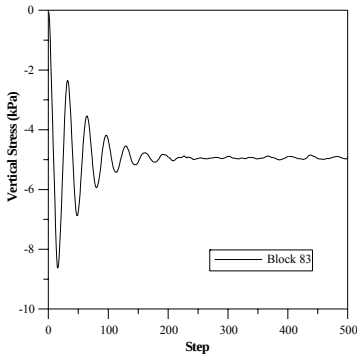

Fig. 36 Simulation results with lower contact spring stiffness and damping

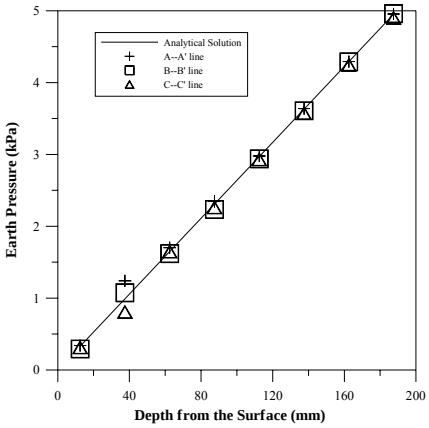

Fig. 37 Illustration of Earth Pressures Change with the Depth

References

This paper refers to the following papers.

- Proceedings of the ISRM International Symposium 3rd ARMS edited by Ohnishi & Aoki, Special Session "Numerical Analysis of Discontinuous Rock Masses",2004.
- Proceedings of the eighth International Conference on the Analysis of Discontinuous Deformation
- Wu Jian-Hong, Doctor Dissertation, "Numerical Analysis of Discontinuous Rock Masses using Discontinuous Deformation Analysis", Kyoto University,2003.

Validation for rock block stability kinematics and its application to rock slope stability evaluation using discontinuous deformation analysis

AIQING WU, XIULI DING, BO LU, QIHUA ZHANG

Yangtze River Scientific Research Institute, Wuhan, 430010, P.R. China

This paper firstly introduces the process in calculation of the contact forces between blocks, and presents a method about the safety factor calculation in DDA. Based on this, the stability validation with a rock block sliding along a double incline has been carried out. Two cases, one with the friction angle (ϕ), and the other with the friction angle (ϕ) and cohesion (C) together, are considered. At last, as an engineering application example, DDA method has been used to analyze the stability of a slope with a weak fault controlled in one hytro-project, and it has been shown that as the contact force calculation in DDA method is based on the rigorous equilibrium equations, DDA method may provides a more reasonable method for stability analysis in rock engineering.

Keywords: DDA; Validation for rock block stability; Rock slope; Stability analysis

1. Introduction

DDA method incorporates dynamics, kinematics, and elastic deformability of the rock in the equilibrium equations of block system. The equilibrium equation is based on minimization of potential energy and uses a penalty method to prevent penetration of blocks. When the geometric contact converges are achieved in total block system, the normal and shear contact forces can be calculated according to the deformation of springs acting at each contact positions. The precision of the contact forces is perhaps the most concern issue for DDA researchers. If it is true, DDA method can be used not only to simulate failure mechanism of block system, but also to evaluate the stability status of rock mass with great precision. Several researchers have studied the kinematical problem about a rock block sliding along one or double incline with given friction angle. The results show quite good agreement of DDA and the theoretical analysis. As in most cases, the parameter cohesion (C) should be considered in stability analysis. The validation of block stability considering simultaneously the friction angle (ϕ) and cohesion (C) is much more challenging.

This paper firstly introduces the process in calculation of the contact forces between blocks, and presents a method about the safety factor calculation in DDA. Based on this, the stability validation with a rock block sliding along one incline has been carried out. Two cases, one with the friction angle (ϕ), and the other with the friction angle (ϕ) and cohesion (C) together, are considered. At last, as an engineering application example, DDA method has been used to analyze the stability of a weak fault controlled slope in one project. It is shown that as the buckling deformation of the sliding slices may affect the utilization of the shear strength, the limit equilibrium method sometimes may provides an over estimation for the stability of a rock slope, and on the other hand, as the contact force calculation in DDA method is based on the rigorous equilibrium equations, DDA method may provide a more reasonable method for stability analysis in rock engineering.

2. Contact forces and safety factor calculation

2.1 contact and contact forces

In DDA method, the total equilibrium equations are derived by minimizing the total potential energy done by forces and stresses acting on blocks. After the equilibrium equations are solved, the block displacement variables are computed. For each contact of the system, the conditions of no-penetration and no-tension are checked and relevant stiff springs are added or removed according to the criteria of penetration at each contact position.

There are three types of contacts of block system, named contact between a convex angle less than 180° and a concave angle great than 180°, contact between an edge and a convex angle, and contact between two convex angles. For each type of the contact, there are corresponding reference lines which can be used to check if penetrations or tensions occur between blocks. There are two rules consisting the criteria of penetration, no inter-penetration between two blocks, and no tension forces exist between two sides.

In the case when inter-penetration occurs at a given position, a 'lock' is applied, which starts from the point and lies at a particular point on the reference line. The 'lock' is to be carried out by adding one or two stiff springs with a given deformed status. Fig.1

shows a corresponding process of a contact between an edge P_2P_3 of block N and a convex angle P_1 of block M according to the iteration solutions of the total equilibrium equations. After solution of the equations, the angle P_1 of block M may pass through the reference line P_2P_3, as in Fig. 1(b). But in fact, the inter-penetration will not occur. Instead, the contact forces R_n and R_s(normal and parallel to the reference line P_2P_3) will be induced. The mechanical contribution of R_n and R_s to the block system is to be replaced by adding relevant stiff springs with given deformation distance (d_n and d_s) and stiffness coefficient k_n and k_s of springs.

Fig.2 shows detailed relative positions of reference line P_2P_3 and an angle before and after the deformation of block M and block N. The inter-penetration between point P_1 and line P_2P_3 can be represented by normal inter-penetration d_n and the possible shear distance d_s. We can define the components R_n' and R_s ′as the named contact force at the contact position between angle P_1 and an edge P_2P_3 by following formulas,

$$\begin{aligned} R_n' &= K_n d_n \\ R_s' &= K_s d_s \end{aligned} \tag{1}$$

where the K_n and K_s are stiffness of normal and shear springs respectively.

The distances d_n and d_s can be calculated according to the coordinates (x_i,y_i) and displacement increment $(u_i,v_i)$of point P_i, i=1,2,3.

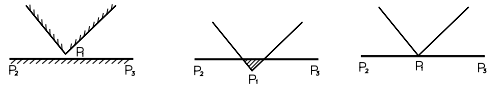

Fig.1. Contact between angle P_1 and edge P_2P_3

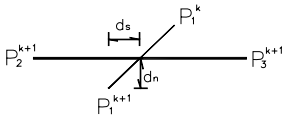

Fig.2. Relative positions before and after iterations

As there are three possible states for each contact, the named contact forces $R_n'$and R_s' have to be modified in further to match the corresponding state of each contact, and at last the real contact force R_n and R_s will be determined as shown by following step (a) to (d).

(a) When the component of the contact force R_n' along the normal of the edge is tensile,

$$R_n' = -K_n d_n \le 0 \tag{2}$$

no lock or stiff spring has been applied. In this case, the contact is open, and no contact force exists. The components R_n and R_s of contact force are zero.

(b) When the normal component R_n' of the contact force is compressive and the shear component of R_s' of the contact force along the reference line is less than shear strength represented by Coloumb's law,

$$R_s' \le R_n' \tan(\phi) + Cl \tag{3}$$

the contact point is fixed, and two stiff springs (perpendicular and parallel to the reference line) will be applied. In this case, the components R_n and R_s of contact force are the same as calculated by formula (1). In formula (3), the parameter ϕ and C are friction angle and cohesion along the reference line, and parameter l is the cohesion length.

(c) When the normal component R_n' of the contact force is compressive and the shear component R_s' of the contact force along the reference line is large enough to cause sliding,

$$R_s' \ge R_n' \tan(\phi) + Cl \tag{4}$$

a stiff spring normal to the reference line is applied to allow the sliding to take place. In this case, the components R_n is the same as calculated by formula (1), but the shear components R_s will be determined by the friction force as defined by following,

$$R_s = R_n \tan(\phi) \tag{5}$$

(d) When criteria of penetration and no tension at all contacts are satisfied, the contact force R_n and R_s calculated above will become the real contact force at the contact positions.

2.2 Safety factor calculation

Assume a potential sliding surface in block system. For blocks above the siding surface, the DDA code will identify automatically the exact contact states for all contacts of blocks above the sliding surface. Assume that there are m_i contacts which perform the above contact state of step (b), and m_j contacts which perform the above contact states of step (c), then we can define safety factor Fs of blocks sliding along a given sliding surface as by following,

$$F_s = \frac{\sum_{i=1}^{m_i} (R_{ni} \tan(\phi_i) + c_i l_i) + \sum_{j=1}^{m_j} R_{nj} \tan(\phi_j)}{\sum_{i=1}^{m_i} R_{si} + \sum_{j=1}^{m_j} R_{nj} \tan(\phi_j)} \tag{6}$$

Where, ϕ_i, ϕ_j, C_i are parameters of friction angle and cohesion. R_{ni}, R_{nj}, R_{si} are normal and shear components of contact forces, and l_i is the cohesion length of a contact.

3. Validation of a single block sliding along incline

In order to evaluate the accuracy for stability analysis with DDA method, a simple model is established here, which consists a single block and a double incline, as shown in fig.3. There are two slopes in the double incline with their dip angles given respectively, the upper one, α_1=30°, and the lower, α_2=15°. The dimension of sliding block is 100cm×50cm (length×height). The distance of the upper slope from point A to B is 8m, and the lower one 10.6m. Different friction angles (ϕ_1, ϕ_2) between the sliding block and inclines are used to investigate the slope stability kinematics of the block. In addition, different combinations of friction angle ϕ_1 and cohesion C are also used as the input strength parameters to study the block sliding stability and its corresponding value of safety factor.

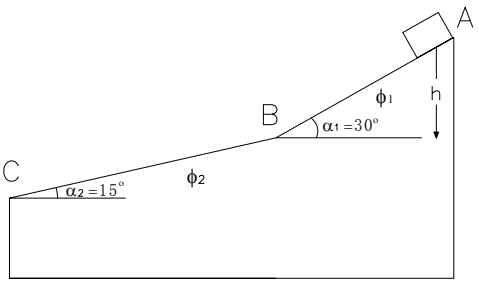

Fig.3. Single block sliding model

3.1 Stability kinematics considering friction angle

In this case, the parameter of cohesion C is assumed to be zero. The calculation here aims purposes in two aspects: (a) by changing the fiction angle ϕ_1, the critical angle for the sliding block from stable state to unstable state is hopeful to be found, and compared to the theoretical results; (b) as the dip angle of upper incline is deeper than lower one, $\alpha_1>\alpha_2$, the proper combinations of friction angles ϕ_1 and ϕ_2 have been chosen as input parameters to investigate the kinematical characteristics of sliding block during its whole sliding process, where the friction angle ϕ_2 of lower incline is assumed to be larger than its dip angle. Here, ϕ_2=25°.

Fig4(a) and (b) show respectively the sliding velocity and sliding distance of the block versus sliding time. When friction angle ϕ_1 is lower than the dip angle α_1 of the upper incline, $\phi_1< \alpha_1$, the block starts to move down, accelerates firstly in the upper incline, and decelerates in the lower incline, and then stops in some place of the lower inline at last.

Firstly, it is clear to see that there are quite different deformation tendencies in the conditions of ϕ_1=29.7° and ϕ_1=30.1°. When the friction angle ϕ_1 is 30.1°, the block is quite stable, but in the condition of ϕ_1=29.7°, there is a notable deformation tendency for block to move down. It is shown that the accuracy for DDA analysis is less then 0.3°.

Secondly, when giving friction angle ϕ_1 different values, such as ϕ_1 =23°, 25°, and 28°, the kinematical characters in aspects of the sliding velocity and sliding distance versus the sliding time show regular kinematical tendencies. The bigger of the friction angle ϕ_1 is given, the lower of the maximum velocity, and the longer of sliding time and the shorter of sliding distance from initiating to stopping. It is shown that DDA method can be used to simulate quantitatively the whole kinematical process of block sliding problems.

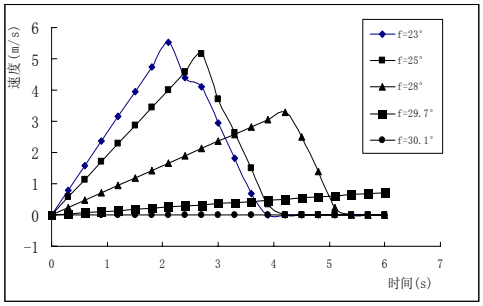

(a) Sliding velocity versus time

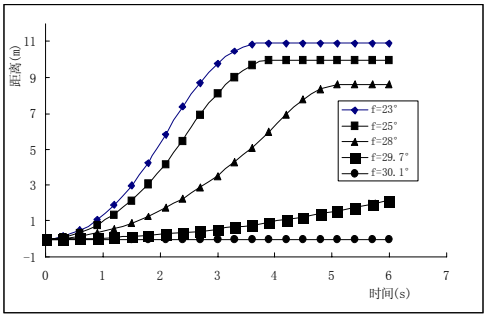

(b) Sliding distance versus time

Fig.4. Results for single block sliding along double incline

3.2 Block stability considering friction and cohesion

The calculation model is shown as in Fig.4. When considering the fiction angle and cohesion, the safety factor for the block sliding along the incline AB can be calculated theoretically. In DDA model, the friction angle ϕ_1 and cohesion C are taken as input parameters. By DDA code, the contact forces acting on the sliding block can be calculated numerically, and then the safety factor Fs is determined.

Fig.5 shows the calculation results by theoretical analysis and by DDA. For each curve in fig.6, the friction angle ϕ_1 is assumed to be a constant, and the cohesion is variable. Here, ϕ_1 is given as 29.7° and 30.1° respectively, and C is from 0.0KPa to 500KPa. It is shown that the results by theoretical and by DDA are nearly the same, and the maximum relative error between the theoretical analysis and DDA is no more than 1.2%. In the above example, the sensitive analysis of the modulus E, stiffness K of springs, and the time increment Δt has been carried out, and their effects are not remarkable.

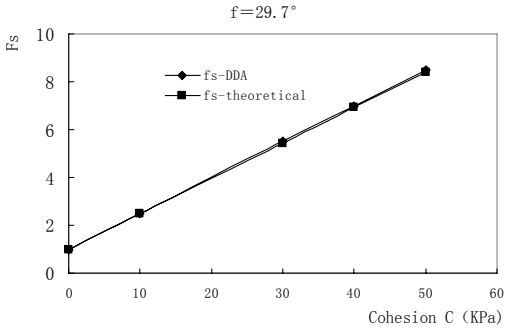

(a) The case of ϕ1=29.7°

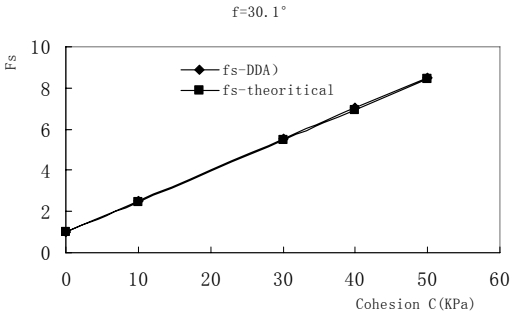

(b) The case of ϕ1=30.1°

Fig.5. Safety factor Fs versus the cohesion C

4. Stability analysis to an actual rock slope

4.1 The stability problem of the rock slope

A rock slope, which will be formed by dam abutment excavation, is located in right bank of one hydro-electric project, the 11th power station in schedule by cascade development in Wujiang River. There is an unfavorable fault, f1, in the right dam abutment. Its strike is nearly parallel to the original rock slope. The stability of the rock slope in the right dam abutment is controlled absolutely by the fault. As the height of the rock slope is more than 100m, and the fault f1 lies not very far from the slope surface after the dam abutment excavation, great concerns have been taken by the designers to the stability evaluation and the valid reinforcement designing for the slope.

Different methods, FLAC-3D and limit equilibrium analysis, etc, have been used to analyze the stability of the slope. When compared their results to that by DDA, it has been shown that DDA method can provide a more reasonable results in aspects of considering both the deformation mechanism and the actual contact forces acting on boundary of slices. Furthermore the results obtained by the static limit equilibrium methods, Sometimes are less conservative as the deformation of slices are not involved during stability analysis, and the anti-sliding forces acting on the slide surface are sometimes over considered.

4.2 Results by limit equilibrium methods

Fig.6 is one of the failure models used in limit equilibrium analysis. For the assumed sliding surface, the fault f1 is from point A to point B, and the segment from point B to point C, which forms the lower part of the sliding surface, is assumed to be produced among rock mass.

Different state limit equilibrium methods, which include Sarma method, Residual Thrust Method (RTM), and Residual Thrust Method Improved (RTMI), etc, have been used to calculate the safety factor. The results are listed in the table below. Determined by the limit equilibrium methods, it is shown that the slope in the condition of the assumed sliding surface still has a proper margin for its stability.

Table 1. Results by limit equilibrium methods

Method	sarma	RTM	RTMI
Safety factor	1.668	1.512	1.484

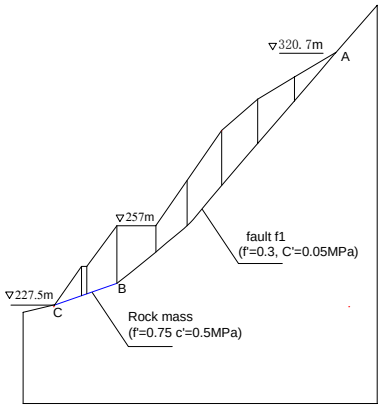

Fig.6. Slices used in limit equilibrium methods

4.3 Results by DDA with no rock bolt

DDA method is used to analyze the stability of the slope. The block system is formed by the slices used in limit equilibrium methods. The strength parameters (friction angle ϕ and cohesion C) in the sliding surface are the same as used in limit equilibrium analysis. The

strength parameters in the vertical separating surfaces and the deformation modulus of blocks are taken from rock mass.

Fig.7 is the deformed blocks by DDA. The corresponding safety factor Fs is less than 1.0. It is shown that the slope is unstable. The failure of the slope is aroused firstly by sliding deformation of the upper blocks, and then by buckling deformation of some blocks with the bottoms separated from the sliding surface by crashing deformation. As the buckling deformation of the upper part of the slope, the shear strength between the blocks and the sliding surface is not utilized efficiently; sliding force acting to the toe of the slope is increased, and results in unstable deformation of the total slope.

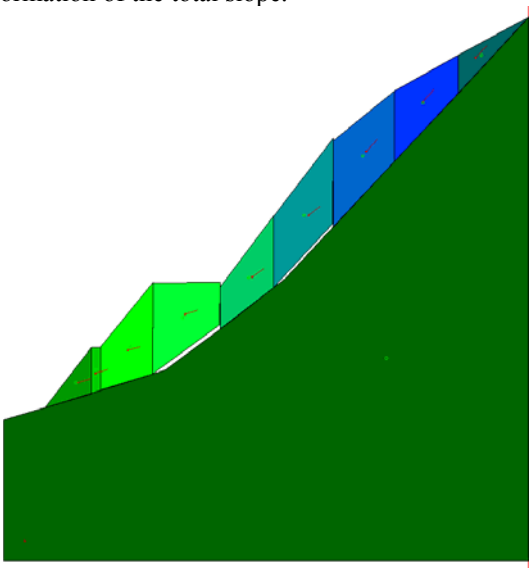

Fig. 7. Deformed blocks by DDA

4.4 Results by DDA with rock bolt

In order to validate the conclusions about the effects of the utilization of shear strength to the stability of the slope, rock bolts, which have been taken as the main measures to strengthen the contact of the block and the sliding surface, are used in DDA calculation. For each block lying on the surface of fault f1 (sliding surface from point A to point B), six rock bolts with diameter of ϕ30mm are installed.

Fig. 8 shows the deformed blocks while the rock bolts reinforcement are considered. In this case the corresponding safety factor Fs is 1.57. It is shown that the slope is quite stable. When compared to results by limit equilibrium methods, the calculated safety factor Fs is reasonable. In other words, it is shown that DDA method may give the contact forces between boundaries of blocks in creditable precision, and in turn provides a more reasonable way for stability analysis in rock engineering.

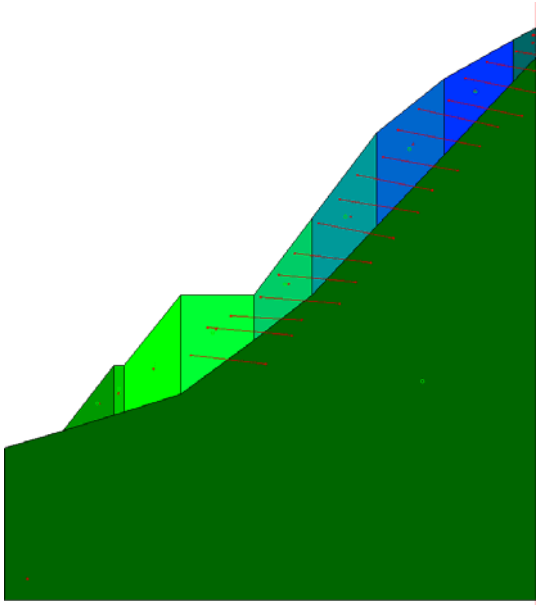

Fig.8. Deformed blocks with rock bolt

5. Conclusions

DDA method incorporates dynamics, kinematics, and elastic deformability of the rock in the equilibrium equations of block system. In past decades, it has been proven that DDA method is a very useful tool especially in dealing with large and discontinuous deformation mechanism of blocks. Sometimes, it can be used to analyze the kinematical simulation problems, such as the falling stone problem, etc. For the calculation of the contact forces between blocks and its further applications for stability analysis with DDA method, very less publishes have been found.

By analyzing a single block sliding along an incline, in conditions of considering friction angle only and considering the friction angle and cohesion together, it has been shown that the accuracy for stability analysis with DDA method is quite acceptable. In the case of single block sliding analysis, the sensibility for friction angle of the sliding surface is no more than 0.3°, and the maximum relative error between the theoretical analysis and DDA is no more than 1.2% .

As the buckling deformation of the sliding slices may affect the utilization of the shear strength, the limit equilibrium method sometimes may provides an over estimation for the stability of high rock slopes. In otherwise, as the contact force calculation in DDA method is based on the rigorous equilibrium equations, DDA method may provides a more reasonable method for stability analysis in rock engineering.

Acknowledgements

This research is supported by Chinese national fund under the contracts of No.50639090 and No. 50539110. The research is also supported by modern hydraulic innovative foundation of the Ministry of

Water and Resources, China, under the contracts of No.XDC2007-10. The authors thank to Dr. Gen-hua Shi for his valuable advice in the field of DDA engineering applications.

References

Shi G.H. Discontinuous deformation analysis: a new numerical model for the statics and dynamics of block systems, Ph.D. Dissertation, Department of Civil Engineering, University of California, Berkeley,1988

Zhao,S., Salami,M.R.,& Rahman,M.S. Simulation of rock toppling failure using discontinuous deformation analysis. In M.R.Salami & D.Banks(eds),Proc. of the first international forum on discontinuous deformation analysis (DDA) and simulations of discontinuous media[C]. Albuquerque:TSI Press,1996,470-479

Maclaughlin,M.M.,Sitar,N., Doolin,D.M., & Abbot,T.S. Investigation of slope stability kinematics using discontinuous deformation analysis. Int. J. Rock Mech. Min. Sci. & Geomech. Abstr. 2001,38:753-762

Maclaughlin,M.M.,Doolin,D.M. & berger E.A., A decade of DDA validation. In Ming Lu (ed.),Development and application of discontinuous modelling for rock engineering, Proceedings of the 6th International Conference on Analysis of Discontinuous Deformation, Balkema,2003,13-3117.

Hatzor,Y.H. & Feintuch, A.The validity of dynamic block displacement prediction using DDA. Int.J. Rock Mech. Min. Sci. & Geomech. Abstr. 2001,38:599-606

Aiqing Wu, Xiuli Ding, Huizhong Li, Gen-hua Shi. Numerical simulation of startup and the whole process characteristics of Qianjiangping Landslied with DDA method[C]. Proce. Of Seventh International Conference on the Analysis of Discontinuous Deformation(ICADD-7). December 10-12,2005, Honolulu, Hawaii, 167-174

Modeling shear resistance of heterogeneous rock joint by using manifold method

G.W. MA[1*], X.M. AN[1], Y.X. ZHOU[2]

[1]School of Civil and Environmental Engineering, Nanyang Technological University, SINGAPORE 639798

[2]Defence Science & Technology Agency, SINGAPORE 109679

(*Email of corresponding author: cgwma@ntu.edu.sg)

The presence of joints may significantly affect the mechanical behavior of rock masses by reducing their capacity to bear shear and tensile loading. Considerable efforts have been contributed to the development of accurate rock joint models. In this paper, a numerical investigation of the mechanical behavior of initially mated artificial joints with saw-tooth shaped asperities is undertaken. Shear response of homogeneous joints is firstly studied. The influences of joint roughness and normal stresses are investigated. Numerical results are compared with theoretical solutions. Good agreements have been observed. Then, material and geometrical heterogeneities for rock joint are incorporated into the manifold method. Numerical results indicate that material heterogeneity will reduce the shear strength. However, its effect is very limited, which is within 8%. In contrast, the shear strength can be increased significantly when the geometrical heterogeneity is introduced. The shear mechanism of rock joint with geometrical heterogeneity is dominated by the largest asperity. Based on this observation, a simple model is proposed to predict its shear strength. The results from the proposed model match well with the numerical results.

Keywords: Shear strength; Homogeneous joint; Material heterogeneity; Geometrical heterogeneity; Manifold method

1. Introduction

The presence of joints may significantly affect the mechanical behavior of rock masses by reducing their capacity to bear shear sand tensile loading. Considerable efforts have been contributed to the development of accurate rock joint models. A lot of shear strength criteria have been proposed. The Coulomb slip criterion is often used to judge the shear failure of a smooth, clean and dry joint:

$$\tau = c + \sigma_n \tan\phi \quad (1)$$

where ϕ is the friction angle, c is the joint cohesion, σ_n is the normal stress.

For rough joints, the shear strength increases with normal stresses linearly as described by the dilatant model (Patton, 1966; Withers, 1964):

$$\tau = \sigma_n \tan(\phi + \alpha) \quad (2)$$

The JRC-JMC model (Barton 1971; Bandis et al 1983; Barton and Bandis 1990) is the most commonly used joint shear criterion, which has the form of

$$\tau = \sigma_n \tan\left[JRC_{mob} \cdot \log_{10}(JCS/\sigma_n) + \phi\right] \quad (3)$$

in which, JRC_{mob} is the joint roughness coefficient which may be mobilized during shearing, JCS is the laboratory scale joint wall compressive strength.

More recently, Zhao (1997a; 1997b) proposed the JRC-JMC shear strength criterion by combining the joint matching coefficient (JMC) into the JRC-JCS model as

$$\tau = \sigma_n \cdot \tan\left[JRC \cdot JMC \cdot \log_{10}(JCS/\sigma_n) + \phi\right] \quad (4)$$

The manifold method (MM) is initially developed by Shi in 1991 (Shi, 1991; 1997). The method is derived from the finite cover approximation theory and gains her name after the mathematical notion of manifold. The MM was developed based on discontinuous deformation analysis (DDA). It preserves all the discrete element modeling characteristics such as kinematics constraints, contact detection and modeling from DDA. However, it employs a number of covers in each block to raise its degrees of freedom (DOFs) to improve the accuracy of stress and displacement field. The MM demonstrates a good consistency with both the conventional finite element method (FEM) and the DDA and applicable to both continuous and discontinuous problems.

In the present paper, a numerical investigation of the mechanical behavior of initially mated artificial joints with tooth shaped asperities is undertaken using the MM. The shear response of homogeneous joints is firstly studied. The numerical results are compared with the theoretical solutions. Then, the material heterogeneity effect and geometrical heterogeneity effect are implemented into the MM models. Their influences on the shear strength of rock joint are investigated.

2. Shear response of homogeneous joint

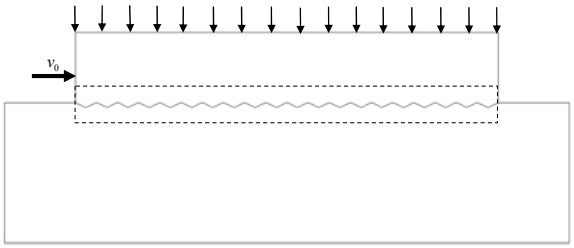

Fig. 1 Schematic view of the direct shear test model

Fig. 1 is the schematic view of the direct shear test model. The joint surface (marked by the dash line box) which consists of 20 asperities divide the model into two halves, namely upper half (60cm×10cm) and lower half (75cm×20cm). The lower half is fixed. A velocity boundary is applied to the left edge of the upper half to provide the shearing displacement. Compressive loading is applied to the top of the specimen to simulate the initial earth stresses. The rock material is assumed elastic without damage with the parameters: density = 2650 kg/m^3; Young's Modulus = 80 GPa; Poisson's Ratio = 0.3. The joint obeys Coulomb slip criterion with three parameters: friction angle = 30°; tensile strength = 0 MPa; cohesion = 0 MPa.

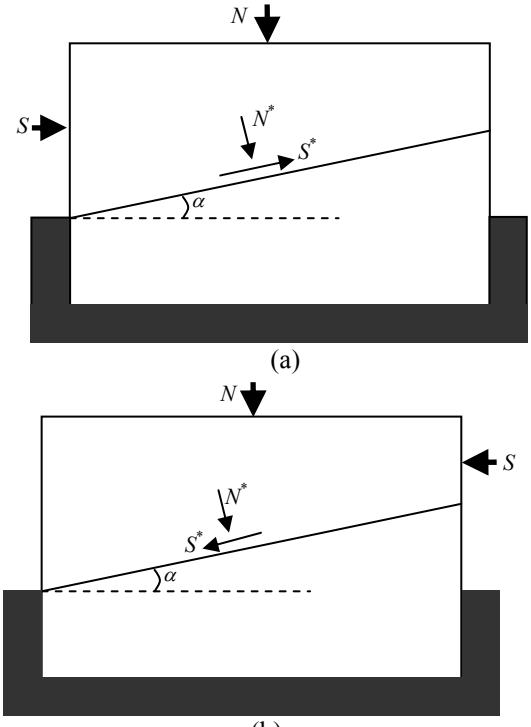

Fig. 2 Illustration of the analytical model for direct shear test: (a) forward shearing; (b) backward shearing

The theoretical solutions of this problem can be derived using the simplified model shown in Fig. 2. The joint surface is inclined at an angle of α to the direction of shear force S.

The shear strength for forward shearing is

$$\tau_F = \sigma \cdot \tan(\phi + \alpha) \quad (5)$$

The shear strength for backward shearing is

$$\tau_B = \sigma \cdot \tan(\phi - \alpha) \quad (6)$$

The offset, which is defined as the difference between the above two shear strengths can be expressed as

$$\Delta\tau = \tau_F - \tau_B = N \cdot \left(\tan(\phi + \alpha) - \tan(\phi - \alpha)\right) \quad (7)$$

Joint roughness is a measure of the inherent joint surface waviness and unevenness relative to the mean plane. It is a very important component of shear strength, especially for undislocated and interlocked joints. The joint roughness is represented by asperity inclination angle in this study. Six cases with various asperity angles of 0°, 5°, 10°, 15°, 20°, and 25° (shown in Fig. 3) are simulated. The shear strengths from numerical modeling are compared with theoretical solutions. Good agreement has been observed.

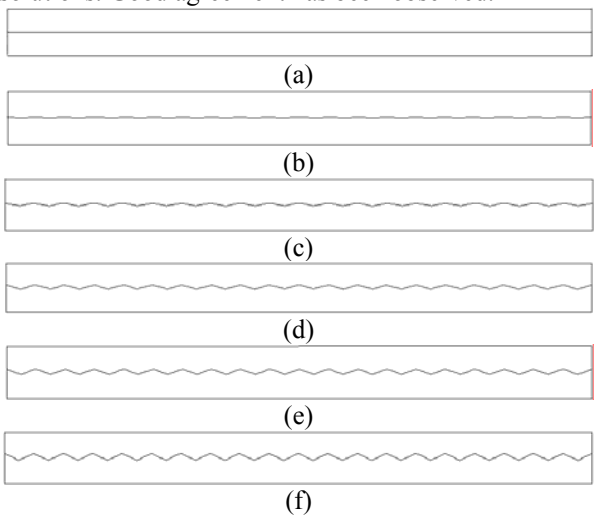

Fig. 3 Illustration of joints with different roughness: (a) 0°; (b) 5°; (c) 10°; (d) 15°; (e) 20°; (f) 25°

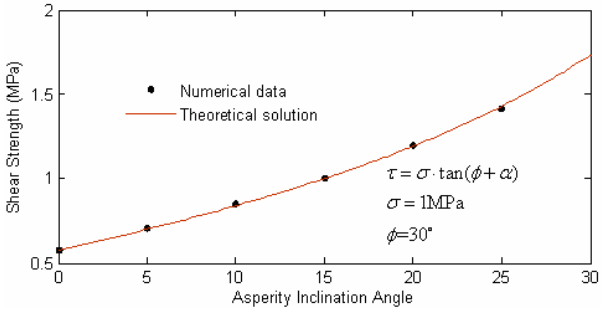

Fig. 4 Comparison of numerical results and theoretical solutions in shear strength for the joint with different roughness

Shear response of rock joint under cyclic loading is also studied. The offset value is compared with the theoretical solution in Fig. 5.

Seven cases with various normal stresses of 0.5 MPa, 1.0 MPa, 2.0 MPa, 3.0 MPa, 4.0 MPa, 5.0 MPa, 6.0 MPa are studied here to investigate the influences of normal stress on the joint shear strength. The

numerical result again matches well with the theoretical solutions. The shear strength increases linearly with the normal stresses.

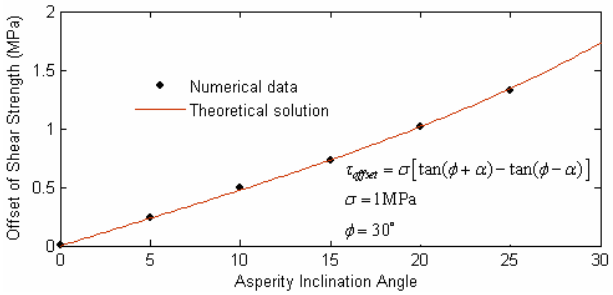

Fig. 5 Comparison of offset value from numerical modeling with the theoretical solution for joints with different roughness

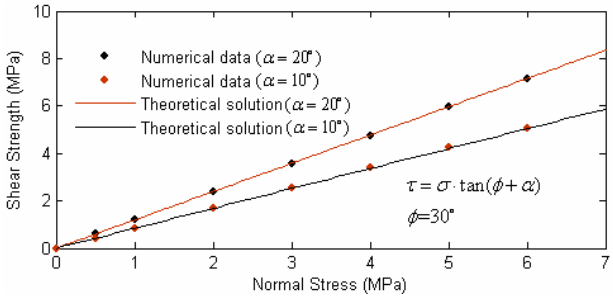

Fig. 6 Comparison of shear strength from numerical modeling with the theoretical solution for the cases with different normal stresses

3. Shear response of rock joint with material heterogeneity

The joint model with 20 geometrically identical asperities is shown in Fig. 7. The joint is described by Coulomb slip law with three parameters, namely friction angle, cohesion and tensile strength. In the present study, cohesion and tensile strength are ignored. In order to model the material heterogeneity effect, each asperity is assigned with different friction angles conforming to a Weibull distribution.

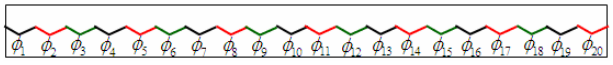

Fig. 7 Illustration of joint model with material heterogeneity

The two-parameter Weibull distribution (Weibull, 1951) can be expressed as

$$f(T) = \frac{m}{\mu}\left(\frac{T}{\mu}\right)^{m-1} \exp\left(-\left(\frac{T}{\mu}\right)^{m}\right) \tag{8}$$

where T is the rock joint parameter, μ is the mean value of T, m is the shape parameter describing the scattering of T.

Here, the friction angles are configured to follow a Weibull distribution. The probability density of the Weibull distribution is shown in Fig. 8. The shape parameter m is a measure of the parameter scattering and defined as a heterogeneity index. A larger m indicates that the material is more homogeneous. When m tends to infinity, the variance tends to zero and an ideal homogeneous rock joint is obtained. Because the Weibull distribution is non-monotone, the cumulative distribution function (shown in Fig. 9) is derived as

$$Q(T) = \int_0^T f(T)dT = 1 - \exp\left(-\left(\frac{T}{\mu}\right)^{m}\right) \tag{9}$$

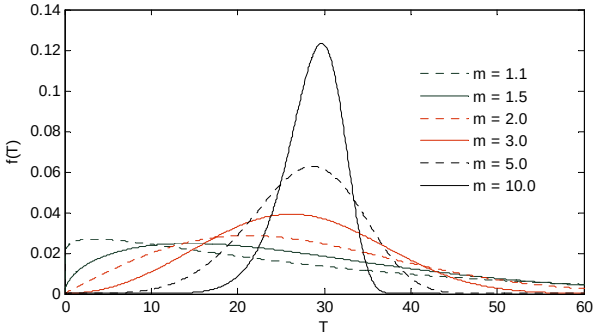

Fig. 8 Probability density of Weibull distribution

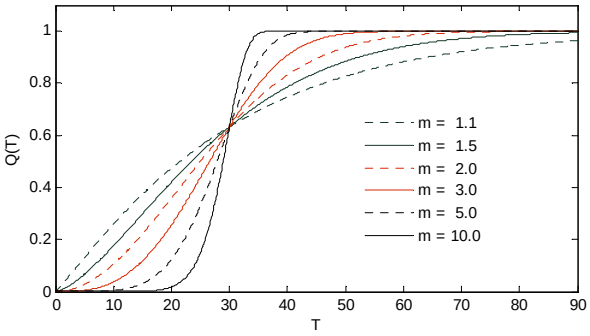

Fig. 9 Cumulative distribution of Weibull distribution

The disorder of the probability distribution for joint friction angles can be achieved by the Monte Carlo method. One simple way is to generate a series of random data which have a uniform distribution between 0 and 1. Then, a series of desired parameters, which conform to Weibull distribution, can be obtained as

$$T = \mu\left(\ln(U(0,1))\right)^{1/m} \tag{10}$$

where $U(0,1)$ represents the random data between 0 and 1 generated by the Monte Carlo method.

The numerical models with various heterogeneity index m of 5, 6, 8, 10, and 15 for four cases with various joint inclination angle of 5°, 10°, 15°, 20° are simulated. The calculated non-dimensional shear strength, which is defined as the shear strength divided by that of homogeneous joint, is plotted in Fig. 10. The numerical results indicate that shear strength is decreased when material heterogeneity is considered. However, its effect is limited within 8%.

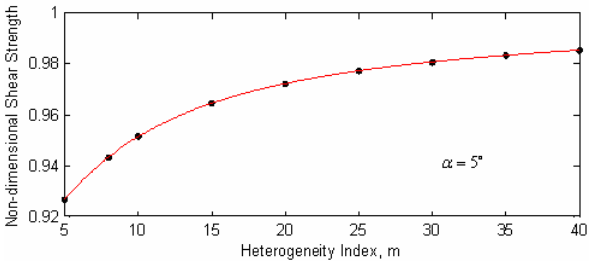

(a)

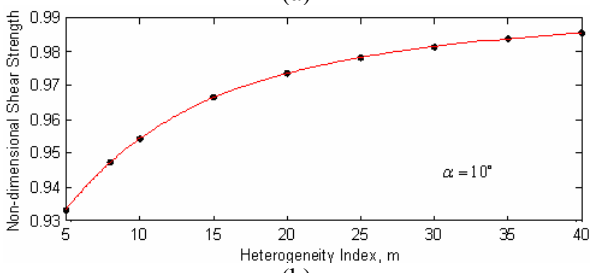

(b)

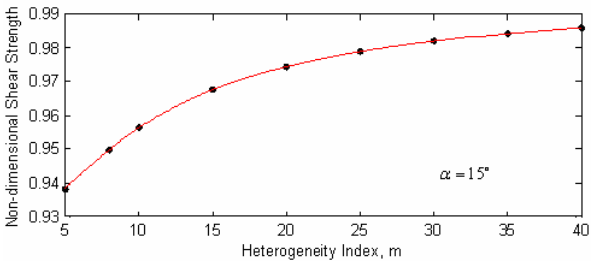

(c)

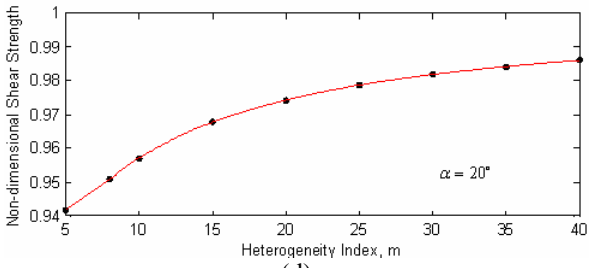

(d)

Fig. 10 Non-dimensional shear strength vs heterogeneity index for four cases with various α of 5°, 10°, 15°, 20°

4. Shear response of rock joint with geometrical heterogeneity

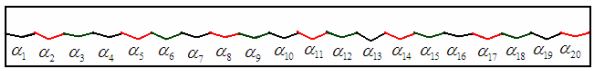

Fig. 11 Illustration of joint surface with geometrical heterogeneity

In order to model geometrical heterogeneity of rock joint (shown in Fig. 11), the asperities are configured with different inclination angles following Weibull distribution.

The following cases are simulated:

1) Five specimens with various heterogeneity indices of 1.1, 2, 3, 5, 10, the mean inclination angle is 5°;
2) Five specimens with various heterogeneity indices of 1.1, 2, 3, 5, 10, the mean inclination angle is 10°;
3) Five specimens with various heterogeneity indices of 1.1, 2, 3, 5, 10, the mean inclination angle is 15°;
4) Seven specimens with various heterogeneity indices of 1.3, 1.4, 1.5, 2, 3, 5, 10, the mean inclination angle is 20°.

In order to save pages, only the configurations of rock joints in case 4 is plotted in Fig. 12 as an illustration.

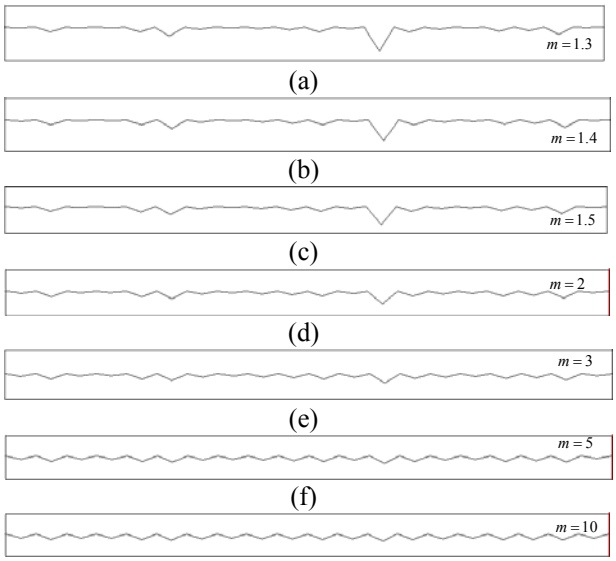

Fig. 12 Configuration of joint surface with various heterogeneity index, mean $\alpha = 20^o$

The non-dimensional shear strength, which is the shear strength normalized by that of the homogeneous joint with the same joint inclination angle, for the four cases are shown in Fig. 13. It can be found that the shear strength can be significantly increased when the geometrical heterogeneity effect is introduced. With the increase of the heterogeneity index, the non-dimensional shear strength decreases sharply and then becomes a relative flat plateau when m is lager than 2.

For homogeneous joint and joint with material heterogeneity, the upper half slides along the surfaces of each asperity of the lower half during the shearing process. However, the shear mechanism becomes much different for the geometrically heterogeneous joint model. After a small shearing displacement, the upper half of the model slides along the surfaces of a few main asperities while most of the asperities will be open.

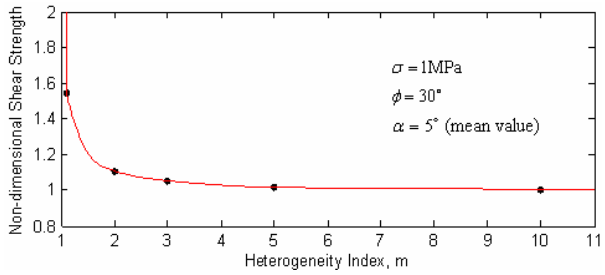

(a)

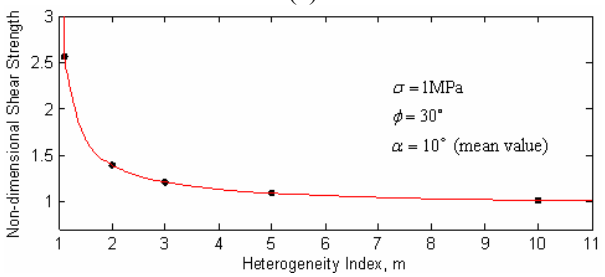

(b)

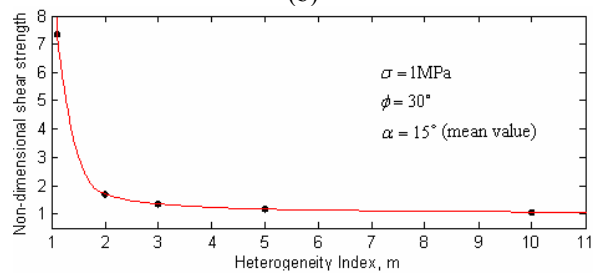

(c)

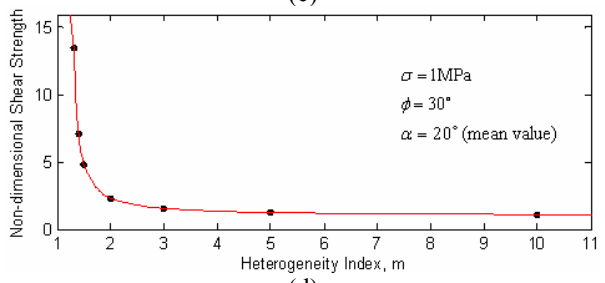

(d)

Fig. 13 Non-dimensional shear strengths of joint with various heterogeneity indices: (a) mean α=5°; (b) mean α=10°; (c) mean α=15°; (d) mean α=20°

The shear response of the rock joint with geometrical heterogeneity is dominated by the largest asperity on the joint surface as shown in Fig. 14. Based on the numerical simulation results, the following shear strength model can be proposed for the rock joint with geometrical heterogeneity:

$$\tau = \sigma \cdot \tan\left(\phi + \max\left(\alpha_1,\ \alpha_2,\ \alpha_3,\ \ldots,\ \alpha_n\right)\right) \qquad (11)$$

where n is the number of asperities in one joint surface, $\max\left(\alpha_1,\ \alpha_2,\ \alpha_3,\ \ldots,\ \alpha_n\right)$ is the inclination angle of the largest asperity.

(a) Step 0

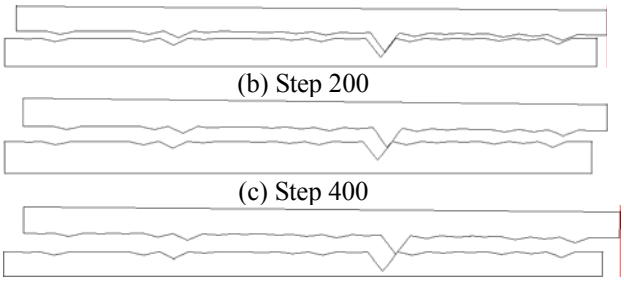

(b) Step 200

(c) Step 400

(d) Step 500

Fig. 14 Shearing process of rock joint, α=15°, m=1.1

The shear strengths from the proposed model are compared with the numerical results in Table 1. Good agreements have been found.

Table 1 Comparison of numerical results with the results from the proposed criterion for the rock joint with geometrical heterogeneity

Shear Strength \ m		1.1 (1.4)	2	3	5	10
5°	Numerical result	1.08	0.77	0.74	0.71	0.70
	Predicted result	1.09	0.84	0.78	0.74	0.72
	Error (%)	0.9	9.1	5.4	4.2	2.9
10°	Numerical result	2.15	1.17	1.01	0.91	0.85
	Predicted result	2.16	1.19	1.03	0.94	0.88
	Error (%)	0.5	1.7	2.0	3.3	3.5
15°	Numerical result	7.33	1.69	1.34	1.15	1.06
	Predicted result	7.89	1.73	1.37	1.18	1.08
	Error (%)	7.6	2.4	2.2	2.6	1.9
20°	Numerical result	8.39	2.72	1.83	1.46	1.30
	Predicted result	9.11	2.74	1.86	1.50	1.33
	Error (%)	8.5	0.7	1.6	2.7	2.3

6. Conclusions

In this paper, a numerical investigation of the mechanical behavior of initially mated artificial joints with saw-tooth shaped asperities is undertaken. Shear response of homogeneous joints is firstly simulated. The influences of joint roughness and normal stresses are investigated. Numerical results are compared with theoretical solutions. Good agreements have been observed. Then, material and geometrical heterogeneities are incorporated into the MM models. Numerical results indicate that material heterogeneity will reduce the shear strength. However, its effect is limited within 8%. In contrast, the shear strength can be increased significantly when the geometrical heterogeneity is introduced. The shear mechanism of rock joint with geometrical heterogeneity is dominated by the largest asperity. Based on this observation, a joint shear strength model is proposed for the joint with geometrical heterogeneity. The shear strengths from the proposed model match well with the numerical results.

The numerical simulation using the MM shows clearly the shear mechanism of heterogeneous rock joints. The results agree well with the analytical solutions which are derived on the forward and

backward shearing model.

It should be highlighted that the MM has great advantage in simulating heterogeneous rock joints. The mathematical cover for different joint roughness is the same, while the physical cover by considering the material and geometrical heterogeneity can be obtained by slightly modifying the homogeneous ones.

References

Bandis S., Lumsden A.C., Barton N.R. Fundamentals of rock joint deformation. *Int. J, Rock Mech. Min. Sci. & Geomech. Abstr*. 1983, Vol. 20: 249-268.

Barton N.R. A relationship between joint roughness and joint shear strength. *Proc. Symp. Rock Fracture*, Nancy, France, 1971, pp.1-8.

Barton N. R., Bandis S. Review of predictive capabilities of JRC-JCS model in engineering practice. *Proc. Int. Conf. Rock Joints*. Leon, Norway, 1990, pp. 603-610.

Patton F.D. Multiple modes of shear failure in rock. *Proc. 1st ISRM Congr*. Lisbon, 1966, pp.509-513.

Shi, G.H. Manifold method of material analysis. *Trans. 9th Army Conf. on Applied Mathematics and Computing*, Minneapolis, Minnesota, 1991, pp.57-76.

Shi G.H. Numerical manifold method, Proc.*2nd Int. Conf. on Analysis of Discontinuous Deformation*, Kyoto, 1997, pp.1-35.

Weibull W. A statistical distribution function of wide applicability. *J. Appl. Phys.* 1951, Vol. 28: 293-297.

Withers J.H. Sliding resistance along discontinuities in rock masses. Ph.D. thesis, University of Illinois, Urbana, 1964.

Zhao J. Joint surface matching and shear strength part A: joint matching coefficient (JMC). *Int. J. Rock Mech. Min. Sci*. 1997a, 34 (2): 173-178.

Zhao J. Joint surface matching and shear strength Part B: JRC-JMC shear strength criterion. *Int. J. Rock Mech. Min. Sci.* 1997b, 34 (2): 179-185.

Analysis of discontinuous deformation of upper rock strata of coal mine

YANG JU, J. P. ZUO

State Key Laboratory of Coal Resources and Safety Mining, School of Mechanics and Civil Engineering,
China University of Mining & Technology, Beijing, 100083, P. R. CHINA

A two-dimensional DDA method has been employed to analyze the discontinuous deformation of upper rock strata during coalmine excavation. A discontinuous block system containing statistically distributed joints and faults has been set up to model the real rock strata based the geological data acquired at the site of excavation. The evolution of stresses in upper rock layers, the movement of immediate roof arched by key blocks, the layer-abscise initiation and the subsidence of rock strata during excavation were simulated. The comparison of numerical analysis and laboratory test shows that the numerical DDA method can effectively model the excavation process and deformation of upper rock strata of a coalmine.

KEYWORDS: discontinuous deformation analysis (DDA); stresses; displacement; deformation; rock strata; mine excavation; great depth.

1. Introduction

A large amount of coal resources have been excavated and utilized to complement the energy supply in China. A negative aspect of booming coal exploitation in China is that the society has suffered severe environmental problems caused by over-excavation, such as environmental pollution, large subsidence and movement of covering surface, the ruin of infields and earthquakes, etc. Moreover, as the result of incessant excavation, the coal reserved at shallow has gradually been exhausted. A fair proportion of coalmines were forced into deep excavation where high earth stresses and high permeable hydraulic pressures occur. This makes the excavation very difficult to handle as compared to the treatment under the shallow conditions.

To maintain the sustainable utilization of coal resources in China and protect the environment, people have paid close attention to the technologies for predicting and controlling deformation and subsidence in rock strata surrounding the tunnels. It has become a critical problem in the theoretical study of rock-strata controlling and mining engineering applications. To our knowledge, a great number of pioneering studies have been carried out regarding to the deformation prediction, numerical simulation for rock strata movement and controlling techniques with the shallow excavation condition [1-12]. However, what we concluded from the shallow conditions may not fit to predict the deformation or displacement of rock strata at depth if accounting the effects of great gravity stress, high geological stress and confining pressure. Thus, to ensure a safe and environmental-friendly mining, it is of great import for us to well understand the properties of deformation and movement of rock strata during deep excavation processes.

Our purpose in this paper is that we attempt to figure out how the stress and the deformation of upper rock strata behave as a deep excavation proceed, using numerical discontinuous deformation analysis method. The *in-situ* deep geological condition has been taken into account.

To our knowledge, a few theoretical or analytical models have been proposed to quantify the deformation and displacement of rock strata during mining [1-2, 7, 9-12]. However, due to the complicated discontinuity and boundary conditions, it is intractable to have an exactly analytical solution of stress and deformation distribution. From this point, numerical simulation has its advantage in solving such problems. Thus, finite difference method (FDM), finite element method (FEM), boundary element method (BEM), known as continuum-based approaches, and discrete element method (DEM), known as discontinuum-based method, have been adopted to compute the movement of rock strata and subsidence of ground surface [1-6, 8]. Despite the success that continuum-based approaches achieved a weak point arose from that the motion (e.g. translation and rotation) of an individual rock block along the interfaces with different scales (e.g. faults, joints and microcracks) cannot be taken into account, since the displacement compatibility between elements must be satisfied. Only the deformation (i.e. strains) of the continuous system can be analyzed. On the other hand, for discontinuum-based approaches (e.g. DEM), the deformation of rigid body is generally not included since it does not produce strains inside the individual rock element. Only the rigid motion of rock elements can be computed in this method. Therefore, it is pretty hard for either continuum-based approaches or discontinuum-based approach to properly evaluate surface

displacement caused by the rock-stratum deformation and/or displacement arising in mine excavations.

Fortunately, based on the consideration of FEM, Dr. Shi (1988) developed a so-called *Discontinuous Deformation Analysis* (DDA) method that can be used to compute not only the deformation of individual elements but also large displacement between elements, including sliding, fracturing, and rotation of the discontinuous rock system [13-15]. In DDA, elements are blocks naturally separated by interfaces existing in rock masses. The equilibrium equations of individual elements are formulated to minimize the total potential energy of system. The static and dynamic equilibrium conditions are automatically satisfied. The solutions to the strain, displacement, and stress can be obtained by solving simultaneous equilibrium equations of the whole blocky system. The elements or blocks used by DDA can be any convex or concave shape, whereas the FEM uses only elements with polygons. Furthermore, displacement, strain, and stress of every individual element can be calculated by incorporating the initial condition and geometric boundary condition of the model. Accordingly, the translation, rotation, and open-close processes of the rock blocks can be simulated. The movement and displacement between the rocks can be determined and therefore the failure criteria of the whole system can be built. DDA method has been successfully applied to civil and mining engineering problems, including landslide, slope stability, stability of dam foundations, tunnel excavation, blasting and earthquake response [16-29]. The researches clearly demonstrate that DDA method can capture stress and large displacement behaviors of discontinuous rock masses when excavation is undertaken.

In this paper we employed DDA to simulate the surface movement and displacement of thick rock strata above the excavation tunnel of a deep coalmine in southern China. The influence of relative motion along the existing geological faults and joints, as well as the deformation of individual rock blocks on the displacement of ground surface has been analyzed. The stress field and its evolution in upper rock strata during excavation have been computed using DDA.

2. Computational model

The outline of geological condition: The coalmines we intend to analyze distribute along both sides of the Huai River in China and there are 13 to 18 coal seams available for mining. The seams are in a monocline structure and most are gently inclined, a few of them are steep seams. The total thickness of the coalmine is about 30 m and the total confirmed reserve of the coalmine comes to approximately 1,470 billion tons between depths of 1000 m and 1200 m. Currently, most of the coalmines in this region have already entered the stage of deep exploration and a large proportion of mines has been excavated at the level of 700 m underground. With the increasing of the excavation depth, the earth temperature rose rapidly and the movements of rock strata became more and more apparent; thus it is exceedingly difficult for workers to support the fractured rock masses and mine safely. Taking stope 2171(1), the working face of coal seam 11-2 of one coal mine in this region, as an example, the working face, which is 1780 m along the line of strike and 206 m in the width of inclination, has nine normal slip faults and is ready for extraction. The thickness of the relatively horizontal coal seam is 1.8 m. The roof of the excavation is comprised of mudstone and sand-mud rock. The ground elevation is between +19 m and +20 m and the elevation of working face is between –729 m and –690 m. The coal was extracted by means of an automatic mechanical system.

DDA model for excavation: Part of the 2171(1) working face has been modeled as a representative case using two-dimensional DDA method. Based on the geological conditions, the practical mining process has been simplified as a two-dimensional plane strain case. The model, 420 m in length and 200 m in height, was fixed along the bottom and lateral boundaries. The distance between the top surface of the model and the ground surface is 500 m. The averaged bulk density of the upper layer rock strata is $\rho = 2.6 \times 10^3\ kg/m^3$. In order to reflect the overburden of the rocks above the model surface up to the actual ground surface, a uniform load is applied to the top boundary of the computation model; that is:

$$\sigma = \rho \cdot g \cdot H \qquad (1)$$

where H refers to the depth of rock between the top boundary of the model and the ground surface. The mechanical parameters of the rock mass adopted in DDA model are listed in the Table 1. Three normal slip faults in the 2171(1) excavation zone, shown in Fig. 1, are included in the DDA computation to analyze the influence of the faults on the large displacement and the failure mode of the upper rock strata. Properties of fault and orientations can be found in Table 2.

Table 1 Mechanical parameters of rock masses

Material	Elastic Modulus (10^4 MPa)	Poisson Ratio	Density (10^3 kg·m^{-3})	Cohesive Strength (MPa)	Internal Friction angle (°)
Rock	1.5	0.25	2.6	15	35
Coal (seams)	0.29	0.3	1.4	1.7	42

Table 2 Geologic properties of working face 2171(1)

Properties of Faults	Dip Direction (degree °)	Slope Angle (degree °)	Property	Drop (meter)
Fe 1	142	45	positive	5.0~6.0
Fe 2	124	57	positive	2.0
Fe 3	139	43	positive	1.7

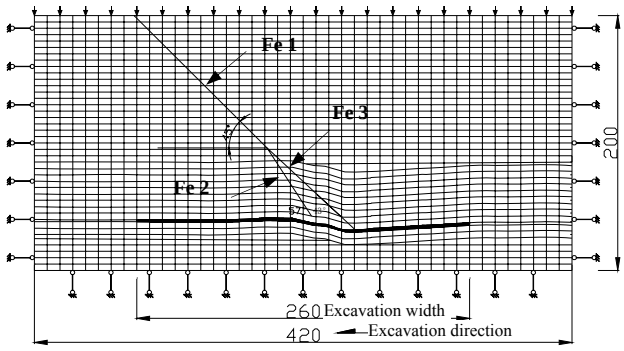

Fig. 1 Two-dimensional DDA model along the tunnel direction

3. Computation results and analyses

Fig.2 and 3 illustrate the stress distribution, deformation, and movement of the upper layer rock strata during mining, respectively. The sequence of coal mining in the numerical simulation is based on the physical extraction sequence of the working face. The real excavation ran 4 meters every day, hence 65 days were needed to complete 260 m long excavation. In the DDA calculation, 2500 time steps were set up to model 60 m physical extraction. The DDA computation results indicate some interesting phenomena as follows.

(1) Before excavating the working area 2171(1), the stresses of the whole mining field mainly behave in the horizontal and vertical direction, due to the uniform gravity effect of the rock strata, indicated by the arrows in Fig.2. In the vicinity of the faults, however, the directions of the principal stresses are altered and relatively large stress concentration fields have formed in this area, as shown in the Fig. 2a.

(2) When mining to the station of 52-meters, the immediate roof created above the space where the coal has been removed is arched by four key blocks, as shown in Fig. 2b. The function of the immediate roof is similar to a freely supported beam through which the load of upper layer rock was passed to the front and back walls of the coal mine, and simultaneously, the degree of stress concentration is rather high in the walls. At this time, the local stress field of the upper rock layer resulted from excavation shaped as a half-ellipse with small radius.

(3) When approaching station 104, the upper layer rock strata began to fall down. The half elliptical local stress field of the upper rock strata, above the extraction space, grew smoothly in the horizontal and vertical directions. The separation and abscises initiated in the rock layers just above the immediate roof, as shown in Fig. 2c. The effect of stress softening can be found in the front and back walls of the coalmine in the working surface at this stage.

(4) When processed to the point of 156-meters, the excavation has passed through the faults. The coal walls at the neighborhood of the faults retain comparatively low strength and therefore relatively large deformation took place. The rock was not strong enough to sustain the freely supported beam; hence the upper layer rock strata began to fall down seriously. In the meantime, the local stress field of the upper rock strata, exiting in the shape of a half-ellipse, was growing step by step, and the rock stratum separation became serious, as shown in Fig. 2d and 3d. The stress concentration, however, is still rather obvious in the wedge created below the intersection of faults Fe 2 and Fe 3.

(5) When reaching the point of 208-meters, the rock strata near the faults broke down in significant areas. Consequently, the high stress concentration in the intersection area of the faults has been lifted. The enlargement of the local stress field, in the shape of a half-ellipse, has reached its maximum size in the vertical direction. The phenomenon of abscises, shown in Figures 3e and 4e, have taken place in various rock strata above the excavation roof.

(6) When approaching the end position of 260-meters, the roof of excavation region has completely subsided. The stress distribution in the area beyond the half-ellipse local field tends to be uniform. The stress concentration still exists in the front of the working face and near the faults. With the advancement of the extraction region, the half-ellipse stress field of the upper layer rock in the horizontal direction continued to extend, but the stress field at the vertical direction remain unchanged, as illustrated in Fig. 2f and 3f.

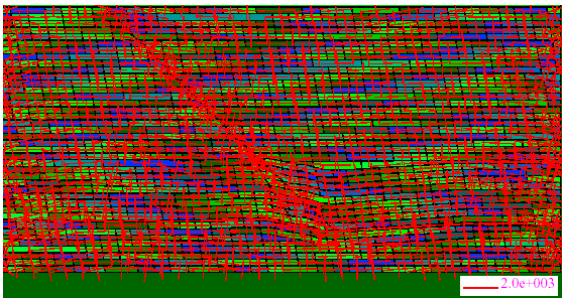

a) Principal stresses and stress concentration before excavation

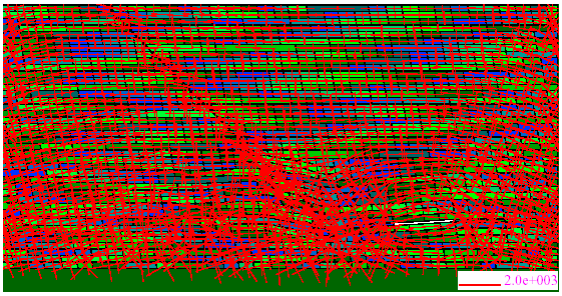

b) The immediate roof arched by key blocks, a half elliptical local stress field initiation and stress concentration when mining to the point of 52-meters (operating 500 steps in DDA)

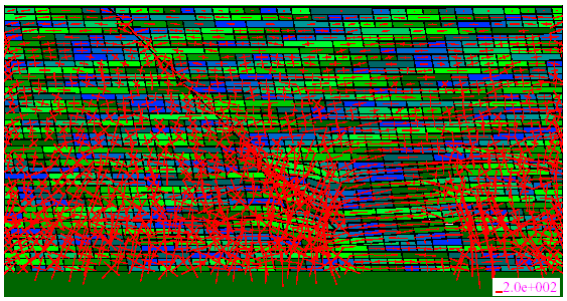

c) The growing half elliptical local stress field near the fault, global stress distribution and abscises initiating in the rock layers when mining to 104-meters (operating 1000 steps in DDA)

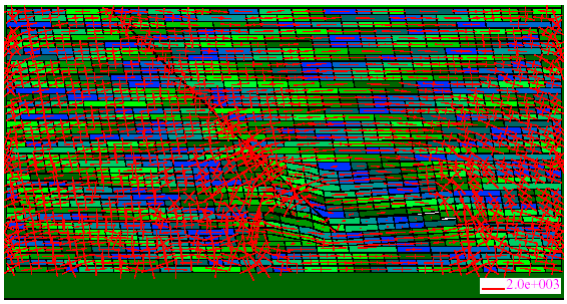

d) The half elliptical local stress field over the faults, rock strata abscising and falling down when excavating to the point of 156-meters (operating 1500 steps in DDA)

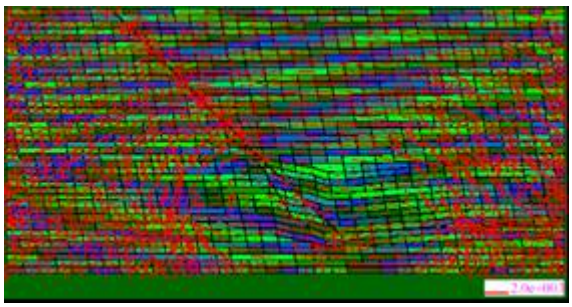

e) The half elliptical local stress field with the maximum size in vertical direction, the descending stress concentration near the faults and apparent layer abscises when mining to the point of 208-meters (operating 2000 steps in DDA)

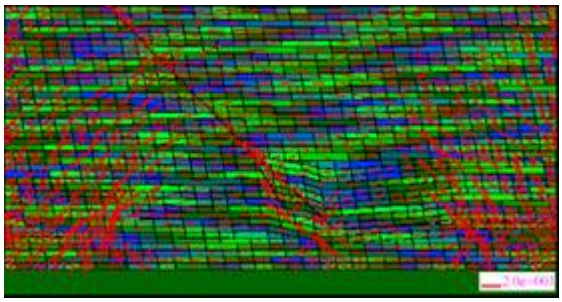

f) The growing local half elliptical stress domain in horizontal direction, completely-subsided roof, low stress concentration near the fault and uniformly-distributed global stresses when mining to the end (operating 2500 steps in DDA)

Fig. 2 The stress distribution in upper rock strata during excavation

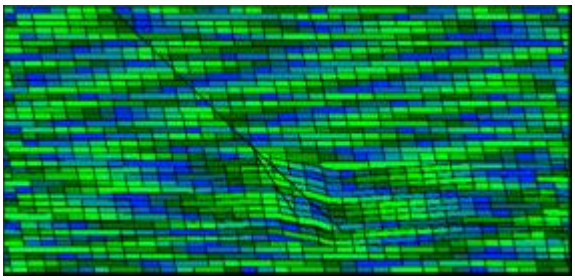

a) Statistically-generated joints, displacement and deformation of blocks before excavation

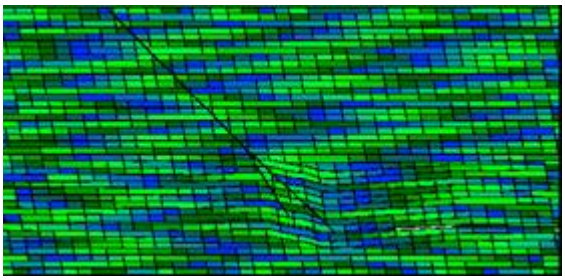

b) The immediate roof arched by key blocks, displacement, and deformation of upper rock strata when mining to 52 meters (operating 500 steps in DDA)

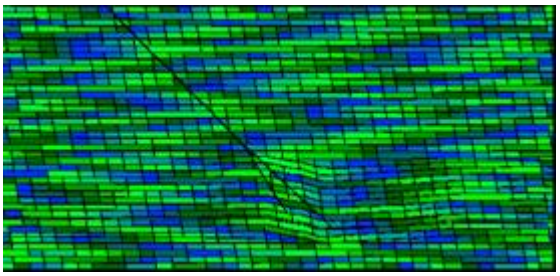

c) The layer separation and abscise initiation, displacement and deformation of blocks when mining to 104 meters (operating 1000 steps in DDA)

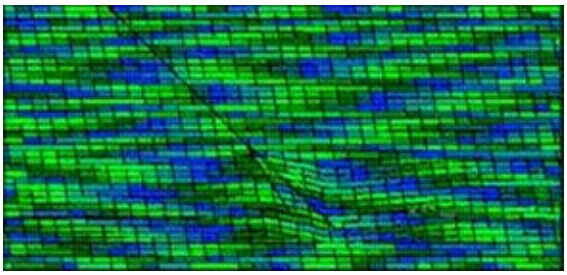

d) The upper rock strata abscising and falling down when excavating to 156 meters (operating 1500 steps in DDA)

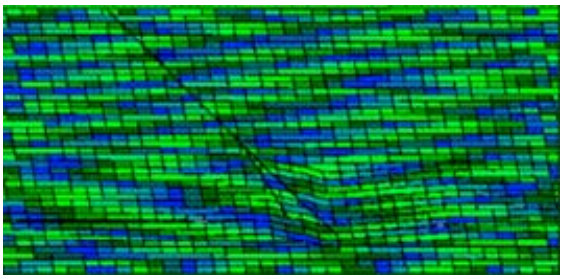

e) The abscise developing in various rock strata above the excavation roof when mining to 208 meters (operating 2000 steps in DDA)

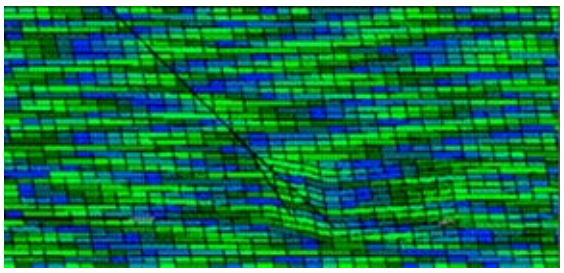

f) The completely-subsided roof, displacement, and deformation of upper rock strata when excavating to 260 meters (operating 2500 steps in DDA)

Fig. 3 The deformation and displacement of upper rock strata during excavation

5. Experimental validation

In order to exam the efficiency of simulation, a modeling experiment of excavation has been carried out. Fig. 4 illustrates the experimental setup. Based on the real size of the excavation area, the total height of tested rock strata was set up to 164.02 m in the model, including 1.8 m coal seam, 8 m rock layer and 156.02 m upper rock strata in height. There are 48 levels from the bottom through the coal seam to the upper board. The model scale is 1:100; and therefore the width, height, and thickness of the model is 4.2 m, 1.64 m and 0.25 m, respectively. The gravity of rock layers exerting on the model is generated by a few screw jacks distributed along the top surface of the model. The material used for model is prepared according to the density and stress similitude principles. The aggregate adopts river sand with grain size less than 1.5 mm; the cementitious matter is gypsum and lime, and the delaminating material used for simulating strata structure is mica powder. The time ratio of modeling excavation is 1:12; the modeling height of excavation is 1.8 cm, the extraction speed is 3.6 cm every two hours, and the total length of the modeling excavation is 260 cm. Many labels were pasted on the surface of each stratum to facilitate the observation of deformation of the rock mass. The strain of the rock mass was measured by means of a strain gauge and displacement of the upper layer rock was recorded by an electronic transit instrument. For more details about model preparation, refer to reference [30].

Fig. 5 shows the deformation and failure pattern of the upper layer rock strata during the excavation. It implies that these experimental results are in consistent with the numerical simulation shown in Figs. 2d~2f and Figs. 3d~3f.

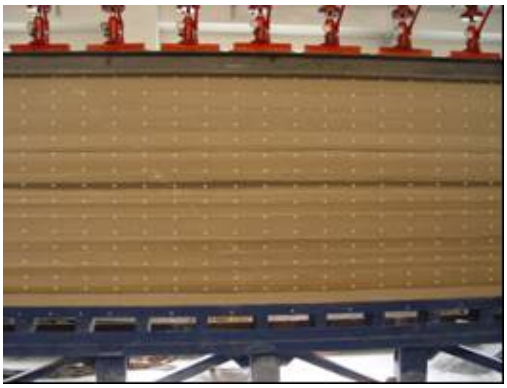

Fig. 4 Photographs of experimental setup

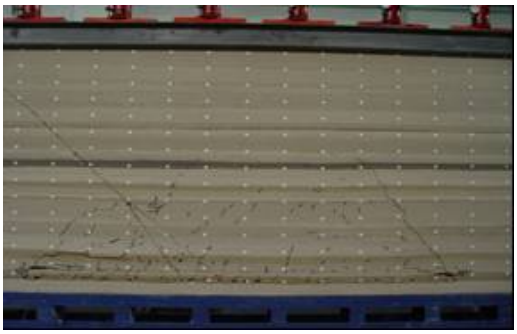

Fig. 5 Experimental observation of deformation and failure of rock strata

6. Conclusions

Based on the DDA method, a discontinuous block system with statistically- generated joints and cracks was applied to analyzing the stress distribution and displacement of upper rock strata during the excavation of a coalmine at 700 meters underneath. The numerical results and experimental validation indicate that the changes of the stress field in rock strata induced by coal extraction, and the displacement, abscises, and subsidence of rock strata, while taking the individual block translation, rotation, and deformation into account, can be efficiently computed by means of DDA method.

It is shown that the half-elliptical stress field of the upper layer rock has initiated during exploration. With the excavation expansion, the local stress field extended in both horizontal and vertical directions. However, when excavating over certain distances, the extension of the stress field stopped in the vertical direction, but successively grew in the horizontal direction. The area where the principle stresses altered can be used to scale the range of abscises or separation of the rock layer during the extraction. The simulation and experiments also show that the immediate roof, at the beginning of excavation, acted like a ‘keystone’ in the discontinuous block system. The effect of interlocking prevented the collapse of fractured blocks. Throughout the extraction, the rupture consecutively happened in different upper rock layers; and,

accordingly, the keystone area, i.e. the interlocked upper layer that supported the loads, moved upwards along with the change of the half-elliptic stress field.

We feel obligated to note that the work done in this paper is just a first attempt to compute the stress and deformation of upper rock strata during the excavation of a coalmine at depth by DDA method. The semi-quantitative analyses for the stress domains, abscises, and span of failed area of upper rock layer have been carried out. Much work related to engineering applications, such as predication of parameters of excavation sequence and the periodic geologically external pressure, needs to be done by DDA.

Acknowledgements

The part of content in this paper has been published in Chinese Journal of Geotechnical Engineering, 2007, 29(2): 268-273.

The authors are grateful for the financial support of National Basic Research Project of China (Grant No. 2002CB412705), Chinese New-Century Outstanding Fellowship Project (Grant No: NCET-05-0215), National Natural Science Foundation of China (Grant No. 50579042) Special thanks go to Dr. Gen-hua Shi for his helpful comments and discussion.

References

1. Guo, W. B., Deng, K. Z. and Zou, Y. F., Research progress and prospects of control technology for surface and overlying strata subsidence. *China Safety Sci. Journal*, 2005; 15(1): 6-10 (in Chinese).
2. Shi, B. M., Yu, Q. X. and Zhou, S. N., Numerical simulation of far-distance rock strata failure and deformation caused by mining protecting stratum. *J. China University Mining Technology,* 2004; 33(3): 259-263 (in Chinese).
3. Ambrozic, T. and Turk, G., Prediction of subsidence due to underground mining by artificial neural networks. *Computers & Geosciences,* 2003; 29(5): 627-637.
4. Guglielmi, Y. Vengeon, J. M., Bertrand, C., Mudry, J., Follacci, J. P. and Giraud, A. Hydro-geochemistry: an investigation tool to evaluate infiltration into large moving rock masses (case study of La Clapiere and Sechilienne alpine landslides). *Bulletin Engng. Geology Environ.,* 2002; 61(4): 311-324.
5. Alejano, L.R. and Ramirez-Oyanguren, P. J., FDM predictive methodology for subsidence due to flat and inclined coal seam mining Taboada. *Int. J. Rock Mech. Min. Sci,* 1999; 36: 475-491
6. Xie, H. P., Zhou, H. W., Wang, J. A., Li, L. Z. and Kwasniewski, M., Application of FLAC to predict ground surface displacement due to coal extraction and its comparative analysis. *Chinese J Rock Mechanics Engineering,* 1999; 18 (4): 397-401 (in Chinese).
7. Xie, H. P., Yu, G.. M., Yang, L. and Zhou, H. W., The influence of proximate fault morphology on ground subsidence due to extraction. *In. J. Rock Mech. Mining Science,* 1998; 35(8): 1107-1111.
8. Yang, G., Chugh, Y. P., Yu, Z. and Salamon, MDG., A numerical approach to subsidence prediction and stress analysis in coal mining using a laminated model. *In. J. Rock Mech. Min. Science & Geomech. Abstr,* 1993; 30(7): 1419-1422.
9. Aston, TRC., Tammemagi, H. Y. and Poon, A. W., A review and evaluation of empirical and analytical subsidence prediction techniques. *Mining Science and Technology,* 1987; 5:(1) 59-69.
10. Salamon, MDG.., Elastic analysis of displacements and stresses induced by the mining of seam or reef deposits - Part 1. Fundamental principles and basic solutions as derived from idealized models. *J S Afr Inst Min Metall,* 1963; 64:128-49.
11. Berry, D. S. and Sales, T. W., An elastic treatment of ground movement due to mining - II. Transversely isotropic ground. *J Mech Phys Solids,* 1961; 9:52-62.
12. Berry, D. S., An elastic treatment of ground movement due to mining - I. Isotropic ground. *J. Mech Phys Solids,* 1960; 8:280-92.
13. Shi, G. H. and Goodman, R. E., Discontinuous deformation Analysis. *Proc. 25th U.S. Symposium on Rock Mech,* 1984, 269-277.
14. Shi, G. H. and Goodman, R. E., Two-dimensional discontinuous deformation analysis. *Int. J. Num. Analy. Methods in Geomech,* 1987; 9: 541-556.
15. Shi, G. H., Discontinuous Deformation Analysis: A new numerical model for the statics and dynamics of block systems. PhD Thesis, Department of Civil Engineering, University of California, Berkeley 1988.
16. Moosavia, M. and Grayelib, R., A model for cable bolt-rock mass interaction: Integration with discontinuous deformation analysis (DDA) algorithm. *Int. J. Rock Mech. & Min Sci,* 2006; 43: 661- 670.
17. Zhang, M., Yang, H. Q. and LI, Z. K., A Coupling Model of the Discontinuous Deformation Analysis Method and the Finite Element Method. *Tsinghua Sci.& Tech.,* 2005; 10(2): 221-226.
18. Wu, J. H., Ohnishi, Y. and Nishiyama, S. Simulation of the mechanical behavior of inclined jointed rock masses during tunnel construction using Discontinuous Deformation Analysis (DDA). *Int. J. Rock Mech. Min. Sci.* 2004; 41(5): 731-743.
19. Hatzor, Y. H., Arzi, A. A., Zaslavsky, Y. and Shapira, A. Dynamic stability analysis of jointed rock slopes using the DDA method: King Herod's Palace, Masada, Israel. *Int. J. Rock Mech. Min. Sci*, 2004; 41(5): 813-832.
20. Yeung, M. R., Jiang, Q. H. and Sun, N. Validation

of block theory and three-dimensional discontinuous deformation analysis as wedge stability analysis methods. *Int. J. Rock Mech. Min. Sci*, 2003; 40(2): 265-275.
21. Song, J. S., Numerical analysis of discontinuous rock masses using modified manifold method. PhD Thesis, Department of Civil Engineering, Kyoto University, 2002.
22. Maclaughlin, M. M., Sitar, N. and Doolin, D. M. and Abbot, T. S., Investigation of slope stability kinetics using discontinuous deformation analysis. *Int. J. Rock Mech. Min Sci,* 2001; 38(5): 753-762.
23. Hatzor, Y. H. and Feintuch, A. The validity of dynamic block displacement prediction using DDA. *Int. J. Rock Mech Min. Sci,* 2001; 38: 599-606.
24. Jing, L. R., Formulation of discontinuous deformation analysis (DDA)-an implicit discrete element model for block systems. *Engineering Geology,* 1998; 49 (3-4): 371-381.
25. Koo, C. Y. and Chern, J. C., Modification of the DDA method for rigid block problems. *Int. J. Rock Mech. Min. Sci. & Geomech. Abstr,* 1998; 35(6): 683-693.
26. Hatzor, Y. H. and Benary, R., The stability of a laminated Voussoir beam: Back analysis of a historic roof collapse using DDA. *Int. J. Rock Mech. Min. Sci. & Geomech. Abstr,* 1998; 35(2): 165-181.
27. Wu, A. Q., Ren, F. and Dong, X. C., A Study on numerical model of DDA and its preliminary application to rock engineering. *Chinese J. Rock Mech. Engineering,* 1997; 16 (5): 411-417 (in Chinese).
28. Lin, C. T., Amader, B., Jung, J. and Dwyer, J., Extensions of Discontinuous Deformation Analysis for Jointed Rock Masses. *Int. J. Rock Mech. Min. Sci. & Geomech. Abstr,* 1996; 33(7): 671-694.
29. Yeung, M. R., Analysis of a mine roof using the DDA method. *Int. J. Rock Mech. Min. Sci. Geomech. Abstr,* 1993; 30(7): 1411-1417.
30. Zhou, H. W., Zuo, J. P., Wang, H.W. and Wang, Z. G., Research report of study on excavation of working face # 2171 (1) of a coal layer 11-2 in Huainan Mining Industrial Corp. China University of Mining & Technology, Beijing, 2005 (in Chinese)

Application of 3D block theory in engineering

XIAOCHU PENG[1] PUJIAN LI[2]

[1] China Institute of Water Resources and Hydropower Research
[2] Northwest Design & Research Institute for Hydroelectric Projects, China Hydroelectric Consultation Group

This paper puts forward for the first time the characterization of block with any degree of complexity and the description of the system of forces in block system.

Keywords: 3D; Block theory; Complex block

1. Introduction

There are many methods used in engineering for the stability analysis of rock slope and tunnels underground, and each has its advantages and shortcomings. At present, a common agreement has been reached between the field of engineering and field of theory, i.e., the stability of rock engineering mainly depends on the system of structure planes, which means that the stability depends on the physical properties and the interdependence between the structure planes. The block system cut by various structure planes has static balance and are stable in natural stress field. However, if the constraint conditions are changed due to external disturbance, the shear force and normal force on the structure plane will change greatly because of the redistribution of internal forces in the block system and sometimes the changes of forces are out of the bearing capacity of structure planes. Thus, if the block on such structure planes is on the boundary and meets the conditions of slumping, it will fail.

After the failure of this block, the boundary conditions of the block system change which will incur redistribution of system of forces of block system and may induce another failure. Hence, a series of chain reaction may be triggered which will cause instability of blocks in large scope. Therefore, if the first patch of instable blocks is stabilized, the whole system will be stable, which will need the least efforts in engineering. What is more, large scale failure or even irreparable damage can be avoided. What mentioned above is just the "Key Block" theory put forward by Shi & Goodman (1989).

Block system bears many loads such as ground stress, seepage force of underground water, structural load and gravity. Since the shape of block is complex, it is very hard to calculate the least supporting force and its direction to stabilize key blocks. Therefore, the traditional analytical stereographic projection method will meet many troubles in its application while solving such problems.

Based on the geometric method put forward in Dr. Shi's block theory, this paper develops programs to model 3D random structure plane and defined structure plane.

2. Modeling of block system

Many block theory programs only define simple convex or concave polyhedron. It is because the authors take a wrong way in the definition of graph; they always divide complex block or loop into many simple convex polyhedrons or convex polygons, then make union-difference calculation of topological graphs, which makes the definition of block too complicated to apply in real calculation. This paper introduces a very simple but effective definition of complex block.

Two factors can be used to exactly define one block, one is the boundary plane of the block, and the other is the normal vector of the plane with direction pointing inward.

Therefore, when search is started in the system of structure plane, if only one structure plane's (defined as mother plane) normal vector is defined and all the other planes connecting with its edges are searched, it can be guaranteed that the normal vector of the plane searched will not penetrate the mother plane, otherwise, it is not the boundary plane of the block searched.

If each plane and its edges are searched without anyone omitted, then the block will be defined. Thus, there is no need to make convex or concave judgment and what we get is a block system with blocks having realistic shape. You may be amazed by the masterpiece of nature when you see the block system you get.

3. Building of force system of block

Block theory holds that the rock cut by many structure planes will form many blocks, each being rigid body with no deformation nor failure; all these blocks form a block system. The deformation of the system occurs on

the structure plane; also, its failure occurs there. The inner forces of the system will become balanced through the deformation of the structure plane.

In this paper, structure plane is believed to be placed with plane springs and all of them have single normal and shear stiffness and Mohr-Coulomb Criterion is adopted as failure criterion.

In this paper, only small deformation is considered, and it is assumed that the block is rigid and cannot deform and that the relative displacement and rotation is very small. Therefore, the normal displacement of boundary planes of each block is very small after the deformation of the block system; it can be taken as a constant.

Normal force forms due to the normal dispalcement of normal plane spring of the structure plane, and shear forces generate because of the displacement of shear spring of the structure plane. However, if two structure planes have the separating normal displacement, no normal tensile stress will generate on the normal spring, then the normal force on the structure plane is 0.

The calculation method of normal force and shear force of spring is introduced below.

3.1 Sub-matrix of normal spring's stiffness

Define the normal vector of one boundary plane of block is $\vec{n}$ $(N_1 \quad N_2 \quad N_3)$, the displacement of point Q_i on the side of block *i* is $(u_i \quad v_i \quad w_i)$; the displacement of corresponding point Q_j on side of block *j* is $(u_j \quad v_j \quad w_j)$; see the figure below.

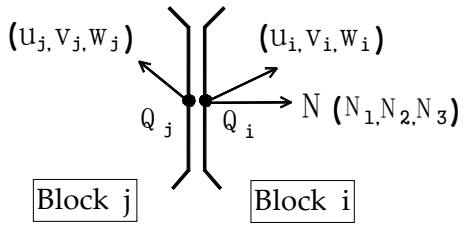

Fig. 1 Definition of normal vector and displacement

The relative displacement $\vec{\delta}$ at point Q can be expressed as:

$$\vec{\delta} = (u_i - u_j)\vec{i} + (v_i - v_j)\vec{j} + (w_i - w_j)\vec{k}$$

The relative displacement in normal direction at point Q can be expressed as:

$$\Delta = \vec{n}.\vec{\delta} = \begin{pmatrix} N_1 & N_2 & N_3 \end{pmatrix} \begin{Bmatrix} u_i - u_j \\ v_i - v_j \\ w_i - w_j \end{Bmatrix} =$$

$$\begin{pmatrix} N_1 & N_2 & N_3 \end{pmatrix} \left(\begin{Bmatrix} u_i \\ v_i \\ w_i \end{Bmatrix} - \begin{Bmatrix} u_j \\ v_j \\ w_j \end{Bmatrix} \right)$$

From the figure, it can be seen that, when $\Delta \le 0$, the springs between two blocks are compressed; when $\Delta \ge 0$, the springs are in tension.

Let $\begin{Bmatrix} u_i \\ v_i \\ w_i \end{Bmatrix} = [T]^{(i)} \{\delta_0\}^{(i)}$ $\quad$ $\begin{Bmatrix} u_j \\ v_j \\ w_j \end{Bmatrix} = [T]^{(j)} \{\delta_0\}^{(j)}$

Where, $\{\delta_0\}^{(i)} = \begin{Bmatrix} u_0 \\ v_0 \\ w_0 \\ \gamma_{x0} \\ \gamma_{y0} \\ \gamma_{z0} \end{Bmatrix}_i$ $\quad$ $\{\delta_0\}^{(j)} = \begin{Bmatrix} u_0 \\ v_0 \\ w_0 \\ \gamma_{x0} \\ \gamma_{y0} \\ \gamma_{z0} \end{Bmatrix}_j$

$\{\delta_0\}^{(i)}$ and $\{\delta_0\}^{(j)}$ are displacement and rotation of the centroid of block i and block j respectively.

$$[T]^{(i)} = \begin{bmatrix} 1 & 0 & 0 & 0 & z - z_{0i} & -(y - y_{0i}) \\ 0 & 1 & 0 & -(z - z_{0i}) & 0 & (x - x_{0i}) \\ 0 & 0 & 1 & (y - y_{0i}) & -(x - x_{0i}) & 0 \end{bmatrix}$$

Where, (x_{0i}, y_{0i}, z_{0i}) is the coordinates of the centroid of block *i*.

$$[T]^{(j)} = \begin{bmatrix} 1 & 0 & 0 & 0 & z - z_{0j} & -(y - y_{0j}) \\ 0 & 1 & 0 & -(z - z_{0j}) & 0 & (x - x_{0j}) \\ 0 & 0 & 1 & (y - y_{0j}) & -(x - x_{0j}) & 0 \end{bmatrix}$$

Where, (x_{0j}, y_{0j}, z_{0j}) is the coordinates of the centroid of block *j*.

Suppose the normal stiffness of springs on the structure plane is a constant, then the potential energy Π_N of the structure plane is,

$$\Pi_N = \frac{1}{2} \iint_{\Omega} p\Delta^2 dA$$

$$\Pi_N = \frac{1}{2}\iint_\Omega p((N_1 \quad N_2 \quad N_3)(\begin{Bmatrix} u_i \\ v_i \\ w_i \end{Bmatrix} - \begin{Bmatrix} u_j \\ v_j \\ w_j \end{Bmatrix}))^2 dA$$

=

$$\frac{p}{2}\iint_\Omega ((N_1 \quad N_2 \quad N_3)([T]^{(i)}\{\delta_0\}^{(i)} - [T]^{(j)}\{\delta_0\}^{(j)}))^2 dA$$

=

$$\frac{p}{2}\iint_\Omega (\sum_{n=1}^{3} N_n (\sum_{m=1}^{6} T^{(i)}{}_{nm} \times \delta^{(i)}{}_{0m} - \sum_{m=1}^{6} T^{(j)}_{nm} \times \delta^{(j)}_{0m}))^2 \, dA$$

By differentiating Π_N and minimizing it, four 6×6 sub-matrix of stiffness can be got and they can be added into $[K_{ii}], [K_{ij}], [K_{ji}], [K_{jj}]$.

$$\frac{\partial \Pi_N}{\partial \delta^{(i)}{}_{0p}} = p\iint_\Omega \sum_{n=1}^{3} N_n (\sum_{p=1}^{6} T^{(i)}_{np} \times \delta^{(i)}_{0p} - \sum_{p=1}^{6} T^{(j)}_{np} \times \delta^{(j)}_{0p}) \times \sum_{n=1}^{3} N_n T^{(i)}_{np} dA$$

$$\frac{\partial^2 \Pi_N}{\partial \delta^{(i)}{}_{0p} \partial \delta^{(i)}{}_{0q}} = p\iint_\Omega (\sum_{n=1}^{3} N_n T^{(i)}_{np})(\sum_{n=1}^{3} N_n T^{(i)}_{nq}) dA$$

$$\Rightarrow \textit{Row } p \textit{ column } q \textit{ in } [K_{ii}]$$

$$\frac{\partial^2 \Pi_N}{\partial \delta^{(i)}{}_{0p} \partial \delta^{(j)}{}_{0q}} = -p\iint_\Omega (\sum_{n=1}^{3} N_n T^{(i)}_{np})(\sum_{n=1}^{3} N_n T^{(j)}_{nq}) dA$$

$$\Rightarrow \textit{Row } p \textit{ column } q \textit{ in } [K_{ij}]$$

$$\frac{\partial \Pi_N}{\partial \delta^{(j)}_{0p}} = -p\iint_\Omega \sum_{n=1}^{3} N_n (\sum_{p=1}^{6} T^{(i)}_{np} \times \delta^{(i)}_{0p} - \sum_{p=1}^{6} T^{(j)}_{np} \times \delta^{(j)}_{0p}) \times \sum_{n=1}^{3} N_n T^{(i)}_{np} dA$$

$$\frac{\partial^2 \Pi_N}{\partial \delta^{(j)}_{0p} \partial \delta^{(j)}_{0q}} = p\iint_\Omega \sum_{n=1}^{3} (N_n \times T^{(j)}_{np}) \times \sum_{n=1}^{3} (N_n \times T^{(j)}_{nq}) dA$$

$$\Rightarrow \textit{Row } p \textit{ column } q \textit{ in } [K_{jj}]$$

$$\frac{\partial^2 \Pi_N}{\partial \delta^{(j)}_{0p} \partial \delta^{(i)}_{0q}} = -p\iint_\Omega \sum_{n=1}^{3} (N_n \times T^{(j)}_{np}) \times \sum_{n=1}^{3} (N_n \times T^{(i)}_{nq}) dA$$

$$\Rightarrow \textit{Row } p \textit{ column } q \textit{ in } [K_{ji}]$$

3.2 Submatrix of stiffness for shear spring

Suppose plane P(a,b,c) passes the original point of the coordinate system, its function is

$$ax+by+cz=0 \qquad (1)$$

where $a2+b2+c2=1$

Suppose one vector is $S(s_1,s_2,s_3)$, its initial point is the original point of the coordinate system. Draw one ray perpendicular to plane P while passing point (s_1,s_2,s_3) , then the function of the line is

$$\begin{cases} x = s_1 + ta \\ y = s_2 + tb \\ z = s_3 + tc \end{cases} \qquad (2)$$

Connecting the cross point of ray and plane P and the original point, the project of vector S on plane P can be obtained.

Substitute equation(2) into equation (1), then

$$a(s_1 + ta) + b(s_2 + tb) + c(s_3 + tc) = 0$$

It can be solved that,

$$t = -(as_1 + bs_2 + cs_3)/(a^2 + b^2 + c^2) = -(as_1 + bs_2 + cs_3)$$

Substitute t into equation(2), then the cross point of the line and plane P can be obtained and the square of the distance between the cross point and the original point is

$$\Delta^2 = (s_1 + ta)^2 + (s_2 + tb)^2 + (s_3 + tc)^2$$

$$= {s_1}^2 + {s_2}^2 + {s_3}^2 + \text{t2(a2+b2+c2)+2t(as1+bs2+cs3)}$$

$$= {s_1}^2 + {s_2}^2 + {s_3}^2 + t^2 + 2t \times (-t)$$

$$= {s_1}^2 + {s_2}^2 + {s_3}^2 - \text{t2}$$

$$= {s_1}^2 + {s_2}^2 + {s_3}^2 - (as_1 + bs_2 + cs_3)^2 \qquad (3)$$

Where, Δ is the project of S on plane P.

Suppose the displacement of point Q on side of block i is $\begin{Bmatrix} u_i \\ v_i \\ w_i \end{Bmatrix}$, and $\begin{Bmatrix} u_j \\ v_j \\ w_j \end{Bmatrix}$ for the corresponding point on side of j. Then, the relative displacement is $\begin{Bmatrix} u_i - u_j \\ v_i - v_j \\ w_i - w_j \end{Bmatrix}$; the project of this relative displacement is its relative shear displacement

$$s_1 = u_i - u_j = \sum_{p=1}^{6} T^{(i)}_{1p} \delta^{(i)}_{0p} - \sum_{p=1}^{6} T^{(j)}_{1p} \delta^{(j)}_{0p}$$

$$s_2 = v_i - v_j = \sum_{p=1}^{6} T^{(i)}_{2p} \delta^{(i)}_{0p} - \sum_{p=1}^{6} T^{(j)}_{2p} \delta^{(j)}_{0p}$$

$$s_3 = w_i - w_j = \sum_{p=1}^{6} T^{(i)}_{3p} \delta^{(i)}_{0p} - \sum_{p=1}^{6} T^{(j)}_{3p} \delta^{(j)}_{0p}$$

Supppose the normal vector of structure plane is (N_1, N_2, N_3), and the shear stiffness is p, then the shear potential Π_s of shear springs is,

$$\Pi_s = \frac{1}{2} p \iint_{\Omega} \Delta^2 dA$$

$$= \frac{1}{2} P \iint_{\Omega} ((1-N_1^2)s_1^2 + (1-N_2^2)S_2^2 + (1-N_3^2)S_3^2 -$$

$$- 2N_1N_2S_1S_2 - 2N_2N_3S_2S_3)dA$$

By differentiating Π_s and minimizing it, four 6×6 submatrix of stiffness can be got.

$$\frac{\partial^2 \Pi_s}{\partial \delta_{0p}^{(i)} \partial \delta_{0q}^{(i)}} \Rightarrow \quad \Rightarrow \textit{Row p column q in } [K_{ii}]$$

$$\frac{\partial^2 \Pi_s}{\partial \delta_{0p}^{(i)} \partial \delta_{0q}^{(j)}} \Rightarrow \quad \Rightarrow \textit{Row p column q in } [K_{ij}]$$

$$\frac{\partial^2 \Pi_s}{\partial \delta_{0jp} \partial \delta_{0jq}} \Rightarrow \quad \Rightarrow \textit{Row p column q in } [K_{jj}]$$

$$\frac{\partial^2 \Pi_s}{\partial \delta_{0jp} \partial \delta_{0iq}} \Rightarrow \Rightarrow \textit{Row p column q in } [K_{ji}]$$

Note: the mechanical meaning of $[K_{ij}]$ in row p column q is: the displacement of block j in direction p(or rotation around axis p) leads to the loading on block i in direction q(or couple around axis q).

3.3 Submatrix of frictional force

The frictional force is:

$$F = p_N \times tg(\varphi) + cA$$

As mentioned above, the projection of relative displacement $\vec{\delta}$ at point Q on boundary plane is:

$$\vec{\delta} - (\vec{n} \cdot \vec{\delta})\vec{n} =$$

$$((u_i - u_j)\vec{i} + (v_i - v_j)\vec{j} + (w_i - w_j)\vec{k}) -$$

$$(N_1 \times (u_i - u_j) + N_2 \times (v_i - v_j) + N_3 \times (w_i - w_j))$$

$$(N_1\vec{i} + N_2\vec{j} + N_3\vec{k})$$

et

$$s = N_1 \times (u_i - u_j) + N_2 \times (v_i - v_j) + N_3 \times (w_i - w_j)$$

Then, the projection of relative displacement at point Q on boundary plane is:

$$\vec{\delta} - (\vec{n} \cdot \vec{\delta})\vec{n} =$$

$$((u_i - u_j) - s \times N_1)\vec{i} + ((v_i - v_j) - s \times N_2)\vec{j} +$$

$$((w_i - w_j) - s \times N_3)\vec{k}$$

Assemble the stiffness sub-matrix of normal and shear spring above into the global stiffness matrix; then assemble the external force on each plane to get the general external force array. By solving the equilibrium equation $[k] \times \{\delta\} = \{f\}$, the displacement of the centroid of each block can be obtained. The relative displacement of structure planes can be obtained according to the displacement of the centroid of two adjacent blocks through transition matrix; then, the normal force and shear force on the structure plane can also be obtained.

The shear force on each structure plane is judged according to Mohr-Coulomb criterion. Those shear forces not meeting the criterion will be taken as external force and be redistributed within the block system. That is, these forces will be balanced by adjusting normal and shear forces on other structure planes.

For the block with external boundary, if the forces on structure plane cannot meet Mohr-Coulomb criterion and the block is movable in the view of topology because of the moving direction caused by shear force or couple, then this block is unstable.

4 Conclusions

The author of this paper has successfully applied 3D block theory in many analyses of projects. This theory can very clearly instruct engineers in taking reinforcing measures in engineering, and because of the 3D effect and clear expression of complex structure planes, engineers can also participate in the analysis and judgment whether the final conclusion is correct or not, which facilitates better communication between researchers and users of the research.

References

Shi Gen-Hua and Goodman R.E. The Key Blocks of Unroolled Joint Trace in Developed Maps of Tunnel Walls Int. J. for Num.and And. Methods Geo. Vol.13,No. 2,Mar-Apr. 1989

Implementation of a trilinear hexahedron mesh into Three-Dimensional Discontinuous Deformation Analysis (3-D DDA)

S.A. BEYABANAKI[1], A. JAFARI[1], M.R. YEUNG[2] and S.O. BIABANAKI[3]

[1] School of Mining Engineering, University College of Engineering, University of Tehran, Tehran, Iran
[2] Department of Civil Engineering, College of Engineering, California State Polytechnic University, Pomona, USA
[3] Department of Civil Engineering, Sharif University of Technology, Tehran, Iran

The Three-Dimensional Discontinuous Deformation Analysis (3-D DDA) with a first-order displacement function was extended by incorporating an eight-node hexahedron mesh into a 3-D block, to enhance 3-D DDA's capabilities of modeling deformable blocks. The matrices of the equilibrium equations for this new model are given in detail. An illustrative example is presented to show the improvement achieved by this model. The calculated results show close agreement with the theoretical solutions.

Keywords: Three-Dimensional Discontinuous Deformation Analysis (3-D DDA); Trilinear hexahedron finite element; Rock block; Numerical method

1. Introduction

The Discontinuous Deformation Analysis (DDA) is well-suited for investigating fractured rock mass behavior important to many geotechnical and structural problems (Shi 1993). In the original DDA formulation, a first-order displacement function was used to model block deformations, which does not allow for variable stress/strain distribution within a block. This approximation precludes the application of the first-order polynomial function to problems with significant stress variations within blocks. This may yield unreasonable results when the block deformation is large or when the geometry of the block is irregular. In two dimensions, to overcome this shortcoming, some approaches have been attempted. One approach adopted was to glue small blocks together in an artificial manner to form a larger block. Ma et al. (1996), Koo et al. (1996) and Hsuing (2001) implemented high-order displacement functions into the DDA algorithm. Shyu (1993), Chang (1994) and Grayeli & Mortazavi (2006) implemented finite element mesh into the original DDA blocks to account for stress variations within the blocks. In 3-D, there have been some published works but they use a linear displacement function as in the original 2-D DDA, so the stresses and strains within each block are constant. This paper presents the implementation of an eight-node hexahedron element into the 3-D DDA algorithm. The program code has been developed, and to demonstrate the capabilities of the modified 3-D DDA code a cantilever beam is analyzed. The calculated results agree well with theoretical solutions.

2. Coupling of 3-D FEM and 3-D DDA

Since 3-D DDA conforms to the principle of minimum total potential energy, the total potential energy is the summation of all potential energy sources for each block. The potential energy formulated in the following sections includes that from initial and induced stresses, point loads, body forces, inertia forces and displacement constraints, as well as the potential energy from the interaction between two elements such as a normal contact. For each of the cases stated above, the element or nodal matrices of stiffness and force are formed by taking the derivatives with respect to displacement variables from the corresponding potential energy. Taking the direct summation of these individual submatrices to form the global stiffness matrix $[K]$ and force matrix $[F]$, the simultaneous equations of equilibrium are then established.

The simultaneous equilibrium equations derived by minimizing the total potential energy for a system with N number of nodes have the following form:

$$\begin{bmatrix} [K_{11}] & [K_{12}] & [K_{13}] & \dots & [K_{1N}] \\ [K_{21}] & [K_{22}] & [K_{23}] & \dots & [K_{2N}] \\ [K_{31}] & [K_{32}] & [K_{33}] & \dots & [K_{3N}] \\ \vdots & \vdots & \vdots & \ddots & \vdots \\ [K_{N1}] & [K_{N2}] & [K_{N3}] & \dots & [K_{NN}] \end{bmatrix} \begin{bmatrix} \{D_1\} \\ \{D_2\} \\ \{D_3\} \\ \vdots \\ \{D_N\} \end{bmatrix} = \begin{bmatrix} \{F_1\} \\ \{F_2\} \\ \{F_3\} \\ \vdots \\ \{F_N\} \end{bmatrix} \tag{1}$$

As in the FEM (Zienkiewicz & Taylor 2000), the nodal displacements are chosen as unknown variables and each node has three degrees-of-freedom for the three-dimensional case. $[K_{ij}]$ in the global stiffness matrix is a 3×3 submatrix and $\{D_i\}$ - the unknown vector, and $\{F_i\}$ - the force vector, are 3×1 submatrices.

3. Derivations of Submatrices of Equilibrium Equation for Hexahedron Elements

The displacement field $\{u\,v\,w\}^T$ of eight-node isoparametric elements can be described as:

$$\begin{Bmatrix} u \\ v \\ w \end{Bmatrix} = \left[\widetilde{N}(x,y,z)\right]_{3\times 24} \{D\}_{24\times 1} \tag{2}$$

Where the matrices of shape function and nodal displacements, respectively, are:

$$[\widetilde{N}(x,y,z)] = \begin{bmatrix} \widetilde{N}_1(x,y,z) & 0 & 0 \\ 0 & \widetilde{N}_1(x,y,z) & 0 \\ 0 & 0 & \widetilde{N}_1(x,y,z) \\ \widetilde{N}_2(x,y,z) & 0 & 0 \\ 0 & \widetilde{N}_2(x,y,z) & 0 \\ 0 & 0 & \widetilde{N}_2(x,y,z) \\ & \vdots & \\ \widetilde{N}_8(x,y,z) & 0 & 0 \\ 0 & \widetilde{N}_8(x,y,z) & 0 \\ 0 & 0 & \widetilde{N}_8(x,y,z) \end{bmatrix}^T \tag{3}$$

$$\{D\} = \{u_1\ v_1\ w_1\ u_2\ v_2\ w_2\ \ldots\ u_8\ v_8\ w_8\}^T \tag{4}$$

Since it is difficult to establish the shape function $[\widetilde{N}(x,y,z)]$ in a simple form to depict the element with a general shape, a transformation from global Cartesian to natural coordinates through mapping is necessary. The shape functions of natural coordinates (ξ,η,ζ) described in a $2\times 2\times 2$ cube with origin $(0,0,0)$ at its center is used to map the eight-node element shape functions of the global Cartesian coordinates.
The interpolation for the global Cartesian coordinates in each element may be expressed in terms of the shape functions as:

$$\begin{cases} x = \sum_{l=1}^{8} N_l(\xi,\eta,\zeta)\, x_l \\ y = \sum_{l=1}^{8} N_l(\xi,\eta,\zeta)\, y_l \\ z = \sum_{l=1}^{8} N_l(\xi,\eta,\zeta)\, z_l \end{cases} \tag{5}$$

Where (x_l, y_l, z_l) $l = 1, 2, \ldots, 8$ are the values of coordinates at the nodes, describing the isoparametric elements.

3.1 Stiffness Matrix

At each time step, the elastic strain energy stored by the stresses of the elements is:

$$\pi_e = \iiint_V \frac{1}{2}\{\varepsilon\}^T.\{\sigma\}\,dxdydz \tag{6}$$

Where

$$\{\varepsilon\} = \{\varepsilon_x\ \ \varepsilon_y\ \ \varepsilon_z\ \ \gamma_{yz}\ \ \gamma_{zx}\ \ \gamma_{xy}\}^T$$

and

$$\{\sigma\} = \{\sigma_x\ \ \sigma_y\ \ \sigma_z\ \ \tau_{yz}\ \ \tau_{zx}\ \ \tau_{xy}\}^T$$

The stress-strain relationship is assumed to be linear at each time step. Therefore:

$$\{\sigma\} = [E].\{\varepsilon\} \tag{7}$$

Where

$$[E] = \frac{E}{(1+\nu)(1-2\nu)} \begin{bmatrix} 1-\nu & \nu & \nu & 0 & 0 & 0 \\ \nu & 1-\nu & \nu & 0 & 0 & 0 \\ \nu & \nu & 1-\nu & 0 & 0 & 0 \\ 0 & 0 & 0 & \frac{1}{2}-\nu & 0 & 0 \\ 0 & 0 & 0 & 0 & \frac{1}{2}-\nu & 0 \\ 0 & 0 & 0 & 0 & 0 & \frac{1}{2}-\nu \end{bmatrix} \tag{8}$$

In which, E and ν are the Young's modulus and Poisson's ratio, respectively.
Based on the small strain theory:

$$\{\varepsilon\} = \begin{bmatrix} \partial/\partial x & 0 & 0 & \partial/\partial y & \partial/\partial z & 0 \\ 0 & \partial/\partial y & 0 & \partial/\partial x & 0 & \partial/\partial z \\ 0 & 0 & \partial/\partial z & 0 & \partial/\partial x & \partial/\partial y \end{bmatrix}^T . \begin{Bmatrix} u \\ v \\ w \end{Bmatrix} = [d].[\widetilde{N}]\{D\} = [B]\{D\} \tag{9}$$

That $[B]$ is a 6×24 matrix for eight-node hexahedron elements.

As in the FEM, the matrix of the strain shape function with respect to the natural coordinates, $[B(\xi,\eta,\zeta)]$, is then obtained. Therefore, the strain energy of element i is described as:

$$\pi_e = \frac{1}{2}\{D_i\}^T \left(\iiint_V [B_i]^T [E_i][B_i]\,dxdydz\right)\{D_i\} \tag{10}$$

After taking derivatives with respect to displacement variables of the strain energy π_e of element i, the 24×24 element stiffness matrix $[K_{ii}]$ is obtained as:

$$\begin{aligned}[K_{ii}] &= \iiint_V [B_i(x,y,z)]^T [E_i][B_i(x,y,z)]\,dxdydz \\ &= \int_{-1}^{1}\int_{-1}^{1}\int_{-1}^{1} [B_i(\xi,\eta,\zeta)]^T [E_i][B_i(\xi,\eta,\zeta)]\left\|J(\xi,\eta,\zeta)\right\| \\ &\qquad d\xi d\eta d\zeta\end{aligned} \tag{11}$$

Where $\|J(\xi,\eta,\zeta)\|$ is the determinant of the Jacobian matrix:

$$[J] = \begin{bmatrix} \frac{\partial x}{\partial \xi} & \frac{\partial x}{\partial \eta} & \frac{\partial x}{\partial \zeta} \\ \frac{\partial y}{\partial \xi} & \frac{\partial y}{\partial \eta} & \frac{\partial y}{\partial \zeta} \\ \frac{\partial z}{\partial \xi} & \frac{\partial z}{\partial \eta} & \frac{\partial z}{\partial \zeta} \end{bmatrix} \tag{12}$$

$[K_{ii}]$ is then added to the simultaneous equilibrium equations.

3.2 Initial Stress

For element i, the potential energy of initial stresses $\{\sigma_i^\circ\}$ is described as:

$$\begin{aligned}\pi_\sigma &= \iiint_V (\varepsilon_{x_i}\sigma_{x_i}^0 + \varepsilon_{y_i}\sigma_{y_i}^0 + \varepsilon_{z_i}\sigma_{z_i}^0 + \gamma_{yz_i}\tau_{yz_i}^0 + \gamma_{zx_i}\tau_{zx_i}^0 \\ &\qquad + \gamma_{xy_i}\tau_{xy_i}^0)\,dxdydz \\ &= \iiint_V \{\varepsilon_i\}^T.\{\sigma_i^0\}\,dxdydz\end{aligned} \tag{13}$$

That is described as:

$$\pi_\sigma = \{D_i\}^T \iiint_V [B_i(x,y,z)]^T \{\sigma_i^\circ(x,y,z)\}\,dxdydz \tag{14}$$

Taking derivatives of the potential energy π_σ, a 24×1 element force matrix $\{F_i\}$ with the following form is added to the global force matrix in the simultaneous equations:

$$\begin{aligned}\{F_i\} &= -\iiint_V [B_i(x,y,z)]^T \{\sigma_i^\circ(x,y,z)\}\,dxdydz \\ &= -\int_{-1}^{1}\int_{-1}^{1}\int_{-1}^{1} [B_i(\xi,\eta,\zeta)]^T \{\sigma_i^\circ(x,y,z)\}\left\|J(\xi,\eta,\zeta)\right\| \\ &\qquad d\xi d\eta d\zeta\end{aligned} \tag{15}$$

3.3 Point Load

The point loading force $\{F_x\ F_y\ F_z\}^T$ acts at point (x,y,z) of element i, the potential energy due the point loading is:

$$\pi_p = -\{u\ v\ w\}\begin{Bmatrix} F_x \\ F_y \\ F_z \end{Bmatrix} \tag{16}$$

For hexahedron isoparametric element i, the potential energy is given by:

$$\begin{aligned}\pi_p &= -\{D_i\}^T [\tilde{N}_i(x,y,z)]^T \begin{Bmatrix} F_x \\ F_y \\ F_z \end{Bmatrix} = -\{D_i\}^T [N_i(\xi,\eta,\zeta)]^T \\ &\quad .\begin{Bmatrix} F_x \\ F_y \\ F_z \end{Bmatrix}\end{aligned} \tag{17}$$

After taking derivatives of the potential energy, the 24×1 element force matrix $\{F_i\}$ is obtained for the eight-node element:

$$\{F_i\} = [N_i(\xi,\eta,\zeta)]^T \begin{Bmatrix} F_x \\ F_y \\ F_z \end{Bmatrix} \tag{18}$$

This is added to the global force matrix in the simultaneous equilibrium equations.

3.4 Force of Inertia

Denote $\{u(t)\ v(t)\ w(t)\}^T$ as the time dependent displacements of any point (x,y,z) of element i. The force of inertia per unit volume is:

$$\begin{Bmatrix} f_x \\ f_y \\ f_z \end{Bmatrix} = -M \frac{\partial^2}{\partial t^2} \begin{Bmatrix} u(t) \\ v(t) \\ w(t) \end{Bmatrix} = -M \left[\tilde{N}_i(x,y,z)\right] \frac{\partial^2 \{D_i\}}{\partial t^2} \tag{19}$$

where M = mass per unit volume.

The potential energy of the inertia force of element i is in the same form as that of the original 3-D DDA and is given by:

$$\pi_i = M\{D_i\}^T \left[\iiint_V \left[\tilde{N}_i(x,y,z)\right]^T \left[\tilde{N}_i(x,y,z)\right] dxdydz \right]$$

$$\frac{\partial^2 \{D_i(0)\}}{\partial t^2} = \{D_i\}^T \left[\iiint_V \left[\tilde{N}_i(x,y,z)\right]^T \left[\tilde{N}_i(x,y,z)\right] dxdydz \right] . \left(\frac{2M}{\Delta^2}\{D_i\} - \frac{2M}{\Delta}\{V_i(0)\} \right) \tag{20}$$

Where Δ is the time step, and $\{V_i(0)\}$ is the element velocity accumulated from the previous time step.

After taking the derivatives with respect to displacement variables of the potential energy $[K_{ii}]$ and $\{F_i\}$ are then added to the simultaneous equilibrium equations:

$$[K_{ii}] = \frac{2M}{\Delta^2} \left[\iiint_V \left[\tilde{N}_i(x,y,z)\right]^T \left[\tilde{N}_i(x,y,z)\right] dxdydz \right] = \frac{2M}{\Delta^2} \left[\int_{-1}^{1}\int_{-1}^{1}\int_{-1}^{1} [N_i(\xi,\eta,\zeta)]^T [N_i(\xi,\eta,\zeta)] \left\|J(\xi,\eta,\zeta)\right\| d\xi d\eta d\zeta \right] \tag{21}$$

$$\{F_i\} = \frac{2M}{\Delta} \left[\iiint_V \left[\tilde{N}_i(x,y,z)\right]^T \left[\tilde{N}_i(x,y,z)\right] dxdydz \right] . \{V_i(0)\} = \frac{2M}{\Delta} \left[\int_{-1}^{1}\int_{-1}^{1}\int_{-1}^{1} [N_i(\xi,\eta,\zeta)]^T [N_i(\xi,\eta,\zeta)] \left\|J(\xi,\eta,\zeta)\right\| d\xi d\eta d\zeta \right] . \{V_i(0)\} \tag{22}$$

3.5 Fixed Point

When a point (x,y,z) in an element i is to be fixed, a very strong constraint spring with stiffness p is used at this point. The energy of the constraint spring can be expressed as:

$$\pi_c = \frac{p}{2} \{u \quad v \quad w\} \begin{Bmatrix} u \\ v \\ w \end{Bmatrix} \tag{23}$$

For hexahedron isoparametric element i, the potential energy is:

$$\pi_c = \frac{p}{2} \{D_i\}^T [N_i(\xi,\eta,\zeta)]^T [N_i(\xi,\eta,\zeta)] \{D_i\} \tag{24}$$

The 24×24 element stiffness matrix $[K_{ii}]$ is obtained after taking the derivatives with respect to displacement variables of the potential energy π_c:

$$[K_{ii}] = p\, [N_i(\xi,\eta,\zeta)]^T [N_i(\xi,\eta,\zeta)] \tag{25}$$

This matrix is then added to the simultaneous equilibrium equations.

4. Verification of the New Modified 3-D DDA

In this section the application of the modified 3-D DDA is presented for a typical example of a cantilever beam subjected to two concentrated loads at its free end.

The cantilever beam geometry shown in Fig. 1 was analyzed using the original 3-D DDA and the modified version with 50 eight-node elements to discretize the beam. Dimensions of the beam are 8 m in length and 1 m in height and width, and the Young's modulus and Poisson's ratio were $E = 3 \times 10^8\ Pa$ and $\nu = 0.2$, respectively.

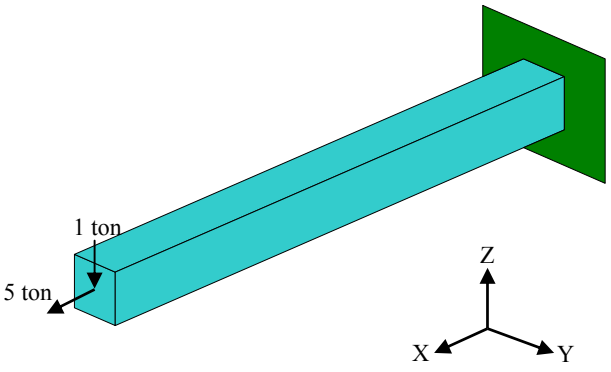

Fig. 1: Cantilever beam subjected to two forces.

The axial deformation along the axis of a beam subjected to an axial load is (Popov 1996):

$$\Delta = \frac{P.x}{A.E} \tag{26}$$

where Δ is the axial deformation; x is the distance from the fixed end; P is a concentrated load acting at the middle point of the free end; A is the cross-sectional area; and E is the Young's modulus of the beam. The closed form solution for the beam deflection (v) along its axis can be written as below (Popov 1996):

$$v = \frac{P}{6EI}(2L^3 - 3L^2x + x^3) \qquad (27)$$

where L is the length of the beam; and I is the moment of inertia of beam cross section. To show the capabilities of the modified 3-D DDA, the beam deformation was simulated. The results are plotted in Figs 2 and 3 for obtained displacements along the X and Z directions, respectively.

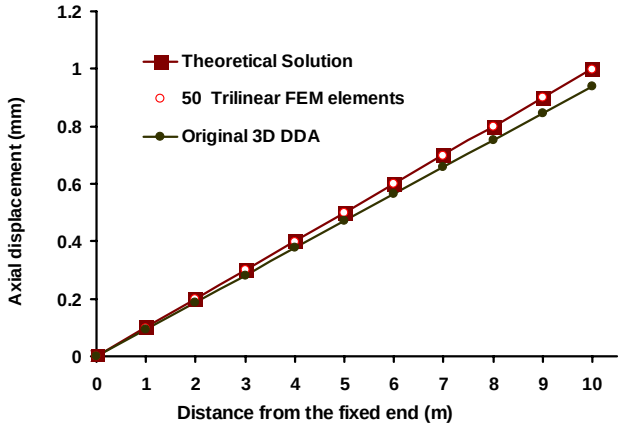

Fig. 2: Axial deformation of the cantilever beam calculated by analytical solution and 3-D DDA.

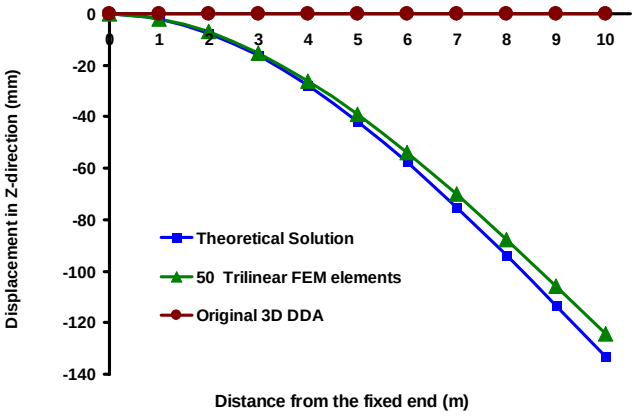

Fig. 3: Deflection of the cantilever beam calculated by analytical solution and 3-D DDA.

Figure 2 shows that the 3-D DDA modeling gives more accurate results when a finite element meshed block is used. As can be seen from Fig. 3, results of the original 3-D DDA is far from the theoretical solutions. Using 50 Trilinear elements to discretize the beam, one can calculate the deflection at the free end that is about 93% of the theoretical value.

5. Conclusions

The main purpose of using a finite element mesh within each block is to improve the deformation capability. In this study, a more powerful version of 3-D DDA method was developed using eight-node hexahedral elements. This enhanced the deformation capability of 3-D DDA significantly, thus making it a more suitable tool for accurate calculations and practical applications. The matrices of the equilibrium equations for this new method were presented. The successful application of the modified 3-D DDA to a problem with known solutions was demonstrated. The calculated results show good agreement with the theoretical solutions; however, it is believed that more verification and refinement of the new 3-D DDA is required to make it a more useful tool for practical applications.

Acknowledgements

The authors would like to thank Dr. Gen-Hua Shi for his valuable comments.

References

Chang, C.S. Nonlinear dynamic discontinues deformation analysis with finite element meshed block system, PhD thesis, Department of Civil Engineering, University of California, Berkeley, 1994.

Grayeli, R. and Mortazavi, A. Discontinuous deformation analysis with second-order finite element meshed block, International Journal for Numerical and Analytical Methods in Geomechanics, 2006, **30**(15), 1545-1561.

Hsuing, S.M. Discontinuous Deformation Analysis (DDA) with nth-order polynomial displacement function, Proceedings of the 38th U.S. Rock Mechanics symposium, Washington D.C., July 7-10, 2001; 1437-1444.

Koo, C.Y. and Chern, J.C. The development of DDA with third order displacement function, Proceedings of the First International Forum on Discontinuous Deformation Analysis (DDA) and Simulations of Discontinuous Media, June 12-14, TSI Press: USA, 1996; 342-349.

Ma, M. Y., Zaman, M. and Zhou, J.H. Discontinuous deformation analysis using the third-order displacement function, Proceedings of the First International Forum on Discontinuous Deformation Analysis (DDA) and Simulations of Discontinuous Media, June 12-14, TSI Press: USA, 1996; 383-394.

Shi, G. H. Block System Modeling by Discontinuous Deformation Analysis, Computational Mechanics Publication: Southampton, U.K. 1993.

Shyu, K.K. Nodal-based Discontinuous Deformation Analysis, PhD thesis, Department of Civil Engineering, University of California, Berkeley. 1993.

Zienkiewicz, O.C. and Taylor, R.L., Finite Element Method, Butterworth Heinemann, London, 2000.

Numerical Simulation of Mechanical Characteristics of Coarse Granular Materials by Discontinuous Deformation Analysis

GUO PEIXI [1,2], LIN SHAOZHONG [2]

[1] Geotechnical Research Institute, Hohai University, Nanjing, P. R. CHINA
[2] DDA center, Yangtze River Scientific Research Institute, Wuhan, P. R. CHINA

In this paper, DDA is used to study the mechanical characteristics of coarse granular materials. In order to establish the numerical simulation specimen, 2-D random particle-generating algorithm of granular materials is studied. Loose particles are randomly generated according to the gradation curve. Under the action of the gravitational load, the packing process of the particles inside a rectangular container is simulated by DDA so that a heap of the particles which contact each other is formed. Based upon the heap, the specimen is then established. Referring to the loading process of the tri-axial laboratory test, 2-D numerical simulation on the mechanical characteristics of coarse granular materials is performed also by the DDA. The stress-strain curves obtained by the numerical simulation are basically in agreement with the results by the tri-axial laboratory test. It indicates the numerical simulation is suitable for the mechanical characteristics research of coarse granular materials. In addition, the distribution of several fabric elements about interaction between particles is also presented.

Keywords: Coarse granular material; Random distribution; Mechanical characteristics; Numerical analysis; Discontinuous Deformation Analysis

1. Introduction

The coarse granular material is the chief material of rock fill dams. There are three methods for the mechanical research of coarse granular materials: indoor test, in situ test and numerical simulation. Because of the limits of the specimen size and the equipment ability, the test can not solve problems such as gradation similarity and complicated loading route. Numerical simulation does not require much labor or many recourses and it is not limited by time and space. The most important benefit is that it has no limit to the size of particles. Therefore it can be a supplement to the indoor test and in situ test.

Coarse granular material is a discontinuous medium. DDA, DEM and PFC, which is based on DEM, are the techniques widely used in the numerical simulation of discontinuous deformation. PFC computation is simple. However, particles are assumed circular discs or spherical balls, which are different from real granular materials in their shapes. A tri-axial test showed the behavior of ball aggregate was classically ideal elastico-plastic and was quite different from that of general granular materials. Therefore, it was undesirable to use circle or ball aggregate to reasonably model the mechanical behavior of coarse granular materials (Cheng & Ding 2006).

DDA and DEM can handle arbitrary polygonal particles and are suitable for the mechanical analysis of coarse granular materials. Liu & Gao (2003) described soil particles by a uniform equilateral polygon with eleven edges and DDA was applied to simulate soil deformation in plane strain. According to the comparison between simulating results and the result of laboratory test, it has been proved that DDA is a powerful tool for analyzing the constitutive relationship for soil.

In this paper, DDA is also used to study the mechanical characteristics of coarse granular materials and particles are randomly generated according to the gradation curve in order to enhance the reality of the numerical simulation.

2 Formation of specimen for numerical simulation

In order to numerically analyze the mechanical characteristics of coarse granular materials, the first step is to generate a specimen with particles which are distributed randomly and contact each other. Random particle-generating algorithms have been studied in the computer simulation of concrete aggregates (Zhang et al 2000; Zhang & Jin 2004; Du & Sun 2006). Concrete aggregates are the skeleton of concrete, in which particles do not contact each other. Because the particles of coarse granular materials contact each other, these algorithms are not suitable for generating the specimen of coarse granular materials, but for reference only.

In this paper, the algorithm proposed by Zhang et al (2000) is used to generate polygonal particles which satisfy the gradation curve of coarse granular materials. These particles are randomly thrown into a given domain, of which the width is same as one of the specimen, and a loose particle system is formed, as shown in figure 1(a). In the throwing process, the intersection between particles is simply judged by the boxes enclosing particles.

The loose particles do not yet meet the requirement of the mechanical simulation. Therefore, it is required to use the loose particles as the initial stage, and then

use DDA to simulate the packing process of particles in the given domain with rigid boundaries. After that, a heap, in which the particles contact each other, is formed, as shown in figure 1(b). After the packing process, the particles below the top boundary of the specimen are selected to form the specimen for the numerical simulation. If a particle intersects with the boundary, its area above the boundary is cut off.

Referring to the tri-axial laboratory test, flexible material is added on the both sides of the specimen and divided into blocks, rigid blocks on the top and the bottom, as shown in figure 2. That two rigid blocks with smooth surfaces are placed on the both sides of the top block is to keep the axial pressure vertical. Applying the side pressure σ_3 on the both sides and the axial pressure σ_1 on the top, the numerical simulation on the deformation of coarse granular materials can be carried out by using DDA.

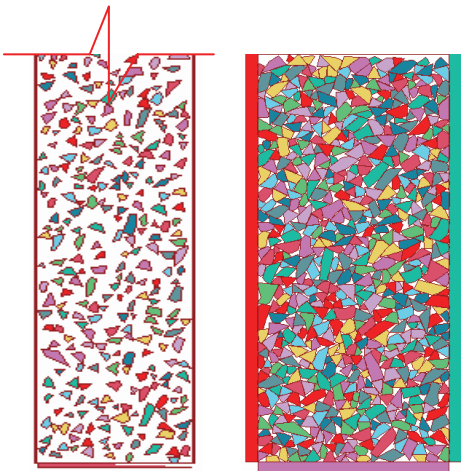

(a) Loose particles （b）heap

Fig. 1 Loose particles and heap

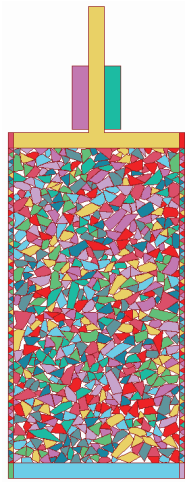

Fig. 2 Numerical simulation model

In figure 1 and figure 2, the particle size is 10mm to 20mm. The width of the specimen is 300mm and the height is 600mm. The particle parameters for the numerical simulation are as follows: E=20GPa, μ=0.2 and δ =25°, C= 0 between particles.

3 Results of numerical simulation

3.1 *Stress vs. strain curves*

The stress vs. strain curves are shown in figure 3, where we can see that the curves obtained by the numerical simulation are basically approximate to the ones by the tri-axial test (Wu 2007).

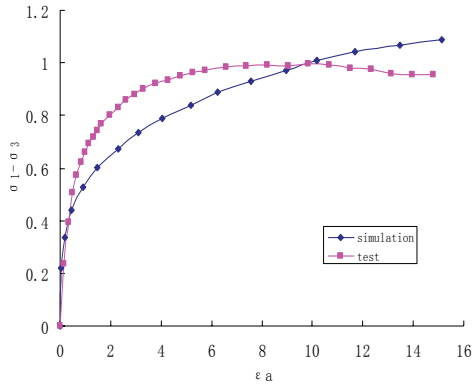

σ_3 = 0.2 MPa

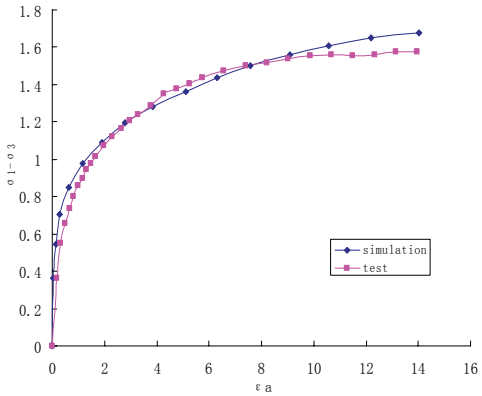

σ_3 = 0.4 MPa

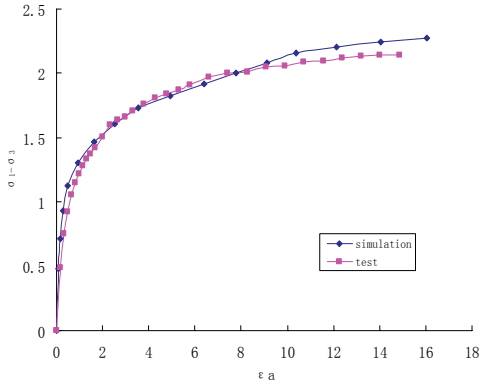

σ_3 = 0.6 Mpa

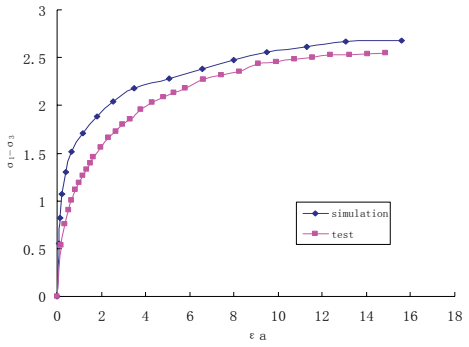

σ_3 =0.8 MPa

Fig. 3 Stress vs. strain curves

3.2 *Fabric elements*

Fabric describes comprehensive characteristics of particle system. It mainly includes space arrangement and interaction of the particles. Fabric elements about the interaction include follows:

Coordination number N_t: the number of particles contacting some particle, an index of the density of material.

Contact normal $\tilde{n}$: the cosine of the normal on contact face. For a contact point, there is a pair of $\tilde{n}$ whose directions are opposite. For a particle system, the orientation of $\tilde{n}$ is described by the distribution of its spherical coordinate, α and β.

Contact force $\tilde{f}$: the interaction forces between particles. As a statistics description, the distribution of their quantity is given.

Branch vector $\tilde{l}$: the lines linking the centers of particles which contact each other. For a particle system, the synthesis effect is described by the distribution, orientation and length of branch vectors.

The coordination number, branch vector and interaction force are shown in figure 4 to 6. From these figures, the changes of the interaction of particles can be seen clearly. With the increasing of the axial pressure, the coordination numbers in the center area decrease distinctly, the branch vectors change little at two ends and become sparse in the center area, the direction of the contact forces tends to vertical and it appears force chains clearly.

3.2 *Particle motion*

Figure 7 to 9 are the displacements at the center of the particles. The movement of the particles is in agreement with that of the tri-axial test with computerized tomography (CT) (Wu 2007). Because of the affect of constraints of the top and bottom blocks, the horizontal displacement of the particles in the upper and lower triangular areas is small. At higher axial pressure, the horizontal displacement in the middle area of two sides is large and symmetrically distributed, the vertical displacement distributes levelly and with maximum at the top, the rotation is small in the upper and lower areas and large in the diagonal areas.

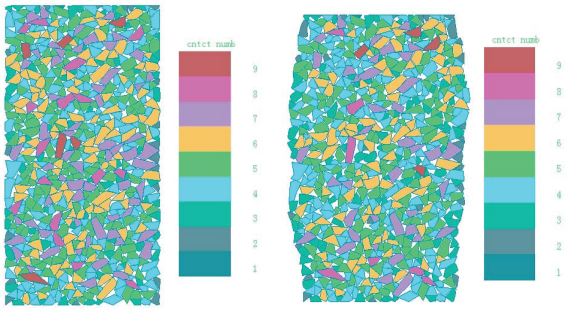

$\sigma_1=\sigma_3=0.4$MPa $\sigma_1=1.68$MPa, $\sigma_3=0.4$MPa

Fig.4 Coordination number

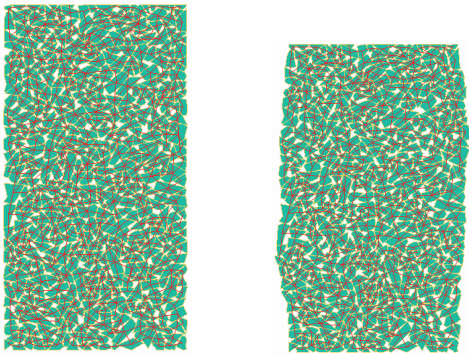

$\sigma_1=\sigma_3=0.4$MPa $\sigma_1=1.68$MPa, $\sigma_3=0.4$MPa

Fig.5 Branch vector

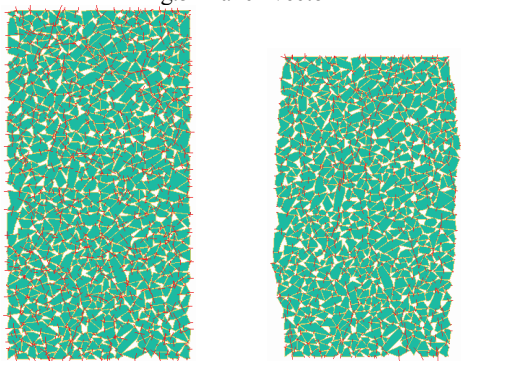

$\sigma_1=\sigma_3=0.4$MPa $\sigma_1=1.68$MPa, $\sigma_3=0.4$MPa

Fig.6 Contact force

The movement of the particles represents the particularity of granular materials and is hardly explained by the continuous mechanics. The study on the fabric elements may provide a new approach for the research of the mechanical characteristics of coarse granular materials.

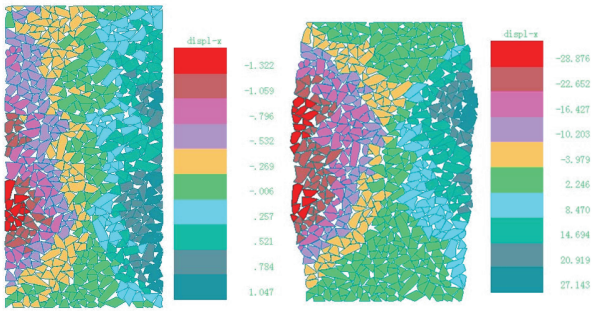

$\sigma_1=\sigma_3=0.4$MPa $\sigma_1=1.68$MPa, $\sigma_3=0.4$MPa

Fig.7 Horizontal displacement (mm)

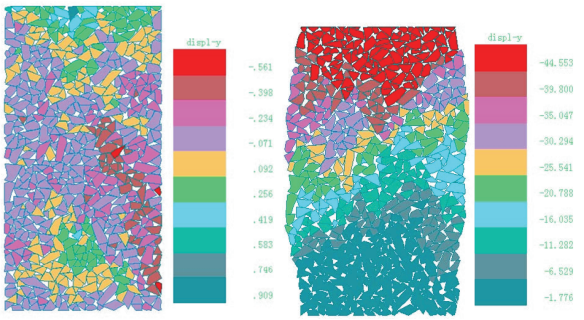

$\sigma_1=\sigma_3=0.4$MPa $\sigma_1=1.68$MPa, $\sigma_3=0.4$MPa

Fig.8 Vertical displacement (mm)

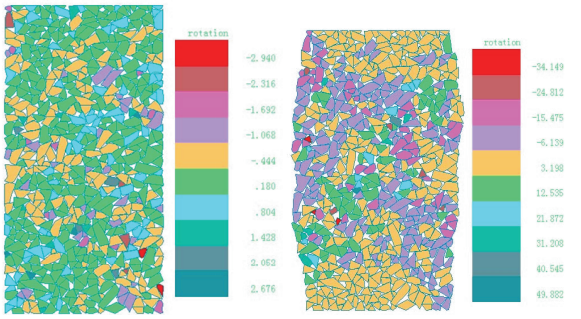

$\sigma_1=\sigma_3=0.4$MPa $\sigma_1=1.68$MPa, $\sigma_3=0.4$MPa

Fig.9 Rotation angle of particle (°)

4 Conclusions

This paper provides an effective method for establishment of the mechanical simulation model of coarse granular materials. In the model the particles satisfy the gradation curve and have random shapes and positions. The results of numerical simulation are in agreement with that of tri-axial test. It shows that DDA is suitable for the mechanical characteristic research of coarse granular materials. The statistics and analysis of fabric elements is been doing. The relationship between fabric elements and macro behaviors of coarse granular materials is to be studied.

References

Cheng Zhanlin, Ding Hongshun. Test Research on Coarse Granular Material. Proceeding of the first symposium on geometrics of hydraulic and hydroelectricity, 2006, pp. 41-47.

Du Chengbin, Sun Liguo. Numerical Simulation of Concrete Aggregates with Arbitrary Shapes and Application. Journal of Hydraulic Engineering, 2006, 6: 662-667.

Liu Guangting, Gao Zhenguo, Random 3-Dimentional Aggregate Structure for Concrete. Journal of Tsinghua University, 2003, 43(8):1120-1123.

Wu Liangping. Fabric Test Research on of the coarse granular material, Master degree thesis. Yangtze River Scientific Research Institute, 2007.

Zhang Guoxin, Li Guangxin, Guo Ruiping. Stress-Strain Relationship for Soil using Discontinuous Deformation Analysis. Journal of Tsinghua University, 2000, 40(8)102-105.

Zhang Jiang, Jin Nanguo. Numerical Simulation Method for Polygonal Aggregate Distribution in Concrete. Journal of Zhejiang University, 2004, 38(5): 581-585.

Fundamental study for slope failure of volcanic soil ground by DDA

T. ISHIKAWA[1], S. KAWAMURA[2], S. MIURA[1] and Y. OHNISHI[3]

[1] Hokkaido University, Kita 13, Nishi 8, Kita-ku, Sapporo, Hokkaido, 060-8628, JAPAN
[2] Muroran Institute of Technology, Muroran, Hokkaido, JAPAN
[3] Kyoto University, Katsura, Kyoto, JAPAN

This paper focuses on how to simulate the slope failure of volcanic soil ground with DDA. DDA simulations of model tests for slope failure of volcanic soil ground are performed to examine the effect of element mesh type and input parameters on the slope stability. Moreover, the validity of DDA simulations for simulating input parameters is examined by comparing numerical results with experimental results. As the results, it is revealed that slip surface can be roughly identified by displacement vectors of each DDA block, and that DDA simulation is similar in the shape and location of slope failure surface to the model test. However, there is a remarkable difference in volume change of volcanic soil ground before and after slope failure. These results indicate that DDA is an effective method to simulate a slope failure of volcanic soil ground, though there is room for further investigation on the modeling method.

Keywords: Slope failure; Volcanic coarse-grained soil; Numerical modeling; DDA

1. Introduction

At the fragmental volcanic soil ground in cold regions like Hokkaido, the north area of Japan, the degradation in the static and dynamic strength of volcanic coarse-grained soils caused by heavy rainfall and cyclic freeze-thaw action often makes the natural disaster such as slope failure at embankment and cut slope or landslide at a subsurface layer worse. However, the synthetic research on disaster preventive measures in Hokkaido is behind in examining how various factors such as freeze-thaw history, rainfall, rise in ground water level at thaw season and earthquake have an influence on the mechanism of slope failure and landslide at fragmental volcanic soil ground individually.

The objective of the research is to examine the applicability of discontinuous analysis to numerical simulation of slope failure which occurs at fragmental rock slope in cold regions and to identify a cause of the slope failure based on the result of numerical experiments. As the fundamental study, this paper focuses on how to simulate the slope failure of volcanic soil ground with DDA (Discontinuous Deformation Analysis, Shi and Goodman (1985)). In this paper, DDA simulations of model tests for slope failure of volcanic soil ground are performed in order to examine the effect of element mesh type and input parameters on the slope stability. Moreover, the validity of DDA simulations for simulating input parameters is examined by comparing numerical results with experimental results.

2. Model rainfall tests of volcanic soil slope

2.1 Experimental conditions

In order to examine the feature of rainfall-induced slope failure for volcanic soil ground, a series of model rainfall tests are performed (Kawamura et al 2007). Here, a model rainfall test was performed until 3 hours or the occurrence of slope failure, and rainfall intensities were 60 or 100mm/hr, which were simulated by using spray-nozzles. During the rainfall tests, the change in pore water pressure, deformation and saturation degree was monitored using pore water pressure transducers and soil moisture meters, especially the deformation behavior was estimated using the Particle Image Velocimetry (PIV) analysis (White et al 2003).

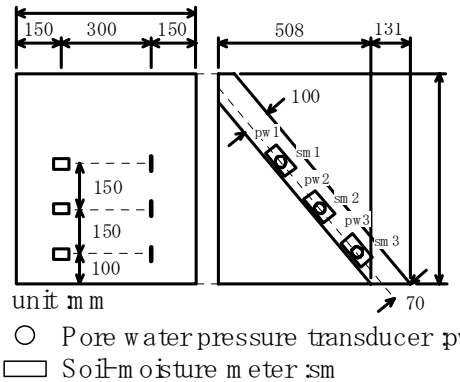

Fig. 1: Typical slope shapes in rainfall test.

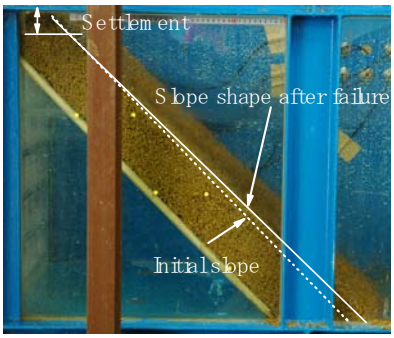

Fig. 2a: Observed deformation after failure at θ=45°.

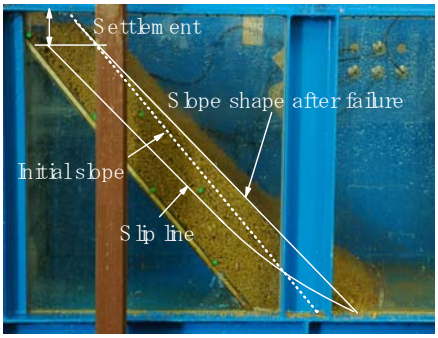

Fig. 2b: Observed deformation after failure at θ=50°.

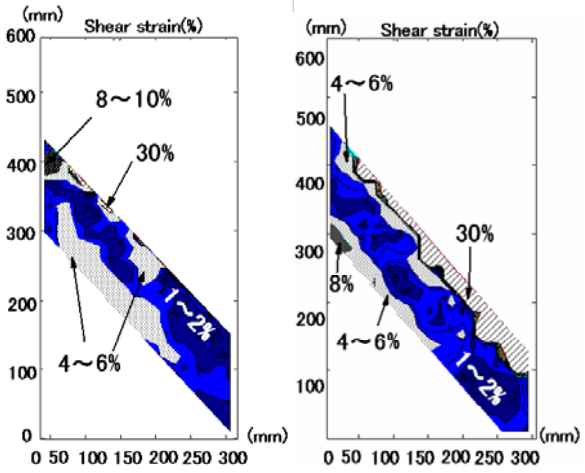

a) θ=45° b) θ=50°

Fig. 3: Shear strain distribution by PIV.

Table 1: Test conditions and slope failure modes.

Slope angle	Rainfall intensity	Base friction	Elapsed time	Failure mode
45°	60mm/h	Smooth	385s	Plane failure
45°	100mm/h	Smooth	258s	Plane failure
45°	60mm/h	Rough	–	No failure
45°	100mm/h	Rough	–	No failure
50°	60mm/h	Smooth	465s	Slip failure
50°	100mm/h	Smooth	496s	Slip failure
50°	60mm/h	Rough	–	No failure
50°	100mm/h	Rough	283s	Slip failure
55°	60mm/h	Smooth	385s	No experiment
55°	100mm/h	Smooth	258s	No experiment
55°	60mm/h	Rough	208s	Slip failure
55°	100mm/h	Rough	213s	Slip failure

Fig. 1 shows a typical shape of model slopes adopted in this study. The soil container was 2,000mm in length, 700mm in depth and 600mm in width, and its front wall was made of a reinforced glass to observe deformation with failure of model slopes. The model slope is in the plane strain state. Each model slope was constructed in a soil container by pluviating Kashiwabara volcanic soil into the soil container and tamping it on an acrylic impermeable layer (foundation) so as to be the desired dry density (ρ_d=0.48g/cm^3) with the variation in the density within ±5%. Additionally, in order to examine the effect of slope angle on the deformation behavior of model slope, slope angle (θ) was set to θ=45°, 50° and 55°. This paper supposes that the friction between volcanic soil slope and foundation can neglect because the original foundation surface is smooth. Furthermore, in some test cases, to increase the surface-roughness, No. 120 sandpapers were glued on the surface. It is called "rough" condition in contrast to the abovementioned "smooth" condition.

Kashiwabara volcanic soil (ρ_s=2.34g/cm^3, ρ_{dmax}=0.623 g/cm^3, ρ_{dmin}=0.462g/cm^3 and D_{50}=1.25mm) is a primary deposition of pyroclasic fall deposit, which originated from the eruption of Shikotsu caldera, and then it is a crushable coarse-grained soil. The details of mechanical behavior of Kashiwabara volcanic soil have been reported by Miura et al (1996).

2.2 Experimental results

Figs. 2 show the deformation after the test of model slopes, which differ in the slope angle. As can be seen in Figs. 2, slope failure occurs with large deformation. In previous study, it was found that large deformation was induced around 10sec after the peak of saturation degree (Kawamura et al 2007). Here, the mechanical behavior on the time at which the shear strain of 4-6% was caused was tentatively regarded as that at failure, because shear strain of 4-6% in the slope occurred at the peak of saturation degree. Comparing Fig.2a (θ=45°) with Fig. 2b (θ=50°), the failure modes of model slopes are different as to the slope angle. For example, a slip failure like circular slip with the settlement of slope crest was observed in case of θ=50°, while a plane failure which compressed model volcanic soil slope in the direction parallel to the foundation surface was observed in case of θ=45°.The scale of slope failure at the former case (θ=50°) was larger than that at the latter case (θ=45°). Figs. 3 show shear strain distributions at the peak of saturation degree (just before failure) obtained from PIV analysis. In Fig. 3a (θ=45°), the shear strain was mainly less than 4-5%, except for some areas of 8-30%, whereas in Fig. 3b (θ=50°), the shear stain more than 30% was confirmed in the large area around the slope surface.

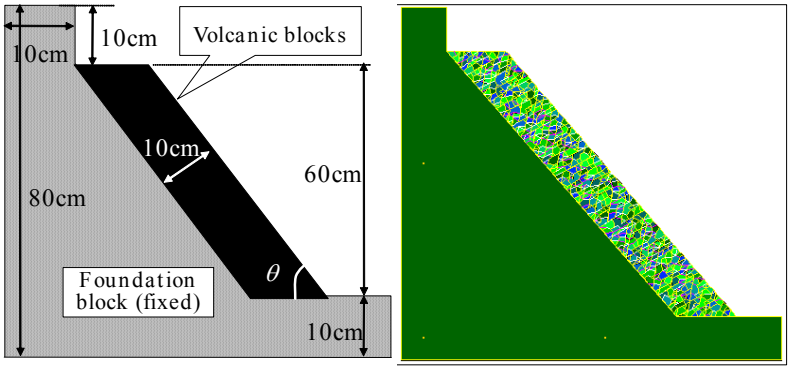

Fig. 4: Schematic diagram of DDA model.

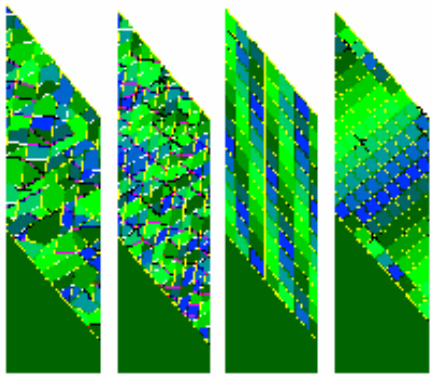

Fig. 5: Schematic diagram of DDA model.

Table 2: Features of DDA models.

Mesh name	Block number	Average diameter
Model A	728	5.6mm
Model B	1424	4.1mm
Model C	677	6.1mm
Model D	635	6.3mm

Table 3: Analytical conditions of DDA simulations.

Name	Slope	Mesh type	Base friction	Friction angle	Failure mode
Case 1	50°	Model A	Smooth	ϕ_μ= 0°	Slip failure
Case 2	50°	Model A	Smooth	ϕ_μ=40°	Slip failure
Case 3	50°	Model A	Rough	ϕ_μ=40°	Slip failure
Case 4	45°	Model A	Smooth	ϕ_μ=40°	Plane failure
Case 5	55°	Model A	Smooth	ϕ_μ=40°	Slip failure
Case 6	50°	Model B	Smooth	ϕ_μ=40°	Slip failure
Case 7	50°	Model C	Smooth	ϕ_μ=40°	Plane failure
Case 8	50°	Model D	Smooth	ϕ_μ=40°	Plane failure

Table 1 summarizes the relationships between failure modes of model slopes and experimental conditions to examine the effect of experimental conditions on the deformation behavior of model slope. Firstly, as for the effect of slope angle, it is revealed that the failure mode of model volcanic soil slope varies depending on the slope angle. According to Table 1, the slip failure was observed in case of a steep slope angle more than θ=50°, and the plane failure was occurred in case of θ=45° as mentioned above, irrespective of the difference in the friction of foundation surface or the rainfall intensity. Secondly, as for the effect of the friction of foundation surface, though the friction of foundation surface has important effects on the occurrence of slope failure and the feasibility of model tests, it has little effect on the failure mode. Thirdly, as for the effect of the rainfall intensity, it hardly affects the failure mode, though there is a difference in the time at which the model slope fails. These results indicate that the slope angle of model volcanic soil ground influences the behavior of slope failure strongly.

3. Analytical conditions of DDA simulations

3.1 Numerical modeling

A series of numerical simulations for rainfall tests of volcanic soil slope were performed with two-dimensional DDA models. Fig. 4 shows the size, dimension and boundary condition of typical DDA model, which simulates the above-mentioned model volcanic soil slope. The DDA model is composed of two types of blocks, that is a large polygon block named "foundation block", which represents the impermeable layer of model slope, and many small blocks named "volcanic blocks," which represent the volcanic soil ground of model slope. Here, the foundation block is fixed. Also, DDA models which slope angle (θ) was set to θ=45°, 50° and 55° were employed, respectively. In DDA simulations, a stability analysis was performed by applying gravity force of 9.8m/s^2 to each DDA model.

A method for modeling volcanic soil ground seems to influence the behavior of slope failure strongly in DDA simulation. Then, this study employs several DDA models which differ in element mesh type. Fig. 5 shows four kinds of element meshes before loading gravity force used in this study, namely a) Random mesh using large DDA blocks (model A), b) Random mesh using small DDA blocks (model B), c) Regular mesh using large DDA blocks with joints parallel to the slope surface and vertical direction (model C), d) Regular mesh using large DDA blocks with joints both parallel and perpendicular to the slope surface (model D). Table 2 shows the feature of DDA models. Table 3 summarizes the analytical conditions of all DDA simulations performed in this paper.

3.2 Input parameters

All DDA blocks are linear elastic blocks under plane-strain condition. In this study, when two DDA blocks come in contact, springs and a slider are created at

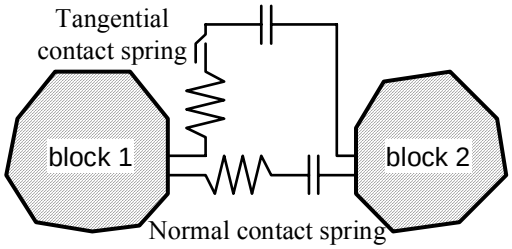

Fig. 6: Contact mechanism of DDA.

Table 4: Material properties of DDA model.

Material property	Volcanic block	Foundation block
Unit mass γ	0.81 g/cm^3	0.81 g/cm^3
Young's modulus E	2.25 GPa	22.5 GPa
Poisson's ratio ν	0.343	0.343
Friction angle ϕ_μ	0º, 40º	0º, 40º
Cohesion C_μ	0 kPa	0 kPa

contact points as shown in Fig. 6. Accordingly, the analytical input parameters of DDA blocks are characterized by the material properties of a block, namely unit mass (γ), Young's modulus (E) and Poisson's ratio (ν), and the interface properties of block edges, namely block friction angle (ϕ_μ) and cohesion of surface (C_μ). Table 4 shows the material properties of blocks and the interface properties of block edges.

As for the material properties, the parameters were set by referring to the experimental conditions of model rainfall tests and element test results of Tomikawa volcanic soil (Ishikawa et al 2007), which mechanical characteristics is similar to Kashiwabara volcanic soil. Here, unit mass (γ) of a volcanic block is set to wet density considering the degree of saturation at failure of volcanic soil slope in model rainfall tests. On the other hand, the interface properties were set by referring to the element test results as follows. The block friction angle (ϕ_μ) between volcanic blocks regards as a parameters ranging from 0° to 40° to examine the effect on the slope stability of DDA models. As for ϕ_μ between a volcanic block and a foundation block, the value was set equal to 0º (smooth) and 40° (rough) to examine the effect. Besides, as for C_μ between all materials, the value was set equal to zero by considering that Kashiwabara volcanic soil is a coarse granular material.

4. Results of DDA simulations

4.1 Effects of analytical conditions

Fig. 7 shows the distribution of displacement vectors for DDA blocks under various analytical conditions. Here, a displacement vector which color is dark shows that a movement of the block is large. In Fig. 7, a slip line for each DDA simulations can be roughly identified by the distribution of displacement vectors. For example, a border of displacement vectors around 2cm may be regarded as a slip line. Then, based on the distribution of displacement vectors, the effect of numerical modeling and input parameters on the deformation behavior of model slope is examined as follows.

First, the effect of analytical conditions except for slope angle on the numerical results is examined under the constant slope angle of θ=50°. As for the effect of element mesh type, in case of regular meshes (case 7 & 8) a slip line parallel to the slope surface, that is the joint direction of model C and D, was observed at the depth of around a one-third of the volcanic soil ground thickness from slope surface, while in case of random mesh (case 2) a slip line reaches the surface at a lower part of model slope, and the shape looks like a circular arc. However, a difference in the deformation behavior of model slope due to the variation in the size of DDA blocks was hardly confirmed.

Furthermore, comparing two results (case 1 & 2) which differ in the block friction angle between volcanic blocks, it is recognized that although the deformation behavior of model slope is not altered regardless of the block friction angle, a location of slip line deepens with an decrease in the block friction angle and under ϕ_μ=0° the whole slope tends to slide down. However, the block friction angle between a volcanic block and a foundation block has little effect on the deformation behavior of model slope in DDA simulations. These results indicate that as for DDA simulations performed in this paper, under the constant slope angle, the failure mode of model volcanic soil slope varies mainly depending on the element mesh type.

Next, the effect of slope angle on the numerical results is examined under keeping the other analytical conditions constant. From Fig. 7, it is confirmed that a location of slip line deepens with an increase in the slope angle, and that the failure mode of model volcanic soil slope seems to be the slip failure in case of a steep slope angle more than θ=50°, while the plane failure can be observed in case of θ=45°. These results indicate that the deformation behavior of model volcanic soil slope varies considerably with the slope angle even if the other analytical conditions are constant.

4.2 Applicability of DDA simulations

The applicability of DDA to the slope failure simulation was examined in terms of the failure mode of volcanic soil slope. Comparing DDA simulations (Fig. 7) with test results under the same experimental

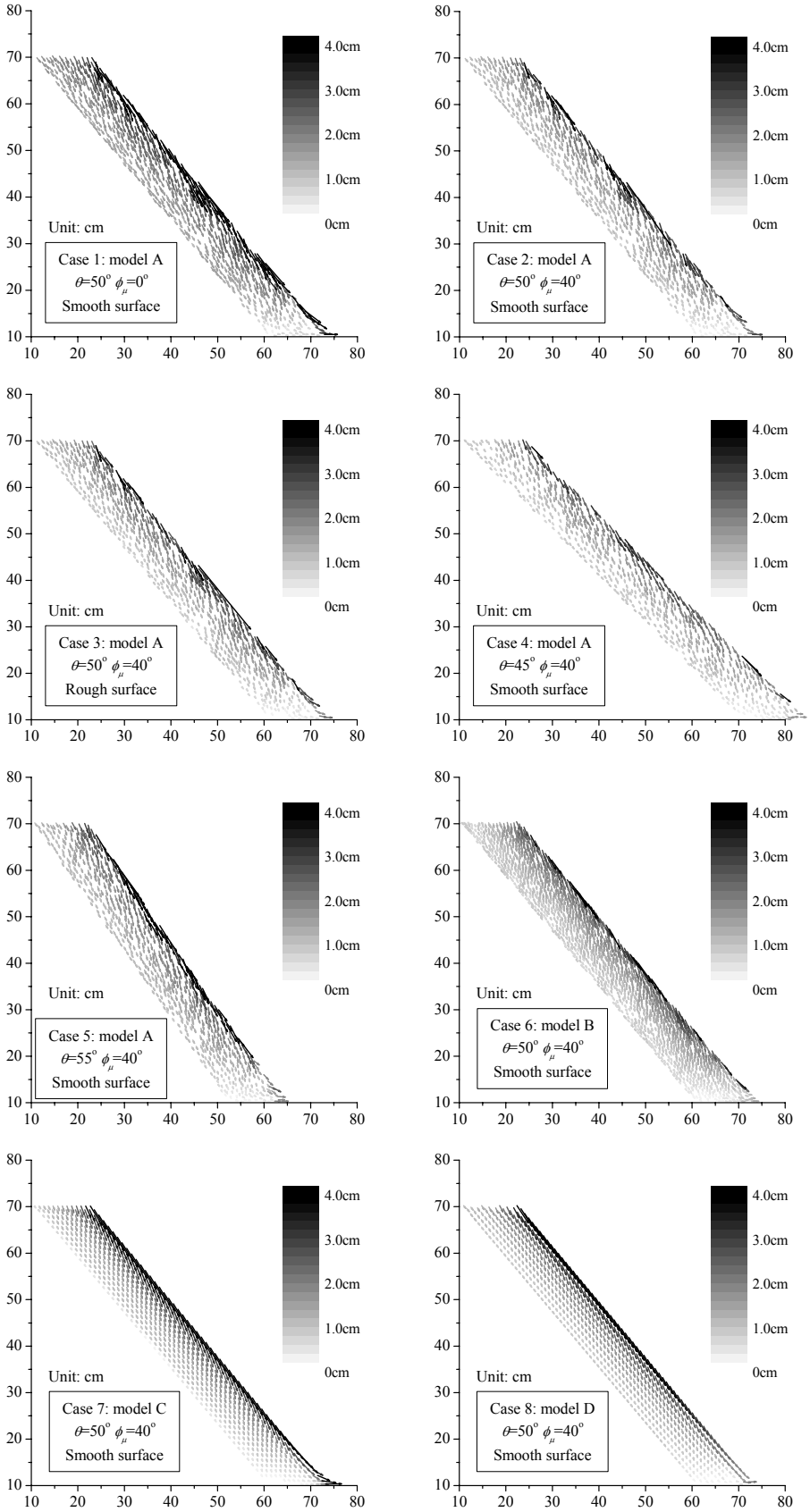

Fig. 7: Distribution of displacement vectors for DDA blocks.

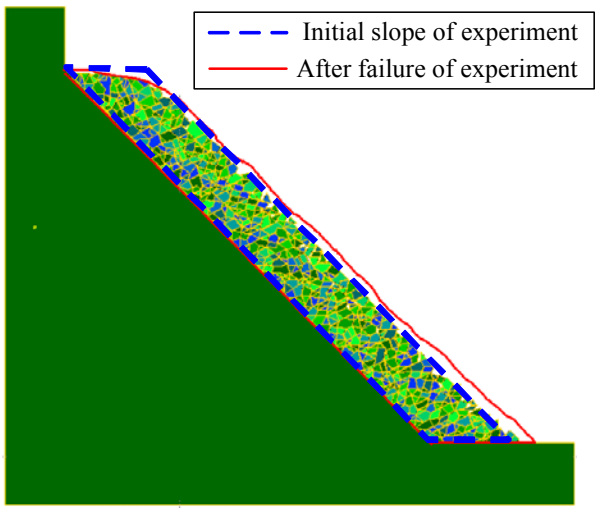

Fig. 8a: Comparison in deformation behavior at θ=45°.

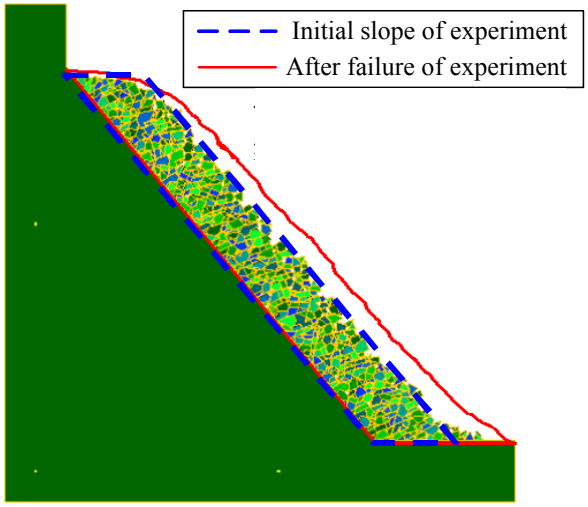

Fig. 8b: Comparison in deformation behavior at θ=50°.

conditions (Fig.2), it is revealed that DDA simulations employing random meshes are qualitatively similar in the shape and location of slope failure surface to the test results, in comparison with DDA simulations employing regular meshes, and the tendency can be confirmed irrespective of the slope angle. These results suggest that DDA is an effective method to simulate a slope failure of volcanic soil ground.

However, there is room for further investigation on the method for modeling a slope composed of crushable volcanic coarse-grained soils. For example, Fig. 8 compares the deformation behavior of DDA model with the deformation of model volcanic soil slope after the rainfall test under the same experimental conditions. There is a remarkable difference in volume change of volcanic soil ground before and after slope failure between DDA simulations and test results in case of θ=50°, whereas a difference in the volume change between both is hardly confirmed in case of θ=45°. The reason may safely be supposed as follows. The mobility of DDA blocks had been restrained due to too strong interlocking between volcanic blocks in DDA models employed in this paper, and as the result, the scale of slope failure in DDA simulation at θ=50° became small compared with the test result. This caused that a remarkable dilatancy behavior of volcanic soil ground with slope failure observed in model rainfall tests could not be simulated by DDA models well.

5. Conclusions

The following conclusions can be obtained;

1. According to rainfall test results, the slope angle of model volcanic soil ground influences the behavior of slope failure strongly.
2. In DDA simulation for slope failure, a slip surface can be roughly identified by displacement vectors of each DDA block.
3. DDA simulation is similar in the shape and location of slope failure surface to the experiment, though there is a remarkable difference in volume change of volcanic soil ground before and after slope failure.

From the above-mentioned results, it can be pointed out that as for DDA simulation performed in this paper, DDA is an effective method to simulate a slope failure of volcanic soil ground, though there is room for further investigation on the method for modeling a slope composed of crushable volcanic coarse-grained soils.

References

Shi, G.H. and Goodman, R.E., Two dimensional discontinuous analysis, *Int. J. Num. Anal. Methods. Geomech*, 9: 541-556, 1985.

White, D.G., Take, W.A. and Bolton, M.D., Soil deformation measurement using particle image velocimetry (PIV) and photogrammetry, *Geotechnique*, 53(7): 619-631, 2003.

Kawamura, S., Kohata, Y. and Ino, H., Rainfall-induced slope failure of volcanic coarse-grained soil in Hokkaido, *Proceedings of 13th Asian Regional Conference, Soil Mechanics and Geotechnical Engineering*, 2007. (in press)

Miura, S., Yagi, K. and Kawamura, S., Static and cyclic shear behavior and particle crushing of volcanic coarse grained soils in Hokkaido, *Journal of Geotechnical Engineering*, *JSCE*, 547(III-36): 159-170, 1996. (in Japanese)

Ishikawa, T., Ozaki, Y. and Miura, S., Influence of degree of saturation on strength characteristics of crushable volcanic coarse-grained soils, *Proceedings of 3rd Asian Conference on Unsaturated Soils*, *Nanjing*, *China*: 223-229, 2007.

Analysis of toppling using three-dimensional Discontinuous Deformation Analysis

M.R. YEUNG [1] and K.L. WONG [2]

[1] Civil Engineering Department, California State Polytechnic University, Pomona, CA 91768, U.S.A.
[2] Unaffiliated, Hong Kong, P.R. China

This paper reports results from a study of toppling as a truly three-dimensional (3D) problem using physical models and 3D Discontinuous Deformation Analysis (3D DDA). It also presents a field case study in which 3D DDA is used to obtain the factor of safety of a toppling rock slope. For the cases studied, 3D DDA results agree well with the physical modeling results not only in terms of the effective failure mode but also in terms of the displacement histories of the blocks in the model. The field case study shows that 3D DDA can be applied in practice to analyze truly 3D behavior of jointed rock masses and to obtain the safety factor of a toppling rock slope through repeated analyses using the shear strength reduction method.

Keywords: Toppling; Three-dimensional Discontinuous Deformation Analysis; 3D DDA; Shear strength reduction method

1. Introduction

A jointed rock slope is susceptible to toppling if the joints dip steeply into the slope. For toppling to be kinematically feasible, it is usually assumed that the strike of the steeply dipping joint set is roughly the same as that of the slope face. With this assumption, the problem can be reduced to a two-dimensional one that can be analyzed by considering a section perpendicular to the slope face. Existing kinematic tests for toppling usually allow for some deviation from the condition that the strike of the joint set is the same as that of the slope face, but the maximum allowable deviation for toppling to be considered kinematically feasible appears to be based on judgment and experience. This paper presents some results from studying toppling as a three-dimensional (3D) problem using physical models and 3D Discontinuous Deformation Analysis (3D DDA). It also presents a field case study in which 3D DDA, along with the shear strength reduction method, is used to calculate the factor of safety of a toppling rock slope.

When viewed as a general 3D problem, the variables that determine whether a jointed rock slope will topple include (1) the geometry of the ground surface including the slope face, which may be characterized by the slope height, slope angle, and the slope length; (2) rock mass characteristics, including the number of joint sets, joint set orientations, joint spacings, joint friction angles, and the intact rock strength; and (3) the lateral confinement in the direction parallel to the length of the slope. In this study, the effects of some of these variables were investigated using physical models and 3D DDA, a numerical model for blocky systems.

2. Physical modeling

A jointed rock slope was modeled as a prismatic rectangular block (the "slope block"), with a height of H, a length of L, and a depth of D, as shown in Figure 1. This slope block rested on an inclined base plane having an inclination angle of α. The slope block was cut by only one joint set that was perpendicular to the top surface of the block. The joint spacing was 2.5 cm, and the friction angle was ϕ. The angle between the strike of the top surface and the trace of a joint on the top surface was defined as the angle δ.

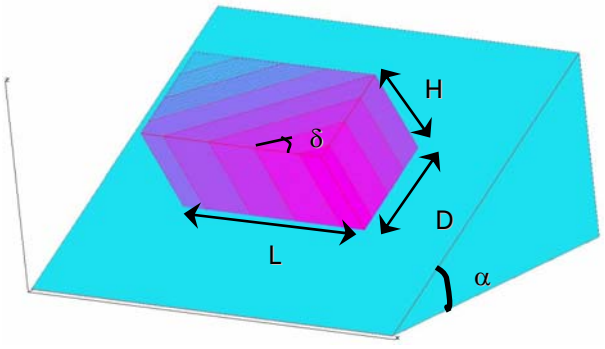

Fig. 1: Configuration of model.

A series of physical models with different combinations of H, L, D, α, ϕ, and δ, as listed in Table 1, was built to study the effects of these variables. The physical models were made of wood. To obtain the three different joint friction angles, the wood surfaces were polished, which gave the lowest ϕ value, and also covered with two different grades of sand paper, giving the two higher ϕ values.

Table 1 Summary of physical modeling cases.

H (cm)	L (cm)	D (cm)	α (°)	ϕ (°)	δ (°)
9.7	20	10	10,20,30, 40,50,60	30,45,65	0,10,20,30, 40,50,60, 70,80,90
5	20	10	10,20,30, 40,50,60	30,45,65	30
9.7	10	10	10,20,30, 40,50,60	30,45,65	30

To perform a physical model test, the slope block was placed on a tilt table set at the desired inclination angle and held in place by a plastic bar across and against the downslope plane of the slope block. The plastic bar was then lifted quickly out of the way of the slope block, and the behavior of the slope block observed. Each physical model was tested twice and video-taped digitally for later analysis.

3. Three-Dimensional DDA

The original DDA developed by Shi and Goodman (1985) is a 2D numerical model for the statics and dynamics of discontinuous block systems. Significant recent development of DDA has been focused on extending the model to 3D (Jiang and Yeung 2004; Yeung et al. 2007).

A 3D DDA computer program was used to analyze all the cases studied using physical models. In addition, to study the effect of lateral confinement parallel to the length of the slope, for each of the cases studied using physical models, the same case is re-analyzed using 3D DDA with the slope block confined on the sides by two fixed blocks, as shown in Figure 2.

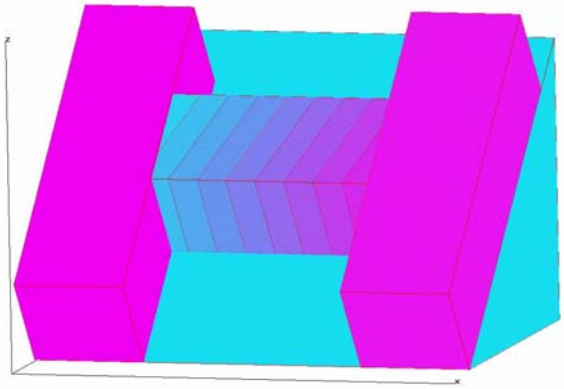

Fig. 2: 3D DDA model confined by two fixed blocks.

4. Summary of physical modeling and 3D DDA results

From the physical model tests, four different failure modes were observed: stability, toppling, toppling and sliding simultaneously (toppling/sliding), and sliding. Figure 3 shows a toppling case from a physical model test. Figure 4 shows the corresponding 3D DDA graphic output for the same case at the same elapsed time.

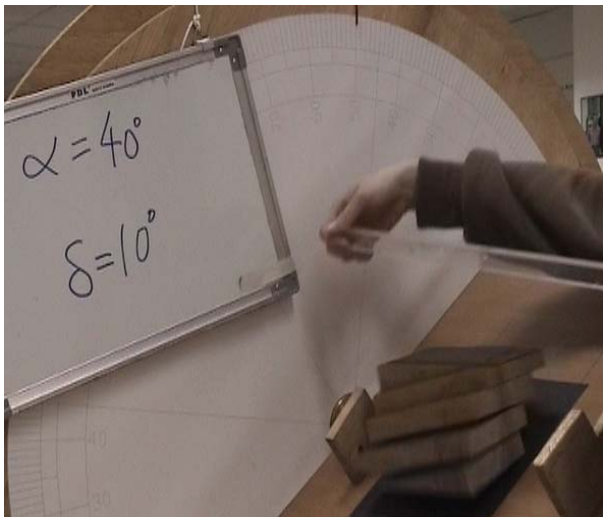

Fig. 3: Toppling in a physical model test.

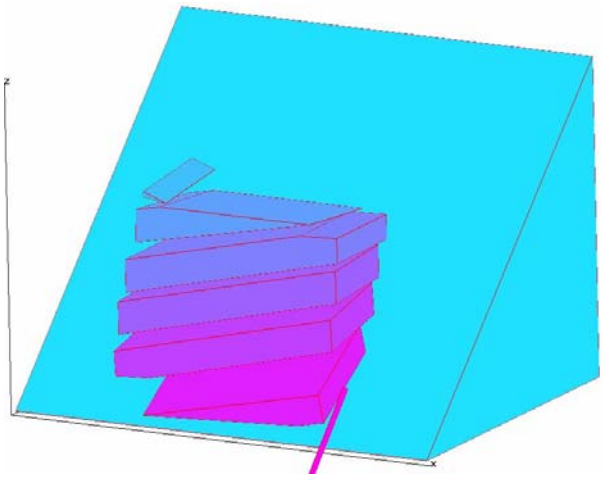

Fig. 4: 3D DDA graphic output for the case shown in Figure 3.

The physical modeling and 3D DDA results show that the tendency for toppling becomes larger if the slope block is taller for the same base width; if the friction angle of all joints is larger; if the base inclination is larger; and if there is no lateral confinement. Furthermore, as the angle δ changes for different cases, there exists a transition δ value that separates the pure toppling cases from other cases (stable, sliding, or toppling/sliding).

For the cases studied, 3D DDA results agree well with the physical modeling results not only in terms of the effective failure mode but also in terms of the displacement histories of the blocks in the model.

5. Field toppling case study

Three-dimensional DDA was used to analyze the stability of a toppling rock slope observed in the field. Shown in Figure 5, this slope was located at Shek O Beach in Hong Kong, P.R. China. Figures 6 and 7 show close-ups of the toppling rock blocks on the slope.

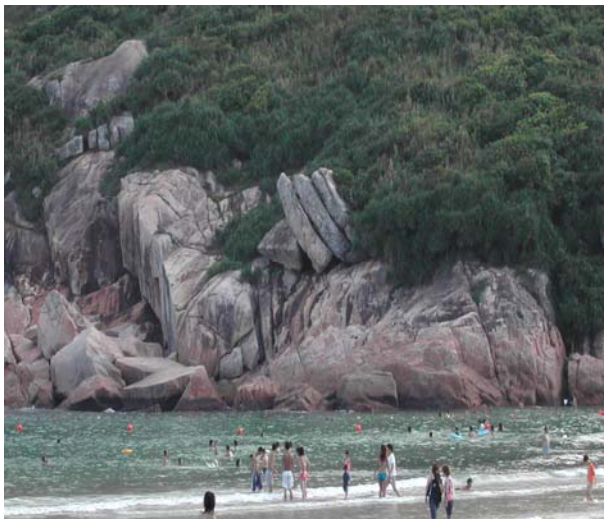

Fig. 5: A toppling rock slope at Shek O Beach, Hong Kong.

Fig. 6: Front view of toppling rock blocks.

Fig. 7: Back view of toppling rock blocks.

The factor of safety of this toppling rock slope was obtained using the shear strength reduction method, i.e. by analyzing the same slope repeatedly with different joint friction angle values to find the friction angle required for limiting equilibrium, $\phi_{required}$.

Based on field measurements, the dimensions of the rock blocks and their arrangement are shown in Figure 8. The intact rock was slightly weathered granite. Intact rock properties assumed in the 3D DDA analyses are as follows: Young's modulus is 50 GPa; Poisson's ratio is 0.25; and the unit weight is 2700 kg/m^3. Joint cohesion and friction angle were assumed to be 0 and 40^o, respectively. For static stability, the blocks were loaded by gravity only.

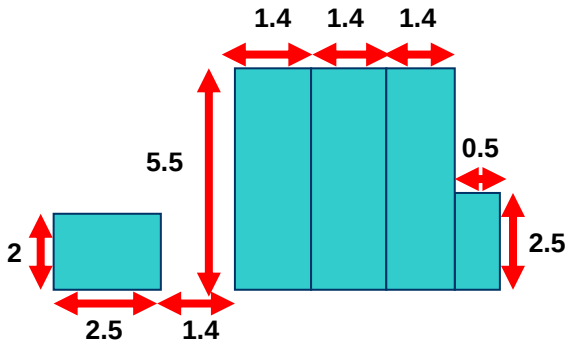

Fig. 8: Dimensions of toppling rock blocks and their arrangement (distances in meters).

The behavior of the rock slope was obtained by 3D DDA and is shown in Figure 9. It can be seen that the behavior obtained by 3D DDA agrees with the observed toppling behavior of the rock slope in the field.

The stability of the rock slope was evaluated by analyzing the slope repeatedly with different friction angles smaller than the available friction angle, $\phi_{available}$, decreasing the friction angle from 40^o by 1^o from analysis to analysis. In this way, the slope was found to

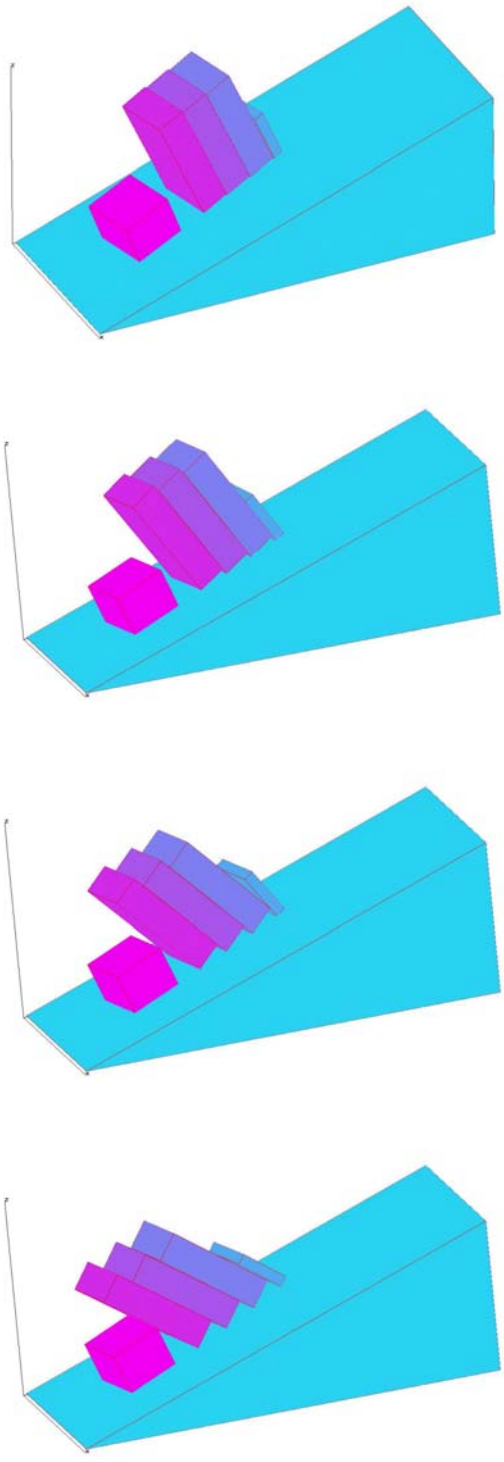

Fig. 9: 3D DDA results for field case with a joint friction angle of 40°.

fail when the friction angle was equal to 26°. The 3D DDA results for this case with a friction angle of 26° is shown in Figure 10. Therefore, the static factor of safety of the slope can be calculated to be the ratio of

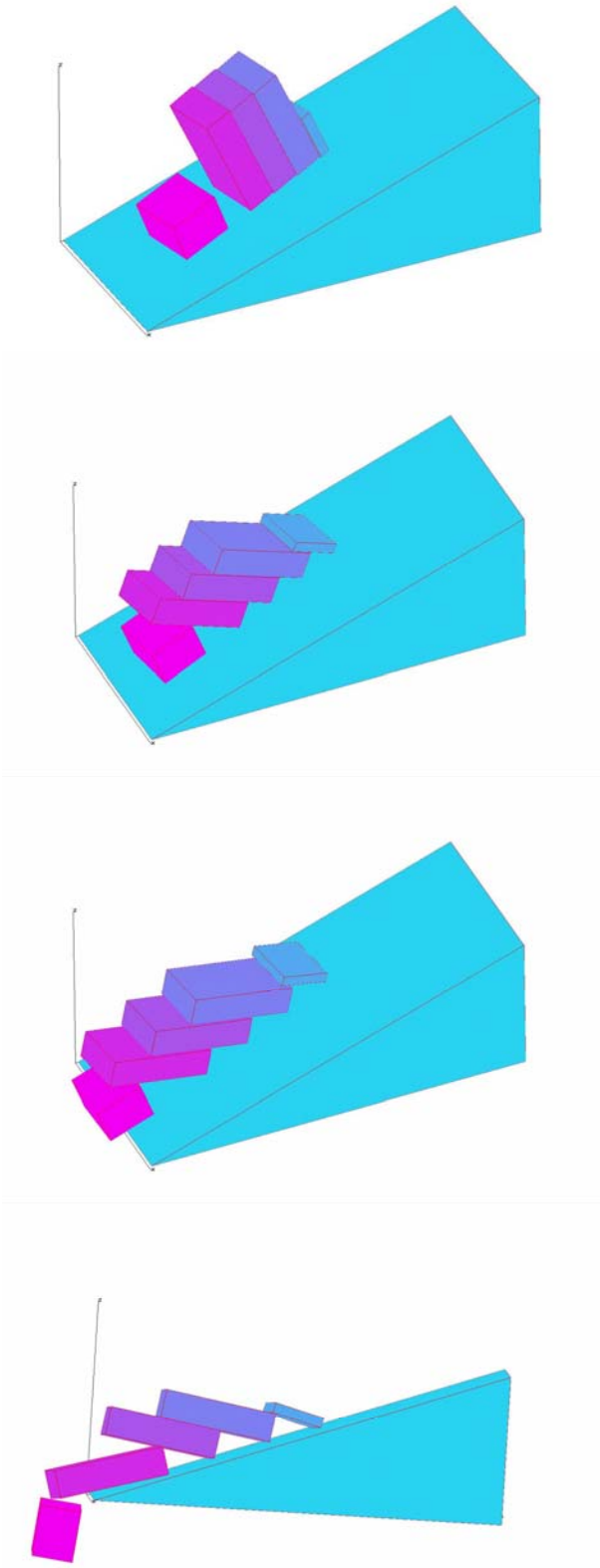

Fig. 10: 3D DDA results for field case with a joint friction angle of 26°.

the tangent of $\phi_{available}$ to the tangent of $\phi_{required}$, or 1.72. This agrees with the observation that the slope is stable under static conditions.

6. Conclusions

This paper reports some results from a study of toppling as a truly 3D problem using physical models and 3D DDA. It also presents a field case study in which 3D DDA is used to obtain the factor of safety of a toppling rock slope.

The physical modeling and 3D DDA results show that the tendency for toppling becomes larger if the slope block is taller for the same base width; if the friction angle of all joints is larger; if the base inclination is larger; and if there is no lateral confinement. Furthermore, as the angle δ changes for different cases, there exists a transition δ value that separates the pure toppling cases from other cases (stable, sliding, or toppling/sliding).

For the cases studied, 3D DDA results agree well with the physical modeling results not only in terms of the effective failure mode but also in terms of the displacement histories of the blocks in the model.

The field case study shows that 3D DDA can be applied in practice to analyze truly 3D behavior of jointed rock masses and to obtain the safety factor of a toppling rock slope through repeated analyses using the shear strength reduction method.

Acknowledgements

The authors would like to thank Drs. Q.H. Jiang and N. Sun for their help with the 3D DDA analyses, and also Mr. N.C. Poon and Mr. Y.F. Lo for their assistance with the physical modeling work.

References

Jiang, Q.H. and Yeung, M.R., A model of point-to-face contact for three-dimensional discontinuous deformation analysis. *Rock Mechanics and Rock Engineering,* 2004, **37**, 95-116.

Shi, G. and Goodman, R. E., Two Dimensional Discontinuous Deformation Analysis. *International Journal for Numerical and Analytical Methods in Geomechanic.* 1985, **9**, 541-556.

Yeung, M.R., Jiang, Q.H. and Sun, N., A model of edge-to-edge contact for three-dimensional discontinuous deformation analysis. *Computers and Geotechnics*. 2007, **34**, 175-186.

Evaluation of shield tunnel segment behavior with digital photogrammetry and discontinuous manifold analysis : A case study of Fushimi Tunnel

M. Ryu [1], T. Nakai [1] Y. OHNISHI[2], Y. ADACHI[3], A. HIGASHIDE[4] & S. MIKI[5]

[1]Earthtech Toyo Corporation, JAPAN; [2]Kyoto University, JAPAN,
[3]Hanshin Expressway Co. Ltd, JAPAN; [4]Obayashi Corporation, JAPAN;
[5]Kiso-Jiban Consultants Co., Ltd., JAPAN,

The Shield Tunnel is adopted in many cases in order to cope with soft ground at urban areas in spite of high cost of using segments. Since the cost of segment takes from 20 to 40% of the whole cost of construction, efforts of cost reduction are required.
First, we explain some conventional design methods of a shield tunnel. Then, we propose application of the Manifold Method(MM) as the rational design method. The MM may be able to treat the rigid body action in the weak foundation appropriately by analyzing segments as blocks.
We also show a plan of examination for actual deformation of tunnel segment by using precise photogrammetry method at the Fushimi Tunnel which is now under construction, which is expected to be used for verification of the MM analysis result.

Keywords: Deformation of Shield Tunnel with segments; Photogrammetry measurement; MM

1. Introduction

The shield driving method is applied to tunnel construction in urban area as a very leading construction for quick accomplishing and because of soft ground. When we compare with the tunnel construction methods, the shield driving method tends to take high cost. Moreover, it is adopted in many cases in order to cope with soft ground of urban areas in spite of high cost caused by using segments. Therefore, efforts of cost reduction are required as urgent necessity. Since the cost of segment takes from 20 to 40% of the whole cost of construction. The rational segment design is required.
The present design remains only in consideration of the action in a tunnel cross section. The possible three-dimensional analysis of taking into consideration not only the inside of a tunnel cross section but the action about the direction of a tunnel axis from now on is needed. For that purpose, we have to build the three-dimensional analysis method and effective observation of segment rings.
As shown in Figure 1, the Fushimi Tunnel is now under construction in the very complex geological condition and two tunnels are passing each other very closely. The authority wants to know what may happen when two tunnel crosses by. The Fushimi Tunnel uses composite segments which have combined advantages of compact, lightweight steel and rigid concrete. No bolts are needed, allowing efficient construction of the large-diameter of l0.82 m tunnel.

The reflective targets for precision photogrammetry was stuck on segment wall, by taking a photograph, the 3-dimensional coordinates of a target were acquired and deformation of tunnel wall was visualized. In comparison with these actual deformation data as shown in Figure 2, stress and strain back analysis with MM are used to evaluate surrounding external pressures to tunnel segment and tunnel.

Fig.1 Observation site of the shield tunnel

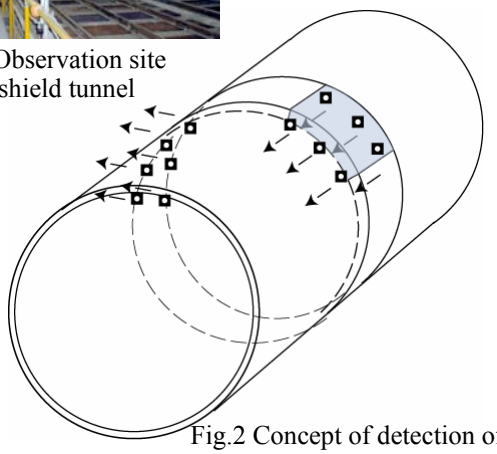

Fig.2 Concept of detection of deformation at each segment by digital camera method

2. Outline of the Fushimi Tunnel

2.1 Tunnel planning

As shown in Figure 3, Fushimi Tunnel is a pair of the two-lane traffic road tunnel being constructed by slurry shield method. The length of the tunnel is 855m each. This tunnel should be constructed in soil and rock geology, cross very busy major railway and water supply canal with very thin cover depth, and excavated under high density residential area. The slurry shield starts to excavate from the Fushimi launching shaft in east direction, turns around at the huge underground yard in rock site which was already constructed by NATM, and comes back to the arriving shaft where the machine started.

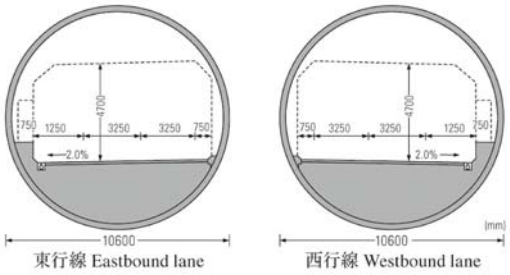

Fig.3 Cross section of Fushimi tunnel

The cover depth is only 4.3m at the water supply canal and about 12m at the two railways.
And the tunnel is planned under high density residential area so that the partial ownership was established and more careful excavation is needed to avoid the settlement the ground above.

2.2 Slurry shield machine

The photo of the machine is shown in Figure 4.
The geological condition varies from soil to intermediate hard rock including crashing zone. Therefore, the machine should be designed to excavate in soil as a slurry shield machine and to excavate in rock like as a TBM.

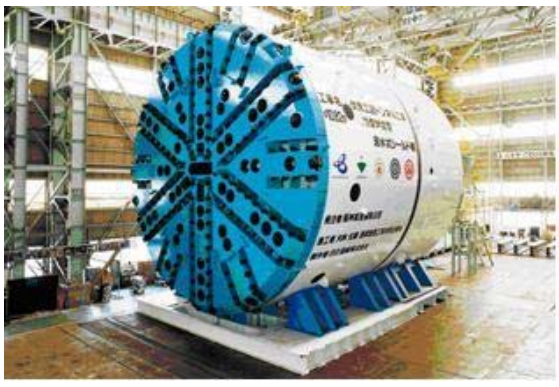

Fig.4 Photo of the slurry shield machine

2.3 Segment

In order to reduce the cost of construction and to enhance the reliability of water resistance of the tunnel, composite segments named "NM segment" are adopted for this tunnel. Figure 5 shows the photo of NM segments. NM segment is a composite segment of steel beam and high strength concrete slabs and it has high strength and high stiffness. The features of NM segment are the followings.

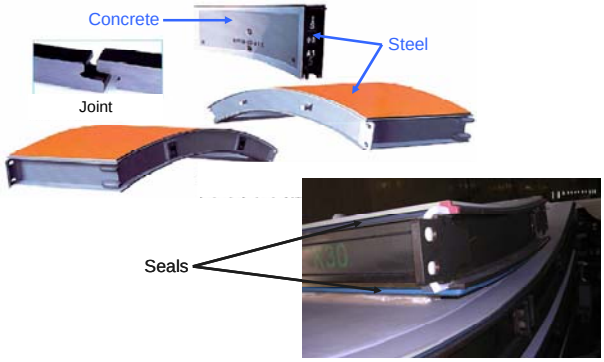

Fig.5 NM segment

In this study, we have equipped the MM with excavation process and material boundaries. Material boundaries, which are the boundary between different material property areas in the same block, have to set without losing easiness of mesh making. In realizing excavation process, it is essential that excavation surfaces work as free surfaces, and contacts and separations between blocks are enabled on the excavation surfaces. This report outlines the excavation process and the material boundary in the MM, and present analysis examples and applications.

3. Deformation analysis using Manifold Method (MM) for shield segment

3.1 The present design method of segments

Shield tunnel consists of segment ring by connecting with bolts etc. and uniting the segment used as a tunnel wall component. For this reason, the rigidity of the joint portion of a segment decreases compared with material itself. Moreover, depending on the way of assembling which shifted the joint position called the Chidorigumi, rings are constructed so that a strong mutual portion may assist the weak portion of a joint where the rigid decrease.
Thus, it becomes most important when designing a segment how the rigid decrease of a joint part is evaluated. Therefore, the structural model of the following segment rings is proposed by the valuation method of this joint until now.

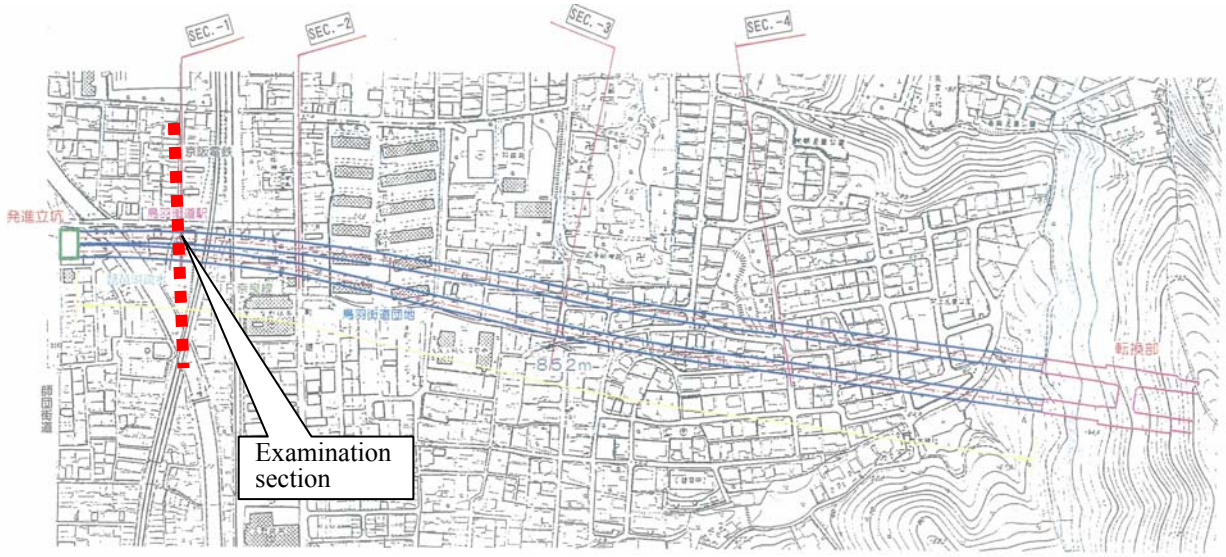

Fig.5 Fushimi Tunnel Plan (Shield Method area)

(1) Consider structure to be a flexural rigidity uniform ring without a segment joint

a) This is a method which is called a conventional method, was proposed around 1960 and has been used widely till the present.

b) Although it is called a correction conventional method and the structural model of a segment ring uses the same model as a conventional method. In order to evaluate the rigid decrease of a joint part, it is the method which introduced the effectiveness rate η of flexural rigidity, and introduced the concept of the premium rate ζ of a moment.

(2) A segment joint is considered to be a multi-hinge system ring.

The model by a multi-hinge system ring is a method used when the circumference of a tunnel is a good condition in many foreign countries, and is calculated by making a segment joint portion into hinge structure. If this method is used, the moment to generate will become quite small and the economical design will be attained. However, the influence of the surround ground around a tunnel is very great, and dangerous for applying to soft ground like Japan.

(3) The ring which has a rotation spring in a segment joint and has a shearing spring in a ring joint

It is called a beam-spring model and evaluated by using a segment main part as a beam by bending in a segment joint part and preparing the rotation spring to a moment in it. Moreover, in order to evaluate the alongside effect by the Chidorigumi, a shearing spring is arranged in a ring joint part.

In this research, it made to model a segment ring in a simple form as actually as possible closely into the plan. By a new method, it enables to analyze the action of the segment, and aims to reduce construction costs.

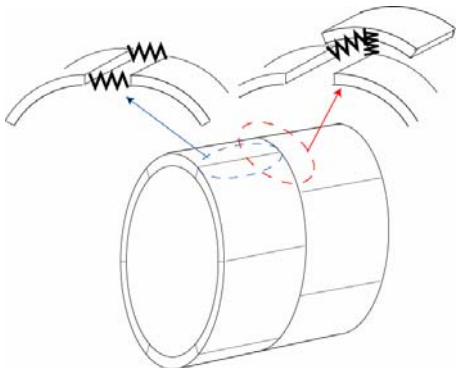

Fig. 6 The concept of a segment design method

3.2 Manifold Method

The Manifold Method (MM) (Shi 1991), as well as Discontinuous Deformation Analysis (DDA) (Shi 1988), is a powerful numerical analysis method to simulate displacement and deformation of rock mass including discontinuous planes such as joint, faults and so on. MM also has an advantage that mathematical meshes (cover) are independent of physical meshes or block boundaries, and mesh making for the analysis became easy.

3.3 Result of analysis in case of Fushimi Tunnel site

As shown as Fig.6, Tunnels comes closer at the end of west side each other.

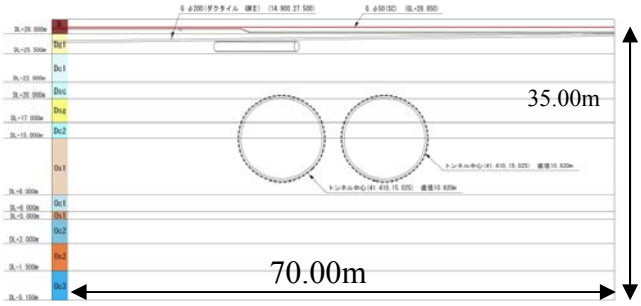

Fig.7 Tunnel arrangement and foundation composition

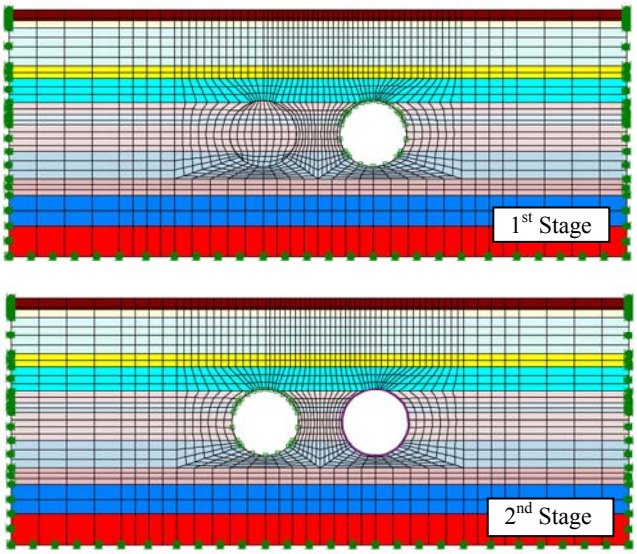

Fig.8 Digging of Eastbound tunnel is carried out first and Westbound tunnel after that.

Table.1 Material properties

Color	Material	E (kN/m^2)	ν	γ (kN/m^3)	C (kN/m^2)	ϕ (°)
	B	2.000E+04	0.45	20.0	0.00	30
	Dg1	4.000E+04	0.35	20.0	0.00	40
	Dc1	2.000E+04	0.40	20.0	100.00	0
	Dsc	2.000E+04	0.40	20.0	150.00	0
	Dsg	4.500E+04	0.35	20.0	0.00	40
	Dc2	2.000E+04	0.40	20.0	100.00	0
	Os1	8.000E+04	0.30	20.0	0.00	40
	Oc1	3.000E+04	0.40	20.0	280.00	0
	Oc2	3.000E+04	0.40	20.0	280.00	0
	Os2	8.000E+04	0.30	20.0	0.00	40
	Oc3	3.000E+04	0.40	20.0	280.00	0
	Segment	33.3+e7	0.30	2516-e3	0.50	

(1) Examination section

As shown in Fig.7, analysis was carried out in neighborhood construction case In addition, the size and soil composition of an analysis section are shown in Figure 8. The composition of analysis -- an analysis position (SEC-1 : STA 120), section width(70.00m), section height(35.00m) number of number6194, cover nodes 339.

(2) Modeling of the shield tunnel

The shield tunnel was approximated by right 12 square shapes, and was made into the outer diameter of 10.6m, and the inside diameter of 10.1m. Moreover, the shield segment was taken as equal 6 division. The shield segment was modeled as a block divided by the discontinuities.

(3) Analysis conditions

- Element conditions

Each element analyzed as a elastic element.

- Boundary conditions

Making the boundary condition of right-and-left both the sides of a section into the roller boundary which fixes displacement of the direction of X, the cross-sectional bottom fixed displacement of the direction of X, and the direction of Y.

- Physical properties value

The material properties of each soil layer supposes that it is the same as prior subsidence FEM analysis also as it is shown in a table.1. In addition, since convergence became slow when it being thought excessive to make the Young's modulus of a segment into the Young's modulus of steel materials, the physical-properties value of the segment was performed as follows.

Young's Modulus : 3.33×10^9 (0.01 times of FEM analysis)

Poisson's ratio : 0.3 Unit weight : 2700kN/m^3

About the physical-properties value of joint, all cohesion set to 0.0 N/m^2, and the internal friction angle was performed as follows.

Between the soil and shield segment : The internal friction angle of soil

Between shield segments : 50 degrees

・Parameter for analysis model

The main analysis parameters were set up as follows.

Normal Penalty Stiffness : 1.0 × 108N/m, Shear Penalty Stiffness : 1.0 × 106N/m, Fix Penalty Stiffness : 1.0×1010N/m

Time Step : 0.01sec, Maximum displacement ratio : 0.0001, 0pen-close Reference : 0.000001

Iteration : 1500 steps

・Stage of analysis

The analysis flow to iteration 1500 times was performed as follows.

1～500 steps : gravity analysis

500 steps : Excavation of Westbound tunnel

600 steps : Introduce of Segment(The stress of the element of shield segment relevance part is set to 0.0, and material properties is changed into the value of segment)

1000 steps : Excavation of Eastbound tunnel

1100 steps : Introduce of Segment(The stress of the element of shield segment relevance part is set to 0.0, and material properties is changed into the value of segment)

1500 steps : End of Analysis

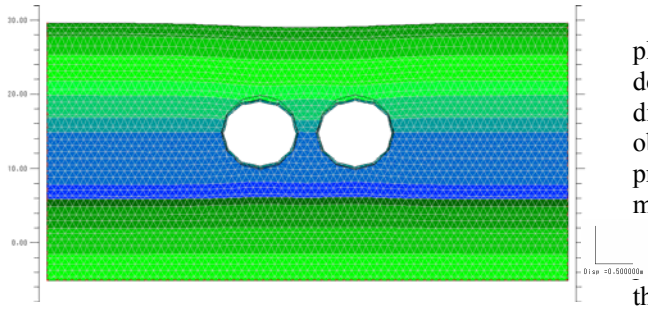

Fig.9 Displacement at the time of the 1500 steps on the basis of 500 steps

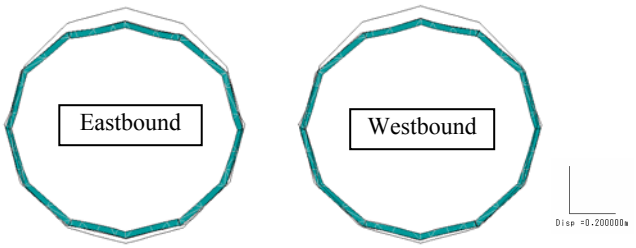

Fig.10 Deformation of Segment Displacement at the time of the 1500 steps on the basis of 500 steps Displacement arrow is expanded by 10 times.

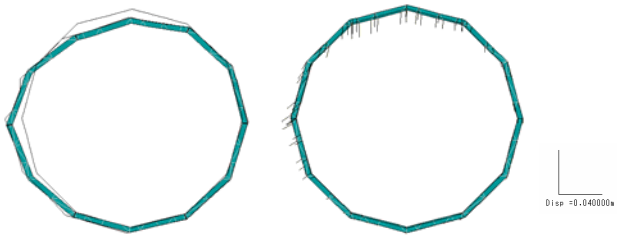

Fig.11 Displacement vector of Westbound tunnel Displacement at the time of the 1500 steps on the basis of 500 steps Displacement arrow is expanded by 50 times.

It is required to verify the function of the designed segment in addition to the rational design method of the segment by the MM method as shown in Fig.10 and 11. Since the three-dimensional arrangement based on Chidorigumi of segment is adopted in many cases, the interaction between segments works in three dimensions.

For this reason, we decided to propose digital photogrammetry as the technique of the ability to observe three-dimensional modification of a segment.

4. Measurement using photogrammetry for shield segment

4.1 Digital photogrammetry

In order to measure the displacements, we need to install the targets that can reflect the flashlight of camera. The fundamental mathematical model of digital photogrammetry is an optical triangulation that describes the perspective transformation from two dimensional image coordinates into three dimensional object space coordinates. The ultimate extension of the principles is to adjust many photogrammetric measurements to ground control values in a single solution known as a bundle adjustment. The analytical process is so named because of the many lights rays that pass through each lens position constituting a bundle of rays. Any object point can be determined as the intersection of the corresponding rays from each of many images.

All parameters describing the perspective transformation process can be also determined without prior knowledge of camera positions and calibration parameters.

The computational model of the bundle adjustment is based on the well-known collinearity equations as shown in Figure 12.:

$$x = \Delta x - c\frac{a_{11}(X-X_0)+a_{12}(Y-Y_0)+a_{13}(Z-Z_0)}{a_{31}(X-X_0)+a_{32}(Y-Y_0)+a_{33}(Z-Z_0)}$$

$$y = \Delta y - c\frac{a_{21}(X-X_0)+a_{22}(Y-Y_0)+a_{23}(Z-Z_0)}{a_{31}(X-X_0)+a_{32}(Y-Y_0)+a_{33}(Z-Z_0)} \qquad (1)$$

where x and y are the observed image coordinates; X_0,Y_0,Z_0 and X,Y,Z are the object space coordinates of the camera positions and object points, respectively; the a's are functions of three rotation angles of each image; $\Delta x, \Delta y$ and c are the interior orientation elements; Δx and Δy are perturbation parameters which describe departures from collinearity due to lens distortion and in-plane and out-of-plane image distortion, c being the focal length. This model including the interior orientation elements is known as a self-calibrating bundle adjustment. This method has the advantage of obtaining high photogrammetric accuracies with cameras having unknown calibration parameters.

The collinearity equations can be recast into the following observation equations by linearization:

$$v = A_1X_1 + A_2X_2 + \Delta \qquad (2)$$

where A_1,A_2 are the design matrices of the unknown exterior orientation elements, vector X_1, and object point coordinates, X_2; Δ is the discrepancy vector, v is the vector of image coordinate residuals. Solution for X_1 and X_2 is according to the method of least-squares.

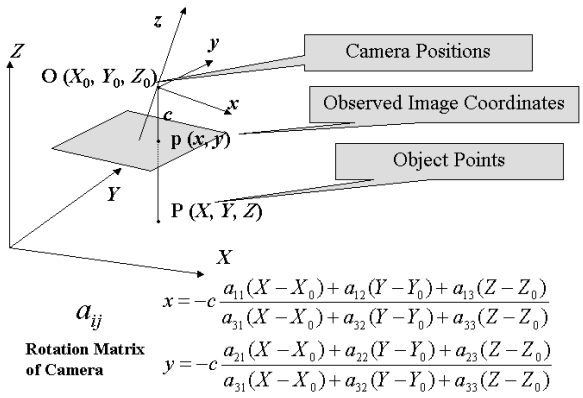

Figure 12. The concept of collinearity equations

4.2 How to apply the method at shield tunnel segment measurement

As seen in the part of analysis, there is difficulty in solving strictly the action between the segments of the structure and the hinge portion of the rigid, very big segment in contact with soft ground, and the direction of an axis. In order to solve these problems, it is necessary to observe the actual action of segments, and it needs to feed it back to the analysis method.
In order to observe deformation, it supposes that each segment is regarded as a rigid body which exercises as a block, and a target is arranged so that the form of a segment can be expressed.
We suggest to apply digital precision photogrammetry so that the monitor of the deformation of the segment ring of the tunnel wall can be carried out in detail. With regard to the unstable segments identified in the MM analysis and the segment borders, displacements of segments along tunnel ring were monitored by photogrammetry right below the observational zone like as nieghboring construction, i.e. crossing Lake Biwa water supply canal and railway crossings of Keihan line and JR Nara line.
During the observation procedure, we plan to install more than 300 targets placed tunnel wall were photographed by the digital photogrammetry technology, at first stage photography will carry out when the Shield machine go through the place and 2nd stage is when the machine come back to the observation zone.

(1)Photographing Equipment
Nikon D80 camera and a 18mm lens of the same manufacturer are selected. Nikon SB-600 Speedlight Flash is used inside the tunnel wall.

(2)Targets
After selecting the camera and lens, the diameter of targets is determined according to the measured distance to ensure the images of the targets could come out in 5 pixel or larger in diameter. The diameter is set at 30mm here. An example of target layout is shown in Figure.13.

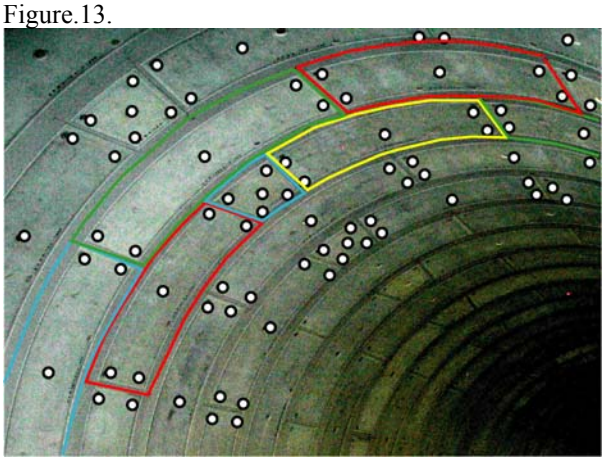

Figure.13 Target Layout (colored lines present boundary of each segment)

(3)Installation of Scales
At the Fushimi Tunnel, it is planned to install scale bars for external measurement. Six to ten 1m-long fiducial scale bars are prepared and installed.

(4)Photographing Conditions
The lens stop was set at F22 at maximum. The infinite focus was selected. The shutter speed and ISO sensitivity were set at 1/250 and 200, respectively.
Photographs were taken for every 6m at 3 points each at both upper and lower locations for each transversal direction.

5. Conclusions

We carried out a basic examination to propose the shield tunnel segment design method using MM. As a result, we recognized that the MM can treat segments as rigid blocks in soil ground appropriately. In examination, we also recognized the necessity to examine the stiffness value between segments.
In order to verify the applicability of the MM, we planned the in-site observation by a photogrammetry method at Fushimi Tunnel, which is now under construction. By comparing the result of MM with actual data of displacement at Fushimi Tunnel, we expect that the result will be fed back to the determination of MM parameters such as Penalty Stiffness.

References

Nakai, T., Ohnishi, Y., Ohtsu, H., Nishiyama, S.& Ryu, M.:Monitoring and Analysis of Tunnel in Discontinuous rock Masses by using Digital Photogrammetry and Key Block Theory at Houou Tunnel, EIT-Kyoto University-AIT Joint

Work-shop on Development of Rock Mechanics and Engineering, pp57-63, 2002

Ohnishi, Y., Nishiyama, S., Nakai, T & Ryu, M.: Monitoring and Analysis of Tunnel in Discontinuous Rock Masses by using Digital Photogrammetry and Key Block Theory, Proceeding of The 5th International Conference on Analysis of Discontinuous Deformation, 2002

Okamoto, A. : General Free Net Theory in Photogrammetry , Intl. Archives of Photogrammetry and Remote Sensing, XXVII-B3, pp.599-608, 1988

Sasaki, T., Morikawa, D., Ishii, D. and Ohnishi, Y., Elastic-Plastic Analysis of Jointed Rock Models by Manifold Method, Proc. Second International Congress on Analysis of Discontinuous Deformation (2nd ICADD), 1997

Shi, G.-H., Manifold Method of Material Analysis, Transactions of 9th Army Conference on Applied Mathematics and Computing, Report No.92-1, U.S. Army Research Office, 1991.

Tamura, T., Adachi, T., Hiromatsu, T. & Sakamoto, H., 3-D Analysis of Shield Tunnel Compose of Perfectly Rigid Segments, Journal of JSCE, No.652/Ⅲ-51.61-72, 2000

A new meshfree displacement approximation mode for DDA method and its application

Ma Yong Zheng, Jiang Wei, Huang Zhe Chong, Zheng Hong

Institute of Rock and Soil Mechanics, Chinese Academy of Sciences, Wuhan 430071, P. R. CHINA

The forward discontinuous deformation analysis method (DDA) adopts complete first order displacement approximations, so it has a simple form of block stiffness sub-matrices and high efficiency. However this displacement function can only describe constant stress or stain within each block, and fails to model complex deformation patterns such as bending or twisting. Some usual improvements include: series of higher order, or sub-blocks meshing, or coupling the DDA method with the Finite Element Method (FEM) or finite difference method. A complete new way of approximating block displacements is suggested here, namely the Moving Least-squares (MLS) approximation. To do so, interpolative nodes should firstly be scattered into blocks or along their borders, it can be looked as coupling DDA with Element Free Galerkin (EFG) method. The advantage of adopting this new displacement approximation mode is mainly that all advantages of Meshfree Methods over meshing methods can be used directly by DDA, such as crack propagation within blocks, block breakage, etc.

Keywords: Discontinuous Deformation Analysis (DDA); Element Free Galerkin (EFG); Meshfree Methods; displacement approximate mode; Move least square (MLS)

1. Introduction

Numerical modeling of geological discontinuities has a long history, the development of the joint element by Goodman et al is a traditional way (Goodman et al 1968), and the complete discrete element methods are created thereafter, e.g. the earlier Discrete Element Method (DEM) by Cundall and the latter DDA by Shi. DDA is comparatively an efficient method based on rigorous mathematical and mechanical theory, and till now, applied to more and more engineering problems, such as underground tunnels and caverns, foundations, slopes, groundwork, as well as earthquakes, demolition impact, particles' motion, etc.

DDA originally adopts first order series as block displacement function, so it has a simpler matrix form compared with finite element method, which makes it very efficient. But it can only describe constant stress or strain within each block, fails to model block bending or twisting or complicated stress fields, even only three constraint points (not along one line) can fix one block. A general series approximation is originally proposed by Shi (1988), different blocks can have different order series as displacement functions (Koo and Chern 1996; Max 1996). Actually series with too high order (≥ 4) leads to numerical vibration (namely Runge phenomenon) and is also difficult to implement, so the order is usually restrict to be not above 3, which can meet the demand for describing block bending, but might has difficulty in analyzing block fracture etc. To investigate block material nonlinear mechanical response, coupling with FEM has been tried by meshing DDA block into finite elements (Chang 1994; Lee 2002). However, this meshing method has difficulties in itself while treating with crack propagation or large deformation. Sub-block meshing of original large blocks has been tried to investigate crack propagation, see Amendei and Lin (1996) and etc.

A totally new displacement approximate mode is proposed here, which never re-mesh large blocks but uses meshfree interpolative nodes scattered into blocks or along the borders, then the MLS approximation procedure is used to evaluate the approximate displacement value at any point of the blocks. This can be looked as coupling the EFG method (Belytschko et al 1994), a thriving numerical method that overcomes the shortages of meshing methods. By this way, DDA can easily treat with block breakage, crack propagation, large deformation, material nonlinear mechanics response etc.

Like FEM, DDA is a typical displacement method with implicit solution of equilibrium equations, block stiffness sub-matrices and force variables are derived by minimizing the total potential energy. For different displacement approximate modes this procedure is similar, but might be different in formula forms. So, in this article, this procedure is repeated while using this new mode, the corresponding formulae are list in section 3. Some numerical examples are tested in section 4, which demonstrate this new method is feasible.

2. The complete first order displacement approximation

DDA displacement function is the complete first order displacement approximation of block displacements. As far as two-dimension is concerned ,each block has six degrees of freedom including translation variables of

rigid body u_0、v_0, rotation angle r_0 and deformation variables of block(normal strain ε_x、ε_y and tangential strain γ_{xy}), as shown below:

$$\mathbf{d}=\begin{pmatrix}u_0 & v_0 & r_0 & \varepsilon_x & \varepsilon_y & \gamma_{xy}\end{pmatrix} \tag{1}$$

The shape matrix is presented as the formula (2):

$$\mathbf{T}=\begin{pmatrix}1 & 0 & -(y-y_0) & (x-x_0) & 0 & (y-y_0)/2\\ 0 & 1 & (x-x_0) & 0 & (y-y_0) & (x-x_0)/2\end{pmatrix} \tag{2}$$

The displacement $\mathbf{u}=\begin{pmatrix}u & v\end{pmatrix}^T$ of any point $\mathbf{x}\begin{pmatrix}x & y\end{pmatrix}$ of the block could be denoted as product of displacement variables as the formula (1) mentioned and the shape matrix (2), shown as the following formula (3):

$$\mathbf{u}=\mathbf{T}\cdot\mathbf{d}^{\mathrm{T}} \tag{3}$$

The above $\mathbf{u}$ is easily proved to be equivalent to the complete first order approximation of block displacements as the following form (4), where a_i and b_i ($i=1,2,3$) are known constants, so the first derivatives of displacements are constant, then block stress and strain are constants.

$$\begin{cases}u=a_1x+a_2y+a_3\\ v=b_1x+b_2y+b_3\end{cases} \tag{4}$$

3. The scheme of DDA with the MLS approximation

3.1 Introduction of the MLS approximation

The MLS approximation proposed by Lancaster and Salkauskas (1981) is used for smoothing and interpolating data, and is latterly adopted by the EFG method to construct trial function and test functions. Suppose a smooth function $\boldsymbol{u(x)}$ defined on domain Ω, with N interpolative nodes, each node $\boldsymbol{x}_i$ valued $\boldsymbol{u(x}_i\boldsymbol{)}$ ($i=1,\cdots,N$), then a local approximation at evaluation point $\boldsymbol{x}$ is $\bar{\mathbf{u}}^h(\mathbf{x},\bar{\mathbf{x}})$:

$$\bar{\mathbf{u}}^h(\mathbf{x},\bar{\mathbf{x}})=\mathbf{p}^T(\bar{\mathbf{x}})\cdot\mathbf{a}(\mathbf{x}) \tag{5}$$

Where $\bar{\mathbf{x}}$ is the position of the local nodes nearby, the vector $\mathbf{p}(\bar{\mathbf{x}})$ is complete polynomial basis with consistency m, the unknown coefficient vector $\mathbf{a}(\mathbf{x})$ is selected by minimizing the following weighted least-squares discrete L2 error norm, shown in the formula (6), $w_i(\mathbf{x})=w(\mathbf{x}-\mathbf{x}_i)$ is the weighting function:

$$\mathbf{J}=\sum_{i=1}^{N}w_i(\mathbf{x})[\bar{\mathbf{u}}^h(\mathbf{x},\bar{\mathbf{x}})-\mathbf{u}(\mathbf{x}_i)]^2 \tag{6}$$

Substitute function (5) to (6), and minimize $\mathbf{J}$ by setting the derivative of $\mathbf{J}$ with respect to $\boldsymbol{a(x)}$ equal to zero, i.e. $\dfrac{\partial\mathbf{J}}{\partial\mathbf{a}(\mathbf{x})}=0$, then $\boldsymbol{a(x)}$ is obtained by:

$$\mathbf{a}(\mathbf{x})=\mathbf{A}(\mathbf{x})^{-1}\cdot\mathbf{B}(\mathbf{x})\cdot\mathbf{d} \tag{7}$$

Where $\mathbf{d}$ represents the node displacements $u(\boldsymbol{x}_i)$, ($i=1,\cdots,N$). The matrix $\mathbf{A(x)}$ called moment matrix, is of size $m\times m$, and has to be inverted, ,see formula (8); The matrix $\mathbf{B(x)}$ is of size $m\times N$,see formula (9):

$$\mathbf{A}(\mathbf{x})=\sum_{i=1}^{N}w_i(\mathbf{x})\mathbf{p}(\mathbf{x}_i)\mathbf{p}^T(\mathbf{x}_i) \tag{8}$$

$$\mathbf{B}(\mathbf{x})=[w_1(\mathbf{x})\mathbf{p}(\mathbf{x}_1),w_2(\mathbf{x})\mathbf{p}(\mathbf{x}_2),\ldots w_N(\mathbf{x})\mathbf{p}(\mathbf{x}_N)] \tag{9}$$

In order to extend this local approximation to the whole domain, the so-called moving-procedure is introduced to achieve a global approximation, usually controlled by the weighting function $w_i(\mathbf{x})$.

$$\mathbf{u}(\mathbf{x})\approx\mathbf{u}^h(\mathbf{x})=\mathbf{u}^h(\mathbf{x},\bar{\mathbf{x}})\big|_{\bar{\mathbf{x}}=\mathbf{x}} \tag{10}$$

Then the shape functions can be presented as:

$$\mathbf{N}(\mathbf{x})=\mathbf{p}^T(\mathbf{x})\mathbf{A}^{-1}(\mathbf{x})\mathbf{B}(\mathbf{x}) \tag{11}$$

The first order partial derivative of shape function $\boldsymbol{N(x)}$ is $\boldsymbol{N}_{,k}$ ($k=1,2$):

$$\mathbf{N}_{,k}=\mathbf{p}^T{}_{,k}(\mathbf{x})[\mathbf{A}^{-1}(\mathbf{x})\mathbf{B}(\mathbf{x})]$$
$$+\mathbf{p}^T(\mathbf{x})[-\mathbf{A}^{-1}\mathbf{A}_{,k}\mathbf{A}^{-1}(\mathbf{x})\mathbf{B}(\mathbf{x})+\mathbf{A}^{-1}(\mathbf{x})\mathbf{B}_{,k}(\mathbf{x})] \tag{12}$$

The MLS approximation has high accuracy and good consistency, as well as smoothness of any order, but the shape function is not interpolating and the calculation task is heavy. In this article, the MLS approximation is adopted as the displacement approximation mode for DDA, of course other similar approximation modes of Meshfree Methods are adoptable.

3.2 The global equations

In this section, the scheme of DDA coupling with a general Meshfree displacement approximation mode is discussed. Firstly, interpolative nodes should be arranged according to each block's geometry, and the nodal displacements are taken as the unknown variables to be solved; so the approximate displacement at any evaluation point can be constructed by the Meshfree displacement approximation mode adopted by DDA, e.g. the MLS approximation. Then according to the procedure of minimizing potential energy, stiffness matrices and force variables are deduced, the unknown

nodal displacements are obtained by solving the established linear algebra equations. This procedure is repeated for each contact open-close iteration step. Finally, after reaching a converged contact status, block displacements, stresses or strains are solved again using the MLS approximation or other similar ones. The above procedures should be repeated at each time step until all the time steps finish. The MLS approximation is adopted in this scheme, to other displacement approximation mode it is similar.

Simultaneous equations system is established as below for a two-dimensional block system. Suppose there are n_i discrete nodes in block i, the unknown displacement sub-vector of node j is $\left(d_i^{1j}, d_i^{2j}\right)$, and the force sub-vector of node j is $\left(p_i^{1j}, p_i^{2j}\right)$, so the displacement sub-vector $\mathbf{d}_i$ and load sub-vector $\mathbf{F}_i$ of block i can be denoted as formula (13) and (14):

$$\mathbf{d_i} = [d_{11}^i, d_{21}^i, \ldots d_{1j}^i, d_{2j}^i, \ldots, d_{1n^i}^i, d_{2n^i}^i]^T \tag{13}$$

$$\mathbf{F_i} = [p_{11}^i, p_{21}^i, \ldots, p_{1j}^i, p_{2j}^i, \ldots, p_{1n}^{i^i}, p_{2n^i}^i]^T \tag{14}$$

For a block system composed of m blocks, the simultaneous equilibrium equations can be established as formula (15).

$$\begin{bmatrix} \mathbf{K}_{11} & \mathbf{K}_{12} & \cdots & \mathbf{K}_{1m} \\ \mathbf{K}_{21} & \mathbf{K}_{22} & \cdots & \mathbf{K}_{2m} \\ \vdots & \vdots & \ddots & \vdots \\ \mathbf{K}_{m1} & \mathbf{K}_{m2} & \cdots & \mathbf{K}_{mm} \end{bmatrix} \begin{bmatrix} \mathbf{d}_1 \\ \mathbf{d}_2 \\ \vdots \\ \mathbf{d}_m \end{bmatrix} = \begin{bmatrix} \mathbf{F}_1 \\ \mathbf{F}_2 \\ \vdots \\ \mathbf{F}_m \end{bmatrix} \tag{15}$$

Where $\mathbf{K_{ii}}$ is the matrix ($2n_i \times 2n_i$) representing the sum of contributing sub-matrices for the block *i*, $\mathbf{K_{ij}}$ is the matrix ($2n_i \times 2n_j$) representing the sum of contributing sub-matrices of contacts between blocks *i* and *j* or other inter-block actions like bolting etc, the global coefficient matrices are positive and symmetrical along the diagonal. $\mathbf{F_i}$ is the matrix of resultant equivalent forces acting on the block *i*. Π represents the potential energy, according to the minimum potential energy principle, we have:

$$\mathbf{K}_{ii} = \frac{\partial^2 \Pi}{\partial \boldsymbol{d}_i^{\,2}}; \mathbf{K}_{ij} = \frac{\partial^2 \Pi}{\partial \mathbf{d}_i \partial \mathbf{d}_j};$$
$$\mathbf{F_i} = -\frac{\partial \Pi(0)}{\partial \boldsymbol{d}_i}; \mathbf{F}_j = -\frac{\partial \Pi(0)}{\partial \mathbf{d}_j} \tag{16}$$

3.3 Extremum of the total potential energy

DDA, as an implicit displacement method, is similar to FEM, which deduces the stiffness matrix and force vector according to the extremum principle of the total potential energy. The variation process is similar for different displacement modes but different in expression form. In this section, many influencing factors are discussed, which contribute to stiffness sub-matrices and force vectors, and include: elastic strain energy, initial stress and strain, inertia, external loads, contact forces and friction forces between blocks, restraint displacements, etc.

3.3.1 Elastic strain energy

The stiffness sub-matrix by minimizing elastic strain energy of the block *i* can be expressed in the general form shown as the right part of the following formula (17) and contribute to sub-matrix $\mathbf{K}_{ii}$. Here the symbol '$\Leftarrow$' represents that the right part is added to the left.

$$\mathbf{K}_{ii} \Leftarrow \int_{\Omega} \mathbf{B}^{\mathbf{T}} \mathbf{D} \mathbf{B} d\boldsymbol{\Omega} \tag{17}$$

Where $\boldsymbol{D}$, called the Young's module matrix, has the same expression as in FEM, and the matrix $\mathbf{B}$ is shown as below:

$$\mathbf{B} = \left[\mathbf{B}_1, \mathbf{B}_2, \ldots, \mathbf{B}_N\right]; \boldsymbol{B}_l = \begin{bmatrix} N_{l,x} & 0 \\ 0 & N_{l,y} \\ N_{l,y} & N_{l,x} \end{bmatrix};$$

$l = 1, \ldots, N$;

N is the number of nodes for the block *i*, $N_{l,k}$ is the first order derivative of the shape function, as shown in formula (12), $k = x, y$.

3.3.2 Initial stress and strain

Suppose the block *i* has the initial stress $\boldsymbol{\sigma_0}$ and the initial strain $\boldsymbol{\varepsilon'_0}$, the equivalent load sub-matrix can be expressed as:

$$\mathbf{F}_i \Leftarrow -\int_{\boldsymbol{\Omega}} \mathbf{C} d\boldsymbol{\Omega} + \int \mathbf{B}^{\mathbf{T}} \mathbf{D} \boldsymbol{\varepsilon'}_0 \, d\boldsymbol{\Omega} \tag{18}$$

Where $\boldsymbol{C} = [\boldsymbol{C_1}, \boldsymbol{C_2}, \ldots, \boldsymbol{C_N}]$,

$\boldsymbol{C}_l = \left[N_{l,x}\sigma_x^0 + N_{l,y}\tau_{xy}^0 \quad N_{l,y}\sigma_y^0 + N_{l,x}\tau_{xy}^0\right], l = 1, \ldots, N$.

3.3.3 Inertia force

Denote ρ as the block density, t the time step of this iteration, $\boldsymbol{v}_0$ the nodal initial velocity. Then the inertia force's contribution to the global equations can be listed as formula (19)- (20).

$$\mathbf{K}_{ii} \Leftarrow \frac{\rho}{t^2} \int_{\Omega} \mathbf{N}^{\mathbf{T}} \mathbf{N} d\Omega \tag{19}$$

$$\mathbf{F}_i \Leftarrow \frac{\rho}{t} \int_{\Omega} \mathbf{N}^{\mathbf{T}} \mathbf{N} d\Omega \cdot \mathbf{V_0} \tag{20}$$

3.3.4 Displacement constraints

Because the MLS shape functions are not interpolative, the penalty method is preserved to impose the essential boundary conditions. The penalty spring stiffness k should be chosen beforehand (usually 40-100 times material Young's modulus). Suppose a constraint displacement $\mathbf{u}_c = \begin{Bmatrix} \mathbf{u}_m \\ \mathbf{v}_m \end{Bmatrix}$ at the point $\mathbf{x}_0$, we have:

$$\mathbf{K}_{ii} \Leftarrow k\mathbf{N}(\mathbf{x}_0)^{\mathbf{T}}\mathbf{N}(\mathbf{x}_0);$$
$$\mathbf{F}_{\mathbf{i}} \Leftarrow k\mathbf{N}(\mathbf{x}_0)^T \cdot \mathbf{u}_c \quad (21)$$

3.3.5 External loads

Generally external loads include fixed loads, distributed loads or volume loads (e.g. gravity), etc. For fixed load $\mathbf{f}_0$, the equivalent load to the global equations is denoted as the following expression (22).

$$\mathbf{F}_i \Leftarrow \mathbf{f}_0 \cdot \mathbf{N} \quad (22)$$

For distributed load $\bar{\mathbf{f}}_0$ along the border Γ, see the formula (23).

$$\mathbf{F}_i \Leftarrow \int \bar{\mathbf{f}}_0 \cdot \mathbf{N} d\Gamma \quad (23)$$

The volume load (such as gravity) $\mathbf{g}_0$ has the equivalent load contribution as the formula (24).

$$\mathbf{F}_i \Leftarrow \int \mathbf{N} d\Omega \cdot \mathbf{g}_0 \quad (24)$$

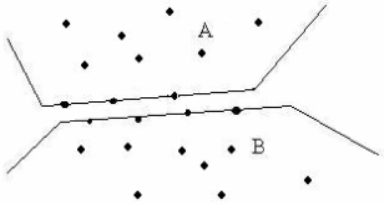

Fig 1 the blocks with possibly intruding

3.3.6 Contacts analysis

The DDA employs so-called point-face contact model suitable for treating with large sliding of blocks or departments between blocks, contacts constraints are 'no tension between blocks and no penetration of one block into another' usually imposed by the penalty spring method (Goodman et al 1968). While this method is adopted again in DDA with this new displacement mode, additionally the nodes on the edges need to be handled as well as block vertices. For the block displacement is nonlinear, overlapping between curve edges is possible and should be avoided, e.g. in Fig 1, the blocks A and B have border nodes possibly intruding into each other block.

Suppose the block i has N^i nodes, the block j has N^j nodes and the spring stiffness p, there is a contact between point p_1 and edge p_2p_3 (the coordinates of point p_k denoted as $(x_k \quad y_k)$, $k = 1,2,3$). The area of triangle composed of the three points p_k is s_0, the edge length l. Then the contributions to the global equations can be denoted as the following formulae (25)- (27):

$$\mathbf{K}_{ii} \Leftarrow p\mathbf{e}^T\mathbf{e}, \quad \mathbf{K}_{jj} \Leftarrow p\mathbf{g}^T\mathbf{g} \quad (25)$$

$$\mathbf{K}_{ij} \Leftarrow p\mathbf{e}^T\mathbf{g}, \quad \mathbf{K}_{ji} \Leftarrow p\mathbf{g}^T\mathbf{e} \quad (26)$$

$$\mathbf{F}_i \Leftarrow -\frac{ps_0\mathbf{e}^T}{l}, \quad \mathbf{F}_j \Leftarrow -\frac{ps_0\mathbf{g}^T}{l} \quad (27)$$

Where components of $\mathbf{e}$ and $\mathbf{g}$ are listed as the following (28)- (29):

$$\mathbf{e}_{\mathbf{I}} = (e_{I1} \quad e_{I2}); \mathbf{e} = (\mathbf{e}_{\mathbf{1}} \quad \cdots \quad \mathbf{e}_{\mathbf{N}});$$
$$I = 1,...,N^i \quad (28)$$

$$\mathbf{g}_{\mathbf{I}} = (g_{I1} \quad g_{I2}); \mathbf{g} = (\mathbf{g}_{\mathbf{1}} \quad \cdots \quad \mathbf{g}_{\mathbf{N}});$$
$$I = 1,...,N^j \quad (29)$$

But components of $\mathbf{e}_{\mathbf{I}}$ or $\mathbf{g}_{\mathbf{I}}$ are different from that with linear displacement mode, for normal spring, the components are listed as:

$$e_{I1} = (y_2 - y_3)N_I^{\mathbf{i}}(x_1, y_1)/l;$$
$$e_{I2} = (x_3 - x_2)N_I^{\mathbf{i}}(x_1, y_1)/l;$$
$$g_{I1} = [(y_3 - y_1)N_I^{\mathbf{j}}(x_2, y_2) + (y_1 - y_2)N_I^{\mathbf{j}}(x_3, y_3)]/l;$$
$$g_{I2} = [(x_1 - x_3)N_I^{\mathbf{j}}(x_2, y_2) + (x_2 - x_1)N_I^{\mathbf{j}}(x_3, y_3)]/l; \quad (30)$$

Similarly, for tangential spring, the components are as:

$$e_{I1} = (x_3 - x_2)N_I^{\mathbf{i}}(x_1, y_1)/l;$$
$$e_{I2} = (y_3 - y_2)N_I^{\mathbf{i}}(x_1, y_1)/l;$$
$$g_{I1} = (x_2 - x_3)N_I^{\mathbf{j}}(x_0, y_0)/l;$$
$$g_{I2} = (y_2 - y_3)N_I^{\mathbf{j}}(x_0, y_0)/l; \quad (31)$$

In function (30)- (31), $N_I^k(\mathbf{x})$ is the shape function; the superscript $k = i, j$ represents the block number.

3.3.7 Friction forces

Suppose a contact between point p_1 of the block i and the edge p_2p_3 of the block j (the coordinate of

point p_k denoted as $(x_k \quad y_k)$, $k = 1,2,3$), the edge length l . The vertical projection of point p_1 to the edge is p_0 (x0, y0), the friction force is denoted as f . Then the equivalent loads to the block i contributed by the friction force can be expressed as:

$$\mathbf{F}_i \Leftarrow -f \cdot \mathbf{H} \tag{32}$$

Where $\mathbf{H}=[H_{11},H_{12},H_{21},H_{22},\cdots H_{N1},H_{N2}]^T$, and the components of $\mathbf{H}$ are as following:

$$H_{I1} = N^{\mathbf{i}}_{I1}(x_1, y_1)(x_3 - x_2)/l;$$
$$H_{I2} = N^{\mathbf{i}}_{I2}(x_1, y_1)(y_3 - y_2)/l; \tag{33}$$

The equivalent loads to the block j :

$$\mathbf{F}_j \Leftarrow f \cdot \mathbf{H} \tag{34}$$

The components of $\mathbf{H}$ are listed as:

$$H_{I1} = N^{\mathbf{j}}_{I1}(x_0, y_0)(x_3 - x_2)/l;$$
$$H_{I2} = N^{\mathbf{j}}_{I2}(x_0, y_0)(y_3 - y_2)/l \tag{35}$$

3.4 output of block stress fields

The block stresses at the end of certain time step are accumulated by all the increments of the time steps before, and are also the initial stresses of the next step, as shown in the following formula (36):

$$\boldsymbol{\sigma} = \sum \Delta\boldsymbol{\sigma} \tag{36}$$

In DDA with linear displacement mode, the stress increment $\overline{\Delta\boldsymbol{\sigma}}$ is the even value of the whole block, obtained by the product of the solved strain increment $\overline{\Delta\boldsymbol{\varepsilon}}$ with **D** (the Young modulus matrix), namely $\overline{\Delta\boldsymbol{\sigma}} = \overline{\Delta\boldsymbol{\varepsilon}} \times \mathbf{D}$. As for the Meshfree displacement approximate mode, the stress increment $\Delta\boldsymbol{\sigma}(\mathbf{x})$ at certain point **x** in the block should be computed as following:

$$\Delta\boldsymbol{\sigma}(\mathbf{x}) = \mathbf{D} \cdot \Delta\boldsymbol{\varepsilon}(\mathbf{x}) = \mathbf{D} \cdot \mathbf{N}'\mathbf{d} \tag{37}$$

Where $\mathbf{N}'$ is the derivative of the shape function.

The total stress $\boldsymbol{\sigma}_i$ of the interpolative node i can be accumulated according to the formulae (36)-(37); while for certain evaluation point $\mathbf{x}$, the stress $\boldsymbol{\sigma}(\mathbf{x})$ should be calculated as the function (38), which corresponds to implement a MLS fit according to the stresses at the influent nodes around.

$$\boldsymbol{\sigma}(\mathbf{x}) = \sum_{i=1}^{n} \mathbf{N}_i(\mathbf{x}) \cdot \boldsymbol{\sigma}_i \tag{38}$$

Here n represents number of the influent nodes around point $\mathbf{x}$ in the block, $\mathbf{N}_i(\mathbf{x})$ is the shape function components of one of the influent node i .

4. Numerical examples

4.1 Example 1. The overlapped beams under point load

Fig 2 shows two overlapped beams fixed on the left side, and the subjacent one suffers a point load P upward (at the right-bottom angle point A) (Zheng et al 2002). The size of each beam is 10m×1m×1m, no friction between the beams, Young modulus 1500MPa,and Poisson's ratio 0.25. Suppose case 1: P=1.5KN corresponds to small deformation problem; and Case 2: P=1.5MN which corresponds to large deformation problem.

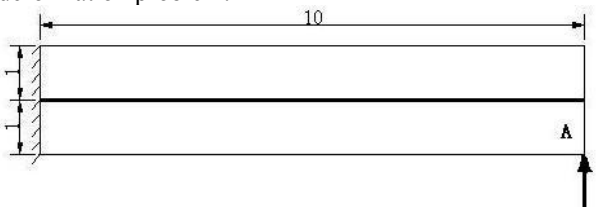

Fig 2 overlapped beams problem

In case 1, the y displacement of the reference point is about 2.02569mm after 50 steps, identical with that in Zheng et al (2002), as shown Fig 3. The stress σ_x field is shown at Fig 4; the max stress value is about

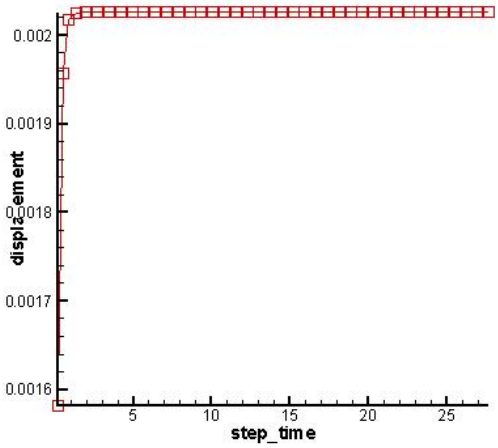

Fig 3 y displacement of point A vs time of case 1

$\pm$ 45Kpa, lies on the left-hand of the beams.

In case 2, large displacements of the two beams occur since the point load P is large, the maximum displacement at A is 1.94913m. The stress field σ_x and the deformed configurations are shown in Fig 5, the max stress value is about $\pm$ 45Mpa, on the left-hand of the beams, which sounds reasonable.

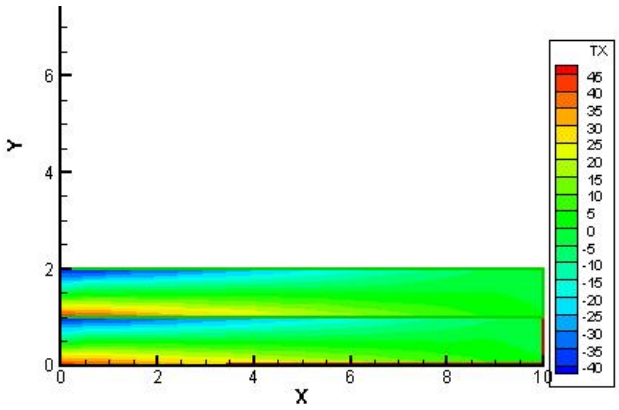

Fig 4 x normal stress and the deformed configuration of case 1

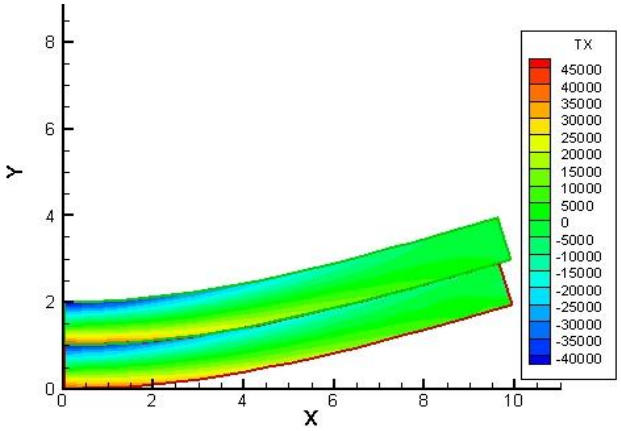

Fig 5 x normal stress and the deformed Configuration in case 2

4.2 Example 2. A slope sliding along the circular failure surface

Suppose a slope sliding along a potential circular sliding surface shown in Fig 6, with height 10m, sloping at angle α=45º, the friction angle Φ=20º, weight ν=20KN/m^3, Poisson ratio μ=0.35,no cohesion force. The slope is separated into several blocks with interpolative nodes scatted shown in Fig 6.

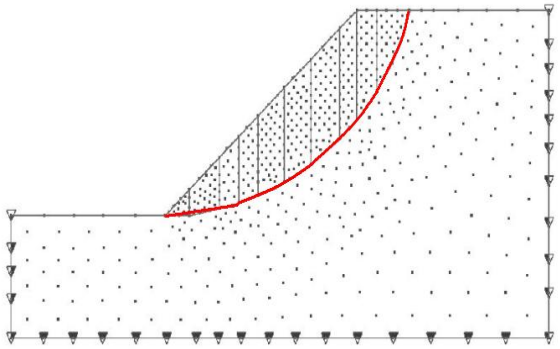

Fig 6 the numerical model of the slope with a circular Sliding surface

The displacement ratio is set 0.001, time-step is automatically set by the DDA program. Fig 7 shows the max principal stress result of the 1st iteration time-step, which indicates that the stress, caused mainly by gravity, increases with the depth and the stress level of small blocks above the sliding surface is relatively lower, from -10KPa to -35KPa.

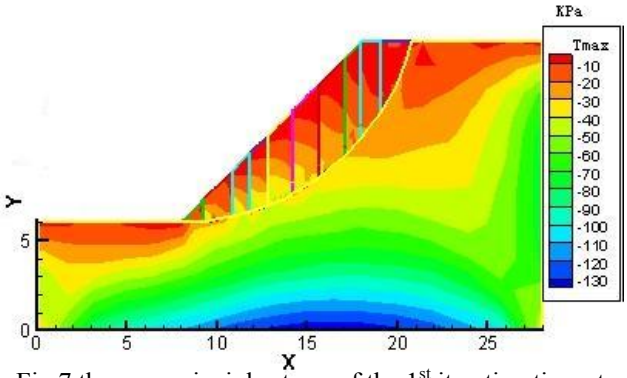

Fig 7 the max principle stress of the 1st iteration time step

For DDA with two different displacement modes, the deformed block configurations (shown in Fig 8-9) at the 100th time step seem to be similar. In Fig 9 the maximal principal stress field is also displayed, which is calculated by DDA with the Meshfree displacement mode.

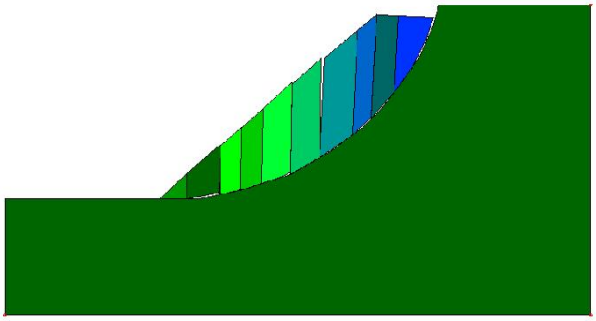

Fig 8 the result of linear mode DDA

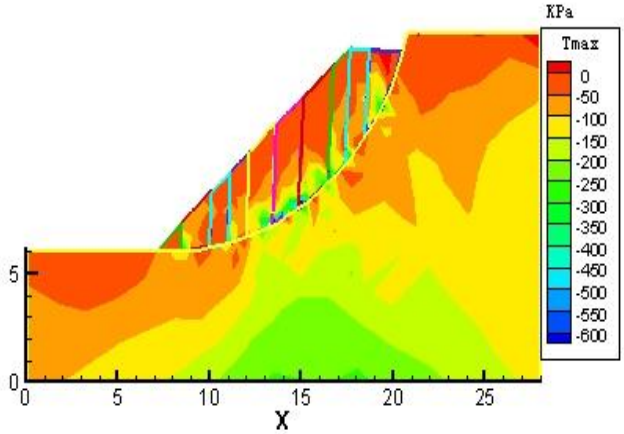

Fig 9 the result of DDA with MLS mode (With maximal principle stress)

4.3 Example 3. An arc beam under fixed load

The numeric model of the arc beam under a fixed load is shown in Fig 10, which is composed by 7 discrete blocks (each forms an isosceles trapezoid 0.42m×0.28m×0.5m×0.5m), the const fixed load -0.05T , Young's modulus 200T/m^2; Poisson ratio μ=0.2, Density ρ=0.1T/m^3,Gravity -1.0T,no friction between blocks.

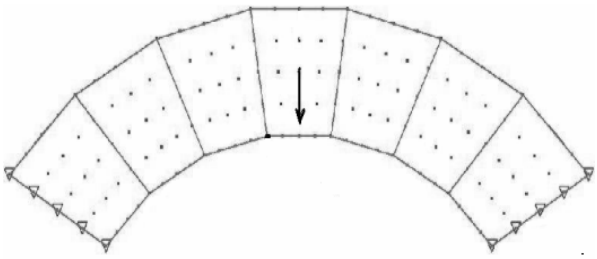

Fig 10 the numeric model of the arc beam model

The block configuration results calculated by DDA with different displacement modes at the 30th time step are very similar shown in Fig 11 and Fig 12. In Fig 12, the block stresses σ_x calculated by DDA with MLS approximate mode are also displayed.

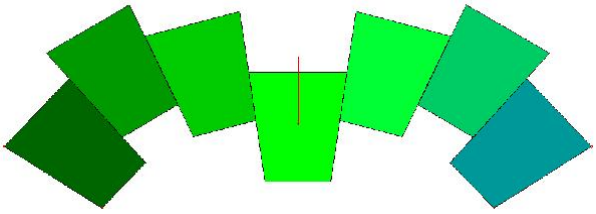

Fig 11 Result of the linear mode DDA

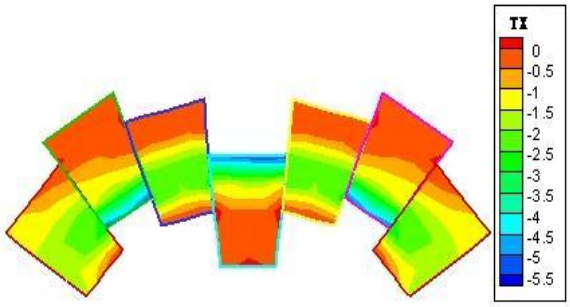

Fig 12 Result of the new mode DDA
(With σ_x normal stress)

The linear mode DDA can get good results of block configurations and displacements, in an other word, blocks with simple geometry and possible simple stresses need not be modeled by displacement approximation functions of high orders.

4.4 Example 4. A collapsing roof

The size of roof is 270m×180m, the bottom blocks (40m×20m) on the left and right side are fixed, the Young's modulus 5000Pa, Poisson ratio 0.3, the density 0.1N/m^3, gravity -0.5N/m^2, and no friction between blocks. Fig 13 shows the result of the linear mode DDA at the 500th iteration time step; and Fig 14 shows the result of the new mode DDA as well as the maximal principal stress field.

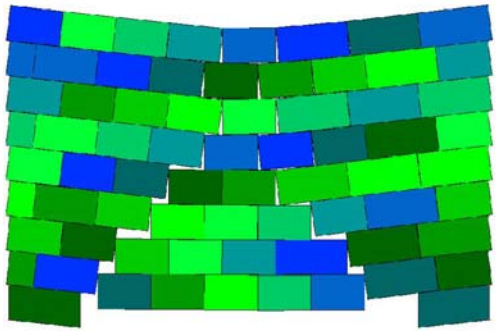

Fig 13 the result of the linear mode DDA

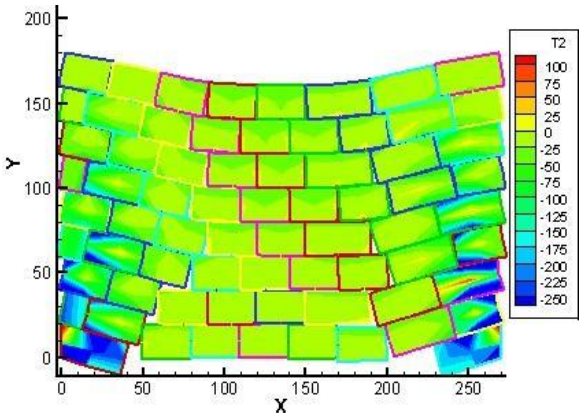

Fig 14 the result of the new mode DDA
(With the principal stress field)

On comparing the above Fig 13 with Fig 14, it is found that there is some slight difference between deformed block configurations, no block bending phenomena occur in Fig 13, but obvious in Fig 14.

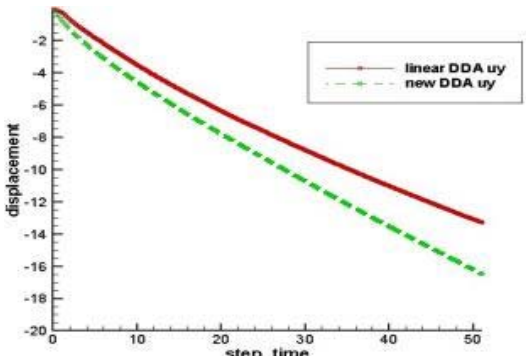

Fig 15 Contrast of displacement sedimentation vs. time at the middle position of the roof's top

Fig 15 shows displacement sedimentation vs. time at the middle position of the roof's top, Obviously the roof sedimentation obtained by the new mode DDA is a little bigger than the solution obtained by DDA with the linear mode, which we call 'block bending effect'.

5. Conclusions

In the original DDA method, a simple linear displacement mode is adopted, which is very suitable for simple block geometry or simple and low stress levels. For complicated block geometries and stresses and deformations (e.g. block bending), displacement functions of high order should be implemented.

In this article, a meshfree displacement approximation mode is adopted, namely the MLS approximation. The application to numerical examples in section 4 shows that the scheme of DDA with the MLS approximation is feasible; contrasts of numerical results of DDA with linear displacement mode and that with MLS approximation show that, except when block bending is not ignorable, the deformed block configurations are very similar for both displacement approximation modes; much more accurate stresses are of course obtained by MLS approximation of block displacement, but much heavier task of calculation is taken too since the MLS shape function is not simple in form.

Strict post error evaluation of strains or stresses should be done but eliminated in this article, for research on this branch in Meshfree Methods seems to be not enough mature before adopted into DDA as a dynamic numerical method.

Further investigations of DDA with this new approximation mode can include several branches, e.g. nonlinear mechanics response of block materials, crack propagation inside the blocks etc.

References

R. E. Goodman, R. Taylor and T. L. Brekke, A Model for the Mechanics of Jointed Rock. Journal of the Soil Mechanics & Foundations Dvi., ASCE,1968,v.94 pp. 637.

Gen-hua Shi. Discontinuous Deformation Analysis—A New Numerical Model for the Statics and Dynamics of Block Systems. Department of Civil Engineering University of California, Berkeley(Ph. D. Thesis），1988.

Koo CY and Chern JC. The development of DDA with third order displacement function. Proceedings of the 1st International Forum on Discontinuous Deformation Analysis (DDA) and Simulations of Discontinuous Media, Berkeley. Albuquerque: TSI Press, 1996, 342-349.

Max Y M. Discontinuous deformation analysis the third order displacement function[A]. In: Proc. of the first International Forum on Discontinuous Deformation Analysis and Simulation of Discontinuous Media[C]. Albuquerque: TSI Press.l996, 383-395

Lee.Seung-Cheol. Linear and Nonlinear modeling of viscous geo-materials with DDA [D]. University of Colorado. 2002

Chiao-Tung Chang. Nonlinear Dynamic Discontinuous Deformation Analysis with Finite Element Meshed Block System. Department of Civil Engineering University of California, Berkeley, (Ph. D. Thesis), 1994.

Amadei B ， Lin Chihsen-Jerry Dwyer, Recent extensions to the DDA method [A]．In: Proc.of the First International Forum on Discontinuous Deformation Analysis (DDA)and Simulations of Discontinuous Media[C]Albuquerque：TSI Press, J 996, J-3O

T. Belytschko, Y. Y. Lu and L. Gu. Element free Galerkin methods[J].Int. J. Numer. Meth. Engng.1994,37:229-256.

Lancaster, P.; Salkauskas, K.: Surfaces Generated by Moving Least Squares Methods. Math. Comput., 1981,37, 141-158.

Zheng Hong, Lee C F, Ge Xiu run, Yue Z Q，A mixed finite element solution for interface problems[J]，Chinese Journal of Rock Mechanics and Engineering Jan, 2002 21(1):1-8

DDA with higher order polynomial displacement functions for large elastic deformation problems

WANG XIAO-BO, DING XIU-LI, LU BO, WU AIQING

Yangtze River Scientific Research Institute, Wuhan, Hubei 430010, P. R. CHINA

The original formulation of DDA (Discontinuous Deformation Analysis) suggests that a higher polynomial displacement function could be used to describe the movement of any point in a two-dimensional (2D) domain. By using series as the displacement approximation, a single block can admit highly sophisticated deformation ability. However, in the higher order case, the large displacement and large deformation are more important in discontinuous cases. As the blocks move or deform, the updating block shapes and positions will produce different block contacts and different interactive forces, which will change the whole block structure and affect the modes of failure in a way more sensitive than in a problem in the continuum mechanics. Therefore, there are two main problems to solve for large deformations. Firstly, when large deformation is involved, even the originally straight edged block will deform to one with curved edges, so the contacts judge among blocks becomes more complex. Secondly, the initial stress of each step starts with the deformed block shape and position resulting from the previous step, the integration domain of initial stress has changed and the initial stress redistributes in the block area, so the integration domain of initial stress for the previous step must be translated to the last step by coordinate translation, moreover, the initial stress functions become more and more complex with the step increasing. For the first problem, the boundary dividing method is adopted. For the later one, the first method is to simply accumulate the coefficients of initial stress functions without considering the changed integration domain, it is easy to do but not always valid for large deformations; The second method is coordinate translation approximation method; this approximation can not only improve the integration accuracy of initial stress, but also enable the initial stress functions to retain the polynomial form and be integrated by Simplex Integration Method. The program was used in an example of a cantilever beam and a comparison was made between results obtained using these proposed methods and other methods in order to demonstrate excellent accuracy and efficiency.

Keywords: DDA; Contacts judge; Integration of initial stress; Coordinate translation; Simplex Integration Method

1. Introduction

The numerical method of Discontinuous Deformation Analysis (DDA) was originally proposed by Dr. Genhua Shi in 1980s. This method directly simulates the behavior of interaction between block joints instead of using the traditional method by decreasing the material strength. It uses the displacements as unknowns and solves the equilibrium equations in the same manner as the matrix analysis of structures in the finite element method. This method is mainly used for large displacements and deformations problems.

In the original formulation (Shi, 1993; 1996), it was suggested that a polynomial displacement function could be used to describe the movement of any point in a two-dimensional (2D) domain. In developing the computer code for DDA, the first order polynomial displacement function approximation was assumed, so that the stress and strain within a block in the model are constant. This approximation limits somewhat the application of DDA in areas where stress concentrations are significant. For example, when computing coal mine excavations, the block bending has to be modeled. While modeling earthquakes, the waves appear in soil or rock layers, which are considered as blocks. The movement of earth crust shows more complex deformation patterns, which include bending and twisting.

By using series as the displacement approximation, a single block can admit highly sophisticated deformation ability. However, in the higher order case, the large displacement and large deformation are more important in discontinuous case. As the blocks move or deform, the updating block shapes and positions will produce different block contacts and different interactive forces, which will change the whole block structure and affect the modes of failure in a way more sensitive than in a problem in the continuum mechanics. Toward this end, an attempt is made to develop a more general approach such that the DDA computer code has the capacity to accept an n-order polynomial displacement function.

2. Displacements and deformations of blocks

The large displacements and deformations are the accumulation of the small displacements and deformations of steps. Within each step, the displacements of all points are small and the displacement functions can be described by series approximation.

2.1 Higher order displacement formulation and series displacement approximation

The displacement function for each block can be generalized in the series form; the displacements of any point *(x, y)* can be represented in general a two dimensional series approximation.

$$\begin{cases} u = \sum_{j=1}^{m} d_{2j-1} f_j(x,y) \\ v = \sum_{j=1}^{m} d_{2j} f_j(x,y) \end{cases} \quad (1.1)$$

where the functions $f_j(x, y)$ are series, and d_{2j-1} , d_{2j} are the coefficients of the series representation. The functions $f_j(x, y)$ are linearly independent, which can be defined as a $(j-1)^{th}$ order polynomial. Let $q = 2m$, formula (1.1) can be written in matrix form:

$$\begin{pmatrix} u \\ v \end{pmatrix} = [T_i][D_i] = \begin{pmatrix} f_1 & 0 & f_2 & 0 & \cdots & f_m & 0 \\ 0 & f_1 & 0 & f_2 & \cdots & 0 & f_m \end{pmatrix} \begin{pmatrix} d_1 \\ d_2 \\ d_3 \\ \vdots \\ d_{q-1} \\ d_q \end{pmatrix} \quad (1.2)$$

where the subscript "*i*" represents the i^{th} block, *(u, v)* are the displacements of point *(x, y)*, $[T_i]$ is a $2 \times q$ matrix and $[D_i]$ is a $q \times 1$ matrix.

$[T_i]$ represents the displacement functions

$$[T_i] = \begin{pmatrix} f_1 & 0 & f_2 & 0 & \cdots & f_m & 0 \\ 0 & f_1 & 0 & f_2 & \cdots & 0 & f_m \end{pmatrix}$$

$[D_i]$ represents the deformation variables $[D_i] = \begin{pmatrix} d_{1i} & d_{2i} & d_{3i} & \cdots & d_{(q-1)i} & d_{qi} \end{pmatrix}^T$

For example, a complete 2-dimensional first order Taylor series expansions about the point (x_0, y_0) can be written in matrix form:

$$\begin{pmatrix} u \\ v \end{pmatrix} = \begin{pmatrix} 1 & 0 & x-x_0 & 0 & y-y_0 & 0 \\ 0 & 1 & 0 & x-x_0 & 0 & y-y_0 \end{pmatrix} \begin{pmatrix} d_1 \\ d_2 \\ d_3 \\ d_4 \\ d_5 \\ d_6 \end{pmatrix} \quad (1.3)$$

where (x_0, y_0) is the coordinates of the gravity center of each block. The series expansions about the point (x_0, y_0) will be more accuracy than ones about the point *(0, 0)*.

2.2 Simultaneous equations with series as displacement function

For the discontinuous deformation analysis, the 89equilibrium equations are established by minimizing the total potential energy and solved directly. The j^{th} order approximation requires $q=(j+1)*(j+2)$ equilibrium equations per block. Also the external forces and internal stresses (σ_x , σ_y , τ_{xy}) reach equilibrium. Individual blocks are connected and form a block system by contacts between blocks and by displacement constraints on single blocks. Assuming there are *n* blocks in the defined block system, the simultaneous equilibrium equations have the form:

$$[K][D] = [F] \text{ or}$$

$$\begin{pmatrix} K_{11} & K_{12} & K_{13} & \cdots & K_{1n} \\ K_{21} & K_{22} & K_{23} & \cdots & K_{2n} \\ K_{31} & K_{32} & K_{33} & \cdots & K_{3n} \\ \vdots & \vdots & \vdots & \ddots & \vdots \\ K_{n1} & K_{n2} & K_{n3} & \cdots & K_{nn} \end{pmatrix} \begin{pmatrix} D_1 \\ D_2 \\ D_3 \\ \vdots \\ D_n \end{pmatrix} = \begin{pmatrix} F_1 \\ F_2 \\ F_3 \\ \vdots \\ F_n \end{pmatrix} \quad (1.4)$$

Because each block has *q* degrees of freedom, each element $[K_{ij}]$ in the coefficient matrix given by equation (1.4) is a $q \times q$ submatrix. $[D_i]$ and $[F_i]$ are $q \times 1$ submatrices where $[D_i]$ represents the deformation variables of block *i*, $[F_i]$ is the loading on block *i* distributed to the deformation variables $[D_i]$. Submatrix $[K_{ii}]$ depends on the material properties of block *i* and $[K_{ij}]$, where $i \neq j$ is defined by the contacts between block *i* and block *j*.

These equilibrium equations are derived by minimizing the total potential energy Π done by the forces and stresses. The following parts are the main formulas of the forward model with series as the block displacement function.

3. Sub matrices of stress, strain of a single block

3.1 Elastic sub matrices

For each displacement step, assume the blocks are linearly elastic, then for conditions of plane stress:

$$\begin{pmatrix} \sigma_x \\ \sigma_y \\ \tau_{xy} \end{pmatrix} = \frac{E}{1-\nu^2} \begin{pmatrix} 1 & \nu & 0 \\ \nu & 1 & 0 \\ 0 & 0 & (1-\nu)/2 \end{pmatrix} \begin{pmatrix} \varepsilon_x \\ \varepsilon_y \\ \gamma_{xy} \end{pmatrix} \quad (1.5)$$

where *E* and ν are for plain stress or plain strain as appropriate.

For the higher order displacement functions, the plane strain is:

$$\begin{pmatrix}\varepsilon_x\\ \varepsilon_y\\ \gamma_{xy}\end{pmatrix}=\begin{pmatrix}\frac{\partial f_1}{\partial x} & 0 & \frac{\partial f_2}{\partial x} & 0 & \cdots & \frac{\partial f_m}{\partial x} & 0\\ 0 & \frac{\partial f_1}{\partial y} & 0 & \frac{\partial f_2}{\partial x} & \cdots & 0 & \frac{\partial f_m}{\partial y}\\ \frac{\partial f_1}{\partial y} & \frac{\partial f_1}{\partial x} & \frac{\partial f_2}{\partial y} & \frac{\partial f_2}{\partial y} & \cdots & \frac{\partial f_m}{\partial y} & \frac{\partial f_m}{\partial x}\end{pmatrix}\begin{pmatrix}d_1\\ d_2\\ d_3\\ \vdots\\ d_{2m-1}\\ d_{2m}\end{pmatrix} \quad (1.6)$$

Denote

$$[E]=\frac{E}{1-\nu^2}\begin{pmatrix}1 & \nu & 0\\ \nu & 1 & 0\\ 0 & 0 & \frac{1-\nu}{2}\end{pmatrix},[B]=\begin{pmatrix}\frac{\partial f_1}{\partial x} & 0 & \cdots & \frac{\partial f_m}{\partial x} & 0\\ 0 & \frac{\partial f_1}{\partial y} & \cdots & 0 & \frac{\partial f_m}{\partial y}\\ \frac{\partial f_1}{\partial y} & \frac{\partial f_1}{\partial x} & \cdots & \frac{\partial f_m}{\partial y} & \frac{\partial f_m}{\partial x}\end{pmatrix}$$

The strain energy Π_e done by the elastic stresses of block *i* is:

$$\Pi_e=\iint\frac{1}{2}(\varepsilon_x\sigma_x+\varepsilon_y\sigma_y+\gamma_{xy}\tau_{xy})dxdy$$

$$=\frac{1}{2}[D_i]^T\left(\iint[B_i]^T[E_i][B_i]dxdy\right)[D_i] \quad (1.7)$$

where the integration is over the entire area of the i^{th} block.

The derivatives are computed to minimize the strain energy Π_e:

$$k_{rs}=\frac{\partial^2\Pi_e}{\partial d_{ri}\partial d_{si}}=\frac{1}{2}\iint[B_i]^T[E_i][B_i]dxdy,\ r,s=1,2,\cdots,q.$$

$[k_{rs}]$ forms a $q\times q$ submatrix:

$$\frac{1}{2}\iint[B_i]^T[E_i][B_i]dxdy\rightarrow[k_{ii}] \quad (1.8)$$

The matrix of (1.8) is added to the submatrix $[K_{ii}]$ in the global equation (1.4).

3.2 Sub matrices of initial stress

For the i^{th} block, the potential energy of the initial stress (σ^0_x, σ^0_y, τ^0_{xy}) is:

$$\Pi_\sigma=-\iint(\varepsilon_x\sigma_x^0+\varepsilon_y\sigma_y^0+\gamma_{xy}\tau_{xy}^0)dxdy$$

$$=-[D_i]^T\iint[B_i]^T\begin{pmatrix}\sigma_x^0 & \sigma_y^0 & \tau_{xy}^0\end{pmatrix}^T dxdy \quad (1.9)$$

where the integration is over the entire area of the i^{th} block, (σ^0_x, σ^0_y, τ^0_{xy}) represents the initial stress functions.

The derivatives are computed to minimize the strain energy Π_σ:

$$f_r=-\frac{\partial\Pi_\sigma}{\partial d_{ri}}=\iint[B_i]^T\begin{pmatrix}\sigma_x^0 & \sigma_y^0 & \tau_{xy}^0\end{pmatrix}^T dxdy,\ r=1,2,\cdots q.$$

which forms a $q\times 1$ sub matrix

$$\iint[B_i]^T\begin{pmatrix}\sigma_x^0 & \sigma_y^0 & \tau_{xy}^0\end{pmatrix}^T dxdy\rightarrow[F_i] \quad (1.10)$$

which is added to $[F_i]$ in the global equations (1.4).

In the series cases the initial stresses (σ^0_x, σ^0_y, τ^0_{xy}) are not necessarily constants, so, the integration of the initial stress is discussed here.

4. Integration of initial stress

In the higher order series cases, the large displacement and large deformation are more important in discontinuous case. As the blocks move or deform, the updating block shapes and positions will make the initial stress redistribute on the block area. So, the initial stress functions will become more and more complex with the step increasing. Because the initial stress of each step starts with the deformed block shape and position resulting from the previous step, then, the integration domain of initial stress will change with the step, therefore, the integration domain of initial stress for the last step must be converted from the previous step by coordinate translation.

4.1 Coordinate translation

Assume that (x, y) is any point of block *i* for the previous step, (x', y') is the same point of the block for the last step (see Fig. 1). As the block moves or deforms, the integration domain of initial stress changes, the domain for the previous step will convert into the one for the previous step.

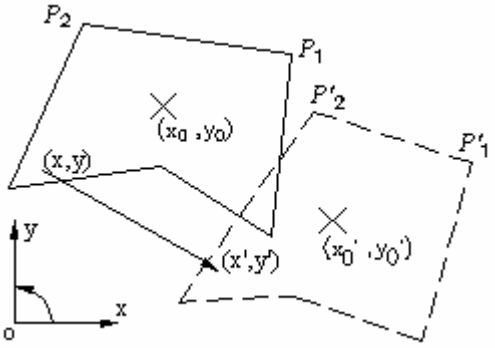

Fig. 1: The movement of a block from the previous step (solid line) to the last step (dash line).

From the previous step to the last step, we have

$$\begin{cases}x'=x+u\\ y'=y+v\end{cases} \quad (1.11)$$

where (u, v) is the displacement of point (x, y), it can be obtained from (1.4).

For obtaining the coordinate translation from the last step to the previous step, we must solve the formula (1.11). Assume we can solve formula (1.11), the coordinate translation will be the following form

$$\begin{cases}x=x'+p(x',y')\\ y=y'+q(x',y')\end{cases} \quad (1.12)$$

To integrate the initial stress for the last step, from formula (1.10), we have

$$\iint [B_i(x',y')]^T \begin{pmatrix}\sigma_x^0 & \sigma_y^0 & \tau_{xy}^0\end{pmatrix}^T dx'dy' = \iint [B_i(x',y')]^T \begin{pmatrix}\sigma_{x'}^0 & \sigma_{y'}^0 & \tau_{x'y'}^0\end{pmatrix}^T dx'dy' \quad (1.14)$$

which is added to $[F_i]$ in the global equations (1.4), where ($\sigma^0{}_x$, $\sigma^0{}_y$, $\tau^0{}_{xy}$) is the initial stress for the previous step.

Obviously, the integrand of formula (1.14) will be more and more complex with the step increasing; therefore, finding the coordinate translation approximation is the way.

4.2 Coordinate translation approximation method

From formula (1.11) to formula (1.14), it suggests that the key issue will be how to deal with coordinate translation (1.11) and (1.12).

The first method is to accumulate the coefficients of initial stress functions without considering the changed integration domain. In this case, we can easily obtain the initial functions and its integrals, but the computation accuracy is not very good.

Another method is the triangle dividing integration method, which is to choose the gravity center of a block, then connect each oriented edge to the gravity center of the block to form a set of triangles. For each triangle of the block, its coordinate translation from the previous step to the next step can be approximately replaced with the linear polynomial functions. The integrals of formula (1.14) on these triangles are computed. The sum of the computed integrals together with their orientation sign will be the correct integral over the whole block. This method can not only improve the integration accuracy of initial stress, but also simplify the initial stress functions and make the integration of initial stress easy to deal with.

Assume (x_0, y_0) is the gravity center of a block for the previous, (x_1, y_1) and (x_2, y_2) are the vertex coordinates of a single triangle. (x_0', y_0') (x'_1, y'_1) and (x'_2, y'_2) are the same points for the last step (see Fig.1). Then, the coordinate translation of the triangle is

$$\begin{cases} x - x_0 = a_1(x' - x_0') + b_1(y' - y_0') \\ y - y_0 = a_2(x' - x_0') + b_2(y' - y_0') \end{cases} \quad (1.15)$$

where (x', y') can be obtained from formula (1.11), four parameters (a_1, a_2, b_1, b_2) are defined by the following equations:

$$\begin{pmatrix} a_1 & 0 & b_1 & 0 \\ 0 & a_1 & 0 & b_1 \\ a_2 & 0 & b_2 & 0 \\ 0 & a_2 & 0 & b_2 \end{pmatrix} \begin{pmatrix} x_1' - x_0' \\ x_2' - x_0' \\ y_1' - y_0' \\ y_1' - y_0' \end{pmatrix} = \begin{pmatrix} x_1 \\ x_2 \\ y_1 \\ y_2 \end{pmatrix} \quad (1.16)$$

Solve the formula (1.16), we can obtain the coefficients of the coordinate translation of each triangle over a block. Then the integrals of formula (1.14) on these triangles can be computed.

5 Contacts judge and block integrations

For block system movements, no tension and no penetration can be allowed between blocks, it is necessary to connect the individual blocks into a block system. When the block system moves or deforms, the blocks are in contact only along the boundary and the non-penetration inequalities can be transformed into the equations when two blocks are in contact.

5.1 Contacts judge of blocks with curved boundary

Assume P_1 is a point before deformation which moves to point P_1 after deformation; P_2P_3 is the reference line and (x_i, y_i) and (u_i, v_i) are the coordinates and displacement increment of P_i, $i = 1, 2, 3$ respectively.

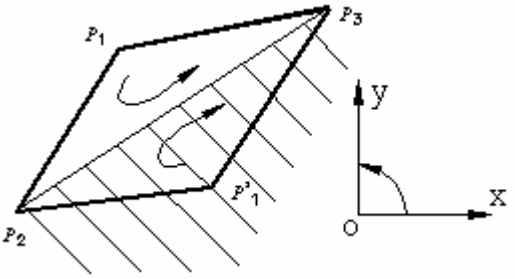

Fig. 2: Criteria where point P_1 passes edge P_2P_3 by rotation direction

If points P_1, P_2 and P_3 rotate in the same sense as the rotation of *ox* to *oy* (see Fig. 2), then P_1 has passed line P_2P_3 and is stated by the inequality:

$$\Delta = \begin{vmatrix} 1 & x_1 + u_1 & y_1 + v_1 \\ 1 & x_2 + u_2 & y_2 + v_2 \\ 1 & x_3 + u_3 & y_3 + v_3 \end{vmatrix} < 0 \quad (1.18)$$

The determinant calculates twice the area of the triangle (P_1 P_2 P_3) which becomes negative when P_1 is located past P_2P_3. The distance d from P_1 to P_2P_3 is

$$d = \frac{\Delta}{\sqrt{(x_2 - x_3)^2 + (y_2 - y_3)^2}} \quad (1.19)$$

Two rules must be observed when contacts are involved:

1. No inter-penetration occurs between the two sides.
2. No tension force exists between the two sides.

In the case when inter-penetration occurs at a given position, a "lock" is applied, which starts from the point and lies along the direction normal to the reference line.

The original contacts judge of DDA is based on that the boundary of a block is straight edges. However, in the case of series displacement approximations (more than one order), the originally straight edged block will deform to one with curved edges, so, the contact judge among blocks becomes more complex. To solve the problem, the simplest way is to substitute the divided edges for the curved edges, which is a good method to judge the contacts of the curved boundary.

5.2 Integrations on a curved block

In the processing of DDA computation, the blocks have general shapes, which can be a block with curved boundary. When large deformation is involved, even the originally straight edged block will deform to one with curved edges. The computations of geological movement require curved edge blocks.

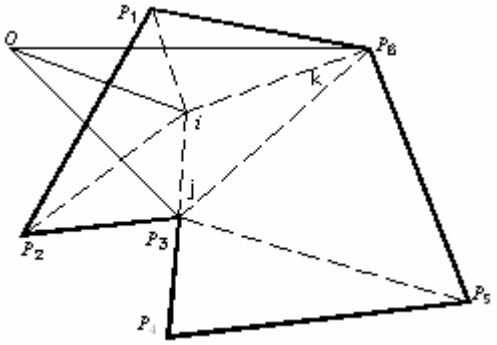

Fig. 3: Integration over a block with m vertices

Assume this block has ordered vertices (see Fig. 3).

$$P_1\ P_2\ P_3 \cdots P_{m-1}\ P_m\ P_{m+1} \quad (P_{m+1} = P_1)$$

where the inside area is always in the left side of the advance direction of the ordered vertices or boundary loop.

For the more general n^{th} order functions such as

$$f(x,y) = \sum_{i+j\le n} a_{ij} x^i y^j \quad (1.20)$$

Considering the integral term of $x^i y^j$, its integration over the block is

$$\iint x^i y^j dxdy = \sum_{k=1}^{m}\left(\sum_{i_1,i_2\ge 0}^{i_1+i_2=i}\sum_{j_1,j_2\ge 0}^{j_1+j_2=j} \frac{i!}{i_1!i_2!}\times\frac{j!}{j_1!j_2!}\rightarrow \right.$$

$$\left. \leftarrow \times x_k^{\,i_1} x_{k+1}^{\,i_2} \times y_k^{\,j_1} y_{k+1}^{\,j_2} \times \frac{(i_1+j_1)!(i_2+j_2)!}{(i+j+2)!} \right)\rightarrow$$

$$\leftarrow \times\left(x_k y_{k+1} - x_{k+1} y_k\right) \quad (1.21)$$

From formula (1.20), its integrals are additive

$$\iint f(x,y)dxdy = \sum_{i+j\le n} a_{ij} \iint x^i y^j dxdy \quad (1.20)$$

then, the analytic solution of the block integration can be derived in the same way with more computations.

The analytic solution can also be applied to the blocks with curved edges.

6 An example of a cantilever beam

The following is an example of a cantilever beam, the vertical displacement at the free end of the cantilever beam is discussed, and a comparison is made between results obtained using these proposed methods and other methods.

6.1 Parameters of the cantilever

Assume there is a cantilever, one end is fixed on a big rigid object, and the other end is free, which is subjected to a vertical force *P* (see Fig.4).

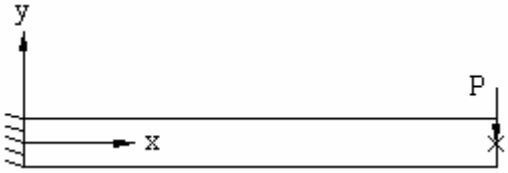

Fig. 4: A cantilever subjected to a vertical force at the mid-point of the free end.

The parameters of the cantilever are

length: *10m,*

cross section: $1m \times 1m$,

material constants: $E=3\times10^5\ kN/m^2$, $\nu=0.2$,

loading: *P=125kN, 250kN, 500kN*, respectively.

boundary condition: three fixed points at the fixed end of the cantilever (two ends and a mid-point).

divided edge: 46

step: 100

6.2 Computation results

The following is the result by the method that simply accumulates the coefficients of initial stress functions without considering the changed integration domain (see Tab. 1).

Tab. 1: The mid-point displacement at the free end of the cantilever beam (unit: m).

P (kN)		Solution of DDA			Theoretical Solution
		1st	*2nd*	*3rd*	
125	*u*	0.000	0.083	0.188	0.16
	v	0.009	1.164	1.667	1.62
250	*u*	0.000	0.229	0.556	0.56
	v	0.017	1.894	2.833	3.02
500	*u*	0.000	0.511	1.308	1.60
	v	0.033	2.776	4.275	4.94

Notes: *u* represents the horizontal displacement, *v* represents the vertical displacement, 1st 2nd 3rd represent the order of the polynomial displacement functions.

The following is the result by the coordinate translation Approximation method which replaces coordinate translation with the linear polynomial functions (see Tab. 2).

Tab. 2: The mid-point displacement at the free end of the cantilever beam (unit: m).

P (kN)		DDA			Theoretical Solution
		1st	*2nd*	*3rd*	
125	*u*	0.000	0.100	0.180	0.16
	v	0.009	1.213	1.713	1.62
250	*u*	0.000	0.298	0.611	0.56
	v	0.017	2.061	3.069	3.02
500	*u*	0.000	0.702	1.712	1.60
	v	0.033	3.112	4.870	4.94

Notes: see the notes of table 1.

The deformations of the cantilever beam are shown in Fig. 5

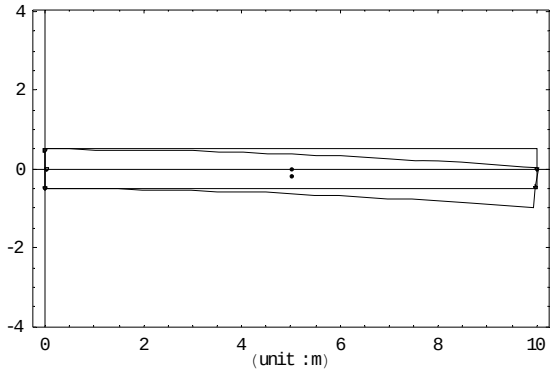

Fig. 5: The deformations of the cantilever beam (*P=125kN, 3rd order displacement functions, step:100*)

7. Conclusions

From Tab. 1, when the loading is lower, the solution of DDA is close to the theoretical solution with higher order. However, when the loading is larger, the result is not very good even if the order is higher. The reason is that we ignore the updated geometry of the block when we integrate the initial stress over the block, the shape of the block changes a lot under the larger loading.

From Tab. 2, the solution of DDA is also close to the theoretical solution with the order increasing. However, in the case of lower loading, the result by the coordinate translation approximations method is not better than the one by the method which accumulates the coefficients of initial stress functions. The reason is that the triangle dividing integration makes the initial integration large than the theoretical value.

So, for obtaining a better result, it is necessary to find a better way to integrate the initial stress of the block.

References

R. E. Goodman and G. H. Shi, 1985. "Block Theory and Its Application to Rock Engineering," Prentice-Hall, Englewood Cliffs, N. J..

G. H. Shi, R. E. Goodman and J. P. Tinucci, 1985. "Application of block theory to simulated joint trace maps," Fundamentals of rock joints, O. Stephansson(ed.), Lulea: Centak Publishers pp. 367-383.

G. H. Shi and R. E. Goodman, 1987. "Stability analysis of infinite block systems using block theory," Proc. Analytical and computational methods in engineering rock mechanics, E. T. Brown, London: Allen and Unwin, pp. 205-245.

Chern, J.C., Koo, C.Y., and S. Chen, Development of Second Order Displacement Function for DDA and Manifold Method, Working Forum on the Manifold Method of Material Analysis, Vol. 1, p. 183-202, U.S. Army Corps of Engineers, Waterways Experiment Station, Vicksburg, MS, 1995. Clatworthy, D., and F. Scheele, A Method of Sub-Meshing in Discontinuous Deformation, Proceedings of the 3rd International Conference on Analysis of Discontinuous Deformation from Theory to Practice, ed. B. Amadei, p. 85-94, June 3-4, 1999, Vail, CO, 1999.

Koo, C.Y., and J.C., Chern, The Development of DDA with Third Order Displacement Function, Working Forum on the Manifold Method of Material Analysis, Vol. 1, p. 342-349, U.S. Army Corps of Engineers, Waterways Experiment Station, Vicksburg, MS, 1997.

Ma, M.Y., M. Zaman, and J.H. Zhu, Discontinuous Deformation Analysis Using the Third Order Displacement Function, Working Forum on the Manifold Method of Material Analysis, Vol. 1, p. 388-394, U.S. Army Corps of Engineers, Waterways Experiment Station, Vicksburg, MS, 1997.

Shi, G.H., Block System Modeling by Discontinuous Deformation Analysis, Topics in Engineering, Volume 11, C.A. Brebbia and J.J. Conner eds., Computational Mechanics Publications, Boston USA, 1993.

Shi, G.H., Modeling Dynamic Rock Failure by Discontinuous Deformation Analysis with Simplex Integration, Proceedings of the 1st North American Rock Mechanics Symposium, Austin, TX, 1994.

Shi, G.H., Discontinuous Deformation Analysis Technical Note, First International Forum on Discontinuous Deformation Analysis, June 12-14, 1996, Berkeley, CA., 1996.

Narrow-phase collision detection based on DDA

ZHAO XIAOFEI, XISHENG FANG and WANG YING

College of Computing and Communication Engineering
Graduate University, Chinese Academy of Sciences,
Beijing 100049, P. R. CHINA

Collision detection (CD) is wildly used in Physics-based animation, CAD/CAM, etc., and CD often becomes the bottleneck. The DDA, which is a numerical simulation technique, can analyze discontinuous rock mass behavior. This paper simulates a car bumps the wall and cars collide with each other based on DDA. The simulation results indicate that DDA can successfully detect the contact of the cars under different conditions in narrow-phase collision detection.

Keywords: DDA; Collision detection: Physics-based animation; Car collision.

1. Introduction

Collision Detection (CD) is a highly-interdisciplinary field, in Physics-based animation, CAD/CAM, computing geometry, VR, robotics, and so on. But what is Collision Detection? When considering collisions with respect to our everyday perception a concise answer would be the task of determining over a given time interval whether any points of the two objects occupy the same location in space simultaneous.

In physics based animation, it tries to benefit from physics by applying physical laws in a simulator in order to animate the movement of objects in a realistic plausible manner. During the course of physics-based animation, objects come in contact with each other. The contact region must be resolved so that objects bounce or slide off each other or come to rest upon each other (Kenny 2005). In order to simulate these effects it is necessary to infer details about the shape of the contact regions. This is the aim of collision detection in physics-based animation. In 1993, Hubbard was the first to introduce the concepts of broad-phase and narrow-phase collision detection in computer graphics area (Hubbard 1993). Since then, a wealth of literature on broad-phase, narrow-phase algorithms and different approaches have been investigated. Broad-phase collision detection lists pairs of potential colliding objects, and the narrow-phase collision detection examines each of these pairs in detail. For each pair of objects, the narrow-phase collision detection determines whether the objects are separated, touching, or penetrating. Narrow-phase collision detection algorithms are naturally divided into four main groups: Spatial Data Structures such as spatial subdivisions and bounding volume hierarchies (Melax 2001), feature-based (Ehmann 2001), simplex-based (Bergen 2001), volume-based (Guendelman 2003), and the major challenges for narrow-phase collision detection are deforming geometry, self-intersections, and penetration depths. The DDA (discontinuous deformation analysis) (Shi 1997) is a numerical simulation technique used to model the motions of rock masses under a wide range of conditions which was originally proposed by Dr. Shi Gen-hua. This paper applied DDA to solve the problems of collision detection in Physics-based animation.

2. The theory of contact in DDA

DDA allows the user to construct models of blocky materials that recognize different loading conditions and interactions between blocks, accounting for friction along block surfaces.

2.1 The summary of DDA

The discontinuous deformation analysis method (DDA) parallels finite element method. It solves a finite element type of mesh where all the elements are real isolated blocks, bounded by preexisting discontinuities. However, it is more general. Whereas, the elements or blocks used by the DDA method can be of any convex or concave shape or even multi-connected polygons with holes, the finite element method encompasses only elements of standard shape. Furthermore, in the DDA method, when block are in contact, Coloumb's law applies to the contact interface, and the simultaneous equilibrium equations are selected and solved for each loading or time increment. In the case of the finite element method the number of unknowns is the sum of the degrees of freedom of all nodes. In the case of DDA method the number of unknowns is the sum of degrees of freedom of all the blocks.

2.2 The theory of contact in discontinuous deformation analysis.

DDA solves a finite element type of mesh where all the elements are real isolated blocks, bounded by preexisting discontinuities, so we have to deal with the discontinuities problem of the boundaries of the blocks. For the movements of discontinuous boundaries, no tension and no penetration must be satisfied between two contact sides. Finding the contacts in each time step, applying stiff springs on contacts, and the discontinuous displacements can be computed (SHI G H. 1988).

Based on the small step displacements, the contacts are defined in the beginning of each time step. Each contact is formed with two sides. All of the pair of two sides that are possible to contact, penetrate or entrance from one to another at the end of time step are defined as contacts. Since practically there are no penetrations on the two sides are allowed on the contacts, so the contacts are merely the entrance positions.

There are two kinds of contacts: angle to edge and angle to angle. The edge to edge contacts can be transferred to angle to edge contact. Assume the maximum step edge rotation is δ. There are the criteria for the contacts:

(1) for angle to edge contact, the minimum distance of the angle vertex to the edge of the contacts is less than 2ρ,
(2) for angle to angle contact, the minimum distance of two angle vertices of the contacts is less than 2ρ,
(3) for angle to edge contact, when the angle vertex translates to the edge without rotation, the maximum overlapping angle of the angle and the edge is less than 2δ,
(4) for angle to angle contact, when the angle vertex translates to the vertex of other angle without rotation, the maximum overlapping angle of the two angles is less than 2δ,

The common sense requirements of no penetration and no tension indeed are inequalities. Coulomb's friction law and limited tension are also inequalities, and inequalities can be simplified to linear inequalities. There are three kinds of linear inequalities:

(1) no penetrations in contacts,
(2) tension force less than tension strength in contacts,
(3) Coulomb's friction law in contacts.

In the computation, an angle to angle contact will be transferred to one or two angle to edge contacts. The theory of contact in DDA can be divided into three parts:

2.2.1 The determinant of contact

In the DDA theory, there are three kinds of contact: angle to angle, angle to edge, edge to edge. They contain one situation that the edge to edge contact can change into two angles to edge contacts. When the minimum distance of two angle vertices of the contacts is less than the given value a and when the angle vertex translates to the vertex of other angle without rotation, the maximum overlapping angle of the two angles is less than a given value b, so we determine the contact belong to angle to angle contact. When the minimum distance of the angle vertex to edge of the contact is less than the given value a and when the angle vertex translates to the edge without rotation, the maximum overlapping angle of the angle and the edge is less than the given value b, so we determine the contact belong to angle to edge contact. The Fig.1 (a), (b) are contacts between two convex angles. The Fig.1 (c) describes a contact between a convex angle less than 180^o and a concave angle greater than 180^o.

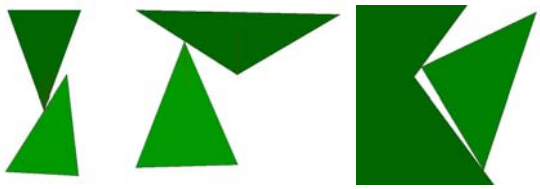

Fig.1: Three kind of contact situation

2.2.2 The computation of the contact force

In the DDA theory, contact force is simulated by spring, there is normal spring and shear spring, when Coulomb's law allows sliding between two sides of boundary contacts, there exist friction forces in two sliding sides if the friction angle is not zero. Contact forces between blocks are made up by these forces. In every time step, we have to choose the lock position (the position of the spring to put), and we have to iterate repeatedly. The iterate process is also the adding-removing process of the stiff spring. There are three modes of contact: open, sliding and lock. If a contact has a tensile contact force from the normal spring, the mode of the contact is open. If the vertical component of the contact force is press and the horizontal component is greater than the critical friction, the mode of contact is sliding. If the vertical component of the contact force is press and the horizontal component is less than the critical friction, the mode of contact is lock. In the sliding state, we need a normal spring and a pair of friction, and in the lock state, we need a normal spring and a shear spring. In the open state, we do not need the contact force. The open-close iterations have to ensure no-penetrations in the open contacts, and no-tensions in the contacts with normal springs. The contact force can be added to the general equation by normal contact matrices, shear contact matrices and friction matrices.

2.2.3 Contact transfer

DDA is computed by time step, all the geometric and physical parameters have to be transferred from the end of the previous time step to the beginning of the next time step. The following items are to be transferred: stresses of each element, strains of each element velocities of each element, geometry of the joint boundaries and elements, all closed contacts. The position and state parameters of the closed contacts have to go to the next step. The geometric parameters and physical parameters of contacts will be transferred: the contact vertex and edge, the position of contact point, the normal displacement and normal force, the shear displacement and shear force, locking or sliding as contact state.

3. Simulation of cars collision

After the heavy traffic accident happened, we have to collect every kinds of data information, in order to analyze and compute the process of the accident (including computer simulation), it so called reappearance of the accident, it can provide the gist to relative department to judge the reason of accident, went behind criminal and civil duty. What's more it can provide the gist to insurance company to determine the compensation.

This paper applies DDA to solve the collision detection problems in Physics-Based animation. In recent years, in animation field we paint the pictures one by one, and we can not simulate the reaction of the objects in the virtual reality about how they collide into each other in reality and real time. This paper makes a try to solve the problems exited in animation using engineering tool. This paper realizes the whole physics process including collision using VC++6.0 compiler, treats the objects in the virtual reality as the simulation objects, uses the boundaries of the objects in the virtual reality as the joints and the shape of the blocks in the DDA program, sets the parameters and the initial condition. We can simulate collision in the real world and it completely corroding with the laws of physics.

3.1 Using block sectioning theory to generating the physics scene

The blocks of the computed block system are the result of sectioning by the existing discontinuities. Therefore blocks with any shapes and any number of vertices can be produced: convex blocks, concave blocks, the union of convex blocks or block containing holes. We know that DDA have the capacity to compute blocks of any shape. But when input these preexisting blocks offered by geologic experts, we can not use the same methods like FEM. Here, real blocks can not be produced by an automatic meshing, as employed in finite element analysis, because the element nodes and edges can be chosen optionally. Computing blocks from input discontinuities is more convenient and more natural.

This paper use AutoCAD to design the physics scene, and through reading the DXF files to get the boundaries information. And then threat the boundaries of the objects in the virtual reality as the joints and the shape of the blocks in the cutting program of DDA. Now we have completed the preprocessing level, the boundaries of the objects are represented by their ordered vertices, where the vertices are rotated clockwise.

3.2 The setting of the physics parameter

This paper used contact theory in DDA to simulate the collision of a car bumps the wall and cars collide. We set the speed at start of a travel and the direction of the travel, than we repaint the locale of the car accident, and simulate the whole process of the collision accident in animation form. In order to measure the true situation, this paper reset the physics parameter, material parameter, speed at start of travel, situation of the loading. At last, we simulate the cars collision relatively according to the real.

3.3 Examples

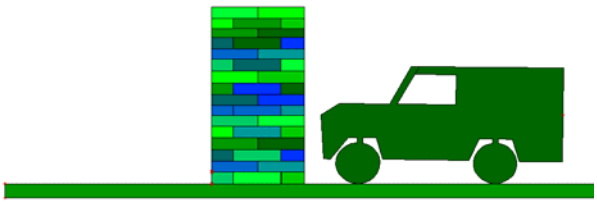

(a)

(b)

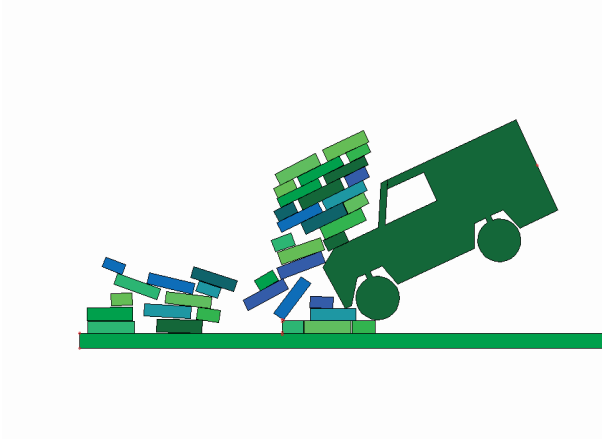

(c)
Fig.2: A car bump the wall

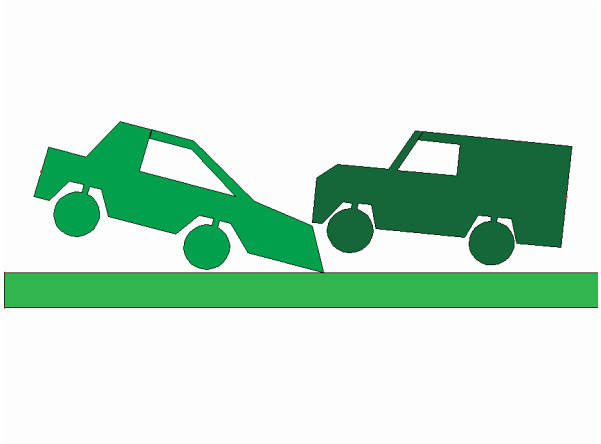

(c)
Fig.3: Collision of two cars

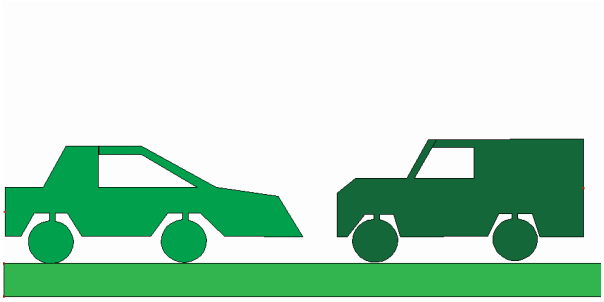

(a)

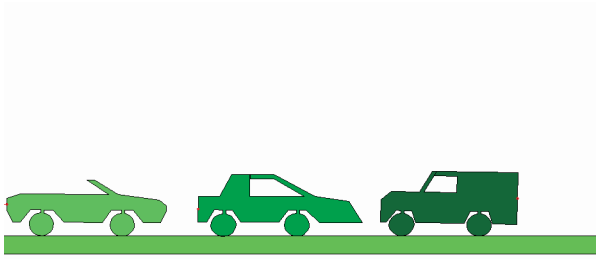

(a)

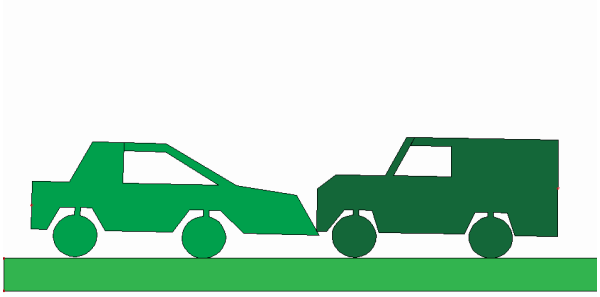

(b)

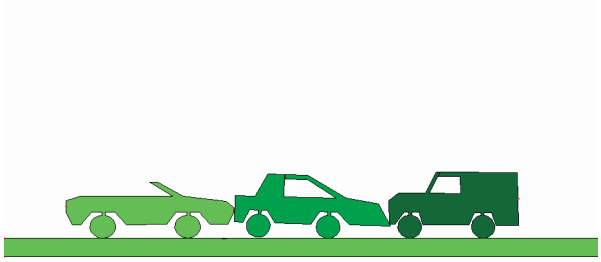

(b)

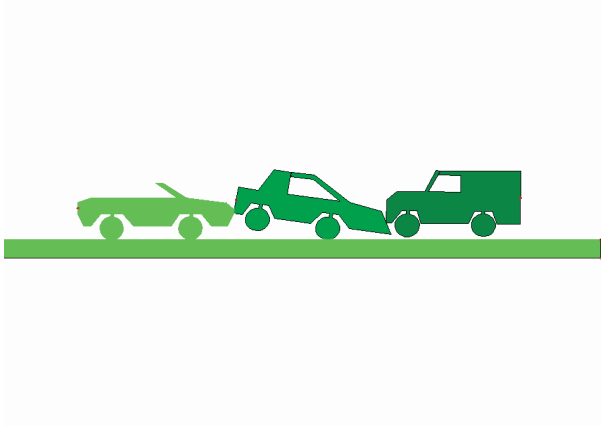

(c)
Fig.4: Collision of three cars

In the Fig.2, (a) is the initial condition. We can see a jeep parking in front of a wall which made up by a pile of stiff bricks, after add a horizontal force on the back the car, it start to run, and bump the wall (see Fig.2, (b)). The Fig.2, (c) shows the final result at the 475th steps. From the Fig.3 and Fig.4 we can see cars collide with each other. The DDA program has successfully detected the collision, and responds to the collision according with the physics law completely.

4. Conclusion

Rigid bodies in the real world do not penetrate each other, and the penetration is impossible due to the contact forces between rigid bodies. In penalty-based multibody animation, a spring-damper system is used for penalizing penetrations. This paper applies DDA for the first time to solve the problems in Physics-Based animation, and the simulation itself proves that the contact theory in DDA can be applied very well in this area.

Reference

Bergen, G.v.d., Proximity queries and penetration depth computation on 3D game objects, *Game Developers Conference*, 2001

Ehmann, S.A and Lin, M.C. Accurate and fast proximity queries between polyhedral using convex surface decomposition. In Chalmers, A. and Rhyne, T.-M., editors *EG 2001 Proceedings*, volume 20(3), pages 500-510, Blackwell Publishing. 2001.

Guendelman, E., Bridson, R., and Fedikiw, R. Nonconvex rigid bodies with stacking, ACM Transaction on Graphics, *Proceedings of ACM SIGGRAPH*, 2003

Hubbard, P.M. Interactive collision detection, In *Proceedings of the IEEE Symposium on Research Frontiers in Virtual Reality*, page 24-32, 1993

Kenny Erleben, Jon Sporring, Knud Henriksen, and Henrik Dohlmann, *Physics-Based Animation*, Preface, Page399, 2005.

Melax, S. Bsp collision detection as used in mdk2 and neverwinter nights, 2001

SHI G H. *Discontinuous deformation analysis: a new numerical model for the statics and dynamics of block systems* [D]. Berkeley: Department of Cilvil Engineering, University of California, 1988.

SHI G H. *Numerical Manifold Method and Discontinuous Deformation Analysis* [M], Jue-min Pei translated. Beijing: Tsinghua University Express, 92-145, 1997.

A fast common plane identification algorithm for 3-D contact problem

J. LIU, Q.D. GENG & X.J. KONG

State Key Laboratory of Offshore and Coastal Engineering,
Dalian University of Technology, Dalian, P. R. CHINA

Determining the contact points between interacting blocks and the associated contact normal is an important and time consuming calculation in the discrete element method (DEM) and the discontinuous deformation analysis (DDA). Common-plane (CP) algorithm is one of the more effective methods for contact detection when dealing with three-dimensional polyhedral or two-dimensional polygonal blocks. A new approach, called fast common plane (FCP) method, is proposed by Nezami et al (2004) to find the common plane for separate blocks. In this paper, the fast common plane identification algorithm is extended to a general case for all contact types and the proof of the algorithm is also provided. FCP approach recognizes that a common plane has identifying characteristics, which dramatically reduce the search space for the common plane. In two-dimensions, the CP is found by checking only 5 possible candidate lines. In three-dimensions, the candidate planes fall within 4 types related to the geometry of the blocks and their relative positions. So the efficiency for CP identification is improved greatly and the accuracy can be guaranteed. Numerical experiments reveal the efficiency of the extended FCP algorithm.

Keywords: Contact detection; Common plane; Discrete element method (DEM); Discontinuous deformation analysis (DDA)

1. Introduction

Although the computer technique has been improved greatly, the huge computational time to detect the contact condition is still a bottleneck in large scale DEM and DDA simulations. For complex block geometries, such as three-dimensional polyhedrons, contact detection computation can even take up to 80% of the total analysis time.

Contact detection in DEM and DDA is usually performed in two independent stages. The first stage, referred to as neighbor search, is merely a rough search that aims to provide a list of all possible blocks in contact. The most recent neighbor searching algorithms include No Binary Search (NBS) contact detection algorithm (Munjiza & Andrew 1998) and DESS algorithm (Perkins & Williams 2001).

The second stage is called geometric resolution. The pairs of contacting blocks obtained from the first stage are examined in more detail to find the contact points (or contact area if distributed contact forces are considered) and calculate the contact forces. Geometric resolution algorithms strongly depend on complexity of the geometric representation of blocks. For example, if the boundaries of the blocks are implicitly represented by a single function $f(x, y, z) = 0$, then a closed form solution is likely to be available (for example refer to Cundall & Stack (1979) for contacts between disks and spheres, Ting et al (1993) for two-dimensional ellipses, and Lin & Ng (1997) for three-dimensional ellipsoids). Efficiency of these contact detection schemes are mostly controlled by the simplicity of the resulting equations.

Where the boundary cannot be represented by a single function $f(x, y, z) = 0$, such as in polygons or polyhedrons, the contact detection can be quite cumbersome. Barbosa (1990) introduced a simple algorithm for contact detection between polyhedrons that requires comparing all the vertices of one block to all faces of the other one and vice versa. The algorithm has a high computational complexity of order $O(N^2)$, with N being the number of vertices. Williams and O'Connor (1995) introduced Discrete Function Representation algorithm which achieves a computational complexity of order $O(N)$. Krishnasamy and Jakiela (1995) and later Feng & Owen (2002) introduced energy-based methods for finding the contact forces, in which a potential energy function is defined for each contact as a function of the overlap area. There are also some other methods are put forward recently, such as penetration edges method (Chueng et al 2006), incision body scheme (Wang et al 2006) and so on.

Cundall (1988) introduced the well-known class of ''Common-Plane'' (CP) methods: "A common plane is a plane that, in some sense, bisects the space between the two contacting blocks''. If the two blocks are in contact, then both will contact with the CP, and if they are not in contact, then neither contacts with the CP. By using CP, the block-to-block contact detection problem reduces to a much faster plane-to-block contact detection problem. Once the CP is established between two blocks, the normal to the CP defines the direction of the contact normal, which in turn defines the direction of the normal contact force between the two blocks. This is especially advantageous for vertex-to-vertex or edge-to-vertex contacts, where the definition of the contact normal is a non-trivial problem. The method has a complexity of order $O(N)$ and has been successfully

implemented in three-dimensional DEM code 3DEC (Itasca 1998) and 3-D DDA (Liu et al 2004).

But it is difficult to get the real CP for the two blocks, and the existing methods for CP identification always need a great amount of calculation and terminate on a saddle-point sometimes. Nezami et al (2004) proposed a fast contact detection algorithm for 3-D DEM and provided the proof for the algorithm for separate blocks. For blocks in contact, an additional step is performed before the algorithm is used, to temporarily separate the contact blocks by translating the two blocks in a direction perpendicular to the CP from the previous time step. On the one hand, the CP for the separate blocks is just an approximate CP for the in-contact blocks. On the other hand, the initial CP is unknown before the DEM or DDA analysis for the initial contact blocks, so the separate operation cannot be accomplished. From the view mentioned above, the current fast common plane (FCP) identification algorithm is limited.

The following sections extend the FCP algorithm to a general case for all types of contact based on rigorous proof of the algorithm. In two-dimensions, the CP is also found by checking only 5 possible candidate planes. In three-dimensions, the candidate planes fall within 4 types related to the geometry of the blocks and their relative positions. Blocks assumed to be convex, while concave blocks can be modeled as a combination of several convex blocks attached to each other. In order to give a completely proof for all type of contact, the separate case is also included in this paper. The second and third sections describe the definition of CP and the conventional algorithm for finding the CP. The fourth and fifth sections give the FCP algorithm and its proof.

2. Definition of the common plane (CP)

The CP is identified by its unit normal, n, and any point V_0 on it, as shown in Fig. 1. For any point V in the space, the "distance" d^V of that point to any arbitrary plane in the space is defined as

$$d^V = n \cdot (V - V_0), \tag{1}$$

where, n is the unit vector normal to the plane and V_0 is any point on that plane. Both V and V_0 are described in a global Cartesian coordinate system. Eq. (1) divides the space into positive and negative half-spaces, with points in positive half-space have positive distances and points in negative half-space have negative distances to the plane. For any polygonal or polyhedral block A the "distance" d_A of the block to any plane in the space is defined as

$$d_A = \begin{cases} \max(d_A^V) & \text{if } d_A^C < 0 \\ \min(d_A^V) & \text{if } d_A^C > 0 \end{cases}, \tag{2}$$

where $d^V{}_A$ is the distance of a vertex V on the block to the plane (Eq. (1)), and $\min\{\cdot\}$ and $\max\{\cdot\}$ represent minimum and maximum values, respectively, taken over all vertices of the block. $d^C{}_A$ is the distance of the centroid of the block to the plane. If a face of the block is parallel to the plane then more vertices can define the distance d_A. $d^C{}_A = 0$ is of no practical interest as the CP will never pass through centroid of a block. Subscripts and superscripts in all equations denote blocks and vertices (points), respectively. The vertex (or each of the vertices) that define the distance in (2) is called the ''closest vertex'' of that block to the plane.

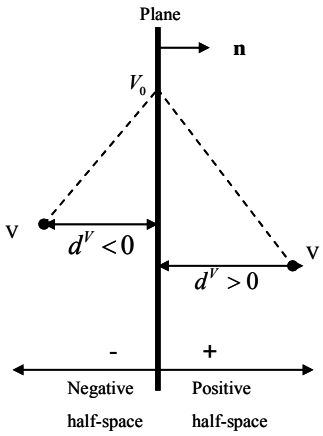

Fig. 1: Definition of distances and sign convention of a point to a plane

For any two blocks **i** and **j**, a CP is the plane which meets the following three conditions:

Condition1.

Centroids of block **i** and block **j** are located on opposite sides of the CP. In this paper it is assumed that the centroid of block **i** is located on the negative side of the CP and that of block **j** on the positive side. (as shown in Table 1)

Condition2.

The gap or overlap, defined as $d_j - d_i$, is a maximum in the mathematical sense.

Condition3.

$$d_i = -d_j$$

Condition 1 guarantees that the *CP* is between the blocks. The gap or overlap, $d_j - d_i$, is only a function of direction n of the CP and is independent on the location of the plane in space. Condition 2 identifies the direction of n by maximizing the gap or minimizing the overlap. Condition 3 specifies the location of the CP by setting $d_i = -d_j$. For separated blocks the gap is always positive ($d_i < 0$ and $d_j > 0$), while for blocks in contact the gap is always negative ($d_i > 0$ and $d_j < 0$) or zero for just in contact ($d_i = 0$ and $d_j = 0$).

Whenever $d_j - d_i >$ TOL, where TOL is a small positive user-defined tolerance, then the blocks are recognized as not in contact, no CP is developed. A "potential contact" is a contact for which $d_j - d_i <$ TOL the blocks are contacted each other or likely to develop new contacts in the next few time steps. A real contact

is a contact for which $d_j - d_i < 0$. Contact points and forces are found only for real contacts.

Table 1. The CP and its distance to the blocks

	two blocks and the CP	distance of the blocks to the CP
separate blocks	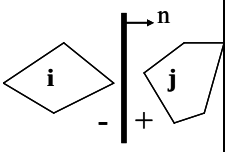	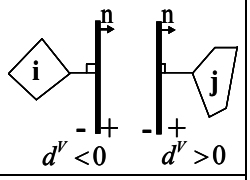
just-contact blocks	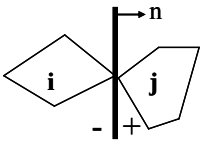	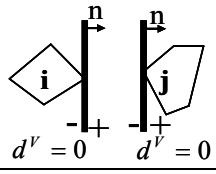
in-contact blocks	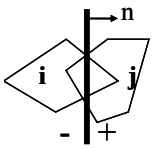	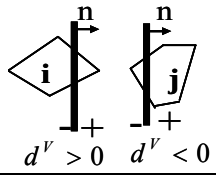

3. The conventional algorithm to position the common plane

Cundall [12] suggests a two-stage procedure to search the CP: the first stage specifies one point on the CP (referred to as the reference point, point *M* in Fig. 2). The second stage is an iterative process, in which a normal vector n, corresponding to the maximum gap, is found by rotating the CP around the reference point. In two-dimensions, the CP is a line and the rotation is performed around the reference point *M*. In three-dimensions, two arbitrary orthogonal axes are chosen in the CP with their origins at the reference point. The CP is then perturbed around each of them in both negative and positive sense. If any perturbation produces a gap larger than that of the current CP, the new CP replaces the current one. In this case, the closest vertices and the reference point is updated based on the newly found CP. If all the perturbations produce smaller gaps than that of the current CP, the next iteration starts with a smaller perturbation. The iteration process starts from an initial guess (either the CP from the previous time step or the perpendicular bisector of the line that connects the centroids of the blocks), and continues until the direction of the CP is found with reasonable accuracy. At any stage of iteration, if the gap exceeds a positive tolerance TOL then the iterative process halts and the contact is deleted. A gap larger than TOL indicates that the blocks are too far from each other to generate a contact. The total number of iterations depends on the accuracy of the initial guess of the CP and the smallest disturbing rotation angle. In general, the algorithm requires a large number of iteration steps. The number of iteration steps is especially high for the first-time formation of the CP, where the initial guess and the actual CP are very different.

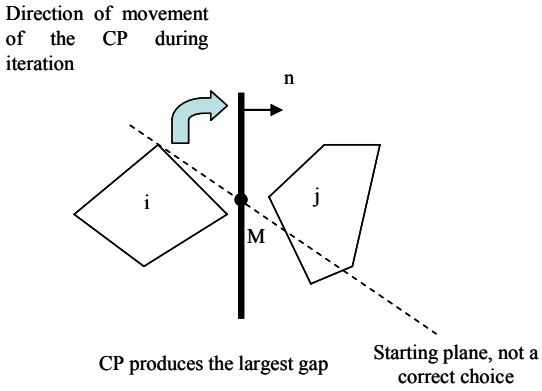

Fig. 2: conventional iterative procedure for finding the CP

4. Fast CP identification for separate and in-contact blocks

When two blocks are not in contact or already in contact, the definition of the CP can be utilized to limit the number of candidate common planes and thus significantly reduce the computational cost of common plane searching.

4.1. CP identification in 2-D

Statement: In two-dimensions, the CP can be found by checking only 5 possible candidate planes.
The following provides a stepwise proof of the statement above leading to identification of the 5 possible candidate planes**.**
Proof: Let *A* and *B* be the closest vertices for blocks i and j, respectively.
(1) *The CP passes through the midpoint M of the segment AB.*

Let θ measure the angle between the *CP* and the perpendicular bisector (*PB*) of the segment *AB* as shown in Fig.3. Then $d_A = |AA_0| = |MA|\cos\theta$ and $d_B = |BB_0| = |MB|\cos\theta$.

The Condition 3 of *CP* definition, $d_A = -d_B$, implies that $|d_A| = |d_B|$ or

$$|MA|\cos\theta = |MB|\cos\theta \Rightarrow |MA| = |MB|.$$

∴ The *CP* should pass through the midpoint *M* of the segment *AB*.

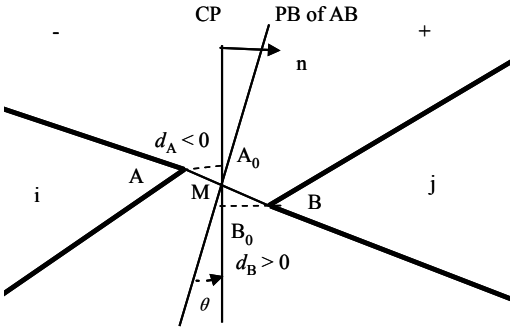

(a) Separate blocks

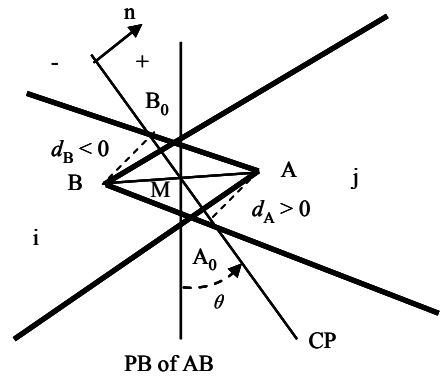

(b) In-contact blocks

Fig. 3: *PB* of the segment *AB* and the *CP* in 2-D

(2) *CP is completely located within the space S.*

The space *S* is the area formed by rays Mm_1, Mm_2, Mm_3 and Mm_4, drawn from the midpoint *M*, parallel to edges AA_1, AA_2, BB_1 and BB_2, respectively (the shaded area in Fig.4).

Assume that line *L*, portion of which is located outside the space *S*, is a candidate *CP* (Fig. 4a). Then, vertex B_2 makes $d_{B2} < d_B$ according to Equation (2). This implies that AB_2 and not *AB* are the closest vertices. This contradicts with *AB* being the closest vertices and the geometric arrangement of the blocks. For in-contact blocks in Fig. 4b, assume the line *PB*, portion of which is located outside the space *S*, is a candidate *CP*. Then, vertex A_2 makes $d_{A2} > d_A$ according to Equation (2). This implies that BA_2 and not *BA* are the closest vertices. This contradicts with *AB* being the closest vertices and the geometric arrangement of the blocks. Therefore, line *L* cannot be a candidate *CP*. Similarly, all lines located partially or completely outside the space *S* cannot be the candidate *CP*. So the *CP* is completely located within the space *S*.

(3) *CP should produce the smallest angle with the PB of the segment AB for separate blocks*

From Fig. 3a, $d_B - d_A = |AB| \cdot \cos\theta$ ($d_B > 0$ and $d_A < 0$, $0 \le \theta < 90$)

From Condition 2, $d_B - d_A$ is maximum

=> $\cos\theta$ is maximum

∴ angle θ is minimum.

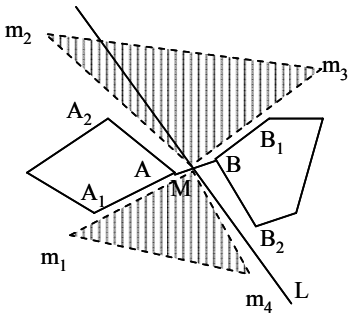

(a) Separate blocks

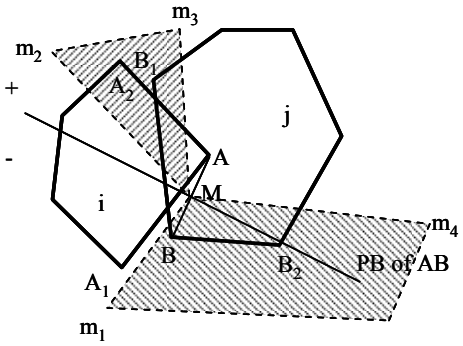

(b) In-contact blocks

Fig. 4: CP is completely located within the space S

(4) *CP should produce the largest angle with the PB of the segment AB for in-contact blocks with PB not completely within the space S*

From Fig. 3b, $d_B - d_A = -|AB| \cdot \cos\theta$ ($d_B < 0$ and $d_A > 0$, $0 \le \theta < 90$)

From Condition 2, $d_B - d_A$ is maximum

=> $\cos\theta$ is minimum

∴ angle θ is maximum.

From separate to overlap of the two blocks, the angle θ transforms from the minimum to the maximum.

(5) *The CP is the PB of the segment AB for in-contact blocks when PB is completely located within the space S.*

Let $f = (d_B - d_A)$. *f* is only the function of angle θ. Then

$$\frac{\partial f}{\partial \theta} = 0 \Rightarrow \sin\theta = 0 .$$

So the plane with $\theta = 0$ is also a candidate plane, which is the *PB* itself when the *PB* is completely located within the space *S*.

(6) *The CP is one of five candidate planes*

The CP is the line that

- is completely located in space *S* from proof (2) and (5), and
- makes the smallest or largest possible angle with the *PB* of the segment *AB* from proof (3) and (4) for separate and in-contact blocks, respectively.

If the *PB* of the segment *AB* is completely located in the space *S* for separate blocks (Fig. 5), then:

From proof (3) the line that makes the smallest possible angle θ with the *PB* is the *PB* itself for separate blocks. The *PB* also satisfies proof (2),

∴ The common plane is the *PB* (type a below).

If the *PB* of the segment *AB* is completely located in the space *S* for in-contact blocks (Fig. 3(b)), then:

From proof (5) the *PB* is a candidate common plane. The *PB* also satisfies proof (2).

∴ The common plane is the *PB* (type a below).

If the *PB* is not located completely inside the space *S* (Fig. 4), then:

- The *PB* is not the common plane.
- The common plane is the line with the smallest possible angle θ to the *PB* for separate blocks (proof 3) and the line with the largest possible angle θ to the *PB* for in-contact blocks (proof 4).

∴ for separate blocks the common plane is one of the boundary rays Mm_1, Mm_2, Mm_3 and Mm_4, (Mm_4 in the Fig. 4a, type b below). Any line inside space *S* other than on the boundaries will make a larger angle θ. For in-contact blocks the common plane is also one of the boundary rays Mm_1, Mm_2, Mm_3 and Mm_4, which also should be within the space *S* (Mm_3 in Fig. 4b, type b below). Any line inside space *S* other than on the boundaries will make a smaller angle θ.

∴ The *CP* is one of the following candidates:

Type a: The perpendicular bisector of the segment *AB*.

Type b: The lines passing through the mid-point of the segment *AB* and parallel to one edge of AA_1 or AA_2 of the block i, or parallel to one edge of BB_1 or BB_2 of the block B.

The number of candidate planes is limited to five. All these *CP* candidates in 2-D are defined as the set of 2DCP.

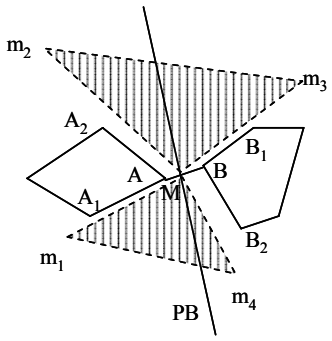

Fig. 5: Perpendicular bisector of segment AB is inside of the space *S*. So it is the *CP*

4.2. CP identification in 3-D

Statement: In three-dimensions the candidate planes fall within 4 types related to the geometry of the blocks and their relative position.

Proof: Let *A* and *B* be the closest vertices of blocks **i** and **j**, respectively.

(1) *The CP passes through the midpoint M of the segment AB*.

Similar to the 2-D case, the *CP* should pass through the midpoint *M* of the segment *AB*. The difference is that both *PB* and *CP* are planes rather than lines, and angle θ measures the dihedral angle between *PB* and *CP* (Fig.6).

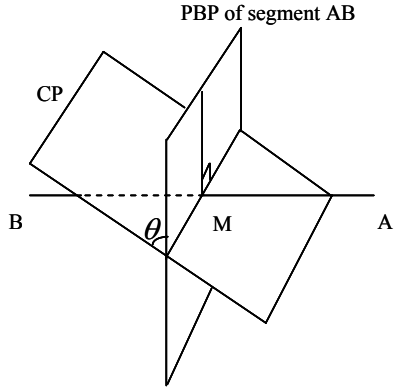

Fig. 6: *PB* plane, *CP* and dihedral angle θ in 3-D

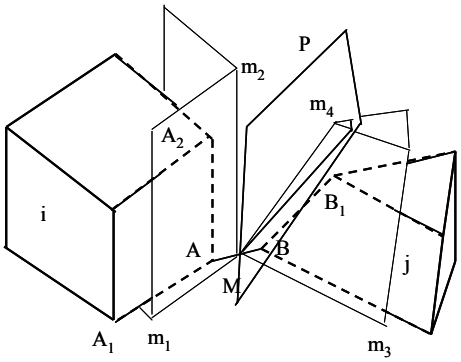

(a) Space *S* for separate blocks

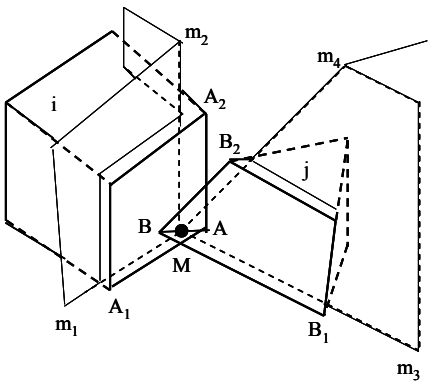

(b) Space *S* for in-contact blocks

Fig. 7: Space *S* constructed by quarter-planes parallel to faces of block i and j.

(2) *The CP is completely located within the space S.*

Rays Mm_1 and Mm_2 drawn parallel to edges AA_1 and AA_2 respectively, define a semi-infinite quarter-plane m_1Mm_2, parallel to face A_1AA_2 of block **i**. In the same way, for every face of block **i** that shares vertex *A*, and for every face of block **j** that shares vertex *B*, a quarter-plane can be constructed, passing through the midpoint

M, parallel to that face. The space bounded between the quarter-planes associated with block **i** form one side, and those associated with block **j** form the other side, defines the space *S* in 3-D as shown in Fig. 7.

Similar to 2-D, any candidate common plane should be completely located inside the space *S*. For separate blocks assume that plane *P*, portion of which is located outside the space *S*, is a candidate *CP* (Fig. 7a). Then, vertex B_1 is closer to this plane than vertex *B*, which contradicts *AB* being the closest vertices. For in-contact blocks the proof is similar to the 2-D case.

∴ The *CP* is completely located within the space *S*.

(3) *The CP should produce the smallest dihedral angle with the PB plane of the segment AB for separate blocks*.

$d_B - d_A = |AB| \cdot \cos\theta$ ($d_B > 0$ and $d_A < 0$, $0 \le \theta < 90$) still holds in 3-D. From Condition 2, maximizing $d_B - d_A$ can lead $\cos\theta$ to a maximum.

∴$d_B - d_A$ is a maximum when dihedral angle θ is a minimum.

(4) *The CP should produce the largest dihedral angle with the PB plane of the segment AB for in-contact blocks with PB not completely within the space S.*

$d_B - d_A = -|AB| \cdot \cos\theta$ ($d_B < 0$ and $d_A > 0$, $0 \le \theta < 90$) also holds in 3-D for in-contact blocks. From Condition 2, maximizing $d_B - d_A$ can lead $\cos\theta$ to a minimum.

∴$d_B - d_A$ is a maximum when dihedral angle θ is a maximum.

(5) *The CP is the PB of the segment AB for in-contact blocks when PB is completely located within the space S.*

Let $f = (d_B - d_A)$. *f* is only the function of angle θ. Based on the extremum theory, we can get

$$\frac{\partial f}{\partial \theta} = 0 \Rightarrow \sin\theta = 0 .$$

So the plane with $\theta = 0$ is also a candidate plane, which is the *PB* itself when the *PB* is completely located within the space *S*.

(6) The CP is one of four different types

The *CP* is the plane that

- is completely located in space *S* from proof (2) and (5), and
- makes the smallest or largest possible angle with the *PBP* of the segment *AB* from proof (3) and (4) for separate and in-contact blocks, respectively.

If the *PB* plane of the segment *AB* is completely located in the space *S* for separate blocks, then:

From proof (3) the plane that makes the smallest possible dihedral angle θ with *PB* is the *PB* itself. The *PB* also satisfies proof (2)

∴ The common plane is the *PB* (type a below).

If the *PB* of the segment *AB* is completely located in the space *S* for in-contact blocks, then:

From proof (5) the *PB* is a candidate common plane. The *PB* also satisfies proof (2),

∴ The common plane is also the *PB* (type a below).

If the *PB* plane is not completely located inside the space *S*, then:

- The *PB* is not the common plane.
- The common plane is the plane with the smallest possible angle θ to the *PB* (proof 3) for separate blocks or the largest possible angle θ to the *PB* (proof 4) for in-contact blocks.

∴ The common plane contains at least one ray from the boundary. Any plane which is completely inside the space *S* and does not contain any of the boundary rays makes a larger dihedral angle θ with *PB* for separate blocks and a smaller angle for in-contact blocks and cannot be a candidate common plane. The number of rays included in *CP* can be used to further categorize it:

• The *CP* contains exactly two boundary rays. If those two rays correspond to the same block, then the *CP* contains the quarter-plane made by those rays. Therefore it is parallel to one of the faces of the blocks (type b).

If those two rays correspond to different blocks, then the *CP* is parallel to corresponding edges from different blocks (type c).

• The *CP* contains exactly one boundary ray. In this case, the *CP* is parallel to the corresponding block edge (type d).

• The *CP* contains more than two boundary rays. Then any two of them can be utilized to identify the *CP* (the result is either type b or type c).

∴ The *CP* is one of the following candidates:

Type a: The *PB* of the segment *AB*.

Type b: The plane passing through the midpoint of the segment *AB*, parallel to one of the faces of block **i** or **j**. For block i, only faces which include the vertex *A* are considered. For block j, only faces which include the vertex *B* are considered.

Type c: The plane passing through the midpoint of segment *AB*, parallel to one edge of block **i** and one edge of block **j**. For block i, only edges which share the vertex *A* are considered. For block j, only edges which share the vertex *B* are considered.

Type d: The plane passing through the midpoint of segment *AB* parallel to one edge from one of the two blocks. The plane can be fully defined by using the Conditions of the common plane. Fig. 8a shows the *CP* containing only one ray (Mm_1), parallel to the edge BB_1 of block j. In this condition, the normal of the *CP* can be calculated by $n = \pm n_{BB_1} \otimes (n_{BB_1} \otimes n_{AB})$, where n_{BB1} and n_{AB} are the unit vector of BB_1 and *AB*, respectively. For in-contact blocks as shown in Fig. 8b, the candidate common plane of type d can be obtained by the similar computation method for separate blocks mentioned above.

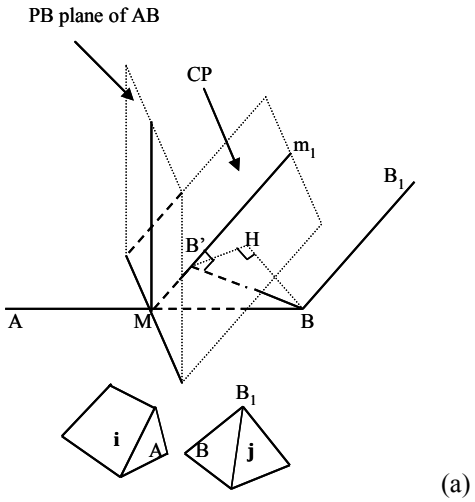

(a)

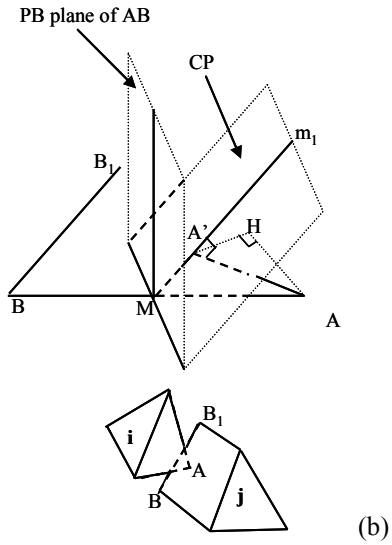

(b)

Fig. 8: Type d, CP is parallel to one edge from the blocks: (a) *CP* is parallel to edge BB_1 from block j for separate blocks; (b) CP is parallel to edge BB_1 from block j for in-contact blocks

The number of candidate planes type is limited to four. All these *CP* candidates in 3-D are defined as the set of 3DCP.

5. Fast CP identification for two just-in-contact blocks

5.1 CP identification in 2-D

Statement: The *CP* is completely located in the space *S*.

Proof: For two just-in-contact blocks the space *S* is shown in Fig.9. Assume that line *L*, portion of which is located not completely within the space *S*, is a candidate *CP* (Fig. 9). Then, vertex B_1 makes $d_{B1} < d_B$ according to Eq. (2). This implies that AB_1 and not AB are the closest vertices. This contradicts with AB being the closest vertices and the geometric arrangement of the blocks. Therefore, line *L* cannot be a candidate *CP*. Similarly all lines located partially or completely outside the space *S* cannot be the candidate *CP*. So the *CP* is completely located within the space *S*.

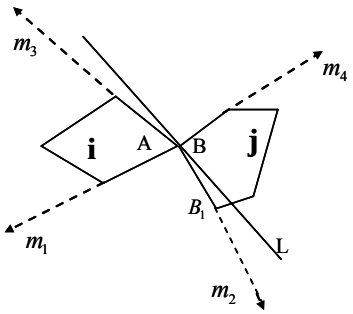

Fig. 9: *CP* is located within the space *S* defined in 2-D

Statement: The *CP* can be found in the set of 2DCP

Proof:

(1) vertex-to-edge or edge-to-edge contact type

For vertex-to-edge or edge-to-edge contact type the space *S* contains just a line that is the contact edge from one of the blocks. This line meets the conditions to be a *CP* and locates within the space *S*. So the *CP* can be found in the set of 2DCP.

(2) vertex-to-vertex contact type

For vertex-to-vertex contact type, there are infinite *CP*s in the space *S* since vertex *A* and *B* are coincide, which indicates that this type of contact is non-smooth and the normal direction is undefined.

Based on the proof above that the *CP* must exit and it is completely located within the space *S*. So the intersection of the space m_1Mm_2 and $m_3'Mm_4'$ is non-zero. $m_3'Mm_4'$ is the diagonally space of m_3Mm_4 as shown in Fig. 10. This intersection makes the space *S*′, which is a subset of the space *S*. Any line located in the space *S*′ is a *CP*, for all these lines meet the conditions to be a *CP*. The boundary of the space *S*′ is determined by two edges from the two blocks. So these two edges from the blocks are the *CP* and the *CP* can be found in the set of 2DCP.

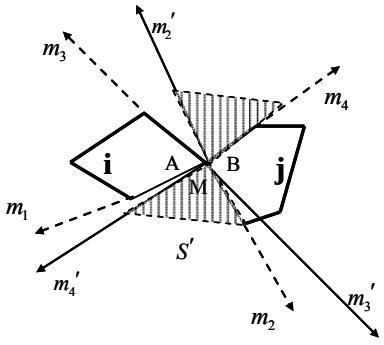

Fig. 10: Subset of the space *S*

Furthermore, in order to get a better *CP*, we can move vertices *A* and *B* along AC_i and BC_j by a distance

of ε (ε << min ($|AC_i|$, $|BC_j|$)) to A' and B', where AC_i and BC_j are the centroids of block i and j, respectively (Fig. 11). So the perpendicular bisector line of the segment $A'B'$ can be defined. If the *PB* is completely located in space *S*, it meets the conditions of *CP* and it is the *CP*. If the *PB* doesn't completely locate in the space *S*, we can also find a CP in the set of 2DCP by the edges from the blocks.

∴ The *CP* can be found in 2DCP.

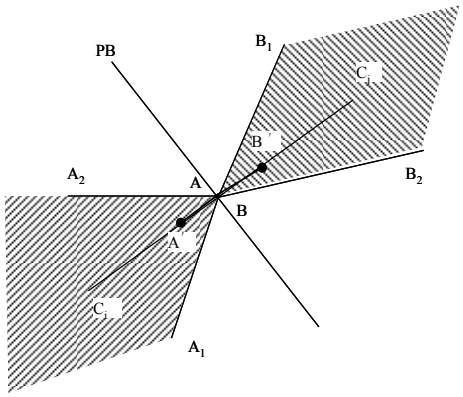

Fig. 11: Moving *A* and *B* to get *PB*

5.2 CP identification in 3-D

Statement: the *CP* is completely located in the space *S*

Proof: Similar to 2-D, any candidate common plane should be completely located inside the space *S*. Assume that plane *P*, portion of which is located outside the space *S*, is a candidate common plane (Fig. 12). Then, vertex B_1 is closer to this plane than vertex *B*, which contradicts *AB* being the closest vertices. Therefore, plane *P* can't be a candidate *CP*, and the *CP* is completely located within the space *S*.

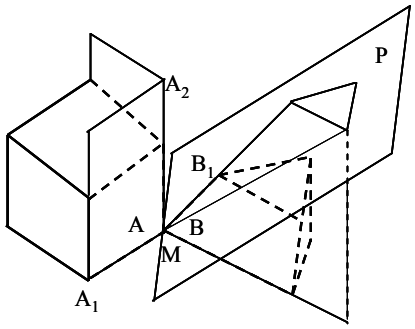

Fig. 12: A plane, partially located outside the space *S*, can't be a *CP* candidate

Statement: The *CP* can be found in the set of 3DCP

Proof: (1) vertex-to-face, edge-to-face, face-to-face contact type

For vertex-to-face, edge-to-face or face-to-face contact type, the space *S* contains just a face that is the contact face from one of the blocks. This face meets the conditions to be a *CP* and locates completely within the space *S*.

∴ The *CP* can be found in the set of 3DCP.

(2) edge-to-edge contact (intersected)

Let *A* and *B* be the closest vertices. With the two edges (assume the contacting edges are AA_1 and BB_1, as shown in Fig.13), the normal $\boldsymbol{n}$ of the *CP* can be defined by $\boldsymbol{n} = AA_1 \times BB_1$, just like type b in 3DCP.

∴ The *CP* can be found in the set of 3DCP.

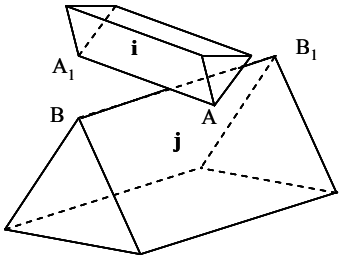

Fig. 13: edge-to-edge (intersected) contact of blocks

(3) edge-to-edge contact (parallel) and vertex-to-edge contact

Let *A* and *B* be the closest vertices. For these two types of contact, the number of *CP* in the space *S* is infinite. Similar to vertex-to-vertex contact in 2-D, we can also find a non-zero space *S'*, which is a subset of the space *S*. The boundary of *S'* is defined by the faces containing *A* from block **i** and the faces containing *B* from block **j**. So these boundary faces of the space *S'* are *CP*s. Furthermore, if *A* and *B* are coincide, then these two vertices can be moved a length of ε towards the centroids of the two blocks as shown in Fig. 11. The perpendicular bisector plane of the segment *A'B'* is the *CP* when it is completely located within the space S. If *A* and *B* are not coincide, then vertex *A* or *B* can be move a length of ε towards its block centroid (moving *B* to B*'* in Fig. 14). A perpendicular line from *B'* to *AB* can be defined, with the pedal point of *B″*. Then the plane passing through *AB* with the normal of *B'B''* is a candidate *CP*. If the plane is completely located in the space *S*, then it is the *CP*.

∴ The *CP* can be found in the set of 3DCP.

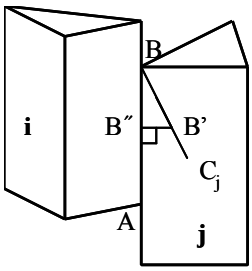

Fig. 14: A candidate *CP* for edge-to-edge contact (parallel)

(4) vertex-to-vertex contact

Similar to 2-D case, there is a non-zero subset *S'* of the space *S*, which is bounded by some faces from the two blocks. So these boundary faces of the space *S'* are *CP*s. Furthermore, vertices *A* and *B* can be moved a

small distance to A' and B' towards the centoids of the blocks. So the perpendicular bisector line of the segment $A'B'$ can be defined. If the PB is completely located in space S, it meets the conditions of CP and it is the CP.

∴ The CP can be found in 3DCP

6. FCP algorithm

The FCP algorithm to find the CP consists of the following steps (Fig. 15):

Step 1. Initial guess: if there is a CP from previous DEM time step then use it as the initial guess for the CP in this time step. Otherwise, set the CP as the PB plane of the line connecting the centroids of the two blocks.

Step 2. Based on the guess CP, find the closest vertices AB in blocks i and j. This can be performed by a quick search of the distances of all the vertices of the blocks to the CP, considering the sign convention for each block. Among all segments such as AB that connect a closest vertex A of block i to a closest vertex B of block j, the one with the shortest length is chosen. If more than one pair of closest vertices have the shortest length (i.e., those vertices are equidistant), then any of them can be chosen to proceed with the algorithm.

Step 3. For the two closest vertices A and B found in Step 2, check all candidate planes of Section 4 and 5 (from type a to type d) and find the one with the largest gap or smallest overlap. If $d_A = d_B = 0$, moving A and/or B a small distance temporarily is needed to define the PB. If any candidate plane produces a gap larger than TOL, then stop the algorithm as the blocks are too far from each other to make any, real or potential, contact. If the gap is less than zero then a real contact is generated.

Step 4. If the CP obtained in Step 3 is the same as the one from Step 2, then it is the correct common plane. Otherwise go to Step 2.

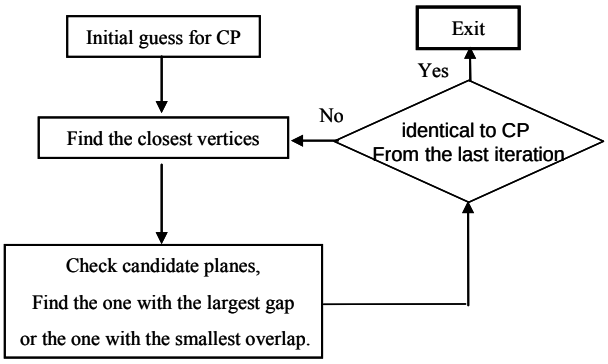

Fig. 15: FCP algorithm

This is an iterative algorithm, with consisting of steps 2–4 in each iteration. The number of iterations required to find the CP is usually very small and the position of the selected CP is accurate. This is mainly because the iteration is done to locate the two closest vertices, rather than the CP itself.

7. Numerical experiments

The numerical experiment below is an example of a gravity dam used by Dr. Shi [12] in 2-D DDA. The gravity dam is modeled as a single block. The bedrock is composed of many blocks by horizontal bedding planes and nearly vertical joints. The loads are the weight of the dam and of the rock blocks and the resultant water pressure acting horizontally on the face of he dam. The base and side borders of the bed rock are fixed. Fig. 16a shows the 3-D view of unmoved blocks before loads are applied. The concave blocks are meshed to several convex sub-blocks for contact detection and contact transfer (as shown in Fig. 16b). Fig. 16c is the result of time step 2000 with friction angle φ =20°.

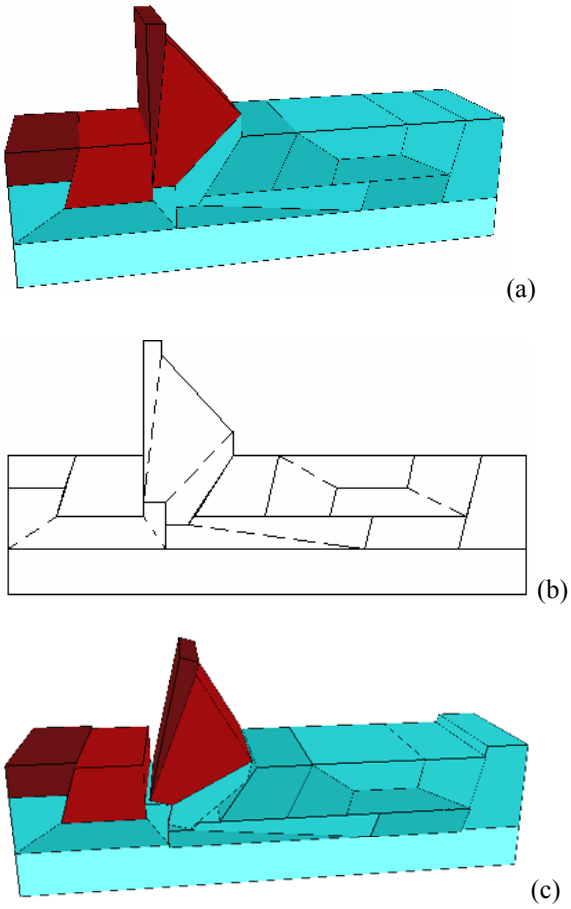

Fig. 16: Numerical experiment of gravity dam: (a) before deformation in 3-D view; (b) concave blocks meshed by several convex blocks; (c) deformed system.

The input data were the following:
number of steps = 2000,
step time interval = 0.005,
unit mass = 0.05,
ratio of maximum displacement = 0.010,

water pressure (F_x , F_y, F_z) = (10 , 0, 0),
block unit weight (f_x , f_y, f_z) = (0 , -0.5, 0),
material constants E = 20, ν = 0.30.

Fig. 17 shows the average computing times of the d_A and d_B (Eq. 2) to get the CP in each contact searching for two blocks using FCP algorithm and the original CP algorithm. In the original CP algorithm, the maximum and minimum rotation angles in the original CP algorithm are 10° and 0.001°, respectively. From Fig. 17 one can find that the FCP algorithm is faster about 100 times than the original one.

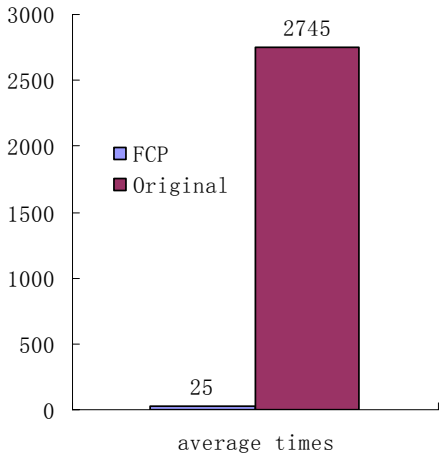

Fig. 17: The efficiency comparison between FCP and original algorithm.

Conclusions

The fast common plane (FCP) algorithm proposed by Nezami et al (2004) for separate blocks is extended to a general case for all contact types and the proof of the algorithm is also given. The algorithm takes advantages of the properties of the CP to limit the research space and reduce candidates of the common plane to five in 2-D and four types of faces in 3-D. With this algorithm, the efficiency of the contact detection can be greatly improved.

References

Barbosa RE. Discrete element models for granular materials and rock masses. PhD thesis, Urbana: Department of Civil and Environmental Engineering, University of Illinois at Urbana Champaign; 1990.

Chueng Y M. Chen W S. Zhang Y. H. New approach to determine three-dimensional contacts in blocks systerm: penetration edges method. ASCE 2006;6(5):303-310

Cundall PA, Strack ODL. A discrete numerical model for granular assemblies. Geotechnique 1979, 29(1): 47–65.

Cundall PA. Formulation of a three-dimensional distinct element model-part I: a scheme to detect and represent contacts in a system composed of many polyhedral blocks. Int J Rock MechMin Sci & Geomech Abstr 1988;25(3):107–16.

Erfan G. Nezami, Youssef M.A. Hashash, Dawei Zhao, Jamsnid Ghaboussi. A fast contact detection algorithm for 3-D discrete element method. Computers and Geotechnics 2004;31:575-587.

Feng YT, Owen DRJ. An energy based corner to contact algorithm. In Cook BK, Jensen rP, Cook BK, Jensen RP, editors. Discrete element methods, numerical modeling of discontinua. Santa Fe, New Mexico, USA; 2002. p. 32–7.

Itasca Consulting Group, I. 3DEC 3-Dimensional distinct element code. User's Manual, 2.0 2.0 2.0; 1998.

Krishnasamy J, Jakiela MJ. A method to resolve ambiguities in corner–corner interactions polygons in the context of motion simulation. Eng Comput 1995;12(2):135–44.

Lin X, Ng TT. A three-dimensional discrete element model using arrays of ellipsoids. Geotechnique 1997, 47(2):319–29.

Liu Jun, Kong Xianjing and Lin Gao. Formulations of the three-dimensional discontinuous deformation analysis method. Acta Mechanica Sinica 2004, 3: 270~282.

Munjiza A, Andrews KRF. NBS contact detection algorithm for bodies of similar size. Int J Numer meth Eng, 1998, 43(1):131–49.

Perkins E, Williams JR. A fast contact detection algorithm insensetive to object size. Eng Comput 2001, 18(1–2): 48–61.

Shi Gen-hua. Discontinuous deformation analysis: A new numerical model for the statics and dynamics of deformable block structures. Int J Engineering Computations 1992,vol.9: 157-168

Ting J, Khwaja M, Meahum LR, Rowell HD. An ellipsed-based discrete elemetn model for granular materials. Int J Numer Anal Meth Geomech 1993;17:603–23.

Wang Jianquan, Lin Gao and Liu Jun. Analysis and improvement of scheme to detect contacts in system composed of 3D convex polyhedral blocks. Chinese Journal of Rock mechanics and Engineering, 2006, 25(11): 2247-2257.

Williams JR, O Connor R. A linear complexity intersection algorithm for discrete element simulations of arbitrary geometries. Int J CAE-Eng Comput, Special Ed Discrete Element Meth 1995, 12(2):185–201.

Application of DDA-FEM coupled method in pavement analysis

C.Y. CAO[1], Y. ZHONG[1] and G.H. SHI[2]

[1]Department of Civil Engineering, Dalian University of Technology, CHINA
[2]DDA Consultant Company, USA

The numerical model coupling three-dimensional discontinuous deformation analysis (3D-DDA) with finite element method (FEM) was developed in the present paper. The displacements and stresses were obtained by proper internal discretization of deformable blocks using finite element meshes while the contacts between the blocks were modeled by DDA method. Based on the variational principle of minimum potential energy, the simultaneous equilibrium equations of the coupled method were then established. A multilayer asphalt concrete pavement subjected to moving vehicle loads was analyzed to illustrate the application of the proposed method. The numerical results demonstrated the validity and the advantages of the coupled method.

Keywords: 3D-DDA-FEM Coupled Method; 3D-DDA; Finite element method; Pavement

1. Introduction

The dynamic displacements and stresses of pavement systems have raised an increasing concern in the field of pavement engineering in recent years. During the past decades many developments in both analysis techniques and materials testing procedures have made it possible to better simulate the dynamic response of pavements to traffic loads and environmental conditions. Various pavement structure models have been generated since 1960s, ranging from an infinite beam on Winkler foundation to a multilayered system over an infinite half space (Monismith 1988). Among them, the multi-layered model is a widely accepted one by researchers and engineers due to its validity and precision. How-ever, the solutions of the problem usually encounter much difficulty and are not satisfactory. It is very complex and difficult for engineers to master the analytical method of multilayer pavements. Although the flexible multilayered pavement system can also be modeled in a discrete manner with finite element method (FEM) using special joint elements, the description of discontinuities is usually difficult and there are often restrictions on the degree of deformation permitted (Cho et al. 1996). Furthermore, the number of locations where discontinuities can be handled is very limited.

The discontinuous deformation analysis (DDA) is a promising discontinuous modeling technique which has great potential for modeling of blocky systems (Shi 1988, 2001). Since it was proposed, DDA has received considerable attention from researchers and practicing engineers throughout the world and has become a useful tool for the analysis of jointed rock mass behaviors. Many scholars have also made great effort to improve it for applications in more widely domains (Pearce et al 2000; Ning and Yang 2006). Although the geometry of the block in DDA can be convex or concave, or even with holes in it, the stress and strain in each block is constant, which is not a realistic assumption, particularly for a big block. Thus, some researchers presented a coupled method called "DDA-FEM Coupled Method" (DFCM) to improve its deformation ability by means of discretizing each block using finite element meshes. The method combines the advantages of the FEM and the DDA so that not only the movements of the block system can be depicted, but the stress distributions in the blocks can also be obtained. It is a good approach to simulate a domain controlled by continuous and discontinuous medium which is not suitable for any single numerical technique.

In this paper, the authors developed the DDA-FEM Coupled Method to solve the problems of moving load and made attempt to apply the DFCM for displacement and stress analysis of pavements. The pavement system is modeled by the multilayered medium; the moving vehicle is presented by a moving concentrated load. The displacement and stress fields are obtained by proper internal discretization of deformable blocks using finite element meshes. The contacts between the deformable blocks were modeled by DDA method. Based on the variational principle of minimum potential energy, the global equilibrium equations of the coupling method were deduced in detail.

2. Formulations of 3D-DDA-FEM coupled method

2.1 Displacements of each element

If the four-node tetrahedrony isoparametric element (Fig. 1) is chosen to be the finite element in DDA blocks, the x-, y-, z-displacements (u, v, w) of an arbitrary point (x, y, z) in each element can be expressed as

$$\begin{bmatrix} u \\ v \\ w \end{bmatrix} = [N_i][D_i] \tag{1}$$

where $[D_i]$ is the nodal displacement vector,

$$[D_i] = [u_1\ v_1\ w_1\ u_2\ v_2\ w_2\ u_3\ v_3\ w_3\ u_4\ v_4\ w_4]^{\mathrm{T}} \tag{2}$$

$[N_i]$ is the matrix of the shape functions of elements.

$$[N_i] = \begin{bmatrix} N_1 & 0 & 0 & \cdots & N_4 & 0 & 0 \\ 0 & N_1 & 0 & \cdots & 0 & N_4 & 0 \\ 0 & 0 & N_1 & \cdots & 0 & 0 & N_4 \end{bmatrix} \tag{3}$$

where $N_1 = \xi$, $N_2 = \eta$, $N_3 = \zeta$, $N_4 = 1-\xi-\eta$; and (ξ_j, η_j, ζ_j) is the natural coordinate of nodes.

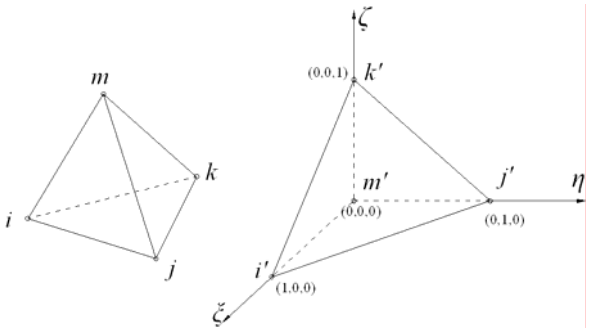

Fig. 1: Tetrahedrony isoparametric element model

In general, a block can be as small as an element or as large as an element mesh, and different meshes can also be put into different blocks if conditions permit (Chang, 1994).

2.2 General equilibrium equations

A number of individual blocks can be connected to form a block system satisfying the constraints between blocks. For a system of *n* blocks and *k* contact, if each DDA block is discretized into m_b finite elements, the total potential energy of the system includes the strain energy of the initial and induced stresses, the external work of the point loadings, body loadings, inertia forces and the displacement constraints, as well as the potential energy of the normal and shear contacts, and friction forces.

The total potential energy Π of the system can be expressed as

$$\Pi = \sum_{b=1}^{n}\sum_{i=1}^{m_b}\Pi_e - \sum_{b=1}^{n}\sum_{i=1}^{m_b}\Pi_w + \sum_{i=1}^{k}(\Pi_n + \Pi_s) \tag{4}$$

where Π_e, Π_w, Π_n, Π_s are the potential energy of each finite element in a block, the work of external forces, the potential energy of the normal spring and the potential energy of the shear spring, respectively.

The element matrices of stiffness and force are formed by taking the derivatives with respect to the displacement variables from the corresponding potential energy. Taking the direct summation of these individual submatrices to form the global stiffness matrix [*K*] and force matrices [*F*], the simultaneous equations of equilibrium are then established.

The simultaneous equilibrium equations derived by minimizing the total potential energy of the system have the following form:

$$\begin{bmatrix} K_{11} & K_{12} & \cdots & K_{1n} \\ K_{21} & K_{22} & \cdots & K_{2n} \\ \vdots & \vdots & \vdots & \vdots \\ K_{n1} & K_{n2} & \cdots & K_{nn} \end{bmatrix} \begin{Bmatrix} D_1 \\ D_2 \\ \vdots \\ D_n \end{Bmatrix} = \begin{Bmatrix} F_1 \\ F_2 \\ \vdots \\ F_n \end{Bmatrix} \tag{5}$$

In the Eq. (5), the nodal displacements [D_i] are chosen unknown variables, [K_{ij}] is a 12×12 submatrix and [F_i] is a 12×1 submatrix.

2.3 Formulation of the elements

Stiffness matrix

The strain energy Π_e of element *i* can be expressed as

$$\Pi_e = \frac{1}{2}\iiint_{v_i}\{\xi_i\}^T\{\sigma_i\}\,dxdydz$$

$$= \frac{1}{2}\{D_i\}^T\iiint_{v_i}[B_i]^T[E_i][B_i]\,dxdydz\{D_i\}$$

$$= \frac{1}{2}\{D_i\}^T\int_{-1}^{1}\int_{-1}^{1}\int_{-1}^{1}[B_i]^T[E_i][B_i]\,|[J]|\,d\xi d\eta d\zeta\{D_i\} \tag{6}$$

where

$$[E_i] = \frac{E}{(1+\nu)(1-2\nu)}\begin{bmatrix} 1-\nu & \nu & \nu & 0 & 0 & 0 \\ \nu & 1-\nu & \nu & 0 & 0 & 0 \\ \nu & \nu & 1-\nu & 0 & 0 & 0 \\ 0 & 0 & 0 & \frac{1-2\nu}{2} & 0 & 0 \\ 0 & 0 & 0 & 0 & \frac{1-2\nu}{2} & 0 \\ 0 & 0 & 0 & 0 & 0 & \frac{1-2\nu}{2} \end{bmatrix}$$

$$[B_i] = \begin{bmatrix} \frac{\partial N_i}{\partial x} & 0 & 0 & \frac{\partial N_i}{\partial y} & 0 & \frac{\partial N_i}{\partial z} \\ 0 & \frac{\partial N_i}{\partial y} & 0 & \frac{\partial N_i}{\partial x} & \frac{\partial N_i}{\partial z} & 0 \\ 0 & 0 & \frac{\partial N_i}{\partial z} & 0 & \frac{\partial N_i}{\partial y} & \frac{\partial N_i}{\partial x} \end{bmatrix}^T$$

i=1, 2, …, 4. *E* and *v* are Young's modulus and Poisson ratio, respectively.

Taking derivatives with respect to the displacement variables from the strain energy Π_e, a 12×12 element stiffness matrix [K_{ii}] is obtained

$$k_{rs}=\frac{\partial^2\Pi_e}{\partial d_{ri}\partial d_{si}}=\int_{-1}^{1}\int_{-1}^{1}\int_{-1}^{1}[B_i]^T[E_i][B_i]\,|[J]|d\xi d\eta d\zeta \quad (7)$$

(r, s=1, 2, ⋯, 12.)

where |[J]| is the determinant of the Jacobian matrix.

$$[J]=\begin{bmatrix}\sum_{j=1}^{8}\frac{\partial N_j}{\partial\xi}x_j & \sum_{j=1}^{8}\frac{\partial N_j}{\partial\xi}x_j & \sum_{j=1}^{8}\frac{\partial N_j}{\partial\xi}x_j\\ \sum_{j=1}^{8}\frac{\partial N_j}{\partial\eta}x_j & \sum_{j=1}^{8}\frac{\partial N_j}{\partial\eta}x_j & \sum_{j=1}^{8}\frac{\partial N_j}{\partial\eta}x_j\\ \sum_{j=1}^{8}\frac{\partial N_j}{\partial\zeta}x_j & \sum_{j=1}^{8}\frac{\partial N_j}{\partial\zeta}x_j & \sum_{j=1}^{8}\frac{\partial N_j}{\partial\zeta}x_j\end{bmatrix}. \quad (8)$$

Inertia force matrix

If the displacement of an arbitrary point (x, y) in i-th element and the mass per unit volume are expressed as $\{u\ v\ w\}$ and M, respectively, the potential energy Π_i of the inertia force is given as

$$\Pi_i=-\iiint_{v_i}\{u\ v\ w\}\begin{Bmatrix}f_x\\f_y\\f_z\end{Bmatrix}dxdydz$$

$$=\{D_i\}^T\iiint_{v_i}[N_i]^T[N_i]dxdydz\left(\frac{2M}{\Delta^2}\{D_i\}-\frac{2M}{\Delta}\{v_i(0)\}\right) \quad (9)$$

The derivatives of Π_i gives

$$k_{rs}=\frac{2M_i}{\Delta^2}\int_{-1}^{1}\int_{-1}^{1}\int_{-1}^{1}[N_i]^T[N_i]\,|[J]|d\xi d\eta d\zeta\rightarrow[K_{ii}] \quad (10)$$

$$f_r=\frac{2M_i\{v_i(0)\}}{\Delta}\int_{-1}^{1}\int_{-1}^{1}\int_{-1}^{1}[N_i]^T[N_i]\,|[J]|d\xi d\eta d\zeta\rightarrow[F_i] \quad (11)$$

(r, s=1, 2, ⋯, 12.)

where Δ is the time step, $\{v_i(0)\}$ is the initial velocity at the beginning of the times step. The velocity at the end of the time step $\{v_i(\Delta)\}$ is calculated by

$$\{v_i(\Delta)\}=\frac{2}{\Delta}\{D_i\}-\{v_i(0)\} \quad (12)$$

Initial stress matrix

For the i-th element, the potential energy of initial stresses $\{\sigma_i^0(x,y,z)\}$ is written as

$$\Pi_\sigma=\iiint_{v_i}\{\varepsilon_i\}^T\{\sigma_i^0(x,y,z)\}dxdydz$$

$$=\{D_i\}^T\int_{-1}^{1}\int_{-1}^{1}\int_{-1}^{1}[B_i]^T\{\sigma_i^0\}\,|[J]|d\xi d\eta d\zeta \quad (13)$$

where $\{\sigma_i^0\}=\{\sigma_\xi^0\ \sigma_\eta^0\ \sigma_\zeta^0\}$. Minimizing Π_σ by taking the derivatives can obtain a 12×1 force submatrix :

$$f_r=-\int_{-1}^{1}\int_{-1}^{1}\int_{-1}^{1}[B_i]^T\{\sigma_i^0\}\,|[J]|d\xi d\eta d\zeta\rightarrow[F_i] \quad (14)$$

(r=1, 2, ⋯, 12.)

Displacement constraint matrix

Assume the point (x, y, z) of element i is constrained with displacement vector of $\{u_c\ v_c\ w_c\}$. Then, the potential energy Π_c related to the constrained spring is

$$\Pi_c=\frac{p}{2}\{u_c\ v_c\ w_c\}\begin{Bmatrix}u_c\\v_c\\w_c\end{Bmatrix}-p\{D_i\}^T[N_i]^T\begin{Bmatrix}u_c\\v_c\\w_c\end{Bmatrix}+\frac{p}{2}\{D_i\}^T[N_i]^T[N_i]\{D_i\} \quad (15)$$

Taking the derivatives of displacement variables from potential energy Π_c can obtain a 12×12 element stiffness matrix [K_{ii}] and a 12×1 element force matrix [F_i] as follow:

$$k_{rs}=\frac{\partial^2\Pi_c}{\partial d_{ri}\partial d_{si}}=p[N_i]^T[N_i]\rightarrow[K_{ii}] \quad (16)$$

$$f_r=-\frac{\partial\Pi_c(0)}{\partial d_{ri}}=p[N_i]^T\begin{Bmatrix}u_c\\v_c\\w_c\end{Bmatrix}\rightarrow[F_i] \quad (17)$$

(r, s=1, 2, ⋯, 12.)

Point loading matrix

The point loading force $(F_x, F_y, F_z)^T$ acts on the point (x, y, z) of element i, then the potential energy of the loading can be written as

$$\Pi_p=-\{u\ v\ w\}\begin{Bmatrix}F_x\\F_y\\F_z\end{Bmatrix}=-\{D_i\}^T[N_i]^T\begin{Bmatrix}F_x\\F_y\\F_z\end{Bmatrix} \quad (18)$$

The derivatives of Π_p gives a 12×1 element force submatrix

$$f_r=-\frac{\partial\Pi_p(0)}{\partial d_{ri}}=[N_i]^T\begin{Bmatrix}F_x\\F_y\\F_z\end{Bmatrix}\rightarrow[F_i] \quad (19)$$

(r=1, 2, ⋯, 12.)

which is added to the [F_i] in the global Eq. (5).

Body loading matrix

Assume $(f_x, f_y, f_z)^T$ is the constant body force loading acting on the volume of element i. The potential energy due to the body loading is expressed as

$$\Pi_v=-\iiint_{v_i}\{u\ v\ w\}\begin{Bmatrix}f_x\\f_y\\f_z\end{Bmatrix}dxdydz$$

$$=-\{D_i\}^T\int_{-1}^{1}\int_{-1}^{1}\int_{-1}^{1}[N_i]^T\,|[J]|d\xi d\eta d\zeta\begin{Bmatrix}f_x\\f_y\\f_z\end{Bmatrix} \quad (20)$$

The derivatives of Π_v at 0 gives a 12×1 element force submatrix

$$f_r = \int_{-1}^{1}\int_{-1}^{1}\int_{-1}^{1}[N_i]^T |[J]| d\xi d\eta d\zeta \begin{Bmatrix} f_x \\ f_y \\ f_z \end{Bmatrix} \rightarrow [F_i], \quad (21)$$

(r=1, 2, ⋯, 12.)

which is added to the $[F_i]$ in the global Eq. (5).

2.4 Contract matrix between adjacent blocks

In the contact theory of 3D-DDA, the requirements of no-penetration, no-tension and Coulomb's law must be satisfied in DDA's block kinematics. When using the four-node isoparametric element, the contract problem can reduce to the relationship of point-face of finite elements. The common-plane method (Cundall, 1988) is used to determine the contact type. Once the contact types and contact faces are determined, all contacts can be converted to one or more point-to-face contacts (Jiang and Yeung, 2004), as shown in Fig. 2.

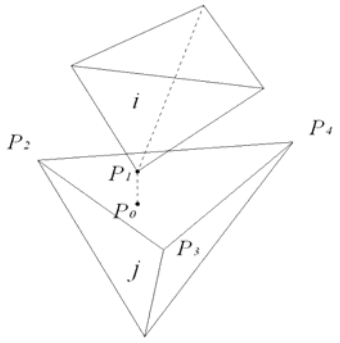

Fig. 2: Point-to-Face Contact Model

Normal spring submatrices

Utilizing the penalty method, a mathematical spring is placed between point P_1 and the contact face P_2 P_3 P_4 in the direction normal to the contact face. Assuming the stiffness of the spring as p_n, the potential energy of the normal spring is given by

$$\Pi_n = \frac{p_n}{2} d_n^2 = \frac{p_n}{2}\left[\frac{S_0}{L} + [G_i]\{D_i\} + [H_j]\{D_j\}\right]^2 \quad (22)$$

where

$$S_0 = \{\mathrm{a\ b\ c}\}\begin{Bmatrix} x_1 - x_0 \\ y_1 - y_0 \\ z_1 - z_0 \end{Bmatrix}, \; L = \sqrt{a^2 + b^2 + c^2} \quad (23)$$

$$[G_i] = \frac{1}{L}\{\mathrm{a\ b\ c}\}[N_i], \quad [H_j] = \frac{1}{L}\{\mathrm{a\ b\ c}\}[N_j] \quad (24)$$

$$a = \begin{vmatrix} y_3 - y_2 & z_3 - z_2 \\ y_4 - y_2 & z_4 - z_2 \end{vmatrix}, \; b = \begin{vmatrix} z_3 - z_2 & x_3 - x_2 \\ z_4 - y_2 & x_4 - x_2 \end{vmatrix}, \; c = \begin{vmatrix} x_3 - x_2 & y_3 - y_2 \\ x_4 - x_2 & y_4 - y_2 \end{vmatrix}.$$

In general, p_n should be a large positive penalty so that it can ensure that the deformation of the spring is much smaller than that of the block. If the value of p_n is large enough, the computational results practically will not depend on the value of p_n. (Shi, 1988).

Taking derivatives with respect to the displacement variables from Π_n obtains four 12×12 submatrices and two 12×1 submatrices which are added to $[K_{ii}]$, $[K_{ij}]$, $[K_{ji}]$, $[K_{jj}]$, $[F_i]$ and $[F_j]$, respectively.

$$k_{rs} = \frac{\partial^2 \Pi_n}{\partial d_{ri} \partial d_{si}} = p_n [G_i]^T [G_i] \rightarrow [K_{ii}] \quad (25)$$

$$k_{rs} = \frac{\partial^2 \Pi_n}{\partial d_{ri} \partial d_{sj}} = p_n [G_i]^T [H_j] \rightarrow [K_{ij}] \quad (26)$$

$$k_{rs} = \frac{\partial^2 \Pi_n}{\partial d_{rj} \partial d_{si}} = p_n [H_j]^T [G_i] \rightarrow [K_{ji}] \quad (27)$$

$$k_{rs} = \frac{\partial^2 \Pi_n}{\partial d_{rj} \partial d_{sj}} = p_n [H_j]^T [H_j] \rightarrow [K_{jj}] \quad (28)$$

$$f_{ri} = -\frac{\partial \Pi_n(0)}{\partial d_{ri}} = -\frac{p_n S_0}{L}[G_i]^T \rightarrow [F_i] \quad (29)$$

$$f_{ri} = -\frac{\partial \Pi_n(0)}{\partial d_{ri}} = -\frac{p_n S_0}{L}[H_j]^T \rightarrow [F_j] \quad (30)$$

(r, s=1, 2, ⋯, 12.)

Shear spring submatrices

It is assumed that the points P_1 and P_0 respectively move to P'_1 and P'_0 after the displacement increments are applied. Let $\vec{L}$ be the projection of $\overrightarrow{p'_0 p'_1}$, the increments of the spring is expressed as

$$d_s = |\vec{L}| = \sqrt{|\overrightarrow{p'_0 p'_1}|^2 - |d_n|^2} \quad (31)$$

Assuming there is a shear spring with the stiffness of p_s between points P_1 and P_0, the potential energy of the shear spring is given by

$$\Pi_s = \frac{p_s}{2} d_s^2 = \frac{p_s}{2}\begin{bmatrix} x_1 + u_1 - x_0 - u_0 \\ y_1 + v_1 - y_0 - v_0 \\ z_1 + w_1 - z_0 - w_0 \end{bmatrix}^T \begin{bmatrix} x_1 + u_1 - x_0 - u_0 \\ y_1 + v_1 - y_0 - v_0 \\ z_1 + w_1 - z_0 - w_0 \end{bmatrix} - \frac{p_s}{2} d_n^2 \quad (32)$$

In general, p_s should be a large positive penalty number. If the value of p_s is large enough, the computational results practically will not depend on the value of p_s.

Minimizing Π_s by taking derivatives, four 12×12 submatrices and two 12×1 submatrices are obtained and added to the submatrices $[K_{ii}]$, $[K_{ij}]$, $[K_{ji}]$, $[K_{jj}]$, $[F_i]$ and $[F_j]$, respectively.

$$k_{rs} = p_s\left([N_i]^T[N_j] + [G_i]^T[G_j]\right) \rightarrow [K_{ii}] \quad (33)$$

$$k_{rs} = -p_s\left([N_i]^T[N_j] + [G_i]^T[H_j]\right) \rightarrow [K_{ij}] \quad (34)$$

$$k_{rs} = -p_s\left([N_i]^T[N_i] - [H_j]^T[G_i]\right) \rightarrow [K_{ji}] \quad (35)$$

$$k_{rs} = p_s\left([N_i]^T[N_i]-[H_j]^T[H_j]\right)\rightarrow[K_{ji}] \quad (36)$$

$$f_{ri} = -p_s\left([N_i]^T\begin{bmatrix}x_1-x_0\\ y_1-y_0\\ z_1-z_0\end{bmatrix}-\frac{S_0}{L}[G_i]^T\right)\rightarrow[F_i] \quad (37)$$

$$f_{rj} = p_s\left([N_i]^T\begin{bmatrix}x_1-x_0\\ y_1-y_0\\ z_1-z_0\end{bmatrix}+\frac{S_0}{L}[H_j]^T\right)\rightarrow[F_i] \quad (38)$$

(r, s=1, 2, ⋯, 12)

Friction force submatrices

For the 3D contact problem, sliding at the contact point may occur in any direction parallel to the contact face. Yeung et al. (2004) propose an iterative procedure for determining the frictional force and the sliding direction. For the point-to-face contact shown in Fig. 2, the point P_1 is on element i and its projection P_0 is on element j. When the sliding happens, a pair of equal and opposite friction forces parallel to the sliding direction is applied, one at the point P_1 and one at the point P_0 on the face. The magnitude and directions of the frictional forces are obtained from the previous iteration. The friction force F is obtained from the normal contact compressive force from the previous iteration:

$$F = p_n \mid d_n \mid \tan\varphi \quad (39)$$

where P_n, d_n and φ are the normal spring stiffness, the normal penetration distance after the previous iteration; and the friction angle, respectively.

The direction of the friction force acting at P_0 is assumed to be in the direction of $\vec{L}$, which is the projection of the vector $\overrightarrow{p_0'p_1'}$, and the direction of the frictional force acting at P_1 is assumed to be opposite to that of $\vec{L}$. Now, let $\vec{n}$ be the unit vector pointing out of the block, then,

$$\vec{L} = \overrightarrow{p_0'p_1'} + \mid d_n \mid \vec{n} = [d\ e\ f] \quad (40)$$

The potential energy of the pair of frictional forces is expressed as

$$\Pi_f = \frac{F}{\mid\vec{L}\mid}[u_1-u_0\ \ v_1-v_0\ \ w_1-w_0][d\ e\ f]^T$$
$$= F\left(\{D_i\}^T[M]-\{D_j\}^T[N]\right) \quad (41)$$

where

$$[M] = \frac{1}{\mid\vec{L}\mid}[N_i(\xi_1,\eta_1,\zeta_1)]^T[d\ e\ f]^T, \quad (42)$$

$$[N] = \frac{1}{\mid\vec{L}\mid}[N_j(\xi_0,\eta_0,\zeta_0)]^T[d\ e\ f]^T. \quad (43)$$

The relevant derivatives of Π_f with respect to d_{ri} and d_{rj} at 0 form two 12×1 submatrices which are added to $[F_i]$ and $[F_j]$ in global Eq. (5), respectively.

$$f_{ri} = -\frac{\partial\Pi_f(0)}{\partial d_{ri}} = -F[M]\rightarrow[F_i], \quad (44)$$

$$f_{rj} = -\frac{\partial\Pi_f(0)}{\partial d_{rj}} = F[N]\rightarrow[F_j]. \quad (45)$$

(r=1, 2, ⋯, 12.)

After iteration, the friction force magnitude and directions are updated according to the results of the iteration.

3. An example of multilayer pavement

As shown in Fig. 3, the pavement structure is described by a multilayer system containing three horizontal layers, which are asphalt concrete layer, base layer and subgrade soil layer, respectively. The parameters of each layer are listed in Table 1. The moving vehicle is presented by a circular distributed load. It is assumed that the length, width and thickness of the 3D model of pavements are respectively 5 m, 5 m and 3 m based on engineering judgment and previous research.

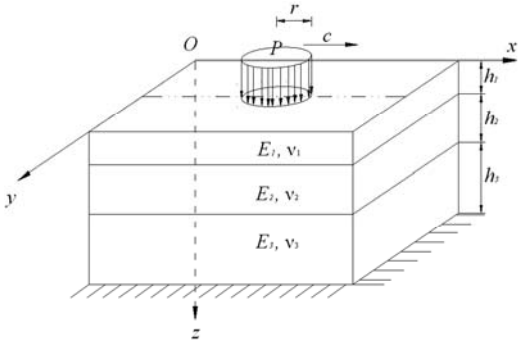

Fig. 3: 3D model of multilayer pavement system

Table 1: Input values of parameters for calculation

Layer	**E** (*MPa*)	***v***	**Thickness** (*cm*)
Asphalt (h_1)	2000	0.25	20
Base (h_2)	400	0.25	40
Subgrade (h_3)	200	0.35	240
Load stress (*kPa*)	500		
Load radius (*mm*)	200		

To compare with analytical solution, it is assumed that the velocity of the load is zero in particular and the load is applied on the original point of *x*-*y* plane. Then, it can be reduced to 2D plane strain problem. In the analysis, each layer of the model is treated as a block of DDA and the blocks are discretized into 45 four-node

element meshes (Fig.4). Full friction between the layers is assumed. The displacements and stresses of the pavement can be obtained by the program of 2D-DFCM, which is developed by the authors. The numerical results are shown in Table 2, where σ_r and σ_z are normal stresses in the directions of r and z, and w is the vertical displacement of the pavement.

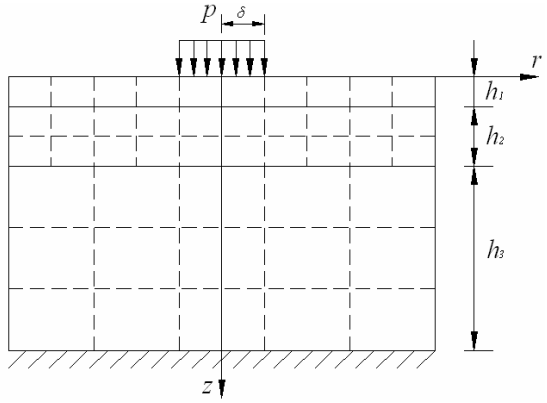

Fig. 4: 2D-DDA-FEM pavement calculation model

Table 2: Numerical results of DFCM

Layer	(*r*, *z*) (*cm*)	Solution	σ_r (*MPa*)	σ_z (*MPa*)	*w* (*mm*)
Asphalt layer	(0, 0)	Analytic	-0.685	-0.500	0.320
		DFCM	-0.685	-0.500	0.319
	(20, 0)	Analytic	-0.288	-0.250	0.261
		DFCM	-0.286	-0.250	0.261
	(30, 0)	Analytic	-0.007	0.000	0.212
		DFCM	-0.007	0.000	0.211
Base layer	(0, 20)	Analytic	0.0107	-0.2051	0.209
		DFCM	0.0103	-0.2030	0.202
Subgrade layer	(0, 60)	Analytic	0.0023	-0.0426	0.182
		DFCM	0.0020	-0.0421	0.176

The results in Table 2 show that the solutions obtained by the DFCM agree very well with the analytical solutions (Zhong and Yin 2006). It demonstrates the validity of the coupled method.

4. Conclusions

The numerical model and formulations of 3D DDA-FEM Coupled Method (3D-DFCM) were developed in the present paper. The displacements and stresses were obtained by proper internal discretization of deformable blocks using finite element meshes. The contacts between the deformable blocks were modeled by DDA. It combines the advantages of the DDA and the FEM so that not only the movements of the block system can be depicted, but the stress distributions in the blocks can also be obtained. A multilayered pavement subjected to moving vehicle loads was investigated by the method. The numerical results demonstrated the validity of the coupled method. The DFCM will have a wide application in complicated rock mass problems and other new fields.

References

Chang C. T., Nonlinear dynamic discontinuous deformation analysis with finite element meshed block system. Ph.D. Thesis, Department of Civil Engineering, University of California at Berkeley, 1994.

Cho Y. H., Mccullough B. F. and Weissmann J., Considerations on finite element method application in pavement structural analysis. Transportation research record 1539, TRB, Washington, D.C., 1996, pp. 96-101.

Jiang Q. H and Yeung M. R., A model of point-to-face contact for three dimensional discontinuous deformation analysis. *Rock Mech Rock Eng*, 2004, 37, 95-116.

Monismith, C.L., Sousa J. and Lysmer J., Modern pavement design technology including dynamic load conditions. SAE, Conference on vehicle-pavement interaction, Indianapolis, Indiana, 1988.

Ning Y.J. and Yang J., Simulation Study of Earth Penetrator Penetrating Underground Structures with the Method of 2D-DDA. Tactical Missile Technology, 2006, 5, 39-43.

Pearce C.J. et al., Computational aspects of the discontinuous deformation analysis framework for modeling concrete fracture, Engineering Fracture Mechanics, 2000, 65, 283-298.

Shi G. H., Discontinuous deformation analysis: a new numerical model for the statics and dynamics of block systems. Ph.D. Thesis, Department of Civil Engineering, University of California at Berkeley, Berkeley, 1988.

Shi G. H., Theory and examples of three dimensional discontinuous deformation analyses. Proceedings of the second Asian rock mechanics symposium, Beijing, China, 2001.

Zhong Y. and Yin J.H., Solution method of layered elastic medium. Beijing, Science Press, 2006.

Application Study of DDA Method in Blasting Numerical Simulation

NING YOU-JUN, YANG JUN and CHEN PENG-WAN

State Key Laboratory of Explosion Science and Technology,
Beijing Institute of Technology, Beijing 100081, China

Simulation of blasting problems is one of the important applications in dynamics for the DDA method. Demolition blasting and rock blasting are two main aspects of blasting engineering and research. In this paper, the blasting demolition process of two brick walls in an anti-terrorism exercise was simulated by the DDA method firstly, and then a typical rock bench blasting was simulated with the DDA code extended by the authors especially for rock blasting simulation. The extensions of the code include: the development of plastic rock constitutive relation, the calculation of damping, the calculation of suppositional cracks, and a temporary way of boundary treatment. With these extensions, the problems of energy dissipation and stress wave reflection at finite boundaries in rock blasting simulation are solved to a certain extent, and the fragment size can be forecasted. According to the simulation results and corresponding analysis, the feasibility of simulating blasting process with DDA method was validated.

Keywords: DDA method; Demolition blasting; Rock blasting; Numerical simulation

1. Introduction

Demolition blasting and rock blasting are two main aspects of blasting engineering. To simulate blasting process with numerical methods is an important way of engineering blasting research. By numerical simulation, the collapse, disassembly of buildings and the formation of blasting piles can be forecasted for demolition blasting; the breakage and fly of rock blocks, the formation of blasting piles, and the blasting fragment size can be forecasted for rock blasting. Thereby the designs of engineering blasting projects can be directed by the numerical results, increasing the reliability and decreasing the failure probability of engineering practice.

In this paper, the numerical DDA method is utilized to simulate the large deformation and large displacement breakage problem of engineering blasting projects. Firstly, the blasting demolition process of two brick walls in an anti-terrorism exercise was simulated respectively by the 2D-DDA and 3D-DDA method, and then a typical rock bench blasting was simulated by the 2D-DDA code extended by the authors especially for rock blasting simulation. The extensions of the code include: the development of plastic rock constitutive relation, the calculation of damping, the calculation of suppositional cracks, and a temporary way of boundary treatment. With these extensions, the problems of energy dissipation and stress wave reflection at finite boundaries in rock blasting simulation are solved to a certain extent, and the fragment size can be forecasted.

2. Brick Wall Blasting Demolition Simulation

As the DDA method is especially developed for the calculation of discontinuous block systems, it's very suitable for the simulation of the blasting demolition process of block structures, such as steer constructions (Hu et al 2002), brick chimneys (Zhao et al 2005), etc.. Zhao et al (2006) also simulated the blasting demolition process of a RCC cofferdam successfully by this method.

In this paper, the blasting demolition process of two brick walls in an anti-terrorism exercise is to be simulated by the DDA method. For the restriction of the actual DDA code, only the collapse and disassembly process of the walls under the effect of self-gravity after the formation of blasting cuts is simulated.

2.1 Calculation models and material parameters

Two brick walls demolished in the exercise is shown in Fig. 1 , and a typical moment of the blasting process is shown in Fig.2. The two brick walls intersect with an angle of 90º and have different breakage styles. The eastern wall is to be simulated with the 2D-DDA method according to its symmetry character, and the southern wall is to be simulated with the 3D-DDA method.

The DDA models of the two walls are shown in Fig.3 (a) and Fig.4 (a) respectively. The eastern wall has a height of 8m with 0.24m thick and 0.2m high bricks. To save calculating time, the southern wall only has a height of 2.4m with 0.4m length bricks.

According to the field material characteristics, the material parameters are set as follows: density of the

walls (hollow bricks) ρ=1800kg/m^3; Yong's modulus E =7000MPa; Poisson's ratio μ=0.22; as only the parameter of friction angle among blocks can be calculated in the actual 3D-DDA code, the friction angles are respectively set as φ_1=15º and φ_2=30º among 2D-DDA bricks and 3D-DDA bricks; cohesion and tensile strength among both 2D-DDA bricks and 3D-DDA bricks are respectively c =0.5MPa and σ_t=0.3MPa.

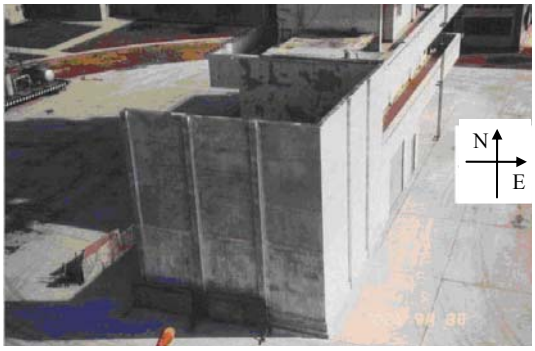

Fig.1: Two brick walls to be demolished


Fig.2: A typical moment during blasting demolition

2.2 Simulation results and the analysis

As the air resistant effect is taken into account, static calculation is used in the simulation of the eastern wall. Dynamic calculation is used in the simulation of the southern wall. Typical moments of the simulation of the two walls are shown in Fig. 3 (b) - (d) and Fig. 4 (b) - (d).

(1) According to the comparison of the simulation results and the field photos, it can be found that the demolition process of the two walls is numerically displayed quite well. As the effect of the blasting vibration is not taken into account, the simulation is carried out approximatively.

(2) The simulated demolition pile of the eastern wall is very close to that in the exercise, but the southern wall has just been disassembled and the calculation stops, which is because of the relatively low development level of 3D-DDA code presently. In the 3D-DDA simulation, as the calculation went on, block invading happened, and the calculation efficiency was fairly low in dynamic calculation.

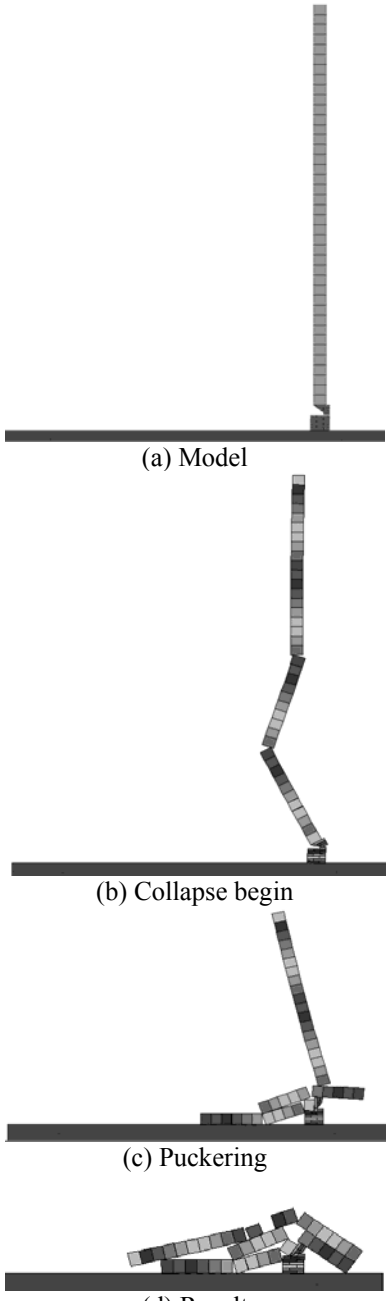
(a) Model

(b) Collapse begin

(c) Puckering

(d) Result

Fig.3: Demolition process of the eastern wall

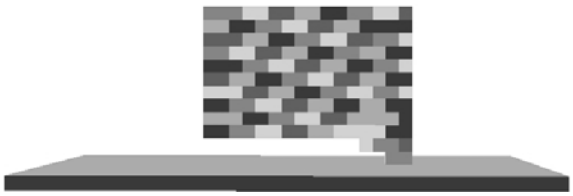
(a) Model

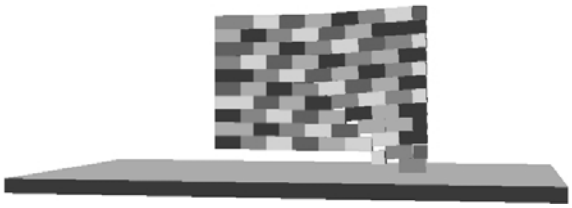

(b) Typical moment 1

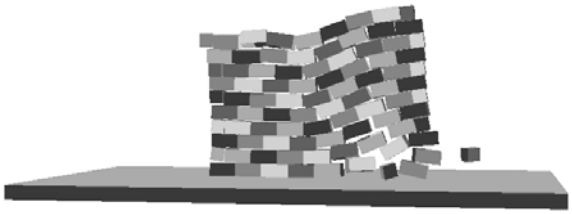

(c) Typical moment 2

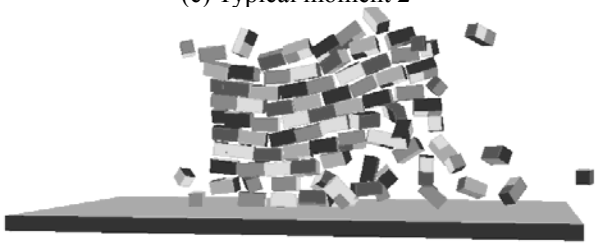

(d) Disassembly

Fig.4: Demolition process of the southern wall

3. Development of 2D-DDA code for rock blasting

For the numerical simulation of rock blasting, the DDA method has its superiority in theory compared with other traditional numerical methods and it meets the characteristics of rock blasting: large deformation, large displacement, with both static and dynamic process (Yang et al 1999). Furthermore, as blocks may be fractured by explosive impact effect during blasting, and for the DDA method, both the growth of initial faults and the generation of new cracks in rock mediums can be calculated, the blasting fragment size can be forecasted by this method (Yang at al 2005).

In the initial edition of 2D-DDA code, the friction among blocks is the main way of the consumption of energy (Shi 1985) and obviously it's not enough in dynamic calculation. Based on their past work in simulating rock blasting by the DDA method (Yang Jun at al, 2005), the authors may try to solve the problem of energy dissipation better in this paper with the development of rock plastic constitutive relation, the calculation of damping and artificial boundary blocks and a more sophisticated calculating method of suppositional cracks. Then a typical rock bench blasting is calculated with the extended code and more satisfying results of block throw and fragment size forecast curves are achieved.

3.1 Plastic constitutive relation

As Drucker-Prager yield criterion is the revise of Mohr-Coulomb yield criterion, the effect of ambient pressure σ_2 to the yield of rock medium is taken into account and this criterion can also reflect the effect of shear stress to the expansion of volume (Cai Mei-feng et al, 2002), so this yield criterion is to be used in the extension of the 2D-DDA code. The criterion can be expressed as follows:

$$f = \alpha I_1 + J^{1/2} - K = 0$$

Where I_1 is the first invariant of stress tensor, J_2 is the second invariant of deviator stress tensor, α and K are material parameters, their relations to cohesion c and internal friction angle ϕ are:

$$\alpha = \frac{2\sin\phi}{\sqrt{3}(3-\sin\phi)}$$

$$K = \frac{6c\cos\phi}{\sqrt{3}(3-\sin\phi)}$$

Using the two dimensional Drucker-Prager yield criterion, the linear strain-hardening plastic constitutive relation of rock medium is added to the 2D-DDA code.

3.2 Damping and boundary treatment

In the simulation of dynamic problems, energy dissipation of materials and structures is revealed by the use of damping matrices. In order to calculate rock blasting with the DDA method, damping matrices are to be added into the 2D-DDA code.

Rayleigh damping is always used in dynamic problems (Cai et al,2002), in which the affect of the system frequency to the damping force is neglected and the damping matrix is predigested as the linear combination of the mass matrix and stiffness matrix:

$$\boldsymbol{C} = \alpha \cdot \boldsymbol{M} + \beta \cdot \boldsymbol{K}$$

where $\boldsymbol{C}$ is the damping matrix; $\boldsymbol{M}$ is the mass matrix; $\boldsymbol{K}$ is the stiffness matrix; α and β are constants independent of frequency. $\alpha \cdot \boldsymbol{M}$ represents the effect of the damping force directly proportional to the particle velocities; $\beta \cdot \boldsymbol{K}$ represents the effect of the damping force directly proportional to the strain velocities.

In the calculation of dynamics, to represent the infinite region of true model with finite calculating region has an unavoidable problem to be solved: stress wave reflection at artificial boundaries. To decrease the effect of artificial boundaries in the simulation, a temporary method is used: blocks along the artificial boundaries are defined as boundary blocks, and for these boundary blocks, the stresses, stains and velocities are not to be inherited at each time step so as to absorb reflected energies.

3.3 Suppositional crack calculation and fragment Size forecast

Under the effect of explosive shock loadings, rock

mass may be terribly destroyed in blasting. Joints, beddings and other existing faults may be tensed and staggered and continuous rock medium may be fractured. For the calculation of the breakage along existing faults, the DDA method can already solve it very well. However, the generation of new cracks and crack propagations can't be calculated by the actual DDA code now. To insure more correct energy dissipation and to forecast the rock blasting fragment size, suppositional cracks may be calculated based on the stress strength criterions of the rock medium.

Because of the fragile property of most rock mediums, they are always fractured by tensile or shear effect. Based on the fact that fractured rock blocks may not have the ability of reserve tensile effect, the following fracture rules for each block in every time step are used in the DDA code:

(1) To judge whether the block is fractured according to the largest main tensile stress and the largest shear stress, if it is fractured, the increasing velocity in this time step, the tensile stresses, the tensile strains of this block may be set as zero.

(2) Once a block is fractured, a crack is recorded for this block. When the crack time for a certain block is beyond a given number (in this paper the given number is 15, which can be estimated by the initial average block area), the block is thought to be crushed and it may not reserve any stress or strain.

Based on the crack times and the open-close conditions of all the blocks in the blasting pile, the representational dimension l can be obtained, and then a Γ - l curve can be drawn to reveal the blasting fragment size distribution (Yang Jun, et al, 2005), where Γ is the percentage of the total volume of blocks that have a smaller representational dimension than a certain value. Then, the G-G-S distribution curve and R-R distribution curve can be drawn as follows (Yang Jun, et al, 1999):

G-G-S distribution: $\log(\Gamma) - \log(l)$;

R-R distribution: $\log(\log(100/(100-\Gamma))) - \log(l)$.

To display the fragment size distribution condition intuitionisticly, a more diplomatic post-processor DG is developed, in which the crack time of each block is revealed by its color. Once a block is crushed, it turns red.

4. A typical rock bench blasting simulation

4.1 Geometrical model and physical parameters

The sketch map of the calculated typical rock bench and its main geometrical parameters are shown in Fig.5. The height of the bench is H =10m and the over drilling depth is H_0 =1m. The height of the explosive column is H_e =7m and the stemming depth is H_s =4m. The width of the bench at the top is 4m and the obliquity is about 70º. As the main crushed zone is not going to be calculated, the diameter of the borehole D =500mm in the model is 5 times (Cai Mei-feng et al, 2002) of that in reality (D_0 =100mm).

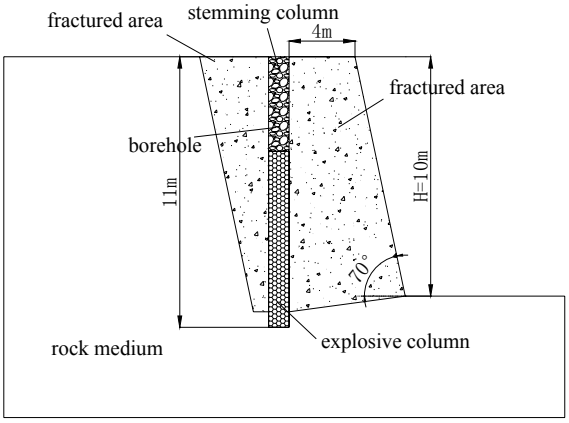

Fig.5: A typical rock bench model

There are mainly three sets of joints distributing in the rock medium, and the block system of this typical rock bench produced by the DDA pre-processor is shown in Fig.6, in which there are 1853 blocks and the average area of the blocks is 0.292m^2, so the representational dimension l is 0.713m. Physical parameters of the rock medium and the joints are shown in Table 1.

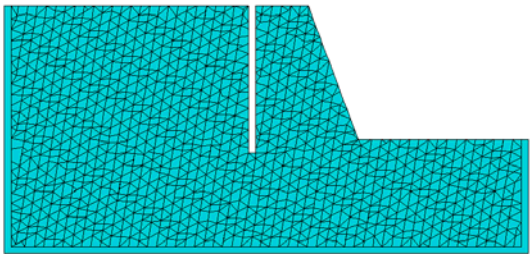

Fig.6: Block system of the rock bench

4.2 Explosive Load Estimation

As the explosive impact effect can't be directly calculated in the actual DDA code, the explosive load should be estimated before simulation. The sketch map of the explosive load history affecting the wall of the borehole is shown in Fig.7.

(1) Load history along the explosive column

For the sect of the borehole at the bottom where the explosion directly acts, the peak value (P_m) of the load can be calculated according to the coupling coefficient of explosive charge and the total lasting time (t_2) can be calculated according to the fly out of the stemming column (Ning et al 2007).

The peak value of the explosion pressure P_m =20MPa, the total lasting time t_2 =10ms, and the peak value time t_1 is 1/10 of t_2, that is 1.0ms.

Table 1: Physical parameters

	Density ρ / (Kg/m^3)	Yong's modulus E / GPa	Poisson ratio μ	Friction angle θ / °	Cohesion c / MPa	Tensile strength σ_t / MPa	Shear strength σ_s / MPa	Compressive strength σ_p / MPa
Rock medium	2600	62	0.25	60	50	5	10	155
Joints	/	/	/	30	0.5	0.2	/	/

(2) Load history along the stemming column

For the sect of the borehole at the top that contains the stemming material, P_m decreases linearly from 20MPa to 7.5MPa. Meanwhile, t_0 increases linearly form 0ms to 8.94ms and t_1 increases linearly from 1.0ms to 9.05ms. All the loads finish at t_2 =10ms, and the rising time (t_1 - t_0) is 1/10 of the total lasting time for all the loads.

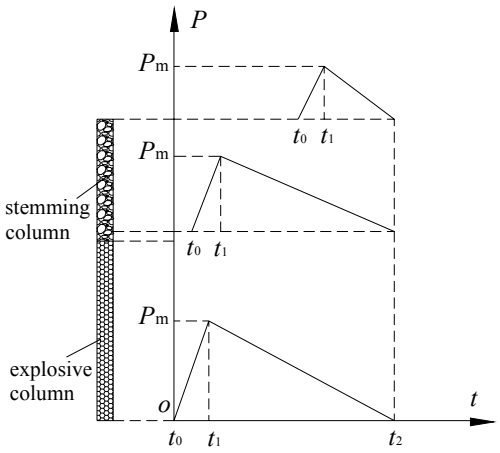

Fig.7: Explosive load history estimation

4.3 Simulation result and fragment size forecast

Four typical moments of the simulation are shown in Fig.8. The movement of the blocks in the bench is displayed, and the rough shape of the blasting pile is obtained as Fig.8 (d). Compared with the past simulation result of rock bench blasting (Yang Jun at al, 2005), the fly of the blocks is controlled much better for the more exact energy dissipation. It can be found that blocks around the borehole are totally crushed and blocks bellow the borehole and at the foot of the bench are cracked terribly. These conclusions are consistent with that in practice.

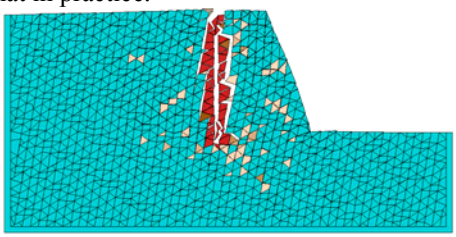

(a) t =0.0915s

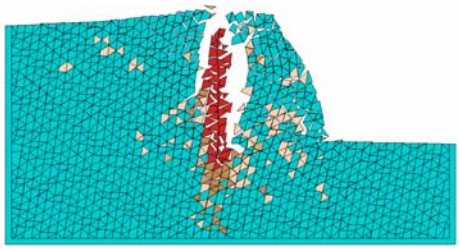

(b) t =0.3520s

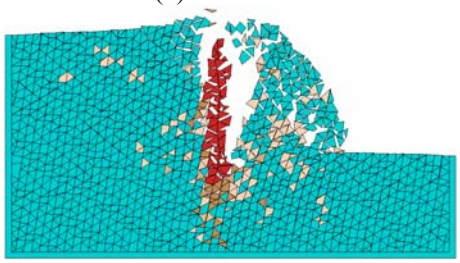

(c) t =0.6493s

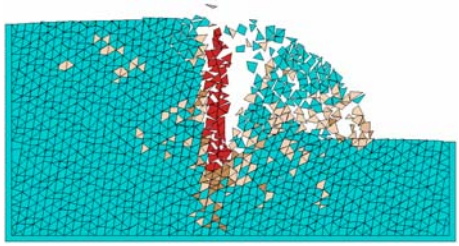

(d) t =0.9772s

Fig.8: Typical moments of simulation

Regretfully, the final formation of the blasting pile is not achieved for the shape aberrance current of some blocks, which may likely be induced by the primary suppositional crack calculation method used in this paper.

According to the crack times and the open-close conditions of the blocks in the rough blasting pile, the Γ-l curve that reveals the fragment size of the rock bench blasting is shown in Fig.9 (a). As most blocks in the bench just separate from each other and are not cracked, the proportion of the blocks with initial representational dimension (0.713 m) is as large as 45%, which means that initial joint density may strongly affect the fragment size. G-G-S distribution and R-R distribution of the fragment size are shown in Fig.9 (b). They both have well linearity as 0.98 and 0.94 respectively.

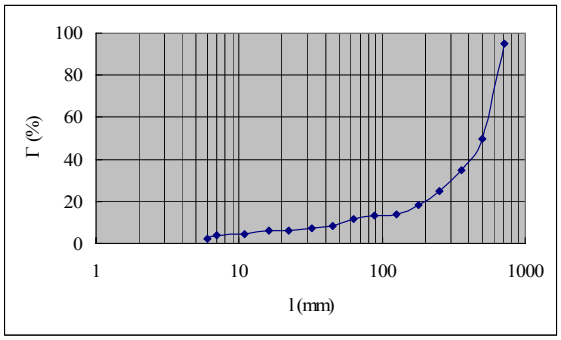

(a) Γ - *l* curve

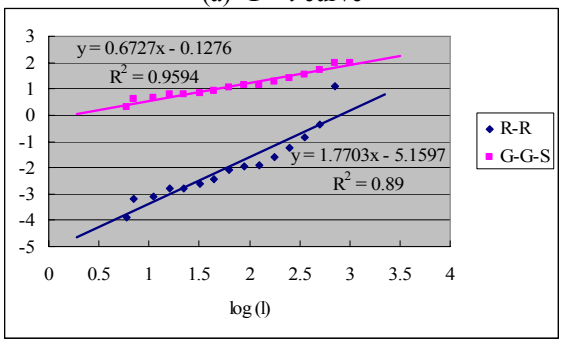

(b) G-G-S and R-R distributions

Fig.9: Blasting fragment size forecast

5 Conclusions and Remarks

(1) The blasting demolition process of two brick walls were respectively simulated by the 2D-DDA and 3D-DDA method, in which the 2D-DDA simulation result was pretty good, while the 3D-DDA simulation result still needs to be improved. Generally, the simulation results were quite close to that in practice.

(2) By the development of rock plastic constitutive relation, the addition of damping matrices, the utilization of artificial boundary blocks and the more sophisticated calculation of suppositional cracks, using the estimated explosive loads acted on the borehole wall, a typical rock bench blasting was simulated by the developed 2D-DDA code, in which the movement of the blocks and the formation process of the blasting pile were displayed numerically, but the final formation of the blasting pile was not achieved.

(3) All the simulation work in this paper indicates the feasibility of simulating engineering blasting process with the DDA method. However, in the demolition blasting simulation, the actual development level of the 3D-DDA method restricted the simulation result; in the rock blasting simulation, the artificial boundary method and the fragment size forecast method used in this paper were primary and temporary.

(4) To simulate engineering blasting better by the DDA method, real artificial boundary techniques and real crack calculation should be carried out in the 2D-DDA code, and the 3D-DDA method also needs to be developed as soon as possible.

References

Cai Mei-feng, He Man-chao, Liu Dong-yan. Rock Mechanics and Engineering, Science Press, 2002.

Hu Wen-jun, Lu Yan-hua. Preliminary Study on Computer Simulation of Blasting Demolition of Steel Construction. *Chinese Journal of Engineering Blasting,* 2002, 8(4), 11-16.

J. Henrych. The Dynamics of Explosion and Its Use, Elsevier Scientific Publishing Company, 1979.

Ning You-jun, Yang Jun. Numerical Simulation of Block Throw and Fragment Size Forecast of Rock Blasting by DDA Method. New Development on Engineering Blasting, 2007, 80-84.

Shi Gen-hua, Goodman R E. Two-dimensional Discontinuous Deformation Analysis. *International Journal for Numerical and Analytical Methods in Geomechanics*, 1985, 9: 541-556.

Yang Jun, Chen Peng-wan, Hu Gang. Modern Blasting Technology, Beijing Institute of Technology Press, 2004.

Yang Jun, Jin Qian-kun, Huang Feng-lei. Rock Blasting Theory Model and Its Numerical Simulation, Science Press, 1999.

Yang Jun, Ning You-jun. Numerical Simulation of Bench Blasting by 2D-DDA Method. Proceedings of ICADD-7, 2005, 159-165.

Zhao Gen, Wang Xiu-jie, Wang Xin-xia, Zhu Xue-xian. DDA Numerical Simulation of Demolition Blasting of TGP's Ⅲ-phrase Upstream RCC Cofferdam. *ACTA MECHANICA SOLID ASINICA*, 2006, 27(S. Issue), 148-154.

Zhao Gen, Zhang Wen-xuan. DDA Numerical Simulation and Demolition of a Brick Chimney by Directional Blasting. *Chinese Journal of Blasting*, 2005, 22(4), 74-76.

Seismic risk estimation from overturning analysis of hellenistic columns using DDA

G. YAGODA [1,2] and Y. H. HATZOR [1]

[1]Dept. of Geological and Environmental Sciences, Ben-Gurion University of the Negev, Beer-Sheva, ISRAEL.
[2]Engineering Geology & Geological Hazards Division, Geological Survey of Israel, Jerusalem, ISRAEL.

We present here back analysis of structural collapse of monolithic granite columns used as supports in a Hellenistic cathedral which was destroyed during a strong earthquake probably in 749 AD. First an existing analytical solution for dynamic rocking of columns is compared with results obtained using the numerical DDA method. We then proceed with forward DDA modeling to obtain the most likely frequency and peak acceleration of the accelerogram which triggered the observed failures, using sinusoidal input functions. While we find that the required PGA for overturning is frequency dependent, we believe that an input frequency of 2 Hz and PGA of 0.6 *g* can explain the observed column failure at Susita.

Keywords: PGA, DDA, Back Analysis, Seismic Risk, Toppling, Dynamic Analysis

1. Introduction

Dynamic stability of masonry structures in regions which suffer from high seismicity is an important issue when assessing the seismic risk associated with such areas. In particular, failure of distinct elements in the structures can be analyzed to estimate the driving motion responsible for the observed damage. In Israel there are several archeological monuments where partial or complete collapse of ancient masonry structures can be observed today. In this paper we present back analyses of topping of monolithic granite columns dated back to the Hellenistic period, which are preserved to this day in the Susita (Hippos) archeological site, located along a northern segment of the seismically active Dead Sea rift valley (Figure 1 A). We use the numerical DDA method (Shi 1993) first to check agreement with a published analytical solution and then to proceed with forward modeling to obtain the most likely characteristics of the seismic motion which triggered the collapse of the columns at Susita.

1.1 Geological Setting

Susita is located at the top of a diamond shaped plateau 350 m above the Sea of Galilee, a rhomb-shaped graben that formed due to a left segmentation on a sinister fault - the Dead Sea transform, and is characterized by relatively high seismicity. From earthquake statistics, strong earthquakes have occurred along the Dead Sea Transform every 80-120 years, the last event recorded in 1927. A horizontal peak ground acceleration greater than 0.3 *g* is reported for this region by SII building code 413 (2004). Archeological excavations of a spectacular cathedral discovered at the site reveal a row of collapsed granite columns, where all columns are lying parallel on the ground (Figure 1B). This observation suggests that the cathedral was destroyed by an earthquake; most probably the great earthquake of 749 AD which caused much documented damage in the region.

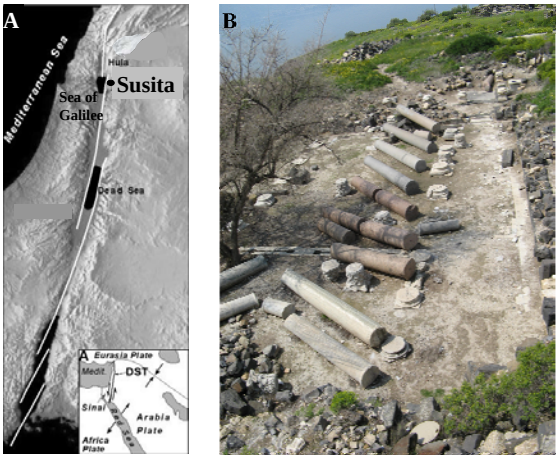

Fig. 1: A) Location map B) The collapsed columns in the Susita cathedral

1.2 Previous Paleo-seismological Studies

Several Paleo-seismic methods have been attempted for the resolution of past ground motions from mapped rock/structural deformations. One common approach is to use trenching through soil profiles in an attempt to identify actual fault traces and date displaced horizons (e.g. Amit et al. 2002). Another is to attempt to work out the required horizontal PGA in a pseudo-static back-analysis of ancient landslides (Yagoda et al. 2007). Finally, where seismically-displaced structural elements can be identified in historic monuments, dynamic back analysis may be attempted (Kamai and

Hatzor, in press). While previous studies focused on dynamic sliding analysis for blocks in ancient masonry structures (Kamai and Hatzor, in press), here we attempt to address a slightly more complicated problem: the dynamic rotation of a shaking column, and to deduce from our analysis the main characteristic (frequency, amplitude) of the driving input motion.

2. Dynamic Column Rotation: Analytical Solution

Makris and Roussos (2000) presented an analytical solution for the rocking of a free standing block under a sinusoidal input function. The two-dimensional solution addresses a rigid rectangular block as shown in Figure 2.

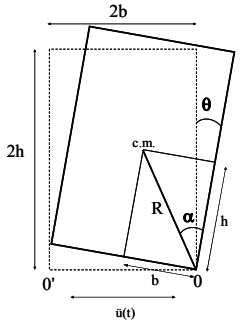

Fig. 2. Sign convention used in this paper

Consider the block diagram in Figure 2. The centers of rotation can be either O or O'. A friction coefficient greater than *b/h* is required for a rocking motion to ensue (Scalia and Sumbatyan 1996). We will assume here that the coefficient of friction is sufficiently high to completely prevent block sliding. Assuming there is no vertical base acceleration, the equations of motion are (Makris and Roussos 2000):

$$I_0\,\ddot{\theta} + mgR\sin(-\alpha-\theta) = -m\ddot{u}_g R\cos(-\alpha-\theta), \theta \le 0 \quad (1)$$

and

$$I_0\,\ddot{\theta} + mgR\sin(\alpha-\theta) = -m\ddot{u}_g R\cos(\alpha-\theta), \theta \ge 0 \quad (2)$$

where I_0 is the mass moment of inertia (in this case $I_0 = 4/3\, mR^2$), m the block mass, and $\ddot{u}_g$ the ground acceleration. All the geometrical parameters are defined in Figure 2. Inserting the definition of I_o into (1) and (2) we get:

$$\ddot{\theta}(t) = -p^2\left\{\sin(\alpha\,\mathrm{sgn}[\theta(t)]-\theta(t)) + \frac{\ddot{u}_g}{g}\cos(\alpha\,\mathrm{sgn}[\theta(t)]-\theta(t))\right\} \quad (3)$$

where $p = \sqrt{3g/4R}$, a measure of the dynamic characteristics of the block. When the block transfers smoothly from rotating around point 0 to rotating around point 0', the ratio between the angular velocity before the impact ($\dot{\theta}_1$) and the angular velocity after the impact ($\dot{\theta}_2$) is called the coefficient of restitution, and is expressed by:

$$r = \frac{\dot{\theta}_2^2}{\dot{\theta}_1^2} = \left[1 - \frac{3}{2}\sin^2\alpha\right]^2 \quad (4)$$

Introduction of the coefficient of restitution as in (4) implies that there is no energy loss due to another interface mechanism such as, for example, sliding or damage at blocks corners. For tall slender blocks characterized by small α equations (1) and (2) can be linearized. Here a solution for ground motion in the form of a sine function $\ddot{u}_g(t) = a_p\sin(\omega_p t + \psi)$ is presented, where a_p, ω_p and ψ are the amplitude, frequency and phase when rocking initiates, respectively.

Using the linearized assumption, equations (1) and (2) become:

$$\ddot{\theta}(t) - p^2\theta(t) = -\frac{a_p}{g}p^2\sin(\omega_p t+\psi) + p^2\alpha, \theta \le 0 \quad (5)$$

and

$$\ddot{\theta}(t) - p^2\theta(t) = -\frac{a_p}{g}p^2\sin(\omega_p t+\psi) - p^2\alpha, \theta \ge 0 \quad (6)$$

Integrating these equations yields:

$$\theta(t) = A_1\sinh(pt) + A_2\cosh(pt) - \alpha + \frac{1}{1+(\omega_p^2/p^2)}\frac{a_p}{g}\sin(\omega_p t+\psi), \theta \le 0 \quad (7)$$

and

$$\theta(t) = A_3\sinh(pt) + A_4\cosh(pt) + \alpha + \frac{1}{1+(\omega_p^2/p^2)}\frac{a_p}{g}\sin(\omega_p t+\psi), \theta \ge 0 \quad (8)$$

and the coefficients of integration are:

$$A_1 = A_3 = \frac{\dot{\theta}_0}{p} - \frac{\omega_p/p}{1+\omega_p^2/p^2}\frac{a_p}{g}\cos(\psi) = \frac{\dot{\theta}_0}{p} - \alpha\frac{\omega_p/p}{1+\omega_p^2/p^2}\frac{\cos(\psi)}{\sin(\psi)} \quad (9)$$

$$A_2 = \theta_0 + \alpha - \frac{1}{1+\left(\omega_p^2/p^2\right)}\frac{a_p}{g}\sin(\psi) \qquad (10)$$
$$= \theta_0 + \alpha - \frac{\alpha}{1+\omega_p^2/p^2}$$

$$A_4 = \theta_0 - \alpha - \frac{1}{1+\left(\omega_p^2/p^2\right)}\frac{a_p}{g}\sin(\psi) \qquad (11)$$
$$= \theta_0 - \alpha - \frac{\alpha}{1+\omega_p^2/p^2}$$

the equations for the angular velocity are given by:

$$\dot{\theta}(t) = pA_1\cosh(pt) + pA_2\sinh(pt) + \frac{\omega_p}{1+\left(\omega_p^2/p^2\right)}\frac{a_p}{g}\cos(\omega_p t+\psi), \theta \le 0 \qquad (12)$$

and

$$\dot{\theta}(t) = pA_3\cosh(pt) + pA_4\sinh(pt) + \frac{\omega_p}{1+\left(\omega_p^2/p^2\right)}\frac{a_p}{g}\cos(\omega_p t+\psi), \theta \ge 0 \qquad (13)$$

3. DDA Validation for Dynamic Column Rotation

The analytical solution for dynamic rotation induced by an input of a half-sine pulse is obtained in two stages: 1) motion simultaneously under the input acceleration function: $\ddot{u}_g(t) = a_p\sin(\omega_p t+\psi)$ from t = 0 to t = 0.5 sec, where here ω is 2π, and the phase angle is $\psi = \sin^{-1}\left(\frac{\alpha g}{a_p}\right)$, and 2) free vibration following pulse termination from t = 0.5 sec onwards. At pulse termination the input acceleration diminishes ($\ddot{u}_g(t) = 0$, hence a_p = 0) and the coefficients of integration are updated for changing rotation angle and angular velocity. Furthermore, following each impact ($@\,\theta = 0$), the angular velocity and the coefficients of integration are recalculated as well.

The analytical and DDA solutions for column width and height of b = 0.2 m and h = 0.6 m are presented in Figure 3. The results on the left hand side of the figure are obtained for amplitude a_p = 5.43 m/s^2 (0.5535g), a value slightly lower than required for overturning, hence only column vibration is obtained. On the right hand side an amplitude of a_p = 5.44 m/s^2 (0.5545g) is used, the minimum value required for overturning, and indeed column overturning is obtained ~ 1.5 sec after pulse termination.

In the DDA model the column rests on a fixed base and is subjected to dynamic input at its centroid. The friction angle along the interface is set to 89 degrees to avoid sliding, as in the analytical solution which ignores sliding. The optimal values for DDA numerical control parameters (*g1*, *g2*) are obtained following the optimization study performed by Tsesarsky et al.(2005). Contact spring stiffness (*g0*) is selected by iterations, until the numerical computation returns the correct value of a_p necessary for column overturning. A remarkably good agreement between the analytical and numerical solutions is suggested by the data presented in Figure 3. The accuracy of the numerical solution can be assessed in terms of the numerical error ($\left|\frac{\theta_{anl.}-\theta_{num.}}{\theta_{anl.}}\right|\cdot 100\%$). As can be seen in Figure 3 after initial perturbations the numerical error rapidly decreases below 1%. Note that the DDA solution deviates from the analytical solution as soon as the first impact between the rocking block and the fixed base occurs. This deviation may be explained by the way damping is addressed in the two methods. While in the analytical solution the motion between impact cycles is restrained following the constant value of the coefficient of restitution, in DDA oscillations at contact points are restrained due to algorithmic damping (see Doolin and Sitar, 2004; Ohnishi et al., 2005). The numerical control parameters used in DDA simulations are: (*k01* = 1, *g2* = 0.0075, *g1* = 0.0025 sec, *g0* = 83*10^6 N/m, E = 3 GPa, ν = 0.25).

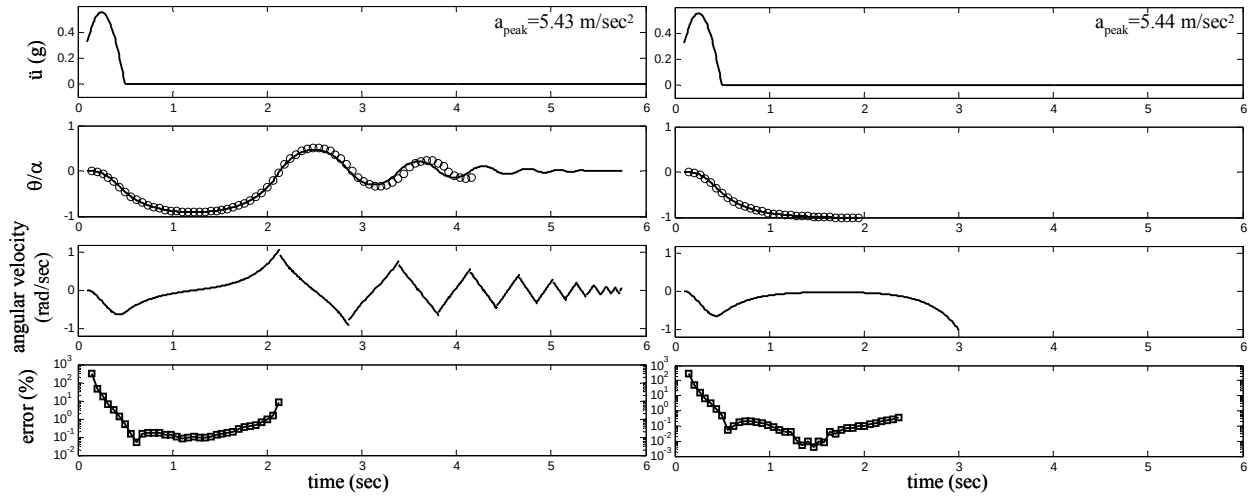

Fig. 3: Solution for dynamic column rotation (b=0.2 m, h=0.6 m). Left: a_p lower than required for toppling, Right: a_p sufficient for column toppling. Solid line - analytical solution, Open circles - DDA results.

The same procedure is repeated to find the solution for a full sine input function, again with $\omega = 2\pi$. The comparison between analytical and numerical solutions is presented in Figure 4 for column width and height of b = 0.5m and h = 1.5m, respectively. Again on the left-hand side a_p is slightly lower and on the right hand side a_p is slightly higher than the peak acceleration required for overturning. The difference between the two values used for input in the two simulations is 0.003 m/s^2 or 0.0001 g(!), suggesting an extremely high DDA accuracy. The spring stiffness found in iterations as before is $g0$ = 64*10^6 N/m, probably because of the difference in column stiffness due to the change in column geometry. The other DDA input parameters are: $k01$ = 1, $g2$ = 0.0075, $g1$ = 0.0025 sec, E = 3 GPa, ν = 0.25. As in the previous validation for a half sine the error remains very small until the first impact occurs, after which the error begins to increase. Naturally from the definition of error which depends on the actual value of θ, greater error is expected for very small values of θ, and vice versa.

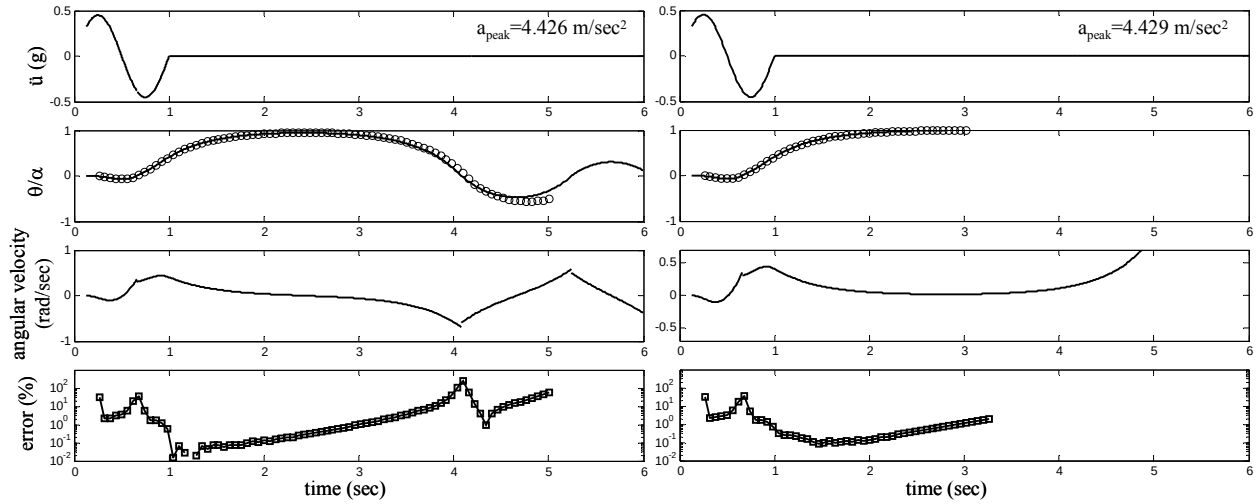

Fig. 4: Solution for dynamic column rotation (b=0.5 m, h=1.5 m). Left: a_p lower than required for toppling, Right: a_p sufficient for column toppling. Solid line - analytical solution, Open circles - DDA results.

4. Column Collapse at the Hellenistic Cathedral, Susita

In Susita, the columns of the Hellenistic cathedral are found lying parallel on the ground in azimuth 70°-250° (Figure 1B). The column bases are typically displaced by 60 to 90 cm from the column pedestals. The columns are made of solid granite, which was brought to the region probably from Egypt (Segal et al., 2004). Model geometry is presented in Figure 5, and the material properties are estimated as follows: E = 40 GPa, ν = 0.18, ρ = 2700 kg/m^3, and friction between column base and pedestal ϕ = 45°. The values of the numerical control parameters are as in the validation study. An optimal contact spring stiffness of $g0$ = 2*10^8 N/m is found by iterations, this time for best fit with the analytical solution but for initial oscillation stage (see Figure 6). The optimal $g0$ value was determined for very low values of θ to avoid sliding deformation.

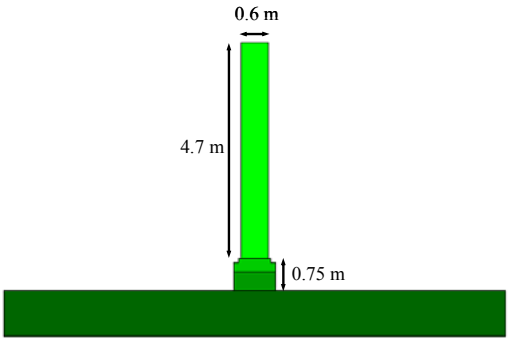

Fig. 5: The structural model used for the columns at Susita

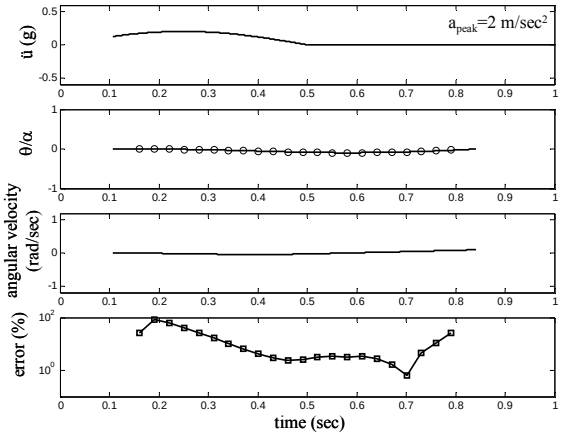

Fig. 6: The best fit solution for contact spring stiffness ($g0$ = 2*10^8 N/m) in the Susita case.

Forward DDA modeling is preformed as a function of frequency and amplitude of the input acceleration function. DDA results for one and three cycles of a sinusoidal input function are presented in Figures 7A and 7B respectively. With a single loading cycle the required amplitude for overturning clearly increases with frequency (Figure 7A). For example, the amplitude required for overturning at 5 Hz is 4.6 g, far greater than the expected PGA for this region, which is 0.3 g. Input loading frequencies of 1 Hz and 2 Hz return PGA values of 0.2 g and 0.6 g respectively, much closer to the expected PGA for this region. The required PGA for overturning also increases with frequency for three loading cycles, but at a smaller rate (Figure 7B).

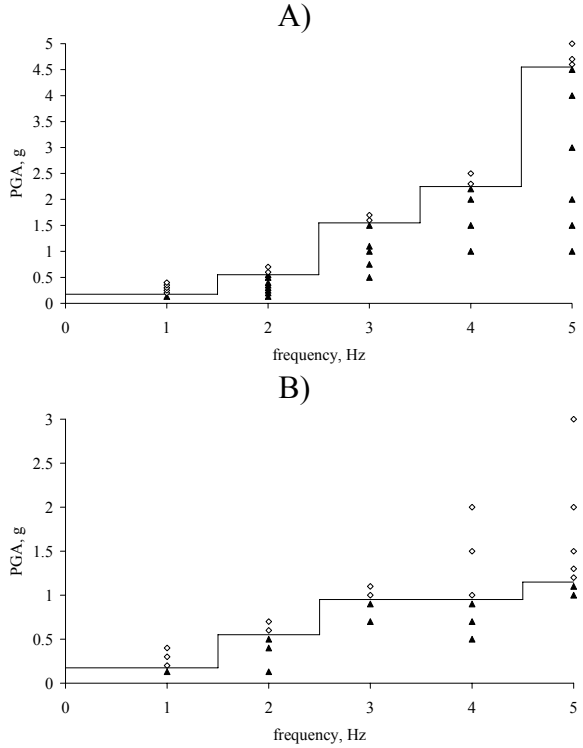

Fig. 7: DDA results for the Susita columns. Required PGA for overturning under one (A) and three (B) cycles of input loading function. Solid Triangles - stable columns, Empty diamonds – overturned columns. Solid line – stability boundary.

5. Discussion and Conclusions

In this paper we have presented an analytical solution for the dynamic rocking and overturning of rectangular columns developed by Makris and Roussos (2000). This problem is very important for seismic risk evaluation of existing structures, but is used here to back analyze a documented failure of monolithic columns which was clearly driven by seismic vibration in a known historic period. The sought products of this exercise are the most likely characteristics of the loading function, primarily the frequency and amplitude of the input acceleration record, for obtaining some constrains on regional seismic risk estimations which are, to date, largely dependent upon

empirical relations between earthquake magnitude, distance, and attenuation models. We use the dynamic DDA method first to check the validity of the numerical solution and then for forward modeling using sinusoidal input loading functions and calibrated numerical control parameters. By using dynamic DDA we relax the restriction of a "non-sliding" boundary at the base, inherent to the analytical solution, and allow the deformation to proceed in a more realistic manner.

Using the existing analytical solution we found by iterations the numerical contact spring stiffness, the value of which greatly influences the results of the numerical computation. We found that the best contact spring stiffness in this case is two orders of magnitude less than the elastic modulus of the column. The iterative procedure used to obtain to best value of numerical contact spring stiffness is recommended for problems where a very high level of accuracy is desired. Naturally selecting to perform this optimization calls for an existing analytical solution for the problem at hand.

We found that the required PGA for overturning increases with input function frequency, as also found by Psycharis et al. (2000). They further found that for low frequencies of 1 Hz or below the required PGA for overturning is independent of the number of loading cycles, since the column will overturn during the first cycle or soon after it. For higher frequencies however, three loading cycles seem to better represent earthquake thresholds. Proceeding with this reasoning we feel that the solution for three loading cycles better represents real earthquakes. Considering the result for three loading cycles (Figure 7B) the required PGA for overturning reaches a constant value of 1 g at frequencies greater than 3 Hz. For both one and three loading cycles realistic PGA values are obtained for 1 Hz and 2 Hz loading frequencies: 0.2 g and 0.6 g, respectively. Considering typical structural amplifications of 2.5 PGA in standard seismic building codes (e.g. NEHRP, 2004), the result of f = 2 Hz and PGA = 0.6 g yields a reasonable ground PGA value of 0.24 g. Another constrain we have on the threshold PGA is the distance between collapsed column base and pedestal which is consistently between 60 and 90 cm in the field. Column collapse under both 1 Hz and 2 Hz frequencies gives reasonable displacement distances of 0.6m and 0.79m, respectively. Further research on the natural frequency of free-standing columns is required before a definite determination of the most likely PGA value can be made.

Acknowledgement

We thank Dr. Shi for providing the latest version of his 2D-DDA code for this research.

References

Amit R., Zilberman E., Enzel Y., and Porat, N. Paleoseismic evidence for time dependency of seismic response on a fault system in the southern Arava Valley, Dead Sea rift, Israel. *Geological Society of America Bulletin,* 2002, **114**(2), 192-206.

Doolin, D.M. and Sitar, N. Time integration in Discontinuous Deformation Analysis. *Journal of Engineering Mechanics,* 2004, **130**, 249-258.

Kamai, R., and Hatzor, Y. H. Numerical analysis of block displacements in ancient masonry structures: a new method to estimate historic ground motions. *International Journal for Numerical and Analytical Methods in Geomechanics,* (in-press).

Makris, N. and Roussos, Y.S. Rocking response of rigid blocks under near-source ground motions. *Geotechnique,* 2000, **50**(3), 243-262.

NEHRP. in Report prepared by the building seismic safety council for the Federal Emergency Management Agency (FEMA 450), Washington, D. C., 2004.

Ohnishi, Y., Nishiyama, S., Sasaki, T. and Nakai, T. The application of DDA to practical rock engineering problems: issues and recent insights. In *Proceedings of ICADD -7,* 2005, Honolulu, Hawaii, 277-287.

Psycharis, I.N., Papastamatiou, D.Y., and Alexandris, A.P. Parametric investigation of the stability of classical columns under harmonic and earthquake excitations. *Earthquake Engineering and Structural Dynamics,* 2000*,* **29**, 1093-1109.

S.I.I. Design provisions for earthquake resistance of structures. The Standards Institution of Israel Code 413, 2nd amendment, 2004.

Scalia, A. and Sumbatyan, M.A. Slide rotation of rigid bodies subjected to a horizontal ground motion. *Earthquake Engineering Structural Dynamic,* 1996, **25**, 1139-1149.

Segal, A., Mlynarczyk, J., Burdajewicz, M., Schuler, M. and Eisenberg, M. Hippos - Susita, fifth season of excavation and summary of all five seasons. Zinman Institute of Archeology*,* University of Haifa, Israel, 2004.

Shi, G.-H. Block System Modeling by Discontinuous Deformation Analysis, *Computational Mechanics Publication,* Southhampton, UK, 1993.

Tsesarsky, M., Hatzor, Y. H., and Sitar N. Dynamic displacement of a block on an inclined plane: analytical, experimental, and DDA results. *Rock Mechanics and Rock Engineering,* 2005, **38**(2), 153 – 167.

Yagoda, G., Katz, O., Amit, R. and Hatzor, Y.H. Estimation of PGA values from back analysis of a large landslide in the eastern margins of the Kineret. In *proceedings of the Israel Geological Society's annual meeting*, Neve Zohar, Israel, 2007.

Effects of dynamic friction on sliding behavior of block in DDA

P. H. DONG [1] and OSADA M.[2]

[1] Graduate School of Science and Engineering, Saitama University, Japan
[2] Geosphere Research Institute, Saitama University, Japan

It is well known that the friction coefficient depends on the displacement and velocity. However, the current DDA program detects the slide at the contact surface by the Mohr-Coulomb criteria. Although DDA analysis is dynamic analysis, the friction coefficient is treated as a constant value. It is in fact that the sliding velocity along the fault is very high; in order of 1m/sec. Consequently, an implementation that considers the effect of dynamic friction should be employed in the DDA program especially in case of analysis the ground deformation by fault movement. This paper presents the effect of dynamic friction that should be implemented in DDA program. The validation of DDA program was firstly performed by verifying the block sliding induced by a sinusoidal motion. Subsequently, the potential rotation of block depends on the geometry and friction at contact surface was observed. Likewise, the constitutive friction law of dynamics friction developed by Dieterich (1979) and Ruina (1983) provided a connection between friction-velocity and time dependence, was used to observe the effects of weakening-friction behaviour. The analysis results showed that the effect of dynamic friction is influenced significantly in case of large slip velocity and slip distance. However, this weakening of sliding resistance may depend on many other factors such as the stiffness of the system, stress, temperature, historical sliding, etc.

Keywords: DDA; Dynamic friction; Constitutive friction law; Block sliding.

1. Introduction

Since it has been reported by Dieterich (1972, 1978, 1979), Ruina (1980) and Dieterich (1981), frictional sliding at surface contact has become a topic of interest in the field of fault mechanics. Therefore, frictional sliding behavior has been studied quite extensively by many researchers within the theoretical and experimental frameworks. As a result, constitutive friction laws, a simulation of the frictional sliding behavior, have been proposed as a powerful tool for investigating the mechanics of fault movement. By range of observations in laboratory experiment over natural fault problems, it has been documented that the weakening of frictional resistance at contact surface is nonlinear behavior of slip distance, slip velocity, stiffness of the system, stress condition, temperature, and history of sliding, etc. A summary of research on constitutive friction laws were performed by Marone (1992, 1998), in which presented the fundamentals of laboratory-derived friction laws and their application to seismic faulting. In addition, a slip-weakening friction law was introduced by Dieterich (1979, 1981), Ruina (1983), Rice (1983), Rice & Ruina (1983), Brace & Byerlee (1966, 1970), etc, in which friction - slip distance and slip velocity dependence is widely used. When sliding occurs, frictional resistance will change from static friction coefficient, μ_s to a lower dynamic friction coefficient, μ_d. A numerical simulation considering the reduction of friction - slip distance, slip velocity dependence are important particularly in case of large slip distance, and slip velocity as it was reported that the sliding velocity along the fault is very high in order of 1m/sec when earthquake occurs.

Although DDA (Shi 1989) is dynamic analysis, it detects the sliding condition at the contact surface by the Mohr-Coulomb criteria where the friction coefficient is treated as a constant value in most DDA program. Therefore, in order to analyse the ground deformation by fault movement effectively, it is very important to incorporate the dynamic friction in the DDA program (Osada and Taniyama 2005).

In this research, a DDA program was implemented, in which weakening friction behaviour is firstly assumed in order to observe the effect of dynamic friction in block sliding. Likewise, the constitutive friction law of dynamic friction, developed by Dieterich (1979) and Ruina (1983) was used, in which provides a connection between friction and velocity, time dependence.

2. Friction coefficient update in DDA program

DDA calculation is controlled by time steps, in which friction can be updated according to the shear displacement and velocity that are obtained after each time of Open-Close calculation. The algorithm of friction coefficient update can be expressed as in fig.1.

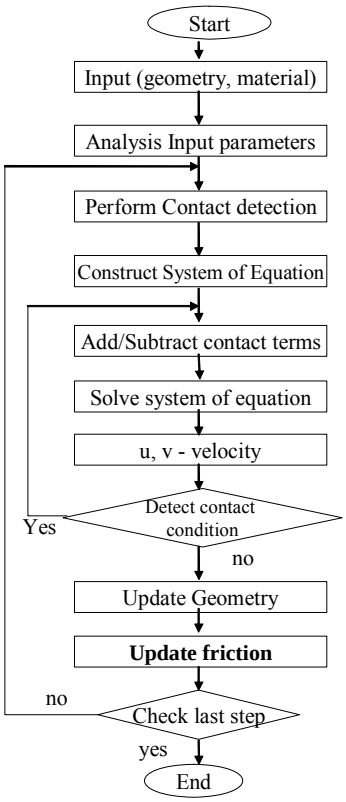

Fig. 1: The algorithm of the friction coefficient update.

3. Validation of DDA

First, the DDA program was validated for the calibration purposes. Because, only an agreement between DDA program and analytical solution will ensure the accuracy of program. In this case, single block sliding on the horizontal plane induces by a sinusoidal motion is studied. Fig. 2 shows the model: Block 1 is fixed in the vertical direction, whereas the horizontal direction is subjected to a sinusoidal load at the centre point. Block 2 with the Height/Width ratio of 0.25 is set as responding block. The acceleration of input motion is expressed as $a_{input} = Asin(\omega t)$ for simplicity.

Since it is being a verification, horizontal sliding only is considered without any rotation or vertical motion. The resistance force in the system is only a friction resistance on the surface contact between the two blocks.

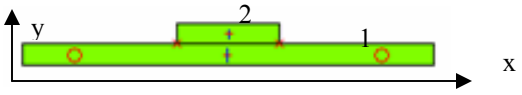

Fig. 2: Blocks system.

The mechanical properties of the blocks used in present DDA program are described in table 1.

Table 1. Mechanical properties of blocks.

Properties	Value
Bulk density ρ (kg/m^3)	2000
Young's Modulus E (GPa)	100
Poison ratio ν	0.3
Cohesion at contact surface *c (kN/m^2)*	0

The block system was set as rigid material with the slender geometry and one degree of freedom in horizontal sliding. Therefore, such an effect of rotation, vertical motion, deformation of block, and cohesive strength do not considerably influence the sliding behaviour of Block 2.

3.1. Analytical Solution

As the model is shown in Fig.2, when Block 1 starts to move, the frictional force pulls Block 2 in the same direction. The relative velocity, $v_r = v_1 - v_2$ between two blocks decides the motion of two blocks. When $v_r = 0$, Block 2 is at rest against the Block 1, when $v_r \neq 0$, the sliding will occurs between two blocks. The analytical solution for this case is implemented by stepwise calculation of time, in which the sign and value of accelerations a_1, a_2 of two blocks are set by the previous conditions. By considering the equilibrium conditions of each block, the analytical solution can be described as follows:

$$
\begin{aligned}
&\textit{If } v_r = 0 \\
&\quad a_1 = a_{input} = A\sin\omega t \\
&\quad \textit{if } m_1|a_1| < m_2 g\mu \\
&\qquad a_2 = a_1 \\
&\quad \textit{else} \\
&\qquad \textit{if } a_1 > 0,\ a_2 = \mu g \\
&\qquad \textit{else } a_2 = -\mu g \\
&\qquad \textit{end} \\
&\quad \textit{end} \\
&\textit{elseif } v_r \neq 0 \\
&\quad \textit{if } v_r > 0 \\
&\qquad a_1 = A\sin\omega t - \mu g;\ a_2 = \mu g \\
&\quad \textit{else} \\
&\qquad a_1 = A\sin\omega t + \mu g;\ a_2 = -\mu g \\
&\quad \textit{end} \\
&\textit{end}
\end{aligned}
\qquad (1)
$$

where μ is the friction coefficient at the contact surface and g is acceleration due to gravity.

3.2. The numerical analysis

The accumulating displacement of the responding Block 2 was calculated with a change of amplitudes,

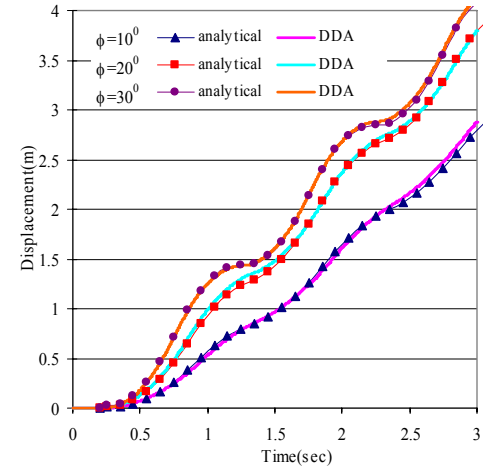

(a)

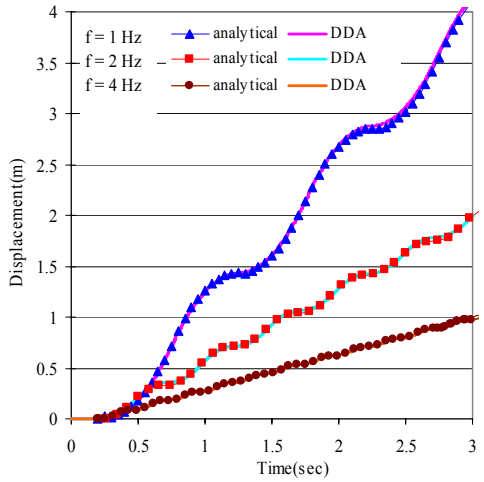

(b)

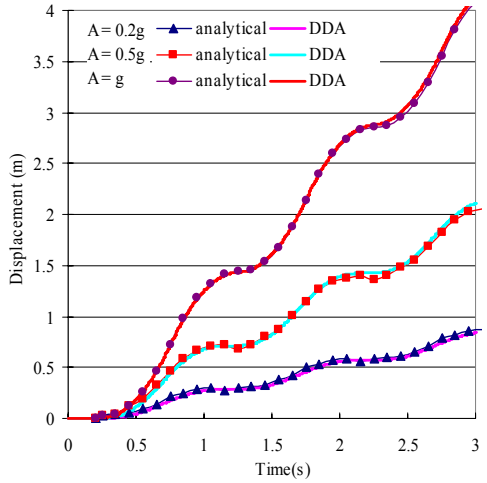

(c)

Fig. 3: The Response of Block 2. Time step Δt= 0.005 sec. 3.a.) Changing frictions with A = g; frequency f = 1Hz. 3.b) Changing frequencies with A = g and ϕ = 30^0. 3.c) Changing A with f=1Hz, ϕ=30^0.

frequencies and friction. A stabilization of normal force is required for the friction force existing on the contact surface. So that, for all cases, the input motion starts to apply only at t = 0.2 sec in order to ensure the vertical motion by self-weight of block 2 is finished.

Fig. 3 shows the comparison between DDA and analytical solution. A remarkable agreement between DDA program and analytical solution (Fig. 3.a, 3.b, 3.c) with changing of friction, frequencies and amplitudes of input motion ensures the performance of DDA program as recommended by Kamai and Hatzor (2005), Tsesarsky, Hatzor, and Sitar (2005). Figure 3.a. presents the displacement of responding Block 2 to changing the friction at the contact surface with the constant input amplitude and input frequency. The good agreement between DDA and analytical solution indicates that the contact condition at the surface contact, induced by normal force and shear force at contact point, is stable as expected. Fig. 3.b. and 3.c. present the accumulating displacement of Block 2 to changing frequencies and amplitudes of input acceleration. These figures reveal the effect of loading velocity to the sliding behaviour. Although, the frequency and amplitude of acceleration are increased 4 times (1 Hz to 4 Hz) in the former and 0.2g to 1.5g in the later (g is acceleration due to gravity), the difference of displacement between DDA and analytical solution is not significant. Hence, it is clear that a wide range of input loading does not influence significantly the agreement of block sliding between DDA and analytical.

3.3. Effect of rotation of block

Subsequently, effect of rotation that may depend on the geometry, input motion loading and friction at surface contact will be discussed. To observe the effect of geometry to rotation, a changing Height/Width ratio of Block 2 will be considered which is called here as geometric parameter $\alpha = h/b$ as shown in fig. 4.

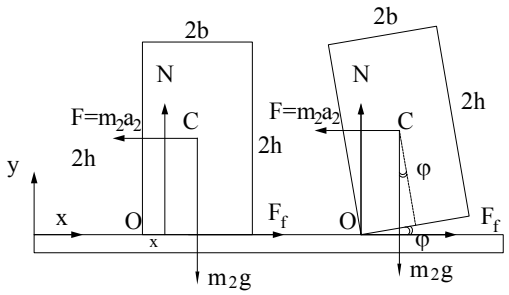

Fig. 4: Overturning of rigid block sliding

The static equilibrium condition of Block 2 for the rigid body (Fig.4):

x direction: $F_f - F = 0$ (2)

y direction: $N - m_2 g = 0$ (3)

Moment round point O:

$$Fh + Nx - m_2 gb = 0 \quad (4)$$

where x is distance from reactive force N to point O, and x = 0 ~b. It follows equations (2), (3), (4) that:

$$x = b - \frac{h}{g} a_2 \quad (5)$$

$$\text{At } x = 0: \; K = \frac{h}{bg} a_2 = \frac{\alpha}{g} a_2 \quad (6)$$

K reveals the ratio of rotational moment over resistant moment from a rotation. Consequently, when K >1, Block 2 starts to rotate. When the exciting force from Block 1 is smaller than friction force existed at the contact surface, Block 2 is a rest relative to Block 1. In contrast, when exciting force is larger than friction force, Block 2 will slide relatively to Block 1 without any rotation. Hence, from the equilibrium condition of Block 2, $a_2 = \mu g$ and $K = \alpha\mu$.

Then, the rotation of block was analysed by DDA. The model in Fig. 4 was studied with a linear acceleration $a = At$ which is subjected at the centre point of Block 1 for simplicity. In these analyses, the initial state of relatively sliding and potential rotation is determined from the contact condition. Basically, the contact condition in DDA is divided into three types, Lock, Close, and Open that depend on the penetration distance of contact point to the contact surface after a repeated calculation of Open-Close of each time step. At the initial state of the loading, the contact condition is detected as Lock condition. Then, an increasing of exciting force induces a change of the contact condition. The rotational condition of Block 2 is realized when a contact point of Block 2 changes to the Open condition whereas the other point is either in Lock or in Close condition. In addition, the sliding condition of Block 2 is detected when both contact points are changed from Lock condition to Close condition. K value is calculated at the initial rotation state as well as sliding of Block 2.

Fig. 5 presents the K-α relation. When α is small such as α = 0.5, K was less than 1 in the range of frictions at the contact surface which implies that Block 2 is only sliding without any rotation. When K > 1, Block 2 is rotated, and a larger K with the same α implies the potential rotation of Block 2 is lower. Likewise, with the same value of friction, the potential rotation of Block 2 increases with the increase of α. Consequently, it can be concluded that the increasing of friction at contact surface or geometric parameter α causes the potential of overturning to be high. However, since it depends on the detection of possible contacts between blocks, the potential rotation of the block depends on the control parameter using in DDA such as penalty parameter, time step size, assumed maximum displacement ratio. For instance, in case of α=2 and ϕ= 30^0 K >1, but a rotation of Block 2 was not occurred. An observation of the effects of control parameters to rotation of block will be performed in the DDA research.

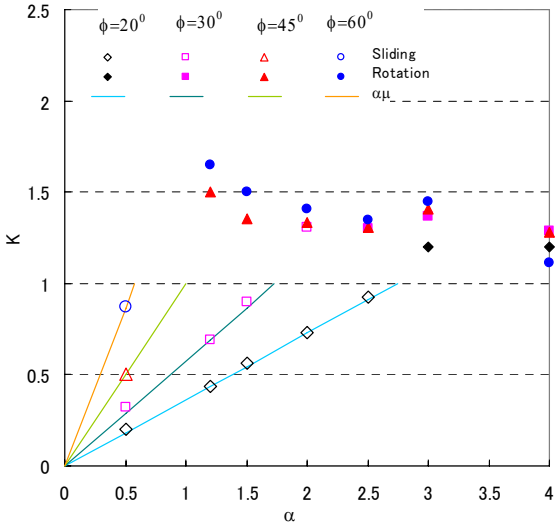

Fig.5: K–α relationship with the amplitude of linear acceleration of A = g; time step Δt= 0.001 sec; assumed maximum displacement ratio, g = 0.001; penalty parameter = 1000 MN/m.

4. Effects of dynamic friction in DDA

When sliding occurs, frictional resistance falls from static friction coefficient, μ_s to a lower dynamic friction coefficient, μ_d. In a possible approach to this weakening-friction, the constitutive friction law of dynamic friction was considered. The Dieterich's original constitutive friction law (1979) was validated by various researchers over the laboratory works on many rock types. One possible constitutive friction equation is slip velocity, and history slip stage dependence which is given by Kanagawa (1996) as follow:

$$\mu = \frac{\tau}{\sigma} = \mu_0 + a \ln(\frac{V}{V_0}) + b\Theta \quad (7)$$

$$\frac{d\Theta}{dt} = -\frac{V}{L}\left\{\Theta + \ln(\frac{V}{V_0})\right\} \quad (8)$$

where μ , τ, σ are the friction coefficient, shear stress, and normal stress respectively; μ_0 is a constant appropriate for steady-state slip at velocity; V_o, V are the frictional slip rates; Θ is a state variable, and a and b, L are experimental parameters; L representing the slip necessary to renew the surface contacts. In

case that dynamic friction is steady state behavior, $d\Theta/dt = 0$, equation (5) can be rewritten as follow:

$$\mu = \mu_0 + (a-b)\ln(\frac{V}{V_0}) \qquad (9)$$

By using equation (9), a DDA program was developed to observe the friction-velocity dependence. In this analysis, the experimental variables *a, b, L* as reported by Dieterich (1979) and Ruina (1983) were used. Again, the same model of block sliding in Fig. 2 is studied.

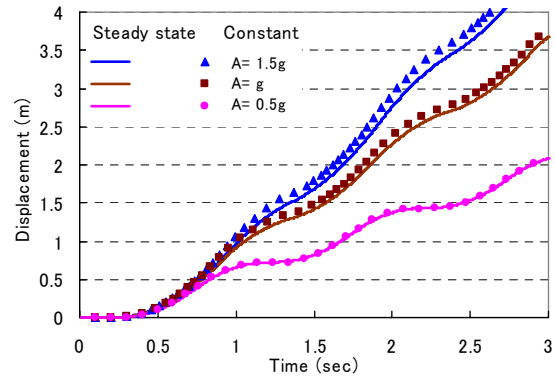

(a)

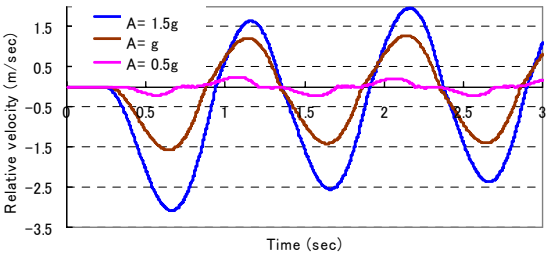

(b)

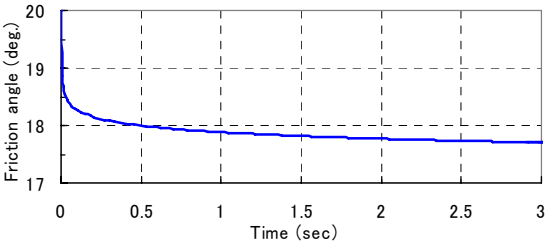

(c)

Fig. 6: Respond of Block 2 when the friction at surface contact is constant and steady state behaviour of reduction to changing amplitudes of acceleration; f = 1 Hz; ϕ_s =20^0; time step Δt= 0.005 sec. 6.a) displacement-time dependence. 6.b) The relative velocity –time. 6.c) the friction-velocity dependence.

Fig.6 presents the respond of Block 2 when the friction at surface contact is constant, and the weakening-friction is considered as steady state behaviour. Fig.6a and Fig. 6.b indicate that a when the sliding velocity increases, the difference of displacement of Block 2 also increase significantly. The displacement of blocks is accumulated after each step and it causes the difference also increase over time. Fig. 6.c presents the friction-velocity dependence. It shows that the amount of friction reduction is larger than 10% in case of the sliding velocity of 0.5 m/sec. However, this weakening of sliding resistance may depend on the stiffness of the system, stress condition, scale effect, etc.

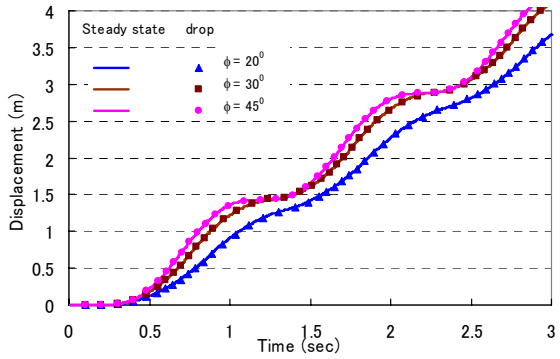

(a)

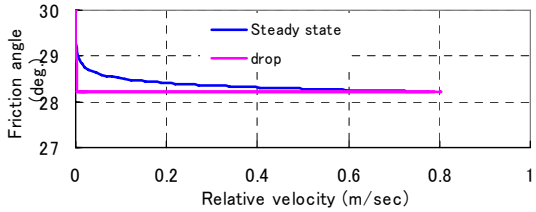

(b)

Fig. 7. The respond of Block 2 when the weakening-friction is as steady state, and sudden change to the sliding velocity; A=g 7.a) Displacement-time dependence. 7.b) The weakening-friction behaviour.

On the other hand, the effect of weakening-friction behaviour on the block sliding were also performed by verifying the respond of Block 2 when the weakening-friction as steady state and sudden change (drop) to the dynamic friction (Fig. 7). With three different static frictions at the contact point 20^0, 30^0, and 45^0, when the weakening-friction is steady state, a reduction of friction of 12.6%, 7.34%, 3.02% respectively was found. With the same amount of reduction, a suddenly change of friction when sliding occurs was analysed. In these cases, the velocity is gradually changed as shown in Fig. 6.b. A good agreement of the displacements of Block 2 in Fig 7.b indicates that sudden drop model of friction can be used as the first approximation to express the effects of the weakening-friction behaviour.

Conclusions

This research is an attempt to explain the dynamic friction behavior which is complicated in nature but it is considered to the most influencing factor for DDA

analysis. From the above analysis, the following conclusions can be drawn:

1. The block sliding behaviour was observed by using DDA. The validation of DDA program was also performed for calibration purpose. Then, the potential rotation of block depends on the geometric parameter and friction at the surface contact that represented by K value was also observed by DDA. However, this effect depends on the control parameter in DDA such as time step size, penalty parameter, assumed maximum of displacement. A research on the effects of these parameters to the potential rotation of block will perform in the further DDA research.

2. The research on dynamic friction in DDA indicated that dynamic friction is influenced significantly by block sliding especially in case of large displacement. Likewise, a considerable reduction of friction has occurred in order larger than 10 % when the weakening-friction as steady state. However, this effect may depend on the other factors such as stress, scale effect, and other control parameters used in DDA. It also pointed out that the effect of weakening-friction behaviour is limited to a small range of sliding velocity. Consequently, a drop of weakening-friction behaviour to the velocity can be used for the first approximation.

Acknowledgement

This study was partly funded by JNES (Japan Nuclear Energy Safety Organization). This support is gratefully acknowledged.

References

Brace, W. F., Byerlee, J. D., Stick-slip as a mechanism for earthquakes. *Science* 153: 990–92, 1966.

Byerlee J. D., Frictional characteristics of granite under high confining pressure. *J. Geophys.Res.,* 1967 72:3639–48.

Byerlee JD, Friction of rocks. *Pure Appl Geophys.* 116:615–26, 1978.

Dieterich J. H., Constitutive properties of faults with simulated gouge. In *Mechanical Behavior of Crustal Rocks*, ed. NL Carter, M Friedman, JM Logan, DW Sterns, *Am. Geophys Union Monogr.*, 24:103–20. Washington, DC: Am. Geophys. Union, 1981.

Dieterich J. H., Modeling of rock friction: 1. Experimental results and constitutive equations, *J. Geophys. Res,* 1979, 84:2161–68.

Doolin, D. M., Sitar, N.. Displacement accuracy of discontinuous deformation analysis method applied to sliding block. *ASCE Journal of Engineering Mechanics,* v. 128, pp. 1158-1168, 2002.

Doolin, M., Sitar, N.. Time integration in discontinuous deformation analysis. *ASCE Journal of Engineering Mechanics,* v. 130, March 2004.

Kamai, R. and Hatzor, Y. H., Dynamic back analysis of structural failures in archaeological sites to obtain paleo-seismic parameters using DDA, *proceeding of ICADD-7*, *Hawaii,* 2005.

Kanagawa, K., Effects of pressure solution on the frictional properties of rocks: Experimental investigations, Tectonics and Metamorphism (The Hara Volume), *SOUBUN Co. Ltd*, 304-313., 1996 (in Japanese).

M. Tsesarsky, Y. H. Hatzor, and N. Sitar, Dynamic Displacement of a Block on an Inclined Plane: Analytical, Experimental and DDA Results, *Rock Mech. Rock Engng.*, 2005, 38 (2), 153–167.

Marone C., Hobbs, B. E., Ord A., Coulomb Constitutive Laws for Friction: Contrasts in Frictional Behavior for Distributed and Localized Shear, pageoph, Wol. 139, No. 2, 1992.

Marone C., Laboratory-derived friction laws and their Application to seismic faulting, Annu. *Rev. Earth Planet. Sci.* 26:643–96, 1998.

Mary Maclaughlin, M., Elizabeth Berger, A., David Doolin, M., A decade of DDA validation, *Proceeding of ICADD 6.*

Osada, M., Taniyama, H., Preliminary consideration for analyzing ground deformation due to fault movement, *proceeding of ICADD-7, Hawaii*, 2005.

Rice J. R., Constitutive relations for fault slip and earthquake instabilities. *Pure Appl. Geophys.* 121:443–75, 1983.

Rice J. R., Ruina A. L., Stability of steady frictional slipping. *J. Appl. Mech.*, 1983, 105:343– 49.

Ruina A., Slip instability and state variable friction laws. *J. Geophys. Res.* 88:10359–70, 1983.

Shi,G-H., Block System Modeling by Discontinuous Deformation Analysis, *Computational Mechanics Publications*, 1989.

Comprehending DDA for a block behavior under dynamic condition

S. AKAO[1], Y. OHNISHI[1], S. NISHIYAMA[1] and T. NISHIMURA[2]

[1]Kyoto University, Kyoto Univ.-Katsura, Nishikyo-ku, Kyoto, 615-8540, JAPAN
[2]Hazama Corp., 2-2-5, Toranomon, Minato-ku, Tokyo, 105-8479, JAPAN

Earthquake is one of the major triggers for rock slope failure and rockfall, which often cause heavy damage to our society. Simulation of the behavior of rock masses during earthquakes is vital for the sake of protecting our society against these disasters. The purpose of this study is to investigate the DDA behavior under dynamic condition. We simulated vibration response of a block on a virtual shaking table, and performed assembled blocks tests on a shaking table and compared with the simulation results by DDA. In consequence, it was found out that DDA can simulate dynamic response of blocks accurately when appropriate input parameters are applied with which frictional force between blocks works well. However, input parameters have a decisive influence on the accuracy of analysis and we expect that the open-close iteration in DDA analysis is related to this phenomenon. Thorough discussion is included in this paper.

Keywords: DDA; dynamic analysis; earthquake problem; shaking table tests

1. Introduction

Earthquake is one of the major triggers for rock slope failure and rockfall, which often cause heavy damage to our society. The safety assessment for rock slopes during earthquakes is necessary so as to protect our society against these disasters, and numerical analysis methods are very useful to simulate behavior of rock masses during earthquakes. Finite element method (FEM) is extensively used as a numerical method for the grounds and rock masses and many vibration analysis systems with FEM have been developed. However FEM have limitations in regard to analysis of discontinuous rock masses because FEM treats objects as continuous media. In contrast, discontinuous deformation analysis (DDA) (Shi and Goodman 1984) is a numerical analysis method which treats objects as discontinuous media and works for analysis of behaviors of discontinuous rock masses. In addition, DDA is known to analyze accurately static and block falling problems and is expected to come into practical use. However, nobody has thoroughly investigated that a system of blocks under earthquake condition can be analyzed by DDA.

The purpose of this study is to investigate DDA behavior under dynamic condition. We simulated vibration response of a block on a virtual shaking table, and did assembled blocks tests on a shaking table and compared with results of simulation by DDA to inspect the applicability of DDA under dynamic condition.

2. A single block behavior under dynamic condition

Investigation of the DDA behavior of a simple vibration problem is vital to inspect the applicability of DDA under dynamic condition. In this paper, we did sensitivity analysis of a block on a virtual shaking table vibrating horizontally to investigate the applicability DDA to vibration problem and the influence of input parameters on analysis results.

2.1 Analytical condition

Fig. 1 shows the analytical model. We input horizontal displacement time history to the lower block, a virtual shaking table, and compared results of DDA to an analytical solution of the response of a single block resting on the virtual shaking table (Kamai and Hazor 2005). The input motion is shown in Fig. 2. The first 0.5 sec. is 'gravity turn-on' routine (MacLaughlin and Sitar 1999) prior to the dynamic analysis. Table 1 shows physical properties of block and parameters used in this analysis. In this analysis, we investigated the influence of mass of a block (m), time interval (h) and contact spring stiffness (k_n) on the analysis results.

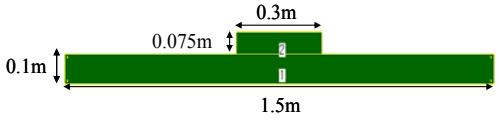

Fig. 1: Analytical model.

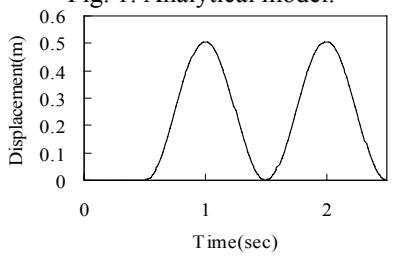

Fig. 2: Input motion.

Table 1: Physical properties of block and parameters used in the analysis

Poisson's Ratio	0.2
Friction Angle(°)	36.4
Young's Modulus(kN/m^2)	1.49×10^7
Unit Weight(kN/m^3)	21.56×10^{-1}-21.56×10^2
Time Interval(sec)	5×10^{-5}-1×10^{-2}
Contact Spring Stiffness(kN/m)	2×10^1-4×10^8

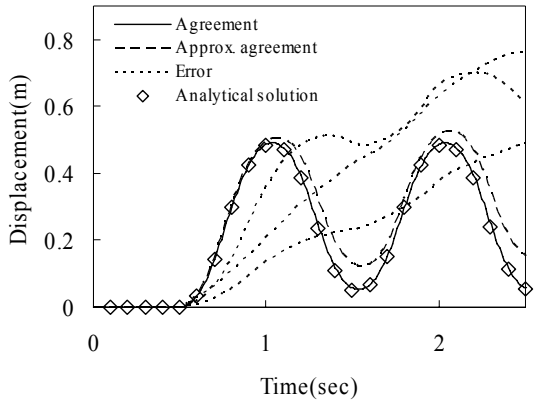

Fig. 3: Classification of result of analysis.

2.2 Method of comparison

We did semi-quantitative assessment by comparing DDA results with the analytical solution of the upper block's displacement plotted on the graph. Results are categorized as 'Agreement', 'Approximately agreement' and 'Error' by the accuracy (Fig. 3).

2.3 Analysis results

Fig. 4 shows the analysis results for different values of mass of the upper block (m) and contact spring stiffness (k_n). This shows that appropriate contact spring stiffness is much lower than the Young's modulus of the block and it increases in proportion to mass. Fig. 5 shows that DDA results agree with the analytical solution well when k_n/m is about 1.0×10^5. However, the range of appropriate stiffness value is limited to only one order, and error is large awfully if contact spring stiffness violates this appropriate range.

Fig. 6 shows the results for different values of time interval (h) and contact spring stiffness (k_n). This figure shows that error is very large with contact spring stiffness less than 1×10^3 kN/m without relation to time interval and that the smaller time interval is, the more the range of appropriate stiffness value broadens. However, too small time interval is inappropriate because the computations with such small time interval make DDA computation a time consuming analysis and a very small time interval makes the solutions unstable (Ohnishi et al 2005).

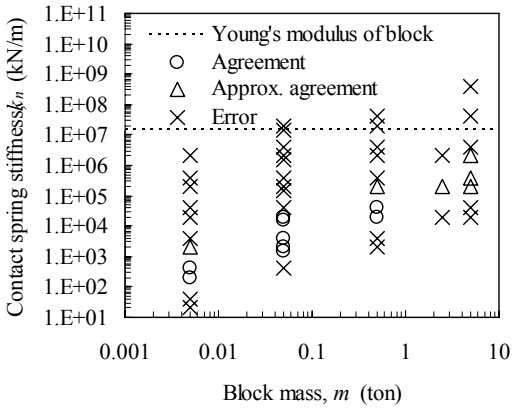

Fig. 4: Analysis results for different values of m and k_n. h=0.001sec.

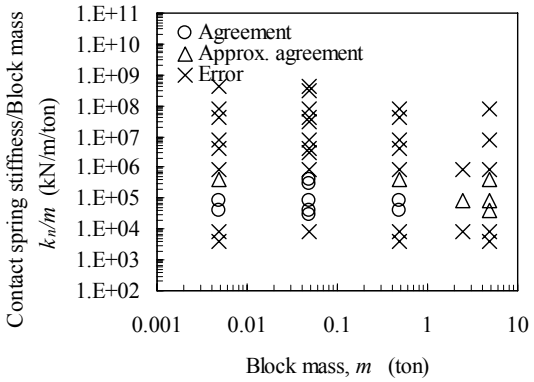

Fig. 5: Analysis results for different values of m and k_n. h=0.001sec.

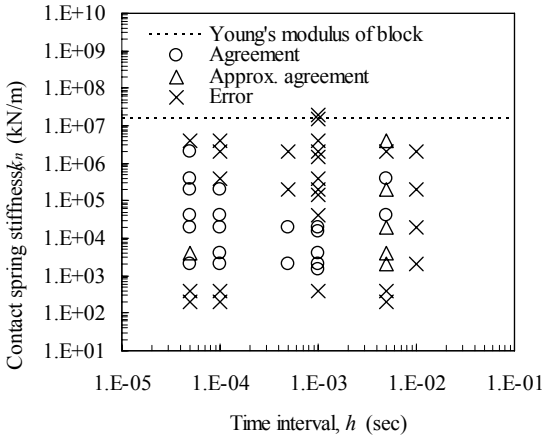

Fig. 6: Analysis results for different values of h and k_n. m=0.0495ton.

2.4 Discussion

In this section, we investigate why accuracy changes variously depending on input parameters, in particular why error is large awfully with input parameters violating appropriate range as in 'Error' case.

2.4.1 Investigation data in detail

In order to find out the reason error is very large as in 'Error' case, we investigate the analysis results in detail. Fig. 7 shows the horizontal and vertical accelerations of the upper block in 'Agree' and 'Error' cases. This figure shows that in 'Agree' case, the horizontal acceleration was calculated $\pm 7.2 m/s^2 = \pm g\tan\varphi$ m/s^2 and the vertical acceleration is calculated $0 m/s^2$ which are equal to theoretical solution, through contact spring makes a little oscillation. In contrast, in 'Error' case, the horizontal acceleration is calculated $0 m/s^2$ and the vertical acceleration is calculated $-9.8 m/s^2$ at the most of the time step, which are the accelerations of free-fall block. This result shows that the error is large awfully because frictional force does not work between two blocks and the upper block is floating in the air.

2.4.2 Stability of solutions

Stability of solutions and accuracy caused by the time integration system might yield large error as in 'Error' case. Hughes (1983) and Doolin and Sitar (2003) present that when we solve a system of equations such as Eq. (1) represents one-dimensional and undamped mass(m)-spring(k) model

$$\ddot{d} + 2\xi\omega\dot{d} + \omega^2 d = f \quad \text{(damping ratio: } \xi = 0\text{)} \tag{1}$$

where

$$\omega = \sqrt{k/m} \tag{2}$$

by the Newmark method ($\beta = 1/2, \gamma = 1$), the spectral radius is represented as follows

$$\rho = \max\left|\lambda_{1,2}\right| \tag{3}$$

where

$$\lambda_{1,2} = A_1 \pm \sqrt{A_1^2 - A_2} \tag{4}$$

$$A_1 = 1 - \left(\Omega^2\left(\gamma + 1/2\right)/2\right)/D \tag{5}$$

$$A_2 = 1 - \left(\Omega^2\left(\gamma - 1\right)\right)/D \tag{6}$$

$$D = 1 + \beta\Omega^2, \Omega = h\sqrt{k/m} \tag{7}$$

It is generally advisable in practice to satisfy slightly stringent conditions to make solutions stable. Hughes (1983) presents the follows conditions should be satisfied to prevent the roots [Eq. (4)] from bifurcating into distinct roots

$$A_1^2 < A_2 \tag{8}$$

The Newmark method satisfies Eq. (8) and the spectral stability requirement when the following conditions hold (Hughes 1983):

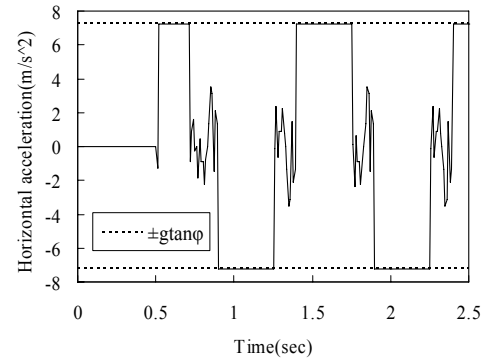

(a)Horizontal acceleration (k_n =2×10^{4}kN/m)

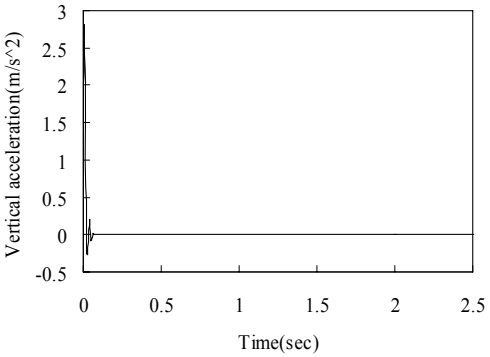

(b)Vertical acceleration (k_n =2×10^{4}kN/m)

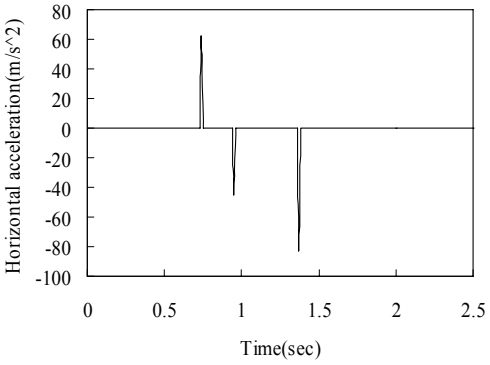

(c) Horizontal acceleration (k_n =2×10^{5}kN/m)

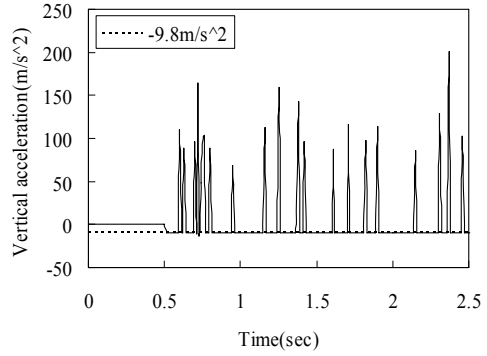

(d) Vertical acceleration (k_n=2×10^{5}kN/m)

Fig. 7: Horizontal and vertical acceleration of the upper block. Block mass and time interval are constant, m=0.0495ton and h=0.001sec.

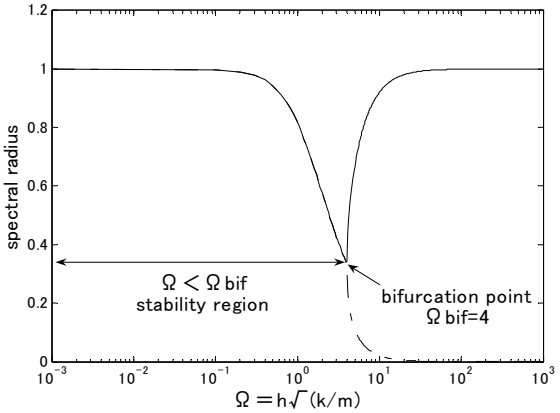

Fig. 8: Spectral radius for Newmark integration.

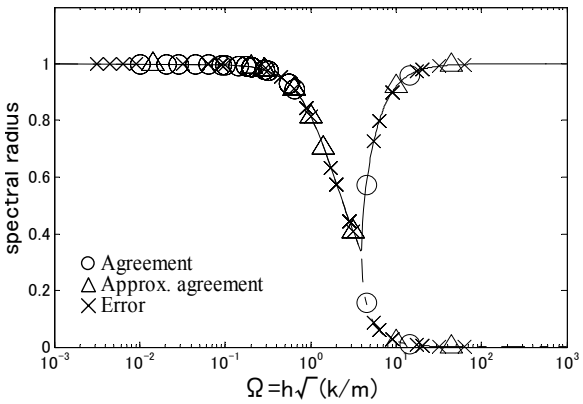

Fig. 9: Distribution of spectral radius calculated from input parameters.

Unconditional

$$0 \le \xi < 1,\ \gamma \ge \tfrac{1}{2},\ \beta \ge \left(\gamma + \tfrac{1}{2}\right)^2 / 4 \tag{9}$$

Conditional

$$0 \le \xi < 1,\ \gamma \ge \tfrac{1}{2},\ \Omega < \Omega_{bif} \tag{10}$$

$$\textit{where}\ \ \Omega_{bif} = \left[\tfrac{1}{4}\left(\gamma + \tfrac{1}{2}\right)^2 - \beta\right]^{-1/2} = 4 \tag{11}$$

When $\beta = 1/2, \gamma = 1$ are used, Eq. (9) are violated, and therefore Eq. (10) should be satisfied in DDA. The details are given in Hughes (1983) and Doolin and Sitar (2003).

When the analysis model (Fig. 1) is simplified into one-dimensional mass-spring model, the spectral radius of this system is illustrated in Fig. 8. We plotted on this figure all input parameters and spectral radius calculated from input parameters used in above analysis (Fig. 9). This figure shows that analytical accuracy does not correlate with spectral radius and many 'Error' cases satisfy Eq. (10). Thus it is difficult to conclude that stability of solutions and accuracy caused by the Newmark method yield large error in this analysis.

2.4.3 Open-close iteration

Contact judgment by open-close iteration might yield large error as in 'Error' case. In DDA, the penalty method is introduced to block-to-block contact and the contact spring prevents penetration of blocks. Then in the case of laminated block model used in this analysis, when contact force by contact spring is too large against block mass, contact spring pushes up the upper block well over open-criteria (Fig. 10) and contact condition is deemed to be non-contact even if it is 'contact' actually. In consequence, even if open-close iteration converges, correct contact judgment is not done and this incorrect judgment yields a condition that does not make frictional force work as in the case of 'Error'. The vertical large force in 'Error' case (Fig. 7-(d)) is caused by too large contact force by spring. In contrast, if contact spring stiffness is too small to push up the upper block, error is large due to over penetration. Thus we believe that soft spring stiffness, but stiff enough to prevent penetration, should be applied to make frictional force work well and incorrect contact judgment by open-close iteration yields large error in dynamic analysis.

3. Shaking table test and simulation by DDA

We performed assembled blocks tests on a shaking table and compared with results of simulation by DDA to inspect the applicability of DDA under dynamic condition (Akao et al 2006).

3.1 Shaking table test

Fig. 11 shows assembled blocks which are composed of cubic concrete blocks, the size of each block is 15cm×15cm×15cm and the density is 2.2ton/m^3. Some sinusoidal input motions which had different frequency and amplitude were used. A typical input motion is shown in Fig. 12. Table 2 shows the cases of input motions and the results of behaviors of the top block in all cases. This table shows that the blocks had various behaviors, stable or topple, depending on input motions. Fig. 13 shows behavior of blocks at 5Hz-700gal vibration, the horizontal displacement of blocks gradually increased with sliding and rotation (locking).

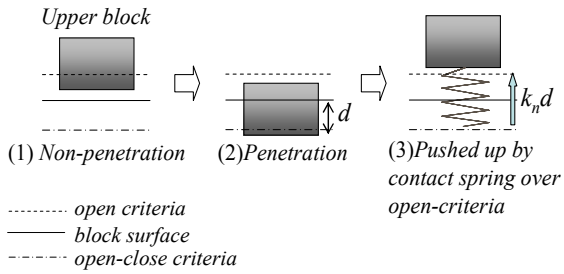

Fig. 10: Contact spring pushes up the upper block well over open-criteria.

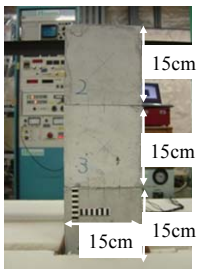

Fig. 11: Experimental model for the shaking table test.

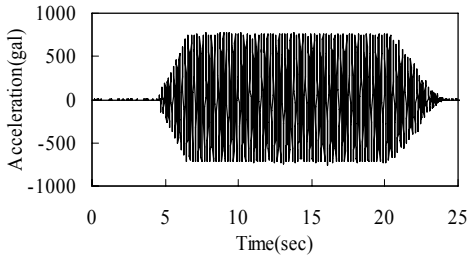

Fig. 12: Typical input motion (3Hz-400gal).

Table 2: Results of block behavior in all cases

Frequency(Hz)	Amplitude(gal)	Behavior
3	400	Stable
3	700	Topple
5	400	Displacement without toppling
5	700	Topple

3.2 Simulation by DDA

The analysis model is shown in Fig. 14 and physical properties of block and parameters used in this analysis are shown in Table 3. Table 4 shows the analysis results of the behaviors of the top blocks and they agree with results of tests. The result of simulation in the case of 5Hz-700gal vibration is shown in Fig. 15. This figure shows that DDA can simulate sliding and rotation (locking) of block seen in the test. Fig. 16 shows the results of horizontal displacement and acceleration spectrum of the top block of DDA and experiments. From these data, horizontal displacement and acceleration spectrum can be expressed well by DDA. Thus, it was proved that DDA can simulate vibration response of assembled blocks well. However, how to determine input parameters was not investigated and further study is necessary.

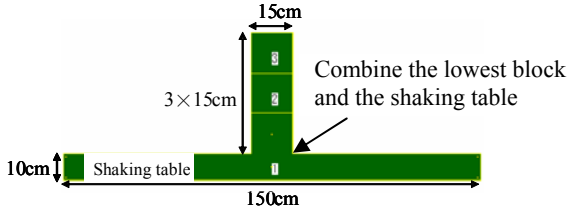

Fig. 14: Analytical model for simulation of the shaking table test.

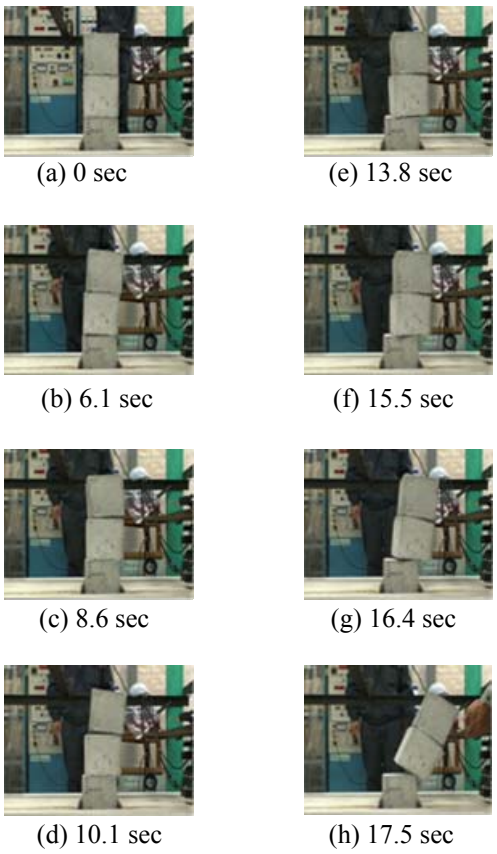

Fig. 13: Block behavior in the case of 5Hz-700gal vibration.

Table 3: Physical properties of block and parameters used in the analysis

Poisson's Ratio	0.2
Friction Angle(°)	36.4
Young's Modulus(kN/m2)	1.49×10^7
Unit Weight(kN/m3)	21.56
Time Interval(sec)	0.001
Contact Spring Stiffness(kN/m)	20000

Table 4: Analytical results of block behavior

Frequency(Hz)	Amplitude(gal)	Behavior
3	400	Stable
3	700	Topple
5	400	Displacement without toppling
5	700	Topple

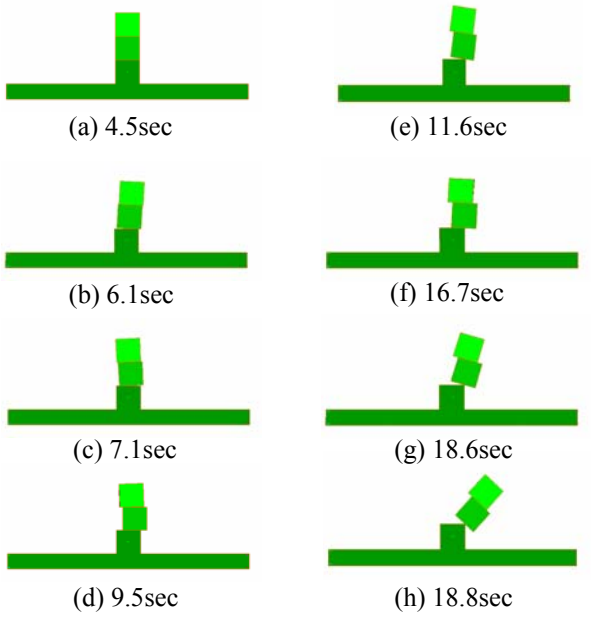

Fig. 15: Result of simulation in the case of 5Hz-700gal vibration

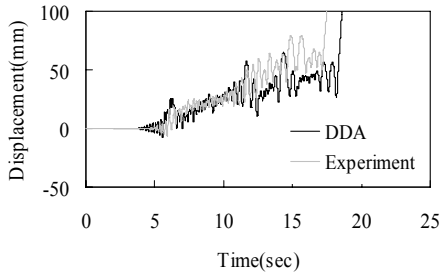

(a) Horizontal displacement of the top block

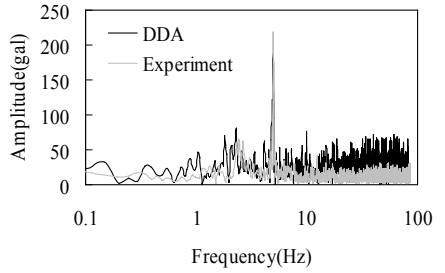

(b) Horizontal acceleration spectrum of the top block

Fig. 16: Comparing DDA result with experimental result (5Hz-700gal vibration).

4. Conclusions

In this study, we inspect the applicability of DDA under dynamic condition by comparing DDA simulation with the analytical solution of a block behavior on the horizontal shaking table and with the results of assembles blocks test on a shaking table. From the first study, it was found out that frictional force between blocks should be represented accurately with the soft contact spring stiffness, but stiff enough to prevent penetration, to simulate block behavior under dynamic condition with high dimensional accuracy by using DDA. In regard to input parameters, we could get appropriate results when kn/m is about 1.0×10^5 and we think that this measure is valid for dynamic problem of a single block. In addition, input parameters have a decisive influence on the accuracy of analysis and error is very large when input parameters are out of appropriate range. We note that this is not because system violates numerical stability condition caused by Newmark method, but because contact judgment of open-close iteration is not done appropriately. From the second study, it was proved that DDA can simulate vibration response of assembled blocks accurately. However, how to determine input parameters was not investigated. Thus, it is difficult to assess the validity of DDA results for actual dynamic problem at this time. We need to explore how to determine contact parameters between blocks more in detail in order to apply DDA to multi-block dynamic problem.

References

Akao, S., Ohnishi, Y., Nishiyama, S., Yano, T., Fukawa, T., Nishimura, T. and Urano, K., Vibration Analysis of laminated blocks by discontinuous deformation analysis, 4th Asian Rock Mechanics Symposium, ISRM International Symposium, 2006.

Doolin, D. M. and Sitar, N., Time Integration in Discontinuous Deformation Analysis, Journal of engineering mechanics, ASCE, 2003, 249-258.

Hughes, T. J. R., Analysis of transient algorithms with particular reference to stability behavior, Computational methods for transient analysis, T. Belytschko and T. J. R. Hughes, eds., Elsevier Science, Amsterdam, 1983.

Kamai, R. and Hatzor, Y. H., Dynamic back analysis of structural failures in archeological sites to obtain paleo-seismic parameters using DDA, Proc. of ICADD-7, 2005, 121-136.

MacLaughlin, M. M. and Sitar, N., A Gravity Turn-On Routine for DDA, Proc. of ICADD-3, 1999, 65-74.

Ohnishi, Y., Nishiyama, S., Sasaki, T. and Nakai, T., The Application of DDA to Practical Rock Engineering Problems: Issues and Recent Insights, Proc. of ICADD-7, 2005, 277-287.

Shi G. H. and Goodman R.E., Discontinuous Deformation Analysis, Proc. 25th U.S. Symposium on Rock Mechanics, 1984, 269-277.

Fundamental studies for dynamic response of simple block structures by DDA

T. SASAKI [1], I. HAGIWARA[1], K. SASAKI[1], Y. OHNISHI[2] and H. ITO[3]

[1]Suncoh Consultants Co. Ltd., Tokyo, JAPAN
[2]Kyoto University, Kyoto, JAPAN
[3]Central Research Institute of Electric Power Industry, Chiba, JAPAN

In order to obtain the relations between the natural frequencies of elastic block structures and applied accelerations, the authors studied several cases of simple block structures under harmonic accelerations by Discontinuous Deformation Analysis (DDA) to prepare for a shaking table experiment under the centrifugal force of a complex block structure. The results show continuum and discontinum models are similar in the small deformation behavior.

Keywords: Dynamic response analysis; DDA; Natural frequency; Amplification rate

1. Introduction

Dynamic response of an elastic body depends on natural frequencies of a structure and frequencies characteristics of an applied acceleration in general. Since, the authors studied earthquake response of actual rock slopes by DDA (Sasaki *et al*. 2004, 2005). But, there are many factors influenced for the response, those are elastic modulus, penalty, boundary conditions, applied acceleration frequencies characteristics and so on. Hence, it was very confused to explain the results.
The purpose of this research is to obtain the relations between the natural frequencies of elastic block structures and applied harmonic accelerations to prepare for the shaking table experiments under the centrifugal force of complex block structures.

2. Outline of the analysis

The dynamic response analysis of elastic bodies with discontinuities includes three parts in theoretically. The first part is the response characteristic of elastic body to natural frequencies with arbitrary boundary conditions and the second part is frequencies characteristics of an applied acceleration. And the third part is collision of blocks with discontinuous planes.

2.1 Governing equations of motions

The governing equation of the potential energy Π^{sys} for large deformations of continuous and discontinuous elastic bodies is given by Hilbert *et al*. (1993):

$$\Pi^{sys} = \sum_{i=1}^{n} \Pi^{(block)i} = \sum_{i=1}^{n} \left(\Pi^{i} + \sum_{j=1}^{m} \Pi^{i,j}_{PL} \right) \quad (1)$$

The first term on the right side of Eq. (1) is the potential energy of the continuum part, and the second term is the potential energy of the contact between blocks. The first term is given on the finite deformation theory by Lubarda and Lee (1981):

$$\Pi^{i} = \int_{V} \frac{\rho^{c}}{\rho^{0}} \left[\tau^{*}_{ij} \delta D_{ij} - \frac{1}{2} \sigma_{ij} \delta (2 D_{ik} D_{kj} - v_{k,i} v_{k,j}) \right] dV - \int_{\Gamma} \bar{t} \cdot u d\Gamma - F(x,y) \int_{V} [\rho(\dot{b} - \ddot{u}) - c\dot{u}] \cdot dV \quad (2)$$

The first term of Eq. (2) is the strain energy of the velocity field, the second term is the surface traction energy, and the third term is the energy of the inertia force and damping force, where, ρ^0 : density before deformation, ρ^c : density after deformation, τ^*_{ij} : Kirchhoff stress velocity, D_{ij} : deformation velocity tensor, σ_{ij} : Cauchy stress, $\ddot{u}$: acceleration, $\dot{u}$: velocity, ρ : unit mass, *b*: body force, *c*: viscosity coefficient, $\bar{t}$: surface traction force, *V*: volume of a block, and Γ : surface area of a block.
The second term on the right side of Eq. (1) is the potential energy of the contact between discontinuous planes, and is evaluated by minimum potential energy theory by using a penalty as follows:

$$\Pi^{i,j}_{PL} = \frac{1}{2} k_N [(u^j - u^i) \cdot n]^2 - \frac{1}{2} k_T [u^j_T - u^i_T]^2 \quad (3)$$

where, k_N: penalty coefficient in the normal direction, k_T: penalty coefficient in the shear direction, $(u^j - u^i) \cdot n$: amount of penetration in the normal direction, u_T: amount of slip in the shear direction, and *n*: direction cosine of the contact plane.

2.2 Discretizations by DDA

DDA (Shi 1989) is formulated from Eq. (1) using the kinematic equations based on Hamilton's principle and minimized potential energy and the equation of motion is expressed by:

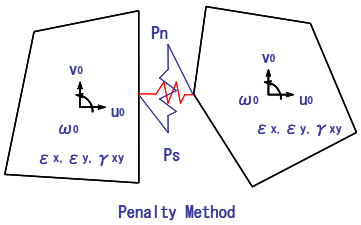

Fig. 1: Unknowns and penalty of DDA (Shi, 1989)

$$M\ \ddot{u} + C\ \dot{u} + K\ u = F \tag{4}$$

where, M: mass matrix, C: viscosity matrix, K: stiffness matrix, F : external force vector, $\ddot{u}$: acceleration, $\dot{u}$: velocity, and u: displacement of the center of a block.

2.3 Numerical integrations

The kinematic equation of motion Eq. (4) is solved by Newmark's β and γ method (Hilbert *et al*., 1993) by using parameters β = 0.5 and γ = 1.0, and the algebraic equation for the increase in displacement is solved for each time increment by the following three equations:

$$\widetilde{K} \cdot \Delta u = \widetilde{F} \tag{5}$$

where,

$$\widetilde{K} = \frac{2}{\Delta t^2} M + \frac{2\eta}{\Delta t} M + \frac{\rho^c}{\rho^0}[K_e + K_s] \tag{6}$$

$$\widetilde{F} = \frac{2}{\Delta t} M \cdot \dot{u} + (\Delta F - \sum \int \sigma dv) - M\,\alpha(t) \tag{7}$$

where, Δu : incremental displacement, K_e : stiffness matrix of linear term, K_s : initial stress matrix caused by rigid rotation, and $\alpha(t)$: time history of earthquake acceleration.

The relations between displacements, velocities and accelerations at an arbitrary point of a block at time t in step i are expressed by the following three equations, respectively.

$$u_i = [D_i] = \frac{\Delta t^2}{2}\frac{\partial^2[D(t)]}{\partial t^2} + \Delta t \frac{\partial[D(t)]}{\partial t} \tag{8}$$

$$\dot{u}_i = \frac{\partial[D(t)]}{\partial t} = \frac{2}{\Delta t}[D_i] - \frac{\partial[D(t-\Delta t)]}{\partial t} = \frac{2}{\Delta t}[D_i] - \dot{u}_{i-1} \tag{9}$$

$$\ddot{u}_i = \frac{\partial^2[D(t)]}{\partial t^2} = \frac{2}{\Delta t^2}[D_i] + \frac{2}{\Delta t}\frac{\partial[D(t-\Delta t)]}{\partial t} = \frac{2}{\Delta t^2}[D_i] - \frac{2}{\Delta t}\dot{u}_{i-1} \tag{10}$$

2.4 Viscosity of a body and frictions

The viscosity matrix C in equation (4) can be rewritten as follows in terms of viscosity η and mass matrix M:

$$C = \eta M \tag{11}$$

The physical meaning of viscosity η is the damping of the elastic block itself, the viscosity of air around the rock surfaces and the vegetation on the surface of a rock slope (Sasaki *et al*. 2004).

On the other hand, in earthquake response analysis it is conventional to prevent the reflection of seismic waves from the boundary to the blocks in the analysis area by using dash pot damping elements as shown in Fig. 2. We therefore introduce Voigt-type viscous damping elements between blocks under the contacts.

The potential energy of the penetration between blocks considering contact viscous damping is expressed by Sasaki *et al*. (2005):

$$\prod_{p\eta} = f_t d = \frac{1}{2}\left(p + \frac{\eta_p}{\Delta t}\right) d^2 \tag{12}$$

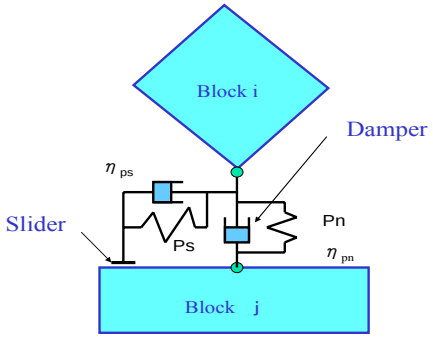

Fig. 2: Viscous damping on contact system

3. Numerical examples

According to the basic concept of numerical models under applied dynamic forces, in an elastic continuous analysis, small displacement is assumed for a model of finite element methods. An earthquake wave comes from the analytical regions at the same time for convenience. On the other hand, in discontinuous analysis for elastic bodies with large deformation by DDA, an earthquake wave comes from the base block and propagates to the upper blocks through penalty springs. Therefore, we applied an earthquake wave only on the base block and the frequency characteristics of the base block depends on the relationship of the applied wave frequency with boundary conditions as a resonance of an amplifications. And in order to obtain the influences of collisions by each block, a single columned, a multi columned and a staggered layered models are examined.

The applied dynamic load are assumed to be harmonic sinusoidal with frequency of 2Hz, 4Hz, 10Hz, 20Hz, 60Hz and a random earthquake wave.

3.1 Single columned six layered model

Fig. 3 shows the case with an input acceleration of 2Hz sinusoidal waves. Fig.4 shows the single column six

layered model. The applied force as acceleration is input at the center of upper point of the base block during from 0.1 second to 1.1second as 2 cycles.

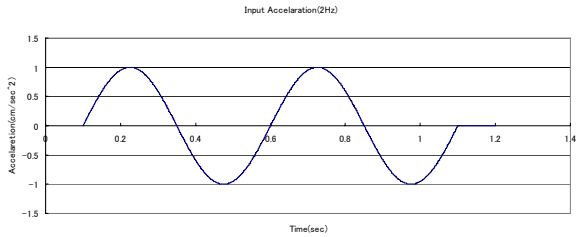

Fig.3: Input acceleration (2Hz sin wave)

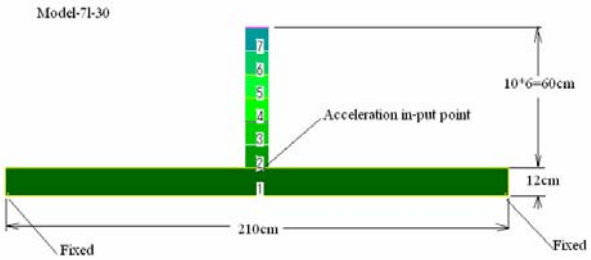

Fig.4: Single column six layered model

Table1. Material properties of the models

Time interval	0.0005sec
Input frequency	2Hz
Elastic modulus(Base block)	200MPa
Elastic modulus(Upper	160MPa
Poisson's Ratio(Base block)	0.2
Poisson's Ratio(Upper blocks)	0.3
Friction angle of the rock	ϕ=30 degrees
Penalty coefficient (Kn)	160MN/m
Penalty coefficient (Ks)	160MN/m
Viscosity coefficient	0.05
Velocity / Energy Ratio	0.81
Unit mass (Base block)	20kN/m^3
Unit mass (Upper blocks)	12kN/m^3

Table 1 shows material properties of the model. In order to get a resonance model between the base block and input applied acceleration, the elastic modulus of base block and the penalty are determined by trial calculations. Fig. 5 shows the acceleration response of each block. The amplification of acceleration ratio for the base block in the presented model is eight times of input acceleration and the upper blocks are eleven to fifteen time. The amplification of acceleration ratios are distribute large to small along to bottom to upper blocks.

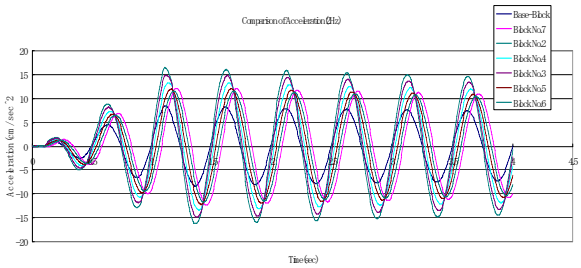

Fig.5: Accelerations response of blocks

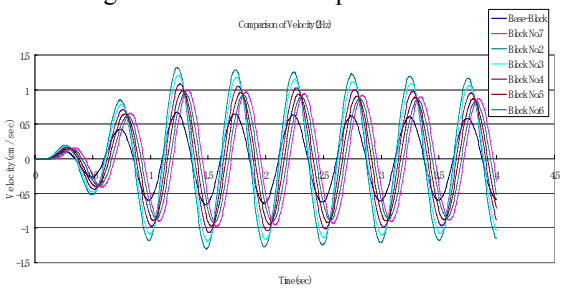

Fig.6: Velocities response of blocks

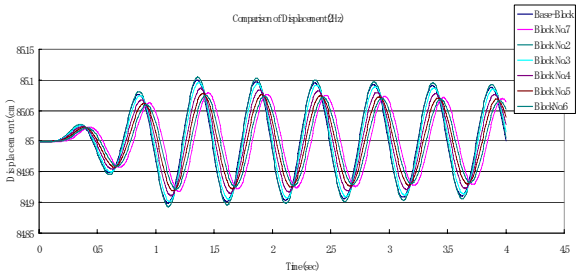

Fig.7: Displacements response of blocks

The time differences of the phase are ordered form bottom to upper blocks. Fig.6 and Fig.7 show the velocities and the displacements response of each block. The amplification ratios are same tendencies of the case of accelerations. Those results agree with the simple one degree of model theory.

3.2 Staggered five layered model

In ordered to obtain the influence of collisions between blocks in the horizontal direction, Fig.8 shows five layered staggered model. Fig.9 shows the acceleration response of the base, the middle and the top block. The base and the top block have same tendencies with the single column six layered model.

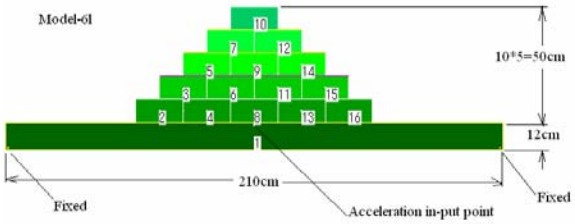

Fig.8: Five layered staggered model

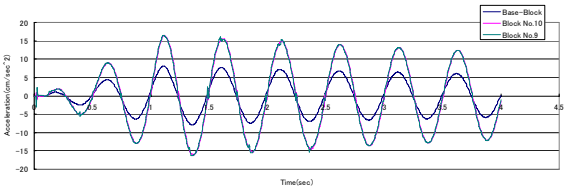

Fig.9: Accelerations response of blocks

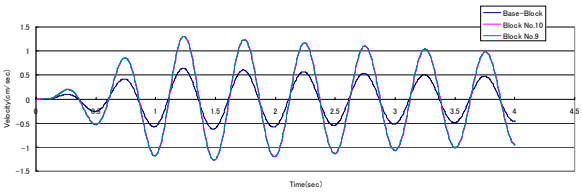

Fig.10: Velocities response of blocks

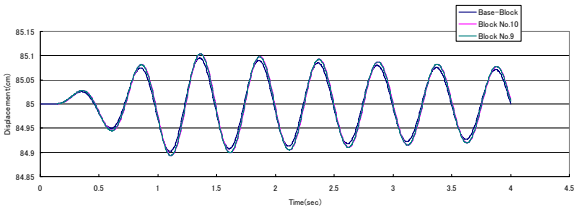

Fig.11: Displacements response of blocks

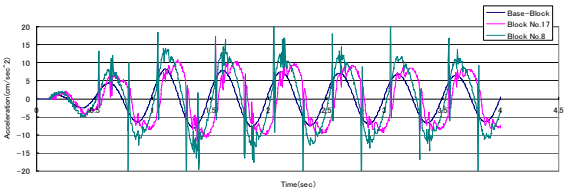

Fig.13: Accelerations response of blocks

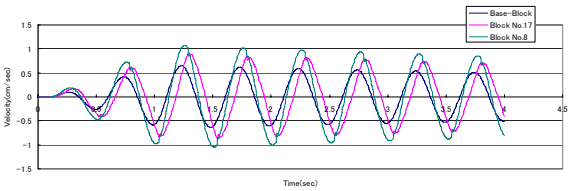

Fig.14: Velocities response of blocks

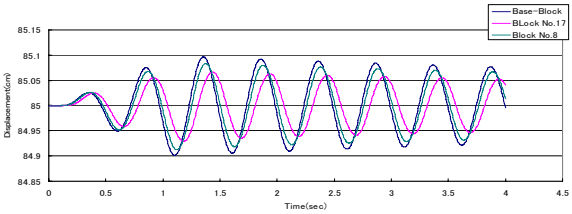

Fig.15: Displacements response of blocks

In order to avoid a letter of stitch at the change points of accelerations directions, acceleration responses are calculated by differentiating velocities directly. Fig.10 and Fig.11 show velocities and displacements response of the base, the middle and the top blocks. The amplification ratios are in the same tendencies of the case of accelerations and there are no influences of collisions by side blocks.

The influence of the collisions of the side blocks appears in a letter of stitch. The amplification ratios are in the same tendencies of the case of accelerations and there are no influences of collisions by the side blocks.

3.3 Five columns six layered model

In order to obtain the influence of collisions between blocks in the horizontal direction and compare with the single column and the staggered model, the five columns six layered model is analyzed. Fig.12 shows five columns six layered model. The material properties and input accelerations are the same as the single column and the staggered models. Fig.13 shows the accelerations response of the base, middle and top block. Influences of collisions by horizontal blocks appear at the change points of accelerations directions of side blocks. This case, accelerations and velocities are calculated form displacements. Fig.14 shows the velocity response and the influences of collisions appear at the middle block. Fig.15 shows the displacements response and no influences of collisions.

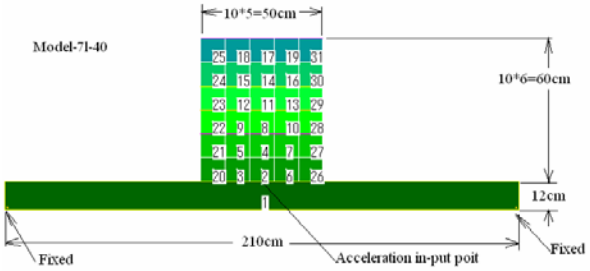

Fig.12: Five columns six layered model

3.4 Random accelerations wave model

In order to obtain the influences of random acceleration waves as earthquake, we applied EL-Centro (N-S) recorded wave for the single column six layered model. Fig.16 shows the accelerations of input point and the response of the base block of two kinds of elastic modulus as 1GPa and 2GPa respectively. The base block amplification of acceleration ratio is 0.5 to 3.0 times of input accelerations.

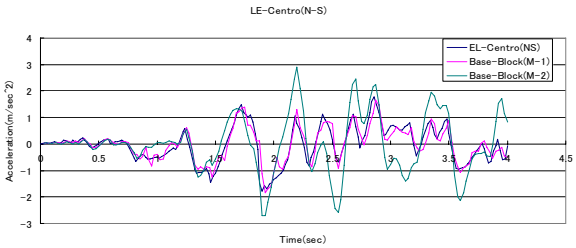

Fig.16: EL –Centro (N-S) input and the base block accelerations response of the two models

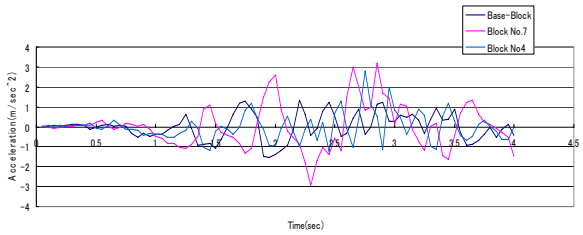

Fig.17: Accelerations response of blocks

In this case, the time interval is 0.005 second. Fig.17 shows the accelerations response of the each block. There are no pulse shape patterns as shown Fig. 9 and Fig. 13 appearing at the middle part of block by collisions of blocks rotations. For this reason, the time interval of random waves input accelerations is ten times of the harmonic sinusoidal wave input cases.

3.5 Shaking table experiments model

Fig.18 shows shaking table experiments of a two dimensional model and blocks were piled in twenty layers and forty columns, the actual tested model was tree dimensional. Table 2 shows material properties of the experiment models and blocks were made by gypsum.

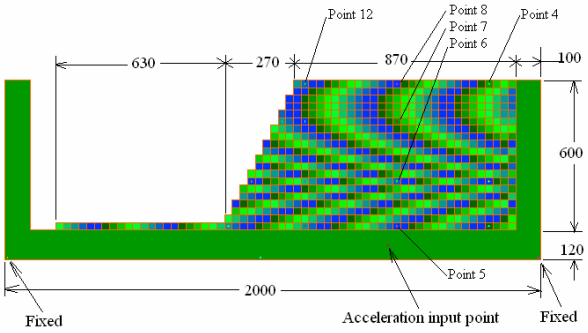

Fig.18: Shaking table experiments model

Table 2. Material properties of model

Time interval	0.0005sec
Input frequency	60Hz
Elastic modulus(Base block)	2GPa
Elastic modulus(Upper blocks)	120MPa
Poisson's Ratio(Base block)	0.15
Poisson's Ratio(Upper blocks)	0.35
Friction angle of the rock	ϕ=30 degrees
Penalty coefficient (Kn)	120MN/m
Penalty coefficient (Ks)	120MN/m
Viscosity coefficient	0.05
Velocity / Energy Ratio	0.81
Unit mass (Base block)	78kN/m^3
Unit mass (Upper blocks)	1.26kN/m^3

Fig.19 shows acceleration of actuator input at base block. The acceleration applied was 60Hz and 30gal at first step, 80gal at second step, 100gal at third step, 200gal at forth step and 300gal at five step. And Fig.20 shows the acceleration response of base block.

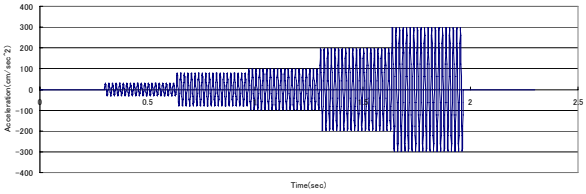

Fig.19: Acceleration of input point

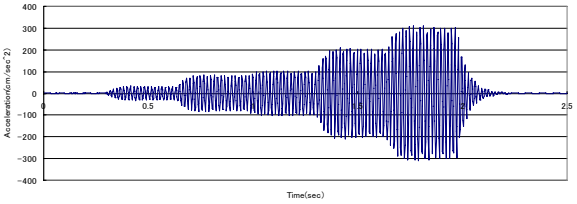

Fig.20: Acceleration response of the base block

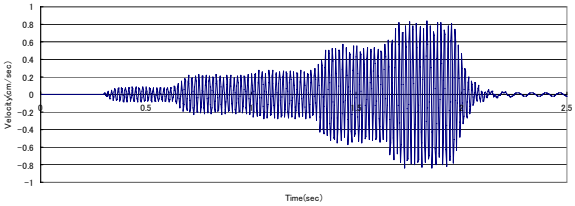

Fig.21: Velocity response of the base block

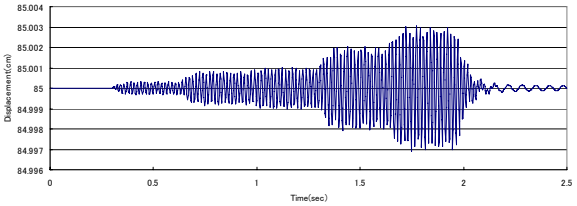

Fig.22: Displacement response of the base block

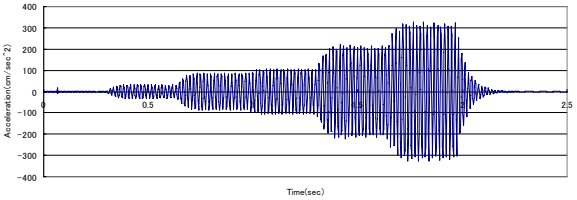

Fig.23: Acceleration response of point No.5

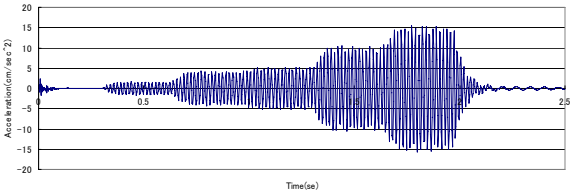

Fig.24: Acceleration response of point No. 6

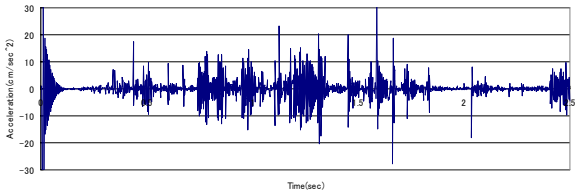

Fig.25: Acceleration response of point No. 7

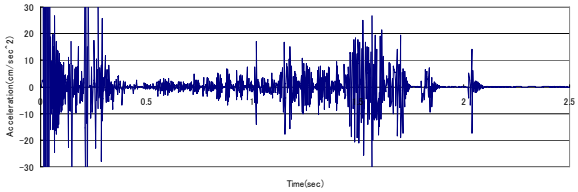

Fig.26: Acceleration response of point No. 8

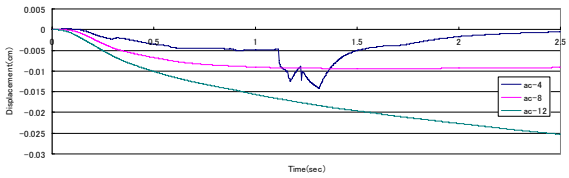

Fig. 27: Displacements response of point No.4, 8, 12

In this case, the base block amplification of acceleration ratio is about thirteen times of the input acceleration and the maximum acceleration is controlled in calculations at the same values of the actuator and the gravity forces by the centrifugal forces was 30G. Fig.21 and Fig.22 show the velocity and the displacement response of the base block. Judging from these results, the natural frequency of the base block is estimated about 20Hz with the boundary conditions.

Fig.23 shows the acceleration of point No.5 in the upper bock as shown in Fig. 18 and amplitude is almost same as the base block.

Fig. 24 shows the acceleration of point No.6 as seven layers from the base block. The rate of amplitude is decreases by 1/15, compared with the base block. Fig. 25 and Fig. 26 show the acceleration response of point No.7 and No.8.

The shape of acceleration mode of the base block disappears and the most response of accelerations is caused by collisions between blocks as pulse shapes.

Fig.27 shows the displacement response of point No.4, 8 and 12 along the surface of model. The displacement of point No.4 as right hand side block, the deformation developed toward the left hand side as slope side at first, and finally turned over and developed toward the right hand side. And the displacement of point 8 and 12 are developed toward the left hand side monotonously. Comparison between a shaking table experiments under the centrifugal force and DDA, the DDA results are relatively conservative, which is the same as what Tsesarsky *et al*. (2002) pointed out and several blocks of the near slope side failed during the experiments.

4. Conclusions

The authors studied the actual natural slopes rock fall by earthquake. However, the real natural models of the boundary conditions and the input earthquake wave frequencies characteristics are complex and vague, so it is very difficult to understand and analyze the results.

Hence, in order to obtain the factors influencing the results, we examined simple block models applying harmonic sinusoidal accelerations prepared for the shaking table experiments under the centrifugal forces and compared the results between the experiments and DDA. The result of wave propagations of the simple column model agrees with the small deformation theory of small acceleration. And the collisions by contacts between blocks influence the response of accelerations significantly for multi columned model, but no influence for the displacements and small for the velocities in harmonic and random wave accelerations. The unnatural stitch accelerations occur in accelerations response in small time intervals by collision between blocks for the multi columned models. This phenomenon can be improved to differentiate displacement results directly by controlling the time interval.

References

Hatzor Y.H., Arzi A.A. and Tsesarsky M., Realistic dynamic analysis of jointed rock slopes using DDA, *Proc. of ICADD-5*, pp. 47-56, BALKEMA, 2002.

Hilbert, L. B. JR, et al., A new discontinuous finite element method for interaction of many deformable bodies in geomechanics, U. C. Berkeley, 1993.

Lubarda , V. A. and Lee, E. H., A correct definition of elastic and plastic deformation and its computational significance, *Jl. of Appl. Mech.*, Vol. 48, pp.35-48, 1981.

Sasaki, T. et al., Earthquake response analysis of a rock falling model by Discontinuous Deformation Analysis, *ISRM Symposium & 3rd Asia Rock Mechanics Symposium* , Millpress, pp1267-1272, 2004.

Sasaki, T. et al., Earthquake response analysis of a rock falling by Discontinuous Deformation Analysis, *Seventh International Conference on the Analysis of Discontinuous Deformation*, pp.137-146, 2005.

Shi G.H. ,Block system modeling by discontinuous deformation analysis, *Univ. of California*, Berkeley, Dept. of Civil Eng. August, 1989.

Tsesarsky M. and Hatzor Y.H., Dynamic block displacement prediction-validation of DDA using analytical solutions and shaking table experiments, *Proc. of ICADD-5*, pp.195-203, BALKEMA, 2002.

Application of discontinuous deformation analysis in prediction analysis of natural dam formation by landslide

E. HAMASAKI [1], A. SASAKI [2], and Y. OHNISHI [3]

[1] Advantechnology, inc., Sendai, JAPAN
[2] Tohoku University, Sendai, JAPAN
[3] Kyoto University, Kyoto, JAPAN

The movement of the landslide was simulated in DDA, and the rock property was estimated when the debris of the landslide form the natural dam in the valley. It is confirmed that the landslide is considered to begin to move when value of the cohesion of the block joint is under 10 KPa and value of the frictional angle of the joint is less than 20 degree. These calculated properties of the joint agree with the general value of the joint of the landslide on this site. In addition, the velocity and the mode of movement of the landslide are examined. As a result, it is caught that the movement of the landslide began from the lower block and spread to the upper block gradually. DDA is useful to examine the sensitivity analysis of the landslide movement.

Keywords: DDA; Landslide; Natural dam; Sanbagawa metamorphic belt; Japan

1. Introduction

When a landslide, situated on a valley side slope, slides downward, the valley is filled up with the debris. As a result, the lake which is created by the natural dam appears in the upper area of the dam. If the natural dam collapses, a debris flow occurs in the downstream and damages the downstream area. Therefore, the countermeasure to the landslide along a river is very important in order to maintain a river system. Although detailed investigation of the landslide are needed to draw up the countermeasure to the landslide, the numerical analysis about the activity conditions of the landslide is significant to draw up the plan of the countermeasure to the landslide (Takeuchi and Hamasaki, 2001). From the above view points, we tried sensitivity analysis by using Discontinuous Deformation Analysis (DDA) (Shi and Goodman 1984) in order to examine the factors which lead to the formation of the natural dam by landslide. There are few examples which solved a landslide problem in DDA (Hamasaki and Sasaki 2004).

2. Study site

Study site is located in Sanbagawa metamorphic belt, which is composed of green-schist and black-schist of Mesozoic, on Shikoku Island in Japan. Many landslides occur in Sanbagawa metamorphic belt because the surface rock of this area is deep weathered (e.g., Terado, 1986). In recent years, these landslides are sliding at heavy rain.

The target slope is located in the valley side slope where many landslides are found. We select a section of the slope for this study because the section of the slope has not been slid yet. The surface part of the rock has been sheared due to intense crushing and subsequent deep weathering. The average angle of the slope is 19°. The scale of the landslide is considered to be 550 m long, 200 m height, if the slope collapses. Slip surface of this landslide is thought to exist about 50m depth from surface of the slope (Fig. 1).

The difference in elevation from the valley bottom to the road is 15 m. The town exists downstream from the spot where the natural dam formation is expected.

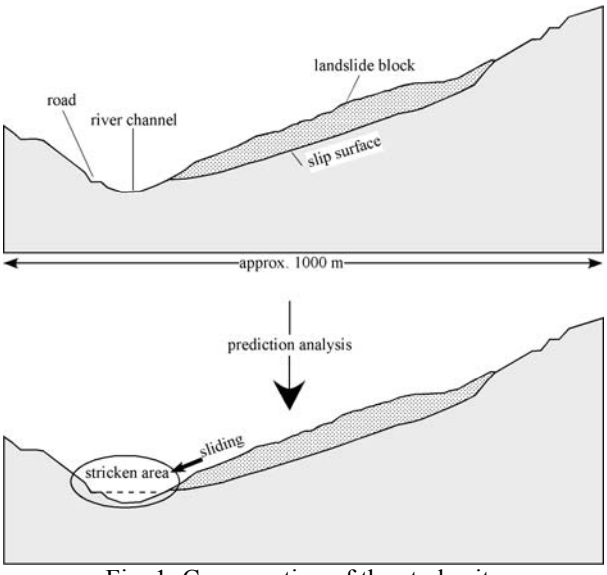

Fig. 1: Cross section of the study site

3. Modeling

3.1 Simulation of formation of the natural dam by landslide

If the landslide occurs on the valley side slope, a lot of debris will bury the valley bottom. The goal of this simulation is to clarify the parameters of the rock property of when the landslide debris fills the valley to the height of the road on the opposite side of the slope. Therefore, DDA simulation will be repeatedly carried out with converting the parameters until the DDA results will be agree with the qualification.

3.2 Block Model of the landslide mass -Voronoi division-

In this case which the DDA model is built up, model of the landslide mass should be divided into fragments with irregular shape because the rocks of the slope is intense crushing and deep weathering as previously described. Thus, we try to divide into construct the block model using the Voronoi division (Fig. 2). As a result, the landslide mass is divided into the 266 fragments (Fig.3).

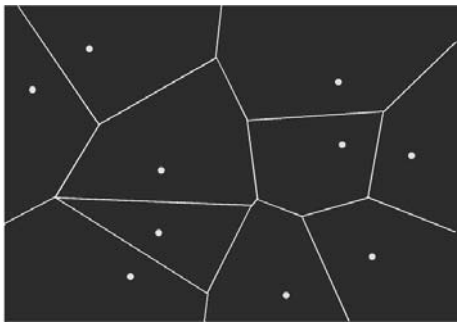

Fig. 2: Division of the block using the Voronoi division.

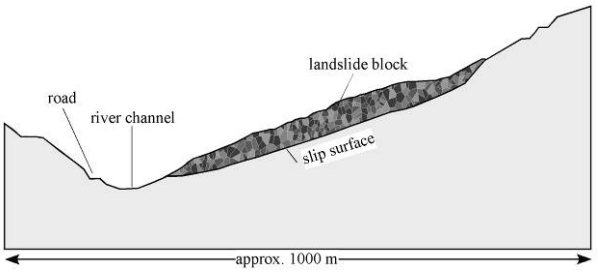

Fig. 3: Block model on this site for DDA using the Voronoi division.

3.3 Parameters for the landslide

The parameters using in the simulation are shown in Table 1. Unit weight of block and Young's module of it are decided from the general data on the landslide in the Sanbagawa metamorphic belt. Poisson ratio and coefficient of attenuation are established from the empirical data of the rock. Frictional angle of joint is varied from 10 to 20 degree. Cohesion of joint is also varied from 5 to 10 KPa.

Table 1. Parameters for the landslide.

Item		Value
Analysis parameters	Displacement Allow Ratio	0.001
	Total Steps	7000
	Maximum Time Step (sec.)	0.1
Block	Unit Weight (KN/m^3)	21.0
	Young's Modules (MPa)	200.0
	Poisson Ratio	0.3
Slope (no displacement)	Unit Weight (KN/m^3)	21.0
	Young's Modules (MPa)	200.0
	Poisson Ratio	0.3
	Coefficient of Attenuation	0.05
Joint	Frictional Angle (degree)	10-20
	Cohesion (KPa)	5.0-10.0
	Tensile Strength (MPa)	0.0

4. Result of the simulation

4.1 Examination of the parameters

First, we tried sensitivity analysis by DDA in order to examine the parameters which are the cohesion of the block joint and the frictional angle of the joint, when the valley is buried up to the height of a road on the opposite side of slope. We confirmed that the landslide mass did not move downward, when value of the cohesion of the block joint is over 11 KPa, and value of the frictional angle of the joint is over 20 degree.

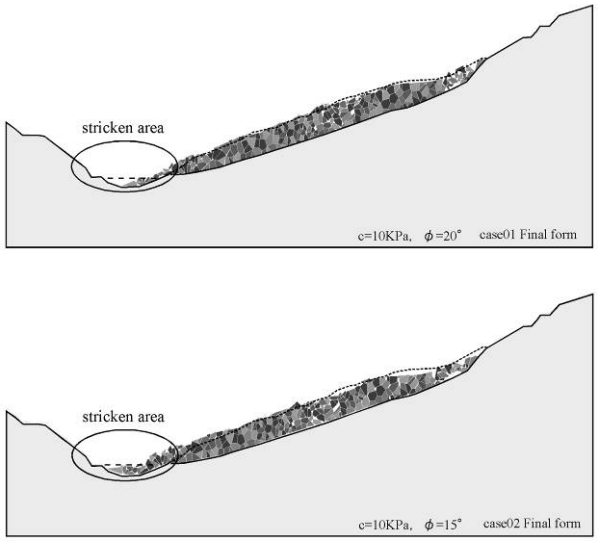

Fig. 4: Final forms of landslide by DDA (c=10 KPa, Φ=20-15°)

Subsequently, we inputted 10 KPa as the cohesion of the block joint, and inputted 20 degree as the frictional angle of the joint (Fig.4; case 01). In this case, the landslide mass moved downward. Although, the tip of the debris reached at river channel, it did not come to bury the valley bottom.

When the cohesion of the joint is 10 KPa, and the frictional angle of the joint is 15 degree, the landslide mass moved downward (Fig.4; case 02). The debris buried the valley bottom, however, the tip of the debris did not reach the height of the road.

In the case that the cohesion of the joint is 5 KPa, and the frictional angle of the joint is 15 degree, the landslide mass moved downward and the top of the debris reached the height of the road (Fig.5; case 03).

Finally, in the case that the cohesion of the joint is 5 KPa, and the frictional angle of the joint is 10 degree, the debris buried the valley completely (Fig.5; case 04).

The above result was arranged in Table 2.

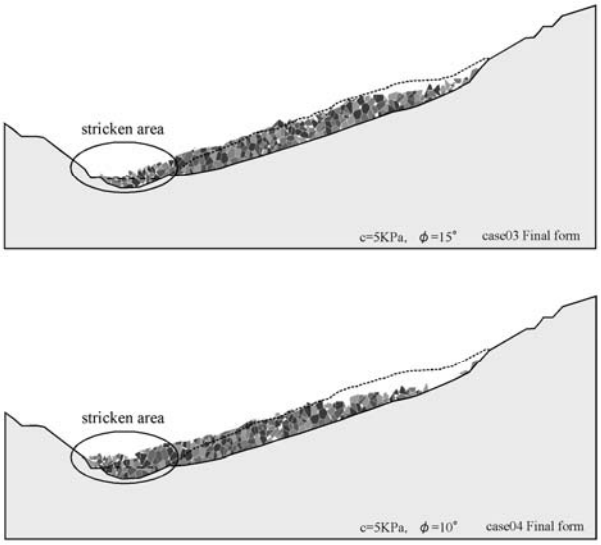

Fig. 5: Final forms of landslide by DDA
(c=5 KPa, ϕ=15-10°)

Table 2. Results of simulations

	cohesion (KPa)	frictional angle (°)	result
case01	10.0	20	no
case02	10.0	15	no
case03	5.0	15	fill
case04	5.0	10	fill

4.2 Velocity of the landslide movement

After parameters of the rock property were determined as case 03, the velocity of landslide movement is estimated.

The landslide mass is divided into 3 parts as follows: no. 2-80 blocks as a lower block, no.81-170 blocks as a middle block, no.171-266 blocks as a upper block (Fig.6). The velocity of the sections is calculated using the average speed of the all blocks of the each section (Fig 7).

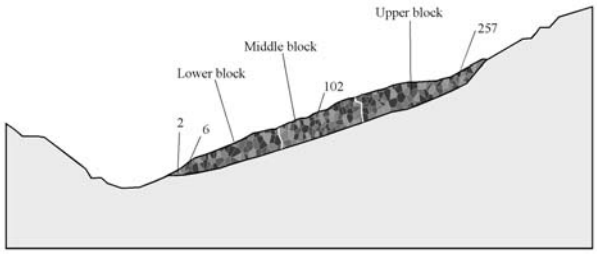

Fig. 6: Final forms of landslide by DDA

Variation of the average movement velocity of the landslide mass is as follows: the peak of movement speed of the lower and middle blocks are recorded at step 11th, and in the upper block, it is recorded at step 6th. It is caught clearly that movement of the landslide have an impact from the lower block to the upper block. The velocity of the lower block picked up gradually until it reached the maximum velocity, and speed is conversely reduced gradually after the maximum velocity. Such variation of the velocity indicates the changes in the mode of movement of landslide. In the early stage, the mode of movement is tension. After maximum velocity recorded, the mode of it changes from tension to compression.

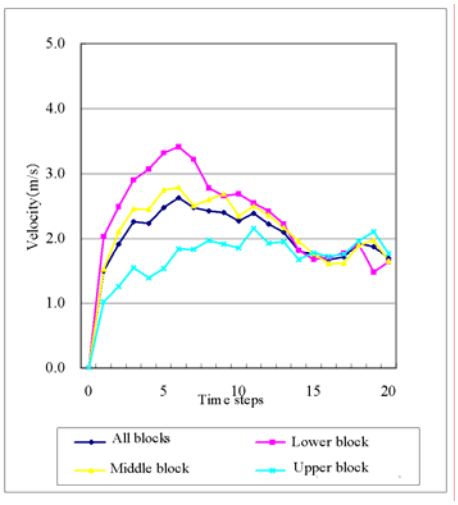

Fig. 7: Average velocity of the each section of the landslide at the case03.

On the other hand, in the middle and upper blocks, the velocity of the blocks fluctuated until it reached the maximum velocity, and subsequently the velocity is

decreased gradually. Such variation of the velocity shows that the tension and the compression are repeated in the middle and upper blocks from the early stages of movement to the end. This mode of movement is considered to agree with the actual landslide movement.

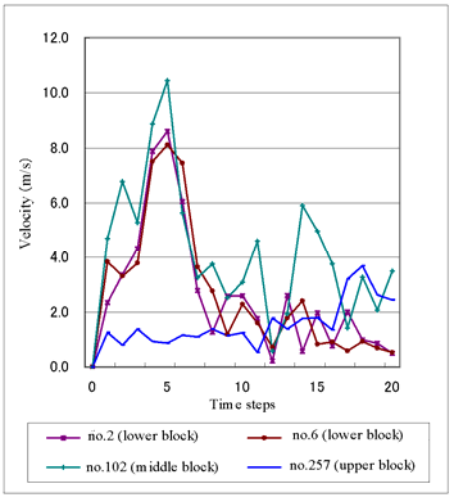

Fig. 8: Velocity of the each block of the landslide at the case03.

Moreover, 4 blocks was extracted from the upper to the lower sections at random, and the velocities of the each block were verified (Fig.8).

The maximum velocities of each block were 10.5 m/sec. (no.102; middle block), 8.6 m/sec. (no.2; lower block), 8.1 m/sec. (no.6; lower block), and 3.7 m/sec. (upper block). The maximum velocity was recorded in step 6th, and it was gradually attenuated the speed until the stop in the lower and middle blocks. On the other hand, in the upper block, the maximum velocity was recorded in step 18th. Such mode of movement shows that the upper block is influenced compression in the early stage of the landslide movement, and the mode of it changes from compression to tension in late stage of the movement.

5. Concluding Remarks

In this study, we carried out the sensitivity analysis by using DDA in order to examine the factors which affect the formation of the natural dam by landslide.

The landslide mass did not move downward, when value of the cohesion of the block joint is over 11 KPa, and value of the frictional angle of the joint is over 20 degree.

The target was filled when the cohesion of the joint is 5 KPa, and the frictional angle of the joint is 15 degree. In that case, the movement of the landslide began from the lower block and spread to the upper block gradually.

DDA methods can be applied to landslide movement. In addition, the displacement process of inner structure of the landslide mass is also in agreement with the actual landslide movement.

References

Hamasaki, E. and Sasaki, A. Study on landslide due to earthquake by using Discontinuous Deformation Analysis. *Proceedings of the ISRM international symposium 3rd ARMS, Millpress, Rotterdam*, 2004, 1253-1256.

Shi, G. H. and Goodman, R. E. Discontinuous deformation analysis. *Proceedings of the 25th U.S. Symposium on Rock Mechanics*, 1984, 269-277.

Takeuchi, N. and Hamasaki, E. Simulation on slope disasters. *Journal of the Japan Society for Computational Engineering and Science*, 2001, **6**, 316-319.

Terado, T. The distribution of landforms caused by large-scale mass movement on Shikoku Island and their regional characteristics. *Memoirs of the Geological Society of Japan*, 1986, **28**, 221-232.

Understanding fracture patterns of rock mass due to blast load – A DDA approach

Z. ZHAO*, J. GU and H. BAO

School of Civil and Environmental Engineering,
Nanyang Technological University, Singapore 639798
(*Email of corresponding author: czzhao@ntu.edu.sg)

Fracture propagation and fragmentation produced by explosive blasting in rock mass is an extremely complex process. Though, laboratory tests on scaled model have been a favorite approach over the past decade, it can only be used for simple cases (simple geometry, small size, simple detonation configuration, etc) due to constraints on cost and reliable measurements. So numerical simulations become an essential complementary tool to investigate the complex wave and fracture propagation phenomena during the blasting process. In this paper, the discontinuous deformation analysis (DDA) is used to simulate the blasting effect on rock mass, to understand the initiation and extension of fractures and eventually the fracture network generation of the rock mass when certain regions of the specimen reach a critical value. A random joint property distribution based on the Weibull distribution is introduced to model the material variation due to the random micro-cracks. The dynamic fracture analysis due to different borehole pressure waveforms (peak pressure, duration, rising time and decaying time) is conducted to verify the fracture patterns of rock mass relating to various conditions. The numerical simulations in general are in good agreement with the theoretical results and close to the relevant experiment findings. The results shown in the paper demonstrate a promising DDA capability in dynamic wave and fracture propagation analyses of rock mass due to blast load.

Keywords: Discontinuous deformation analysis; Weibull distribution; Blasting; Fracture propagation

1. Introduction

Drilled boreholes are widely used for many engineering applications, including drilling and blasting, stimulating oil and gas wells, hydraulic fracturing for geothermal reservoirs, breaking apart rocks with an expansive demolition agent (Sang 2003). Although borehole pressure has been well known by researchers for decades for resource recovery and construction, the mechanism by which rock is broken apart under pressure in a borehole is still not understood well, especially when the borehole is under dynamic loading like blasting. The laboratory scaled blast tests have provided some important guidelines for field practice through the observation of the behavior of down-scaled specimens (Rossmanith et al. 2005), also valuable theoretical study is proceeded based on the theory of elastic wave propagation and fracture mechanics (Rossmanith and Uenishi 2006). But the numerical simulation for modeling the total fracture process is still very limited.

The discontinuous deformation analysis (DDA) has been widely used to model the motions of blocky masses. As the blocks in a DDA model are all independent with each other, the nodes on the interface of the blocks are originally assigned double nodes. Each block boundary can be easily considered as a potential crack, and the crack opening or sliding can be determined based on appropriate strength criteria. So the DDA is very suitable to be used for fracture propagation analysis.

The purpose of this paper is to use the DDA to investigate on how the borehole pressure waveform in rock affects the dynamic fracture propagation and patterns in the scaled blast test. It is necessary to consider the fracture effects associated with the material properties and external forces to control rock fracturing. As rock is an inhomogeneous material, fracturing can be treated as a stochastic process. The material heterogeneity effect is studied by assigning rock joints with different tensile strengths conforming to the Weibull distribution. The effect of the stress-loading rate on the fracturing process will be also studied.

2. Unique features of the DDA

The original "Discontinuous Deformation Analysis (DDA)" was introduced by Shi (1988). As a new discrete element method, many studies on the DDA have been carried out over the last decade, and its applications have been extended to many rock engineering areas (Yin et al 2002; MacLaughlin et al. 2003; Hatzor et al. 2004).

Compared with the other numerical methods, the DDA has several unique features on rock mass analysis which can be generalized as follows:

(1) Its block system seems to resemble the distinct element method but it also more closely parallels the finite element method in the whole problem solving procedure. As a displacement-based implicit method, it can provide satisfying accuracy.
(2) The blocks forming the "elements" of the "mesh" can be any shape or size, even contain holes, which are all independent with each other. The nodes on the interface of the blocks are originally assigned double nodes and there is no need to insert zero-thickness interface elements with double nodes along each line of the block system as commonly used in the FEM.
(3) The whole block system can be considered as a continuous field before block separation appears, just like in a typical FEM analysis. All blocks are glutted together during the analysis when the inter-block stress is less than the joint strength. Block relative movements start to occur when the inter-block stress exceeds the joint property (i.e. opening when the normal stress exceeds the tensile strength, and sliding when the shear stress exceeds the shear strength based on Coulomb's friction law).

Based on the above features, it is ideal to use the block boundary as a potential crack in DDA. A developed DDA program special for the crack propagation analysis is constructed. A series of numerical simulations are carried out to study the rock fracture propagation in the next sections.

3. Numerical simulation and model description

3.1 Model description

A numerical model with borehole was constructed by the DDA. It consists of a blast hole in rock with a free outer boundary, as shown in Fig. 1. The radius of the model and borehole were 0.4m and 0.03m, respectively. The models are divided into quadrangle blocks illustrated in Fig. 2. 1800 blocks with separate joint boundaries are considered. Several measured points have been set along the positive direction of x coordinate for the stress and displacement output. The parameters and calculation conditions are listed in Table 1.

To generate the various applied borehole pressure waveforms, a general form of the applied pressure pulse function (Ito, 1968) was applied as the loading history in the program:

$$P = P_b \xi \left[e^{-\alpha t} - e^{-\beta t} \right] \quad (1)$$

where P_b denote the maximum pressure pulse, α and β are constants for the changes in the rising time

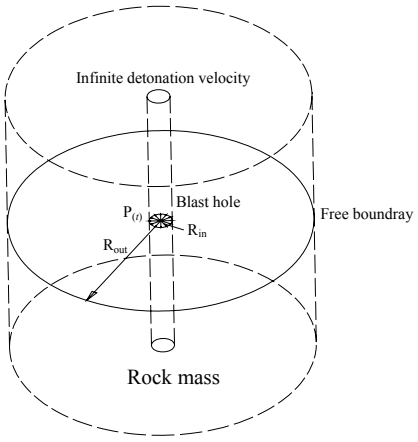

Fig. 1: Geometry of the analysis model

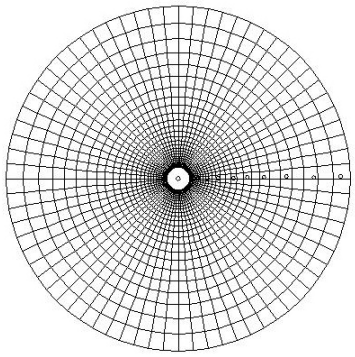

Fig. 2: DDA blocks layout for analysis model

Table 1: Parameters for the analysis model

Parameter	Value
Problem type	Plane strain
Density (kg/m^3)	2650
Poisson's ratio ν	0.3
Elastic modulus E (GPa)	60
Maximum pressure pulse (MPa)	30
Friction angle of joint (°)	30
Cohesion of joint (MPa)	66
Average tensile strength of joint (MPa)	15
Time step Δt (μs)	0.5-2
Total analysis time	(2-5)×loading times till results stable
Factor of successive over-relaxation iteration (SOR)	1.6
Coefficient of uniformity m	2, 5, 20 and 500

and decaying time. Fig. 3 shows the applied pressure-time history with maximum pressure at time t_0 and different β/α ratios.

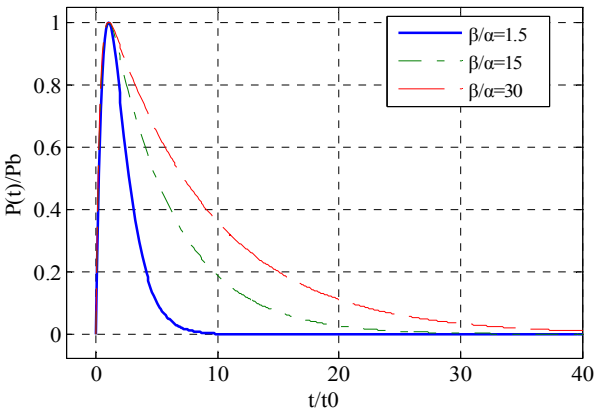

Fig. 3: Pressure-time curves for applied pressure pulses

3.2 Material heterogeneity

As a geological material, heterogeneity is the most intrinsic character of rock mass which can be tested in the mechanics experiments. The results show that the rock sample has very large dispersion on its strength behavior. In this study, the material heterogeneity is modeled with the Weibull distribution.

Although the heterogeneity of rock is characterized by heterogeneity in both the strength and elastic modulus, it is difficult to determine both non-homogeneities experimentally. Therefore, it is reasonable to consider the joint strength of the rock mass as a function of microstructures to account for the heterogeneity while using a constant elastic modulus. To consider this material heterogeneity, random numbers satisfying the Weibull's distribution were generated to give the spatial distribution of the microscopic properties in the analysis model.

The two-parameter Weibull distribution could be expressed as:

$$f(T) = \frac{m}{\mu}\left(\frac{T}{\mu}\right)^{m-1} \exp\left(-\left(\frac{T}{\mu}\right)^{m}\right) \qquad (2)$$

where μ is the mean value, m is the shape parameter describing the probability distribution parameter T which can be obtained as:

$$T = \mu\left(\ln(U(0,1))\right)^{1/m} \qquad (3)$$

where $U(0,1)$ represents the random data between 0 and 1 generated by Monte Carlo method.

The average value $E(T)$ can be expressed as:

$$E(T) = \mu \cdot \Gamma\left(1+\frac{1}{m}\right) \qquad (4)$$

where Γ is the gamma function. Different μ is used to keep the same value of $E(T)$ which makes the numerical models under the same strength conditions.

The tensile strength of rock joint is chosen to conform to the Weibull distribution. Fig. 4 shows the Weibull distribution with the shape parameter m and the mean value 15 MPa. From this figure, it can be seen that the presence of the shape parameter m allows Weibull function to take a wide variety of shape. The shape parameter m can be defined as the heterogeneity index. A smaller m implies more heterogeneous and m=∞ means material is homogeneous.

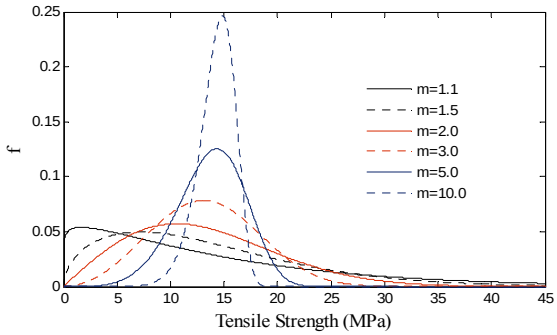

Fig. 4: Probability density of Weibull distribution

In our study, three cases for m=2, 5 and 20 were performed to examine the influence of rock mass heterogeneity on fracture patterns.

4. Fracture propagation simulation results and discussion

4.1 Fracture propagation simulation

The rising time t_0 varies between 10, 50 and 250μs with β/α=1.5 and 30 to investigate the dynamic fracture processes due to the applied pressure waveforms. For simplicity, decaying time is two time that of rising one when β/α=1.5 while 6 times that of rising one if β/α=30.

The formation of the fracture patterns in all cases will experience the process of cracks initiation, propagation and arrest. First, the radial tensile fractures start from the vicinity of the compressive failure zone. After that, the tensile stress field causes the radial cracks to run, which is followed by stress releases around the running cracks. The differences in the crack growth are mainly due to pulse and shape of the applied pressure, specimen dimension and the distribution of the material imperfections. Finally, all the cracks arrest and the final fracture patterns forms. The attenuated waveforms may be still active in the material for a long time, but it has no influence on the final cracks patterns.

Although the same maximum pressure was applied to all of the models, the stress field in the rock model

varied significantly with increases in the rising time. The different stress fields resulted in different fracture processes for each model. When t_0=10 and 50μs, the stress field generated a compressive fracture zone around the borehole with radial tensile cracks in its vicinity which arrest quickly. When t_0=250μs, radial tensile cracks developed in the vicinity of the borehole and propagate continuously to form long cracks. The results of the final fracture patterns in scaled blast model under different conditions are shown in Fig. 5. In every time step, the program will automatically check all joint boundaries with the Mohr's and cut off criteria. For the gray back color specimen, all the joint boundary lines are drawn gray at first. If the strength boundaries reach the criteria, it indicates a failure of the rock mass in the region, cracks will initiate indicated by black lines in the next time step.

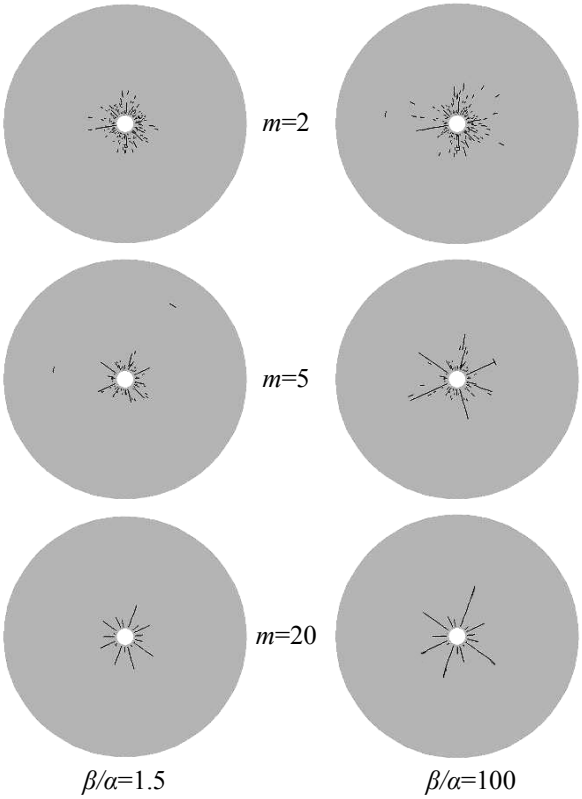

(a)

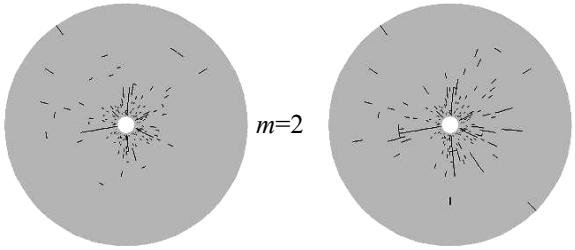

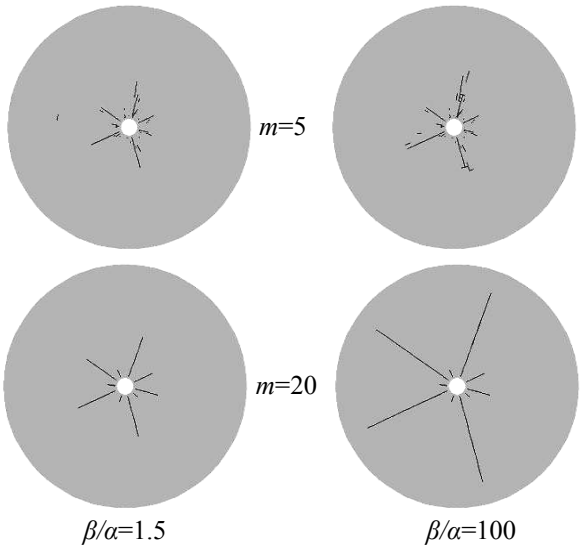

(b)

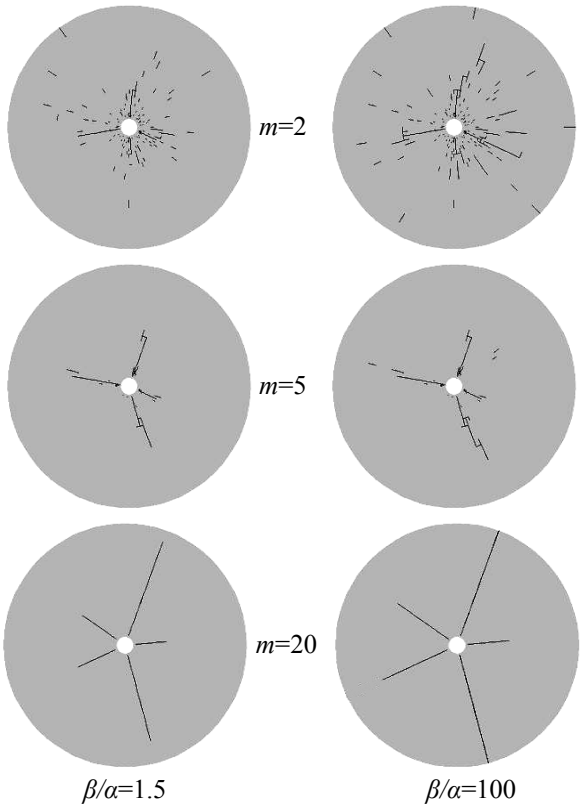

(c)

Fig. 5: Fracture patterns:
(a) t_0=10us; (b) t_0=50us; (c) t_0=250us

4.2 Numerical result discussions

4.2.1 Initial loading rate on the fracture processes

Fig. 5 shows that the fracture processes are markedly affected by the rising time of the pressure that is applied to the borehole wall. In Fig. 5(a), intense short cracks around the vicinity forms with several cracks propagating a little longer. The fast stress release affects crack propagation and results in shorter cracks. While in Fig. 5(c), the interval of the cracks is larger and stress released between the cracks has little effect on the growth of adjacent cracks which results in longer crack extensions. This implies that the fracture processes are closely associated with initial pressure loading rates applied to the borehole. A high stress-loading rate increases the number of radial cracks and leads to intense stress release around the running cracks; at lower stress-loading rates, the number of cracks and crack arrest caused by stress released at adjacent cracks were reduced but led to longer crack extension (Hirata et al., 1999).

4.2.2 Influence of the β/α

The parameter of β/α controls the decaying time of the waveforms. Under the same rising time loading, more energy affects on the specimen if the decaying time is longer. But from the results in Fig. 5, it indicates that only when the rising time is small, the final patterns will be different. As seen in Fig. 5(a) and (b), both the number and length of the cracks increase compared with the case under the short decaying time. But when the rising time becomes longer as in Fig. 5(c), there were little significant differences in the fracture zone; only the length of cracks increased as the decaying time increased. These findings indicate that the fracture patterns were affected to a greater extent by the rising time than the decaying time. Therefore, it is possible that if the rising time becomes significantly long, then the maximum extension of the tensile radial cracks will not be very dependent on the increase in the decaying time. This result agrees well with the known fracture processes of work obtained using static borehole pressures. For static borehole pressures, the crack extension depends on the maximum value of the applied pressure.

4.2.3 Influence of the heterogeneity

The shape parameter m from small to large decides the rock mass from totally heterogeneous to uniform. From Fig. 5, it shows that there have great differences on the final fracture patterns under different m. This indicates that the heterogeneity of rock mass can strongly affect fracture processes and fracture patterns. When m is small, the number of the cracks increases substantially and fracture patterns become very chaotic (Dally et al., 1975), the final fracture patterns are hard to estimate and this sufficiently account for the effect of the large extent of the material dispersion. When m=20 as shown in Fig. 5 (c), the number and length of the cracks become similar as the simulation when $m=\infty$, only the shape and position of the cracks are different.

4.2.4 Effect of the maximum pulse

The variance of the waveforms mainly depends on both the loading time and loading value. In this section, a larger maximum pressure pulse is considered to observe its influence. The case in Fig. 5 (b) when β/α=30 is taken as a comparison. All other parameters are the same but the maximum pressure pulse becomes twice that of the original case. One more case for m=500, which corresponds to a uniform material, is modeled.

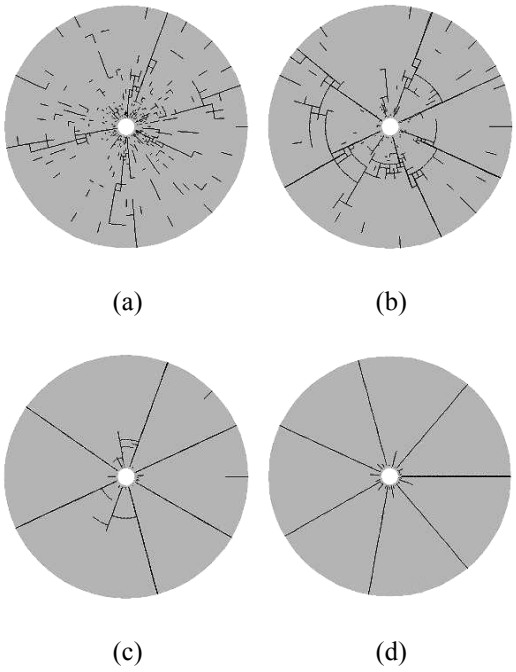

Fig. 6: Fracture patterns for a larger maximum pulse with β/α=100
(a) m=2; (b) m=5; (c) m=20; (d) m=500

The final fracture patterns are shown in Fig. 6. The fracture patterns differ in the shape and position compared with that in the Fig. 5 (b). More cracks initiate and propagate longer. When the attenuated pressure waves hit the free surface, it reflected back as a tensile stress wave towards the center of the borehole. Spalling is possible in certain areas if the resulting stress amplitude is stronger than the critical fracture strength of the material. This indicates that when the maximum pressure pulse is large, it will become a primary influence on the final fracture patterns. The effect of the reflection waves should be cautiously

considered. Spalling and pie-shape cracks will occur due to the large reflected tensile stress. When m=500, the material of rock mass becomes more homogeneous. This can be seen in Fig. 6 (d) the fracture pattern is nearly symmetrical.

5. Conclusions

In studying what happens in a real blast, it has been common to use the numerical methods to simulate the fracture processes on a laboratory scaled blast model. In this paper, numerical studies are carried out for various applied pressure forms and material heterogeneity to investigate their influences on the dynamic fracture processes in rock by the DDA approach.

The simulation shows that the fracture patterns are mostly affected by the rising time than the decaying time. A higher stress-loading rate increased the number of radial cracks, but the rapid stress released from adjacent cracks affected crack extension and resulted in shorter cracks. At lower stress-loading rate, few cracks initiate but propagate longer. The heterogeneity of rock mass can strongly affect fracture processes. The number of the cracks increased as the shape parameter m decreased while the length of the cracks increased as the shape parameter m increased. Finally, the effect of the maximum pulse is considered. The larger pulse value will generate more severe fracture patterns and its reflection effect will become important. Spalling and pie-shape cracks are observed due to the reflection of the waveforms.

References

Dally J.W., Fourney W.L. and Holloway D.C., Influence of containment of the bore hole pressure on explosive-induced fracture. *Int.J. Rock Mech*, 1975, Min. 12:5-12.

Hatzor Y.H., Arzib A.A., Zaslavskyc Y. and Shapira A., Dynamic stability analysis of jointed rock slopes using the DDA method: King Herod's Palace Masada, Israel. *Int. J. Rock Mech Min*, 2004, 41, 813-832.

Hirata A., Yoshinaga T., Matsunaga H. and Kaneko K., Measurement of growth of tension crack by X-ray computed tomography. *Proc. Japan-Korea Joint Symposium on Rock Engineering*, Japan, 1999,587-592

Ito I., Rock mechanics related to blasting. *J. Jpn Explosive Society*, 1968, 29(4), 246-267.

MacLaughlin M.M., Elizabeth A.B. and Doolin D.M., A decade of DDA validation. *In: Proceedings of the Sixth International Conference on Analysis of Discontinuous Deformation*, Norway, 2003, 13-31.

Rossmanith H.P., Hochholdinger V.A. and Uenishi K., Understanding size and boundary effects in scaled model blasts-plane problems. *Fragblast*, 2005, V9(2), 83-125.

Rossmanith H.P., Uenishi K., On size and boundary effects in scaled model blasts-fractures and fragmentation patterns. *Fragblast*, 2006, V10(3-4), 163-211.

Sang H.C., Dynamic fracture process analysis on rock and its application to fragmentation control in blasting. *PhD thesis*, Hokkaido University, Japan, 2003.

Shi G.H., Discontinuous deformation analysis: a new numerical model for the statics, dynamics of block system. *PhD thesis*, Berkeley, University of California, 1988.

Yin K.L., Jiang Q.H. and Wang Y., Numerical simulation on the movement process of Xintan landslide by DDA method. *Chinese Journal of Rock Mechanics and Engineering*, 2002, 21(7), 959-962.

Simulation of simple shear tests using DEM

J. Wang[1], H.S. Yu[1] and P. Langston[2]

[1]School of Civil Engineering, University of Nottingham, UK
[2]School of Chemical, Environmental and Mining engineering, University of Nottingham, UK

The discrete element method (DEM) has established itself as a very useful numerical method for modeling particle assemblies. It is an effective and convenient tool to investigate the complex behavior of granular materials.
The simple shear test is used widely in geotechnical research and practice. Understanding the limitation of simple shear experiments in laboratory, this paper presents a complementary micromechanics-based approach that performs numerical simulations of quasi-static shear deformation of an assembly of polydisperse spheres in the simple shear test. A three dimensional (3D) DEM model of a particle assembly with wall boundaries is used to obtain the macroscopic stress-strain behavior during simple shear tests. Constant volume and constant normal pressure simple shear tests are performed under a wide range of parameters. Detailed information is obtained about the evolution of shear stress and strain associated with the micromechanics occurring at the particle scale. The simulation work includes two major parts: sample preparation and sample testing.
The study investigates the non-coaxial behavior of granular materials in simple shear tests. It shows that the principal axes of stress and strain rate are generally not coincident during simple shear deformation. This paper also explores the stress-dilation relation for shear deformation of frictional granular materials. These results show that there is an inverse relationship between the top wall's vertical displacement and applied vertical pressure during simple shear tests. The future objective is to incorporate these observations into constitutive models.

Keywords: Discrete element method; Three-dimensional model; Non-coaxility; Dilatancy

1. Introduction

The simple shear test is used widely in geotechnical research and practice. During this test, the principal stress rotation is the main aspect of this loading (Ishihara 1983). The mechanical behavior of granular materials under this loading condition has been long observed and recognized in soil tests using experimental devices and numerical simulation (Yu & Yuan 2005, 2006; Yang 2006; Jiang 2003, 2005) . But it was difficult to determine the principal stress direction in the laboratory tests without using certain assumptions (Roscoe 1965). Understanding the limitation of lab experiments, this paper presents a complementary micromechanics-based approach that performs numerical simulations of quasi-static shear deformation of an assembly of polydisperse spheres in the simple shear test. It is shown that the principal axes of stress and strain rate are generally not coincident during simple shear deformation. It is also evident that constitutive relations cannot be sufficiently formulated in the principal stress space unless non-coaxial behavior is taken into account. It is therefore important to examine the effects of the non-coaxial behavior and incorporate such effects in constitutive models.

2. Theoretical model

The discrete element method (DEM) has established itself as a very useful numerical method for modeling particle assemblies. It is an effective and convenient tool to investigate the sophisticated behavior of granular materials. In this method the interaction of the particles is viewed as a transient problem with states of equilibrium developing whenever the internal forces balance (Cundall 1979; Strack & Cundall 1984). The principle of DEM is to track in a time stepping simulation, the trajectory and rotation of each element in a system to evaluate its position and orientation (Asmar & Langston 2002; Langston 1995), and then to calculate the interactions between the elements themselves and also between the elements and their environment**,** The interactions will then subsequently affect the element positions. The equations (1) to (5) show the normal particle interaction (particle to particle and particle-wall) and the equilibrium of motion.

$$F = K_n \Delta n \tag{1}$$

$$\frac{\partial^2 x}{\partial t^2} = \frac{1}{m_0}\sum_{k=1}^{p} F^k \tag{2}$$

$$\frac{\partial^2 \theta}{\partial t^2} = \frac{1}{I_0}\sum_{k=1}^{p} M^k \tag{3}$$

$$\begin{aligned} \dot{x}_{t+\Delta t} &= \dot{x}_t + \ddot{x}_1 \Delta t \\ x_{t+\Delta t} &= x_t + 0.5(\dot{x}_t + \dot{x}_{t+\Delta t}) \end{aligned} \tag{4}$$

$$\begin{aligned} \theta_{t+\Delta t} &= \dot{\theta}_t + \ddot{\theta}_1 \Delta t \\ \theta_{t+\Delta t} &= \theta_t + 0.5(\dot{\theta}_t + \dot{\theta}_{t+\Delta t}) \end{aligned} \tag{5}$$

Where K_n is the stiffness of particles or walls, Δn is the overlap between the particles or the

particle with wall, m_0 is the mass of particles, t is the time, Δt is the time step, is determined by the maximum stiffness and smallest mass of particle, I_0 is the moment of inertia, k is the number of contact, x, θ are the transitional and rotational displacements; and F, M : are the contact force and moment acting on particle.

The contact force, particle-particle and particle-wall, considered in this model include elastic, friction and damping forces. All these forces are classified as normal and tangential components based on the direction of the acting force. The resultant force produced on the particle is the total of all these forces and any external forces from boundary. In this simulation, total normal force and total shear force acting on the boundaries are calculated. By dividing these forces by the areas on which they act, the average normal stresses and average shear stresses are obtained.

In this paper, an investigation of granular material behavior in the simple shear test is reported, the principal stress direction, principal strain increment direction and dilation during simple shear deformation are examined.

3. DEM tests

3.1. Sample preparation

In this simulation, particle radium has an approximately normal distribution between 0.6 cm and 1.8 cm. The mechanical properties of all the particles are given in Table 1. These parameters unless indicated otherwise, are used for all the simple shear simulation.

Table 1: Materials properties in simulation

DEM parameters and material properties	**Selected value**
Number of particles	4000
Frictional coefficient of particle and wall	0.6
Stiffness (Gpa)	10
Time-step (s)	0.0002

During testing actual particle packing arrangement is expected to have a significant influence on the shear behavior. The resulting packing's heterogeneity and response to testing
depend on the techniques used in the sample preparation phase. So the sample generating process should be carried out carefully.

There are many possible procedures for generating an initial configuration of sample before applying simple shear tests on it. As shown in Fig 1, all particles are allowed to drop randomly under gravity into a container. This container will form the ultimate simple shear test box.

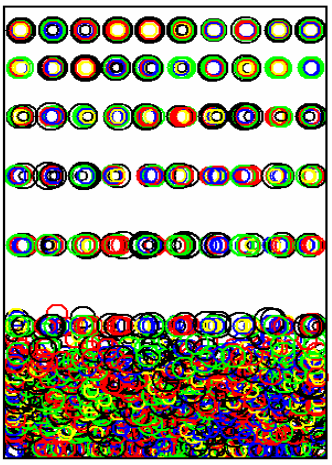

Fig 1: Sample preparation in filling phase

The number of particles dropped at a time is limited by the cross sectional area of this container. In order to reduce the non-homogeneity of the sample, all the particles are randomly dropped in such a manner that no frictional force is allowed to develop within the particles and between the particles and the walls. Both friction coefficients are set to zero.

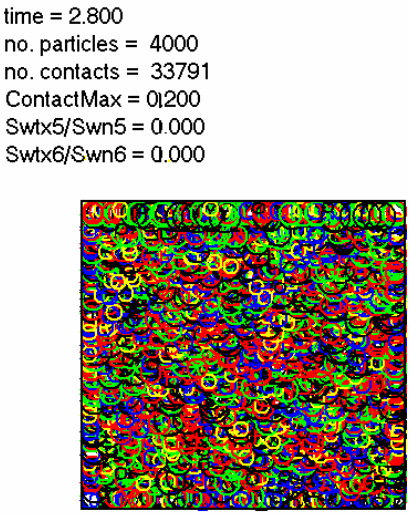

Fig 2: Sample preparation in compacting phase

Once all the particles have settled, the top wall is introduced and the compression is carried out by lowering the top wall to a certain height, as shown in Fig 2, this picture shows the particle's position during compacting phase. The other five walls are kept fixed during this time. Then the top wall is stabilized at this specific position; the sample is given enough time to achieve a state of new

equilibrium with all particles velocities approaching zero.

During the filling phase, gravity is acting upon the particles, which means that the lower layers are inevitably denser than the upper layers within the sample; in order to reduce this non-homogeneity, gravity is released. The gravity release is initiated during compaction. Eventually the sample will settle down and the normal stresses of particles acting on walls will converge to a stable state. At this stage the sample is saved as the initial configuration for the shear tests, the six walls of the container will act as the shear box in simple shear testing. Once the shearing starts, the friction will be turned on till the simulation stops.

During compacting, the stresses stabilized quickly after gravity is released. After many tests, it can be verified the final stress state of the sample is influenced by the compacting force but not by the gravity release time. In this paper, the initial stress state of sample used in constant volume test and constant normal pressure test is same, K_0 representing the initial ratio of horizontal normal stress to vertical normal stress acting on the sample, both of them are 0.52. Fig 1, 2, 4 and 7 are all the front views for xoz plane, this is a 3D simulation with the sphere positions projected onto the 2D page.

4. Numerical results and discussion

In this paper, constant volume and constant normal pressure simple shear tests are performed under the same initial state.

The simple shear condition is performed by rotating the two vertical walls at a constant angular velocity. At the same time, the top and bottom wall are translated with a compatible horizontal velocity in the opposite directions. As shown in Fig 3, in which the dashed line indicates the initial sample position. This is also the principle of simple shear test used in the laboratory. In this simulation the average normal stresses and average shear stresses on the boundaries are calculated.

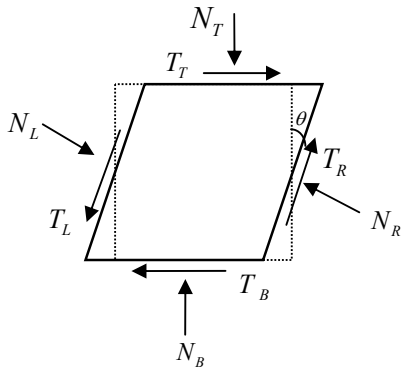

Fig 3: Scheme in simple shear test

4.1 Constant volume test results

Fig 4 shows the configuration of this simulation in constant volume simple shear tests, this picture is a front view for xoz plane, it shows the particle's velocity vector during the shearing.

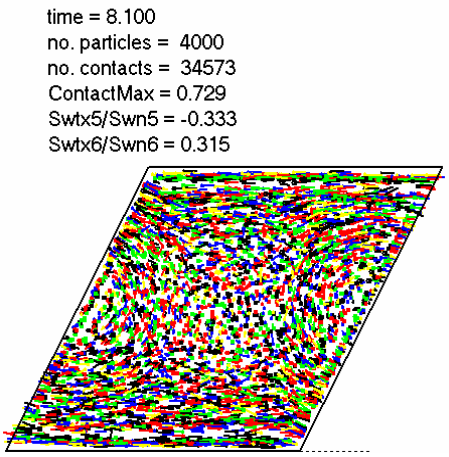

Fig 4: Constant volume simple shear test

It can be seen from Fig 5 that with increasing shear strain, the ratio of shear stress to normal stress rapidly rises to a peak value first and then gradually decreases. When shear strain is developed to 0.35, the stress ratio is stable around the value of 0.36, after that the stress ratio oscillates slightly around this value. This similar result is obtained in constant normal pressure simple shear test, as shown in Fig 8.

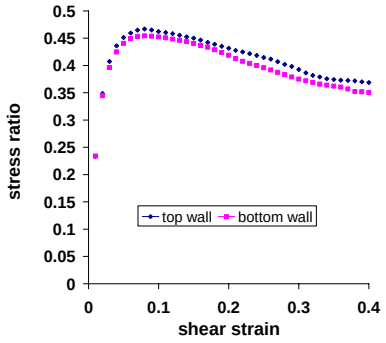

Fig 5: Ratio of shear stress to normal stress

The orientation of the major principal stress inclined to horizontal plane during the constant volume shearing is presented in Fig 6. In this case, initially, the principal stress direction is 90 degrees to horizontal plane because the K_0 is 0.52. With the increasing shearing strain, it decreases to 45 degrees and rotates counter-clock wise. In constant volume test, which keeps the top wall's height constant in order to achieve the constant volume condition during the shear deformation, the principal strain increment direction is fixed at 45 degree inclined to horizontal plane. It can be seen that the principal stress direction is not coincident with the principal strain increment at the beginning of shear.

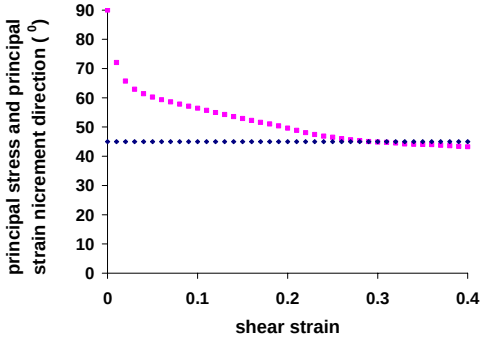

Fig 6: Principal stress direction inclined to horizontal plane

4.2 Constant normal pressure test results

With the same sample, constant normal pressure simple shear test is carried out under the same compacting pressure as in section 3. Fig 7 is a front view for xoz plane, in which the particle's velocity vector is shown during this simulation.

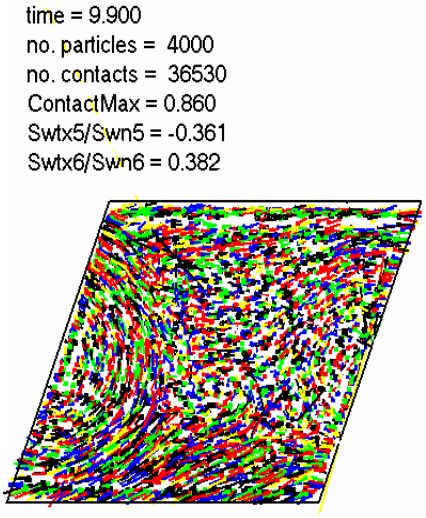

Fig 7: Constant normal pressure test

From Fig 8 it can be seen that the stress ratio of shear stress to normal stress during the shear deformation is similar to that in constant volume test. Both the top wall and bottom wall are increased to a peak point followed by a falling trend.

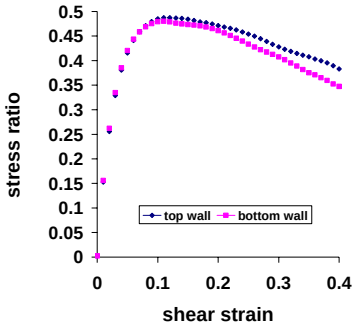

Fig 8: Ratio of shear stress to normal stress

In constant normal pressure test, the top wall and bottom wall are relaxed, both of them can be moved up or down by the force acting on them. From Fig 9, it can be seen that in the constant normal pressure simple shear test the sample dilated slightly at the beginning of shearing, as the sample was sheared further, the vertical displacement of both top and bottom wall increased and the volume of the sample started to expand.

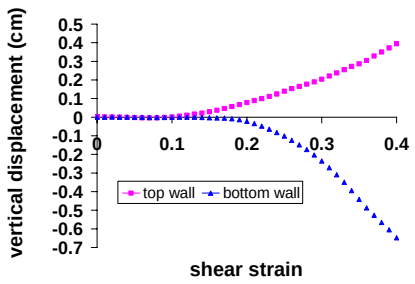

Fig 9: Vertical displacement

From Fig 10 it can be seen that the principal stress and principal strain increment direction are not coincident during the constant normal pressure simple shear tests. The initial K_0 is 0.52, the principal stress direction is 90 degree inclined to horizontal plane, the principal stress increment is 45 degree inclined to horizontal plane. With increasing shear strain, the principal stress direction decreased to 45 degree in an anti-clock wise direction, the principal strain increment direction oscillates near 45 degree inclined to horizontal plane.

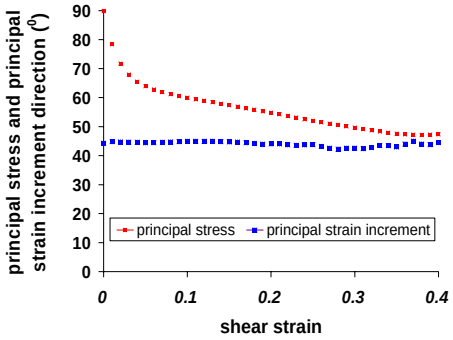

Fig 10: Principal stress direction and principal strain increment direction inclined to horizontal plane

5. Conclusion

This paper investigates the non-coaxial behavior of granular materials in simple shear tests using DEM. It shows that DEM is a valid and convenient tool to be used this area. It is shown that the principal axes of stress and strain rate are generally not coincident during simple shear deformation. This paper also explores the stress-dilation relation for shear deformations of frictional granular materials. The result shows that there is an inverse relationship between the top wall's vertical displacement and applied vertical pressure during simple shear tests. The future objective is to incorporate these observations into constitutive models.

References

Asmar, B.N., Langston, P.A., Matchett, A.J., Walters, J.K., Validation tests on a distinct element model of vibrating cohesive particle systems. *Computers and Chemical Engieering,* 2002, (26), 785-802.

Cundall, P.A., & Strack, O.D.L., A discrete numerical model for granular assemblies. *Geotechnique,* 1979, 29(1), 47-65.

Ishihara, K., Soil response in cyclic loading induced by earthquakes, traffic and waves. *Proc,7th Asia Regional Conf. on Soil Mechanics and Foundation Engineering,* 1983, (2),.42-46.

Jiang, M. J., Harris, D. and Yu, H.S., Kinematic models for non-coaxiality granular materials. Part I and Part II*, Int. J. Num. Anal. Meth. Geomech, 2005, (29), 643-689.*

Jiang, M.J., Konrad,M.J., Leroueil, S., An efficient technique for generating homogeneous specimens for DEM studies, *Computers and Geotechnics,* 2003, (30), 579-597.

Langston, P.A., Discrete element simulation of granular flow in 2d and 3d hoppers: Dependence of discharge rate and wall stress on particle interactions. *Chemical Engineering Science,* 1995, (50), 967-987.

Langston, P.A., Tuzun, U., and Heyes, D.M., Continuous potential discrete particle simulations of stress and velocity fields in funnel flow hoppers. *Powder Technology,* 1995, (85), 153-169.

Roscoe, K.H., Discussion on shear strength and consolidation. *Proc of 6th Int.Conf. Soil Mech.,* 1965, (3).

Strack, O.D.L., Cundall, P.A., Fundamental studies of fabric in granular materials*, interim report to National Science Foundation*, Department of Civil and Mineral Engineering, University of Minnesota, Minneapolis, Minnesota,1984, pp. 53.

Yang, Y., and Yu, H.S., Numerical simulations of simple shear with non-coaxial soil models. *International Journal for Numerical and Analytical Methods in Geomechanics,* 2006, (30), 1-19.

Yu, H.S., Yuan X., The importance of accounting for non-coaxial behaviour in modelling soil-structure interaction, *Proceedings of the 11th IACMAG, Invited Issue Paper,* 2005, (4), 709-718.

Yu, H.S., Yuan, X., On a class of non-coaxial plasticity models for granular soils. *Proceedings of the Royal Society of London,*2006, Series A, (462),725-748.

A discontinuous sub-block meso-damage evolution model for rock mass

He-hua ZHU, Shi-min WANG, Yong-chang CAI

Department of Geotechnical Engineering, Tongji University, Shanghai 200092，China

As an effective numerical simulation method, DDA is used in the stability evaluation of rook mass widely although it has some limitations. The failure of rock mass is due to crack propagation between rock maases and the failure within the rock. In the existing DDA methods, the first factor is taken into account usually. Some researchers consider the second factor using fracture mechanics. But remeshing makes the computation complex, and sometimes even difficult. In this paper, a discontinuous sub-block meso-damage evolution model is proposed. In the new model, each block is divided into smaller sub-blocks. There are two kinds of contacts between sub-blocks. One is continuous and the other is discontinuous. The continuity condition can change along the sub-block contacts and the continuous contacts can convert into discontinuous ones using Mohr-Coulomb criterion. The two kinds of contacts are modeled using the Augmented Lagrangian Method. The failure of rock mass is a progressive process. There is damage in rock mass before it loses stability. So the meso-damage mechanics is introduced into the new model. The tensile damage and shearing damage in the sub-block are considered.

Keywords: Discontinuous sub-block; Augmented Lagrangian Method; Meso-damage; Rock mass

1. Introduction

Rock masses are always dissected by joints, faults and other discontinuities which control the failure and sliding of the mass. Most rock masses are discontinuous over a wide range of scales, from macroscopic to microscopic. In sedimentary rocks the two major sources of discontinuities are bedding planes and joints, the intersection of which form the so-called blocky rock mass (Terzaghi 1946). Excavation of an underground opening in a blocky rock mass disturbs the initial equilibrium, and the stresses in the rock mass tend to readjust until new equilibrium is attained. Failure occurs when the stresses can no longer readjust to form a stable, load resisting structure. This may occur either when the material strength is exceeded at some locations, or when movements of rock blocks preclude the development of a stable geometric configuration (Michael 2004). Numerical method is an effective way to solve the failure of rock mass. With numerical methods, the response of rock masses to loading and unloading is modeled. These methods include the Finite Element Method (FEM), the Boundary Element Method (BEM) and the Discrete Element Method (DEM). Although rock mass discontinuities can be modeled in a discrete manner with FEM and BEM methods using special joint elements (Goodman 1976; Crouch 1983), the descriptions of discontinuities are usually difficult and there are often restrictions on the degree of deformation permitted.

The Discontinuous Deformation Analysis (DDA) method is a new method which was proposed by Shi in the late 1980s (Shi 1988). Computer programs based on the method were developed and some applications were presented in the thesis, as well as in more recent papers (Shi 1989, 1990; Ke 1994; Yeung 1994). Large displacements and deformations are considered under both static and dynamic loadings. Some extensions to the method are presented later (Chihen 1996; Cheng 1998).

The failure of rock mass is due to crack propagation between the rocks and the failure within the rock. In the existing DDA methods, the first factor is taken into account usually. Some researchers consider the second factor using fracture mechanics (Chihen 1996). The failure of rock mass is a progressive process and there is damage in rock mass before it loses stability. But up to today, the meso-damage mechanics is not introduced into the DDA method.

At the outset, this paper reviews some of the basic concepts of the DDA method. Then, with the failure and damage in the rock block considered, a Discontinuous Sub-Block Meso-Damage Evolution Model for Rock mass is brought up.

2. A brief introduction to DDA

In the DDA method, the blocks can be of any convex or concave shape. When blocks are in contact, Coulomb's law applies to the contact interfaces, and the simultaneous equilibrium equations are selected and solved at each loading or time increment. The large

displacements and deformations are the accumulation of small displacements and deformations at each time step. Within each time step, the displacements of all points are small, hence the displacements can be reasonably represented by first order approximations.

2.1 Block deformations and displacements

By adopting first order displacement approximations, the DDA method assumes that each block has constant stresses and strains throughout. The displacements (u,v) at any point (x,y) in a block i, can be related in two dimensions to six displacement variables

$$D_i = (d_1, d_2, d_3, d_4, d_5, d_6) = (u_0 \;\; v_0 \;\; r_0 \;\; \varepsilon_x \;\; \varepsilon_y \;\; \gamma_{xy})^T \tag{1}$$

where (u_0, v_0) is the rigid body translation at a specific point (x_0, y_0) within the block, r_0 is the rotation angle of the block with a rotation center at (x_0, y_0), and ε_x, ε_y and γ_{xy} are the normal and shear strains in the block. The complete first order approximation of block displacements takes the following form

$$\begin{bmatrix} u_i \\ v_i \end{bmatrix} = [T_i][D_i] \tag{2}$$

where

$$T_i = \begin{pmatrix} 1 & 0 & -(y-y_0) & (x-x_0) & 0 & (y-y_0)/2 \\ 0 & 1 & (x-x_0) & 0 & (y-y_0) & (x-x_0)/2 \end{pmatrix} \tag{3}$$

This equation enables the calculation of the displacements at any point (x,y) within the block (in particular, at the corners), when the displacements are given at the center of rotation and when the strains (constant within the block) are known. In the two-dimensional formulation of the DDA method, the center of rotation with coordinates (x_0, y_0) coincides with the centroid with coordinates (x_c, y_c).

2.2 Simultaneous equilibrium equations

In the DDA method, individual blocks form a system of blocks through contacts among blocks and displacement constraints on single blocks. Assuming that n blocks are defined in the block system, the simultaneous equilibrium equations can be written in matrix form as follows

$$\begin{bmatrix} K_{11} & K_{12} & K_{13} & \cdots & K_{1n} \\ K_{21} & K_{22} & K_{23} & \cdots & K_{2n} \\ K_{31} & K_{32} & K_{33} & \cdots & K_{3n} \\ \vdots & \vdots & \vdots & \ddots & \vdots \\ K_{n1} & K_{n2} & K_{n3} & \cdots & K_{nn} \end{bmatrix} \begin{bmatrix} D_1 \\ D_2 \\ D_3 \\ \vdots \\ D_n \end{bmatrix} = \begin{bmatrix} F_1 \\ F_2 \\ F_3 \\ \vdots \\ F_n \end{bmatrix} \tag{4}$$

where each coefficient K is defined by the contacts between blocks i and j. Since each block i has six degrees of freedom defined by the components of D_i in equation (1), each K_{ij} in equation (4) is itself a 6×6 sub-matrix. Also, each F_i is a 6×1 sub-matrix that represents the loading on block i.

The simultaneous equations (4) were derived by minimizing the total potential energy of the block system. The ith row of equation (4) consists of six linear equations

$$\frac{\partial \prod}{\partial d_{ri}} = 0, \qquad r = 1,\ 2,\ \cdots,\ 6 \tag{5}$$

where the d_{ri} is the deformation variable of block i. The total potential energy is the summation over all the potential energy sources, i.e. individual stresses and forces. The potential energy of each force or stress, and their derivatives are computed separately. The derivatives

$$\frac{\partial^2 \prod}{\partial d_{ri} \partial d_{sj}}, \qquad r,\ s = 1,\ 2,\ \cdots,\ 6 \tag{6}$$

are the coefficients of unknown d_{sj} of the equilibrium equations (4) for variable d_{ri}. All terms of equation (6) form a 6×6 sub-matrix, which is sub-matrix K_{ij} in equation (4). Equation (6) implies that matrix K in equation (4) is symmetric. The derivatives

$$-\frac{\partial \prod(0)}{\partial d_{ri}}, \qquad r = 1,\ 2,\ \cdots,\ 6 \tag{7}$$

are the free terms of equation (5) which are shifted to the right hand side of equation (4). All these terms form a 6×1 sub-matrix, which is added to the sub-matrix F_i.

2.3 The open-close iteration

The DDA method assumes all blocks are connected through sp rings with a stiffness of P. The penetrated point at the contact will be pushed back along the shortest path by the stiff spring. It is necessary to impose the no-tension and no-penetration constraints.

A contact spring is added when blocks are in contact and is removed when blocks are separate. Iteration should be realized by adding and/ or removing springs in a trial-error manner until the convergence condition is met. This iteration is named as "Open-Close" iteration (Max, 1995).

There are three types of contact: penetration, opening and sliding. Mohr-Coulomb criterion is applied on the interface between blocks:

(1) if $R_n = -Pd \le 0$, no spring is applied;

(2) if $R_s > C + R_n \tan\varphi$, only normal spring is applied;

(3) if $0 < R_s \le C + R_n \tan\varphi$, springs are applied in two directions , and no sliding is allowed.

3. Discontinuous sub-block model

Discontinuous Sun-Block model is the extension of the origin DDA method. In the Discontinuous Sub-Block model, the displacement of sub-block and the simultaneous equilibrium equations of the sub-block system are same as the origin DDA method. Each block is divided into smaller sub-blocks artificially as the sub-block analysis method. This can increase the accuracy of the DDA method and its ability to resolve stress variations. Differently, there are two kinds of contacts between sub-blocks in Discontinuous Sub-Block model. One is continuous and the other is discontinuous. The continuity condition can change along the sub-block contacts and the continuous contacts can convert into discontinuous ones using Mohr-Coulomb criterion. The two kinds of contacts are themselves modeled using the Augmented Lagrangian Method. Thus the continuous problem, discontinuous problem and their combination all can be solved by Discontinuous Sun-Block model.

3.1 Contacts between sub-blocks

In the existing DDA methods, open-close iteration can be performed only on contacts which are on the joint between the blocks. The failure in the rock block can not be modeled. Some researchers consider the second factor using fracture mechanics (Chihen 1996). But remeshing makes the computation complex even difficult. In Discontinuous Sub-Block model, rock mass is divided into rock blocks and the rock blocks are divided into smaller sub-blocks which is so small that we can think it as homogeneous body in meso-scope. The contacts on the joint in macro scope are defined as discontinuous contacts, and the other contacts are defined as continuous contacts. In the open-close iteration, the continuous contacts can convert into discontinuous ones using Mohr-Coulomb criterion, but not vice versa.

3.2 Adapted open-close iteration

In the existing DDA methods, open-close iteration can be performed only on contacts which are on the joint between the blocks. So the failure in the rock block can not be modeled. In Discontinuous Sub-Block model, considering the crack between the sub-blocks within the rock block. So a adapted open-close iteration can be described as follows:

(1) if the contact is continuous and $R_n = -Pd \le -\tau_T$, the normal spring is removed;

(2) if the contact is discontinuous and $R_n = -Pd \le 0$, the normal spring is removed;

(3) if the contact is continuous and $R_s > \tau_c$, the shear spring is removed, and the friction is applied;

(4) if the contact is discontinuous and $R_s > C + R_n \tan\varphi$, the shear spring is removed, and the friction is applied;

(5) if the contact is continuous and $0 < R_s \le \tau_c$, the springs are applied in two directions, and no friction is allowed;

(6) if the contact is discontinuous and $0 < R_s \le C + R_n \tan\varphi$, the springs are applied in two directions , and no friction is allowed.

4. Discontinuous Sub-Block Meso-Damage Evolution Model

Damage is an essential characteristic of rock mass. It appears in the rock block before the failure of rock mass. Modeling the rock sub-block's failure with meso-damage mechanics is an effective method. In Discontinuous Sub-Block Meso-Damage Evolution Model, the effect of the sub-block's damage to the rock mass failure is reflected by introducing the meso-damage mechanics.

4.1 Definition of damage variable

In meso-scope view, rock sub-block is anisotropic. The scalar quantity damage variable can satisfy the need. In Discontinuous Sub-Block Meso-Damage Evolution Model, the tensile damage and the shear damage are considered. Therefore, two damage evolution equations are established, and each one has its damage variable separately. In tensile damage evolution equation, the tensile strain is taken as its damage variable. And in the shear damage evolution equation, the shear strain is taken as its damage variable.

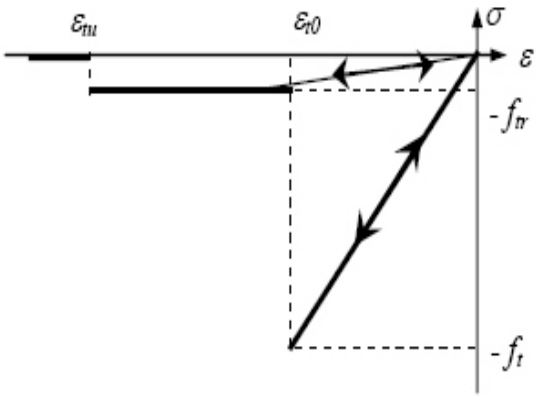

Fig. 1: Elastic damage constitutive curve for rock under uniaxial tensile load.

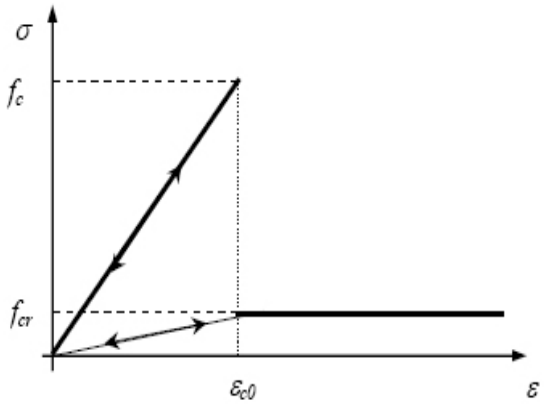

Fig. 2: Rock's elastic damage constitutive curve under uniaxial compress load.

4.2 Tensile damage evolution equation

The elastic damage constitutive curve for rock under uniaxial tensile load is assumed as shown in Fig.1. Accordingly, the form of the damage variable can be described as follows:

$$D=\begin{cases} 0 & \varepsilon_{t0}<\overline{\varepsilon}<0 \\ 1-\dfrac{\lambda\varepsilon_{t0}}{\overline{\varepsilon}} & \varepsilon_{tu}<\overline{\varepsilon}<\varepsilon_{t0} \\ 1 & \overline{\varepsilon}<\varepsilon_{tu} \end{cases} \tag{8}$$

where, λ is the remnants strength coefficient. ε_{t0} is the tensile strain according with elastic ultimate. ε_{tu} is the ultimate tensile strain. $\overline{\varepsilon}$ is the equivalent tensile strain and it can be defined as the following form

$$\overline{\varepsilon}=\sqrt{\langle-\varepsilon_x\rangle^2+\langle-\varepsilon_y\rangle^2} \tag{9}$$

where, ε_x and ε_y are the dominating tensile strain in X and Y direction separately.

4.3 Shear damage evolution equation

Homoplastically, based on the rock's elastic damage constitutive curve under uniaxial compress load as shown in Fig.2, the corresponding form of the damage variable can be described as follows:

$$D=\begin{cases} 0 & \varepsilon_1<\varepsilon_{c0} \\ 1-\dfrac{\lambda\varepsilon_{c0}}{\varepsilon_1} & \varepsilon_1\geq\varepsilon_{c0} \end{cases} \tag{10}$$

where, ε_{c0} the max dominating compress strain when the max dominating compress stress reach its uniaxial compress strength.

5. Conclusions

In this paper, a new method – Discontinuous Sub-Block Meso-Damage Evolution Model is brought forward based on the basic theory of DDA method. The meso-damage in the sub-block and the crake within the rock block are considered in the new model. Not only the discontinuous problems, but also the continuous can be solved with the same method

References

Cheng, Y. M., "Advancements and Improvement in Discontinuous deformation Analysis", *Computers and Geotechnics*, Vol. 22, No. 2, pp. 153-163, 1998.

Chihen T. Lin, Bernard Amadei, Joseph Jung, Jerry Dwyer. Extensions of discontinuous deformation analysis for jointed rock masses[J].*Int. J. Rock Mech. Min. Sci. di Geomech. Abstr*. 1996,Vol. 33, No.7. pp.671-694.

Crouch S. L. and Starfield A. M. *Boundary Element Methods in Solid Mechanics*. Allen and Unwin, London (1983).

Goodman R. E. and St. John C. Finite element analysis for discontinuous rocks. *In Numerical Methods in Geotechnical Engineering*. McGraw-Hill, New York (1976).

Ke T. C. and Goodman R. E. Discontinuous deformation analysis and the artificial joint concept. *Proc. 1st North American Rock Mechanics Symposium*, pp. 599-606. Austin, Balkema (1994).

Max Ma. *Discontinuous deformation analysis*. IACMAG 1995 ,6 : 4-6.

Shi G.-H. and Goodman E. E. Generalization of two-dimensional continuous deformation analysis for forward modeling. *Int. J. Num. & Anal. Method in Geomech.* 13, 359-380 (1989).

Shi G.-H. Forward and backward discontinuous deformation analysis of rock systems. *Proc. Int.*

Conf. on Rock Joints, pp. 731-743. Loen, Norway. Balkema (1990).

Shi, G-H. *Discontinuous deformation analysis – a new numerical method for the statics and dynamics of block system*. Ph.D. Thesis, Department of Civil Engineering, University of California, Berkley (1988).

Steindorfer, A., 1997. *Short-term prediction of rock mass behavior in tunneling by advanced analysis of displacement monitoring data*. Ph.D. Thesis, Department of Civil Engineering, Graz University of Technology.

Sulem, J., Panet, M., Guenot, A., 1987. Closure analysis in deep tunnels. *Int. J. Rock. Mech. Min. Sci*. 24, 145-154.

Yeung M. R. and Klein S. J. Application of the discontinuous deformation analysis to the evaluation of rock reinforcement for tunnel stabilization. *Proc. 1st North. American Rock Mechanics Symposium*, pp. 607-614. Austin, Balkema (1994).

Analysis of block deformation characteristics and its stability under high in-situ stress

SHI Guangbin[1,2] HE Min[1,2]
[1]Xi′an University of Technology, Xi′an 710048, China
[2]Northwest Investigation Design & Research Institute, Xi′an 710065, China

Laxiwa powerhouse is a lager cavern located in high in-situ stress region with stresses ranging from 10MPa to 30MPa. Faults f10, f12 and f24 are revealed in region A of cavern upstream wall. By lower hemisphere joint plane projection, Faults f10, f12 and f24 can form key blocks with excavation face. The block volume is 2103m^3, area of excavation face is 468m^2. During cavern excavation, block deformation keeps increasing slowly under action of excavation. The maximum rate of rock deformation reaches 1.22mm/d in a monitoring cycle (7 days). By analysis with theory of block movement, the sliding type is two-face slide (they are f10 and f12). Under cohesion force C=0.0 and friction angle φ =21.8 °, the factor of safety is 1.30; based on block deformation monitoring and stability analysis, only conventional support to block is necessary. After monitoring for 598 days, the block deformation attains 38.9mm. The present average rate of rock deformation is 0.0018mm/d, and it is convergent s, which shows the block is stable. From this example, if the factor of safety for the block is satisfied, and block deformation does not influence other structure, block deformation during excavation may be allowable, and no special reinforcement measures are necessary for blocks.

Keywords: Laxiwa power house; lager cavern; high in-situ stress region; block deformation; monitor

1 Introduction

The powerhouse of Laxiwa hydropower station consists of the main powerhouse, transformer chamber, surge-chamber tunnel, which lay out in a parallel manner and the clearances of the tunnels are 50.0m and 36.0m. The arrangement plan is shown in Figure 1. The excavation section of three large tunnels is 311.75m×30.0m×74.84m (length×width×height) for the main powerhouse, 232.60m×29.0m×51.5m (length×with×height) for transformer tunnel, and Φ29.6m×69.0m (diameter × height) for surge-chamber tunnel.

Considering the factors of fault, fracture, the direction of the maximum in-situ stress and the block characteristic, the trend of tunnels axis is determined as NE25° and the overburden depth of the tunnels is about 150m～466m.

The geological conditions are as follows: More than 90% of surrounding rock is I, II grade and III grade is less than 10%; the fault and fracture are not development with a small scale and good trait and a characteristic of hardness structural surface.

3D in-situ stress measurement indicates that the maximum principal stress reaches 29.0MPa with a trend of SN and a dip angle of 25°, dipping to the river valley; the maximum intermediate principal stress is about 15MPa with a trend of NEE~SEE and a dip angle of 20°, dipping to the mountain. The minimum principal stress is about 10MPa and almost vertical. It is concluded that the in-situ stresses of the project area are very high.

The main powerhouse was excavated from 9 Nov 2003 and finished in September 2006.The tunnel is divided into nine layers for blasting excavation and the excavation and anchorage support sequences are shown in Figure 2 in details. The upstream wall of the tunnel numbering area A is exposed to faults f10, f12 and f24, as shown in Figure 3.and the characteristics of f11 and f12 are identical with an interval of 5 m ~8m.

The supporting system for the wall includes 1500KN prestressed anchorage cable with an interval of 4.5m×6.0m and a length of 20m, bolts with diameter of 32mm and an interval of

3.0m×3.0m and a length of 9.0m; bolts with diameter of 28mm and a interval of 3.0m×3.0m and a length of 4.5m, steel fiber shotcrete with a thickness of 15cm.

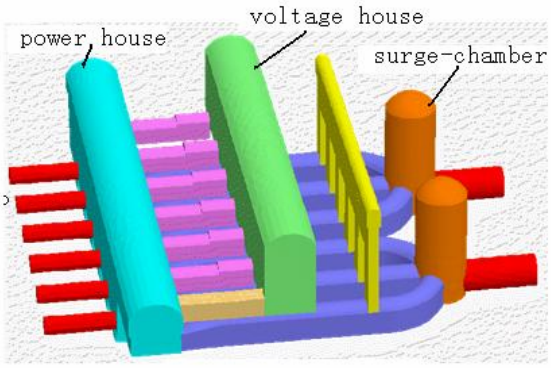

Fig.1 Cavern layout

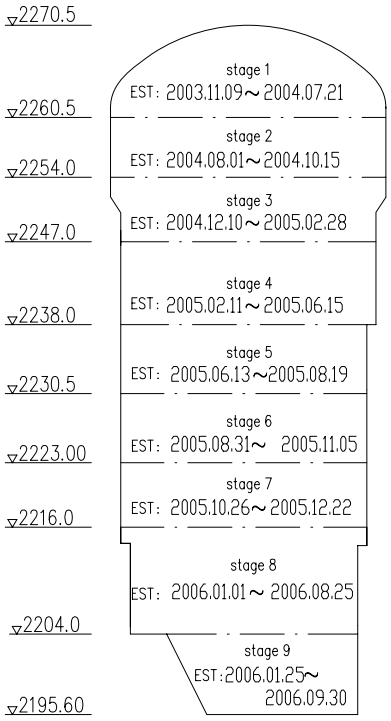

Fig.2 cavern excavation sequence

2 Fault properties

The strikes of the major faults such as f10, f12 and f24 are shown in Table 1. Structure face of f10, f11, f12 and f22 is 5cm～10cm in width and 1cm～5cm for f24; 1cm width for L202. There are filling calcium or crushed stone in structure face. The influence thickness of lower half space of f12 is 2 meters. If the apex height of block is bigger than 5 meters, its cohesion C=0.04MPa～0.05MPa, and friction angle φ =21.8 °~33.0°; smaller than 5 meters or equal to 5 meters, its cohesion C=0.02MPa～0.03MPa, and friction angle φ =19.2 °～21.80°.

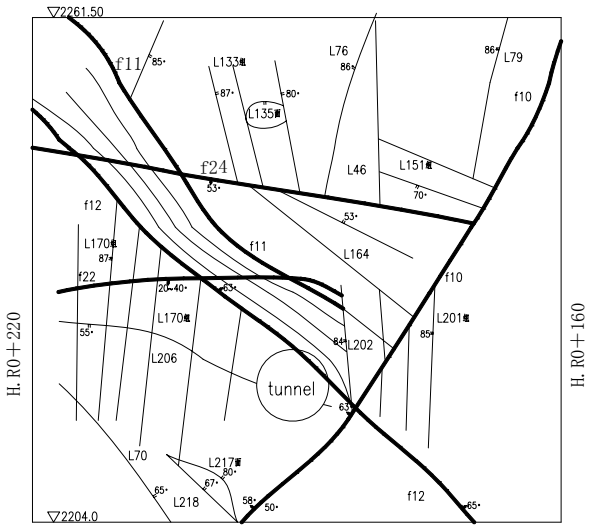

Fig.3 fault and joint in Region A

Table 1 fault and joint parameters

fault	trend	Dip direction	dip
f10	NW305°	SW	63°
f12	NW340°	NE	63°
f24	NE30°	NW	53°
f22	NW355°	SW	30°
L202	NE50°	SE	84°

3 Analysis of block deformation characteristics

3.1 Design of block deformation monitor

The excavation of the fourth stage of the main powerhouse, from the elevation of 2238.0m to 2247.0m, was completed on June 15, 2005, when Faults f10, f11, f12 and f24 were brought to light. Faults f11 and f10 are basically parallel. According to the strike of f10 and f12, it is estimated that these two faults may intersect at one point at the elevation of 2217.0, higher than the ultimate design excavation elevation of 2195.6. It is indicated that Faults f10, f12 and f24 can form key blocks by lower hemisphere joint plane projection. In order to

investigate the deformation and stability of the block during next excavation stages, a set of multipoint displacement meter (M402-XZ1) was installed on the upper left corner of the block (shown in Figure 4) and the location of four anchorage points of the multipoint displacement meter are 2.0 m, 5.0 m, 15.0 m, 30.0m away from the head respectively.

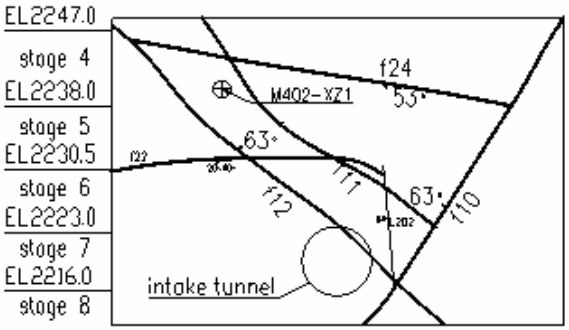

Fig.4 Location of multipoint displacement meter

3.2 Characteristics of block deformation

The record of the multipoint displacement meter started on August 22, 2005, when the excavation of the first five stages has been completed. So the meters recorded the unloading deformation induced by the excavation from the sixth stage to the ninth stage. The monitored displacement is plotted in Figure 5. The displacement induced by the excavation of eighth stage and ninth stage is 19.98mm and 10.84mm respectively and the mean daily rate of change is 0.40mm/d and 0.12mm/d. At the beginning of the seventh stage**,** the maximal daily mean rate of change reaches 1.22 mm/d at an individual monitoring period (a week). The deformation begins to converge at the time of the excavation of the ninth stage and daily displacement rate of change is 0.0018 mm/d at present. By April 12, 2007 (598 days after installation), the total measured displacement is 38.9mm.

In the light of routine, the excavation of the fifth stage and sixth stage has great influence on the deformation of the measuring point. Because the multipoint displacement meter began to record when the excavation of the fifth stage has completed, no displacement can be recorded certainly. However, the total displacement is just 2.42mm during the excavation of the sixth stage. It is so small and much less than the displacement during the excavation of seventh stage and eighth stage, just 12% of the displacement during the excavation of the seventh stage and 22% of the displacement of the excavation, respectively. Why is this? There may be mainly two causes as follows:

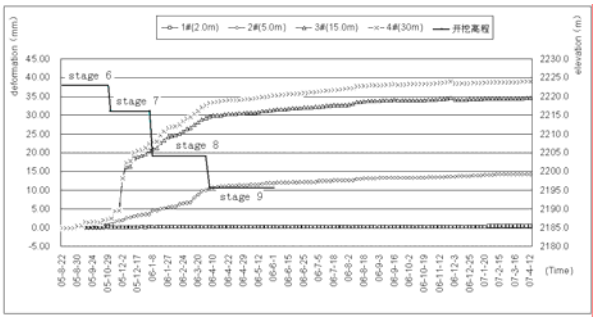

Fig.5 progress curve of M402-XZ1

(1) The block or fault are brought to light gradually

It is known from Figure 4 that the space face of the block II formed by f22, f12 and L202 was not exposed when the excavation of the sixth stage was completed. But after the excavation of the seventh stage was finished, the space face of the block II was exposed completely. and faults f12 and f10 with a width 5 cm ~ 10 cm, the elasticity modulus of filling medium is only 2.0GPa, just 11% of the rock mass modulus 18GPa in other zones and also the structure places developed between fault of f11 and f12; the modulus of rock mass in the zone are about 10.0GPa, lower than that of other zones. Along with excavation unloading, the deformation of the structure surface and the weak zone can obviously increase and some structure surfaces even can open, which can be found in the tunnel (intake tunnel) vertical to the main powerhouse wall, shown in Figure 6. The excavation of the eighth stage is only close to block 02. Its excavation must affect the deformation of block 02. While block 02 is in block 01, the deformation of block 02 must affect block 01. So the block or fault may produce an evident effect on the deformation of rock.

(2) Effect of energy accumulating and releasing

In the condition of high in-situ stress, excavation caused stresses in rock mass to discharge

and redistribute. Because granite is hard rock with high elasticity modulus and good integrity, with excavation of overlying rock masses, the geo-stress of the surrounding rock adjust continually and may induce energy accumulating in the underlying rock. When the rock in those zones was excavated, the energy will release suddenly and induce large deformation of overlying rock. It can be verified that during excavation of the seventh stage, cracks were yielded in the shotcrete between stage 4 and stage 6 and cracks were mainly located in the zones between faultsf 11 and f12 with a width of1.0~2.0mm and a length of 35m.

The reason of the deformation of the rock mass in zones A is not slip displacement along the structure , but deformation induced by excavation releasing, which can be explained by stress/strain analysis by finite element and stability analysis using block theory as follows.

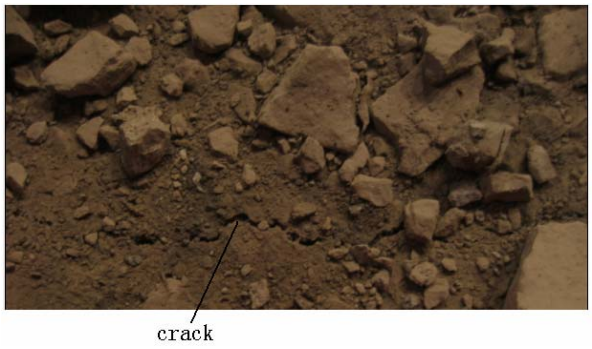

Fig.6 fault or joint open

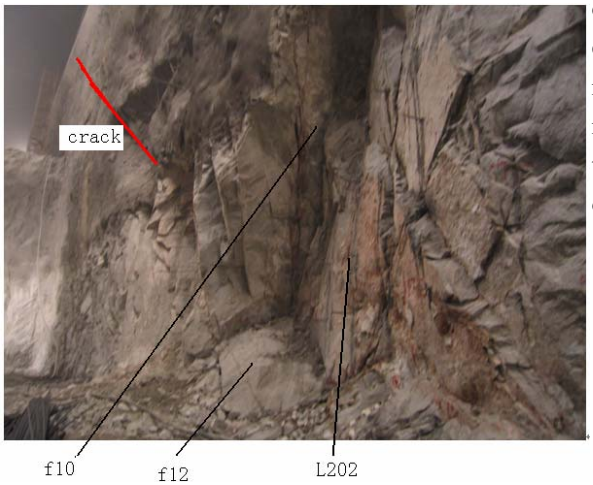

Fig.7 shotcrete crack

4 Deformation analysis using finite element

To quantify the deformation induced by excavation unloading from step 5 to step 9, 3-D finite element analysis is implemented. The following sections give a brief description of analysis model and results.

4.1 Analysis model

Fault f12, f10, f12 and other faults is modeled with equivalent joint elements. The rock is modeled with hexahedral element with 6 nodes or tetrahedron with 4 nodes. The 3-D finite element mesh is shown in Figure 8. The specified parameters of rock mass are given: 15GPa～18GPa for rock modulus, c=1.3 MPa for rock cohesion, φ =52°for internal angle of rock mass and The modulus of equivalent joint element is about2GPa～8GPa.

4.2 Analysis of deformation

The deformation induced by excavation unloading from step 6 to step 9 is illustrated in Figure 9: curve ① labeled for measuring data, curve ② labeled for computation results with finite element. It can be seen from that measuring displacement and computing displacement during period of excavating step 6 to step 9 is consistent on the rule. With consideration of faults, the total displacement reached 77 mm and without consideration of faults, the total displacements reached 21 mm. The difference between the two results is about 21 mm. It can be concluded from that the influence of excavation on the deformation of the surrounding rock is obvious.

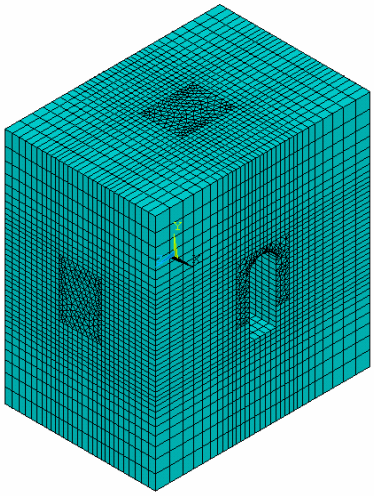

Fig.8 3-D mesh of analysis model

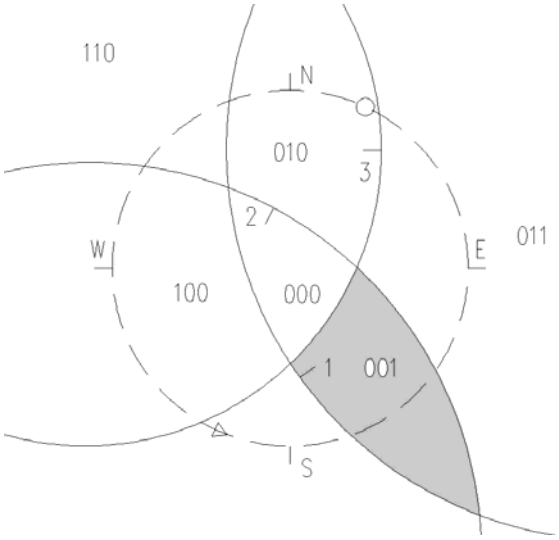

Fig. 10 Stereography projection of JP1

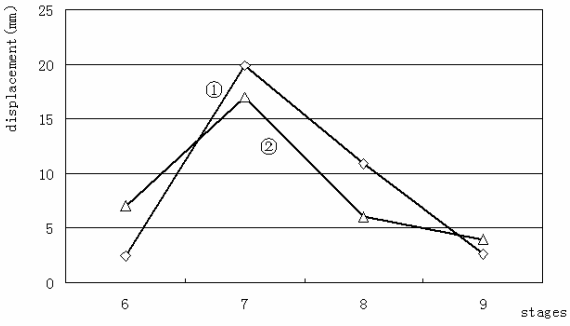

Fig. 9 Comparison between the calculated displacement and the measured displacement

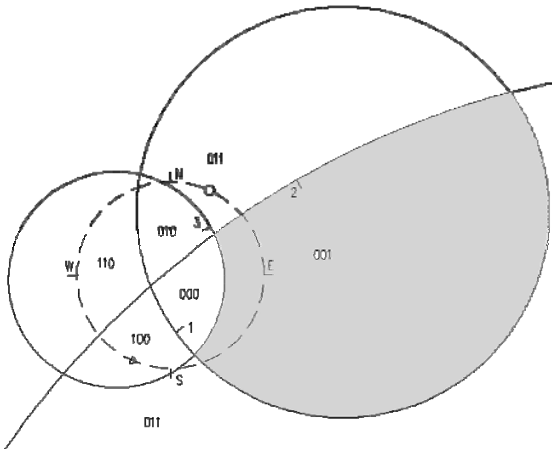

Fig. 11 Stereography projection of JP2

5 Analysis of block stability

5.1 Analysis of joint stereography projection

Stereography projection of f12, f10 and f24 is illustrated in Figure 10 and stereography projection of f12, L202 and f22 is illustrated in Figure 11. It can be known that JP1 is located in the upper half space of f10 and f12 and lower half space of f24 and JP2 is located in the upper half space of f10 and L202 and lower half space of f22. So the code for JP 1 is 001 and the code for JP 2 is also 001. Both JP1 and JP2 are not null from Figures 10 and 11 and also both of them are included in SP of upstream wall. It is concluded that block 01 and block 02 exist and are movable. The sliding mode of block 01 is sliding along f10 and f12 and the sliding mode of block 02 is sliding along f12.

Block 01 has a volume of 2103 m^3, an excavation face area of 473m^2 and an apex height of 13.3 m and Block 02 has a volume of 126 m^3, an excavation face area of 100m^2 and an apex height of 3.8m. The sketch of two blocks is illustrated in Figures 12 and 13 respectively.

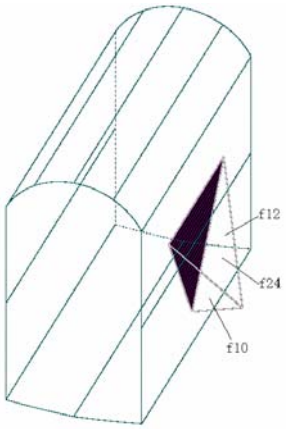

Fig.12 sketch of block 01

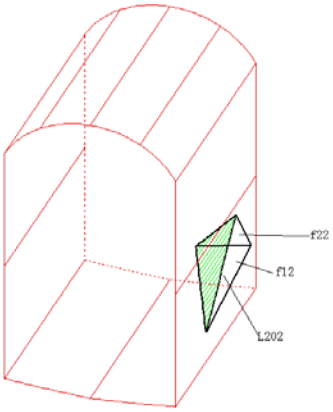

Fig.13 sketch of block 02

5.2 Design of anchorage system

5.2.1 Stability criteria for blocks

There is no clear criteria for blocks now and in order to evaluate the stability of the blocks, with the reference of Classification & design safety standard of hydropower projects, Technical code for building slope engineering and design code of hydropower slope engineering, the design allowable safety factor is defined as [k]=1.25

5.2.2 Design of anchorage system

The stability of up wall of the tunnel is determined by the stability of block 1 and block 2 and the stability of block 1 and block 2 is the main basis for anchoring measures. Analysis of block stability under different shear strength parameters is implemented without consideration of in-situ stress and water pressure. The results are illustrate in Tables 2 and 3.

Table 2 Safety factor of block 01

No.	Cohesion C (MPa)	Friction angle φ (°)	Safety factor	
			Without anchorage	With anchorage
1	0.0	21.8	1.29	1.94
2	0.0	33.0	2.09	2.83
3	0.04	21.8	2.02	2.67
4	0.04	33.0	2.82	3.56
5	0.05	21.8	2.20	2.85
6	0.05	33.0	3.00	3.74

Table 3 Safety factor of block 02

No.	Cohesion C (MPa)	Friction angle φ (°)	Safety factor	
			Without anchorage	With anchorage
1	0.0	19.2	0.18	1.27
2	0.0	21.8	0.20	1.37
3	0.02	19.2	0.43	1.52
4	0.03	21.8	0.46	1.63
5	0.02	19.2	0.56	1.65
6	0.03	21.8	0.60	1.77

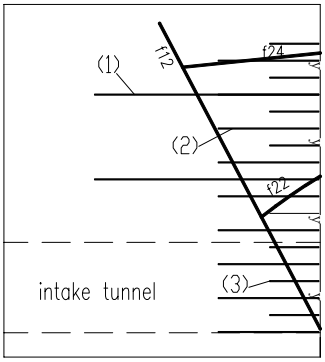

Fig.14 sketch of anchorage system

(1)-Cable,T=1500KN, length=20m, spacing 4.5m×6.0m;

(2)-Bolt, diameter 32mm, length =9.0m, spacing 3.0m×3.0m;

(3)-Bolt, diameter 28mm, length =4.5m, spacing 3.0m×3.0m.

There are some results from Tables 2 and 3:

（1）Block 01

Without anchorage, if C=0.04MPa~0.05MPa, the safety factor is about 2.09~3.00, larger than the design allowable safety factor 1.25; if C=0.0, the safety factor is about 1.29~20.9, also larger than the design allowable safety factor 1.25; the block is stable and only conventional measures are needed. The detail anchorage system is shown in Figure 14 and after anchoring, the safety factor is about 1.94~3.74.

(2）Block 02

Without anchorage, if C=0.0MPa, the safety factor is about 0.18~0.20, smaller than the design allowable safety factor 1.25; if C=0.02~0.03MPa, the safety factor is about 0.43~0.60, also smaller than design allowable safety factor 1.25; with system anchorage measures, the safety factor reaches 1.27~1.77, larger than design allowable safety factor 1.25.

It can be concluded that the two blocks are stable and can not slide. The deformation is the reason of excavation unloading.

6 Anchorage design of tunnel portal

It can be seen from Figure 3, there is an intake tunnel with a diameter of 8.2 m through the lower half space of f12, its excavation may induce instability of the. Some bodies should be reinforced in the section of AB in the tunnel entrance. But the authors think that it is not necessary, because the intersection part of the intake tunnel with blocks are small with a volume 4.0m^3 (shown in figures 15~17) and also the blocks are stability from analysis above. However in the course of excavating the section AB, blasting Charge volume should be controlled and also should strengthen support in the tunnel portal.

7 Conclusions

The following conclusions can be drawn from the above analysis:

(1) The deformation of rock mass in zone A is due to excavation unloading instead of sliding.

(2) Blocks with routine anchorage system are stable

(3) In the condition of high in-situ stress, excavation unloading leads to apparent increase of rock mass and sometimes, the deformation change rate reaches 1.2mm/d. But if blocks are stable and the deformation does not influence the safety of other structures, it should allow block to deform to some extent and no other reinforcement measures are needed.

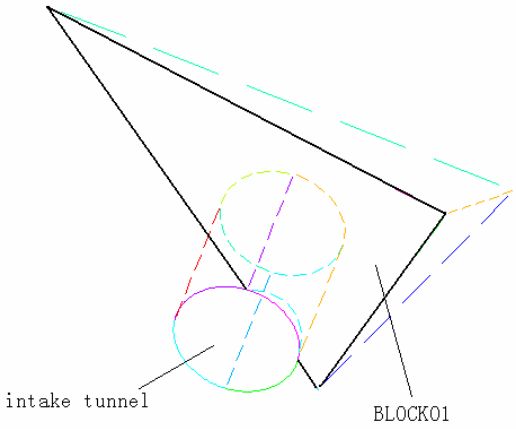

Fig .15 3-D perspective

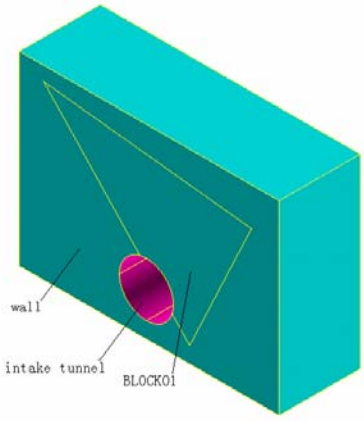

Fig. 16 3-D solid

Fig .17 cut part

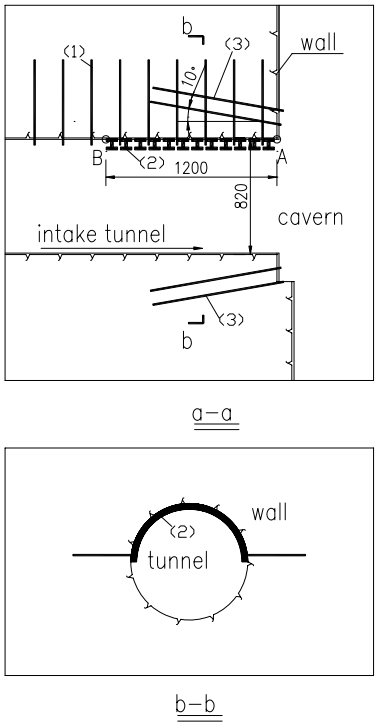

Fig.18 Strengthening support to tunnel portal

(1)- Bolts with diameters of 32 mm, length =6.0m,spacing 2.0m×2.0m

(2)- "I"shape steel，one of every 1.0 metre

(3)- Bolts with diameters of 32 mm, length =9.0m spacing 1.0m×1.0m

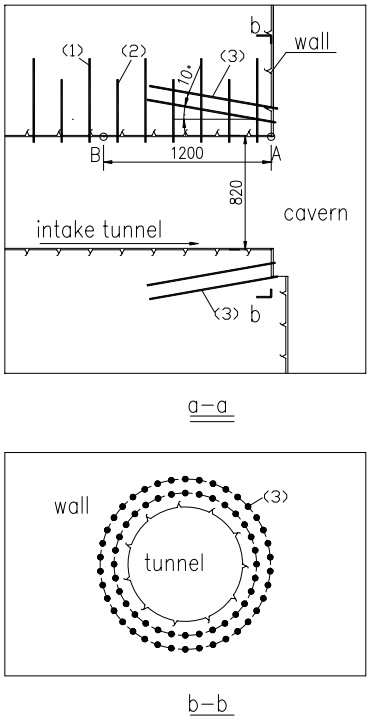

Fig .19 system support to tunnel portal

(1)- Bolts with diameters of 32 mm, length =6.0m spacing @ 4.0m×4.0m

(2)- Blots with diameters of 28 mm, length =4.5m spacing @ 4.0m×4.0m

(3)- Blots with diameters of 32 mm, length =9.0m spacing @ 1.0m×1.0m

References

Liu jinhua, Lu zuheng. Block Theory and Its application To Rock Engineering[M].China Beijing: Water Resourcesand Electric Power Press, 1988

Yang tianjun, JU guanghong. Geologic report on underground house of Laxiwa waterpower station [R]. China Xi'an: Northwest Investigation Design & Research Institute, 2006

Shi guangbin. Analysis report of monitoring data on underground house of Laxiwa waterpower station [R]. China Xi'an: Northwest Investigation Design & Research Institute, 2006

Shi guangbin. Rock deformation Analysis of cavern excavation unload under high in-situ stress [R]. China Xi'an: Northwest Investigation Design & Research Institute, 2006

Shi guangbin. Analysis report of block stability on underground house of Laxiwa waterpower station [R]. China Xi'an: Northwest Investigation Design & Research Institute, 2006

Automatic Generation of 2D Physical Cover in Numerical Manifold Method

WEN XIN, FANG XISHENG and WANG YING

College of Computing and Communication Engineering Graduate University,
Chinese Academy of Sciences, Beijing, P.R.CHINA

Automatic generation of 2D physical cover in numerical manifold method (NMM) is very important for engineering applications even it is a difficult subject. This paper analyzes the data structure of CAD graphics files, and designs an effective integration interface between AutoCAD software and NMM program. Besides, this paper implements the automatic generation of mathematical cover through dividing the whole area by regular equilateral triangles. These efforts greatly improve the computational efficiency and accuracy of NMM program.

Keywords: Numerical manifold method; Physical cover; Mathematical cover; AutoCAD; Data structure

1. Introduction

Numerical manifold method(NMM) can compute the movements and deformations of structures or materials(Shi 1992), and it has been applied in the construction process of some great hydroelectric power stations in China such as Laxiwa hydroelectric power station in Qinghai province and Jinping hydroelectric power station in Sichuan province. The applications of NMM program in these occasions demonstrate its predominant capability of structure analysis.

Generation of physical cover in the pre-processing period is the foundation of subsequent NMM computation. The research on the automatic generation of physical cover is very important for engineering application even it is a difficult project. The first difficult one is to design an effective integration interface between CAD systems and NMM program, and the second is how to generate mathematical cover automatically. This paper analyzes the data structure of CAD graphics files, designs an effective integration interface between AutoCAD software and NMM program, and then implements the automatic generation of mathematical cover through dividing the whole area by regular equilateral triangles.

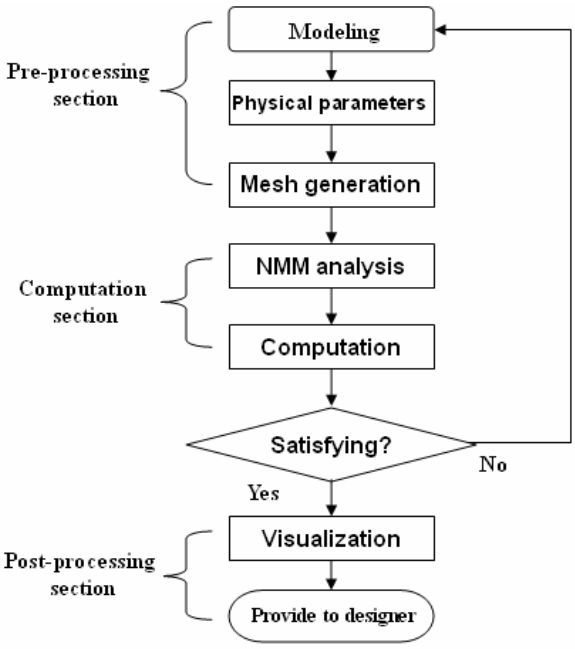

Fig. 1: Process of NMM program.

2. Analysis of NMM Program

NMM program is made up of three major sections, including pre-processing section, computation section and post-processing section. Pre-processing section is to accomplish the generation of physical cover, which consists of model-establishing and mathematical mesh generation; Computation section is to compute the stress and strain of the model under the function of different kinds of load conditions in use of NMM; Post-processing section is to display the computing results in graphics which helps the analysis.

Computation section is almost mature, most of the time of program applications is spent in pre-processing period and post-processing period. Especially, in the present, the construction of engineering analytical models is very time-consuming and of low efficiency because the modeling functions which NMM program provides itself are very limited and engineers are not familiar with them. Currently there are many software that can produce object models, such as AutoCAD, I-DEAS, SolidEdge and Pro/E, etc. AutoCAD is the most popular software in the field of architectural and

mechanical design. It has very powerful graphic editing functions which facilitate engineers a lot and has become their favorite CAD software in China(Xu 2003). Thus modeling in AutoCAD can prevent much repeating work. Therefore, research on the effective integration between AutoCAD software and NMM program replaces that of the development of NMM program's modeling functions in this paper.

The first thing to do is to analyze the data structure of the input files of NMM program. NMM program's input files include two types of files: file MC for geometry information storing and the other for physical parameters storing. A geometry information file MC which is converted from a DXF file generated by AutoCAD contains three parts of data which is stored in a specific way as follow:

- Geometry data of the entity: Geometry data of entities' boundaries and joints and their materials
- Geometry data of special points: Geometry data of fixed point, load points, measure points and hole points.
- Mathematical cover division parameter.

3. Implementation of Integration

3.1 AutoCAD File Format

AutoCAD is a universal graphics software whose file formats includes DWG, DWB and DXF. DXF files enable the interchange of drawings between AutoCAD and other programs such as programs written in senior programming language or other CAD systems. Although DXF is not a standard, but as a result of the popularity of AutoCAD software, DXF grew to be one of the mainstream graphics data interchange standards.

Essentially a DXF file is composed of pairs of codes and associated values. The codes, known as group codes, indicate the type of value that follows. Using these group code and value pairs, a DXF file is organized into sections, including HEADER, CLASSES, TABLES, BLOCK, ENTITIES and OBJECTS, which are composed of records, which in turn are composed of a group code and a data item. Each group code and value are on their own line in the DXF file(Xu 2003). For example, the first line of one group code is "8" which indicates LAYER, and the second line is "0" which indicates the LAYER's number is 0. The information that we need is mainly geometry information which is located in the section of ENTITIES(Qin 2004). Take a simple graphics—a line's DXF file for example, part of the file content is as follows:

```
……  // omission of the previous content
0  // indication of a new section
SECTION
2
ENTITIES  // section of ENTITIES
0
LINE  // indication of the entity of a line
5
2B
330
1 F
l00  // subclass indication
AcDbEntity
8  // layer where the entity is located.
0  // number 0 layer
62  // color of the line
7  // white
100  // subclass indication
AcDbLine
10  // indicates that the next line is X coordinate of the
    // beginning point of the line
108.7645299018547
20  // indicates that the next line is Y coordinate of the
    // beginning point of the line
165.6432764085351
30  //indicates that the next line is Z coordinate of the
    //beginning point of the line
0.0
11  // indicates that the next line is X coordinate of the
    // end point of the line
287.1809547623936
21  // indicates that the next line is Y coordinate of the
    // end point of the line
354.9818475835924
31  // indicates that the next line is Z coordinate of the
    // end point of the line
0.0
0
ENDSEC  // indication of the end of the section
……
0
EOF  // end of file
```

Fig. 2: A white line in AutoCAD

3.2 Implementation of Integration

What integration should accomplish is to abstract the geometry information of the model and endow them

with material parameters. Considering the different characteristics of AutoCAD DXF files and NMM program input files, this paper designs an effective method to implement integration. Since most of the engineering drawings are two-dimensional, we only consider 2D applications and neglect 3D occasions(Zhu 2002, Suresh 2003). When engineers are drawing a model, different types of entities are represented by different colors or different explanative texts. The integration tool in this paper recognizes the differences by colors, that is: for different joints and boundaries, material 1 uses color 1, material 2 uses color2, material 3 uses color 3; Special points are represented by special graphics shapes. This paper uses small circles of specified radius to represent special points, and the coordinate of the center of the circle is that of the special point, different kinds of special points are discerned by different colors as well.

When programming on the platform of VisualC++6.0 to read a DXF file, different geometry information is abstracted according to the recognition of the differences of group code key words and the relative positions in a DXF file, then it is written into a new file MC according to the format of the input file of the NMM program. Besides, at the end of the new file, the mathematical cover division parameter is specified to be a default value. If the computation and analytical results are not satisfying, it can be modified.

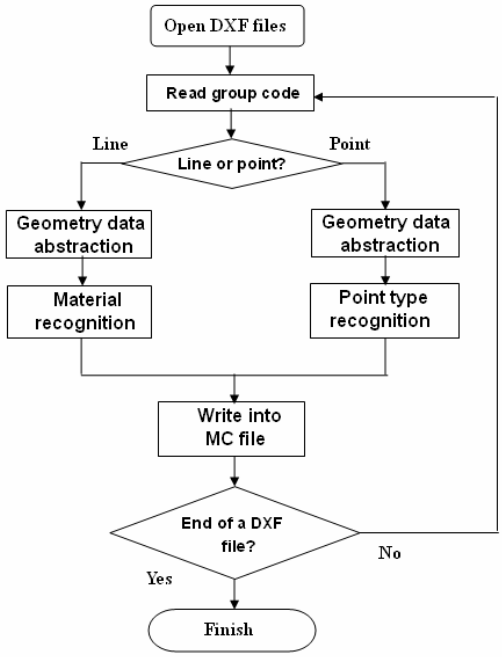

Fig. 3: Process of the integration program

4. Automatic Generation of Physical Cover

Since equilateral triangles are optimized mesh elements, this paper adopts the method of dividing the whole area by equilateral triangles automatically, then joints or block boundaries of different shapes divide a mathematical cover into two or more completely disconnected domains shown in figure 4 and figure 5, these domains form physical cover which is the foundation of NMM computation(Shi 1997, Shi 1992).

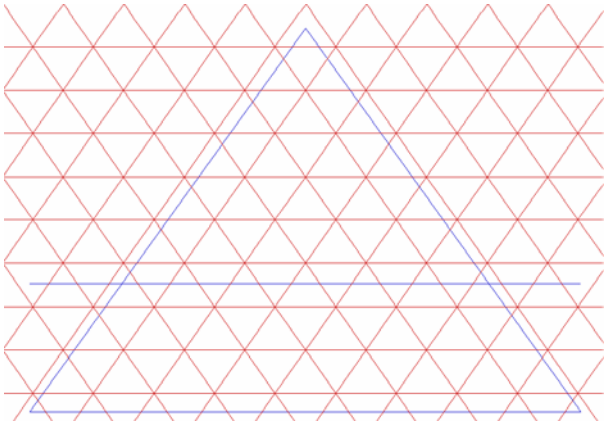

Fig. 4: Mathematical cover generation

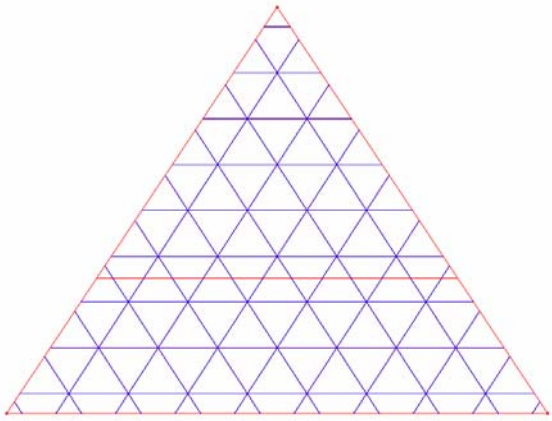

Fig. 5: Physical cover generation

Analysis steps are as follows:

(1) Model construction in AutoCAD, and save as DXF files
(2) Convert DXF files to input files of NMM program
(3) Physical cover generation
(4) Analysis on data generated by physical cover, and form graphics display.

This paper takes two examples to illustrate the integration process in engineering analysis applications. The first one is to analyze a destructive model of deformation of an arch, and the second one is to analyze a destructive model of deformation of rocks with horizontal thin layers. The first one illustrates NMM's capability of dealing with conventional situations with big blocks, and the second one

illustrates NMM's special capability of dealing with very thin structures effectively.

4.1 A Destructive Model of Deformation of An Arch

In this example, the arch to be analyzed consists of seven big blocks. Four fixed points are located in the left and right side of the arch, and the load point is located in the center of the third block from left to right. After the process of AutoCAD modeling and file format conversion, mathematical cover and physical cover of the model are generated automatically, finally, the deformation result is displayed.

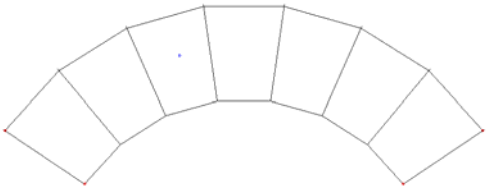

Fig. 6: Model construction of an arch in AutoCAD

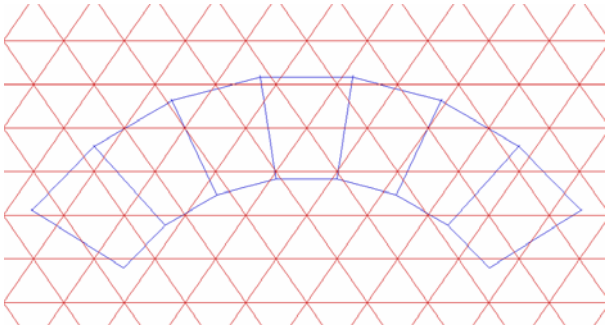

Fig. 7: Automatic generation of mathematical cover

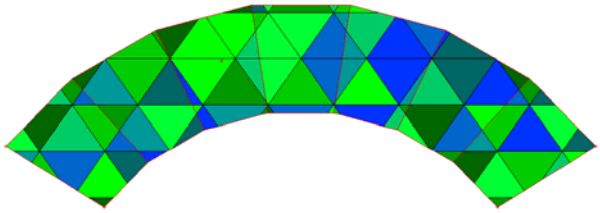

Fig. 8: Analytical model generated by physical cover

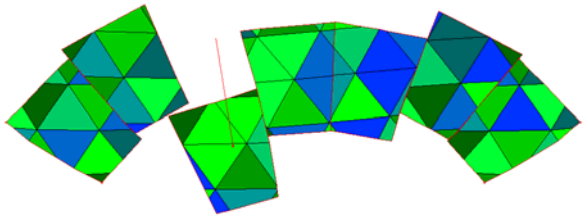

Fig. 9: Deformation analysis

4.2 A Destructive Model of Deformation of Rocks With Horizontal Thin Layers

In this example, the rocks to be analyzed consist of eight horizontal thin layers. Ten fixed points are located at the bottom of the supporter of the rocks, and the load point is located in the middle of top rock layer. After the process of AutoCAD modeling and file format conversion, mathematical cover and physical cover of the model are generated automatically, finally, the deformation result is displayed.

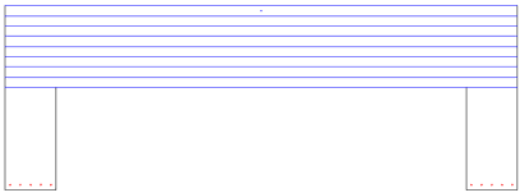

Fig. 10: Model construction of rocks with layers in AutoCAD

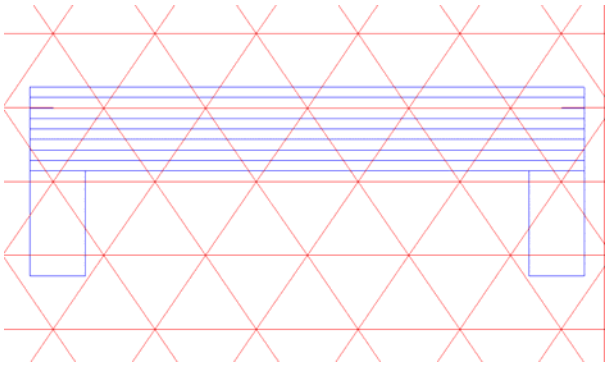

Fig. 11: Automatic generation of mathematical cover

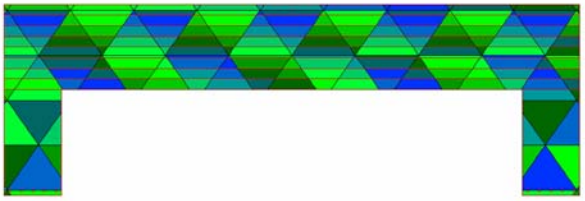

Fig. 12: Analytical model generated by physical cover

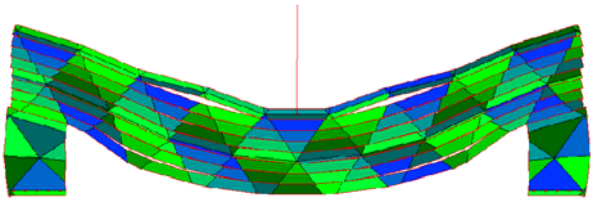

Fig. 13: Deformation analysis

5. Conclusions

Based on the analysis and comparison of DXF file format of AutoCAD software and the input file format MC of NMM program, this paper designs an effective interface tool for connecting two different systems on the platform of VisualC++6.0, and implements the effective integration between two systems. Besides, this paper implements the automatic generation of mathematical cover through dividing the whole area by regular equilateral triangles. Automatic generation of 2D physical cover comes into being after the implementation of the work above. These efforts will save much time in the pre-processing period of NMM program, and will improve the computational efficiency and accuracy of it.

References

Shi G.H. Manifold Method of Material Analysis. C. *Transactions of the Ninth Army Conference on Applied Mathematics and Computing*. Minneapolis, Minnesoda, USA, 1992, 51-57.

Xu W.D. Interface Design of FORTRAN and AutoCAD and its Applications in Finite Element Analysis. *J. Journal of Fuzhou University* (Natural Science), 2003, 31(2), 186-190.

Qin W.X., Wu J and Wu S.H. Study and Realization of Seamless Link between FEM Software and Universal Graphics Software. *J. Rock and Soil Mechanics*，2004, 25(1), 614-618.

Zhu H.S., Ai Z.J., and Deng J.T. Analysis of the Integration Between CAD and CAE. *J. Computer Engineering and Design*, 2002, 23(9), 22-25.

Suresh K. Automating the CAD/CAE Dimensional Reduction Process. J. *Proceedings of the eighth ACM symposium on solid modeling and applications*, Seattle, Washington, USA, 2003, 76–85.

Shi G.H. *Numerical Manifold Method and Discontinuous Deformation Analysis*. M. Pei J.M. translated. Tsinghua University Press, Beijing, 1997, 3-14.

Shi G.H. Manifold Method. C. *Fractured and Jointed Rock Masses*, Lake Tahoe, California, USA, 1992.

On the onset and propagation of shear band in undrained geomaterials

E.G. SEPTANIKA[1,2] and V. THAKUR [3]

[1] Geoengineering Division, Delft University of Technology, The Netherlands
[2] PLAXIS BV, Delft, The Netherlands
[3] ICG and Geotechnical Division, NTNU, Trondheim, Norway

This paper presents a discontinuous approach for describing failure in geomaterials using the PUM/X-FEM taking into account for the pore water effect. For undrained case, it has been assumed that shear band initiation and propagation is related to the induced pore pressure at the tip. Once the shear band is initiated, the softening behavior is governed by the instantaneous loss of cohesion due to the increase of sliding. Hence, the proposed onset/propagation criterion of shear band (discontinuity) is based on a pore-pressure jump. The orientation is based on an averaged gradient of incremental displacements at the tip of the progressing shear band. This approach has been implemented in the Finite Element Program PLAXIS, and utilized to model failure of geomaterials. The verification study of the proposed the initiation/propagation procedure has been performed for biaxial test, shear test and passive retaining wall problem.

Keywords: Shear band; discontinuity; Undrained geomaterials; Softening; PUM/X-FEM

1. Introduction

Modeling of failure in geomaterials requires an adequate description of shearbanding phenomena. Discontinuous approach provides a tool that describes displacement jumps across the shear band in a proper way. Recently, the previous PUM/X-FEM framework as described in Septanika et al (2005a) has been extended by taking into account for undrained behavior in fully saturated media and the pore pressure effects. As pointed out by e.g. Meschke and Dumstorff (2004), the onset/propagation criterion appears to play an important role towards a robust modeling of progressive growth of the shear band. In addition to the previous studies (Vermeer et al 2004, Septanika et al 2005a, 2005b) this paper is focused on shear band initiation/propagation in undrained geomaterials. Undrained instability in geo-material can be observed either due to the shear induced pore pressure or due to the instantaneous loss of cohesion. Shear induced pore pressure can be a crucial factor to govern the strain softening behavior of the geomaterial but not essentially a real material (cohesion or frictional angle) softening itself. Apparently, undrained instability does not only cause the displacement jump at the shear band, but also the jump in pore pressure. Within the shear band additional pore pressure development might be observed, i.e. induced by the large shear deformation in the localized zone. Keeping this in view, a new onset criterion has been considered based on pore-pressure jump at the localized zone. The orientation is approximated based on an averaged gradient of incremental displacements at the tip of the progressing shear band. The developed PUM/X-FEM framework, the proposed initiation/propagation and the orientation algorithms have been implemented in the PLAXIS Finite Element Code for Soil and Rock Analyses. This paper shortly describes the mainframe of the developed discontinuous approach for modeling (progressive) failure in undrained geomaterials.

2. Background

The undrained behavior of fully saturated media is characterized by a change in the excess pore pressure. The total stress consists of the effective stress part in the soil skeleton and the pore pressure part in the pore water (Terzaghi 1943). Shear induced pore pressure can be a crucial factor to govern the failure behavior of the geomaterial.

2.1 PUM/X-FEM for fully saturated media

The point of departure is the two separate weak equations (as defined in e.g. Wells and Sluys 2001) governing the equilibrium of a body Ω which bounded by the boundary Γ and crossed by discontinuity Γ_d

$$\int_{\Omega} \mathbf{B}^{\mathrm{T}} \boldsymbol{\sigma}\, d\Omega = \int_{\Gamma_u} \mathbf{N}^{\mathrm{T}} \mathbf{t}_u\, d\Gamma \tag{1}$$

$$\int_{\Omega^+} \mathbf{B}^{\mathrm{T}} \boldsymbol{\sigma}\, d\Omega + \int_{\Gamma_d} \mathbf{N}^{\mathrm{T}} \mathbf{t}\, d\Gamma = \int_{\Gamma_u} \mathcal{H}_{\Gamma} \mathbf{N}^{\mathrm{T}} \mathbf{t}_u\, d\Gamma \tag{2}$$

Where $\mathbf{B} = \nabla^s \mathbf{N}$, $\mathbf{N}$ is a shape function matrix, $\boldsymbol{\sigma}$ is the Cauchy stress tensor in a vector notation, $\mathbf{t}_u$ is external traction forces along the boundary Γ_u and $\mathbf{t}$ is the tractions at discontinuity Γ_d, $\mathcal{H}_{\Gamma}$ is the Heaviside function and Ω^+ is the so-called active region. For undrained media, the total stress $\boldsymbol{\sigma}$ consists of the

effective stress part $\boldsymbol{\sigma}$' and the pore water part $\boldsymbol{\sigma}_w$. Note that by assuming the change of pore pressure is related to the volumetric strain of the continuum, one can eliminate the pore pressure degrees of freedom. After substitutions of the stresses into the above weak equations and linearization, one arrives at the incremental-iterative finite element formulation

$$\begin{bmatrix} \mathbf{K}^u_{aa} & \mathbf{K}^u_{ab} \\ \mathbf{K}^u_{ba} & \mathbf{K}^u_{ab} + \mathbf{K}^u_{bb} \end{bmatrix} \begin{Bmatrix} \Delta\mathbf{a} \\ \Delta\mathbf{b} \end{Bmatrix} = \begin{Bmatrix} \mathbf{R}_a \\ \mathbf{R}_b \end{Bmatrix} \tag{3}$$

$$\mathbf{K}^u_{aa} = \int_\Omega \mathbf{B}^T \mathbf{D}^u \mathbf{B}\, d\Omega \tag{4a}$$

$$\mathbf{K}^u_{ab} = (\mathbf{K}^u_{ba})^T = \int_{\Omega^+} \mathbf{B}^T \mathbf{D}^u \mathbf{B}\, d\Omega \tag{4b}$$

$$\mathbf{K}^u_{bb} = \int_{\Gamma_d} \mathbf{N}^T \mathbf{T}^u \mathbf{N}\, d\Gamma \tag{4c}$$

$$\mathbf{R}_a = \mathbf{f}^{ext}_a - \mathbf{f}^{int}_a \tag{4d}$$

$$\mathbf{R}_b = \mathbf{f}^{ext}_b - \mathbf{f}^{int}_b \tag{4e}$$

where $\Delta\mathbf{a}$ and $\Delta\mathbf{b}$ are the increments in the regular nodal displacements and the enhanced displacements (jumps), $\mathbf{D}^u$ represents the elastic stiffness matrix for the undrained case, $\mathbf{f}^{ext}_a$ and $\mathbf{f}^{int}_a$ represent the external and internal forces according to the regular degrees of freedom, while $\mathbf{f}^{ext}_b$ and $\mathbf{f}^{int}_b$ are the forces corresponding to the enhanced degrees of freedom.

2.2 Constitutive model

Without referring to any particular plasticity model, the governing equation for the intact soil continuum, discontinuity and the pore water can be formulated as

$$\dot{\boldsymbol{\sigma}}' = \mathbf{D}^e (\dot{\boldsymbol{\varepsilon}} - \dot{\boldsymbol{\varepsilon}}^p),\ \dot{\boldsymbol{\varepsilon}}^p = \dot{\lambda} \frac{\partial g}{\partial \boldsymbol{\sigma}},\ f = f(\boldsymbol{\sigma}, q) \le 0 \tag{5}$$

$$\dot{\mathbf{t}} = \mathbf{T}^e (\dot{\mathbf{b}}_\Gamma - \dot{\mathbf{b}}^p_\Gamma),\quad \dot{\mathbf{b}}^p_\Gamma = \dot{\lambda}_\Gamma \frac{\partial \mu}{\partial \mathbf{t}},\ \phi = \phi(\mathbf{t}, \kappa) \le 0 \tag{6}$$

$$\dot{\boldsymbol{\sigma}}_w = \frac{K_w}{n} \dot{\boldsymbol{\varepsilon}}_v \tag{7}$$

where $\dot{\boldsymbol{\varepsilon}}$ and $\dot{\boldsymbol{\varepsilon}}^p$ are the strain rate and the plastic part of the strain rate, $\dot{\lambda}$ is the rate of plastic multiplier, f and g are the yield function and the plastic potential function, q is an internal variable (to accommodate e.g. hardening behavior), $\mathbf{D}^e$ is the elastic stiffness matrix, $\mathbf{T}^e$ represents the pseudo stiffness matrix of the discontinuity, $\mathbf{b}^p_\Gamma$ represents the "plastic part" of the jump, $\mathbf{b}_\Gamma$ represents the total jump, $\dot{\lambda}_\Gamma$ is the rate of plastic multiplier at discontinuity, ϕ and μ are the discrete yield function and the plastic potential function of discontinuity, κ is an internal variable (related to e.g. the state of sliding/cracking at discontinuity), K_w is the bulk modulus of water, n is the porosity and $\dot{\boldsymbol{\varepsilon}}_v$ is the rate of volumetric strain.

2.3 Onset stresses and tractions

It is worth to mention that the stresses and tractions at the onset of shear band have to be properly determined to maintain the global equilibrium. For the continuum, the total onset stress $\boldsymbol{\sigma}_0$ is determined from the effective part $\boldsymbol{\sigma}'_0$ and the pore water part $\boldsymbol{\sigma}_{w0}$ (which can be determined using standard plasticity analyses)

$$\boldsymbol{\sigma}_0 = \boldsymbol{\sigma}'_0 + \boldsymbol{\sigma}_{w0} \tag{8}$$

Similarly, the total onset traction $\mathbf{t}_0$ at discontinuity can be also divided into the effective part $\mathbf{t}'_0$ and the pore pressure part $\mathbf{t}_{w0}$

$$\mathbf{t}_0 = \mathbf{t}'_0 + \mathbf{t}_{w0} \tag{9}$$

3. Onset/propagation criterion

The onset criterion for the undrained case is based on a sudden jump of the pore pressure in the localized zone with respect to continuum pore pressure. Due to shearing $\Delta\gamma$ induced pore pressure Δp will be developed in the continuum, which can be generally expressed as

$$\Delta p \sim \alpha . \Delta\gamma \tag{10}$$

For the Mohr-Coulomb based plasticity models, the constant α depends on the shear modulus G, Poisson's ratio ν, friction angle φ and dilation angle ψ. In the localized zone at the tip of the shear band, the amount of shearing will be much larger than outside the localized zone. The corresponding induced pore pressure $\Delta p_{localized}$ will be much higher than the average Δp in the continuum. Hence, for undrained case it is assumed that the shear band will be initiated and propagated when the tip region undergoes plastic deformation and the following criterion is met

$$\Delta p_{localized} \ge M . \Delta p \tag{11}$$

where M is a user-defined threshold value.

For determination of the shear band orientation, an incremental displacement function $\Delta V \equiv \Delta V(\mathbf{x})$ is first generated based on the nodal solutions $\{\Delta\mathbf{V_i}\}$. The Gaussian value at (ξ, η, ζ) is then interpolated using the element shape function matrix $\mathbf{N}$, i.e.

$$\Delta V(\xi, \eta, \zeta) = \mathbf{N}\ \{\Delta\mathbf{V_i}\} \tag{12}$$

The orientation simply follows from the derivatives of ΔV with respect to the spatial coordinates. To obtain more reliable information for the initial orientation, the incremental displacements around the tip have been averaged using a Gaussian weight function (see also Septanika et al 2005b).

4. Numerical examples

The following examples are based on the results of current implementation and purposed to illustrate its capability in modeling shear band initiation and propagation in undrained geomaterials. The soil plasticity model is according to the standard Mohr-Coulomb model in the PLAXIS Finite Element Code for Soil and Rock Analyses. To model the softening, it is assumed that the cohesion c_Γ at discontinuity is decreased linearly by the increase of sliding, i.e. $c_\Gamma = c_0 - h_c.|b_s|$ with c_0 is the initial cohesion of the continuum, h_c is the softening modulus at discontinuity and $|b_s|$ is previous attained maximum sliding of the shear band. For the simplicity, the analyses have been performed using 6-noded triangular plane-strain elements.

4.1 Biaxial test

In the homogeneous stresses situation the shear band will occur spontaneously, since the onset criterion will be reached at all points at the same times. In the present approach, the start point of the shear band (the trigger point) can be set manually or automatically. In case of homogeneous stresses, the shear band will be straight and its orientation is related to the frictional angle of the continuum. For biaxial test, the sample is first loaded isotropically under drained condition, in which the vertical stress and the lateral stress are equal $\sigma_v = \sigma_h = \sigma$. Then the lateral stress σ_h is kept constant at 100 kPa while the top surface is pushed downward by means of prescribed displacement (under undrained condition). The applied force is linearly decayed by the increase of the sliding along the shear band, according to the presumed linear softening model. The force at the peak is related to the vertical stress at the onset of plasticity (i.e. when $c_\Gamma = c_0$) and the residual force is governed the lateral stress σ_h. Fig. 1(a)-1(c) show the deformed mesh in a biaxial test, the pore pressure distribution at the residual state and the corresponding force-displacement curve. The pore pressure outside the shear band is decreasing to its residual value, while inside the band additional pore pressure is generated in accordance with the localized shear deformation at the band. The residual state is achieved when $c_\Gamma = 0$ and $\sigma_v \sim \sigma_h$ (i.e. with the width of 6 m, the applied vertical force at the residual state is around 600 kN).

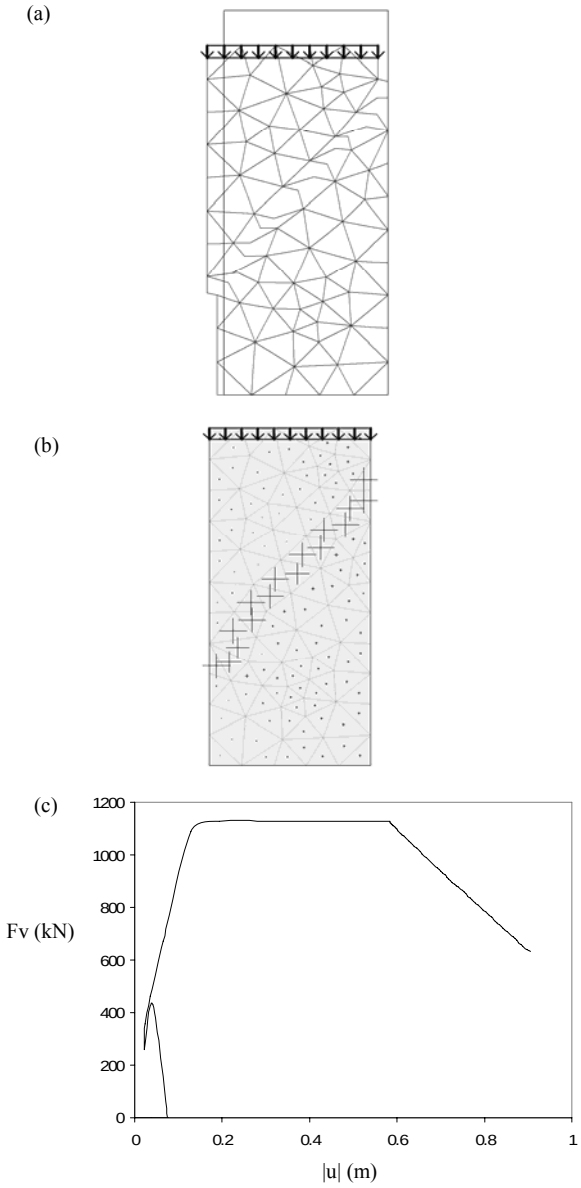

Fig.1(a): Deformed mesh in biaxial test,
(b): Pore pressure at residual state
(c): Force-displacement curve.

4.2 Shear test

The second example considers shear band formation during a shear test in which the pre-peak stress state is characterized by a homogeneous distribution of the shear stress. For this purpose the sample is first loaded by a constant shear stress τ (with $\sigma_v = \sigma_h = 0$), after that the top surface is pushed to the right by means of prescribed displacement (under undrained condition). Similarly as before, the stresses during the softening are governed by Δc. The corresponding deformed mesh pattern, the pore pressure contour and the force-displacement curve are shown in Fig. 2(a)-(c). Due to the fact that no lateral stress is being imposed and

generated, the applied force will decay to the residual cohesion (slightly above zero). It is clearly seen that the pore pressures are very dominant in the region being crossed by the shear band

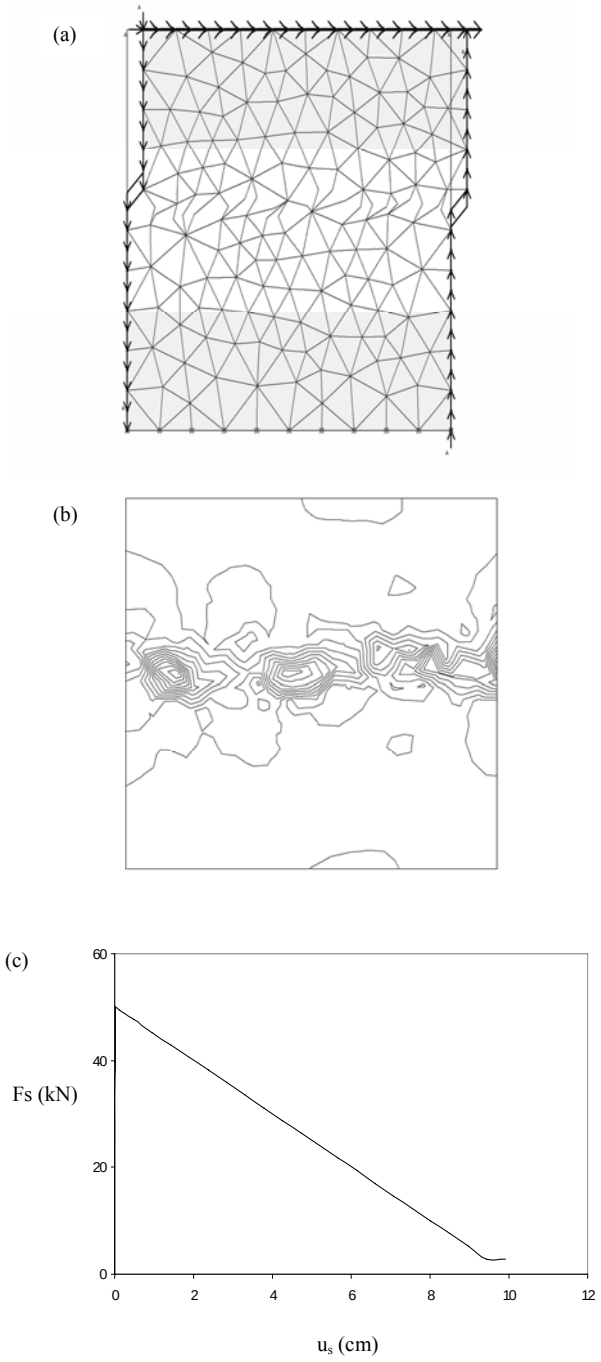

Fig.2(a): Deformed mesh in pure shear test,
(b): Pore pressure contour at residual state,
(c): Force-displacement curve.

4.3 Passive wall problem

The third example considers shear band formation in passive soil-retaining wall case. Due to soil weight effect the vertical stress varies linearly with depth and during K0-procedure lateral stresses are generated based on K0 values. The free right edge is pushed to the left by means of prescribed displacement. Under the present condition, small portion of shear band will be initiated starting at the toe of the wall. Then it propagates slowly up to few elements, until suddenly a spontaneous formation of the shear band will occur. Leading to a slightly curve shear band nearby the toe, followed by a more or less straight shear band up to the top surface as shown in Fig. 3(a). The corresponding pore pressure distribution at the residual state and the force-displacement curve is shown in Fig. 3(b)-(c). The pore pressure in the region around the toe is strongly affected by the imposed boundary condition. However, at the shear band significant residual pore pressure is also observed. Outside the band and the toe region relative smaller residual pore pressures are observed. Note also that the global distribution of pore pressure outside the shear band is affected by the inhomogeneous state of onset stresses. The force at the peak is related to the stresses at the onset of the shear band (i.e. when $c_\Gamma = c_0$) and the residual force corresponds to the stresses for $c = 0$.

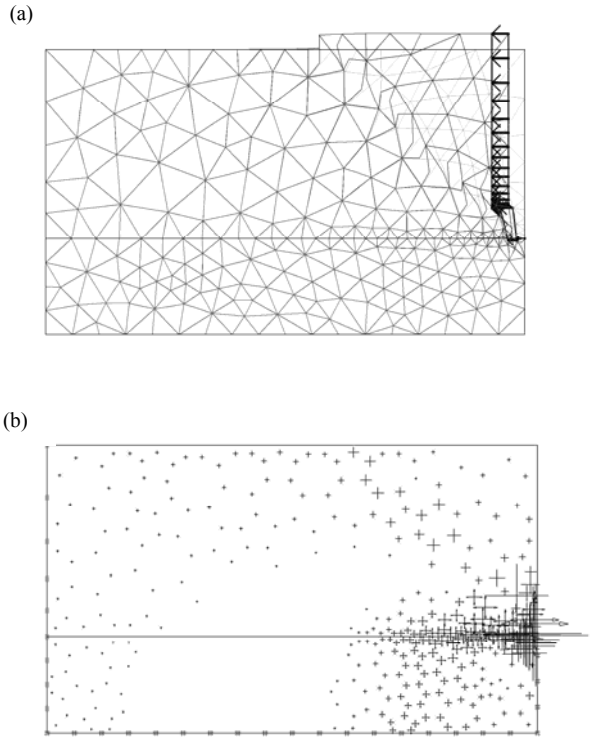

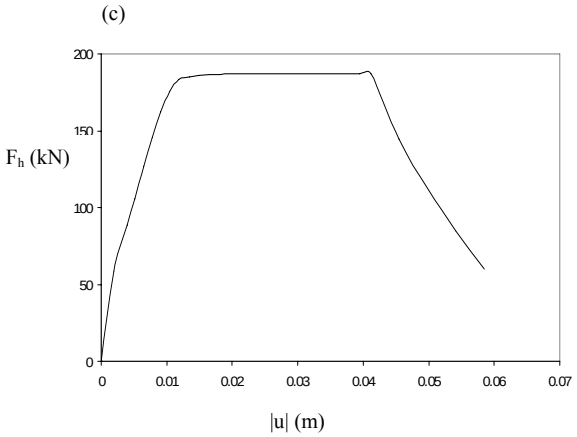

Fig.3(a): Deformed mesh in passive wall test,
(b): Pore pressure at residual state,
(c): Force-displacement curve.

5. Conclusions

This paper presents a discontinuous approach based on the PUM/X-FEM mainframe, considering undrained behavior in fully saturated geomaterials. Undrained effect is included by assuming that the total stress is the sum of the effective part and the pore pressure part. In addition to the drained case, a new onset/propagation criterion for the shear band has been added based on pore-pressure jump criterion. The shear band is inserted element wisely as soon as the pore pressure jump exceeds the presumed threshold value. The orientation of the shear band is determined based on the gradient of the incremental displacement function. The applicability of the proposed approach has been illustrated by considering some standard cases of (progressive) failure in geomaterials. In the near future, more study will be performed regarding the extension onto the coupled deformation-pore pressure problem (such as consolidation) and the application of the developed PUM/X-FEM mainframe in simulating real situations. This research is supported by the Dutch Technology Foundation STW (Project DCB 6368).

References

Meschke G. and Dumstorff P., Discontinuous representation of brittle failure. *Proceedings of 2nd International Symposium on Continuous and Discontinuous Modeling of Cohesive Frictional Materials*, 2004, Stuttgart, 339-352.

Septanika, E.G. Bonnier, P.B. and Brinkgreve, R.B.J., Modeling progressive sliding/cracking in geomechanics. *International Conference on Mechanical Engineering ICME*, 2005a, Bangladesh, AM-01, 1-5.

Septanika, E.G. and Brinkgreve, R.B.J., Progressive shear band model for soil retaining wall problem. *7th International Conference on Analysis of Discontinuous Deformation ICADD-7*, 2005b, Hawaii, 257-264.

Terzaghi, K. Theoretical Soil Mechanics, John Wiley and Sons, New York, 1943.

Vermeer P.A., Vogler U., Septanika E.G. and Stelzer O. A strong discontinuity method without locking. *Proceedings of 2nd International Symposium on Continuous and Discontinuous Modeling of Cohesive Frictional Materials*, 2004, Stuttgart, 381-396.

Wells G.N. and Sluys L.J. A new method for modeling cohesive cracks using finite elements. *International Journal for Numerical Methods in Engineering*, 2001, 50(12), 2667-2682.

Failure process simulation of Meihua Arch Dam by 3-D mode discrete element method

JIN FENG[1], ZHANG CHONG[1,2], WANG RENKUN[2], FENG XUEMIN[2]

[1] State Key Laboratory of Hydroscience and Engineering, Tsinghua University, Beijing 100084, China
[2] Chengdu Hydroelectric Investigation & Design Institute of SPC, Chengdu, 610072, China

The 3-D mode distinct element method (3MDEM) is an efficient numerical method to simulate the mechanical behaviors of small and finite deformation in both continuous medium and discontinuous ones. It is developed from the distinct element method, and has the advantage of fewer degree of freedom and higher precision. The failure process of Meihua Arch Dam in 1981 is simulated by 3MDEM. Results demonstrate that the cause of the rapid collapse of the dam is the upward sliding of the dam body along the peripheral joint, which lacks of enough shear resistance, under the load of the thrust due to the pressure of the reservoir.

Keywords: discrete element method (DEM); discontinuum; numerical computation

1. Introduction

To simulate the failure process of an arch dam-foundation system, numerical methods are required to obtain accurate deformation and stress in small-deformation phase, and to reasonably deal with motion of the block system in post-cracking phase. The continuum mechanics methods, such as Finite Element Method, Boundary Element Method, Mesh-less Method, etc., are not good at simulating block systems, because: ① these methods can not update the contact mode between discontinuous interfaces during block motion. ②these methods can not detect new contact between blocks. ③these methods can not analyze block systems with many discontinuous interfaces, especially when blocks can slide along these interfaces with fairly large deformation, therefore unable to simulate the whole failure process of dams. Discontinuum mechanics methods, such as DDA and DEM, which can reasonably take finite displacement and finite rotation into consideration, overcome the above limitations. However, the accuracy and efficiency of these methods are not good enough in simulation of small deformation of continuous medium. So, developing an effective method simulating the whole failure process of block system from continuous status to discontinuous one, and from small deformation phase to finite displacement one is an attractive work. Numerical Manifold Method (NMM) is one of these efforts, but at present it is only applied in two dimensional and simple problems.

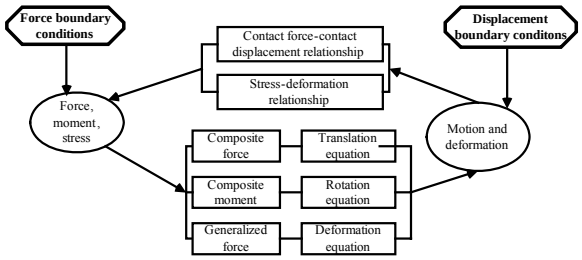

Fig. 1 Flow diagram of 3MDEM

On the basis of the distinct element method brought forward by Cundall (Cundall, 1988, Hart, et al. 1988), 3-D mode discrete element method (3MDEM) (Zhang et al. 2007) is proposed for simulating the whole failure process of hydraulic structures from continuous status

National Natural Science Foundation of China: 90510018
National Natural Science Foundation of China: 50539020

to discontinuous one, and from small deformation phase to finite displacement one. It has high computation efficiency and good numerical stability. The computation flow diagram of 3MDEM is illustrated in Fig 1.

In this paper, the whole failure process of Meihua Arch Dam simulated by 3MDEM is presented. Meihua Arch Dam (Nu et al. 1995), located in Fujian Province in south-east China, is a cylinder-shape arch dam with fixed center and constant outer radius of arch ring, and with a height of 22m and a crest length of about 72.6m. It was built as a masonry structure composed of cement mortar and rags, and peripheral joints between the dam body and its artificial concrete abutment had been set, whose surfaces were coated with bitumen and polyvinyl chloride with the coefficient of friction of maybe only 0.3. The dam collapsed in September 1981, shortly after completed in May of the same year without any warning sign. Residual base foundation in both bank after collapsed are shown in Fig 2. Field investigations indicated that the failure occurred possibly due to the upward and downstream sliding of the dam along a peripheral joint. The computation by 3MDEM simulates the failure process of the dam, and the analysis results agree well with the field investigations.

a. Left abutment

b. Right abutment

Fig. 2 Residual base foundation in both abutments after collapsed

2. Comparison of simulation results by Abaqus, 3DEC and 3MDEM

The block mesh of the Meihua arch dam by 3MDEM is shown in Fig. 3. Average block size is 1m. According to the construction materials of Meihua Project, the blocks of dam body have a modulus of elasticity of 8GPa, a Poisson's ratio of 0.3 and a density of 2360kg/m^3.

In order to compare with FEM Software ABAQUS, (Cui 2001) and DEM Software 3DEC(Hou et al. 2005) under small deformation phase, the strength in peripheral joint and dam interface are selected large enough at first. In this case, the foundation is assumed with rigid block in all ABAQUS, 3DEC and 3MDEM. The gravity load and reservoir water pressure are taken into account and applied to the arch dam body at one step.

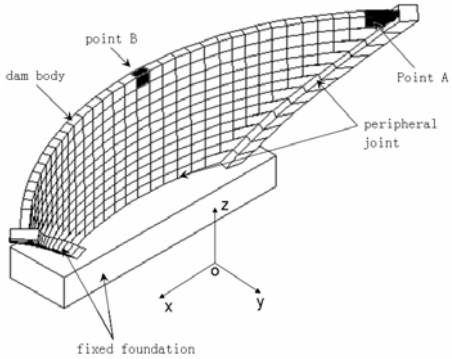

Fig. 3 arch dam computation block mesh
（Point A: displacement monitoring point）

In 3MDEM, only one layer block is employed with the 21 deformation modes. No tetrahedron difference element is needed. The results of 3MDEM, ABAQUS and 3DEC are illustrated in Fig. 4. The computation results of the stresses and displacements are in concordance with each other. The result shows that 3MDEM is an efficient method for continuum simulation.

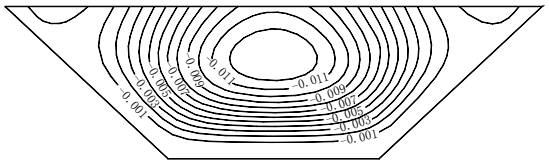

ABAQUS result

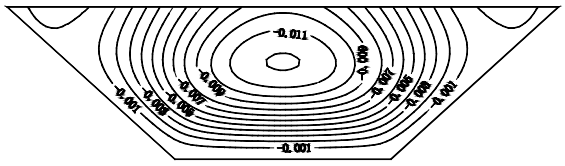

3DEC result

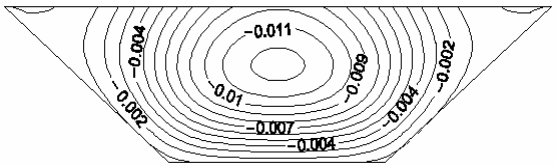

3MDEM result

(a) The longitudinal displacement of arch dam (+: upstream)

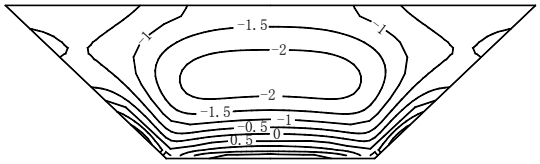

ABAQUS result

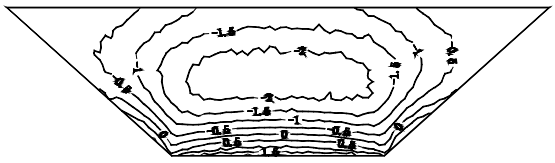

3DEC result

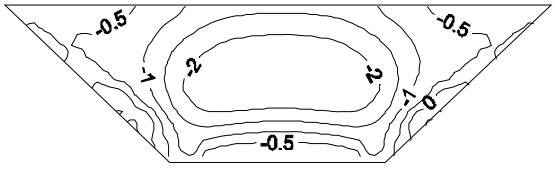

3MDEM result

(b) arch stress in upstream surface (+: tensile stress)

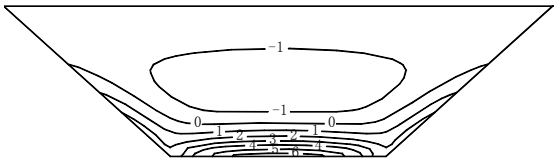

ABAQUS result

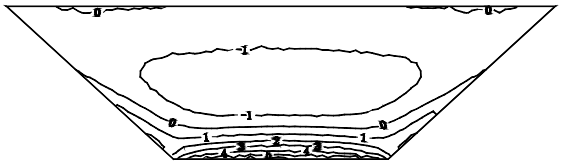

3DEC result

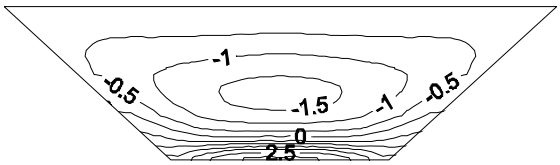

3MDEM result

(c) vertical stress in upstream surface (+: tensile stress)

Fig. 4 Comparison of simulation results by ABAQUS, 3DEC and 3MDEM

In order to get good enough results, hexahedron 20 nodes element with the size of about 1m is used in ABAQUS. Tetrahedron element with size of 0.2m is needed in 3DEC. The number of degree of freedom is three times the node numbers in ABAQUS and 3DEC, while in 3MDEM, the number of degree of freedom are 27 times the number of blocks. The comparison of degree of freedom and time step are listed in table 1. It demonstrates that 3MDEM is an efficient numerical method to simulate the mechanical behaviors of small and finite deformation in both continuous medium and discontinuous ones.

Table 1 Comparison of Computational efficiency

method	Degree of freedom	Time step(s)
FEM	19584	
3DEC	448974	2.213×10^{-5}
3MDEM	7425	1.0×10^{-4}

3. displacement and stress of Meihua Arch Dam

Since the peripheral joint of Meihua arch dam did not reach the top of the dam. The interface between the

dam body and the artificial concrete foundation except for the top layer is modeled as the peripheral joint. To simulate the strength of the dam body, the tensile strength, cohesion and friction coefficient of all interfaces between dam body blocks are set as 0.6MPa, 0.6MPa and 1.0, respectively. Due to the coating of asphalt along the peripheral joint, the cohesion and tensile strength of peripheral joint is set to zero, while the friction coefficient *f* of the peripheral joint is chosen as 0.75 or 0.7 to study the effects on stability. The reservoir water pressure is loaded by five steps, the elevation of water are 38.25m, 40.75m, 44.50m, 47.20m and 50.20m, respectively the corresponding depth of water are3.75m, 6.25m, 10.0m, 12.7m, 15.7m.

The displacement histories of point A in the top left of the arch (shown in Fig. 3) is illustrated in Fig. 5. When *f*=0.75, with increasing water level, the displacements of point A are rapidly convergent and stable. But the final displacement of point A is fairly large and increasing rapidly when the elevation of water reaches 50.20m. This phenomenon may mean that the arch dam approaches critical situation when *f* is equal to 0.75 and under full reservoir. When *f*=0.7, the displacements of Point A remain stable until the elevation of water exceeds 47.20m. But when the elevation of water reaches 50.20m, the displacements of point A are no longer convergent, namely collapse of the arch dam.

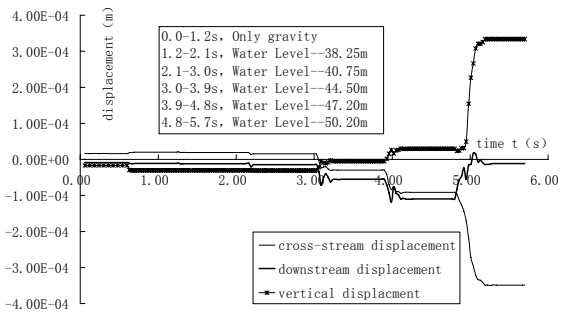

（a） *f*=0.75

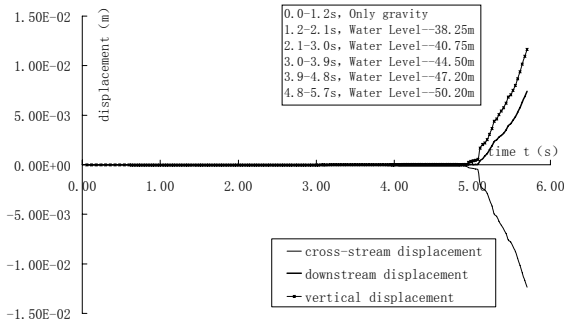

（b） *f*=0.7

Fig. 5 displacement of point A under different *f*

The displacement vectorgraph is shown in Fig. 6. When dam is stable, for example under *f*=0.75 and full reservoir, the displacement along the peripheral joint is small and the magnitude gradually decreases from bottom to top. But when dam becomes unstable, such as under *f*=0.7 and full reservoir, the displacement along the peripheral joint is very large and the magnitude gradually increases from bottom to top. Some sliding along peripheral joint occurs. The vectors in the right of Fig.6 is reference vectors (unit :m).

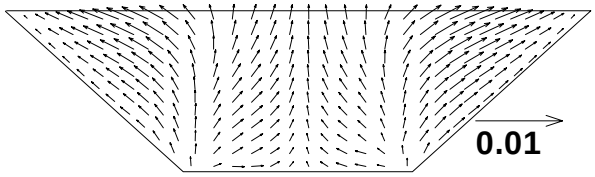

(a) *f*=0.75，full reservoir, after stability

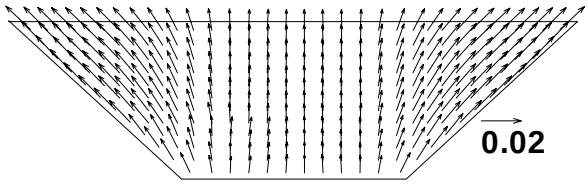

(b) *f*=0.70，full reservoir， end of computation

Fig. 6 displacement vectorgraph in dam face

The crack pattern of the dam interfaces is shown in Fig. 7. Under the full reservoir and *f*=0.75, the peripheral joints are all failed, but the top layer interface between arch dam body and foundation still keeps intact. The dam is stable. But when *f*=0.7, all interfaces between arch dam body and foundation are all failed. The dam began to slide upward along the peripheral joint.

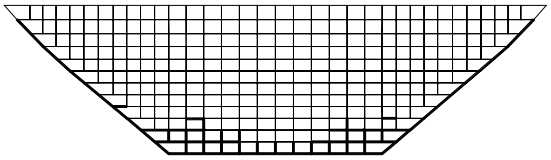

(a) f=0.75，full reservoir, after stability

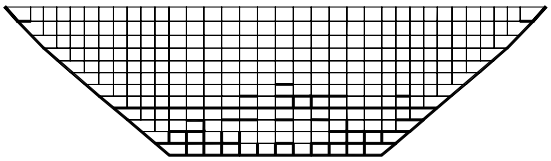

(b) f=0.70，full reservoir，end of computation

Fig. 7 cracking pattern of the interface
(Bold lines indicates craks.)

The stress contours are shown in Fig. 8 and Fig. 9. when f = 0.75, the dam keeps stable. Due to the opening of the peripheral joint, the bearing capacity of cantilevers reduces. Some loads are transferred to the arches. So, the upstream horizontal stresses are larger than that of intact dam (without peripheral joints) shown in Fig. 4, and upstream bottom vertical tensile stresses vanish.

Comparing the result of f=0.75 and f=0.7, the stress redistribution is very significant due to the damage of the dam. In detail, upstream horizontal stress and vertical stress increase with the damage process.

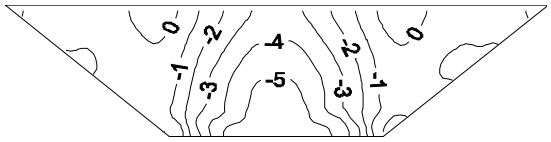

（a）f=0.75

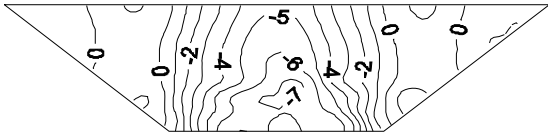

（b）f=0.70

Fig. 8　full reservoir, horizontal stress in upstream

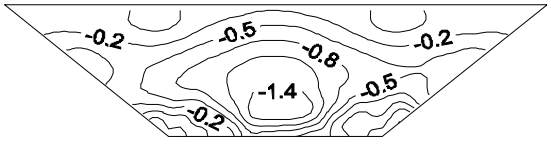

（a）f=0.75

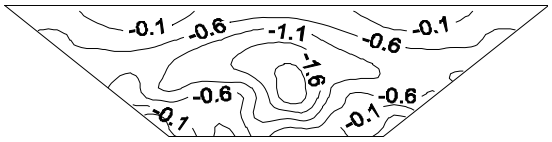

（b）f=0.70

Fig. 9 full reservoir，vertical stress in upstream

4. Failure process of Meihua Arch Dam

To speed up the simulation process, f=0.6 and full reservoir load case are analyzed to simulate the failure progress, which are shown in Fig. 10. In Fig. 10, (a-1) and (b-1) are zoom out of left abutment of (a) and (b). Under the load of water pressure, the dam body moves upward along the peripheral joint at first (fig. 10 (b-1)). Then bottom blocks are pushed to downstream. The bottom blocks movement makes the upper arch rotating to upstream lightly. At last, all blocks are pushed to downstream.

The failure mechanism of Meihua Arch Dam can be concluded: Under the load of the water pressure, when the shear resistance of the peripheral joint is less than the shear stress along the peripheral joint, the dam body slides upward along the peripheral joint. This movement causes further the vertical stress in the bottom area exceeds the tensile strength and the horizontal cracking of lower dam body occurs. Then, redistribution of stresses makes the arch stress exceed the tensile strength and the lower arches collapse. This failure pattern expands upward. This eventually leads to whole dam failure.

It is also noted that the arches is broken firstly in the middle part. Then the whole dam fails like the opening of the door, same as one eyewitness's description.

In short, Meihua Arch Dam failure is mainly due to the peripheral joints due to improper design.

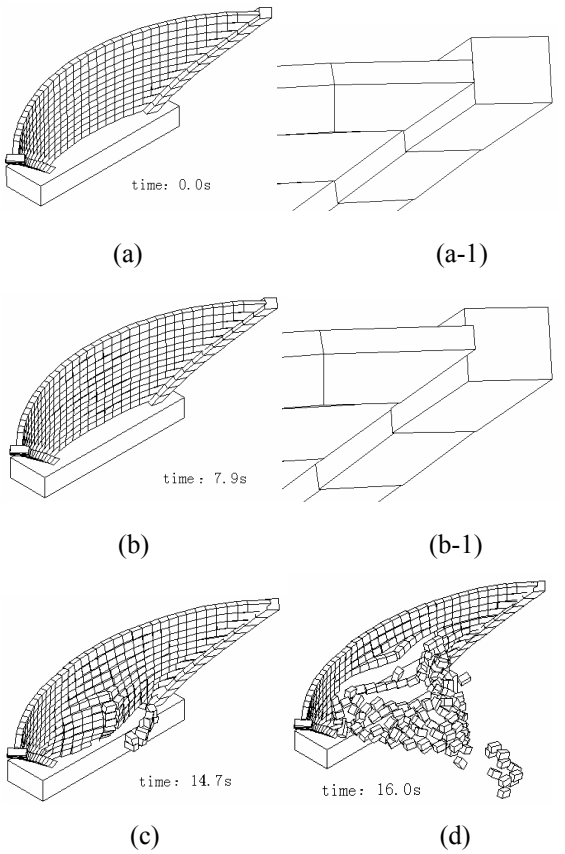

(a) (a-1)

(b) (b-1)

(c) (d)

Fig. 10 Failure process of Meihua Arch Dam

5 Conclusion

(1) As an efficient numerical method to simulate the mechanical behaviors of discontinuous problems, 3MDEM can model finite translation and rotation of blocks, hold a new contact detection method (Zhang Chong, et al. 2006), simulate linear and nonlinear behavior of block material and nonlinear interface and analyze static and/or dynamics problems. It has a great potential for the analysis of static or dynamic stability against sliding of concrete dams and/or slopes.

(2) In small deformation phase, 3MDEM can give as good result as FEM. While in small deformation phase, 3MDEM can simulate failure process similar to 3DEC.

(3) The failure process of Meihua Arch Dam in 1981 is simulated by 3MDEM. Results demonstrates that the thrust due to the reservoir load leads to the upward sliding of the dam body along the peripheral joint which has not enough shear resistance, thus causing the rapid collapse of the dam.

5. acknowledgment

The constructive suggestion from Professors Zhang Chuhan and Wang Guanglun in Tsinghua University are grateful. The work has been supported by National Natural Science Foundation of China (90510018 and 50539020).

References

Cui Yuzhu, Numerical Modeling of Continuum and Discontinuous media and its application to safety analysis of arch dam-foundation systems[D], Beijing: Tsinghua University, 2001

Cundall, P. A. Formulation of three-dimensional distinct element model, Part I, A scheme to detect and represent contact in system composed of many polyhedral blocks. Int J Rock Mech Min Sci & Geomech Abstr, 1988, 25(3): 107-116.

Hart R, Cundall P. A, Lemos J. Formulation of three-dimensional distinct element model, Part Ⅱ, Mechanical calculation for motion and interaction of a system composed of many polyhedral blocks. Int J Rock Mech Min Sci & Geomech Abstr, 1988, 25(3): 117-125.

Hou Yanli, Zhang Chong, Zhang Chuhan, Jin Feng, Simulation of upward-sliding failure of interface in arch dams by deformable distinct elements[J], Chinese Journal of Geotechnical Engineering, 2005,27(6):657-661

Nu Naihua, Jiang Zhongsheng, dam accident and safety. Acrh dam, Beijing, China WaterPower Press, 1995

Zhang Chong, Jin Feng Hou Yanli, 3D block field contact detection algorithm based on visibility and post-round, Chinese Journal of Rock Mechanics and Engineering, 2006, 25(11): 2292-2297.

Zhang Chong, Jin Feng, Hou Yanli, 3-D simple deformable distinct element method ,Chinese Journal of Geotechnical Engineering, 2007, 29(4): 6-10

Elasto-Plastic Discontinuous Deformation Analysis Using Mohr-Coulomb Model

R. GRAYELI[1] and A. MORTAZAVI[2]

Mahab Ghods Consulting Engineers, Vahid Dastgerdy Ave. Tehran, IRAN
[2] Associate Prof., Department of Mining & Metallurgical Eng., Amirkabir University of Technology, Tehran, IRAN

In the original DDA formulation (Shi, 1988), a linear displacement function is used for blocks. Accordingly, stress and strain within each block are assumed constant and this is an inappropriate representation of stress/strain state for a real block. In the present paper, the authors propose to use a simple internal discretization scheme which, is based on Delaunay type mesh generation scheme. This approach was used to calculate the stress and strain distributions within each block. The DDA formulation was obtained based on a Finite Element discretization. The well known elasto-plastic yield criterion of Mohr-Coulomb was incorporated into the modified DDA code using a discrete time system. The numerical implementation of the criterion involves an elastic trial for the stress increment at the first computational step for each element. The corresponding stresses are then evaluated and if they violate the yield criteria (i.e. if the stress state lies above the yield function in the generalized stress space), plastic deformations take place. In this study, only the elastic part of the strain increment can contribute to the stress increment. The obtained results were compared against analytical results as well as the results obtained from the well known commercial software (FLAC, Itasca Consulting). A fairly good agreement was achieved between DDA results, analytical solution, and FLAC results.

Keywords: DDA, Triangular Discretization, Jointed Rock Mass, Elasto-Plastic modelling

1. Introduction

Numerical methods in geomechanics can be classified into two main groups: continuum methods and discontinuous methods. Examples of continuum methods are; the finite element method (FEM), the boundary element method (BEM), and the finite difference method (FDM). These methods are now fully developed and have been successfully used in many applications. These classical methods, however, face great difficulties when dealing with discontinuous media. Rock mass discontinuities can be modeled in a discrete manner with FEM and BEM methods using special joint elements (Jing and Hudson 2002). However, these methods are incapable of simulating the behavior of blocky media, in particular discontinuous rock mass. On the other hand, discontinuum methods such as discrete element method (DEM) introduced by Cundall (Wang et al 2000), and discontinuous deformation analysis (DDA) established by Shi (1993), are now well developed and can be used to simulate the behavior of the discontinuous media. The discontinuous deformation analysis (DDA) method is a promising discontinuum modeling technique which has great potentials for modeling of blocky systems. Large displacement and deformation are considered under both static and dynamic loading conditions. Various modifications to the original DDA formulation have been reported in the rock mechanics literature (Lin et al 1996; Kin et al 1999). In the original DDA formulation, a first order polynomial displacement function was assumed for block deformation, which do not allow for variable stress/strain distribution within a block. This approximation precludes the application of the first order polynomial function to problems with significant stress variations within blocks. To overcome this shortcoming, many researchers have adapted various approaches to overcome this shortcoming of DDA (Chang et al 1996; Koo and Chern 1996; Ma et al 1996; Shi 1996; Jing 1998; Chen et al 1998; Hsiung 2001). This paper presents the implementation of a nonlinear material behavior model into the DDA algorithm employing triangular elements within the DDA blocks. The new code was developed in C++ environment and to demonstrate the capability of the modified DDA code the typical example of stress distribution around circular tunnels at depth was analyzed. The analysis results were compared against analytical and other commercial program results. The following sections describe the implementation procedure and the analysis results.

2. Displacement approximation

In the displacement-based finite element method the primary unknown quantity is the displacement field, which varies over the problem domain. In two dimensional plane strain situations, the displacement

field is characterized by two global displacement vectors u and v, in the x and y directions respectively. In this study a three node triangular element was used for discretization of discrete DDA blocks. The major advantage of these elements is their simplicity and flexibility in terms of mesh generation.

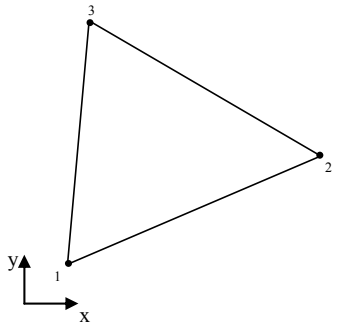

Fig. 1: Geometry of the three-node triangular element.

Each element consists of 3 nodes and has 6 degrees of freedom in the *x* and *y* directions. The displacement vector for the employed element can be written as below:

$$[D_i] = [u_1 \quad u_2 \quad u_3 \quad v_1 \quad v_2 \quad v_3]^T \qquad (1)$$

The displacement function of the three-node triangular element can be written in the following fashion:

$$\begin{aligned} u &= a_1 + a_2 x + a_3 y \\ v &= b_1 + b_2 x + b_3 y \end{aligned} \qquad (2)$$

The 6 unknown coefficients a_1, a_2, a_3 and b_1, b_2, b_3 can be expressed in terms of nodal displacements by substituting the nodal coordinates into the above equations. The element is positively oriented when three nodes are arranged counter-clockwise and the total displacement field of the element, *e,* can be written as blow:

$$\begin{bmatrix} u \\ v \end{bmatrix} = [T^{(e)}][X^{(e)}][D^{(e)}] \qquad (3)$$

where

$$\left[T^{(e)}\right] = \begin{bmatrix} 1 & x & y & 0 & 0 & 0 \\ 0 & 0 & 0 & 1 & x & y \end{bmatrix},$$

$$[X^{(e)}] = \begin{bmatrix} n_c & n_0 \\ n_0 & n_c \end{bmatrix} \qquad (4)$$

and,

$$n_c = \begin{bmatrix} 1 & x_1 & y_1 \\ 1 & x_2 & y_2 \\ 1 & x_3 & y_3 \end{bmatrix}^{-1}, \; n_0 = \begin{bmatrix} 0 & 0 & 0 \\ 0 & 0 & 0 \\ 0 & 0 & 0 \end{bmatrix} \qquad (5)$$

3. DDA formulation based on three-node triangular element

In the discontinuous deformation analysis method, the equilibrium equations are established by minimizing the total potential energy induced into the system and solved. The total potential energy, Π_t of a system with *N* number of nodes has the following form (Shi 1993):

$$\Pi_t = \frac{1}{2}[D_t]^T [K_t][D_t] + [D_t]^T [F_t] + C \qquad (6)$$

where

$$[K_t] = \begin{bmatrix} k_{11} & k_{12} & k_{13} & \cdots & k_{1n} \\ k_{21} & k_{22} & k_{23} & \cdots & k_{2n} \\ k_{31} & k_{32} & k_{33} & \cdots & k_{3n} \\ \vdots & \vdots & \vdots & \ddots & \vdots \\ k_{n1} & k_{n2} & k_{n3} & \cdots & k_{nn} \end{bmatrix},$$

$$[D_t] = \begin{bmatrix} d_1 \\ d_2 \\ d_3 \\ \vdots \\ d_n \end{bmatrix}, [F_t] = \begin{bmatrix} f_1 \\ f_2 \\ f_3 \\ \vdots \\ f_n \end{bmatrix} \qquad (7)$$

In Eq. (6), *C* is the energy produced by friction force. Elements K_{ij} and K_{ii} in the coefficient matrix, given by Eq. (6), are *2×2* submatrices and elements d_i , f_i are 2×1 submatrices. By minimizing the total potential energy function, Π_t, which is written based on system forces and stresses, the equilibrium equations can be derived. The global system of equations has the form of:

$$[K_t][D_t] = [F_t] \qquad (8)$$

For a system with *N* node, the global stiffness matrix will be *2N×2N* in size. In Eq. (6) the off-diagonal contributions to the system matrix will exist only if the blocks are in contact. In other words, the existence of sub-matrices K_{ij} and K_{ji} is the result of contact between two elements. The following sections briefly demonstrate the determination of various sub-matrices required to set up the global equilibrium equation

3.1 Stiffness matrix

The strain energy Π_e due to the elastic stresses of element *e* can be written as:

$$\Pi_e = \frac{1}{2}\iint \{\varepsilon\}^T \{\sigma\} dxdy = \frac{1}{2}\left[D^{(e)}\right]^T \iint \left[X^{(e)}\right]^T [B]^T [E][B]\left[X^{(e)}\right] dxdy \left[D^{(e)}\right] \tag{9}$$

where,

$$\{\sigma\} = [D]\{\varepsilon\},$$

$$[D] = \frac{E}{(1+\nu)(1-2\nu)}\begin{bmatrix} 1-\nu & \nu & 0 \\ \nu & 1-\nu & 0 \\ 0 & 0 & \frac{1-2\nu}{2} \end{bmatrix} \quad \text{and}$$

$$[B] = \begin{bmatrix} \frac{\partial u}{\partial x} \\ \frac{\partial v}{\partial y} \\ \frac{\partial u}{\partial y} + \frac{\partial v}{\partial x} \end{bmatrix} \tag{10}$$

Hence, by minimizing the above energy function with respect to the displacement variables the stiffness term associated with elastic stresses can be calculated as below and added to the global $[K_t]$ matrix:

$$\left[X^{(e)}\right]^T \iint [B]^T [E][B] dxdy \left[X^{(e)}\right] \rightarrow \left[K_{i(r)\,i(s)}\right] \quad r,s = 1 \cdots 3 \tag{11}$$

where,

i(1), the number of the first node of element.
i(2), the number of the second node of element.
i(3), the number of the third node of element.

It should be noted that the elements in $[B_i]$ matrix contain $x^{n_1} y^{n_2}$ terms, where n_1 and n_2 are non-negative integers. It should be realized that the, integration of Eq. (11) is not straightforward. The higher the order of the polynomial functions, the more difficult the integrating would be. Shi (1996) proposed the *2D* and *3D* simplex integration scheme, which allow for the integration of high order polynomials. The presented research has adopted the integration method proposed by Shi.

4. Elasto-plastic behaviour

The basic principle in analyzing the elasto-plastic behaviour is to decompose the total strain into two components and express it in terms of elastic and plastic strain components as below:

$$\varepsilon^t = \varepsilon^e + \varepsilon^p \tag{12}$$

Hooke's law is used to relate the stress rates to the elastic strain rates. Substitution of Eq. (12) into Hooke's law leads to:

$$\sigma^e = \left[D^e\right] \varepsilon^e = \left[D^e\right] (\varepsilon^t - \varepsilon^p) \tag{13}$$

According to the flow rule theory of plasticity (Hill, 1950), plastic strain rates are proportional to the derivative of the yield function with respect to the stresses. This means that the plastic strain can be represented as vectors perpendicular to the yield surface. This classical form of the theory is referred to as associated plasticity. However, for Mohr-Coulomb type yield functions (Eq. 14), the theory of associated plasticity leads to an over prediction of dilatancy.

$$f = \frac{1}{2}(\sigma_1 - \sigma_3) + \frac{1}{2}(\sigma_1 + \sigma_3)\sin\phi - c\cos\phi \tag{14}$$

Therefore, in addition to the yield function, a plastic potential function, *g,* is introduced. The case $g = f$ is denoted as associated plasticity. In general, the plastic strain rates are written as:

$$\varepsilon^p = \lambda \frac{\partial g}{\partial \sigma} \tag{15}$$

in which λ is the plastic multiplier.

The above equations can be used to obtain the following relationship between the effective stress rates and strain rates for elasto-plasticity (Smith & Griffith, 1982; Vermeer & de Borst, 1984):

$$\sigma = \left(\left[D^e\right] - \alpha \frac{\left[D^e\right]\frac{\partial g}{\partial \sigma}\frac{\partial f^T}{\partial \sigma}\left[D^e\right]}{\frac{\partial f}{\partial \sigma}\left[D^e\right]\frac{\partial g^T}{\partial \sigma}} \right) \tag{16}$$

The parameter α is used as a switch. If the material behaviour is elastic, the value of α is equal to zero, whilst for plasticity, the value of α is equal to unity.
To implement the Mohr-Coulomb criteria into *DDA*, for each element initially the elastic stress component is computed and added to the previous stress components. Accordingly, stress increments are calculated by application of Hooke's law to the total strain increment for the step and principal stress components, σ_1, σ_3 are calculated and ordered. If these stresses violate the composite yield criterion (Eq. 14), a correction must be applied to the stresses to determine the new stress state.

5. Verification of the modified DDA

This section presents the application of the modified DDA to a typical example of circular tunnel in an infinite medium with elasto-plastic behaviour. In this

verification example displacement field was evaluated for the case of a circular tunnel in an infinite elasto-plastic medium subjected to a constant in-situ stress field. The problem geometry as depicted in Figure 4 and the analytical solutions to the problem are taken from 1(Jaeger and Cook 1976).

The extension of yielded zone around opening, R_o, is given analytically based on the solution given by Salencon (1969):

$$R_0 = a\left(\frac{2}{K_p+1}\frac{P_0+\frac{q}{K_p-1}}{P_i+\frac{q}{K_p-1}}\right)^{1/(k_p-1)} \tag{17}$$

In the above equation a is the opening radius and C and ϕ are cohesion and friction angle respectively. Other parameters are defined as below:

$$K_P = \frac{1+\sin\phi}{1-\sin\phi} \tag{18}$$

$$q = 2c\tan(45+\phi/2) \tag{19}$$

$P0$ = initial in-situ stress,
Pi = internal pressure

The radial stress at the elastic-plastic interface is given by:

$$\sigma_{re} = \frac{1}{K_p+1}(2P_0 - q) \tag{20}$$

and tangential stress, radial stress, and radial displacement within the elastic zone are described by the following equations:

$$\sigma_r = P_0 - (P_0 - \sigma_{re})\left(\frac{R_0}{r}\right)^2 \tag{21}$$

$$\sigma_\theta = P_0 + (P_0 + \sigma_{re})\left(\frac{R_0}{r}\right)^2 \tag{22}$$

$$u_r = \frac{R_0^2}{2G}\left(P_0 - \frac{2P_0 - q}{K_p+1}\right)\frac{1}{r} \tag{23}$$

where r is the distance from the field point (x,y) to the center of the opening. The stresses and radial displacement within the plastic zone are given by:

$$\sigma_r = -\frac{q}{K_P-1} + \left(P_i + \frac{q}{K_P-1}\right)\left(\frac{r}{a}\right)^{(K_P-1)} \tag{24}$$

$$\sigma_\theta = -\frac{q}{K_P-1} + K_P\left(P_i + \frac{q}{K_P-1}\right)\left(\frac{r}{a}\right)^{(K_P-1)} \tag{25}$$

$$u_r = \frac{r}{2G}(2\nu-1)\left(P_0 + \frac{q}{K_P-1}\right) + \frac{(1-\nu)(K_P{}^2-1)}{K_P+K_{Ps}}\left(P_i+\frac{q}{K_P-1}\right)\left(\frac{R_0}{a}\right)^{(K_P-1)}\left(\frac{R_0}{a}\right)^{(K_{Ps}+1)} + \left(\frac{(1-\nu)(K_PK_{Ps}+1)}{K_P+K_{Ps}} - \nu\right)\left(P_i+\frac{q}{K_P-1}\right)\left(\frac{r}{a}\right)^{(K_P-1)} \tag{26}$$

where

$$K_{Ps} = \frac{1+\sin\psi}{1-\sin\psi} \tag{27}$$

ψ= Dilation angle, ν= Poisson's Ratio, G = Shear modulus

In the given analytical solution P_1 and P_2 are far field stress components in the x and y directions.

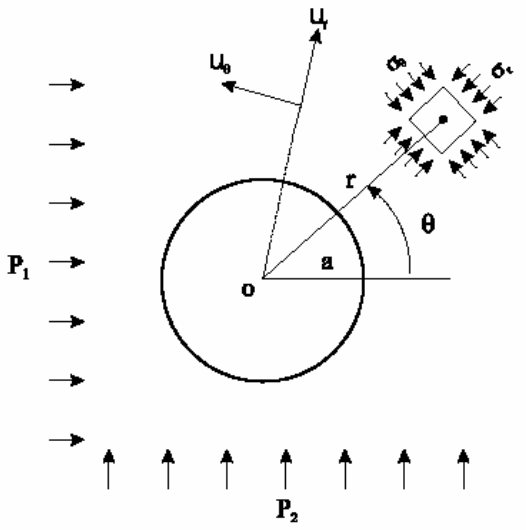

Fig. 2: Cylindrical hole in an infinite elastic medium (Jaeger and Cook 1976).

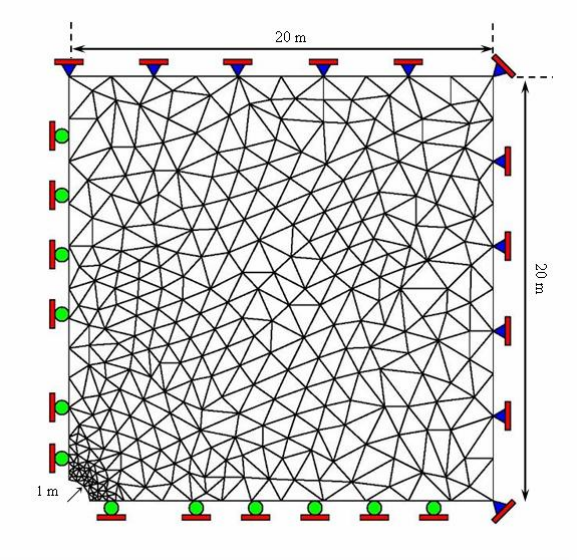

Fig. 3: DDA model of a Circular tunnel in an infinite elastic medium.

In order to verify and further illustrate the capabilities of the modified DDA, the well known commercial code FLAC (Itasca Consulting) was used. The DDA model and applied boundary condition are shown in Figure 3. A similar model was analyzed with the FLAC code and DDA results were compared against analytical and FLAC results.
The input data used in the DDA analysis are as below:

E = 5 GPa, ν=0.2, $\sigma_{x0} = \sigma_{y0} = P_1 = P_2 = -10$ MPa and r = 1m, *Cohesion* = 0.5 MPa, *Friction angle* = 30° and *Dilation angle* = 0°

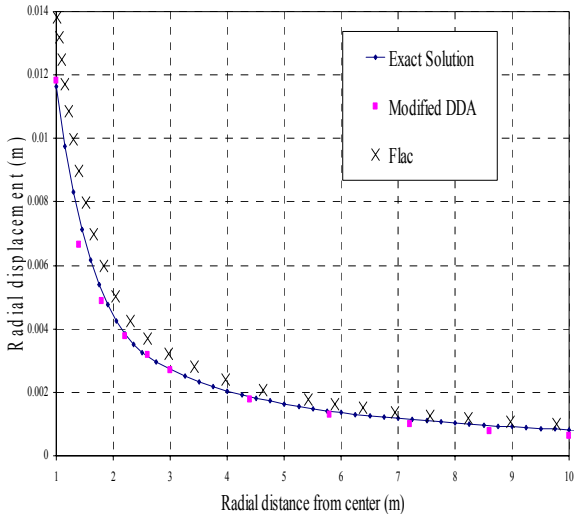

Fig. 4: Comparison of u_r distribution for the circular tunnel in an infinite Mohr-Coulomb medium.

Figure 4 compares the radial displacement distribution obtained from the analytical solution, FLAC, and the modified DDA code. With regard to the obtained results, the displacement field calculated by the modified DDA agrees well with analytical solution. Additionally, the extension of yielded/plastic zone was evaluated by the modified DDA, FLAC, and analytical solution. From the analytical solution the radius of plastic zone was calculated to be 2.505 m (Eq. 17) (from the opening center). The radius of yielded zone calculated by the modified DDA is about 2.56 m which is in good agreement with the analytical solution. Moreover, in the FLAC the extension of failure zone around opening was calculated to be about 2.78 m. A summary of results obtained by DDA and FLAC are illustrated in Figure 5.

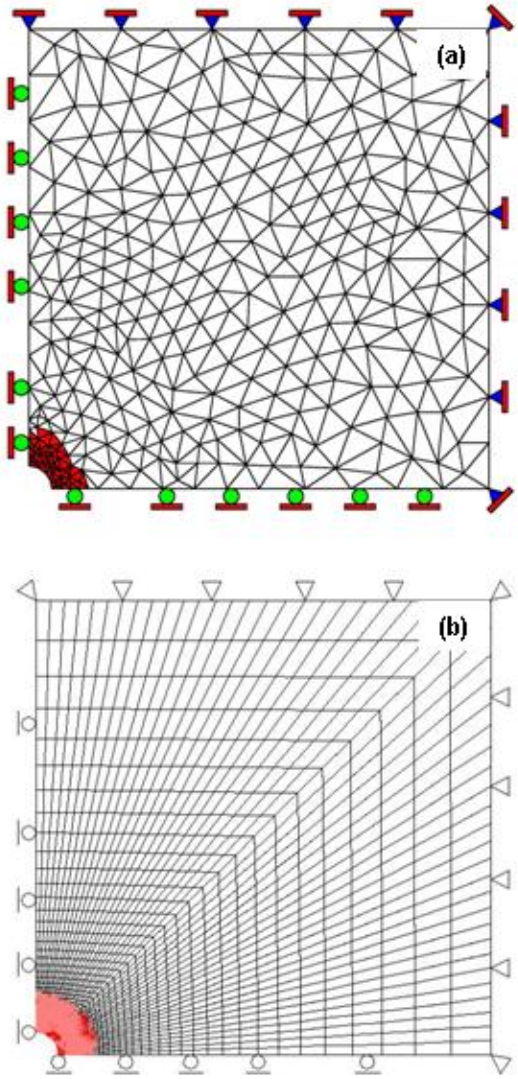

Fig. 5: Calculated radius of plastic region around the opening by a) modified DDA, and b) FLAC

4. Conclusions

The main purpose of using a finite element mesh within each block is to improve its deformation capability. By adding the finite element mesh into each block it is possible to take advantages of the continuum mechanic principles used in FEM and the discontinuum mechanics used by the DDA method. Coupling continuum and discontinuum mechanics allows for simulation of complex problems involving material fracturing, dynamic behavior and nonlinear behavior. In this study, a more powerful version of DDA method was developed using the three-node triangular elements and Mohr-Coulomb constitutive law. This enhanced the deformation capability of DDA significantly, thus, making it a more suitable tool for accurate calculations and practical applications. In this study the successful application of the modified DDA to problem with known solutions was demonstrated. The calculated results show close agreement with the results obtained form theoretical solutions and a commercial program. However, it is believed that more verification and refinement of the new DDA is required. Considering the discontinuum modeling capabilities of DDA, the modified code, with further verifications, has great potential for modeling of practical problems.

References

Chang CT, Moteiro P, Nemati K, Shyu K. Behavior of marble under compression, *Journal of Material in Civil Engineering,* 1996; 8:157-170 1996.

Chen G, Ohnishi Y, Ito T. Development of High-Order Manifold Method, *International Journal of Numerical Method in Engineering* 1998; 43: 685-712.

FLAC. Fast Lagrangian Analysis of Continua (FLAC), *Itasca Consulting Group*, Minneapolis, MN, USA (1998).

Hsiung SM. Discontinuous Deformation Analysis (DDA) with nth Order Polynomial Displacement Functions, *38th U.S. Rock Mechanics Symposium*, July 7-10, Washington, DC, 2001.

Jaeger, J. C., and N. G. W. Cook. Fundamentals of Rock Mechanics, *3rd Ed. London: Chapman and Hall*, 1976.

Jing L, Hudson JA. Numerical method in rock mechanics, *International Journal of Rock Mechanics & Mining Sciences,* 2002; 39: 409-427.

Jing L. Formulation of discontinuous deformation analysis (DDA) an implicit discrete element model for block systems, *International Journal of Engineering Geology,* 1998; 49: 371–81.

Kim Y, Amadei B, Pan E. Modelling the effect of water, excavation sequence and rock reinforcement with discontinuous deformation analysis, *International Journal of Rock Mechanics & Mining Sciences,* 1999; 36: 949-970

Koo CY, Chern JC. The development of DDA with third order displacement function, *Discontinuous Deformation Analysis (DDA) and simulations of Discontinuous Media*, M. R. Salami and Don Banks Editor.

Lin CT, Amadei B, Jung J, Dwyer J. Extension of discontinuous deformation analysis for jointed rock masses, *International Journal of Rock Mechanics & Mining Sciences & Geomechanical Abstract,* 1996; 33: 671-694.

Ma MY, Zaman M, Zhu JH. Discontinuous Deformation Analysis Using the Third Order Displacement Function, *Discontinuous Deformation Analysis (DDA) and simulations of Discontinuous Media*, M. R. Salami and Don Banks Editor, 1996.

Shi GH, Block System Modeling by Discontinuous Deformation Analysis, *Computational Mechanics Publication*, Southampton. UK. 1993.

Shi GH, Manifold method, *Discontinuous Deformation Analysis (DDA) and simulations of Discontinuous Media*, M. R. Salami and Don Banks Editor, 1996.

Shi GH. Simplex integration for manifold method, FEM, DDA and analytical analysis, *Discontinuous Deformation Analysis (DDA) and Simulation of Discontinuous Media*, TSI Press, Mexico, 1996..

Wang Z, Lia Y, Wang S, Yang Z. Numerical simulation of the geomechanical processes in rock engineering. *International Journal of Rock Mechanics & Mining Sciences,* 2000; 37: 499-507.

Nonlinear analysis of Riedel shearing test by using mesh dividing method in HPM

R. MIHARA[1] and N. TAKEUCHI[2]

[1] Graduate School of Art and Technology, Hosei University (JIP Techno-Science Corporation), Tokyo, Japan
[2] Dep. of Art and Technology, Hosei University, Tokyo, Japan

In the Riedel shearing test, the soil specimen is put on the two boards, and the board is removed in shearing direction. This test is a technique for investigating the influence that causes it for the ground level by damaging the bed rock. However, it is difficult to observe the damage shape and the strain distribution from the shearing test. Then, the numerical analysis was performed by using the hybrid-type penalty method. HPM applies the concept of the spring of RBSM in Lagrange multiplier and assumes independent displacement field to each sub-domain. This paper reports the Riedel shearing test and numerical analysis by using the mesh dividing method in HPM.

Keywords: Riedel shearing test; Hybrid-type penalty method (HPM); mesh dividing method

1. Introduction

We proposed the hybrid-type penalty method (HPM) which applied the concept of the penalty method to the principle of hybrid-type virtual work. This model has succeeded the advantage of RBSM (Rigid Bodies-Spring Model) that discrete limit analysis can be performed efficiently and the accuracy of an elastic solution improves.
In the hybrid displacement model, the compatibility of the displacement is loosened a little and it introduces into variational formulation, using Lagrange multiplier to the subsidiary condition. In HPM, the concept of the spring of RBSM is applied to the Lagrange multiplier. Compatibility of the displacement on the intersection boundary is approximately introduced using the penalty function as a spring constant. So that, HPM can assume a displacement field independent in sub-domain. Therefore, HPM doesn't share degree of freedom by the node like FEM, and the node is used only to recognize the configuration of sub-domain.
We analyzed the crack initiation problems using linear displacement field which has rigid displacement and strain for arbitrary point in the sub-domain. In this analysis, the displacement for the elastic problems had the same accuracy as the constant strain element of FEM, and the collapse load for the elasto-plastic problems had the same accuracy as the limit load of RBSM existed.
HPM assumes a displacement field independent in sub-domain and because compatibility requirements of the intersection boundary on adjacent sub-domain are secured by using the penalty method, the displacement field can be assumed regardless of the shape of sub-domain. However, excellent accuracy was not obtained when shape other than the triangle were used at the linear displacement field, and the division of arbitrary shape was difficult. To solve such a problem, it proposes the method of applying the second-order displacement field where the inclination of the strain was added to HPM.
First, the brief formulation of this model is presented. Secondly, an analysis example is illustrated.

2. Governing equation and hybrid-type virtual work

2.1 Governing equation

Let $\Omega \subset \mathbb{R}^{n_{dim}}$, with $(1 \le n_{dim} \le 3)$, be the reference configuration of a continuum body with smooth boundary $\Gamma := \partial\Omega$ and closure $\overline{\Omega} := \Omega \cup \partial\Omega$. Here $\mathbb{R}^{n_{dim}}$ is the n_{dim} dimensional Euclidean space.

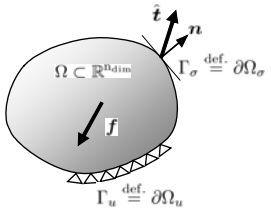

Fig. 1: Reference configuration Ω and smooth boundary $\partial\Omega$

The local form of the equilibrium equation for a deformable body can be written by

$$\operatorname{div}\boldsymbol{\sigma} + \boldsymbol{f} = 0 \qquad \text{in } \Omega \qquad (1)$$
$$\boldsymbol{\sigma} = \boldsymbol{\sigma}^t \qquad \text{in } \Omega \qquad (2)$$

where $\boldsymbol{f} : \Omega \to \mathbb{R}^{n_{dim}}$ is the body force per unit volume, $\boldsymbol{\sigma} : \overline{\Omega} \to \mathbb{S}$ is the Cauchy stress tensor respectively. Here $\mathbb{S} = \mathbb{R}^{(n_{dim}+1)\cdot n_{dim}/2}$ is the vector space of symmetric rank-two tensor and $\boldsymbol{e}_i$ is the standard base vector of $\mathbb{R}^{n_{dim}}$, so that the stress tensor becomes $\boldsymbol{\sigma} = \sigma_{ij}\boldsymbol{e}_i \otimes \boldsymbol{e}_j$, where $\otimes$ denotes a tensor product. $\boldsymbol{u} : \overline{\Omega} \to \mathbb{R}^{n_{dim}}$ is a displacement field of particles with

reference position $\boldsymbol{x} \in \Omega$. We write $\boldsymbol{u}(\boldsymbol{x})$ and denote the infinitesimal strain tensor by

$$\boldsymbol{\varepsilon} = \boldsymbol{\nabla}^s \boldsymbol{u} \overset{\text{def.}}{=} \frac{1}{2}\left[\boldsymbol{\nabla}\boldsymbol{u} + (\boldsymbol{\nabla}\boldsymbol{u})^t\right] \tag{3}$$

where $\boldsymbol{\nabla} := (\partial/\partial x_i)\boldsymbol{e}_i$ is the differential vector operator, $\boldsymbol{\nabla}^s$ shows the symmetry part of $\boldsymbol{\nabla}$.
In what follows, we assume that the boundary $\Gamma = \Gamma_u \cup \Gamma_\sigma$.

$$\overline{\Gamma} = \overline{\Gamma_u \cup \Gamma_\sigma} \ , \ \ \Gamma_u \cap \Gamma_\sigma = \emptyset \tag{4}$$

Here $\Gamma_u := \partial_u \Omega \subset \partial\Omega$ where displacement are prescribed as

$$\boldsymbol{u}|_{\Gamma_u} = \hat{\boldsymbol{u}} \ \ (\text{given}) \tag{5}$$

Where as $\Gamma_\sigma := \partial_\sigma \Omega \subset \partial\Omega$ where tractions $t := \sigma n$ are prescribed as

$$\boldsymbol{\sigma}|_{\Gamma_\sigma}\, \hat{\boldsymbol{n}} = \hat{\boldsymbol{t}} \ \ (\text{given}) \tag{6}$$

Here $\hat{\boldsymbol{n}}$ is the field normal to the boundary Γ_σ. The constitutive equation to the elastic body is provided as follows by the use of the elasticity tensor $\boldsymbol{C}$.

$$\boldsymbol{\sigma} = \boldsymbol{C} : \boldsymbol{\varepsilon} \tag{7}$$

2.2 Virtual work equation (weak forms)

We let $\mathbb{U}$ denote the space of admissible displacement field, define as

$$\mathbb{U} \overset{\text{def.}}{=} \{\boldsymbol{u} : \Omega \to \mathbb{R}^{\text{n}_{\text{dim}}} \mid \boldsymbol{u}|_{\Gamma_u} = \hat{\boldsymbol{u}}\} \tag{8}$$

And, let $\mathbb{V}$ denote the space of admissible virtual displacement field, define as

$$\mathbb{V} \overset{\text{def.}}{=} \{\delta\boldsymbol{u} : \Omega \to \mathbb{R}^{\text{n}_{\text{dim}}} \mid \delta\boldsymbol{u}|_{\Gamma_u} = \boldsymbol{0}\} \tag{9}$$

We can now use Equation (1) and integrate volume of the body to give a weak statement of the static equilibrium of the body as,

$$\delta W := \int_\Omega (\text{div}\, \boldsymbol{\sigma} + \boldsymbol{f}) \cdot \delta\boldsymbol{u}\, dV = 0 \ {}^\forall\delta\boldsymbol{u} \in \mathbb{V} \tag{10}$$

A more common and useful expression can be derived to give the divergence of the vector $\boldsymbol{\sigma}\delta\boldsymbol{u}$ as,

$$\text{div}(\boldsymbol{\sigma}\delta\boldsymbol{u}) = (\text{div}\boldsymbol{\sigma}) \cdot \delta\boldsymbol{u} + \boldsymbol{\sigma} : \text{grad}\ \delta\boldsymbol{u} \tag{11}$$

Using this equation together with the Gauss theorem enable Equation (10) to be rewritten as,

$$\int_\Omega \boldsymbol{\sigma} : \text{grad}\delta\boldsymbol{u}\, dV - \int_\Omega \boldsymbol{f}\cdot\delta\boldsymbol{u} dV - \int_{\Gamma_\sigma} \hat{\boldsymbol{t}}\cdot\delta\boldsymbol{u}\, dS = 0 \ {}_\forall\delta\boldsymbol{u} \in \mathbb{V} \tag{12}$$

This equation is virtual work equation. If $\boldsymbol{u}$ is the weighing function, this is a weak forms. It is $\mathbb{U} \subset \mathbb{H}^1(\Omega)$ and $\mathbb{V} \subset \mathbb{H}^1(\Omega)$ where denotes the Sobolev space $\mathbb{H}^1(\Omega)$ of function possessing space integrable derivatives.

2.3 Hybrid-type virtual work equation

Let Ω consist of M sub-domains $\Omega^{(e)} \subset \Omega$ with the closed boundary $\Gamma^{(e)} := \partial\Omega^{(e)}$ as shown in Figure 2.

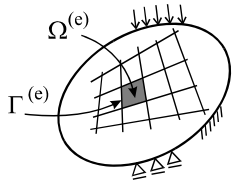

Fig. 2: Sub-domain $\Omega^{(e)}$

That is,

$$\Omega = \bigcup_{e=1}^{M} \Omega^{(e)} \ \text{here,}\ \Omega^{(r)} \cap \Omega^{(q)} = 0 \quad (r \neq q) \tag{13}$$

In what follows, we assume that the closure $\overline{\Omega}^{(e)} := \Omega^{(e)} \cup \partial\Omega^{(e)}$.

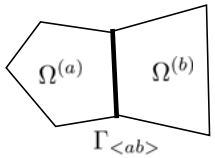

Fig. 3: Common boundary $\Gamma_{<ab>}$ of sub-domain $\Omega^{(a)}$ and $\Omega^{(b)}$

We let $\Gamma_{<ab>}$ denote the common boundary in two sub-domain $\Omega^{(a)}$ and $\Omega^{(b)}$ adjoined as shown in Figure 3, define as,

$$\Gamma_{<ab>} \overset{\text{def.}}{=} \Gamma^{(a)} \cap \Gamma^{(b)} \tag{14}$$

Relative to $\widetilde{\boldsymbol{u}}^{(a)}$ and $\widetilde{\boldsymbol{u}}^{(b)}$ which are the displacement on the intersection boundary $\Gamma_{<ab>}$ in sub-domain $\Omega^{(a)}$ and $\Omega^{(b)}$,

$$\widetilde{\boldsymbol{u}}^{(a)} = \widetilde{\boldsymbol{u}}^{(b)} \qquad \text{on}\ \Gamma_{<ab>} \tag{15}$$

This subsidiary condition is introduced into the framework of the variational expression with Lagrange multipliers $\boldsymbol{\lambda}$ as follows:

$$H_{ab} \overset{\text{def.}}{=} \delta \int_{\Gamma_{<ab>}} \boldsymbol{\lambda}\cdot(\widetilde{\boldsymbol{u}}^{(a)} - \widetilde{\boldsymbol{u}}^{(b)})\, dS \tag{16}$$

where $\delta(\bullet)$ shows the variation of $(\bullet)$.
The hybrid type virtual work equation can be described as follows about *N* intersection boundary.

$$\sum_{e=1}^{M}\left(\int_{\Omega^{(e)}} \boldsymbol{\sigma} : \text{grad}(\delta\boldsymbol{u}) dV - \int_{\Omega^{(e)}} \boldsymbol{f}\cdot\delta\boldsymbol{u}\, dV\right) - \sum_{s=1}^{N}\left(\delta\int_{\Gamma_{<s>}} \boldsymbol{\lambda}\cdot(\widetilde{\boldsymbol{u}}^{(a)} - \widetilde{\boldsymbol{u}}^{(b)})\, dS\right) - \int_{\Gamma_\sigma} \hat{\boldsymbol{t}}\cdot\delta\boldsymbol{u}\, dS = 0 \quad {}^\forall\delta\boldsymbol{u} \in \mathbb{V} \tag{17}$$

Physical meaning of the Lagrange multiplier $\boldsymbol{\lambda}$ is equal to the surface force on the intersection boundary $\Gamma_{<ab>}$.

$$\boldsymbol{\lambda} = \boldsymbol{t}^{(a)}(\tilde{\boldsymbol{u}}^{(a)}) = -\boldsymbol{t}^{(b)}(\tilde{\boldsymbol{u}}^{(b)}) \tag{18}$$

where $\boldsymbol{t}^{(a)}$ and $\boldsymbol{t}^{(b)}$ are the surface force on the intersection boundary $\Gamma_{<ab>}$ in sub-domain $\Omega^{(a)}$ and $\Omega^{(b)}$.

3. Discretization equation

3.1 Lagrange multiplier and penalty

Physical meaning of the Lagrange multiplier $\boldsymbol{\lambda}$ is equal to the surface force on the intersection boundary as described in Section 2. Generally, in a hybrid-type variational principle, this multiplier is dealt with as an unknown parameter.
Since it has the meaning that Lagrange multiplier $\boldsymbol{\lambda}$ is the surface force on the boundary $\Gamma_{<ab>}$ in sub-domain $\Omega^{(a)}$ and $\Omega^{(b)}$, the surface force is defined as follows:

$$\boldsymbol{\lambda}_{<ab>} = \boldsymbol{k} \cdot \boldsymbol{\delta}_{<ab>} \tag{19}$$

Here, $\boldsymbol{\delta}_{<ab>}$ shows relative displacement on the sub-domain boundary $\Gamma_{<ab>}$, and it is shown in two dimensional problem as follows.

$$\begin{Bmatrix} \lambda_{n<ab>} \\ \lambda_{t<ab>} \end{Bmatrix} = \begin{bmatrix} k_n & 0 \\ 0 & k_t \end{bmatrix} \begin{Bmatrix} \delta_{n<ab>} \\ \delta_{t<ab>} \end{Bmatrix} \tag{20}$$

where, $\delta_{n<ab>}$, $\delta_{t<ab>}$ are relative displacement in the normal and the tangential direction to the sub-domain boundary $\Gamma_{<ab>}$. Similarly, $\lambda_{n<ab>}$, $\lambda_{t<ab>}$ are Lagrange multipliers in the normal and tangential direction of the surface forces. The hybrid type penalty method can be described as follows by penalty function $\boldsymbol{\lambda}$ use as coefficient k.

$$k_n = k_t = p \tag{21}$$

3.2 Discretization equation by matrix form

When equation (17) is rewritten by the matrix form to make the discretization equation, it is possible to describe it as follows:

$$\sum_{e=1}^{M}\left(\int_{\Omega^{(e)}} [\boldsymbol{L}\delta\boldsymbol{u}]^t \boldsymbol{D}\boldsymbol{L}\boldsymbol{u} dV - \int_{\Omega^{(e)}} \delta\boldsymbol{u}^t \boldsymbol{f} dV - \int_{\Gamma_\sigma} \delta\boldsymbol{u}^t \hat{\boldsymbol{T}} dS\right) + \sum_{s=1}^{N}\left(\delta \int_{\Gamma_{<s>}} \boldsymbol{\delta}^t \boldsymbol{k} \boldsymbol{\delta}\, dS\right) = 0 \tag{22}$$

In a plane stress of two dimensions, each coefficient is as follows:

$$\boldsymbol{L}^t = \begin{bmatrix} \frac{\partial}{\partial x} & 0 & \frac{\partial}{\partial y} \\ 0 & \frac{\partial}{\partial y} & \frac{\partial}{\partial x} \end{bmatrix}, \quad \boldsymbol{D} = \frac{E}{1-\nu^2}\begin{bmatrix} 1 & \nu & 0 \\ \nu & 1 & 0 \\ 0 & 0 & \frac{1-\nu}{2} \end{bmatrix}$$

$$\boldsymbol{f} = \begin{Bmatrix} f_x \\ f_y \end{Bmatrix}, \quad \boldsymbol{u} = \begin{Bmatrix} u \\ v \end{Bmatrix}, \quad \delta\boldsymbol{u} = \begin{Bmatrix} \delta u \\ \delta v \end{Bmatrix}, \quad \hat{\boldsymbol{T}} = \begin{Bmatrix} \hat{t_n} \\ \hat{t_t} \end{Bmatrix}$$

Here, E and ν are the elastic coefficient and Poisson ratio. f_x and f_y show the body force in the direction of x and y, u and v are the displacements of the direction of x and y, δu and δv are virtual displacement in the direction of x and y, $\hat{t}_n$, $\hat{t}_t$ are the given surface force in the normal and tangential direction on the boundary.
The displacement shown by the second order function in Equation (23) is substituted for Equation(24). Similarly, we assumed virtual displacement as follows:

$$\boldsymbol{u}^{(e)} = \boldsymbol{N}_d^{(e)}\boldsymbol{d}^{(e)} + \boldsymbol{N}_\varepsilon^{(e)}\boldsymbol{\varepsilon}^{(e)} + \boldsymbol{N}_g^{(e)}\boldsymbol{\varepsilon}_x^{(e)} \tag{23}$$

$$\delta\boldsymbol{u}^{(e)} = \boldsymbol{N}_d^{(e)}\delta\boldsymbol{d}^{(e)} + \boldsymbol{N}_\varepsilon^{(e)}\delta\boldsymbol{\varepsilon}^{(e)} + \boldsymbol{N}_g^{(e)}\delta\boldsymbol{\varepsilon}_x^{(e)} \tag{24}$$

To make the discretization equation, equation (23) and equation (24) are changed as follows.

$$\boldsymbol{u}^{(e)} = \boldsymbol{N}^{(e)}\boldsymbol{U}^{(e)}, \; \delta\boldsymbol{u}^{(e)} = \boldsymbol{N}^{(e)}\delta\boldsymbol{U}^{(e)} \tag{25}$$

Therefore, the following expression is obtained.

$$\boldsymbol{L}\boldsymbol{u}^{(e)} = \boldsymbol{L}\boldsymbol{N}^{(e)}\boldsymbol{U}^{(e)} = \boldsymbol{B}^{(e)}\boldsymbol{U}^{(e)} \tag{26}$$

here,

$$\boldsymbol{B}^{(e)} = \boldsymbol{L}\boldsymbol{N}^{(e)}$$

The following is obtained by substituting these relation for Equation (22).

$$\delta\boldsymbol{U}^t\left(\sum_{e=1}^{M}\boldsymbol{K}^{(e)} + \sum_{s=1}^{N}\boldsymbol{K}_{<s>}\right)\boldsymbol{U} - \delta\boldsymbol{U}^t\left(\sum_{e=1}^{M}\boldsymbol{P}^{(e)}\right) = 0 \tag{27}$$

Since Virtual displacement $\delta\boldsymbol{U}$ of equation (27) is arbitrary, we obtain the following discretized equations.

$$\boldsymbol{K}\boldsymbol{U} = \boldsymbol{P} \tag{28}$$

Here, $\boldsymbol{K}$ and $\boldsymbol{P}$ are as follows.

$$\boldsymbol{K} = \sum_{e=1}^{M}\boldsymbol{K}^{(e)} + \sum_{s=1}^{N}\boldsymbol{K}_{<s>} \tag{29}$$

$$\boldsymbol{P} = \sum_{e=1}^{M}\boldsymbol{P}^{(e)} \tag{30}$$

The discretization equation of this model becomes a simultaneous linear equation shown in equation (28). Left coefficient matrix $\boldsymbol{K}$ consists of stiffness in the sub domain and subsidiary condition on the intersection boundary for the adjacent sub-domain. The discontinuous phenomenon of opening etc. can be expressed without changing degree of freedom by changing the value of of equation (27) to zero.

4. Nonlinear Numerical algorithm

In this paper, it was corrected that Yamada's r_{min} method was able to be used for the open stress problem, and applied to a nonlinear analysis of HPM. Here, f is the yield function, $\boldsymbol{\lambda}$ is the surface force, $\Delta\boldsymbol{\lambda}$ is the

incremental surface force, the increment rate r satisfies the following expressions.

$$\boldsymbol{f}(\boldsymbol{\lambda}+r\cdot\Delta\boldsymbol{\lambda})\le 0 \tag{31}$$

Moreover, when equation (31) is satisfied, the plasticity strain increment and the state of the stress are updated according to the flow rule.
This increment ratio r is calculated based on yield criterion, and calculates all the surface force. In this paper, the load increment ratio calculates re-contact after the tension destruction and the tension destruction. The tension destruction is shown as follows.

$$(\boldsymbol{\lambda}_n + r\cdot\Delta\boldsymbol{\lambda}) = F_t \tag{32}$$

At the same time, re-contact after the tension destruction becomes equation (32) by using relative displacement.

$$(\delta_n + r\cdot\Delta\delta_n) = 0 \tag{33}$$

Here, when relative displacement is zero, it is assumed to be re-contact. A minimum increment ratio at the increment ratio calculated above is assumed to be a load increment ratio. At this time, when the current value and the value after the increment are assumed to be n and $n+1$,

$$\boldsymbol{\lambda}^{n+1} = \boldsymbol{\lambda}^{n} + r\cdot\Delta\boldsymbol{\lambda} \tag{34}$$

The surface force after the increment is sure to exist right above or in yield surface.
Here, load $\boldsymbol{P}$ is divided into some increment loads $\Delta\boldsymbol{p}$. At this time, if the load value in an arbitrary step is assumed to be $\Delta\boldsymbol{p}^{(i)}$, and the load increment ratio is assumed to be r_i, residual load $\Delta\boldsymbol{p}^{(i+1)}$ is shown equation (35).

$$\Delta\boldsymbol{P}^{(i+1)} = (1-r_i)\Delta\boldsymbol{P}^{(i)} \tag{35}$$

When the initial increment load is assumed to be $\Delta\boldsymbol{p}$, the residual increment loads of n step are as follows.

$$\Delta\boldsymbol{P}^{(i+1)} = \prod(1-r_i)\Delta\boldsymbol{P} \quad (r_o = 0) \tag{36}$$

The penalty value of the boundary is assumed to be zero when the tension destruction is caused in an arbitrary boundary and the flow of surface force is intercepted. The surface force of the boundary is distributed to a related sub-domain as opening force. The opening force in boundaries of S turn is calculated by the next equation.

$$\boldsymbol{F}_{<s>} = -\int_{\Gamma_{<s>}} \boldsymbol{B}_{<s>}\boldsymbol{\lambda}_{<s>}\,d\Gamma \tag{37}$$

The residual load is added to the distributed opening force and the increment calculation in the next step is done. The iterative calculation is done until all initial loads and opening force are used completely. Total r_{total} of the load increment ratio is shown in equation (38).

$$r_{total} = \sum_{k=1}^{n}\left\{\prod_{i=k}^{n-1}(1-r_i)\right\} \tag{38}$$

It is assumed convergence in $r_{total} = 1$. Moreover, the same technique as the r_{min} method in a conventional load increment method is used except for the opening force.

5. Mesh dividing algorithm

5.1 Calculation of strain energy

In this paper, the shearing strain energy was used for the index of the mesh dividing. The method of calculating the shearing strain energy is described as follows. The shearing strain energy is calculated by using shearing strain γ_{xy} and area A in sub-domain.

$$\text{Shearing strain energy} = \frac{1}{2}\gamma_{xy}^2 A \tag{39}$$

Total strain energy is calculated by using stress, strain and area in each sub-domain.

$$\text{Total strain energy} = \frac{1}{2}[\boldsymbol{\sigma}]^T[\boldsymbol{\varepsilon}]A \tag{40}$$

The mesh dividing is done in sub-domain where the strain energy becomes the maximum in all sub-domains.

5.2 Convergence determination of mesh dividing

The convergence determination of mesh dividing is judged because of the error margin of the average shearing strain energy of a sub-domain and the maximum shearing strain energy of all sub-domain.

$$\frac{1}{2}\int_{\Omega^{(e)}}\gamma_{xy}^2 dA\Big|_{max} - \frac{1}{2M}\int_{\Omega^{(e)}}\gamma_{xy}^2 dA < \varepsilon \tag{41}$$

6. Comparison with Riedel shearing test

6.1 Experimental result

The test equipment is shown in Figure 4. The boundary condition is shown Figure 5. During tests, the board on the side is removed. And, the specimen makes only the influence by the board shear direction. The specimen is shown in Figure 6.

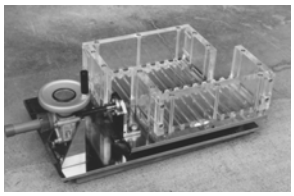

Fig. 4: Test equipment

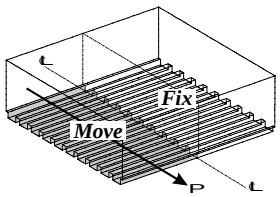

Fig. 5: boundary condition

(Plane-view)

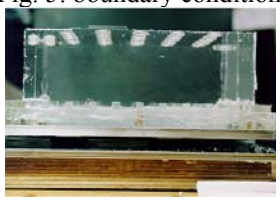

(Side-view)

(Silicon)

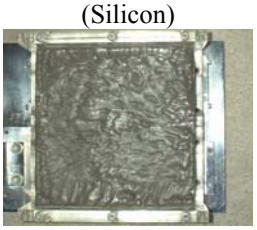

(Clay)

Fig. 6: Specimen

The test result of the silicon model is shown in Figure 7. The crack that occurred in a base progressed with spiral shape with increase of displacement.

(Plane-view)

(Side-view)

(Front-view)

Fig. 7: Result of silicon model

The test result of the clay model is shown in Figure 8. The crack that occurred in the model side has expanded with increase of displacement. Moreover, the crack of the surface of the model became going side by side shape according to an increase in displacement.

(thickness=5.0cm)

(thickness=10.0cm)

Fig. 8: Result of clay model

6.2 Numerical Result

The analytical model is shown in Figure 9. This analysis gives displacement from the use of a plane model to the model side. Moreover, an initial model is shown in the left picture, and the mesh dividing model is shown in the right picture. In addition, an analytical model of RBSM and FEM used for the comparison with HPM is shown in Figure 10.

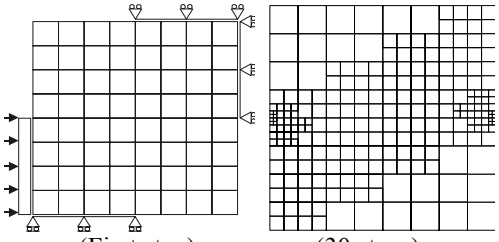

(First step) (30 steps)

Fig. 9: Analytical model (HPM)

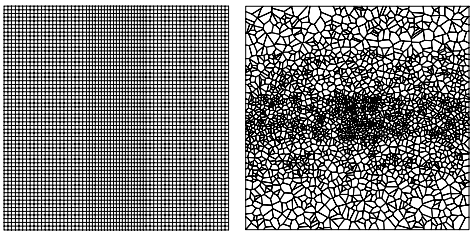

(FEM-Model) (RBSM-Model)

Fig. 10: Analytical model (FEM and RBSM)

The displacement mode of HPM showed the same tendency as RBSM and FEM as shown in Figure 11. Moreover, the tendency to which displacement was localized in the displacement boundary part became the same.

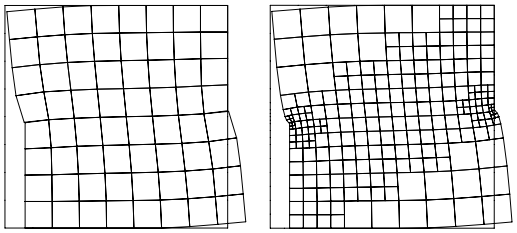

(HPM-First step) (HPM-30 steps)

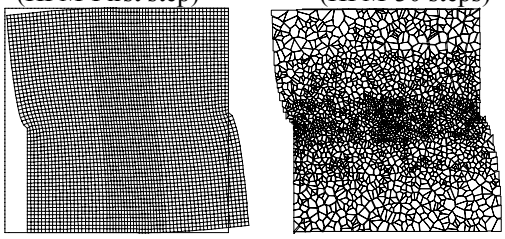

(FEM-Model) (RBSM-Model)

Fig. 11: Displacement mode

The crack pattern by the 2 dimensional nonlinear analysis is shown in Figure 12. The crack initiation by

FEM distribute widely. However, HPM and RBSM were localized in the displacement boundary part.

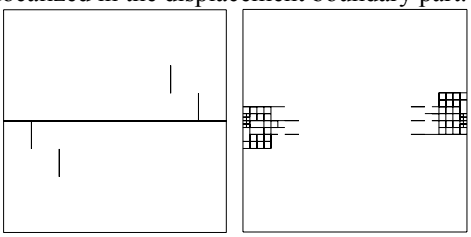

(HPM-First step) (HPM-30 steps)

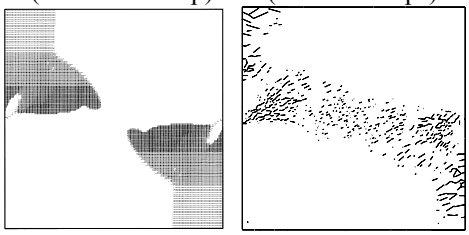

(FEM-Model) (RBSM-Model)

Fig. 12: Crack mode

The maximum shearing strain is shown in Figure 13. The area where the maximum shearing strain was high became the same type as the test result. The maximum shearing strain was localized along with the division of the mesh. And, the same tendency as FEM could be shown by a small number of elements.

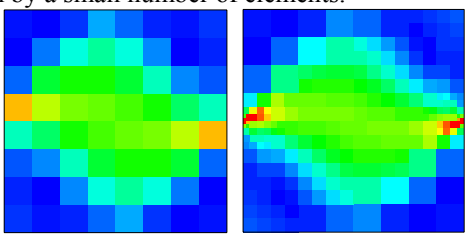

(HPM-First step) (HPM-30 steps)

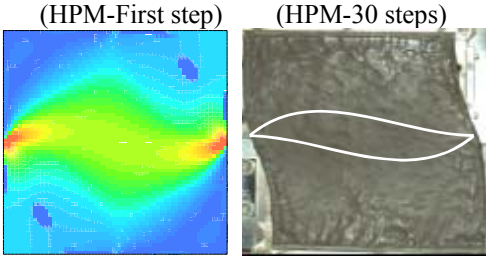

(FEM-Model) (Experiment result)

Fig. 13: Maximum shearing strain

7. Conclusions

This paper reported the result of the Riedel shearing test and a numerical result for the nonlinear analysis by using the mesh dividing method. HPM divides a whole area into sub-domain, and the displacement field is defined independently in each sub-domain. At this time, the node of the area doesn't have degree of freedom from the use only to recognize shape like FEM. Therefore, the middle node need not be installed like FEM. This means an arbitrary area can be subdivided as shown by the example of the numerical analysis as the node doesn't worry. That is, in the problem that strong nonlinear appears locally, it is thought that the improvement of accuracy can be attempted by dividing again partially.

1. HPM using mesh dividing method was able to obtain the same tendency as FEM by a small number of elements.
2. The dividing of the element was repeated in the area where the crack had occurred a lot during tests. Moreover, the tendency to which the shearing strain was localized can be obtained.
3. The shape of the area where the elements are refined showed shape similar to the area where the going side by side crack had been caused during tests. Moreover, the direction of displacement show the same tendency with the area where the high shearing strain was generated by 45 degrees in the direction.

The study in this paper was conducted based on a plane model. It is scheduled to analyze it according to a solid model in the future.

References

T.Kawai, New element models in discrete structural analysis, J. of the Society of Naval Architects of Japan No. 141, pp187-193, 1977.

K.Washizu, Variational Method in Elasticity and Plasticity, Pergamon, 1975.

N.Takeuchi,H.Ohki,A.Kambayashi and M.Kusabuka, Non-linear analysis by using discrete model applied penalty method in hybrid displacement model, Transactions of Japan Society for Computational Engineering and Science Paper No. 20010002, 2001.

R.Mihara and N.Takeuchi, Material nonlinear analysis using bybrid-type penalty method assumed second-order displacement field, ICADD-7, 2005

C.Frits and H.Feenstra, DIANA User's Manual, TNO, 2002.

Rock Block Identification and Block Size Determination of Rock Mass

J.S. SONG*, Y. OHNISHI and S. NISHIYAMA

Division of Urban & Environment Eng., School of Civil Eng., Kyoto Univ., Kyoto, 615-8540, JAPAN

In this paper, the topological properties of 3D blocks are described, and 3D topological data model is proposed. An algorithm of automatically identifying rock blocks is then presented. Based on object-oriented approach, a block tracing program is developed to identify rock blocks. In the program, the discontinuities in rock mass are treated as flat planes with or without finite size. Using the geometrical and topological information of joints as input data, the block tracing program can identify all possible 3D blocks (convex or concave) through four steps, namely, intersection calculation, tree cutting, 2D block tracing and 3D block tracing. The volume of rock blocks can be easily calculated by using of 3D simplex integration without dividing it into small blocks. An example is used to demonstrate and verify the effectiveness and accuracy of block tracing program that can identify both convex and concave polyhedron and calculate their volume. This block tracing program can be used as a pre-process for discrete element method (DEM), block theory, discontinuous deformation analysis (DDA) and manifold method (MM).

Keywords: Rock blocks, 3D topological data model, Block tracing program, Block size

1. Introduction

The rock masses are, by nature, discontinuous materials that contain many discontinuities such as fractures, joints, faults, shear planes and shear zones, which intersecting rock divide the rock mass into blocks with a great variety of sizes and shapes (Fig. 1). The rock block sizes (block volume or joint spacing) and block shapes are extremely important parameters influencing the behavior of rock masses in underground opening and surface cuttings.

Fig. 1: Rock blocks formed by joints (from www.rock.mass.net)

There are mainly two kinds of joints, joint sets that compose of parallel oriented joints, and random (irregular) joints that do not belong to any joint set. The block sizes are result of the joint spacing, the number of joint sets, and the size and persistence of the joints. Block shape depends mainly on the differences between the joint set spacing. Dearman (1991) presented typical block shapes or jointing patterns where regular jointing exists. In most cases, however, there is no regular jointing pattern. Random joints further complicate the block sizes and shapes. The sizes and the shapes of the rock blocks surrounding an underground excavation may also determine whether the rock masses will behave as a continuous material, or as a discontinuous material. Correspondingly the most suitable numerical methods of analysis, the continuum modeling or discontinuum modeling, are chosen to investigate the stability of underground excavation and slope.

Because measurements mostly are made on 2-dimensional surfaces and 1-dimensional borehole, it is difficult to measure block size directly. So some crude estimations of block sizes are proposed by several researchers. Block sizes are typically estimated by following indices, Block Volume (Vb), Rock Quality Designation (RQD), Volumetric Joint Count (Jv), and Block Size Index (Ib). These indices are also a reduction ratio of the strength of intact rock. But these methods do not quantify the actual block size and block size distribution.

Several numerical methods including block theory (Goodman 1985), discrete element method (Cundall 1988), discontinuous deformation analysis (Shi 1988) and manifold method (Song 2006) are used to study the stability problems. But accurately identifying rock blocks and determining their properties (size, mass, volume etc) are critical success factors of numerical simulation of slope failure or tunnel collapse.

The block generation language by Heliot (1988) and rock block identification algorithm developed by Warburton (1983), both as pre-processor of 3DEC code, used infinitely large discontinuous faces and could detect only convex blocks. Maerz and Germain (1996) used the semi-infinite joint sets to cut a fixed volume of space (rock mass) into rock blocks. The assumption in calculating rock block volume is that all blocks are convex. Jing (2000) introduced finite size of joints in his block constructing system, but only regular face (rectangular) of blocks were identified. Lu (2002) proposed block identification algorithm that could find both convex and concave polyhedra, but no block volume calculation was provided. So in this paper, a 3D topological data model is firstly proposed. Then a general block tracing program is developed to identify rock block with complex geometry (convex or concave). Thirdly rock block size determination is discussed. Finally an example is used to verify the correctness and accuracy of block tracing program.

2. 3D data model of rock blocks

Rock blocks (polyhedra) have two kinds of properties: topological properties such as number of vertices, edges, faces and their relationships; and metric properties that include mass, weight, volume, lengths of edges and areas of faces etc.

The number of rock blocks and their size distribution are affected by fracture or joint's size, orientation, and spacing. The joints are usually considered to be smooth and planar, with either regular (rectangular, circular or elliptical) or irregular shapes and of finite or infinite size (compared with the scope of target space). Joints may parallel, overlap or intersect with each other and intersected edges and vertices are formed. Fig. 2 shows typical intersection patterns of three planes.

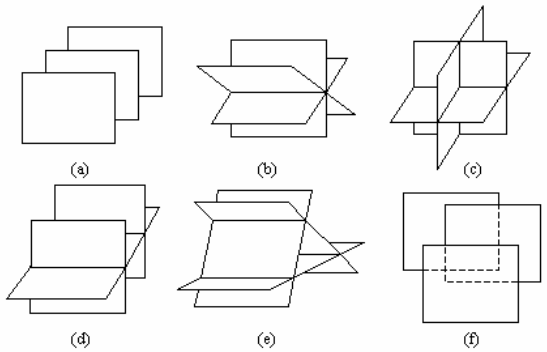

Fig. 2: Possible intersection patterns of three planes (modified from Sunday Dan, 2001)

Topology is a unified high-level abstraction of geometrical information. Adjacency topology describes the adjacency of topological primitives such as vertices, edges, faces, and solids. In this paper, some basic concepts of combinatorial topology are introduced and a hierarchy of data model is proposed. According to properties of rock mass, four abstract objects, point, line, surface and body, are used to represent their geometric properties related shape, size and position. These objects are built of four topological primitives namely vertex, edge, face, solid, i.e. 0,1,2,3 simplexes. Based on study of geometrical and topological properties of 3D rock blocks, a 3D topological data model is proposed to describe rock blocks (Fig. 3).

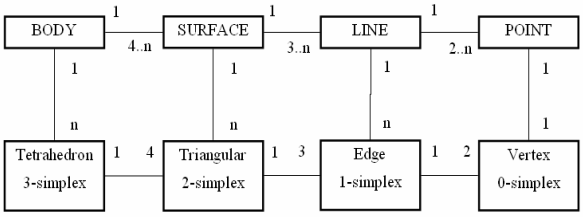

Fig. 3: 3D data model of rock blocks

3. Block tracing program

Discontinuities such as fractures, joints divide rock mass into many rock blocks. So the rock blocks have parts or whole surfaces of fractures as their surfaces. Some fractures can be intersected by many other fractures, forming many closed face loops that may serve as surfaces of newly formed blocks. There are four steps to identify 3D rock blocks. (1) Intersection calculation: All the intersected edges and vertices are calculated using the geometrical data of fractures. (2) Tree Cutting: This paper develops a tree cutting program to delete wire edges or dangling planes because they are non-manifold. (3) 2D block tracing: Extended from 2D block tracing program of DDA (Shi, 1988), a 2D block tracing program is developed and used to find face-loops for all given surfaces. (4) 3D block tracing: Based on the 3D topological data model of 3D rock blocks, the 3D block tracing is finally built to identify rock blocks (both convex and concave polyhedra). The flowchart of 3D block tracing program is shown in Fig. 4.

4. Block Size Determination

The block sizes are result of the joint spacing, the number of joint sets, and the size and persistence of the joints. It is time-consuming to calculate volume of individual blocks. When irregular joints exist, it is more difficult to determine the actual size and shape of formed blocks. So an equivalent block volume is usually used to simplify the determination of block sizes and shapes. On the contrary, the block tracing system, using joint sets or random joint as input data, can identify all blocks with complex geometry (convex or concave) and can accurately compute the actual

volume of block by 3D simplex integration method (Song 2007).

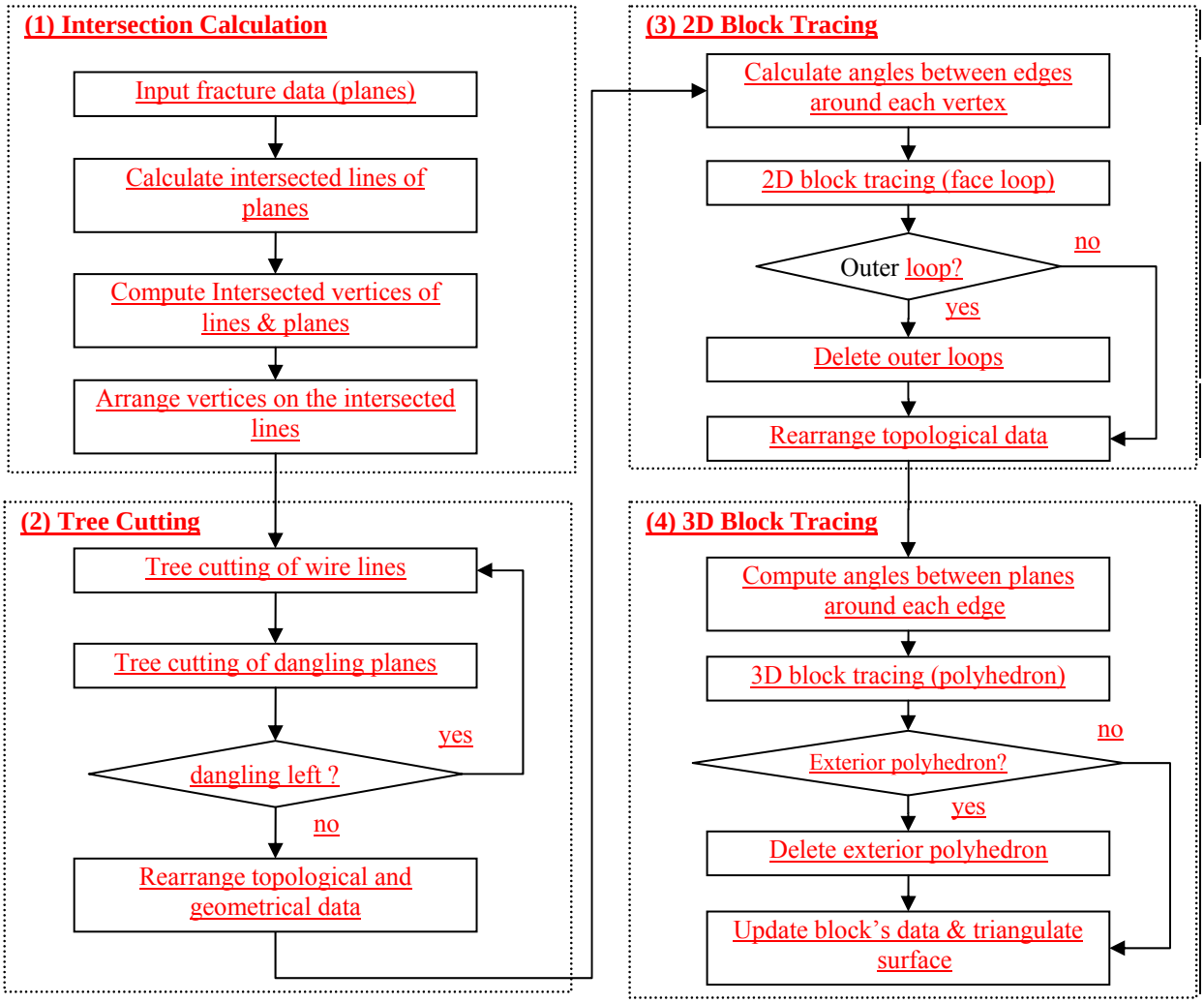

Figure 4: Flow chart of 3D block tracing program

4.1 Block Volume from Joint Spacing

This method uses joint spacing of regular joint sets to determine block volume. The joint spacing or average joint spacing is perpendicular spacing between joints with the same joint set. When three joint sets intersect with each other and divide the rock masses into blocks (Fig. 5). The block volume can simply calculated from joint spacing (Palmstron 1996).

$$V = \frac{S1 \times S2 \times S3}{\sin\gamma 1 \times \sin\gamma 2 \times \sin\gamma 3} \qquad (1)$$

Where γ1,γ2,γ3 are the angles between joint set, and S1, S2, S3 are the spacing between individual joints in each joint set.

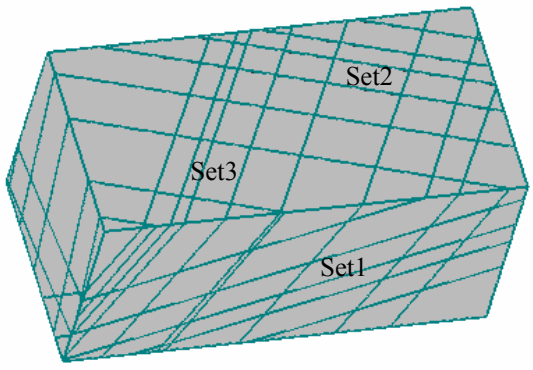

Fig. 5: Joint set and joint spacing

4.2 Block volume from 3D simplex integration

Suppose a general block has *n* polygon surfaces. A general polygon surface, no matter convex or concave, can be triangulated into *m* triangles ($P_{j1}P_{j2}P_{j3}$) mentioned above in block tracing program. Choose an arbitrary point as P_0, inside or outside the block, usually at origin (*0,0,0*), the volume of the block can be an algebraic sum of 3D simplex integration on each tetrahedron $P_0\,P_{j1}P_{j2}P_{j3}$ by equation (2).

$$V = \sum_{i=1}^{n}\sum_{j=1}^{m} V_{p_{j0}p_{j1}p_{j2}p_{j3}} = \frac{1}{6}\sum_{i=1}^{n}\sum_{j=1}^{m}(J_j) \qquad (2)$$

Where J is Jacobi determinant.

5. Examples

To verify block tracing program is to check 1) all formed block are identified without block left, 2) the geometrical parameters are accurately calculated. So in this paper, a simple example is used to verify the correctness and accuracy of 3D block tracing program. Take a cube of 2 units in length, 1 in height and 1 in width as a master block. Then cut the cube with 10 fractures with finite size (Fig. 6(a)). In the intersection calculation step, 4 lines are intersected by 2 fractures and cube. But the 4 intersected lines can not form any block. Therefore they are removed by tree-cutting program. Finally six blocks, 2 concave and 4 convex polyhedra, are identified (Fig. 6(b). The topological information and geometrical information are listed in table 1. From the table, we can find that the total volume of 6 small blocks (2 concave and 4 convex polyhedra) is equal to original volume of cube. The geometrical parameters of blocks are accurately calculated. Volume calculation using 3D simplex integration quantitatively verifies the accuracy of block tracing program. This example demonstrates that the block tracing program can effectively and accurately identify all the blocks formed by fractures.

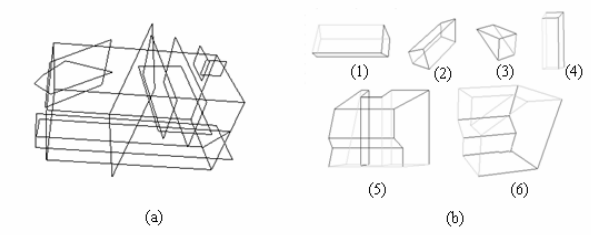

Fig. 6: An example of block identification: (a) a cube cut by 10 finite size fractures (b) Identified 6 blocks (4 convex and 2 concave polyhedra).

Table 1: Topological and geometrical data of identified blocks and original cube

Block	Type	Face	Edge	Vertex	Volume
block 1	convex	6	12	8	0.137450
block 2	convex	6	12	8	0.102550
block 3	convex	5	9	6	0.048000
block 4	convex	6	12	8	0.090000
block 5	concave	12	28	20	0.822550
block 6	concave	10	24	16	0.799450
SUM	-	-	-	-	2.000000
Cube	convex	6	12	8	2.000000

6. Conclusions

Based on analyzing of the topological properties of 3D rock blocks, this paper proposes the 3D topological data model and develops a new block tracing program that can identify both convex and concave polyhedra. Using the geometrical and topological information, any polyhedron with complex geometry can be traced through four steps, intersection calculation, tree cutting, 2D block tracing and 3D block tracing. An example demonstrates and verifies that all blocks can be identified successfully with no small block left. The actual block volume can be accurately computed by using of 3D simplex integration, a computationally efficient method. This block tracing program can provide more accurate information of rock masses for final design and optimization of excavation and support onsite. It can also be used as a pre-process tool for 3DEC, DDA, MM, etc.

References

Cundall PA. Formulation of a three-dimensional distinct element model - Part I. A scheme to detect and represent contacts in a system composed of many polyhedral blocks. *Int J Rock Mech Min Sci and Geomech Abstr* 1988;25(3):107-16.

Dearman W.R. *Engineering geological mapping*. Butterworth - Heinemann Ltd., Oxford, 1991.

Goodman RE, Shi GH. *Block theory and its application to rock engineering*. Prentice-Hall, 1985.

Hart RD, Cundall PA, Lemos J. Formulation of a three-dimensional distinct element model - Part II. Mechanical calculations of a system composed of many polyhedral blocks. *Int J Rock Mech Min Sci and Geomech Abstr* 1988;25(3):117-26.

Heiliot D. Generating a blocky rock mass. *Int J Rock Mech Min Sci and Geomech Abstr* 1988;25(3):127-38.

Jing L., Block sytem construction for three-dimensional discrete element models of fractured rocks. *Int. J. Rock Mech. Min. Sci. & Geomech. Abstr*. 37 4 (2000), pp. 645-659.

Lu Jun, Systematic identification of polyhedral rock blocks with arbitrary joints and faults. *Computers and Geotechnics* 29 (2002) 49-23.

Maerz NH, Germain P. Block size determination around underground openings using simulations. *Proceedings of the FRAGBLAST 5 Workshop on Measurement of Blast Fragmentation*, Montreal, Quebec, Canada, 23-24 Aug., 1996, PP.215-223.

Palmtron A., Characterizing rock masses by the RMI for use in practical engineering. Part 1: *Tunnelling and Underground Space Technology*, Vol. 11, No. 2, pp 175-186. Part2: Vol.11, No. 3, pp 287-303.

Shi Gen-hua, *Discontinuous Deformation Analysis a new numerical model for the statics and dynamics of block systems*. Ph.D. Thesis, University of California, Berkeley, USA, 1988.

Shi Gen-hua, Simplex Integration for Manifold Method, FEM, DDA and Analytical Analysis. in M. R. Salami and D. Banks eds. *Discontinuous Deformation Analysis (DDA) and Simulations of Discontinuous Media,* TSI Press, Albuquerque, New Mexico, 1996, pp. 205-262.

Shi GH, Goodman RE. Two dimensional discontinuous deformation analysis. *Int J Num Analy Mech Geomech* 1989;9(6):541-56.

Song J., Ohnishi Y., Nishiyama S. High order displacement function on rectangular element of manifold method. *In: 7th World Congress on Computational Mechanics*. Los Angeles, USA, 2006. P1515.

Song J., Ohnishi Y., Nishiyama S. Rock Block Identification and 3D Simplex Integration. *In: 2007 International Symposium on Computational Mechanics.* Beijing, China, 2007.

Sunday, Dan. 2001c. Intersection of line, segment and plane in 3d and 3d. www.softsurfer.com.

Warburton PM. Application of a new computer model for reconstructing blocky block geometry analysis single block stability and identifying keystones. *In: Proc 5th Int Congress on Rock Mechanics*, Melbourne, 1983. p. F225¯F230

3-D Mode Discrete Element Method

ZHANG CHONG[1,2], JIN FENG[1], WANG RENKUN[2], FENG XUEMIN[2]

[1] State Key Laboratory of Hydroscience and Engineering，Tsinghua University，Beijing, 100084, China
[2] Chengdu Hydroelectric Investigation & Design Institute of SPC, Chengdu, 610072, China

For block systems that satisfy small strain, finite displacement and finite rotation conditions, a 3-dimensional mode deformable discrete element method (3MDEM) is presented. It is an efficient numerical method to simulate mechanical behaviors of nonlinear, large deformation and dynamic problems. First, the equations including the motion and deformation are derived. Second, under the small deformation condition, the motion of deformable blocks can be decomposed into rigid body motion and deformation. Third, based on several deformation modes, the deformation of blocks can be expressed by the combination of deformation modes, which can be decoupled under given conditions. Regarding the deformation simulation of blocks, 3MDEM is more efficient than 3DEC developed by ITASCA. Numerical verification shows that the displacements and stresses obtained by 3MDEM is coherence with that obtained by FEM under the condition of small deformation. Under the large deformation condition, the simulation results of structures by 3MDEM agree well with that by 3DEC.

Keywords: Discrete element method (DEM); Discontinuum; Numerical method; Finite deformation

1. Introduction

The Discrete or Distinct Element Method (DEM) was first proposed by Cundall (Cundall, 1971) to study slope stability problems in jointed rock masses. In this method the rock messes is simulated as a system of interacting rigid blocks in two-dimensional. This method was then extended by Cundall et al. (Cundall 1988; Hart et al. 1988; Cundall 1980; 3DEC manual) to deformable elements and to three-dimensional. Many other investigators also studied this method in various aspects (Williams et al. 1985, 1987; Bardet et al. 1985; Butkovich et al. 1988, etc.). In China, Wang et al. applied this method in the numerical analysis of jointed rock masses and successfully simulated the natural break-down process of rock body (Wang, et al 1991). Zhang et al. applied this method to study slope stability problems in rock mechanics, to perform static and dynamic stability analysis of arch dams, and introduced corresponding engineering criterion to evaluate the instability potential (Zhang et al 1997; Zhang et al 2006)

The DEM distinguishes itself from the FEM by modeling its objects as systems of discontinuous bodies that interact with each other. Bodies may be rigid or deformable. Based on Newton's second law, kinetic equation is built, and an explicit time-marching scheme is used to solve the equations of motion directly, which can be used to simulate the structure real-time responses from small deformation phase to final failure of systems.

In three-dimensional DEM deformable algorithms, a finite difference tetrahedral meshing technique is generally adopted to model individual blocks, within which physical quantities such as mass and resultant forces are distributed to the nodes. The nodal displacements are then used as basic unknowns to establish the global equations, which are explicit progressively solved in time domain. For engineering problems in large-scale structures such as simulation of a dam-foundation system, this method may require a quite large number of nodes in addition to a very small time step to obtain a reasonable result.

Ideas based on modal decomposition have been induced to simplify the deformation within a discrete element or block.(William et al. 1985, 1987; Shi 1992). The 3MDEM has been built as an efficient method to model bodies of complicated shape that deform in a simple manner (Zhang 2007). In this paper, we assume the translation and rotation of blocks is finite, but the strain is fairly small, so it is reasonable to suppose that the density, volume and inertia moment of blocks will remain constant during the total deformation progress.
A 3-D formulation of mode discrete element method (3MDEM), which can be adopted to solve large-scale engineering problems more efficiently and a modal method to simplify stress-strain relationship inside discrete blocks is presented.

2. Kinematics equations

The motion and deformation of an individual block can be decomposed into three type motions in small deformation condition, there are block translation,

rotation and deformation. This paragraph will only give the description of block rotation and deformation because the translation is too easy, which is not necessary to be further analyzed. Regarding the assumption of small deformation for each individual block, the density, volume, moment of inertia of each block will remain constant.

Generally, in dealing with multi-body systems, three types of coordinate systems are required. The first is global coordinate system that is fixed and represents a unique standard for all blocks in the systems. This coordinate system will be named frame *a*, whose base vector is $\boldsymbol{e}^{a}$ and coordinate is described by lowercase letter *x*, *y* and *z*. In addition to this frame, we assign a body frame to each block which is named frame *b*, whose base vector is $\boldsymbol{e}^{b}$ and coordinate is described by capital letter *X*, *Y* and *Z*. This frame is located in the gravity centre of each block, and the orientation of coordinate is chosen to parallel with principal axis of inertia of each block. The third frame is superposition with frame *b* for each block at the beginning of each time step and its orientation remains steady in the time step. This frame is called reference frame and named frame *b'*.

The symbol ${}^{C}\dot{v}_{i}^{D}$ is defined as ith component exhibited in frame D of the derivative in frame C of vector v.

2.1Rotation of a block

Considering the fixed-spindle rotation of a block from time t to $t+\Delta t$, the block rotates degree θ around axis $\boldsymbol{p}$. The vector $\boldsymbol{p}$ is the unit vector of rotation axis.

Generally, transformation matrix $A^{b'b}$ between frame *b* and frame *b'* is:

$$A^{b'b} = \cos\theta \mathrm{I}_3 + (1-\cos\theta)pp^T + \sin\theta\tilde{p} \qquad (1)$$

Where $\tilde{p}$ is skew symmetric matrix given by

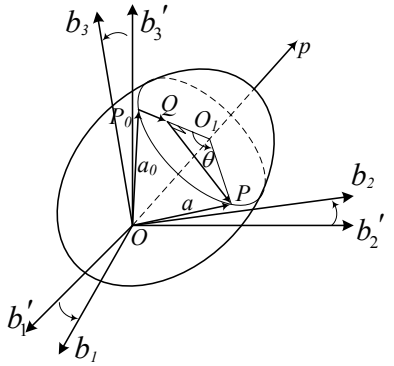

Fig 1 fixed-axis rotation of a block

$$\tilde{p} = \begin{bmatrix} 0 & -p_3 & p_2 \\ p_3 & 0 & -p_1 \\ -p_2 & p_1 & 0 \end{bmatrix} \qquad (2)$$

In which p_1, p_2 and p_3 are the components of the vector $\boldsymbol{p}$.

The angular velocity vector of the block is ω, whose corresponding skew symmetric matrix is $\tilde{\omega}$. According to multi-body dynamics (Hong Jiazhen, 1998), $\tilde{\omega}$ can be written as:

$$\tilde{\omega}^{b} = A^{bb'}\dot{A}^{b'b} \qquad (3)$$

Subsituted intoEq. (1), then Eq. (3) can be written as:

$$\tilde{\omega}^{b} = \tilde{p}\dot{\theta} + (1-\cos\theta)(p\dot{p}^{T} - \dot{p}p^{T}) - \sin\theta\dot{\tilde{p}} \qquad (4)$$

From Eq. (4), the angular velocity vector does not superpose with rotation axis vector. But regarding the small time step in the 3MDEM, the rotation angle and movement of rotation axis is small enough. That is to say Eq. (4) can be simplified as:

$$\tilde{\omega}^{b} = \tilde{p}\dot{\theta} \qquad (5)$$

Written in vector form:

$$\boldsymbol{\omega} = \boldsymbol{p}\dot{\theta} \qquad (6)$$

So in 3MDEM, the rotation of blocks can be simulated as many small fixed-spindle rotations. For each time step, the direction of rotation axis vector of small fixed-spindle rotations is equal to that of the angular velocity vector. The rotation degree is $|\omega|\Delta t$, where, Δt is time step.

2.2 Deformation of a block

The deformation of a block is assumed as the summation of deformation modes. In frame *b*, the coordinate of mass points in the block is independent of the rigid movement of the block. So, new coordinate of mass point can be written as

$$X(t+\Delta t) = X(t) + \Phi\Delta\alpha \qquad (7)$$

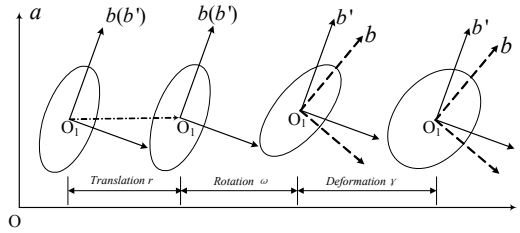

Fig 2 the decomposition of the movement and deformation

Where, X represents the coordinate vector of mass point of the block in frame b; The matrix Φ is a mode matrix, which is the $3\times s$ matrix, three lines is accord with coordinate X, Y, Z; s columns is accord with s deformation modes. $\Delta\alpha$ represents the increment matrix of deformation mode coefficient α in Δt.

But in frame a, the coordinate of mass point is not only relate with the deformation but also the rigid movement of the block. As shown in Fig. 2, the coordinates of mass point in frame a should be written as:

$$\begin{aligned} x^a(t+\Delta t) &= x^a_{O1}(t) + r^a(t) \\ &+ A^{ab'}(A^{b'b}X^b(t)) + A^{ab'}(A^{b'b}\Phi^b\Delta\alpha^b) \end{aligned} \tag{8}$$

Where, r represents the translation component of the block.

3. Kinetics equations

In 3MDEM, the system is an assembly of 3D discrete blocks. The interface between blocks can be joint, fissure, cracks, and artificial cut plane, where linear or nonlinear contact constitutive equations can be applied. In block, the deformation modes are used to decompose the deformation. Explicit step by step relaxation method is used to calculate the mode coefficients as well block translation displacement and rotation degree. Then, the whole history of movement and stresses of every block can be obtained.

From the continuum mechanics theory, the deformation can be represented by Cauchy strain tensor in the small deformation phase and by Green strain tensor in finite deformation phase. But in large rotation and small strain phase, only the movement of the blocks is usually focused. The stress state of blocks is no longer important. So in this paper, the Cauchy strain tensor is used for whole movement.

3.1 Dynamics equation of mass points

As show in Fig. 3, global frame is frame a: $oxyz$, body frame is frame b: $OXYZ$. The position vector of mass point $\boldsymbol{R_0}$ is u, then in any time, the position vector $\boldsymbol{r}$ of this point (point P) in frame a is:

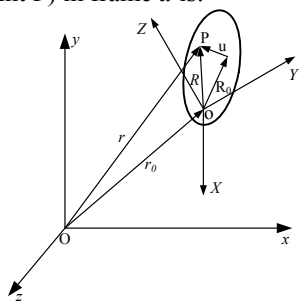

Fig. 3 Position vector decomposition of a particle in block

$$\boldsymbol{r} = \boldsymbol{r}_o + \boldsymbol{R} = \boldsymbol{r}_o + \boldsymbol{R}_0 + \boldsymbol{u} \tag{9}$$

Where, $\boldsymbol{r_0}$ is the position vector of $\boldsymbol{O_b}$, the origin of frame b. In frame a, $\boldsymbol{r_0}$ can be used to denote the translation of the block. $\boldsymbol{R_0}$ is the vector from $\boldsymbol{O_b}$ to mass point. Under the small strain condition, for a given point, the vector expressed in frame b does not change in time, but in frame a it change step by step. The change denotes the rigid rotation of the block. So $\boldsymbol{r_0}$ and $\boldsymbol{R_0}$ give the rigid movement of the block. As shown in Fig. 3, $\boldsymbol{u}$ expresses the deformation of the mass point $\boldsymbol{R_0}$. In a word, three items in the right of Eq. (9) represent the translation, rotation and deformation of the block.

From the elastic mechanics, for any point $\boldsymbol{r}$ in individual block, that have followed balanced equation in frame a:

$$\rho\ddot{\boldsymbol{r}} = \boldsymbol{f} + \nabla\cdot\boldsymbol{\sigma} \tag{10}$$

Where ρ is density of the point; $\boldsymbol{f}$ is the external force acted at the point. $\boldsymbol{\sigma}$ is the stress of the point.

Give the expression of Eq. (10) in frame b:

$$\begin{aligned} &\rho[{}^b\ddot{\boldsymbol{r}} + 2\boldsymbol{\omega}\times{}^b\dot{\boldsymbol{r}} + \dot{\boldsymbol{\omega}}\times{}^b\boldsymbol{r} + \boldsymbol{\omega}\times(\boldsymbol{\omega}\times{}^b\boldsymbol{r})] \\ &= \boldsymbol{f} + \nabla^b\cdot\boldsymbol{\sigma} \end{aligned} \tag{11}$$

Substituting Eq. 9 into Eq. 11, and then considering in frame b, $\boldsymbol{R_0}$ corresponds to a mass point in block, so its derivative in frame b is equal zero. Last, the following equations are always right:

$$\begin{aligned} &{}^b\ddot{\boldsymbol{r}}_o + 2\boldsymbol{\omega}\times{}^b\dot{\boldsymbol{r}}_o + \dot{\boldsymbol{\omega}}\times\boldsymbol{r}_o + \boldsymbol{\omega}\times(\boldsymbol{\omega}\times\boldsymbol{r}_o) = {}^a\ddot{\boldsymbol{r}}_o \\ &{}^b\dot{\boldsymbol{r}}_o + \boldsymbol{\omega}\times\boldsymbol{r}_o = {}^a\dot{\boldsymbol{r}}_o \end{aligned} \tag{12}$$

That has:

$$\rho\,{}^{a}\ddot{\boldsymbol{r}}_o+\rho[\dot{\boldsymbol{\omega}}\times\boldsymbol{R}_0+\boldsymbol{\omega}\times(\boldsymbol{\omega}\times\boldsymbol{R}_0)]$$
$$+\rho[{}^{b}\ddot{\boldsymbol{u}}+2\boldsymbol{\omega}\times{}^{b}\dot{\boldsymbol{u}}+\dot{\omega}\times\boldsymbol{u}+\boldsymbol{\omega}\times(\boldsymbol{\omega}\times\boldsymbol{u})] \quad (13)$$
$$=\boldsymbol{f}+\nabla^{b}\cdot\boldsymbol{\sigma}$$

This is the dynamics equation of mass points, where three items in the left side represent the translation, rotation and deformation, respectively.

3.2 Translation equation of a block

The translation of a block can be represented by the displacement of its gravity center. Directly integrating Eq. (13) in frame *a*, the integral of rotation item will be zero. Under small strain condition, the integral of deformation item is approximate to zero. Eq. (13) could be written as:

$$\int\rho\,{}^{a}\ddot{\boldsymbol{r}}_o dV=\int\boldsymbol{f}dV+\int\nabla^{b}\cdot\boldsymbol{\sigma}dV \quad (14)$$

On the force boundary Γ:

$$\boldsymbol{F}=\boldsymbol{F}_0 \quad (15)$$

Applying Green formula, expressed in index form:

$$m\,{}^{a}\ddot{r}_{oi}=\int f_i dV+\int F_{oi}d\Gamma \quad (16)$$

Where, m is the mass of the block, $\boldsymbol{f}$ is body force which include gravity, $\boldsymbol{F_0}$ is boundary force including contact force.

3.3 Rotation equation of a block

The rotation of frame *b* relative to frame *a* could be used to denote the rotation of the block. Integrating Eq. (16) multiplied by $\boldsymbol{R}_0^b$ in frame *b*, the integral of translation part should be equal 0, the integral of deformation part can be neglected under small strain condition. Then,

$$\int\boldsymbol{R}_0^b\times\boldsymbol{\rho}[\dot{\boldsymbol{\omega}}^b\times\boldsymbol{R}_0^b+\boldsymbol{\omega}^b\times(\boldsymbol{\omega}^b\times\boldsymbol{R}_0^b)]dV$$
$$=\int\boldsymbol{R}_0^b\times\boldsymbol{f}^b dV+\int\boldsymbol{R}_0^b\times(\nabla^b\cdot\boldsymbol{\sigma}^b)dV \quad (17)$$

Substituting boundary condition into Eq. (17) and employing Green formula, one can obtain:

$$\begin{aligned}&I_1\dot{\omega}_1-(I_2-I_3)\omega_2\omega_3=M_1\\&I_2\dot{\omega}_2-(I_3-I_1)\omega_3\omega_1=M_2\\&I_3\dot{\omega}_3-(I_1-I_2)\omega_1\omega_2=M_3\end{aligned} \quad (18)$$

Where I_1、I_2、I_3 are the moment of inertia of block in frame *b*. M_1、 M_2、 M_3 are moment around three coordinate axis of frame *b*.

3.4 Deformation equation of a block

Rewrite Eq. (13) in frame *b*, and then substitute into deformation modes which are shown in Eq. (7). Multiplying Φ^T in the front and applying small strain condition, the integral should be

$$\int_V\rho\Phi^T\,{}^{a}\ddot{r}_0^b dV+\int_V\rho\Phi^T[\dot{\tilde{\omega}}^b R_0^b]dV$$
$$+\int_V\rho\Phi^T\Phi\ddot{\alpha}dV= \quad (19)$$
$$\int_V\Phi^T f^b dV+\int_V\Phi^T(\nabla^b\cdot\sigma^b)dV$$

Substituting boundary condition and applying Green formula, Eq. (19) can be expressed in index form as:

$$\int_V\rho\Phi_{ik}\Phi_{ij}\ddot{a}_j dV=\int_V\Phi_{jk}f_j^b dV+\int_S\Phi_{jk}F_{oj}^b d\Gamma_2$$
$$-\int_V\Phi_{ki,j}^T\sigma_{ij}^B dV-\int_V\rho\Phi_{jk}\,{}^{a}\ddot{r}_{0j}^b dV$$
$$-\int_V\rho\Phi_{jk}[\dot{\tilde{\omega}}_{ji}^b R_{0i}^b]dV \quad (20)$$

Lets:

$$\begin{aligned}M&=\int_V\rho\Phi_{ik}\Phi_{ij}dV\\S_A&=\int_V\Phi_{jk}f_j^b dV+\int_S\Phi_{jk}F_{oj}^b d\Gamma_2\\S_I&=\int_V\Phi_{ki,j}^T\sigma_{ij}^B dV\\S_T&=\int_V\rho\Phi_{jk}\,{}^{a}\ddot{r}_{0j}^b dV+\int_V\rho\Phi_{jk}[\dot{\tilde{\omega}}_{ji}^b R_{0i}^b]dV\end{aligned} \quad (21)$$

Where M, S_A, S_I and S_T are general mass matrix, general external force matrix, general internal force matrix and couple matrix of rigid movement. Substitute Eq. (21) into Eq. (20), that has:

$$M\ddot{a}=S_A-S_I-S_T \quad (22)$$

If the deformation modes satisfy the following conditions:

$$\begin{aligned}&\int\phi^N dV=0\\&\int\phi^N\cdot\phi^L dV=0,\quad \text{当}L\neq N\end{aligned} \quad (23)$$

Then all deformation mode that is in Eq.(23) will be decoupled from each other, and couple vector of rigid movement will be zero. Eq. (23) can be simplified as:

$$m^L \ddot{\alpha}^L = S_A^L - S_I^L \tag{24}$$

m^L, S_A^L and S_I^L are L^{th} row diagonal element of matrix M, S_A and S_I, respectively.

3.5 Contact forces between blocks

Normal and tangential springs are used to express the contact force between blocks. For each contact, the relationship between contact force increment and contact displacement increment is assumed as (Cui Yuzhu, 2001):

$$\begin{aligned} \Delta \boldsymbol{F}_n &= -K_n \Delta \boldsymbol{u}_n A_c \\ \Delta \boldsymbol{F}_s &= -K_s \Delta \boldsymbol{u}_s A_c \end{aligned} \tag{25}$$

Where, K_n and K_s are contact stiffness in normal and tangential direction. $\boldsymbol{\Delta u_n}$ and $\boldsymbol{\Delta u_s}$ are displacement increment in normal and tangential direction. $\boldsymbol{\Delta F_n}$ and $\boldsymbol{\Delta F_s}$ are spring force increment in normal and tangential direction. A_c is contact area.

To simulate nonlinear mechanical property of interface, Mohr-Column criterion is employed in interfaces. That is:

$$\begin{cases} \boldsymbol{F}_n = 0, \ \boldsymbol{F}_s = 0 & \text{当} F_n \geq TA_c \\ \boldsymbol{F}_s = \boldsymbol{F}_s (f |\boldsymbol{F}_n| + cA_c) / |\boldsymbol{F}_s| & \text{当} F_s > f|F_n| + \mathrm{c}A_c \end{cases} \tag{26}$$

Where T is tensile strength, c is cohesion, f is friction coefficient. To simulate the failure of an interface, T and c could be reduced to zero after the first failure of the interface.

3.5 Elastic force in a block

Applying linear elastic constitutive equations, the block stress increment is:

$$\Delta \sigma_{ij} = \lambda(\Delta \varepsilon_v)\delta_{ij} + 2\mu \Delta \varepsilon_{ij} \tag{27}$$

Where, λ and μ are Lame's constant. δ_{ij} is Kroneker- δ. The strain increment:

$$\Delta \varepsilon_v = \Delta \varepsilon_{xx} + \Delta \varepsilon_{yy} + \Delta \varepsilon_{zz} \tag{28}$$

Considering the relationship between strain and displacement, the stress increment can be written in:

$$\Delta \sigma_{ij} = \left[\lambda \left(\frac{\partial \phi_k}{\partial x_k}\right)\delta_{ij} + \mu \left(\frac{\partial \phi_i}{\partial x_j} + \frac{\partial \phi_j}{\partial x_i}\right) \right] \Delta \alpha \tag{29}$$

At the beginning and end of the step, the position of frame b relative to frame a has changed. So the stress at the beginning of step must be modified, and the stress of the step end can be obtained by adding the stress increment:

$$\boldsymbol{\sigma}(t + \Delta t) = \boldsymbol{\sigma}_r(t) + \Delta \boldsymbol{\sigma} \tag{30}$$

Where $\sigma_r(t)$ is the modified stress in step beginning.

Then the general elastic force of a block can be obtained by integral according Eq.(21).

4 Deformation mode selection

The 21 deformation modes are selected in this paper, which have been listed in Table 1 and Table 2. which could be classed into 5 categories, namely, tension modes, shear modes, first bending modes, second bending modes and second order tension modes.

Table 1 first order mode

tension mode			shear mode		
ϕ^1	ϕ^2	ϕ^3	ϕ^4	ϕ^5	ϕ^6
X	0	0	Y	Z	0
0	Y	0	X	0	Z
0	0	Z	0	X	Y

Table 2 second order mode

first bend mode						second order tension mode			second bend mode					
ϕ^8	ϕ^9	ϕ^{10}	ϕ^{12}	ϕ^{13}	ϕ^{14}	ϕ^7	ϕ^{11}	ϕ^{15}	ϕ^{16}	ϕ^{17}	ϕ^{18}	ϕ^{19}	ϕ^{20}	ϕ^{21}
Y^2	Z^2	0	0	0	0	X^2	0	0	XY	XZ	0	0	0	0
0	0	X^2	Z^2	0	0	0	Y^2	0	0	0	YX	YZ	0	0
0	0	0	0	X^2	Y^2	0	0	Z^2	0	0	0	0	ZX	ZY

Obviously, if only the six first order modes listed in table 1 are selected, these modes will satisfy the orthogonal conditions given in Eq. (23). Then mode of deformation equation can be decoupled from each other as shown in Eq.(24).

5 Examples

5.1 Cantilever beam

To verify the accuracy of 3MDEM under small deformation, a cantilever beam as shown in fig. 4, which left end is fixed, is analyzed. The cantilever has a span of 30m, a high of 3m and a thickness of 1m, a

modulus of elasticity of 24GPa, a Poisson's ratio of 0.2 and a density of 2400kg/m^3. the gravity acceleration is 9.8m/s^2, whose direction is in opposition of *Y* axis.

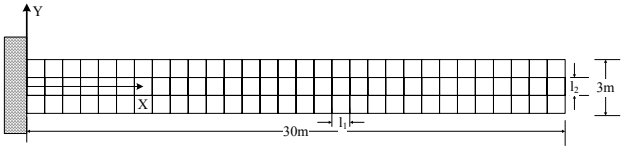

Fig. 4 example of a cantilever

To simulate continuum material, the tensile strength is set as large enough. So the interface between blocks can not be abrupt or slip.

When block size is 3.0×3.0 (unit m, same in the following), the normal stresses by 3MDEM is good enough comparing with the result by FEM with linear element size of 0.2×0.2, as shown in Fig. 5a. When block size is 1.0×1.0, the shear stresses by 3MDEM obtain good results, as shown in Fig. 5b. The 3DEC software can also obtain similar results if the blocks is much smaller. It is because 21 modes employed in 3MDEM include all second order bend mode, while FEM and 3DEC only has a constant or linear deformation modes in their elements or blocks.

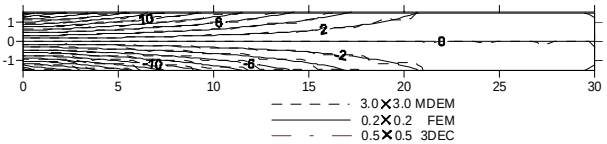

(a) the beam stress comparison in size 3×3

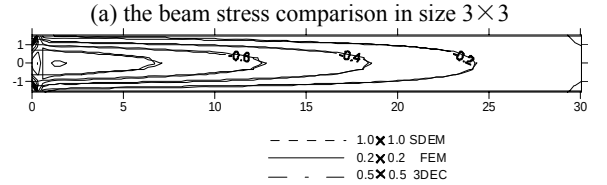

(b) the shear stress comparison in size 1 × 1

Fig. 5 comparison of the displacement and the stress

5.2 Impacting simulation of pillar

As show in fig. 6, a pillar with high of 30m, width of 3m, thickness of 1m, is cut into 10 blocks, whose size is 3×3×1(unit:m). The pillar has a modulus of elasticity of 24GPa, a Poisson's ratio of 0.2 and a density of 2400kg/m^3. the gravity acceleration is 9.8m/s^2. All interfaces between blocks have same property: the tensile strength and cohesion is zero, the friction coefficient *f* is 0.5, the normal stiffness is 50GPa, and the tangential stiffness is 20.8GPa. One block numbered 11 impact this pillar at the speed of 50m/s. In this problem, contact relation will change continually, and contact detection method will be well tested.

Two results with block size 3×3 and 0.5×0.5 are shown in Fig. 6. The result with block size 0.5×0.5 by 3DEC is also shown in fig 6c. The collision process is reasonable and the results by 3MDEM and 3DEC are similar. Because there are air damping in 3DEC but air damping free in 3MDEM, the flight distance of the blocks by two methods are different.

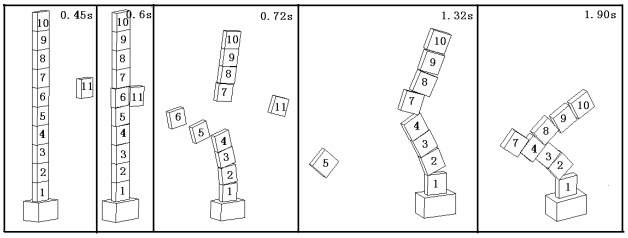

(a)block size 3×3，3MDEM result

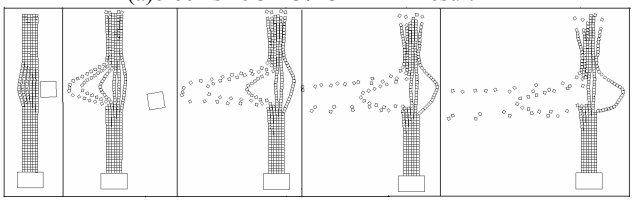

(b)block size 0.5×0.5，3MDEM result

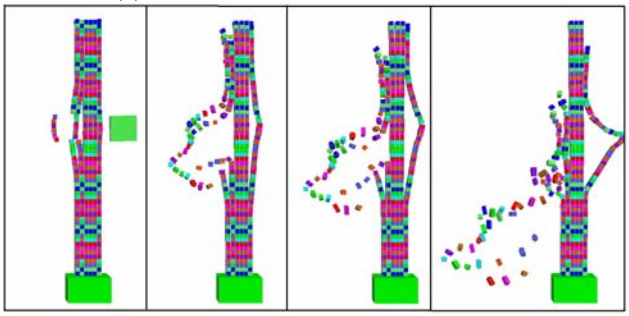

(c)block size 0.5×0.5，3DEC result

Fig. 6 Simulation of a discontinuous column against push

5.3 Wave transmit through interface

A pillar with high of 40m cutted into 40 blocks, which has a length of 1m, a width of 1m and a thickness of 1m. The bottom is fixed, and all other faces are free. The pillar has a modulus of elasticity of 24GPa, a Poisson's ratio of 0.2 and a density of 2400kg/m^3. In the middle of pillar, there is a discontinuous interface whose strength is 10MPa or 0.2MPa. The strength of all other interface is set large enough.

At time zero, a sinusoidal velocity wave is input at the bottom of pillar, the wave has a frequency of 1Hz, and a velocity of 0.1m/s，which is equivalent to input stress wave with amplitude of 0.8MPa. At top of the pillar, 1-D viscous boundary is used to avoid wave reflection, which was first brought out in 1969 by Lysmer and Kuhlemeyer.

The comparison of input wave and response at the top of pillar is shown in Fig.7. If the tensile strength of middle interface is larger than 0.8MPa, as shown in Fig.7a, velocity wave can propagate perfectly to the top of pillar. The time lag should be 0.013s in theory and the lag of 0.012s is given by 3MDEM. If the tensile strength of middle interface is only 0.2MPa，the compress phase of the wave can propagate to the top of pillar, but tensile phase will reflect and transmit at the middle interface, as shown in Fig. 7b. The amplitude of the transmission wave should be 0.025m/s in theory.

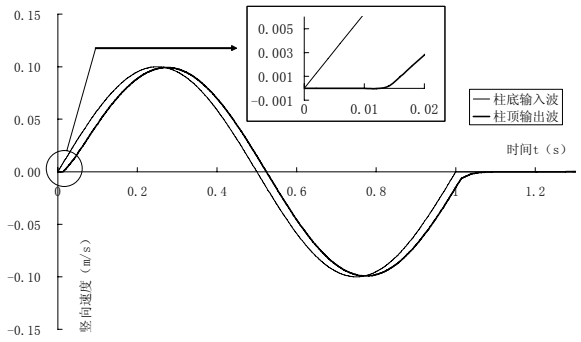

(a) tensile strength of interface is big enough

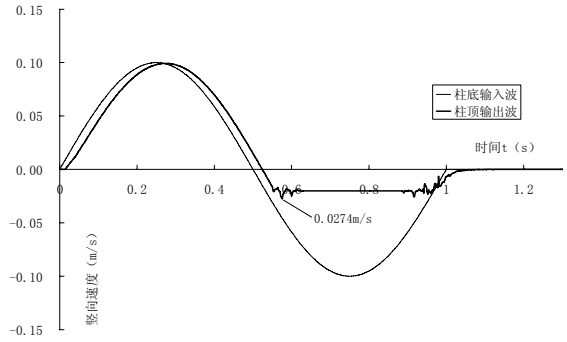

(b) tensile strength of interface is 0.2MPa.

Fig. 7 Transmission and reflection of incident harmonic wave at a discontinuity interface

6 Conclusion

In this paper, 3-D method discrete element method, which is an efficient numerical method for simulating mechanical behaviors of nonlinear, large deformation and dynamic problems, is presented. Due to the tetrahedron meshing technique employed in 3DEC, the number of degree of freedom calculated in 3MDEM will be much smaller than that in 3DEC.

The verification examples demonstrate that 3MDEM is not only able to calculate mechanical behavior of continuum, but also simulate large displacement, large rotation and dynamic problems for block systems. It has great potential in structure and geotechnical engineering fields.

7 Acknowledgment

The constructive suggestion from Professors Zhang Chuhan and Wang Guanglun in Tsinghua University are grateful. The work has been supported by National Natural Science Foundation of China (90510018 and 50539020).

Reference

Bardet, J.-P, and R.F. Scott, Seismic stability of fractured rock mass with the distinct element method, *Research and Engineering Applications in Rock Masses*, Vol.2. 139-150

Butkovich, T.R., O.R. Walton, F.E. Heuze, insights in Cratering Phenomenology provided by discrete element modeling, *Proceeding of the 29th U.S. Symposium*, 1988: 359-368

Cui Yuzhu, *Numerical Modeling of Continuum and Discontinuous media and its application to safety analysis of arch dam-foundation systems*[D], Beijing: Tsinghua University, 2001. (in chinese)

Cundall P. A. Computer model for simulating progressive large scale movements in blocky systems[J]. *Proc. Symp. Int. Soci. Rock Mech*., Nancy, France, Vol. 1, paper No.Ⅱ-8，1971

Cundall P. A. *UDEC-A generalized discrete element program of modeling jointed rock*[R]. European Research Office, U.S. Army, 1980.

Cundall, P. A. Formulation of three-dimensional discrete element model, Part I, A scheme to detect and represent contact in system composed of many polyhedral blocks[J]. *Int. J Rock Mech. Min Sci. & Geomech Abstr*, 1988, 25(3): 107-116.

Hart R, Cundall P. A, Lemos J. Formulation of three-dimensional discrete element model, PartⅡ, Mechanical calculation for motion and interaction of a system composed of many polyhedral blocks[J]. *Int J Rock Mech. Min Sci & Geomech Abstr,* 1988, 25(3): 117-125.

Hong Jiazhen, *Computational Dynamics of Multibody Systems*, Higher Education Press, 1998(in chinese)

Itasca, *3DEC - 3 Dimensional discrete element code, Version 3.0, User's manual*[R], Itasca Consulting Group, Inc. USA.

J. R. Williams, G. G.W. Mustoe. Modal methods for the analysis of discrete systems, *Computers and Geotechnics* 1987, 4, 1-19

J. R. Williams, G.Hocking, G. G.W.Mustoe, The theoretical basis of the discrete element method, *Proceedings of the NUMETA conference*, Swansea, 1985:7-11

Lysmer J., R. Kuhlemeyer, Finite dynamic model for infinite media, *J. Eng. Mech*., Div. ASCE, 95:EM4, 1969

Shi Genhua, Discontinuous deformation analysis: A new numerical model for the statics and dynamics of deformable block structures, *Engineering Computations*, 1992.9.

Wang Yongjia, Xin Jibo, *The discrete element method and its application in geotechnical engineering*[M], Northeastern Polytechnical University Press, 1991,9.(in chinese)

Zhang Chong, Hou Yanli, Jin Feng, Zhang Chuhan, The analysis of arch dam abutment stability by 3-D deformable discrete element method[J], *Chinese Journal of rock mechanics and engineering*, 2006, 28(6) (in chinese)

Zhang Chong, Jin Feng, Hou Yanli, 3-D simple deformable discrete element method, 2007, 29(4): 6-10

Zhang Chuhan, Pekau, O. A. Jin Feng, Wang Guanglun, Application of discrete element method in dynamic analysis of high rock slopes and blocky structures[J]. *Soil Dynamics and Earthquake Engineering*, 1997, 16: 385-394.

Numerical studies on dynamic friction mechanism of blocky rock system using manifold method

G.W. MA[1*], X.M. AN[1], M.Y. WANG[2]

[1]School of Civil and Environmental Engineering, Nanyang Technological University, SINGAPORE 639798

[2]Engineering Institute, PLA University of Science and Technology, Nanjing, CHINA 210007

(*Email of corresponding author: cgwma@ntu.edu.sg)

When a dynamic pulse loading is applied to the top of a blocky rock system, the frictional force between the blocks in the lateral direction can be reduced significantly or even disappear, which is known as an ultra low friction phenomenon. This phenomenon has drawn a lot of attentions of researchers. However, it has not been well understood because of its complexity. In this paper, the dynamic friction mechanism of blocky rock system is numerically investigated using manifold method. The parametric studies with respect to loading duration, loading intensity and loading shape of the pulse have been carried out. Numerical results indicate that the loading duration has a great influence on the frictional force between two blocks. When the loading frequency is around the natural frequency of the blocky rock system, the frictional force will be severely reduced. Loading intensity favors the reduction of the frictional forces. Larger loading intensity will lead to lower frictional force. Loading shape also has some influences on the frictional force because of different energy involved in each loading. The ultra low friction phenomenon has been discussed based on the numerical simulation results. It is due to the vibration of the blocky rock system induced by the applied pulse loading.

Keywords: Dynamic friction mechanism; Blocky rock system; Frictional force; Ultra low friction phenomenon; Manifold method

1. Introduction

When a pulse loading is applied to the top of a blocky rock system, the frictional force between the blocks in the lateral direction can be reduced significantly or even disappear, which is known as a ultra low friction phenomenon. This phenomenon has drawn a lot of attentions of researchers. However, it has not been fully understood because of its complexity (Wang, 2006).

The manifold method (MM) is initially developed by Shi in 1991 (Shi, 1991; 1997). The method is derived from the finite cover approximation theory and gains her name after the mathematical notion of manifold. The MM was developed based on discontinuous deformation analysis (DDA). It preserves all the discrete element modeling characteristics such as kinematics constraints, contact detection and modeling from DDA. However, it employs a number of covers in each block to raise its degrees of freedom (DOFs) to improve the accuracy of stress and displacement field. The MM demonstrates a good consistency with both the conventional finite element method (FEM) and the DDA and applicable to both continuous and discontinuous problems.

In this paper, the dynamic friction mechanism of a blocky rock system is numerically investigated using MM. The parametric studies with respect to the duration, intensity and shape of the pulse loading will be carried out. Some preliminary interpretation to the ultra low friction phenomenon will be given.

2. Numerical studies of friction dynamic mechanism of a blocky rock system

2.1 Numerical model

Fig. 1 shows the numerical model for the dynamic friction analysis. The dimension of the block is 0.4 m×0.2 m. The bottom of lower block is fixed. A dynamic load is applied to the top of the system. The material for the rock block is assumed elastic with the properties of: Density = 2650 kg/m3, Young's Modulus = 80 GPa, Poisson's Ratio = 0.3. The joint is obeying Coulomb's slip law with three parameters of: Friction angle = 30°, Cohesion = 0 MPa, Tensile strength = 0 MPa.

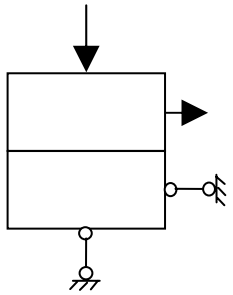

Fig. 1 Numerical model for two block rock system

With only gravitational loading, the theoretical solution of the static frictional force between the two blocks is

$$F = \tan\phi \cdot mg = 1.224N \quad (1)$$

For the MM modeling, firstly the gravitational loading is applied. The frictional force between the two blocks is depicted in Fig. 2. It can be found that the frictional force converges to the theoretical solution after the initial period of vibration. The pulse loading is applied 2 ms later than the gravitational loading when the gravity induced frictional force becomes stable. The parametric studies of loading duration, loading intensity, loading shape are carried out and discussed in the following three sections respectively.

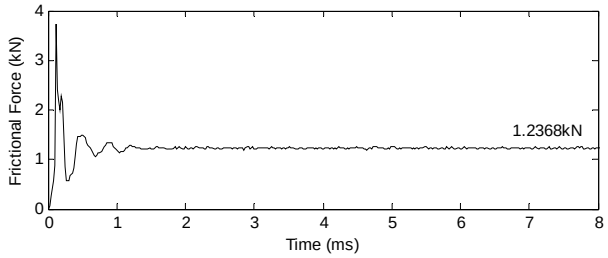

Fig. 2 Gravity induced frictional force between two blocks

2.2 Loading duration effect

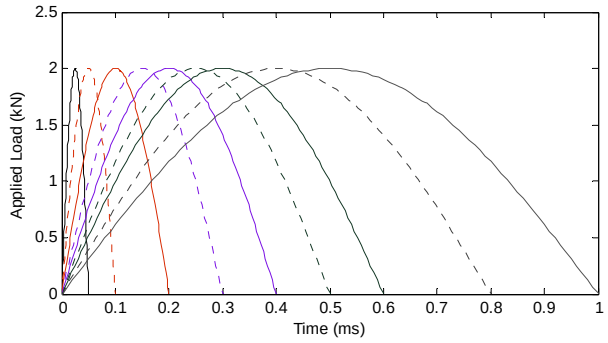

Fig. 3 Loadings with fixed intensity of 2.0kN and various durations of 0.05ms, 0.1ms, 0.2ms, 0.3ms, 0.4ms, 0.5ms, 0.6ms, 0.8ms, and 1.0ms

In order to investigate the influence of the loading duration effect on the frictional force, several loadings with fixed loading intensity 2.0 kN and various loading durations of 0.05 ms, 0.1 ms, 0.2 ms, 0.3 ms, 0.4 ms, 0.5 ms, 0.6 ms, 0.8 ms, and 1.0 ms (shown in Fig. 3) are applied to the top of the system.

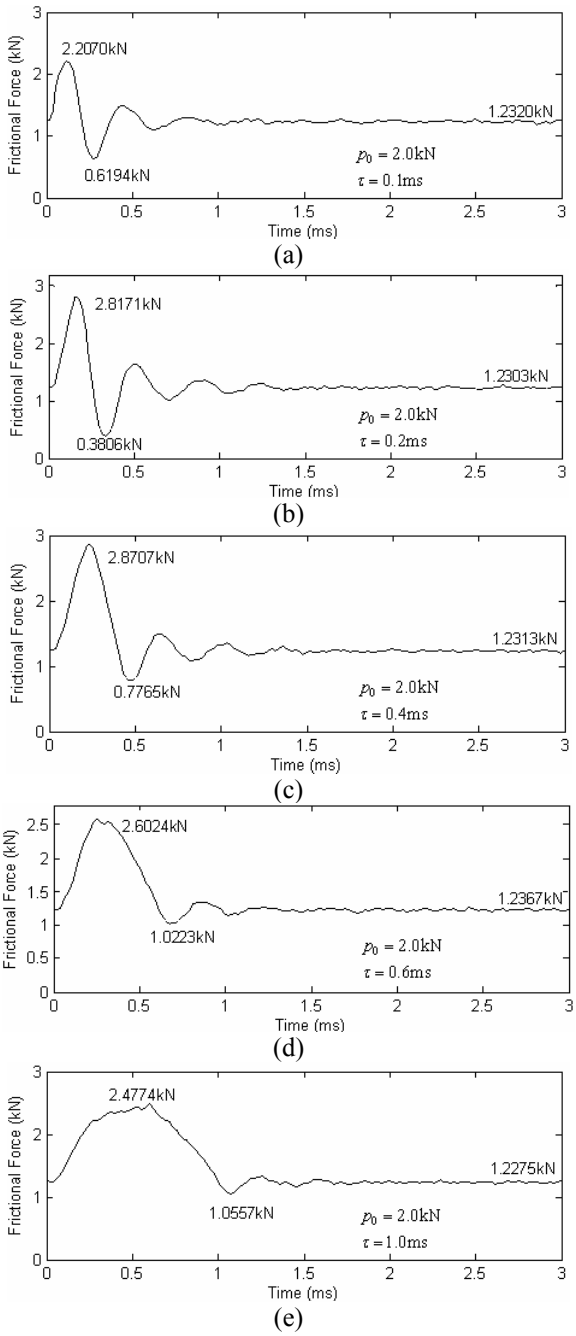

Fig. 4 Frictional force time histories of the model under the loading with various duration of: (a) 0.1ms; (b) 0.2ms; (c) 0.4ms; (d) 0.6ms; (e) 1.0ms

The frictional forces of several cases are shown in Fig. 4. It can be found that the frictional force vibrates around the static frictional force. The minimum frictional force, which is also the critical force to move the top block in the horizontal direction, will be lower than the static frictional force. In other words, numerical results indicates that it will become easier to move the first block when a pulse loading applied to the top of the blocky rock system.

The relationship between the minimum frictional force and the loading duration is plotted in Fig. 5. The

minimum frictional force appears when the loading duration is 0.2 ms.

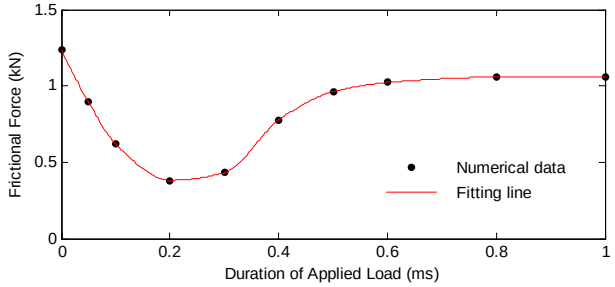

Fig. 5 Relationship between minimum frictional force and loading duration

The natural frequency of the two block system can be derived based on a simplified two degrees of freedom (DOFs) mass-spring model shown in Fig. 6.

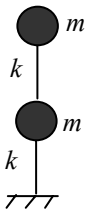

Fig. 6 Simplified model for the two block system

The governing equation is

$$\begin{bmatrix} m & 0 \\ 0 & m \end{bmatrix} \begin{Bmatrix} \ddot{v}_1 \\ \ddot{v}_2 \end{Bmatrix} + \begin{bmatrix} 2k & -k \\ -k & k \end{bmatrix} \begin{Bmatrix} v_1 \\ v_2 \end{Bmatrix} = 0 \quad (2)$$

where

$$m = \rho \cdot V = 2650 \times 0.4 \times 0.2 \times 1 = 212kg$$

$$k = \frac{EA}{l} = \frac{(8 \times 10^{10}) \times 0.4 \times 1}{0.2} = 1.6 \times 10^{11} N/m$$

Then,

$$\begin{vmatrix} 2k - \omega^2 m & -k \\ -k & k - \omega^2 m \end{vmatrix} = 0 \quad (3)$$

Lastly, we get the first natural frequency as

$$\omega_1 = 16978.7 rad/s \quad (4)$$

The frequency of the loading with duration of 0.2 ms is 15708.0 rad/s, which is very close to the natural frequency of the two block system. So, we can conclude that the pulse loading will be most effective to reduce the frictional force only when its loading frequency is around the natural frequency of the blocky rock system.

2.3 Loading intensity effect

In order to investigate the loading intensity effect on the frictional force, a series of loadings with fixed duration of 0.2 ms and various intensities of 0.5 kN, 1.0 kN, 1.5 kN, 2.0 kN, 2.2 kN, 2.4 kN, and 2.45 kN (shown in Fig. 7) are applied to the two block system. The frictional forces for several cases are plotted in Fig. 8. The relationship between minimum frictional force and loading intensity is depicted in Fig. 9. Numerical results indicate that the minimum frictional force decreases with the loading intensity linearly. In other words, the loading intensity favors the reduction of frictional force. Larger loading intensity will lead to lower frictional force.

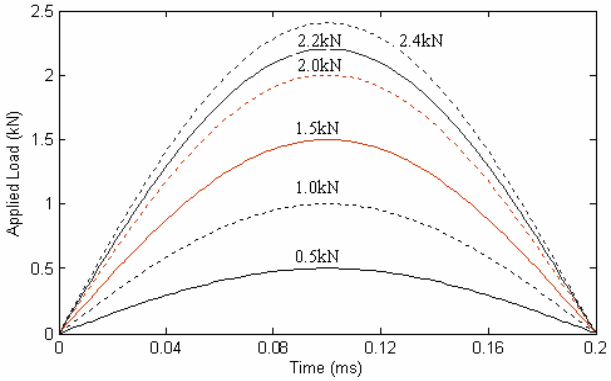

Fig. 7 Loadings with fixed duration of 0.2 ms and various peaks of 0.5 kN, 1.0 kN, 1.5 kN, 2.0 kN, 2.2 kN, 2.4 kN, and 2.45 kN

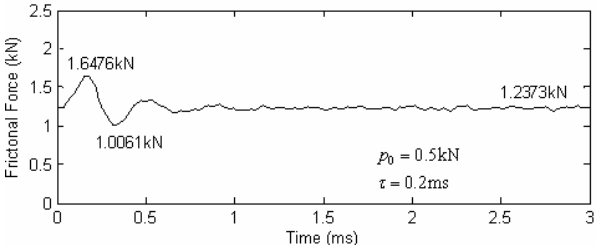

(a)

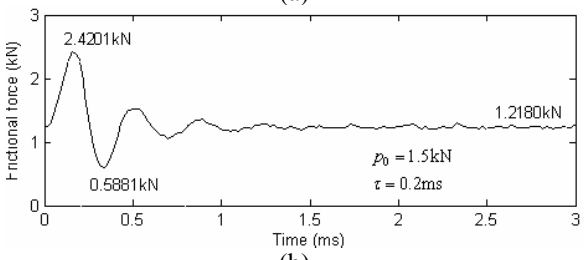

(b)

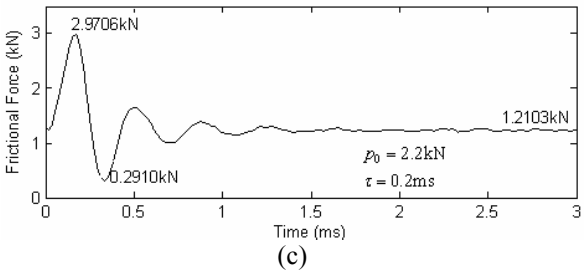

(c)

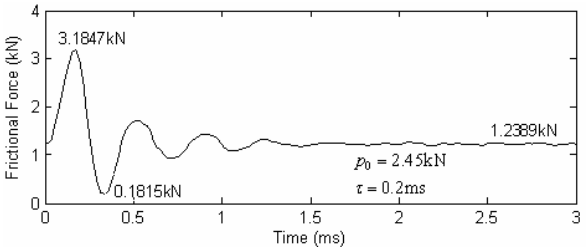

(d)

Fig. 8 Frictional forces under dynamic loadings with fixed duration of 0.2 ms and various peaks of: (a) 0.5 kN; (b) 1.5 kN; (c) 2.2 kN; (d) 2.45 kN

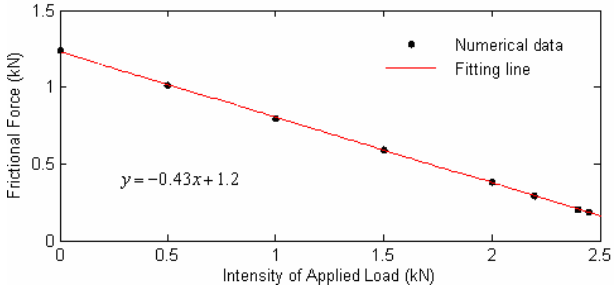

Fig. 9 Relationship between minimum frictional force and loading intensity

2.3 Loading shape effect

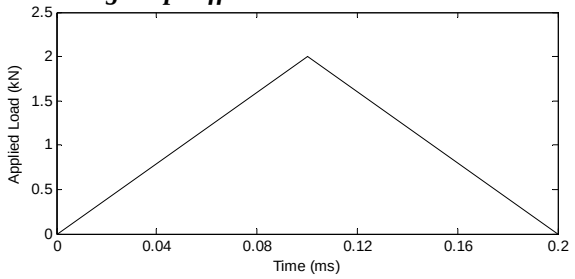

(a)

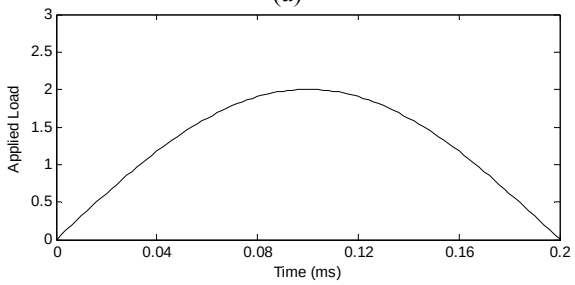

(b)

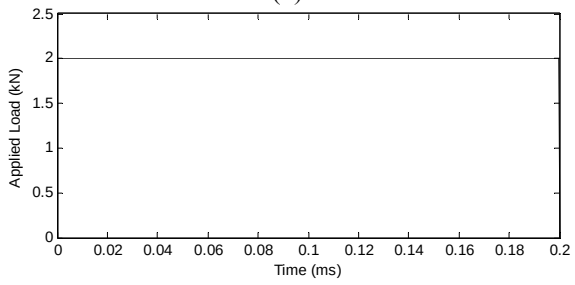

(c)

Fig. 10 Loadings with three different loading shapes: (a) triangular loading; (b) half0sinusoidal loading; (c) rectangular loading

In order to investigate the loading shape effect, the loadings with three loading shapes (shown in Fig. 10), namely triangular loading, half-sinusoidal loading, and rectangular loading are applied to the top of the two block system.

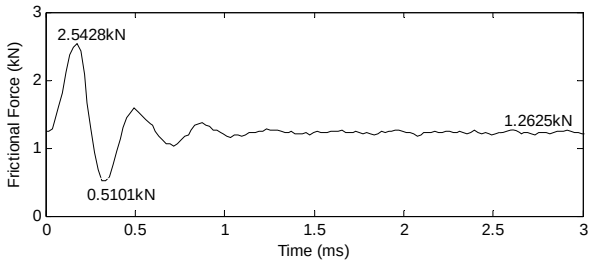

(a)

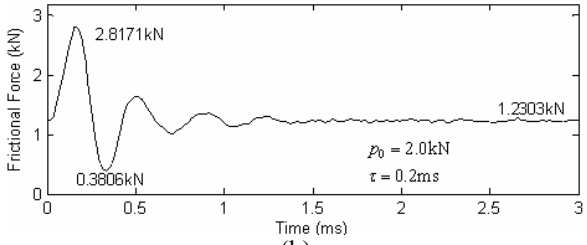

(b)

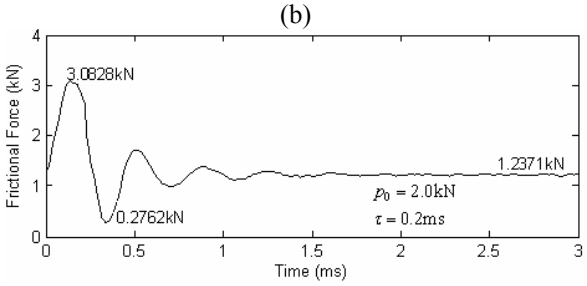

(c)

Fig. 11 Frictional forces between the two blocks under three loadings with various loading shapes: (a) triangular loading; (b) half-sinusoidal loading; (c) rectangular loading

The corresponding frictional forces are plotted in Fig. 11. The minimum frictional force from the triangular loading is the highest, while that from the rectangular loading is the lowest. The minimum frictional force from half-sine loading is between them. This difference may be due to the different energy involved in each loading.

3. Discussions and conclusions

The dynamic friction mechanism of a blocky rock system is numerical investigated using a two block system model. With only gravitational loading, the frictional force in the lateral direction between two blocks is a constant. The critical force, the lowest force to move the top block, will also be a constant equal to the frictional force. However, when a pulse loading is applied to the top of the system, vibration of the block

system will be observed, which leads to the vibration of the frictional force around the static frictional force. The minimum frictional force, which is also the critical force to move the top block, will be lower than the static frictional force. It means that it becomes easier to move the top block in the lateral direction. This is the ultra low friction phenomenon. This phenomenon is due to the pulse loading induced blocky rock system vibration. Parametric studies of loading duration, loading intensity, and loading shape effect are carried out. Numerical results demonstrate that the pulse loading is most effective to reduce the frictional force only when its loading frequency is around the natural frequency of the blocky system. Loading intensity favors the reduction of frictional force. Larger loading intensity will lead to lower minimum frictional force. Loading shape also has some influences on the frictional force, which may be due to different energy involved in each loading.

References

Shi, G.H. Manifold method of material analysis. *Trans. 9th Army Conf. on Applied Mathematics and Computing*, Minneapolis, Minnesota, 1991, pp.57-76.

Shi G.H. Numerical manifold method, Proc.*2nd Int. Conf. on Analysis of Discontinuous Deformation*, Kyoto, 1997, pp.1-35.

Wang H.L. Studies on dynamic mechanism of block rock system. Master Thesis. PLA University of Science and Technology, Nanjing, China, 2006.

Application of numerical manifold method in fluid-solid interaction harmonic analysis

SU HAIDONG[1] and HUANG YUYING[2]
[1] DDA Center, Yangtze River Scientific Research Institute, Wuhan, China
[2]School of Civil Eng. & Mechanic, HUST, Wuhan, China

Numerical Manifold Method (NMM) is first applied to fluid-solid interaction analysis in this paper. Based on rectangular mathematical meshes and simplex integration, high-order NMM equations are presented for two-dimensional fluid-solid interaction harmonic analysis, concerning inviscid, irrotational, incompressible potential flow and undamped structures. Known value of fluid pressure is introduced via Lagrange multiplier method. It is also proposed that cover of analytical series is applied to simulate infinite fluid field, which can greatly decrease unknowns to be solved. Given examples of computing frequencies and harmonic responses prove the validity and high efficiency of the approach, suggesting that NMM is very suitable for combination of numerical solutions and analytical solutions.

Keywords: High-order numerical manifold method; Fluid-solid interaction; Combination of numerical solutions and analytical solutions

1. Introduction

Based on mathematical manifold of modern mathematics, numerical manifold method (NMM) was proposed by Shi (1992). NMM is capable of solving continuum and discontinuum problems and has a bright future in computation mechanics.

In NMM, the entire material volume is divided into many finite covers overlapped each other which are also named physical covers. They are formed by two independent cover systems: one is mathematical mesh defining only the fine or rough approximations; the other is physical mesh defining the boundaries of the material volume and the interfaces of different material zones. On each cover, an independent local cover function is defined, which can be constants, polynomials or other series (including series of analytical solution). These functions are connected together to form a global function on the entire material volume by means of weighted average via weight functions. The common part of these covers is named manifold element whose shape can be assumed arbitrarily. Element matrices are usually calculated exactly by means of simplex integration.

By now, researches on NMM are almost about solid structures. Readers can refer to Wang et al (2003) and Li et al (2004). This paper applies NMM to fluid-solid interaction (coupling) analysis. It is preliminary considered that NMM has following advantages in the new region:

(1) By virtue of the independence of mathematical meshes from physical meshes, it is not requested that mathematical meshes should strictly satisfy the geometric boundaries of structures and fluid field, so element subdivision is convenient to be carried out.

(2) Benefited from the property of p-version, computational precision can be improved by adding number of series terms of the local cover functions without subdividing mathematical meshes.

(3) In some special area of fluid field, such as infinite field, we can use analytical series as cover functions to improve computational efficiency because number of unknowns to be solved is greatly reduced.

We shall make some remarks on (3). As we all know, for infinite field problems or singular point problems, classical approach of using analytical series converges much quickly than numerical approach, but it is limited to the domains of regular shape and simple boundary conditions. Then people have the idea of combination of numerical solutions and analytical solutions: numerical approach is used in domains of complicated shape, while in some regions,

such as infinite field, analytical solutions can be adopted. However, a new difficulty is encountered: because the types of the unknowns are different (the unknowns of numerical solutions are field freedoms, but the unknowns of analytical solutions are series coefficients), it is not easy to deal with the compatibility problem on their interface. For example, Huang (1988) computed frequencies of a dam and water interaction system involving a regular infinite fluid field, using finite element method (FEM) to simulate near field and a series solution to represent the far infinite field. Although the method was more effective than pure FEM, the procedure was very complicated: a local variational principle was introduced, and a functional was derived to satisfy both governing equations and all boundary conditions (including the compatibility of the FEM freedoms and the series coefficients on their interface). Now we can solve this problem conveniently by NMM in the way that covers of numerical solutions and cover of analytical solutions are linked together simply by means of weight functions.

In this paper, high-order NMM equations are presented for two-dimensional fluid-solid interaction harmonic analysis. Preliminary research is also done on using cover of analytical solution to simulate infinite fluid field.

2. Governing equations and boundary conditions

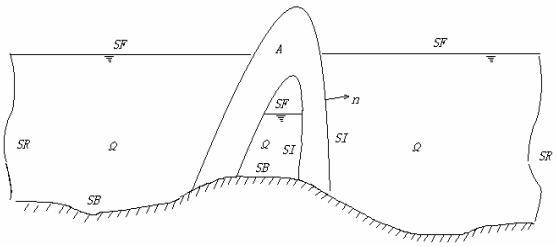

Fig. 1: Fluid-solid interaction system.

A fluid-solid coupling system is shown in Fig.1, in which, solid structure *A* is an undumped elastic body, and fluid field Ω is inviscid, irrotational, incompressible. *m*, ρ are mass density of solid and fluid, respectively.

Governing equation of fluid pressure *p* is

$$\nabla^2 p = 0 \quad \text{in} \quad \Omega . \tag{1}$$

Boundary conditions are:

$p = 0$ on free surface S_F, (gravitational wave is neglected);

$\frac{\partial p}{\partial n} = 0$ on fixed boundary S_B and infinite boundary S_R;

$\frac{\partial p}{\partial n} = -\rho \ddot{u}_n$ on fluid-solid interface S_I (u_n is normal displacement of the structure on it), reflecting coupling action of structure and fluid.

FEM expression of the coupling vibration system is

$$\begin{bmatrix} [M_s] & [0] \\ \rho[G] & [0] \end{bmatrix} \begin{Bmatrix} \{\ddot{D}\} \\ \{\ddot{P}\} \end{Bmatrix} + \begin{bmatrix} [K_s] & -[G]^T \\ [0] & [H] \end{bmatrix} \begin{Bmatrix} \{D\} \\ \{P\} \end{Bmatrix} = \begin{Bmatrix} \{F_0\} \\ -\{Q_0\} \end{Bmatrix} \tag{2}$$

in which, $[D]$ is displacement vector of the structure; $[P]$ is pressure vector of the fluid field; $\{F_0\}$ is dynamic vector loading on the structure (not including fluid pressure); $\{Q_0\}$ is known exciting vector or given boundary moving vector in fluid field; $[M_s]$ and $[K_s]$ are mass matrix and stiffness matrix of the structure, respectively; $[H]$ is fluid matrix and $[G]$ is coupling matrix. Expression of all these matrices can be seen in Huang (1998).

Now we discuss the harmonic vibration of the system.

Let $\{F_0\} = \{f_0\}e^{i\omega t}$, $\{Q_0\} = \{q_0\}e^{i\omega t}$, $\{P\} = \{p\}e^{i\omega t}$, $\{D\} = \{d\}e^{i\omega t}$ (ω denotes the circular frequency of the system, $\mathrm{i} = \sqrt{-1}$), then we have

$$\begin{bmatrix} [K_s] - \omega^2[M_s] & -[G]^T \\ -\rho\omega^2[G] & [H] \end{bmatrix} \begin{Bmatrix} \{d\} \\ \{p\} \end{Bmatrix} = \begin{Bmatrix} \{f_0\} \\ -\{q_0\} \end{Bmatrix} . \tag{3}$$

In the case of free vibration, let $\{f_0\} = \{q_0\} = \{0\}$ and eliminate $\{p\}$, we obtain the equation for modal analysis

$$\left([K_s] - \omega^2([M_s] + [M_w])\right)\{d\} = \{0\} \tag{4}$$

in which $[M_w] = \rho[G]^T[H]^{-1}[G]$ is called added mass.

3. Expressions in manifold method

3.1 Description of displacement and fluid pressure

At present, FEM meshes are often employed to define finite covers of NMM. All elements connected

with any FEM node form a mathematical cover. The FEM shape function is the weight function here. A rectangular mathematical mesh with its four covers is shown in Fig.2, whose weight function is

$$w_i = \frac{1}{4}(1+\varepsilon_0)(1+\eta_0) \tag{5}$$

with $\varepsilon_0 = \varepsilon_i \varepsilon$, $\eta_0 = \eta_i \eta$ in which (ε_i, η_i) and (ε, η) are local coordinates of each node and any point in the mesh, respectively, $i = 1,2,3,4$.

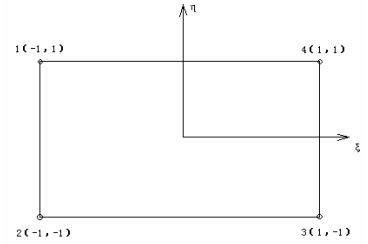

Fig. 2: A rectangular mathematical mesh and four covers.

The polynomial series is in most common use as local cover functions. Computational accuracy is improved when terms and order of the series increase. In two dimensions, polynomials are given as $x^{n-k}y^k$ in which k is repeated from *0* to n order. The total number of terms is $m=(1+n)(n+2)/2$. For example, *0* to *2* order polynomial cover functions are combined to

$\{t\}=\{1 \quad x \quad y \quad x^2 \quad xy \quad y^2\}$.

Matrices of displacement and fluid pressure in a rectangular mesh are

$$[T_s]=[T_{s1} \quad T_{s2} \quad T_{s3} \quad T_{s4}],$$

$$[T_w]=[T_{w1} \quad T_{w2} \quad T_{w3} \quad T_{w4}], \tag{6}$$

respectively, where T_{si}, T_{wi} are covers of *i*-th node as $[T_{si}]=[T_{i1} \quad T_{i2} \quad \ldots \quad T_{im}]_s$, $[T_{wi}]=[T_{i1} \quad T_{i2} \quad \ldots \quad T_{im}]_w$, with $[T_{ij}] = w_i \begin{bmatrix} t(j) & 0 \\ 0 & t(j) \end{bmatrix}$ for displacement field, and $[T_{ij}] = w_i t(j)$ for fluid field ($i=1,2,3,4, j=1, \ldots, m$).

$\begin{Bmatrix} u \\ v \end{Bmatrix} = [T_s]\{d^{(e)}\}$ and $p = [T_w]\{p^{(e)}\}$ represent displacement and fluid pressure in the element, respectively, where $\{d^{(e)}\}$, $\{p^{(e)}\}$ are unknowns (coefficients of polynomial series).

3.2 System equations in the form of manifold method

With respect to manifold method using in this paper, only description of physical field is different from FEM. Thus, we can use the same system Eqs. (2) to (4). Element stiffness matrix $[K_s^{(e)}]$ and mass matrix $[M_s^e]$ for the structure in NMM can be referred to Shi (1992) or Su et al (2005a). Sub-matrix of $[H^{(e)}]$ for fluid element is

$$[H_{ij}] = \int_\Omega \left(\frac{\partial [T_{wi}]^T}{\partial x} \frac{\partial [T_{wj}]}{\partial x} + \frac{\partial [T_{wi}]^T}{\partial y} \frac{\partial [T_{wj}]}{\partial y} \right) d\Omega , \tag{7}$$

in which $i,j=1,2,3,4$. Expression of the coupling matrix will be given later on.

3.3 Introduction of known boundary conditions

Hard springs are used to introduce fixed boundary conditions on structure (Shi, 1992). We shall discuss how to introduce the known boundary conditions to matrix [*H*] in fluid field, that is, $p = 0$ on free surface S_F .

In NMM, pre-process is simplified because mathematical meshes need not satisfy physical boundaries strictly. However, known freedom can not be eliminated directly as what is usually done in FEM. One approach is using the third boundary condition of Laplace equation, $\frac{\partial p}{\partial n} - \beta(p - p_a) = 0$ (on Γ_q), to simulate the first condition $p - p_a = 0$ (on Γ_p), (p_a and $\bar{q}$ are known, β is a coefficient). That is, $p = p_a$ when $\beta \to \infty$. This is called penalty function method, similar to the hard spring of the solid. However, artificial large number β will have a bad effect on the inversion of [*H*], resulting in an unture frequency computed by Eq. (4). So Lagrange multiplier method is used in this paper. Define functional as

$$\Pi = \int_{\Omega}\left(\frac{1}{2}(\frac{\partial p}{\partial x})^2 + \frac{1}{2}(\frac{\partial p}{\partial y})^2\right)d\Omega - \int_{\Gamma_q} p\bar{q}d\Gamma + \int_{\Gamma_p}\lambda(p-p_a)d\Gamma \quad (8)$$

in which $\Gamma_p = S_F, \Gamma_q = S_B + S_R + S_I$, λ is the Lagrange multiplier. After applying variation to Eq.(8), governing equation of Eq.(1) and all boundary conditions are all satisfied automatically due to the arbitrary of δp and $\delta\lambda$, and we get $\lambda = -\frac{\partial p}{\partial n}$. Now substituting $\lambda = -\frac{\partial p}{\partial n}$ into Eq. (8), we obtain a new functional

$$\Pi = \int_{\Omega}\left(\frac{1}{2}(\frac{\partial p}{\partial x})^2 + \frac{1}{2}(\frac{\partial p}{\partial y})^2\right)d\Omega - \int_{\Gamma_q} p\bar{q}d\Gamma - \int_{\Gamma_p}\frac{\partial p}{\partial n}(p-p_a)d\Gamma \quad (9)$$

Variations of this functional lead to a matrix form

$$[H]\{p\} = \{q_1\} + \{q_2\} \quad (10)$$

in which $[H]=[H_0]+[H_p]$, $[H_0]$ is calculated by Eq. (7),

$$[H_p] = -\sum_e [H_p^{(e)}] = -\sum_e \int_{\Gamma_p^{(e)}}\left([T]^T\frac{\partial}{\partial n}[T] + \frac{\partial}{\partial n}[T]^T[T]\right)d\Gamma \quad (11)$$

$$\{q_1\} = \sum_e \int_{\Gamma_p^{(e)}}\left(\frac{\partial}{\partial x}[T]^T p_a\right)d\Gamma, \quad (12)$$

$$\{q_2\} = \sum_e \int_{\Gamma_q^{(e)}}\left([T]^T\bar{q}\right)d\Gamma. \quad (13)$$

3.4 Coupling matrix $[G]$

On fluid-solid interface S_I shown in Fig. 1, n_x and n_y are direction cosines of the outward normal n, and $\bar{q} = \frac{\partial p}{\partial n} = -\rho\ddot{u}_n$. In the element linked to the interface, according to Eq. (13) we have

$$\{q_2\} = -\sum_e \rho \int_{S_I^{(e)}}[T_w]^T\begin{bmatrix} n_x & n_y\end{bmatrix}[T_s]dS_I\left\{\ddot{d}\right\}. \quad (14)$$

Then we obtain the element coupling matrix

$$\left[G^{(e)}\right] = \rho\int_{S_I^{(e)}}[T_w]^T\begin{bmatrix} n_x & n_y\end{bmatrix}[T_s]dS_I. \quad (15)$$

Simplex integration is used in the integration of the above equations, including one and two dimensional simplex.

4. Analytical solution cover of infinite fluid field

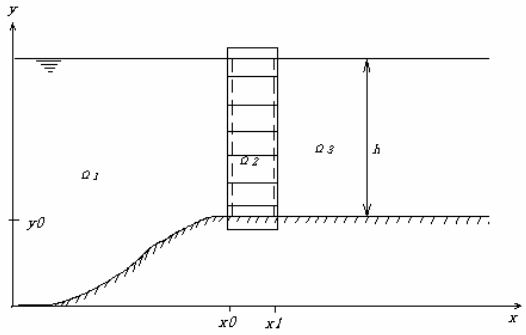

Fig. 3: Fluid field including an infinite domain of equal depth, rectangles are manifold meshes of Ω_2.

Fluid field Ω shown in Fig.3, including an infinite domain of equal depth h, is divided into three parts, $\Omega = \Omega_1 + \Omega_2 + \Omega_3$, which are domain Ω_1 ($x<x_0$) for numerical solutions, transition domain Ω_2 ($x_0<x<x_1$), and domain Ω_3 ($x>x_1$) for analytical solution, respectively. In Ω_3, analytical solution for Laplace equation is

$$\bar{p}(x,y) = \sum_n A_n e^{-\alpha_n x}\cos\alpha_n(y-y_0), \quad (16)$$

in which, $\alpha_n = \frac{(2n-1)\pi}{2h}$, $n=1,2,...$, A_n are unknowns to be solved. It is easy to check that Eq. (16) satisfies the governing equation and all the boundary conditions in Ω_3. Thus, after variations all integrals in Eq. (9) are equal to zero and can be ignored in Ω_3. At the same time, we still adopt numerical solutions based on polynomial cover functions in Ω_1.

We shall discuss the treatment of the transition domain Ω_2 (rectangular meshes of Ω_2 are shown in Fig.3). Two schemes are considered in this paper: One is the traditional four covers shown in Fig.2, in which numerical covers on the 1,2 nodes, while analytical covers on 3,4 nodes, and weight functions are the same as Eq.(5); The other is three covers shown in Fig.4 where the third cover represents analytical series, and the weight function w_3 becomes $w_3 = \frac{1}{2}(1+\xi)$.

Then the three covers in the element are

$[T]=[T_1 \quad T_2 \quad T_3]$,

where, T_1, T_2 are the same as those in Eq. (6), while

$$T_3 = w_3 \bar{p} = \sum_n A_n w_3 e^{-\alpha_n x} \cos\alpha_n (y - y_0) \,. \qquad (17)$$

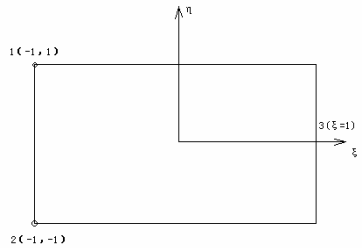

Fig. 4: Three covers in a rectangular mathematical mesh.

Computation shows that these two schemes achieve very close results. However, the three covers scheme is more reasonable theoretically and can save computation amount.

Because there is not formula of simplex integration for Eq. (17) by now, numerical integration is performed. In addition, the value of the function $e^{-\alpha_n x}$ goes little when x goes large, leading to bad condition of the matrix when solving the equations. So we rewrite Eq. (16) as

$$\bar{p}(x,y) = \sum_n A_n e^{-\alpha_n (x - x_0)} \cos\alpha_n (y - y_0) \qquad (18)$$

5. Examples

We select the example in Huang (1988), concerning a coupling system of a cantilever and fluid shown in Fig.5. The cantilever beam has a width of 1m. The length of the beam is the same as the depth of the fluid field h=10m. Young's modulus E of solid is 3×10^6 kN/m^2, Poisson's ratio u is 0.2. Density of solid m is 20, 10, 5, 3.33 times of the density of fluid ρ (=0.1kN/m^3), respectively. Rectangles in the figure are manifold meshes. One can see that the meshes do not agree with the boundaries of the structure or the fluid. For example, the meshes of the first column comprise solid and fluid material. Fluid field is discretized to meshes at a distance of 30m from the beam in x direction. Via trial calculation, it is considered that the fluid field has been discretized far enough.

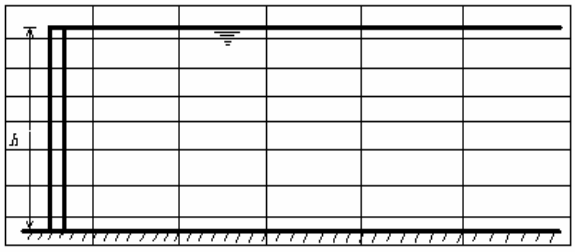

Fig. 5: Fluid-beam interaction system and NMM meshes.

5.1 Compute base frequency of the system

We apply one order polynomial cover functions to the structure to improve the precision of the displacements, and only 0 order to the fluid to consider the added mass. Tab.1 shows the results. It can be seen that frequencies (with or without fluid) are very exact.

Tab.1 Base frequency of the beam (rad/s)

$\rho h/m$	Wet frequency ω_1	frequency of the structure without fluid ω_{01}			ω_1/ω_{01}		
	numerical solutions	numerical solutions	analytical solutions*	relative error (%)	numerical solutions	series solutions*	relative error (%)
0.5	1.175	1.238	1.243	-0.40	0.949	0.947	0.21
1.0	1.585	1.750	1.758	-0.46	0.906	0.900	0.66
2.0	2.063	2.475	2.486	-0.44	0.834	0.825	1.09
3.0	2.352	3.032	3.045	-0.43	0.776	0.766	1.31

*series solutions in Huang (1988) adopt 6 terms of series

5.2 Harmonic responses analysis

Compute harmonic responses according to Eq. (3). A horizontal exciting force acts on the top of the beam, with the amplitude of 10*kN* and frequency of 10*rad/s*. Density of solid m = 1kN/m^3. One order polynomial cover functions are used in structure and fluid field. The deformation of the beam is the same as the results with FEM. Maximum displacement on the top is 0.0345m, close to 0.0364m of FEM. Via trial calculation, number of finite elements is at least 240, while number of manifold meshes is only 48. It can be seen that high order NMM with less number of meshes can obtain the same precision as FEM with much more elements.

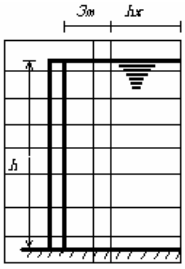

Fig. 6: NMM meshes considering analytical solutions.

Tab.2 Wet frequency ω_1 (considering analytical cover)

$\rho h/m$	$h_x = 2m$		$h_x = 4m$		$h_x = 10m$	
	n=5	n=20	n=5	n=20	n=5	n=20
0.5	1.172	1.165	1.174	1.175	1.178	1.177
1.0	1.579	1.560	1.584	1.584	1.592	1.590
2.0	2.049	2.008	2.060	2.061	2.078	2.074
3.0	2.331	2.271	2.347	2.350	2.374	2.369

h_x is the length of the transition domain, and n is the number of terms of analytical series

It can be seen from the table that, when considering analytical cover, wet frequency ω_1 are close to those in Tab.1. For example, when $\rho h/m = 3$, ω_1 is between 2.271 and 2.374, ω_1/ω_{01} is between 0.7490 and 0.7830. Comparing with the series solution result 0.7661, relative errors are under 2.2%. Moreover, 5 terms of analytical series can give an enough precision, meaning a very quick covergency. The length of the transition domain h_x affects the results to some extent. It can not be very small or very large. When $h_x = 4m$, almost the same results as Tab.1 are obtained.

5.3 Compute frequency considering analytical solution

Shown in Fig.6, Discretized domain for numerical solutions of the fluid field is at a distance of only 3m from the beam in x direction. Considering analytical cover to simulate the infinite field, we obtain wet frequency ω_1 listed in Tab.2, in which some results show the effect of length h_x of the transition domain and number of terms n for analytical series

6. Conclusions

In this paper, some preliminary researches have been done on fluid-solid interaction analysis using numerical manifold method. Further work should be done considering conditions of free surface, compressibility of fluid, damp of structure and so on, or transient dynamic analysis.

This paper makes a significant attempt to combine numerical solutions and analytic solutions together using NMM. The good results suggest that NMM should be very suitable for the combination, much easier than usual approaches. Although the research is preliminary, the method can be spread to many occasions where classical analytical solutions can play a great role.

With respect to nonlinear analysis concerning large displacement of structure and large disturbance of fluid, arbitrary shape of manifold elements presents a possibility of using fixed mathematical meshes to calculate large deformation of the structure (Su et al, 2005b). Thus, solid and fluid can be conveniently solved with the same fixed background meshes to settle the problem of incompatibility on the interface of solid and fluid. Therefore, it is very important to study NMM in the region of fluid-solid coupling analysis.

The authors are grateful to Dr. Shi for his valuable suggestions on the research.

References

Shi Genhua. Manifold method of material analysis. *Transactions of the Ninth Army Conference on Applied Mathematics and Computing,* Minneapolis, Minnesoda, 1992, 51-78.

Wang Zhiyin, Li Yunpeng. Numerical manifold method and its development (in Chinese). *Advances in Mechanics*. 2003, 33(2), 261-266.

Li Shuchen, Cheng Yumin. Numerical manifold method and its applications in rock mechanics (in Chinese). *Advances in Mechanics*. 2004, 34(4), 446-454.

Huang Yuying. Fundamental Theory of Structure Vibration Analysis (in Chinese), Huazhong Technical Institute Press, 1988.

Su Haidong, Xie Xiaoling, Chen Qin. Application of high-order numerical manifold method in static analysis (in Chinese). *Journal of Yangtze River Scientific Research Institute.* 2005a, 22(5), 74-77.

Su Haidong, Xie Xiaoling. Preliminary research on solving large displacement problem using numerical manifold method with fixed mathematical meshes. In: *Proc of the Seventh International Conference on the Analysis of Discontinuous Deformation,* December 10-12, 2005b, Honolulu, Hawaii, 175-182.

Structure failure simulation by Numerical Manifold Method

Guoxin ZHANG[1], Yan ZHAO[1], Jia HA[2]
[1]China Institute of Water Resources and Hydropower Research, Beijing 100038，China
[2] Yellow River Engineering Consulting Ltd., Zhengzhou 450003, China

By improving the simulation method of contact and contact forces, adding the seepage action and the function of tracing the propagation of cracks, the Numerical Manifold Method proposed by Shi is developed which can simulate the discontinuity of block system, the tensile or shear failure, the crack propagation in the intact rock, and the structure failure very well. The algorithms and programs of manifold method are used to simulate the bend-tension failure and toppling instability of rock slop. Considering the crack propagation and seepage action, they are used to simulate the process of crack initiation and propagation in Wuqiangxi ship lock with the rise of water level. The failure mode simulated numerically agrees well with the real, which presents the mechanism of structure failure over again. It shows that the method put forward and the program developed in this paper can effectively simulate the structure failure and can give scientific suggestion for support design.

Keywords: Second-order Manifold Method; Structure failure; Seepage; Crack propagation; Contact

1. Introduction

The structure failures such as slope instability, ship lock and dam failure have brought great losses to human life and properties. Numerical methods not only can simulate discontinuities such as joints and cracks, the large deformation after the failure of rock body but also can simulate the failure of intact rock mass, which cannot be solved well by methods based on discontinuous mechanics such as DEM and DDA or methods based on continuous mechanics such as FEM. Numerical Manifold Method (NMM) is a numerical method proposed by Shi (1997) in the early 1990s. This method takes the advantages of continuous method and discontinuous method. By using the concept of 'Cover' and two sets of grid (math grid and physical grid), not only can it calculate the deformation and stress inside blocks as Finite Element Method do, but also can it simulate block systems as the DDA does. Zhang and co-authors (Zhang et al 2001; Zhang & Peng 2002; Zhang et al 2002) greatly extended the original NMM proposed by Shi, and adopted the second-order Manifold Method, and the fracture mechanics algorithm is added to trace the propagation of cracks. The extended NMM not only can simulate multi-cracks propagation but can simulate the process of tension and shearing failure, as well as coupling analysis of seepage and
deformation. By the extended Manifold method, the bend-tension failure, toppling failure and the crack initiation and propagation in Wuqiangxi ship lock with the rise of water level are simulated in this paper.

2. Failure simulation by Numerical Manifold Method

Structures mainly have two kinds of failure types: the first one is failure along weak parts, for example, joints, cracks, weak interlayer and construction joints of concrete structures etc; the second is the failure within continuum. To simulate the first type of failure, the numerical method should not only correctly calculate the

contact stress, simulate the opening and sliding of interfaces but also should simulate the failure process when the interfaces have tensile strength or shear strength. To simulate the second type of failure, the numerical method should be able to simulate the cracks' occurrence and propagation and the shear failure of continuum. The extended NMM in this paper can simulate both of the two types of failure.

Assume that the failure of existing discontinuities follows Mohr-Coulomb's law. Taking σ_n as the normal stress and τ_s as the shearing stress on a joint, the failure criterion is defined as bellow: Mohr-Coulomb criterion is adopted for the case that cracks propagate along existing failure faces. Namely,

For tensile failure, $\sigma_{\mathrm{n}} = \sigma_{\mathrm{t}}$

and shear failure: $\tau_s = c$ $\sigma_{\mathrm{n}} > 0$ and $\sigma_{\mathrm{n}} < \sigma_{\mathrm{t}}$

$$\tau_{\mathrm{s}} = c - \sigma_{\mathrm{n}} \tan\varphi \qquad \sigma_{\mathrm{n}} < 0 \qquad (1)$$

where σ_n —normal stress (positive for tension),

τ_s —tangential stress, ϕ —friction angle,

σ_t —tensile strength, and *c*—cohesion.

The occurrence of new cracks in continuum follows tensile strength criterion and the crack's propagation follows the stress intensity factor criterion of fracture mechanics theory. When the stress intensity factor of the crack tip reaches the limit value, the crack begins to propagate. This limit value is called fracture toughness.

In this paper, the field of displacement and stress are firstly calculated by the second-order Manifold Method program developed by Zhang; then a subdomain around the crack tip is cut out and the circumambient displacements calculated by NMM along the edge cut out are taken as the displacement boundary of the submodel. By using the singular basic solution which takes the singularity of the crack tip into account and the Kelvin basic solution, the integral equation of the boundary is constructed. Then the stress intensity factor is calculated by the Boundary Element Method. Finally, it judges whether the crack will propagate or not and the direction of propagation, if cracks occur, by max circumferential stress criterion (Chen 1984). The crack growth angle θ_0 is determined by the equation below:

$$K_{\mathrm{I}} \sin\theta_0 + K_{\mathrm{II}} \left(3\cos\theta_0 - 1\right) = 0 \qquad (2)$$

$$\theta_0 = \begin{cases} 2\arctan\left(\dfrac{|\mathrm{K_I}| - \sqrt{K_{\mathrm{I}}^2 + 8K_{\mathrm{II}}^2}}{4K_{\mathrm{II}}}\right) & K_{\mathrm{II}} \neq 0 \\ 0 & K_{\mathrm{II}} = 0 \end{cases} \quad (3$$

The crack criteria of crack composed by I- Ⅱ based on max circumferential stress criterion is:

$$\cos\frac{\theta_0}{2}\left[K_{\mathrm{I}} \cos^2\frac{\theta_0}{2} - \frac{3}{2} K_{\mathrm{II}} \sin\theta_0\right] = K_{\mathrm{Ic}} \quad (4)$$

θ_0 is the angle between crack propagation direction and the initial crack.

The combination of second-order Manifold Method and Boundary Element Method can correctly calculate the stress intensity factor of crack tip. When the crack occurs and propagates, the mesh need not be plotted again, it only needs changing the corresponding physical boundary and mathematics cover. The method can be referred in the paper by Zhang et al (2001).

3. The coupling action of seepage and deformation

Coupling problem is inevitable in the simulation of structural failure induced by water pressure. When cracks occur in the structure subject to the action of water pressure, water comes in and seepage pressure is developed. The seepage pressure may lead to the opening of crack or even further propagation. And the change in width and length of cracks will affect the seepage field in reverse. Therefore, it can be concluded that there is a coupled interaction between seepage and deformation in structures including cracks, fissures and joints.

For a crack segment *i* shown in Fig.1, node *j* and node *k* are its two ends, L_i , its length, b_i, its width, Q^i , the discharge through the crack , H_j and H_k are water heads at two ends.

According to Darcy's law, we have

$$Q_{\alpha i}^{i} = K_i (\frac{\Delta H_i}{L_i})^{\alpha_i} b_i \qquad (5)$$

where K_i is the hydraulic conductivity， ΔH_i , the difference in water head between two ends and α_i , an exponent. Hydraulic conductivity K_i and exponent α_i , are related to crack surface roughness and flow pattern.

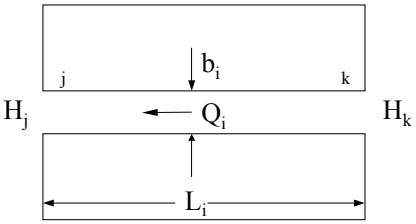

Fig. 1 Joint seepage model

Let $$G_i = \frac{K_i b_i}{L_i^{\alpha_i}} \Delta H^{\alpha_i - 1} \qquad (6)$$

For crack *i*, there is

$$\begin{Bmatrix} Q_k^i \\ Q_j^i \end{Bmatrix} = G_i \begin{bmatrix} 1 & -1 \\ -1 & 1 \end{bmatrix} \begin{Bmatrix} H_k^i \\ H_j^i \end{Bmatrix}$$

Assuming balance of flow at all nodes, the assembly of all the crack elements of mesh yields the following governing equation with nodal water heads as unknowns:

$$G \cdot H = C \qquad (7)$$

where C is the vector of known nodal discharges or water heads.

All the water heads of nodes at certain time can be obtained by solving Equation 7. Hence the seepage pressure in cracks can be determined. The equivalent nodal loads of element i due to the seepage pressure in cracks can be written as in Fig.2:

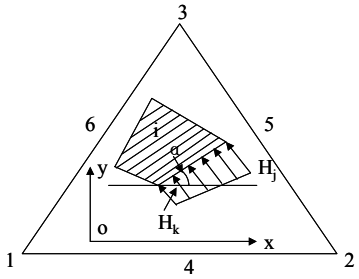

Fig.2 Block with water pressure

$$T_i(x_k, y_k)[H] + T_i(x_{k+1}, y_{k+1})[G] \rightarrow F_i \qquad (8)$$

$$[H] = \begin{bmatrix} \frac{L}{3} f_{xk} + \frac{L}{6} f_{xk+1} \\ \frac{L}{3} f_{yk} + \frac{L}{6} f_{yk+1} \end{bmatrix} \qquad [G] = \begin{bmatrix} \frac{L}{6} f_{xk} + \frac{L}{3} f_{xk+1} \\ \frac{L}{6} f_{yk} + \frac{L}{3} f_{yk+1} \end{bmatrix}$$

$$f_{xk} = -h_k \sin\alpha \,, \quad f_{yk} = h_k \cos\alpha$$

where L is the side length subject to water pressure, α, included angle between side $\overline{kk+1}$ and the axis *x*.

The nodal water heads in Eq. 7 are the same as those in Eq. 8. Water heads and openings of cracks interact with each other, as expressed in Eqs.7 and 8. Iteration method is employed to find the solution.

4. Simulation of flexural failure of rock slope

The flexural failure often happen on the front of slope, and the rock masses occur the cantilever bend accompanying with the tension cracks. The cracks propagate and parallel to the aspect at last. The model in Fig.3 is used to simulate one simple example of flexural failure. The calculation parameters are： specific weight P=24.5kN/m3, elastic modulus E=1000MPa， Poisson 's ratio ν=0.2，Penalty=9800000kN/ m，the maximal time step △t=0.01s. The slope only bears weight in the first time, and along with the increasing of load at a fixed rate, we can see that the top block occur the flexural failure. The fig.4 shows the failure state in the four different times.

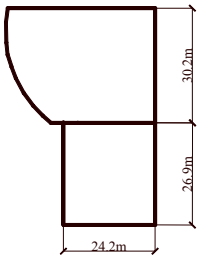

Fig.3 Flexural failure model

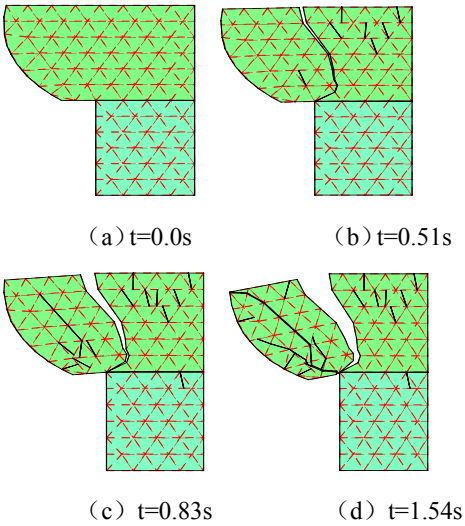

（a）t=0.0s （b）t=0.51s

（c） t=0.83s （d） t=1.54s

Fig.4 Flexural failure of rock slope

5. Simulation of toppling failure of slope without rock bridges

Toppling is usually occurs in the layered rock slope whose structural characteristic is that the bedding plane of the rock and the slope has the same strike but opposite dips. If there is one or many sets of joints along the slope cutting the rock bedding into discrete blocks, the possibility of toppling failure is even higher.

Taking the test mode introduced in the paper by Wang et al (1996) as an example, NMM is used to simulate the failure mode of the model. The model is 64cm high, 93cm long and has totally eleven blocks, see Figure 5. The joint plane is perpendicular to the bedding plane, the elastic modulus of the block is 620MPa and the specific weight is 10.0kN/m^3, and the cohesion between all the contact planes is 0. The failure mode of the blocks is calculated by NMM with various friction angles ϕ, and the results can be referred in Fig. 6.

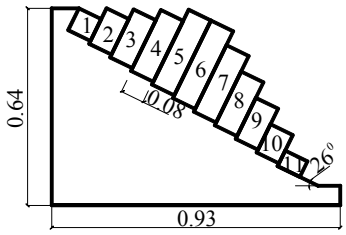

Fig.5. Toppling failure model

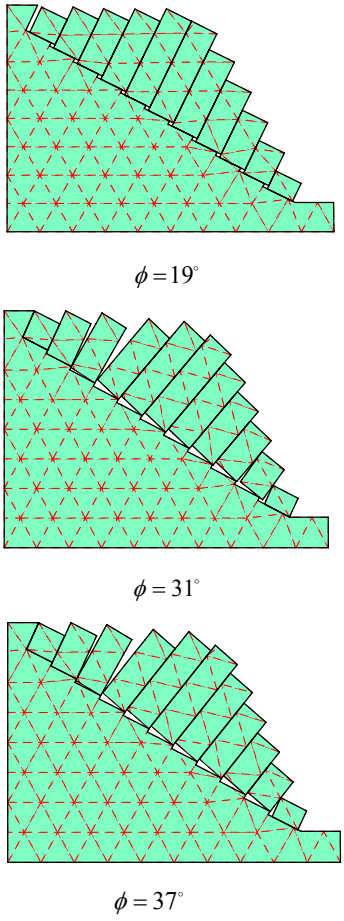

Fig 6. Failure modes with different ϕ values of the bedding plane

From the deformation mode of the slope with different ϕ we can see that:

(1) According to the results of simulation: If $\phi \le 26^\circ$, that is, when ϕ is less than the dip angle of the slope, all blocks cannot keep stable.

(2) From the simulation process of NMM, it can

be clearly seen that when $\tan\alpha \le \tan\phi$, Goodman's classification (Goodman & Bray 1976) of blocks on the slope into groups of stability, toppling, and sliding is reasonable. As the parameters change, the quantities of blocks in different groups are different, and the toppling blocks can also slide. Between blocks, it is plane contact rather than point contact. This contact mode, being different from the Goodman's mode that only considers the point contact, is in better accordance with practical requirements.

6. Simulation of toppling failure of slope considering the fracture of rock bridges

In the paper by Wang et al (1996), a centrifuge test was conducted on a slope model, and in this paper we simulate the slope failure by NMM using the same model and parameters. The computation model is shown in Fig.7, which is made of plaster with some joints incised in the model. The height of the model is 67.5 cm and the total length of the section is 71.65 cm. The angle of reverse dip of bedding plane is 60^o; the dip angle of joints is 60^o; the angle between bedding plane and joint is 60^o and the connectivity of joints paralleling to the direction of the slope is 0.70. For parameters of blocks: elastic modulus is 2×10^3 MPa; the tensile strength is 1.58MPa. For parameters of joints: the friction angle is 37^o; the tensile strength is 0.01MPa and cohesion is 0.065MPa. According to results of tests, the fracture toughness K_{IC} is $0.5MPa/m^{1/2}$. To simulate the loading mode of centrifuge, vertically downward body force is gradually added at a fixed rate.

Fig.8 shows the deformation states under the different centrifugal forces. From which it can be seen that during the failure of the slope, some joints and cracks develop first; then the blocks on the top begin to tilt and move downward; the blocks at the toe of the slope bend around the toe of the slope and the other blocks topple gradually and the rotation angle increases as the increase of load. Finally, the cracks and joints coalesce and form a transverse failure plane which is a zigzag line in profile.

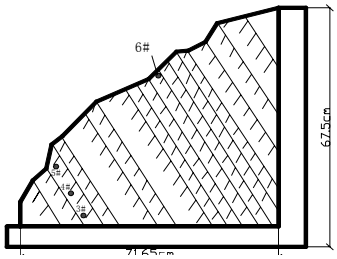

Fig. 7 Computation model of manifold method

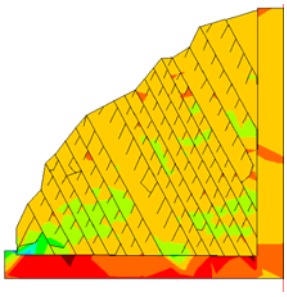

(a)F=99.85g

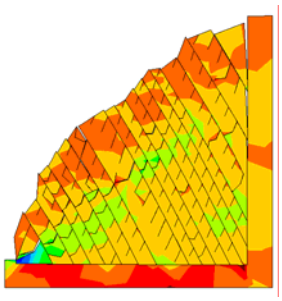

(b)F=127.21g

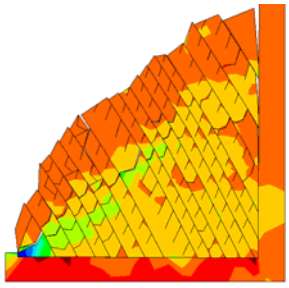

(c)F=127.225g

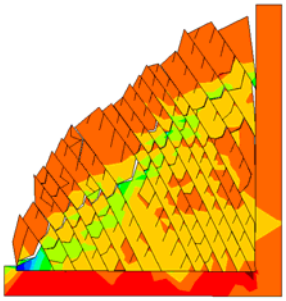

(d)F=127.24g

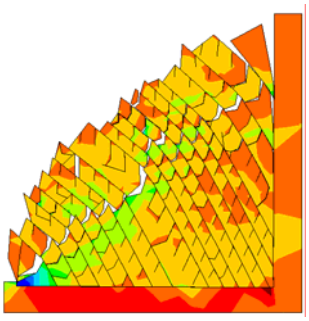

(e)F=127.266g

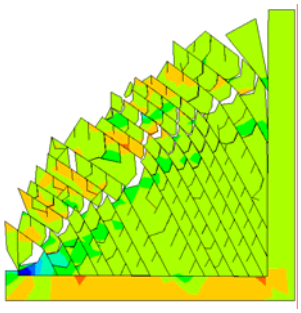

(f) F=127.275g

Fig.8 Slope failure model of with different centrifugal forces by Manifold Method

7. Hydraulic fracture simulation of the Wuqiangxi ship lock

As shown in Fig.9, the Wuqiangxi ship lock was put into operation in April 1995 and large deformation occurred at the lock crest in January 2001 when the water level reached 107.7m. After the ship lock was emptied, a great number of longitudinal cracks with spacing of about 0.8-1.0m were found on the chamber floor. The floor and the side walls were split apart at the corners. There were also cracks in some sections of the lock chamber. The extended manifold method is used to simulate the ship lock failure. The properties of concrete listed in Table 1.

Fig. 10 shows the crack patterns in the lock chamber with different water levels. The stress at the corner of lock chamber reaches the tensile strength of concrete and cracks emerge when water level rises to 105m. When the water level reaches 107.0m, cracks in the floor are nearly coalescent. When water level reaches 108.0m, a lot of coalescent cracks are found in the floor and cracks at the corner of chamber floor develop even downwards to the filling and emptied culvert or deep into the concrete. Cracks at the corner of the large gallery in the middle run downwards into the foundation. Due to the pulling out action of reinforcing bars after major cracks occur, many minor cracks are found bending to major ones at the bottom of the large gallery. In the meantime cracks are also found at the corner of two small galleries. When it reaches the maximum design water level of 110.5m, cracks at two corners of the left small gallery extend deep into concrete. Two semicircular through failure faces are formed at two sides of the chamber floor. They are due to the pulling out action of reinforcing bars and water seepage pressure

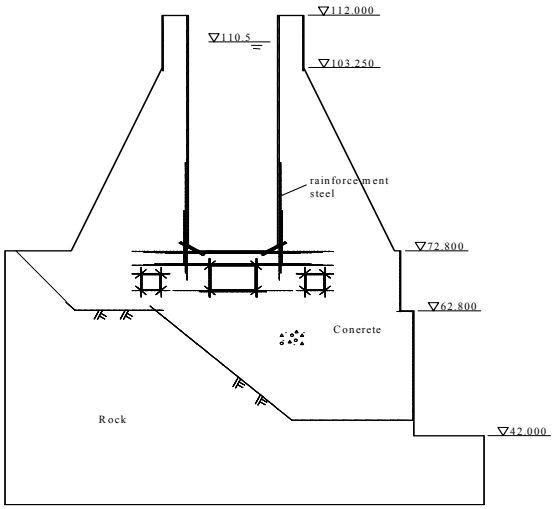

Fig. 9 The profile of the Wuqiangxi Ship Lock

Table.1 The properties of concrete

Elastic modulus （GPa）	Tensile strength （MPa）	Poisson's ratio	Specific weight （T/m^3）	Intensity (MPa)	Fracture toughness($\cdot MPa\sqrt{m}$)
25~29	2.0~2.5	0.17	2.45	2.0	2.0

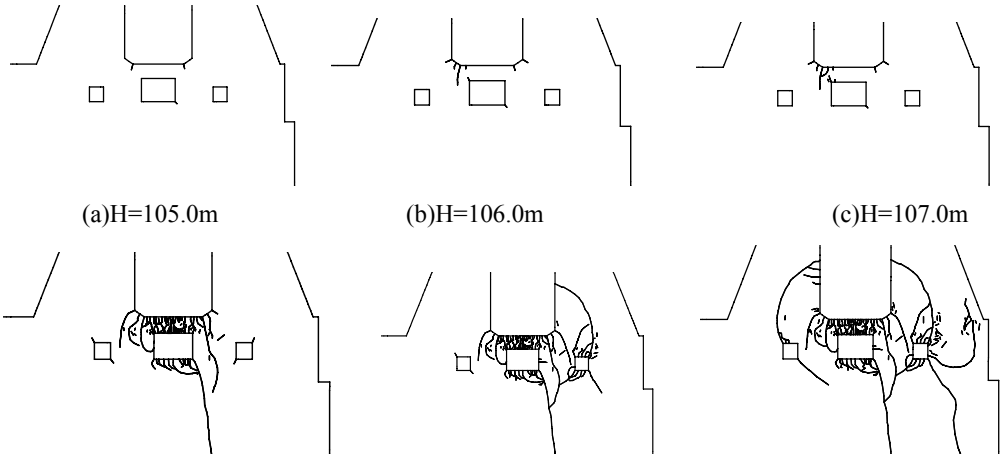

(a)H=105.0m (b)H=106.0m (c)H=107.0m

(d)H=108.0m (e)H=109.0m (f)H=110.5m

Fig. 10 The failure Pattern considering seepage pressure

8. Conclusions

The extended second-order Manifold Method not only can simulate the failure mechanism of structures from continuous to discontinuities, and the contact and contact stresses, but also can trace crack propagation successfully. The cracked section can be automatically searched and pre-setting of cracked section is not necessary, therefore it can accurately simulate the failure mechanism of highly discontinuous structures.

From several case studies in this paper, it can be seen that NMM is objective and reasonable in simulating the failure mode of structure. It can solve

problems that existing numerical methods cannot solve. NMM has advantages and broad application prospects in the simulating of the structure failure.

References

Chen, Z .Y. General case of multiple crack problems in infinite plate[J].Engng. Fracture Mech,1984, 20(5): 591-598.

Goodman, R. E. Bray, J. W. Toppling of slopes [J]. Proceeding of the Specialty Conference on Rock Engineering for Foundations and Slopes ASCE/Boulder Colorado. 1976，201-234

Shi, G. H. Translated by Pei Juemin.Numerical manifold method and discontinuous deformation analysis[M]. Beijing:Tsinghua University Press,1997

Wang, X. G. Zhang, J. H. Zhao, Y. Z. et al. Investigations on mechanism of slope toppling failure by centrifuge model testing[J]. Chinese Journal of Geotechnical Engineering，1996，18(5)：14-21

Zhang, G. X. Wang, G. L. Pei, J. M. Structure failure analysis based on manifold method [J]. Chinese Journal of Rock Mechanics and Engineering,2001，20(3)：281-287.

Zhang, G. X. Peng, J. Second-order manifold method in structure failure analysis[J]. Acta Mechnica Sinica, 2002，34(2)：261-269.

Zhang, G. X. Sugiura, Y. et al. The second order manifold with six node triangle mesh[J]. J. Struct.Mech. Earthquake Eng.，JSCE，2002，696/Ⅰ-58:1-9.

Application of key block theory and DDA to the stability analysis of Underground Powerhouseof Jinping Hydropower Station I

CHEN WEN and DENG JIAN-HUI
Sichuan University, P. R. CHINA

The underground powerhouse of Jinping Hydropower Station Ⅰ is large in scale and deeply buried in green marble and green schist with high in situ stress. The surrounding rock mainly belongs to III 1 and it has 4 groups of fissures and 2 sets of faults. The severely disked rock cores and rib-spallings in drilling hole indicate the plant is in high in situ stress area. In this paper, the key block theory and DDA are adopted for the stability analysis of the underground powerhouse of Jinping Hydropower Station Ⅰ. At first, the key blocks and its influence to the stability of the cavity are identified by key block theory. Then the displacement and the damage condition are examined by DDA. The calculation results show that the key blocks mainly lay on the roof in huge volume. They are dense in upstream side in small volume and bare in downstream side, and there just a few lying on the middle of the downstream wall. After excavation the roof collapsed seriously, and the wall on both sides damaged, especially in the downstream. After installation of bolt reinforcement, the number of falling blocks reduced significantly. The result shows that applying key block theory and DDA together is helpful to understand the damage mechanism of the underground rock wall and check the validity of the reinforcement.

Keywords: Key Block Theory; DDA; Underground powerhouse; High stress; Stability analysis.

1. Introduction

Rock is a natural material, the wide range of internal fissures and joints make it discontinuous. Since discontinuity is of great importance to the deformation and stress of the rock, the normal method, such as FEM, which deals with the rock as a continuous material has many limitations. In order to consider the influence of discontinuous structure to the stability of rock masses, DDA and key block theory are used more and more widely in engineering project. The key block theory can take water pressure into account (Huang et al 2001). It was used in underground cavity and high slope with random fissures and orientated faults (Zhang et al 2004). Recently, some new achievements of key blocks in these years were introduced, such as assuming the max length of the block and anchorage calculation. The key block theory was applied into the stability analysis of the whole underground cavities (Mao et al 2005). DDA has been used in underground project and slope project, considering the influence of excavation, blasting, reinforcement and underground water (Liu & Li 2004; Wu et al 2003; Wu et al 2006; Liu & Kong 2007). In this paper, the author firstly presents the advantages of these two methods, then apply them together in the stability analysis of the underground powerhouse of Jinping Hydropower Station I, and finally show that the key block theory and DDA complement each other and it is helpful to understand the damage mechanism of the underground rock wall and check the validity of the reinforcement.

2 Principles

1)DDA (Discontinuous Deformation Analysis) was put forward by Shi and Goodman in 1985. It's a numerical analysis method using discontinuous medium model and dynamic and static mechanics to reflect rock's large displacement and deformation. Allowing for the complication of rock mass, DDA considered the block system which is divided by structure plane as analysis element. And according to minimum potential energy principle, DDA takes the generalized displacement (rigid, rotation and deformation) as its primary unknowns to establish a balance equation, adding stiffness, quality and load submatrix et.al. to the equation for coefficient solution, and it adopts penalty function to ensure there is no inserting and stretching during moving and deforming. It adds or deletes springs at the contact point in iterations according to entering judgment.

2) The key block theory is a method perfected by Shi and Goodman in 1985. It firstly uses Stereographic Projection to find types of removable blocks, if the Joint Pyramids (the one formed by fissures) fully falls in the Space Pyramids (the space formed by free faces opposite rock) of the intersected rock wall, they are called removable block. And then use the limitation balance way to check whether they can move by residual sliding force in mechanics, if so they are called key blocks, the one that will move firstly if there is not enough prevention and its movement will make the blocks nearby move immediately which may do damage to the rock wall.

3) The advantage of combining key block theory and DDA :① in the manifestation term, 3D-DDA is immature and 2D-DDA is only a plane model, it can not tell the three dimensional situation of the underground cavity, it's weak in understanding the distribution of the firstly-fall blocks, and their influences to the stability of the whole cavity. While key block theory is a 3D method, it focuses on finding key blocks on the excavation surface and it can show the three dimensional relationship or plane-graph of key blocks and the free faces.②In theoretical terms ,although on the surface key blocks

theory uses pure geometric way to analyze the stability of rocks basing on stereographic projection , it can only consider the shear strength and rigid movement of the structure, while DDA use dynamic and static mechanics to reflect the displacement and deformation of structure, Yet they both do research in block system under skin. Since both of them have a strict theory, if we combined them together, each result can perfect another one, we can not only know the distribution of the firstly-fall blocks and their damage to the cavity, but also the movement character of the cavity section, this is helpful to understand the destroy law of the underground cavity and check the validity of the enforcement design.

3 The stability analysis of the rock wall in Jinping Hydropower Station Ⅰ

3.1 The geology survey

Jinping Hydropower Station Ⅰ which has 6 generators with a total installed capacity of 3.6 million kilowatts lies on the main stream of Yalong river, where Muli and Yanyuan, (two counties of Liangshan Yi nation-Sichuan Autonomous Prefecture) bound up. This underground powerhouse is one of the biggest underground projects under construction, with a horizon line of N65 °W, a length of 276.99 m, a width of 25.60 m and a height of 68.80 m. It is located in green marble and green schist, mainly covering T2-3 $^{Z2(2\backslash3\backslash4)}$ strata in rock III 1. The disked rock cores and sloughing in drilling holes and exploratory holes indicate that the Power Station lies in high stress area. The σ1 of rock masses is normally 25~30MPa, and 35.7~40.4MPa at most，whose direction is between N36°W and N67°W, and N51°W at average, and it is nearly perpendicular to the bank strike, with a dig varying from 3° to 57°.

The advantage direction of festival fractures: ① N40~60 ° E, NW ∠ 15~30 °, parallel fissures, whose general space is 1~3 m, and 2~4m in extend, some especial extension length is 10m, mainly straight, rough and closed; ② N50~70 ° E, SE∠ 50~80 ° whose general space is 1~3 m, extending far, straightly, and roughly;③N50~70°W, NE (SW) ∠ 80~90°, generally the space is large and rolls roughly and closely, some especial ones puff about 0.5~3cm wide, and others partly extruded to belts whose band space is 0.1~0.5m filled with a small amount of debris and mud with a width of 3~5m and a extension of 15~50m;④N50~70°E, SE∠ 50~80° partly extruded to belts , its characters is essentially similar to Group 3 .

3.2 Block system mesh generation

When applying key block theory and DDA to the deformation of underground rock wall, at first it should get the block system by Monte Carlo according to the statistics of the fissures in the underground cavity. The data of the fissures is showed in Table.1. Since the third group and the forth group both have two dip directions, the four groups fissures are divided to four combinations, showed in Table 2 .

Table 1 Parameters of 4 groups fissures in the underground powerhouse

Serial num	Dip direction	Dip	Average spacing /m	Bridge /m	Random （0~0.5）
1	320°	25°	2	4	0.2
2	150°	65°	2	10	0.2
3	30°/210°	85°	5	35	0.35
4	60°/240°	85°	5	35	0.35

Table 2 the relationship of fissures combination

combination	the relationship of fissures combination
1	1、2、3-1、4-1
2	1、2、3-2、4-1
3	1、2、3-1、4-2
4	1、2、3-2、4-2

P.S. X-1 is the fissure in NE dip direction of NO.X group;
X-2 is the fissure in SW dip direction of NO.X group.

3.3 coefficients and initial stresses

1) The material properties for rocks: allowing for nearly all blocks belong to green marble and green schist in T2-3 Z 2(2\3\4) strata, so consider all the blocks as one material. Elastic modulus is 30Gpa; Poisson's ratio is 0.25; and unit weight of rock2700Kg/m3.

2) The material properties for all discontinuities: Friction angle of all discontinuities is 25°; Cohesion of all discontinuities is 0; Tensile strength of all discontinuities is 0.

3) Entering coefficient: 0.0005mm.Elastic modulus of spring is 100Gpa.

4) Initial stress: consider the initial stress state of measured point P340 as the initial stress state of the underground powerhouse, σ1 is 34.35 MPa, with a direction of 114°，and its dip is 49°; σ2 is 15.06 MPa, with a direction of 14°, and its dip is 9°; σ3 is 10.09 MPa, with a direction is 227°, and its dip is 40°.

3.4 the result of key block theory

Firstly use key block theory to display the distribution of the firstly-fall blocks. By comparing the block volume, the contract area, the safety factor of the four fissures combinations it preliminary confirm the combination 3 to be the most dangerous situation, whose volume of the key blocks is the largest, the contract area is spread wide and the average length of the block can get to12m at most. In this paper only take combination as the key block theory example.

After analyzed by stereographic projection and limit balance calculation and kick off blocks in high safety factor or in gentle slope angle, or with a narrow body, Finally, the block 1100，1010，1111 are considered as key blocks, marked by rectangle in

Fig.1. More information is told in table 3.

In Fig.1 1010 is the serial number of the joint pyramid (the sense of the serial number referred to the reference [10]), 0.67is the unit residual sliding force (dimensionless) under self-weight.

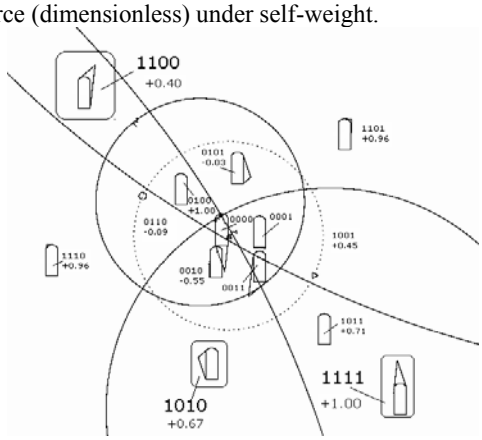

Fig.1 sliding coefficients and positions of blocks

Table 3 the information of key blocks

Serial num	Sliding direction	Residual sliding force	Safety factor	Block Volume /m3	Contact area /m^2
1100	Slide following 3rd and 4th fissure planes	0.40	0.58	6114.44	2246.85
1010	The same as 1100	0.67	0.25	4198.8	984.6
1111	Fall off	1	0	6214.1	513

The relationships between key blocks and the underground powerhouse are showed in Fig.2

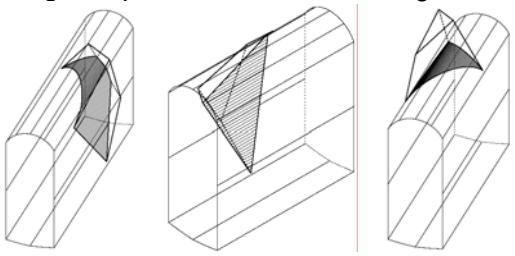

a. (1100) b. (1010) c. (1111)

Fig.2 the relationship between the key block and the underground cavity

Block 1110 is located in the downstream side of the plant; showed in Fig.2 (a), although its safety factor is higher than block 1010 and 1111, yet it has a big volume, once it moves it will cause enormous damage.

Block 1010 is located in the upstream side of the plant, showed in Fig.2 (b), with a smaller volume and a smaller contact area, but the average block length is nearly 4m long and its safety factor is low, so it may slide off when there is some blasting vibration

Block 1111 is located in the roof, showed in Fig.2(c), with a big volume and a zero safety factor, so when the whole border excavated to expose without instant preventions this block will fall off.

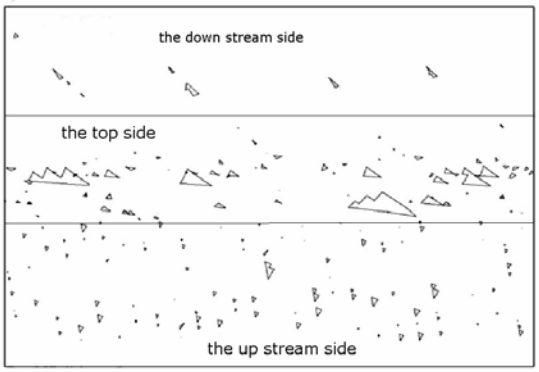

Fig.3 the expansion plane of key blocks

After the key blocks are identified and a series of sketches of the relationship between the single key block and the plant are drawn, in further step the relationship between whole key blocks and the plant can be obtained by the expansion plane. Fig.3 shows that the key blocks in the roof are more and larger than them in other sides, and their movements will cause falling down of a big area of removable blocks in the plant roof. The key blocks in the upstream side are in a small volume but a big amount, which increases the destroying probability of the upstream side and needs more reinforcement; key blocks in downstream side are less than the upstream but much bigger, once it moves, it may cause a big area of removable blocks move in downstream side.

3.5 Simulation result by DDA

The distribution of the firstly-fall blocks is determined by the key block theory in last section, and in this section the damage situation of the four fissure combinations by DDA are compared, as shown in Fig. 4. On one hand, in order to verify the correctness of the most dangerous situation found by the key block theory; on the other hand, in order to understand the damage progress of the cavity.

Combination1 is shown in Fig.4 (a). The roof moves firstly and falls off together. In the upstream side, at first the upper ones move and then push the lower ones. In the downstream side, the lower ones move and tract the upper ones to move.

Combination2 is shown in Fig.4 (b). The upstream side moves firstly. The upper ones in upstream side push the lower ones, and then make it dump and crack down. In the roof, the ones near the downstream side move firstly.

Combination3 is shown in Fig.4(c). The upstream side moves firstly. The upper ones in upstream side push out the triangle block at first, and then the upper ones dump following the triangle block. In the roof, the ones near the downstream side move firstly, and the whole roof collapse together. In the downstream side, the lower ones firstly move and tract the upper ones to move.

Combination4 is shown in Fig.4 (d), the downstream side moves firstly. The lower ones in downstream slide at first and then take the upper ones move together. The ones in the roof collapse together,

which vacate space for new collapsing. The upper ones in the upstream side pushed the lower ones.

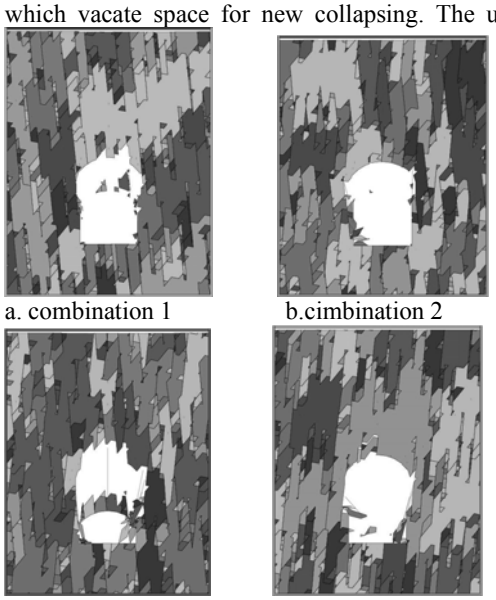

a. combination 1 b.cimbination 2

c. combination 3 d. combination 4

Fig.4 Damage pattern under different fissure combination

From the result of DDA, it's easy to see that in all the combinations the roof collapses. Furthermore, except in combination 2, the falling blocks in the roof is more than 50% of total. The damage barely occurs in the downstream wall, once it takes place, it usually the middle of the wall fail firstly, the blocks above may then foolows the movement; and the blocks in the upstream side is that the upper blocks move firstly, and push the blocks in the middle side, and sometimes the blocks in the middle move firstly.

After comparing the DDA result of the four combinations, it is shown that combination 3 is the most dangerous situation whose roof collapse as a whole, and both walls destroyed, especially the downstream side. This result verifies the conclusion from the results by the key block theory, that the key blocks in the roof are more and larger than those in other sides, and their movement will cause more blocks in the roof fall down; The key blocks in the upstream side are in a small volume but in big amount, which increases the damage probability of the upstream side and needs more reinforcement; key blocks in downstream side are less than the upstream but much larger, once it moves, it may cause a big area of removable blocks in downstream side.

The locations of the measurement points and the dimension of the model are showed in Fig. 5, and the monitoring data are showed in fig.6 .From Fig. 6 it's easy to find out that when the block moves (before fly freely), its horizontal displacement is close to zero, smaller than the vertical one, which proves the main damage form is dropping not horizontal extrusion.

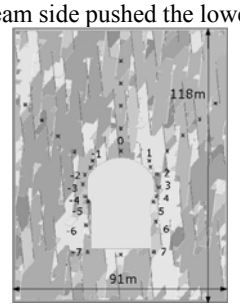

Fig.5 the layout of the measured points

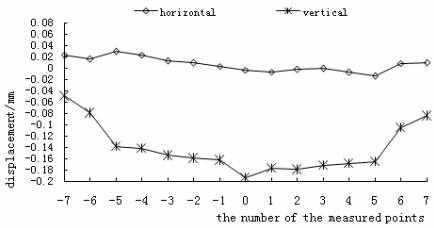

Fig.6 the displacements of the measured points by DDA

3.5 Effect of bolt reinforcement

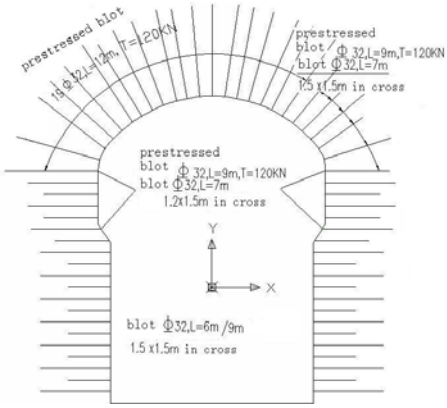

Fig.7 the plan of bolt in the powerhouse

7m and 6m normal blots and 9m prestressed bolt with a prestressing force of 120 KN are used for the reinforcement with the arrangement shown in Fig. 7. All bolts are 32mm in diameter. The bolts are numbered in clockwise direction.

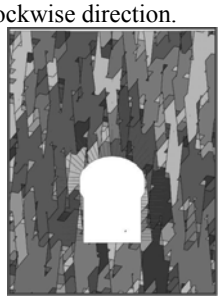

Fig.8 the result of combination 3 after anchorage

Fig.8 proves that after reinforcement the stability of the underground house improves, and there is only a few and small blocks without arched falling down. Among the 63 blots, the forces in only 9 blots are larger than 70kN, and they are in the roof and

downstream side. The largest one is 170kN, in the middle of the downstream side. And the forces in other blots are all under 50kN. The bolt tensions are all under the allowable limits, which shows bolt reinforcement is an effective way.

4. Conclusions

1) In this paper, the author firstly present the advantages of these two methods, then apply them together in the stability analysis of the underground powerhouse of Jinping Hydropower Station I. it use the key block theory's 3D advantage to fill up 2D-DDA's shortcomings; visa verse, it use 2D-DDA to get the displacement in order to offset key block theory's defect that it's only a rigid geometric way.

2)The result of key block theory showed that the blocks in the roof always firstly fall down if it is exposed without instant preventions, since its big volume and spread contact area. The blocks in upstream side is spread wide than those in downstream, so the upstream side destroyed more easily than the downstream side, but since the ones in downstream side is large in volume and contact areas, once slide occurs it may do a worse damage .And the result of DDA also find out the combination 3 is the most dangerous one, with the whole roof collapsing, and both walls damaged, especially the downstream side. This verifies the results by the key block theory,

3) After the bolt reinforcement is installed, the number of falling blocks reduced significantly, only a few blocks without bolt reinforcement fall. And all the tension stresses in bolts are under the limits which show the anchorage is valid.

4)However, this paper is only a basic discussion without taking many influencing factors into account, such as the two sets of faults, the character of the crack filling, and the interaction of underground cavities excavation and so on. The model will be modified further to consider all the factors.

References

Huang zhengjia, Wu aiqing, Sheng qian. Usage of block theory in Three Gorges Projects [J]. Chinese Journal of Rock Mechanics and Engineering. 2001，20（5）：648~652）

Liu Jinhua, Lu Zuhang. Block theory and its application to stability analysis of rock engineering [M]. Beijing：Water Resources and Electric Power Press,1988.(In Chinese))

Liu Jun， Kong Xiao-jing，Numerical simulation of behavior of jointed rock masses during tunneling and lining of tunnels. [J] Rock and Soil Mechanics, 2007，28（2）:321-326.)

Liu Jun, Li Zhongkui. Current situation and development of DDA method.[J]. Chinese Journal of Rock Mechanics and Engineering. 2004,23(5):839-845)

Mao Hai-he，Xia Cai-chu，Zhang Zi-xin,et al. Application of stereo-analytical method for blocktheory to the stability of longtan hydropower station underground power-house[J].Chinese Journal of Rock Mechanics and Engineering. 2005. 24(8): 1308 ~ 1314.

Shi G H., Discontinuous Deformation Analysis and Simulations of Discontinuous Media [M]. Translated by Pei Juemin. Beijing： TSI Press,1997.(In Chinese))

Wu Aiqing, Ding Xiuli , CHEN Shenghong ,et al. Researchers on Deformation and Failure characters of an underground powerhouse with complicated geological conditions by DDA method.[J]. Chinese Journal of Rock Mechanics and Engineering. 2006,25(1):1-8)

Wu Aiqing, Zhu Hong, Li Xinguang.A method for block stability analysis considering a general water pressure distribution model acting on the block surfaces[J].Chinese Journal of Rock Mechanics and Engineering 2000，6（z19）：936~940

Wu Yue, Wang Zemin Xu Shaoquan. Discontinuous Deformation Analysis and Its Application to the Deformation Forecast of Dangerous Lianziya Cliff. [J]. Geomatics and Information Science of Wuhan University 2003.28（5）：573-576)

Xue Xicheng，The Planar Analysis of Initial Stress Field within the Area of Lubuge Underground Hydropower House[J]， Chinese Jounal of Geotechnical Engineering，1986，8（5））

Zhang Qihua, Wu Aiqing, Shi Genhua. Application of Key Block Theroy to analysis of rock stability for underground plant in Baise hydroproject [J]. Chinese Journal of Rock Mechanics and Engineering. 2004,23(5):2609-2614)

A simulation technology of deformable objects using Numerical Manifold Method

TINGTING LIU, XISHENG FANG, and WANG YING

College of Computing and Communication Engineering
Graduate University, Chinese Academy of Sciences
Beijing 100049, China

Deformable objects simulation and animation, which is widely used in CAD/CAM, surgery simulation and computer games, has been an issue of computer graphics. A mechanical model uniformly including continuous constrains such as gravity and discontinuous constrains resulting from collisions with other objects has not been developed. It becomes a bottleneck of precise analysis following Newton's Law. This paper develops a general mechanical model making use of the advantage of numerical manifold method. This model solves a global equation including continuous and discontinuous constrains and can compute collisions efficiently and accurately for deformable objects.

Keywords: Numerical manifold method; Continuous deformation; Contact; Finite covers

1. Introduction

Deformable objects seem to have gained increasing interest during recent years. Objects in real life all seem to be deformable at some level. Deformable objects simulation has important applications in biomedical engineering, surgery simulation and computer games. Because CPUs and GPUs today are both advanced and powerful, it is possible to simulate and animate deformable objects interactively.

In 1987 Terzopoulos et al. presented a continuum model for simulating elastic curves, surfaces, and solids, which pioneered the field of computer graphics by introducing physically-based simulation. In the following year three models have been developed including finite difference, finite element and mass-and-spring lattice models. Now FEM has been a significant method for flexible simulation. In 1989 Gourret et al. advocated the FEM for simulating a human hand grasping a ball, and in 1992 Chen et al. used the FEM for muscle simulation. An implicit finite element method was used to simulate elastic solids in contact (Hirota 2001). They used this method for simulating the muscles in a bending knee. Significant effort has been placed into accelerating FEM calculations including recent approaches that precompute and cache various quantities (Mulla 2001), modal analysis (Chen 1992), and approximations to local rotations (Debunne 2000).Contact handling of non-penetrating elastic objects is the key in simulation. In traditional methods, contact forces are often defined as discontinuous functions of deformation, which leads to poor convergence characteristics. This problem becomes especially serious in areas with complicated self-contact. This paper will present a new modal called "numerical manifold method" for the dynamics of deformable objects that covers contacts and continuous deformation as well as free motion.

2. Numerical Manifold Method

Based upon mathematical manifold, this numerical manifold method is a newly developed general numerical method. This method computes the movements and deformations of structures or materials. The meshes of the numerical manifold method are finite covers.

These physical meshes provide the means to consider both jointed and continuous materials, and even different material phases (i. e. solid, gas or liquid). A brief listing of a few of the advantages of the manifold method follows: (1) free surface and flexible boundaries; (2) analysis not hindered by boundary conditions; (3) free form elements (any shape); (4) conservation of energy; (5) obeys Coulomb's law; (6) very small to very large deformation; (7) static and dynamics possible; (8) analytically correct; (9) continuous and discontinuous analysis (Gen-hua Shi 1997).

2.1 Finite covers

The mathematical mesh is chosen by users, consists of finite overlapping covers which occupy the whole material volume. The conventional meshes and regions, such as regular grids, finite element meshes or convergent regions of series, can be transferred to finite mathematical covers.

The physical mesh includes the boundaries of the material volume, joints, blocks and the interfaces of different material zones. The physical mesh represents material conditions which can not be chosen artificially.

The physical cover system is formed by both mathematical covers and physical meshes. It is the materials contained in the mathematical cover.

We will introduce finite covers formed by finite element nodes and physical boundaries. In fig. 1, the mathematical cover V1 of node 1 has only one element 1 2 3. The mathematical cover V2 of node 2 has three elements1 2 3, 2 4 5 and 2 5 3, and the mathematical covers V3 and V5 of node 2 and node 3 also have three elements including the node. The nodes 4 and 6 have one element. The physical cover of V1 has only one 11. The mathematical covers V2, V3, V4, V5, V6 are divided into two physical covers by the boundaries and joins.

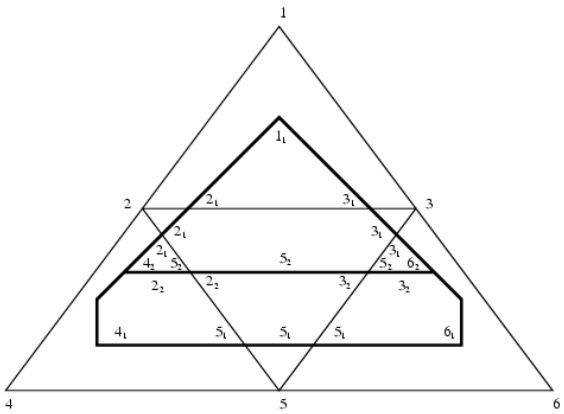

Fig. 1: The finite covers of numerical manifold method

Under manifold method, the "elements" and "nodes" here are the extensions of their FEM counterparts. The elements of the manifold are the common regions or the intersections of the physical covers. The nodes of the manifold method are the physical covers. Using the new nodes and elements, the joints can open and slide, the blocks can move away and the continuous area of the material body can still be connected. In fig. 1, the only joint inside the material divided completely the material to two disconnected parts, and any manifold element divided by this joint have completely different nodes or physical cover numbers. Therefore the two manifold elements are free to move independently (Shi 1997).

2.2 Contact theory

Manifold method processes the contact problem in the material boundaries or joints. The forces between two contact faces obey Coulomb's law, and no tension and no penetration can be allowed between blocks. When the penetration between two blocks happens, we can add very stiff springs or penalties to lock the movement in one or two directions. The global equations have to be solved repeatedly while selecting the lock or constraining positions. Using this method, even a block system with tension and penetration can be corrected by the selection of lock positions a few times. The contact force can be computed precisely in manifold method.

3. The deformation simulation

Our main idea is to simulate flexible objects without imposing restrictions on shape or geometrical environment using the manifold method. Essentially speaking, we use the extended finite element method which makes use of finite cover approach compared with the traditional finite element method, because we use the finite element mesh as the mathematical covers. Using the finite cover systems, continuous or discontinuous materials can be computed in a mathematically consistent manner. Furthermore, the model has the theory processing collision detection and contact response.

The first step is the generation of physical mesh. We just viewed the boundaries and joints of all geometric models in the environment as the physical mesh. We can found geometric models using the tools such as 3Dsmax, Maya and AutoCAD. Then, we use finite element mesh as mathematical cover. An often-used tessellation for surfaces is a triangular mesh. The corresponding tessellation for volumes is a tetrahedral mesh.

3.1 Elastic objects with Manifold Method Models

Manifold method like finite element method is a procedure for obtaining numerical approximations to the solution of boundary value problems. The general idea is to formulate a deformation of a solid as formula (1),

$$ku = f \tag{1}$$

where k is a symmetric, positive definite, stiffness matrix, u is a vector of nodal displacements, and f is a vector of external node forces. The goal is to solve for the value of u. To simplify the problem, the entire computational domain is replaced by the union of disjoint subdomains. These subdomains are the intersections of the physical covers. In computer animations, the Linear Elastostatics Model is typically used. It uses the following assumptions: (1) The deformations involved are small, in which case the relationship between stress and strain are well approximated by a linear model; (2) Only elastic materials are considered, thereby ignoring the viscous stress; (3) Only isotropic materials are considered, which implies that elasticity matrix can be described by two parameters only. (4) The object is in static equilibrium, which allows us to ignore inertia forces. The relationship between stress and strain, is given by formula (2),

$$\begin{Bmatrix} \delta_x \\ \delta_y \\ \tau_{xy} \end{Bmatrix} = \frac{E}{1-\nu^2} \begin{pmatrix} 1 & \nu & 0 \\ \nu & 1 & 0 \\ 0 & 0 & \frac{1-\nu}{2} \end{pmatrix} \begin{Bmatrix} \varepsilon_x \\ \varepsilon_y \\ \gamma_{xy} \end{Bmatrix} \qquad (2)$$

where E is young's modulus. Young's modulus is a measure of instretchability, such that a large Young's modulus implies that the material is hard to stretch. The coefficient $-1<\nu\leq 1/2$ is the Poisson's ratio, and it is only in rare instances negative. The Poisson's ratio describes how much a material contracts in the direction transverse to stretching. Typical values are 1/2 for incompressible materials such as rubber, 0.33 for steel, and almost 0 for rock.

3.2 Contact handling

The complexity of a contact problem depends on the type of contact. There are two distinct classes of problems - the two-body contact problem and the self-contact problem. In most engineering applications, the deformations of those nearly-rigid parts are not large enough to cause self-contact unless the purpose of the simulation is to analyze the destruction of the mechanical structures. Therefore, many algorithms are designed exclusively for two-body problems. In biomechanical applications, on the other hand, the building materials are often very flexible; hence there are more chances for self-contact.

Manifold method applies stiff springs on contacts. There are normal stiff springs and shear stiff springs. If friction coefficient is not zero, a pair of shear sliding forces is added possibly. There are three modes: open, sliding, lock for every contact. In open mode, the component of contact Rn along the normal of the edge is tensile, and no lock or stiff springs are applied. In sliding mode, the normal component Rn of the contact force is compressive and the shear component of Rs of the contact force along the reference line is large enough to cause sliding, and a stiff spring normal to the reference line is applied to allow the sliding to take place along the angle of the reference edge. Here, a pair of frictions is applied in the sliding direction. In close mode, the normal component Rn of the contact force is compressive and the shear component of Rs of the contact force along the reference line is less than that from Coloumb's law. Here, the contact point is fixed or both directions are locked and there is no sliding allowed. Within each time step, the global equations have to be solved repeatedly while selecting the lock positions. This process is called open-close iterations. We need judge the mode to add or remove stiff springs when each step iteration starts. The computation of manifold method follows time steps. The closed contact points should go to next time step and find new representing contacts. The closed contacts of the previous time step will be transferred to the next time step, if the contacts are found in the same contact position.

4. Examples

In order to illustrate the manifold method technique, we simulate several examples using simple isotropic linear elasticity to calculate the stress. The results are shown in fig. 2, fig. 3 and fig. 4. In fig. 2, the material of the elastic object is young's modulus E 5 and the Poisson's ratio ν 0.24. The one end of the object is fixed and the other end is added a point load to. The object is unfolded following the time steps. The process includes the contact between the same object. In fig. 3, a rigid ball collapses into a square consisting of several little elastic blocks, and there are joints in the right green block. The material of the elastic blocks is young's modulus E 150 and the Poisson's ratio ν 0.24. Otherwise, we add a rightward point load to the right green block. The process includes contacts between different blocks and contacts between joints of the same block. In fig. 4, a plastic sphere is pulled through rigid running gears. The material of the sphere is young's modulus E 0.5 and the Poisson's ratio ν 0.5. These figures show that the contact is non-penetrable and this method is fit for the deformable objects with joints and the contacts between the deformable objects.

(a)

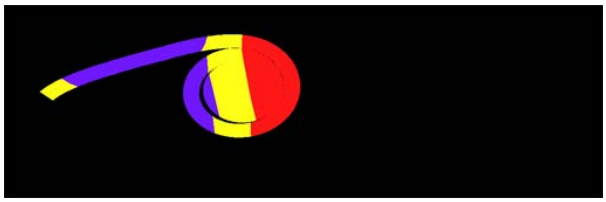

(b)

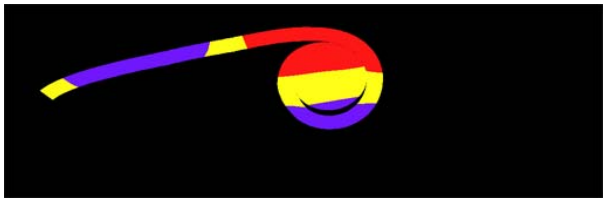

(c)

(d)

Fig. 2: A elastic object is being unfolded.

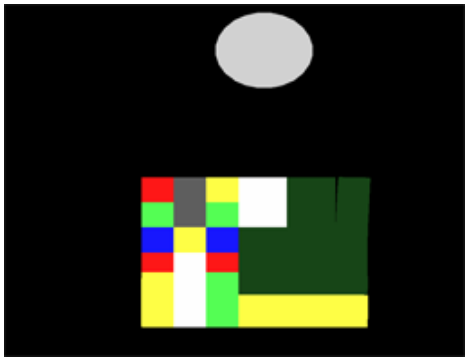

(a)

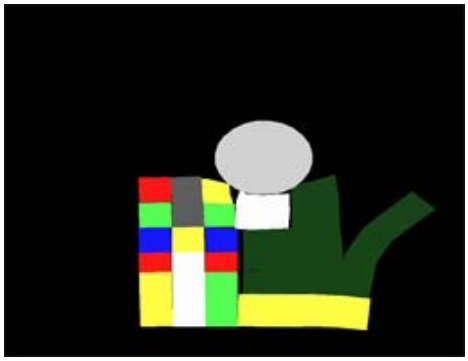

(b)

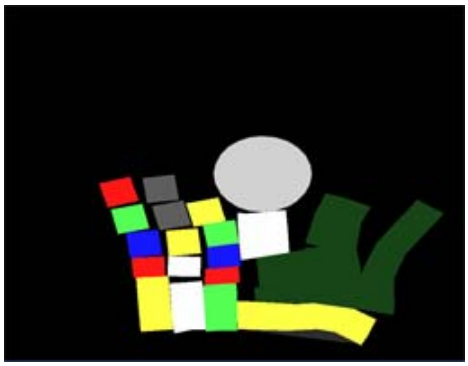

(c)

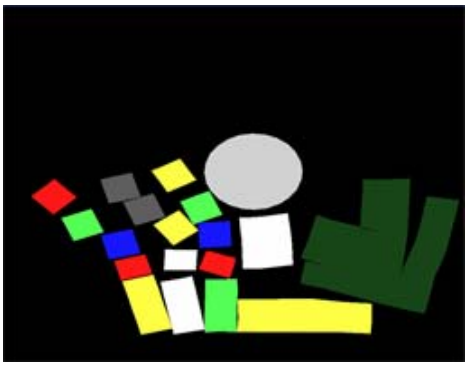

(d)

Fig. 3: A ball collapses into a square consisting of several little elastic blocks, and there are joints in the right green block.

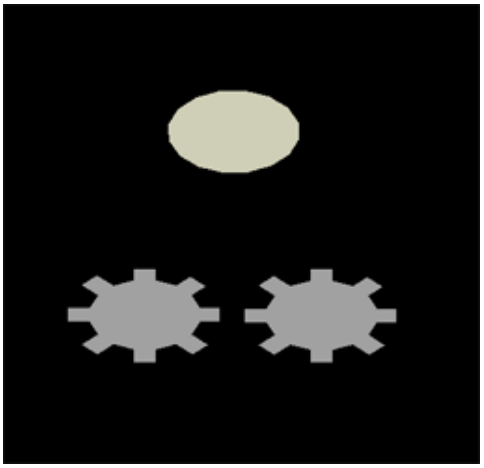

(a)

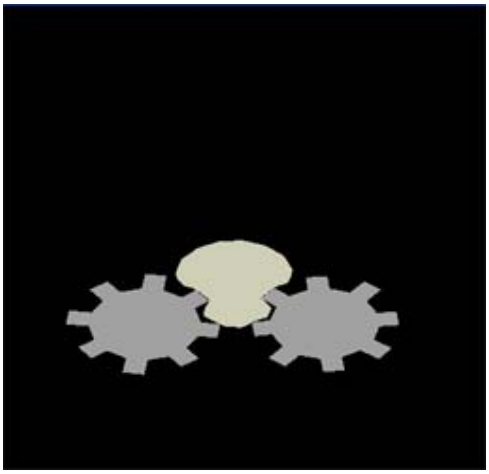

(b)

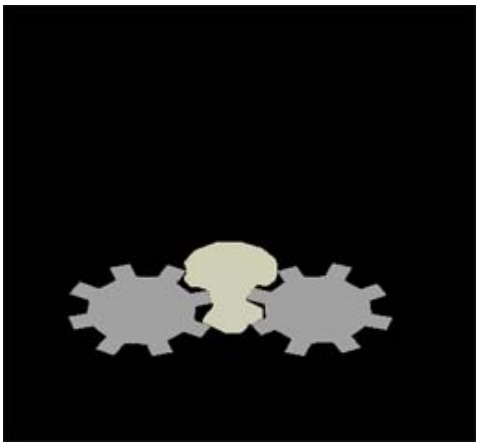

(c)

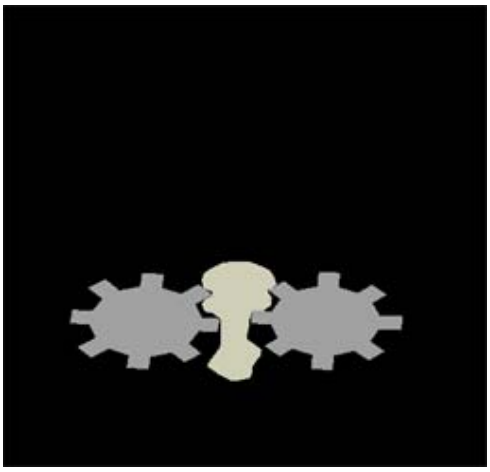

(d)

Fig. 4: A plastic sphere is pulled through rigid running gears.

5. Conclusions

Numerical manifold method introduces a new idea “the finite cover system” to handle contacts between surfaces. Continuous and discontinuous deformation can be computed in a mathematically consistent manner using the finite cover system. Furthermore, FEM for continua is a special case of this numerical manifold method. In the current development stage of numerical manifold method, by using finite cover approach, the extended finite element method can compute more flexible and visible deformation and movement. We have demonstrated this method for flexible objects simulation which can cover contacts and continuous deformation as well as free motion. We have implicated the simple isotropic linear elasticity in two dimensions. The method presented unifies the continuous and discontinuous deformation, and have the advantages at contact problem.

References

Chen, D. T. and Zeltzer, D.. Pump it up: computer animation of a biomechanically based model of muscle using the finite element method. In *Proceedings of the 19th annual conference on Computer Graphics and Interactive Techniques*, ACM Press, 1992, 89-98.

Debunne, G., Desbrun, M., Cani, M.-P., and Barr, A.. Adaptive simulation of soft bodies in real-time. *In Comput. Anim.* Philadelphia, USA, 2000, 133-144.

Gen-hua Shi. *Numerical Manifold Method and Discontinuous Deformation Analysis*[M]. Jue-ming Pei translated. Beijing: Tsinghua University Express, 1997, 3-89.

Gourret, J. P., Magnenat-Thalmann, N., and Thalmann, D.. Simulation of object and human skin deformation in grasping task. *Computer Graphics*, 1989, 23(3):21-31.

Hirota, G., Fisher, S., State, A., Lee, C., and Fuchs, H.. An implicit finite element method for elastic solids in contact. *In Computer Animation,* Seoul, South Korea, 2001.

Muller, M., McMillan, L., Dorsey, J., and Jagnow, R.. Real-time simulation of deformation and fracture of stiff materials. *In Comput. Anim. and Sim. '01*, *Proc. Eurographics Workshop*, Eurographics Assoc, 2001, 99-111.

Terzopoulos, D., Platt, J., Barr, A., and Fleischer, K.. Elastic deformable models. *In Computer Graphics*, 1987, 21(4): 205-214.

Study on geometrical identification of stochastic block in block theory

ZHANG QIHUA and WU AIQING
Key Laboratory of Geotechnical Mechanics and Engineering of Ministry of Water Resources, Yangtze River Scientific Research Institute, Wuhan 430010, P. R. China

Since the block theory was brought forward by Goodman and Shi in 1985, it has been becoming an important tool in rock engineering stability analysis as more and more researches and applications were performed. As we all know that discontinuities in rock mass develop statistically, that is, their geometrical parameters like trace length, spacing and orientation are probabilistic. So the blocks cut by discontinuities must be stochastic, that means the shapes, sizes and locations of blocks are stochastic. The paper put forward the methodology for geometrical analysis of stochastic block based on three-dimensional simulating network of discontinuities by using geometry, statistics and computer knowledge. Moreover, on the basis of the results of geometrical analysis, the statistic properties of size, average size and overlaying ratio (of blocks' planes area in surface to excavation surface area) of stochastic blocks can be analyzed, in order to recognize the features of stochastic blocks, estimate quantitatively harmfulness of key blocks and help to design support. These researches will be introduced later.

The paper first summarizes systematically the researches of simulating network of discontinuities, tree cutting, primary loops finding, and analysis of the probable maximum region of blocks. Then, with the proposed approach of combination of intersections of joint traces, the realistic 3-D stochastic blocks are identified. The systematic processes of stochastic block identification are sketched. Some other problems are studied such as searching the blocks located in the edge of slope surfaces or the roof of tunnel, so as to form the approach of geometrical identification of stochastic block in slope and tunnel. Case studies indicate the geometrical analysis of stochastic block can meet the needs of practical engineering analysis pretty well and give some meaningful results.

Keywords: Block theory; Stochastic block; Simulating network of discontinuities; Geometrical identification

1 Introduction

Rock masses are composed of rock blocks and discontinuities generally. Discontinuities including faults, joints, bedding planes, fractures, etc, divide rock mass into blocks with various sizes and shapes. Discontinuities may vary greatly in different rock masses. Rock deformation and failure often result from opening, closing and shearing of discontinuities, which control rock mass stability hereby.

The block theory was proposed by Goodman and Shi (1985). Classical block theory assumes discontinuities as infinite plane, blocks cut by discontinuities and excavation surface(s) as rigid bodies, analyzes the removability of block by using geometry and topology methods, determines the probable unstable block or key block by incorporating comparatively simple mechanics analysis, and studies support forces of key blocks. Block theory has been studied and applied widely in rock engineering from then on.

Discontinuities can be grouped into major and minor discontinuities simply. The geometrical and mechanical properties of the former, such as faults, are deterministic. The geometrical and mechanical properties of the latter represented by joints, are probabilistic generally. The research work in this paper focuses on joints. The terms of joints and discontinuities may be used arbitrarily in the paper. The locations, sizes, shapes of block cut by joints must be probabilistic accordingly. So stochastic block

analysis has been proposed and studied (Shi & Goodman 1989; Wu et al 1991; Hatzor 1993; Goodman 1995; Shi 2002; Zhang 2004).

From literature review, we can describe stochastic block analysis by the following steps. (1) modeling 3-D probabilistic network of discontinuities by using Monte Carlo and computer technologies, based on geostatistic analysis of orientations, trace lengths, spacings of discontinuities; (2) identifying the stochastic blocks from 3-D modeling network of discontinuities by using block theory and geometry; (3) calculating blocks' volume, area of blocks' planes and overlaying ratio of blocks' faces area to excavation face area, analyzing them statistically so as to recognize the inherent geometric features, estimate quantitatively hazardousness of stochastic blocks and help to design rock block support (Zhang 2004). In the paper, the methodology of identifying of stochastic blocks from modeling network are introduced and discussed in detail, which is called as geometrical analysis of stochastic block. On the other hand, analyzing block size, average size and overlaying ratio statistically will be introduced by the other paper, which is called as statistical analysis of stochastic block correspondingly.

Polar equal-area plot, scanline (Priest & Hudson 1976, 1981) and sampling windows (Kulatilake & Wu 1984) were developed to infer statistic distribution models of orientations, trace lengths and spacings of discontinuities. Based on the statistic distributions, by employing Monte Carlo simulating methods, discontinuities network can be modeled (Wu et al 1991; Zhang 2004; Kulatilake et al 1993).

Based on modeling of discontinuities network, stochastic blocks can be identified. Some literatures identified stochastic blocks in 2-D. Shi & Goodman (1989), Wu et al (1991) and Shi (2002) identified stochastic blocks in 3-D with the processes of generating joint trace map, tree cutting, finding primary loops in the unrolled joint trace map, and delimiting maximum probable regions of blocks. So there was an implicit assumption that joints having traces in the excavation surfaces extend far enough so as to form block by their mutual intersections. However, maximum probable regions of blocks are not the same as the true 3-D blocks in fact, due to the finite extents of joints. All in all, the 3-D stochastic block identifying from modeling network of discontinuities should be studied further.

The paper proposes an approach for identification of 3-D stochastic block based on the methods by Shi & Goodman (1989) and Wu et al (1991). A few case studies are illustrated with the new approach.

2 Main procedures of geometrical analysis of stochastic block

Processes of geometrical analysis of stochastic block are shown in Fig.1. The main analysis processes are discussed as follows.

2.1 Statistic analysis of discontinuities geometrical parameters

Some geostatistic methods and statistic distributions of orientations, extents and spacing of discontinuities are summarized briefly as follows in here.

The shape of discontinuities is assumed as typical geometric figure before network modeling. Snow (1970), Baecher (1978) and Barton (1978) assumed the shape of discontinuities as circular or ellipse disk. Pan (1989) summarized some typical models of discontinuities shape. In general, circular disk is used in discontinuities network modeling for the sake of simplification, so does the present paper.

Polar equal-area projection is usually used in statistic analysis of discontinuities orientations and clusters. Literatures showed hemispherical normal distribution, normal distribution or log-normal distribution are suitable to represent the statistic distributions of discontinuities orientations.

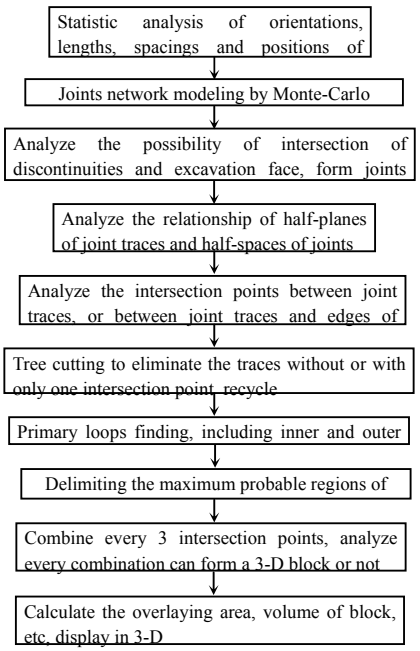

Fig.1 Main procedures of geometrical analysis of stochastic block

Scanline survey is used usually to analyze statistically discontinuity spacing. Research results showed the negative exponential distribution is most suitable for describing the statistic distribution of discontinuity spacing.

Scanline and sampling windows are used often in statistic analysis of discontinuity trace length. Research results indicated both gamma and negative exponential distributions are suitable for describing the statistic distribution of trace length.

Locations of discontinuities, i.e., the centers of circular disk fit uniform distribution.

Since the discontinuities geometry pattern may vary statistically from one to another rock mass region, different homogeneous regions should be segmented, then statistic analysis of locations, orientations, trace lengths and spacings of discontinuities are performed in different homogeneous regions.

2.2 Monte-Carlo modeling of 3-D discontinuities network

3-D discontinuities network modeling can be carried out according to probabilistic distributions of geometric parameters of discontinuities, i.e., location, orientation, spacing and trace length. Discontinuities are assumed as circular disks located randomly in 3-D space. Every discontinuity is determined by a set of parameters: dip direction, dip, radius and coordinates of disk center.

If the orientation of discontinuities is assumed to fit normal distributions, the maximum likelihood estimators of mean μ and variance σ are:

$$\mu = \frac{1}{n}\sum_{i=1}^{n} X_i \text{ , } \quad \sigma^2 = \frac{1}{n}\sum_{i=1}^{n}(X_i - \mu)^2 \tag{1}$$

Where, X_i is the observations (a sample) of random variable X which represents the dip and dip direction here. Variable X can be obtained by solving equation (2):

$$X = \mu + (\sqrt{\frac{12}{n}}\sum_{i=1}^{n}\theta_i - \frac{\sqrt{12n}}{2})\sigma \tag{2}$$

Where, θ_i is the uniform random variable which can be obtained by computer; n is integer and can be set as $n = 36$.

Log-normal variable X can be obtained by solving equation (3):

$$X = \exp(\mu + (\sqrt{\frac{12}{n}}\sum_{i=1}^{n}\theta_i - \frac{\sqrt{12n}}{2})\sigma) \tag{3}$$

Where, the maximum likelihood estimators of μ and σ can be obtained by equation (4):

$$\mu = \frac{1}{n}\sum_{i=1}^{n}\ln(X_i) \text{ , } \sigma^2 = \frac{1}{n}\sum_{i=1}^{n}(\ln X_i - \mu)^2 \tag{4}$$

Negative exponential distribution is suitable for representing the distributions of spacings or trace lengths of discontinuities. Negative exponential variable can be obtained by solving equation (5) depending on a single parameter μ:

$$X = -\mu \ln \theta_i \tag{5}$$

μ is the mean of variable X and can be estimated by X_i using equation (1).

The mean of discontinuity radius r_j of the *i*th discontinuities set can be calculated by equation (6) as discontinuities assumed as circular disks:

$$r_i = 2l_i / \pi \tag{6}$$

Where, l_j is the mean of trance length of the *i*th discontinuities set.

Volumetric frequency of the *i*th discontinuities set λ_i can be expressed as follows (Wu 1993):

$$\lambda_i = (2\pi \cdot s_i \cdot r_i^2)^{-1} \tag{7}$$

Where, s_i is the mean of discontinuity spacing of the *i*th discontinuities set.

If the volume of the considered slope or cavern is determined, then take a region big enough whose boundary is bigger than slope or cavern boundary as 3~5 times mean trace length. In the region, the number of discontinuities N is:

$$N = V_b \cdot \sum_{j=1}^{m}\lambda_j \tag{8}$$

Where, V_b is the volume of the region; m is the number of the discontinuity sets.

Assuming the positions of the circular disks are represented by uniform distribution, we can determine the locations of the center of every discontinuity by employing Monte-Carlo simulation according to the discontinuities number N.

Hereto, the 3-D geometric information of discontinuities is determined. With respect to the deterministic discontinuities such as faults, their information can be input directly to form 3-D modeling network of discontinuities.

2.3 Joint trace of discontinuities

According to statistic distributions of discontinuity geometric parameters and Monte-Carlo simulation, 3-D network of discontinuities can be generated. Then, by judging every discontinuity disc intersect excavation surface(s) or not, if yes, it must have a

trace in excavation surface(s), so we can obtain the trace map of discontinuities. Fig.2 is the trace map of one simulating test of 3 joint sets.

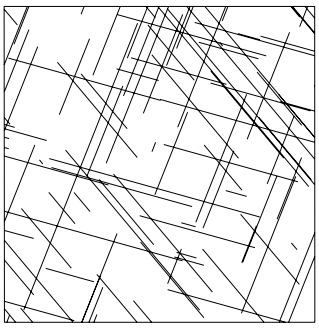

Fig.2 Joint traces in excavation surface

2.4 Relations between half-plane of trace and half-space of joint

In the block theory, joint pyramid is denoted by a string of binary digits. The number 0 defines the half-space above a plane, the number 1 defines the half-space below a plane. Thus number 110 denotes the joint pyramid which is simultaneously below plane 1, below plane 2 and above plane 3. Block is the intersection of joint pyramid and excavation plane.

However, joint trace map is two dimensional relative to open face of typical direction, but the joint pyramid is three dimensional. In order to search a certain kind of block formed by the particular JP codes from the joint trace map, relations between half-plane of trace and half-space of joint has to be determined.

Firstly, let us establish the local coordinate of a plane. As shown in Fig.3, $\vec{X}$, $\vec{Y}$, $\vec{Z}$ are the three axes of the global coordinate. Three axes $\vec{A}_1$, $\vec{A}_2$, $\vec{A}_3$ of the local coordinate of a plane can be calculated by equations (9), (10), (11) (Zhang 2004):

$$\vec{A}_3 = \vec{F} \tag{9}$$

$$\vec{A}_1 = \vec{Z} \times \vec{F} \tag{10}$$

$$\vec{A}_2 = \vec{A}_3 \times \vec{A}_1 \tag{11}$$

Where, $\vec{F}$ is upward normal vector and can be calculated according to the inclination of the plane. $\vec{Z} = \{0 \quad 0 \quad 1\}$.

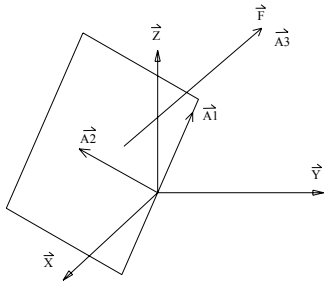

Fig.3 The relationship between global and local coordinate

Then, the issue can be discussed. As shown in Fig.4, P_0 denotes excavation plane, $\vec{A}_2$ denotes an axis of local coordinate of the excavation plane. P_i denotes a joint, $\vec{n}_i$ is its unit normal vector inclines upward. E_1E_2 is the joint trace in excavation plane.

Within plane P_0 , if $\vec{n}_i \cdot \vec{A}_2 > 0$, the upper/lower half-plane of E_1E_2 is corresponding to the upper/lower half-space of P_i . If $\vec{n}_i \cdot \vec{A}_2 < 0$, the upper/lower half-plane of E_1E_2 is corresponding to the lower/upper half-space of P_i .

After establishing the relations above, the spaces of the joints which form block can be expressed by the half-planes of the corresponding joint traces. So block searching from the joint trace map becomes possible.

Half-plane of joint trace can be signified by "trace direction" which can be defined by oriented segment of two vertexes of the trace. Within local coordinate system, trace direction is anticlockwise. In Fig.4, $\overrightarrow{E_1E_2}$ indicates upper half-plane, then $\overrightarrow{E_2E_1}$ indicates the lower half-plane, with the equation $\overrightarrow{E_1E_2} = -\overrightarrow{E_2E_1}$.

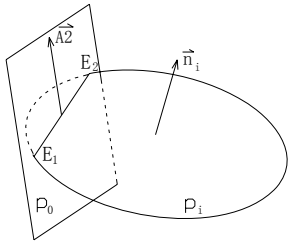

Fig.4 Sketch of relations between half-plane of trace and half-space of joint

2.5 Tree cutting, primary loops finding

Tree cutting and primary loops finding were discussed by Shi (1989). Now the meaning of tree cutting and primary loops finding is introduced briefly in here.

The purpose of tree cutting: before stochastic blocks identifying, eliminate the traces without or with only one intersection point, analyze cyclically until traces

intersect with each other.

Primary loops finding: start from an intersection (starting point), find the next adjacent point according to the sorting order of direction angles of every intersection connected with the starting point. Then take the next adjacent point as the starting point, find its next adjacent point. Iterate the processes until the loops are closed. During the loops finding, every trace segment is found back and forth twice, which means the directions of different loops in the same segment are reversed.

There are 2 kinds of closed loops, inner loops with intersections connected anti-clockwise, and outer loops with intersections connected clockwise. Inner loops are smallest, which also named as basic loops, do not contain lines or closed loops. Outer loops are the biggest loops of contiguous region. Fig.5 shows the closed loops corresponding to Fig.2.

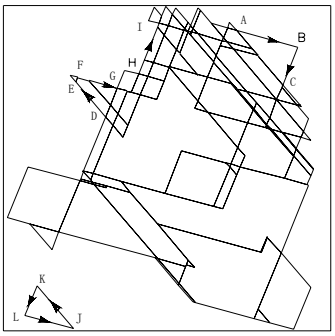

Fig.5 Closed loops

2.6 Maximum probable regions of blocks

Maximum probable regions of stochastic blocks can be identified through the closed loops. Along the outer loops, when "the segment direction" of adjacent intersections is identical to "joint trace direction", this segment is deleted, then the other segments of the inner loop relative to this segment is set as the outer loop segment. This procedure has to be carried out for all outer loops and iterate until no more segment can be deleted.

The maximum probable regions of stochastic blocks identified are shown as Fig.6.

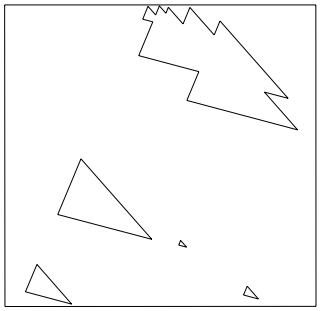

Fig.6 Probable maximum region of stochastic blocks

2.7 3-D blocks identification

Maximum probable regions of stochastic blocks are recognized in 2-D excavation face. But the joints are not always long enough to form the closed blocks in 3-D. Maximum probable regions of stochastic blocks are not the same as real blocks occurrence as the joints are finite.

Tetrahedron formed by three discontinuities and one free face is the most common style in practical engineering and easy to be studied. Blocks formed by more than three discontinuities (with free face) occur seldom and often overlap wholly or partially with the tetrahedron. So, analysis tetrahedron can meet the needs of most engineering applications.

Stochastic blocks may locate within one free face, or in the edge or corner of free faces. The former means one free face engages in block cutting, the latter means two or more than two free faces do. Now the former is discussed, the later will be discussed subsequently.

Since stochastic blocks may overlap together, a loop may belong to two or more than two different blocks, the analyses become difficult.

The paper presents the approach named as intersections combination to identify the realistic 3-D blocks. Every three intersections which are within every probable maximum region of stochastic blocks are combined together. The combination may or may not be the three intersections of a realistic block in opening face. There are two ways to judge. One is as steps (1), (2), (3), (4) as follows, the other as steps (1), (4), (5).

Step1: Analyze whether every combination of three intersections is in three traces and closed, so to get the closed triangle.

Step2: Order the intersections of every combination. As shown in Fig.7, the directions of segment 12, 23, 31 after ordered are identical to the corresponding trace directions.

Step3: Analyze the rotation directions of intersections. Within local coordinate system, trace direction is anticlockwise by appointment, so the rotation direction of intersections of every combination is anti-clockwise also. From Fig.7 we know the left is correct and the right should be deleted.

Step4: Judge whether the corresponding joints of every combination intersect and calculate the intersection point, judge whether the distance between the intersection point and every joint center is smaller than the radius of every joint. If yes, the combination can form a realistic block which is the target we search.

Step5: Judge whether the intersection of joints is within the excavation space (within the rock mass). If yes, the combination is the target we search.

Related to Fig.2, Fig.5 and Fig.6, the stochastic blocks searched are shown in Fig.8 and Fig.9.

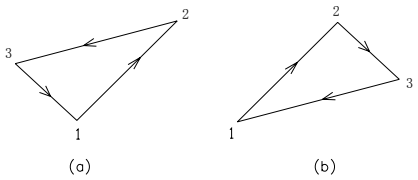

Fig.7 Rotation direction of intersections

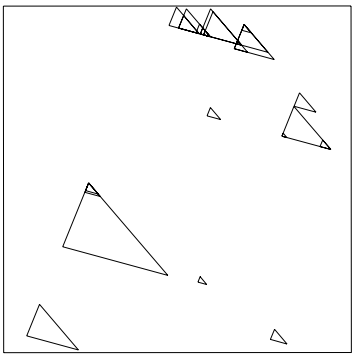

Fig.8 Stochastic blocks in excavation surface (2-D display)

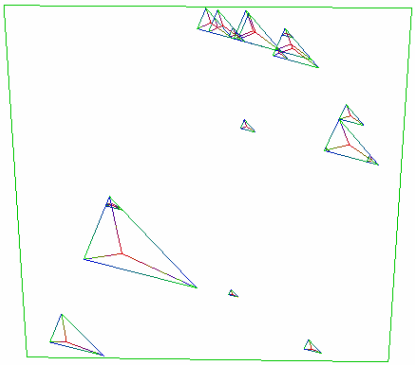

Fig.9 3-D stochastic blocks

2.8 Blocks searching located in the edge

Some block is situated on the edge of slope or tunnel. Fig.10 is the traces map of two adjacent surfaces of a slope. There are 4 stochastic blocks after searched, as shown in Fig 11.

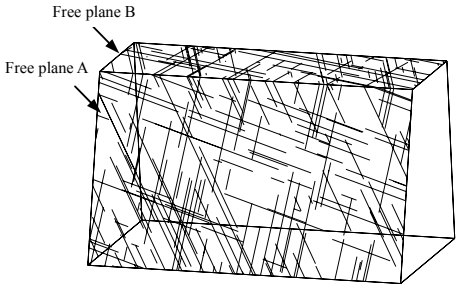

Fig.10 Joint traces map in two excavation surfaces

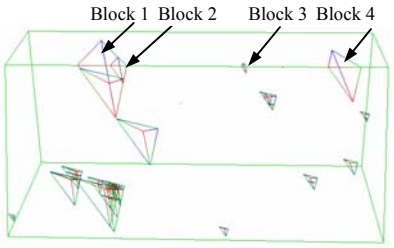

Fig.11 Stochastic blocks display (Including 4 blocks in the edge of two surfaces)

2.9 Blocks searching in the roof of tunnel

The searching procedure is omitted. The results are sketched with Fig.12 and Fig.13.

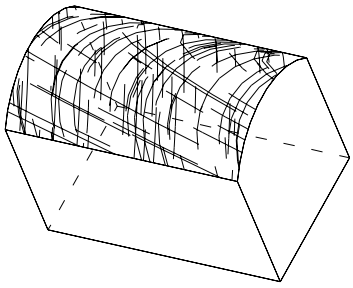

Fig.12 Joint traces in roof of tunnel

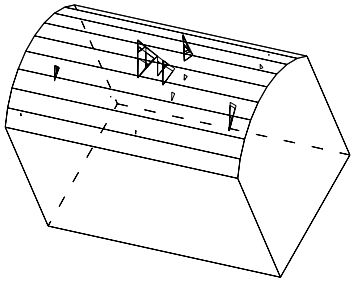

Fig.13 Stochastic block in roof

2.10 Computation of overlaying area of stochastic block

Based on the results of geometrical analysis, the sizes, average sizes and overlaying area of stochastic blocks can be computed, in order to evaluate quantitatively the possible failure of blocks and thus to help in support design.

Overlaying area is the area of face of stochastic block in free surface. Distribution of stochastic blocks in free surface is shown in Fig.14(d). Every triangle of different size is the face of stochastic block in free surface. Some stochastic blocks overlap, the bigger block embraces the smaller one (See Fig.9). The computation of overlaying area means to delimit the range of blocks in free face and compute it, so the area overlapped should not be computed repetitively.

The inner loops which belong to the stochastic blocks are identified, and the area of all these loops is computed. According to the meaning of inner loops, inner loops are smallest and do not contain other closed loops, loops must not overlap, an inner loop situates either within one (or some) stochastic block(s) or not. Therefore, repetitive computation of area of stochastic blocks is not necessary when the overlap can be avoided.

There are 31 stochastic blocks by computing inp Fig.14(d). By computation, the area of free face is 900m^2, the overlaying area of stochastic is 48.82m^2, so the overlaying ratio is 5.42%.

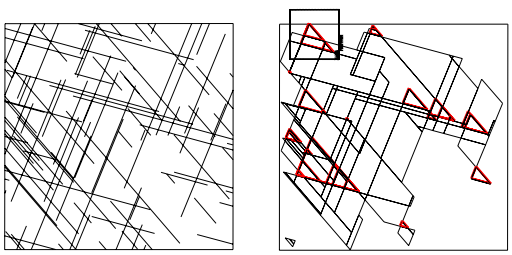

(a) (b)

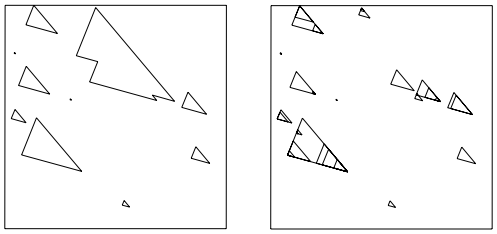

Fig.14 Overlay area of blocks in excavation surfaces (a) Joint traces; (b) closed loops; (c) Probable maximum regions; (d) stochastic blocks in excavation surfaces

3 Case study

One hydropower station is located in south China. The span of underground plant is 20.7m, the height and length of plant is simulated as 33m and 50m. The rock of plant region is dolerite. The geometrical parameters of joints in rock mass are shown in Tab.1. As the geological statistic analysis is not performed deeply enough, the variances of dip and dip direction are assumed as 2°, the other parameters are realistic. Dip and dip direction follow normal distribution, trace length and spacing follow exponential distribution.

Tab.1 Geometrical parameters of joints in rock mass

Joint set	Dip(°)		Dip direction(°)		Trace length(m)	Spacing (m)
	Mean	variance	Mean	variance	Mean	Mean
①	53	2	202	2	6.5	3
②	58	2	330	2	6	2
③	68	2	105	2	5	2.5

According to stereographic projection, JP 011 may form block with excavation surface in upstream wall of underground plant. The results of stochastic block searching are shown in Fig.15 of one test of Monte-Carlo simulation. By calculation of this time simulation, the overlaying ratio is 15.8%.

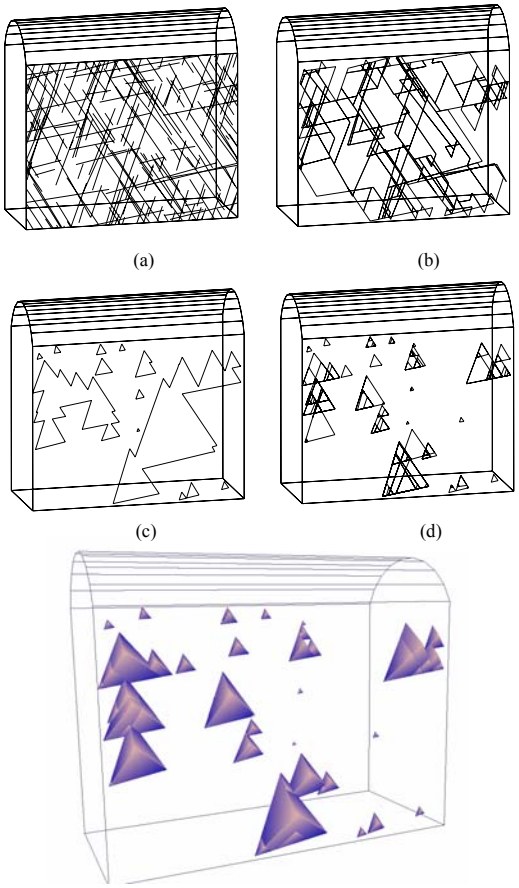

(a) (b) (c) (d) (e)

Fig.15 Stochastic block searching in underground plant

(a) Joint traces; (b) closed loops; (c) Probable maximum regions; (d) stochastic blocks in excavation surfaces; (e) Blocks shown in 3-D with OPENGL

Different results of stochastic block searching, i.e., the locations, sizes and overlaying area, are obtained with different simulation sample of joint system. With the other simulation test, the results are shown in Fig.16~Fig.19, in which the same joints network are used to form different joint traces map and to find the stochastic blocks in different excavation surfaces.

From Fig.16~Fig.19, we can find clearly that in the upstream wall, JP 011 forms blocks with excavation face, yet in the downstream wall, JP 100 does. In the left wall, JP 110 forms blocks with excavation face, yet in the right wall, JP 001 does. In the roof, JP 111 forms blocks with excavation face, yet in the floor, JP 000 does. This phenomenon is concerned a general proposition in block theory. Stochastic blocks in the upstream and downstream walls are much more numerous (developed) than in the left and right walls. The blocks in the left and right walls are much more slender than in the upstream and downstream walls.

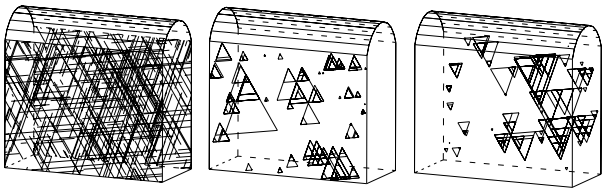

(a) (b) (c)

Fig.16 Stochastic blocks searched in the upstream and downstream walls of underground plant

(a) Joint traces map (b) block 011 in the upstream wall (c) block 100 in the downstream wall

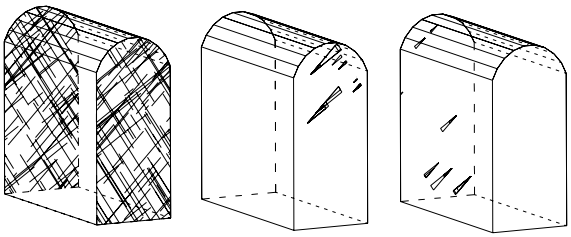

(a) (b) (c)

Fig.17 Stochastic blocks searched in the left and right walls

(a) Joint traces map (b) block 110 in the left wall (c) block 001 in the right wall

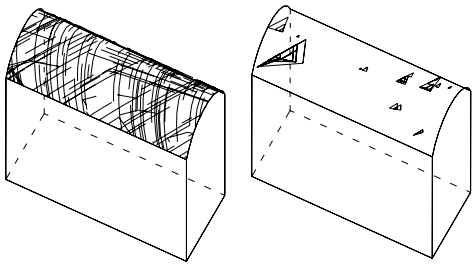

(a) (b)

Fig.18 Stochastic blocks searched in the roof

(a) Joint traces map (b) block 111 in the roof

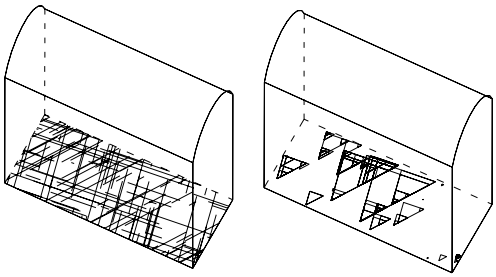

Fig.19 Stochastic block searched in the floor

(a) Joint traces map (b) block 000 in the floor

So the blocks in the upstream and downstream

walls should be paid more attentions. Stereographic projection with no consideration of joint cohesion by Shi's program shows the blocks in the upstream wall are key blocks, the sliding mode is single-face. So the systematic anchor is necessary in the upstream wall. While the blocks in the downstream are more stable as the sliding mode is double-face.

As different simulating tests give different results, the support measures can not be suggested with only one time test. Statistic analysis based on the results of stochastic block geometrical identification can yield the distributions of the size, the average size and the overlaying ratio of stochastic block with dozens of or hundreds of simulation tests. So the quantitative analysis of spacing and length of anchor can be implemented.

4 Concluding remarks and future work

The paper studies geometric identification of 3-D stochastic blocks. Main analysis processes are outlined, with some key steps are discussed in detail. Case study indicates the geometrical identification of stochastic block proposed in the paper can meet the needs of practical engineering analysis pretty well and give some meaningful results.

Based on the results of stochastic block geometrical identification, statistic analysis can yield the distributions of the size, the average size and the overlaying ratio of stochastic block. These results can be used to instruct support design and evaluate the possible damage or failure of stochastic block. These researches will be introduced in future.

Acknowledgements

The research in the paper is supported by the Chinese Natural Science Foundation (No.50509003).

References

Goodman R. E., Shi G H. Block theory and its application to rock engineering, *Englewood Cliffs, New Jersey: Prentice-Hall, Inc.*, 1985

Goodman R.E. Thirty-fifth Rankine lecture: Block theory and its application. *Geotechnique*. 45(3): 383~423, 1995

Hatzor Y. The block failure likelihood: A contribution to rock engineering in blocky rock masses. *Int. J. Rock Mech. Min. Sci. & Geomech. Abstr*..30(7): 1591-1597,1993

Heliot D. Generating a block rock mass. *Int. J. Rock Mech. Min. Sci. & Geomech. Abstr*, 25(3): 127~138, 1988

Kulatilake P. H. S. W., Wathugala D. N., Stephansson O. Joint network modeling with a validation exercise in Stripa mine, Sweden. . *Int. J. Rock Mech. Min. Sci. & Geomech. Abstr.*, 30(5): 503~526, 1993

Lee I.M, Park J.K. Stability analysis of tunnel keyblock: a case study[J].*Tunnel Analysis*, 15(4): 453~462, 2000

Mauldon M. Keyblock probabilities and size distributions: a first model for impersistent 2-D fractures. *Int. J. Rock Mech. Min. Sci. & Geomech. Abstr.,* 32(6): 575~583, 1995

Priest S.D., Hudson J. A. Estimation of Discontinuity Spacing and Trace Length Using Scanline Surveys. *Int. J. Rock Mech. Min. Sci. & Geomech. Abstr.*, Vol.18: 183~197, 1981

Shapiro A, Delport J L. Statistical analysis of jointed rock data. *Int. J. Rock Mech. Min. Sci. & Geomech. Abstr.*, 28(5): 375~382, 1991

Shi G H, Goodman R E. The Key Blocks of Unrolled Joint Traces in Developed Maps of Tunnel Walls, *International Journal for Numerical and Analytical Methods in Geomechanics.* Vol. 13: 131~158, 1989

Shi G H, Single and multiple block limit equilibrium of key block method and discontinuous deformation analysis, In: *Y.H. Hatzor (ed), Stability of Rock Structures Proceedings of the Fifth International Conference on Analysis of Discontinuous Deformation,* 3~43, Balkema, 2002

Wu A Q, Ren F, Guo Y. Study on block random distribution and anchor design for joint rock excavation. *Journal of Yangtze River Scientific Research Institute*, 8(4): 27~34, 1991 (in Chinese)

Wu F Q. Principles of Statistical Mechanics of Rock Masses. *Wuhan: China University of Geosciences Press,* 1993. (in Chinese)

Zhang Q H. Basic study on application of block theory and development of analytical software. *Ph.D thesis, Wuhan University, Wuhan, China,* 2004 (in Chinese)

Numerical Simulation of different fracture pattern in diametrically loaded discs of rock material by Manifold Method

WANG BING-CHEN, YANG JUN, NING YOU-JUN and CHEN PENG-WAN

State Key Laboratory of Explosion Science and Technology,
Beijing institute of Technology, Beijing 10081, China

To investigate the influence of a tensile stress gradient (B. Van de Steen, 2005) on fracture initiation and fracture growth in rock material, a configuration, consisting of a diametrically loaded disc with a hole on the diameter perpendicular to the loaded diameter is used. Depending on the diameter and the eccentricity of the hole, the disc splits along the loaded diameter or macro-fracture starts at the hole, However the tensile stresses at the top and the bottom of the hole are for nearly all cases considerably higher than the stresses along the loaded diameter and than the macroscopic tensile strength of the material, determined by conventional Brazilian test. Manifold Method (G. H. Shi, 1991) provides a unified framework for solving problems with both continuous and discontinues media, In this paper, by introducing a criterion of crack initiation and propagation, the second order manifold method is used to simulate the particular fracturing behavior, and the result has greatly consistence with experiment, which shows the different fracture pattern in diametrically loaded discs of rock material

Keywords: Rock material; Fracture pattern; Brazilian test; Numerical simulation; Manifold Method

1. Introduction

Rock breakage has a wide range of forms, and the fracture initiation and fracture growth in rock material is a complex progress. Van de Steen has systematically studied the theory of influence of a tensile stress gradient on fracture initiation and growth in rock material, and numerical simulation wee conducted using the boundary element code DIGS. Stress gradients induced by excavations in rock depend on the configuration and the size of the excavation and on the loading conditions. For the same pre-excavation in situ stress, the stress gradients around, e.g., a5-m diameter tunnel or around a 32-m drill hole differ considerably: the stress pattern is self-similar but obviously, for the smaller hole, the stress reduces to the field stress over a shorter distance. Similarly, the stress gradients at the corners of a rectangular tunnel differ considerably from the stress gradient around a circular tunnel. Stress gradients not only occur on the macro-scale but also on a micro-scale. High stress gradients exist in the vicinity of flaws, at grain contacts or at pores in the material.

In recent years, numerical simulation of rock damage has drawn tremendous attention of researchers across the world. In general, numerical methods can be classified into two types. One belongs to the category of continuum mechanics, such as Finite Element Method, the other belongs to the category of discontinuous deformation, including DEM and DDA. The former one is capable of accurately analyzing the deformation and stress distribution, but has difficulties in simulating discontinuous deformation, e.g. rock fracture and block movement. The later one can be utilized to model the behavior of discontinuous or block systems, but accurate calculation of stress distribution inside blocks remains a challenge.

Manifold Method proposed by Shi a new numerical method, which provides a unified framework for solving problems with both continuous and discontinuous media. By employing the concept of cover and two sets of meshes, manifold method combines the advantages of FEM and Discontinuous Deformation Analysis. It can only deal with discontinuities, contact, large deformation and block movement as DDA, but also provide the stress distribution inside each block accurately as FEM can. The numerical model of the original MM possesses only the first-order accuracy, leading to dissatisfaction in simulating problems that need high accuracy in displacement. Zhang (2000) developed the second order manifold methodwith six node triangle mesh. In the present paper the second order MM is applied to study the fracture initiation and growth in rock material.

In this paper, first the conventional Brazilian test is simulated by Manifold Method, also a series of numerical simulations of a diametrically loaded disc containing a hole are done, which are compared with the experiment results, and it shows how the fracture pattern is controlled as the size of the hole changes in the presence of material defects.

2. Criterion of crack initiation and propagation

Manifold method (Zhang 1999) can simulate the initiation and the expansion of fractures along combined surface, points and math grids in any

direction, it can be used for stability analysis, damage analysis and structure initiation, and any other problems related with discontinues structure. Manifold method has adapted two covers, so it has great advantage in simulating fracture initiation. Different criteria (Zhang 2002) are used in the initiation of new cracks and the growth of existing cracks. For the initiation of new cracks, a stress-based criterion, Mohr-Coulomb's Law with three parameters, is considered. It assumed that new cracks initiate if: (a), the first principle stress is larger than the tensile strength of the material, or (b), the maximum shear stress is larger than the shear strength of the material. The failure criterion can then be expressed as:
Tensile failure:

$$\sigma_1 = \sigma_0 \tag{1}$$

Shear failure:

$$(\sigma_1 - \sigma_3)/2 = c\,,$$
$$\text{if } (\sigma_1 + \sigma_3)/2 > 0 \text{ and } 0 < \sigma_1 < T_0 \tag{2}$$
$$(\sigma_1 - \sigma_3)/2 = c\cos\phi - (\sigma_1 + \sigma_3)\sin(\phi/2)\,,$$
$$\text{if } (\sigma_1 + \sigma_3)/2 < 0 \text{ and } 0 < \sigma_1 < T_0 \tag{3}$$

where σ_1 and σ_3 are the first and third principal stresses, T_0 is the tensile strength, c is the cohesion and ϕ is the friction angle.

For the existing cracks, the fracture toughness K_{IC} of the material is taken as the fracture criterion, and the maximum circumferential stress theory is adapted to determine the direction of crack growth measured from the current crack line θ

$$K_I \sin\theta + K_{II}(3\cos\theta - 1) = 0 \tag{4}$$

The fracture criterion for a mix mode problem takes the form as:

$$\cos(\theta/2)[K_I \sin^2(\theta/2) - 1.5K_{II}\sin\theta] = K_{IC} \tag{5}$$

3.Experiment sample configuration and observation

In the Brazilian test configuration, a disc is loaded diametrically, inducing an almost uniform tensile stress in the direction perpendicular to the loading along most of the loaded diameter. When a hole is drilled parallel to the sample axis and centred on the diameter perpendicular to the loaded diameter (a configuration further referred to as the disc with a hole, Fig.1), the material above and below the hole is subjected to a rapidly decreasing tensile stress. A linear elastic analysis of the stress distribution shows that the maximum tensile stress at the surface of the hole decrease as the distance between the centre of the disc and the centre of the hole increases (Fig.1). It was further shown that an increase in the radius a of the hole leads to a decrease in the stress gradient (Van de Seen, 2001; Van de Seen and Vervoort, 2001). Except for small holes (a/R≤0.08) in combination with a large eccentricity (e/R≥0.8), the tensile stress at the top and the bottom of the hole is larger than the tensile stress along the loaded diameter. Based on the theories above many experiments were done to show the different fracturing pattern as the radius and location of the drilled hole changes.

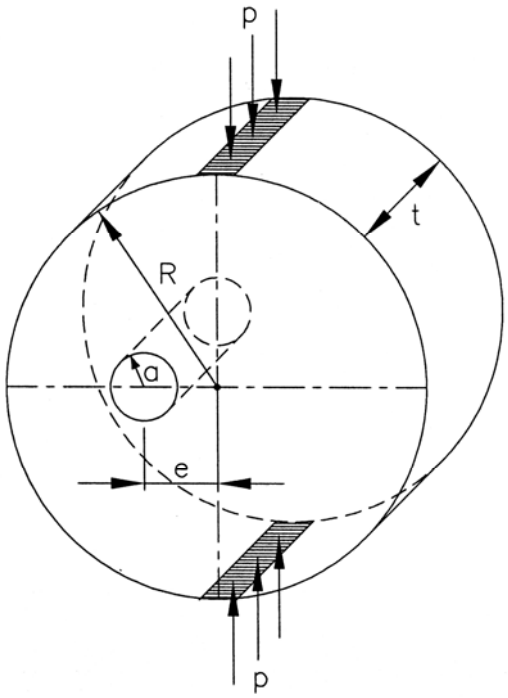

Fig.1: Diametrically loaded disc with a hole: geometrical configuration

4. Simulation of the fracturing behavior by manifold method

To better simulate the experiment situations and avoid the partial damage, here we use two slabs parallel to each other to press the disc in the loading direction. Then it can assure that the contact between the disc and the two slabs is a little segment, which can effectively avoid force loading. In the course of the loading the slabs must not be bended, so the rigidity of the slabs is better than the rock material. Table1 lists the rock material properties and parameters used in the simulation of the disc according to experiment research.

Table1. Material parameters of a rock (R=37.5cm)

	Young modulus E_P/GPa	Poisson ratio v	Density ρ/ (ton/m^3)	Friction angle θ/°	Cohesion c/ MPa	Tensile strength σ_t/MPa	Fracture Toughness K_{IC}/(MN/m$^{3/2}$)
Rock media	25	0.3	2.5	30	15	1.5	5.6
Joint	-	-	-	30	15	1.5	-

4.1 Fracture pattern obtained with a tension in the conventional Brazilian test

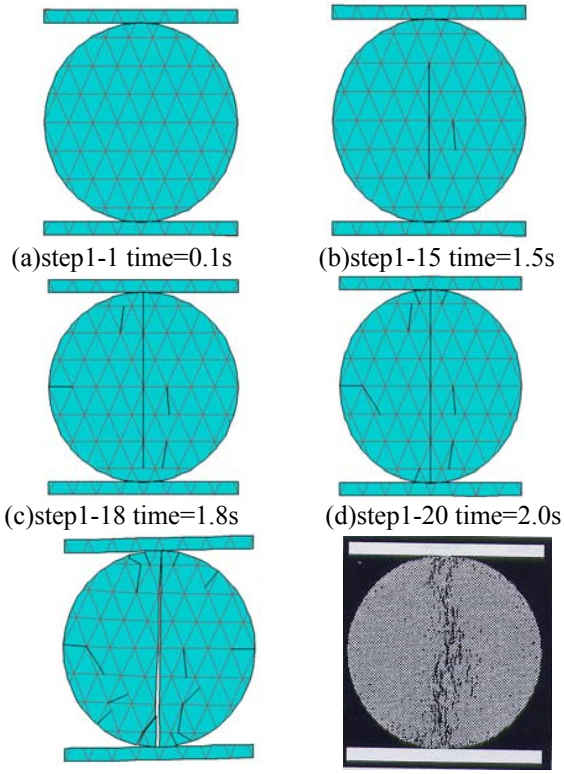

(a)step1-1 time=0.1s (b)step1-15 time=1.5s (c)step1-18 time=1.8s (d)step1-20 time=2.0s (e)step1-25 time=2.5s (f) FEM result

Fig. 2: Fracture pattern in the conventional Brazilian test

Firstly, Fracture pattern with a tension in the conventional Brazilian test is simulated. From the process of the damage, by the step1-15 the formation of the primary fracture appears in the diameter direction, and then it develop along the diameter towards the contact surface, finally it run through the whole Brazilian disc. The result can perfectly prove that it is arc contact between the disc and the two slabs. However, there is much controversy about the fracture initiation mechanism and location in the conventional Brazilian test. Colback (1966) argued that a curved fracture path point to fracture initiation in shear near one of the platens, there is little or no discussion that the fracture grows in tension. The NMM simulation result also cannot be used to determine whether the fracture initiates in tension or in shear. When the fracture path is strictly diametrical, a shear mechanism can still be responsible for fracture initiation.

4.2 Fracture formation in a diametrically loaded disc with a small hole

In particular the same radius disc, in which a 5cm hole drilled with an eccentricity of 20cm, is also simulated. And the 5cm hole is further called the 'small' hole.

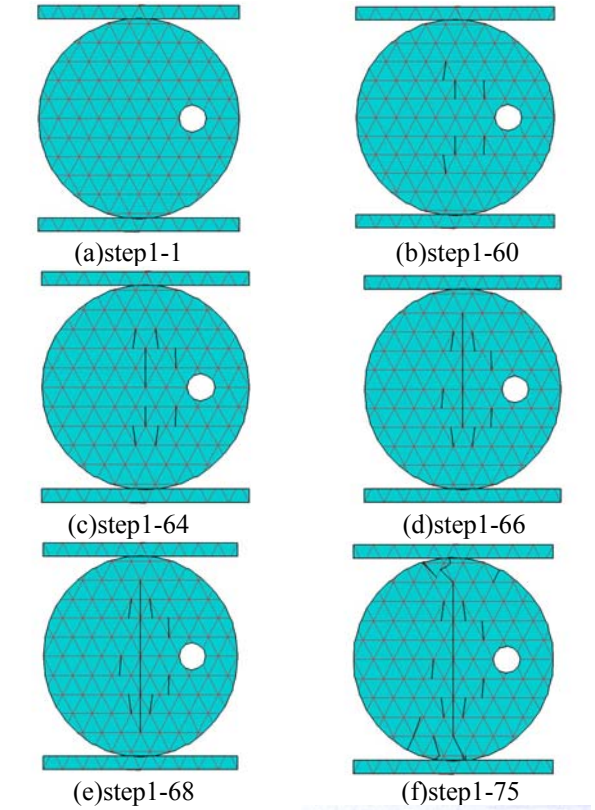

(a)step1-1 (b)step1-60 (c)step1-64 (d)step1-66 (e)step1-68 (f)step1-75

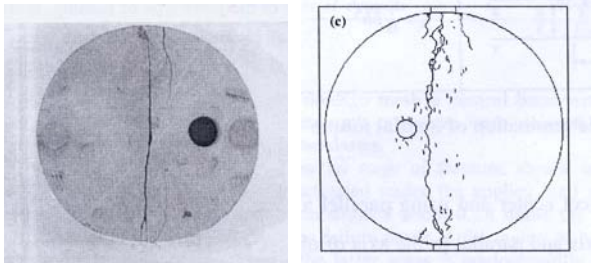

Experiment result Simulation result by B. Van de Steen

Fig. 3: Fracture formation in a diametrically loaded disc with a small hole

From fig.3 we can see that the 'small' hole disc finally failed consistently along the loaded diameter without intersect the hole. In the initial stage of fracture, some title fractures firstly appeared around the loaded diameter, but the additional fractures around the small

hole is very rare. By the step1-66 a predominant fracture also developed along the loading diameter towards the contact surface. At last once the primary fracture has fully developed, secondary tensile fracture may start to grow from the edge of the disc. The simulation result by Manifold Method is in good agreement with the result of experiment and the result Simulated by B. Van de Steen in fig.3.

4.3 Fracture formation in a diametrically loaded disc with a large hole

The stress gradient is affected by the diameter and the eccentricity of the hole, a diametrically loaded disc which has a 10cm diameter hole drilled with an eccentricity of 15cm is also simulated by Manifold Method. And the 10mm hole is further called the 'big' hole.

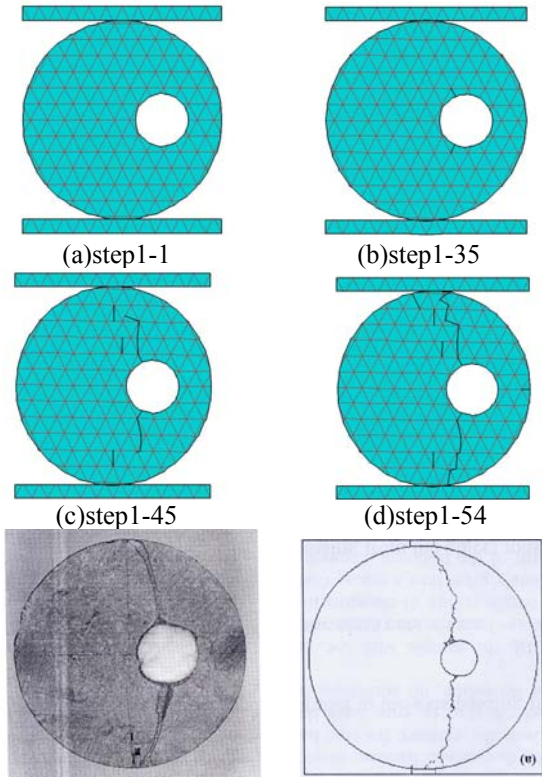

(a)step1-1 (b)step1-35

(c)step1-45 (d)step1-54

(e)Experiment result (f) Simulation result by B. Van de Steen

Fig. 4: Fracture formation in a diametrically loaded disc with a large hole

From the result of the simulation we can see that the disc finally failed at the hole surface, the fracture split starting from the top and bottom of the hole towards the contact surface. By the step1-35 the fracture first initiated, and then some unstable micro-fracture along the loaded diameter and two stable fracture growing from the hole towards the platen contacts are presented, while the activity at the centre of the disc remains very limited until the primary fractures have almost reach the platen contacts. The typical fractures can also be observed in the samples in the laboratory experiments, and the process of the damage is very close to the experiment results.

5. Conclusions

A diametrically loaded disc is a versatile, easy to prepare and easy to test configuration to study, in general, fracture initiation and growth in the brittle rocks are more specially the effect of a stress gradient. A change in the hole diameter and in the eccentricity of the hole position suffice to vary the tensile stress and the stress gradient at the hole surface. The conventional Brazilian test without a hole was experimentally observed. The failure often occurs as a diametrical splitting of the disc without interesting the hole. The laboratory observations of the development of the fracturing in the disc with a hole were successfully simulated by Manifold Method. The simulation demonstrate that the presence of pre-existing flaws serves to explain the effect of different hole size in the formation of primary fracture features either from the hole surface or in the form of a diameter fracture that does not intersect the hole. The simulation result has great consistence with the experiment results, and it shows the general development trend of fractures under such complex condition, but for further validation of the theory such as stress distribution, it also needs to be further studied. The results demonstrate that the manifold method is an effective method in the study of rock failure from a continuous mass to a discontinuous mass in brittle materials, and exhibits some advantages to conventional numerical methods. The results also provide further insights and a new method in the research of the related issues.

References

B. Van de Steen, A. Vervoort, J. A. L. Napier. Observed and Simulated Fracture Pattern in Diametrically Loaded Discs of Rock Material. *International Journal for Fracture*, 2005, 131:35-52.

G. H. Shi. Manifold Method of Material Analysis, Proc. Ninth Army Conference on Applied Mathematics and Computing, 1991, 51-76.

G. H. Shi, R. E. Goodman. Discontinuous Deformation Analysis, Processing of the 25th US Symposium of Rock Mechanics, 1984, 269-277.

Zhang G X, Sugiura Y, et al. The Second Order Manifold Method with Six Node Triangle Mesh. *J. Struct. Mech. Earthquake Eng. JSCE*, 2002, 696/I-58:1-9.

Zhang G X, Sugiura Y, Hasagawa H. Fracture Simulation Using Manifold and Singular Boundary Element Methold. *J. of Geotech. Eng. JSCE*, 1999, 624/III-47:1-10.

Zhang G X, Sugiura Y, Hasagawa H, F. Q. Chen. Fifth International Conference on Computational Structures Technology and the Second International Conference on Engineering Computational Technology, 2000.p61.

Manifold method simulation of the crack evolution of tunnels with different sections under different lateral pressures

QIAN YING, YANG JUN and NING YOU-JUN

State Key Laboratory of Explosion Science and Technology,
Beijing Institute of Technology, Beijing 100081, China

In this paper, the second order Manifold Method (NMM^{2D}) program is used to simulate the crack initiation and propagation of tunnels with different cross sections (which are circle, rectangular, straight-wall-top-arch (SWTA)). The crack evolution characters of tunnels with different sections under a variety of lateral pressure coefficients are given. The study proves that NMM^{2D} is a valid numerical simulation software in design of tunneling engineering.

Keywords: Numerical simulation; Manifold method; Crack evolution; Confining pressure

1. Introduction

The surrounding rock mass failure is always considered in tunneling engineering. Underground space is being widely used, with ceaselessly exploring living space. For examples tunnels, laneways, underground caverns, underground oil tanks and so on, they are built in a great number. At the same time, more problems are encountered in tunneling engineering, such as tunnel floor heave, rib spalling, collapse, ground subsidence aroused by subway excavation and so on. So studying the crack evolution laws of tunnels with different sections under different lateral pressures are significant.

In present, there are lots of the reports about the surrounding rock mass failure of tunnel used by various numerical analysis methods. These methods include Finite Element Method (FEM) (Yang et al,1989), Boundary Element Method (BEM), Displace Discontinuous Method (DDM) (Napier et al, 1992) and $PFPA^{2D}$ (Fu et al, 2000 and Zhao et al, 2004). It is well known that stress concentration maybe initiate cracks and speed growth of cracks. In addition, crack propagation relates with stress state and confining pressure influences stress distribution. So confining pressure need to be considered. For validating above views, using by NMM^{2D} program, authors studied the failure model of tunnels. The crack evolution laws of tunnels with different sections under different ground pressures were gained.

2. Basic concepts of manifold method

NMM can not only calculate large deformation, block contact and movement but also provide element stress and strain as FEM. And it can availably calculate the process from small deformation of continuous block to big deformation of discontinuous block (Shi, 1997). In order to illuminate its main character, a manifold model about tunnel problem is shown in Fig.1. Firstly, the triangle elements make up of mathematic mesh, shown in Fig.1 (a). Secondly, rock mass and tunnel set up its physical mesh, shown in Fig.1 (b). Finally, the mathematic mesh covers on the physical mesh, the part of the mathematic mesh and the physical mesh superposition make up of manifold mesh, shown in Fig.1 (c). The mathematic mesh denotes deformation of whole system using shape function. And the physical mesh represents the bound of discontinuous block. By introducing the concept of a cover and two sets of meshes, the manifold method combines the advantages of the FEM and DDA.

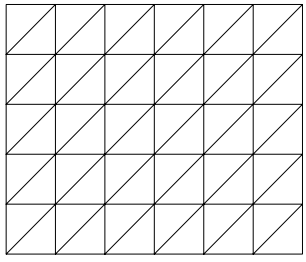

(a) Triangle mathematical mesh

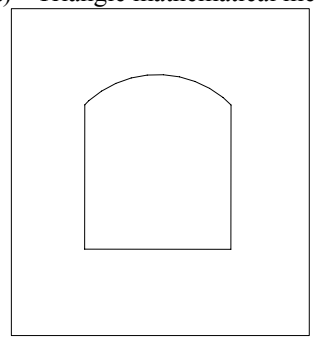

(b) Physical mesh of tunnel

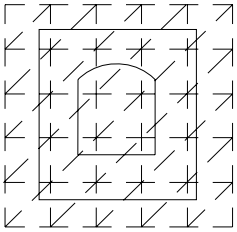

(c) Manifold model mesh

Fig.1: Basic conception of manifold method

Manifold method provides an easier way to simulate crack propagation. Different criteria are used in the new crack initiation and the growth of existing cracks (Zhang et al, 1999). Fracture criteria using the SIF can only be used for existing cracks. For the initiation of new crack, Mohr-Coulomb's law with there parameters is taken as the failure criterion for new cracks. Take σ_1 and σ_3 to indicate the first and third principal stresses, the failure criterion can be expressed as:

Tensile failure:

$$\sigma_1 = T_0$$

Shearing failure:

if $\frac{\sigma_1+\sigma_2}{2} > 0$ and $0 < \sigma_1 < T_0$

$$\frac{\sigma_1-\sigma_3}{2} = C$$

if $\frac{\sigma_1+\sigma_2}{2} < 0$ and $0 < \sigma_1 < T_0$

$$\frac{\sigma_1-\sigma_3}{2} = C\cos\phi - \frac{\sigma_1+\sigma_3}{2}\sin\phi$$

Where T_0 is the tensile strength of the material, C is the cohesion and φ is the friction angle.

For existing cracks, the fracture toughness K_{IC} of material is taken as the fracture criterion, and the maximum circumferential stress theory is adopted to determine the direction θ_0 of crack growth measured from the current crack line by the following equation:

$$K_I \sin\theta + K_{II}(3\cos\theta - 1) = 0$$

The fracture criterion for mix mode problem takes the form as:

$$\cos\frac{\theta_0}{2}(K_I \cos^2\frac{\theta_0}{2} - \frac{3}{2}K_{II}\sin\theta_0) = K_{IC}$$

3. The common tunneling engineering simulation and results analysis

In this paper, new crack initiation and crack propagation of tunnels with different sections, which are circular, rectangular, straight-wall-top-arch (SWTA), are simulated under different lateral pressure coefficients (λ). The lateral pressure coefficient equals that the horizontal pressure value divides the vertical stress peak value.

3.1 Calculation model

The model is a rectangular sample, its width is 20m and its height is 18m. The circle tunnel's radius is 3m. The rectangular tunnel's height is 3m, its width is 6m. The straight-wall-top-arch's width is 2.83m, its height is 3.41m. Physical parameters of the rock medium and joint are shown in Table 1.

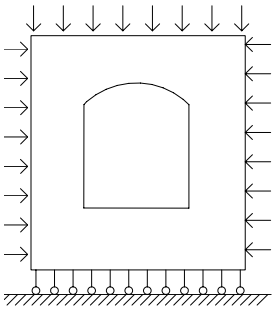

Fig.2: Sample model

The sample bottom is fixed boundary, its top and lateral pressure adopt invariable force load. The top stress peak value reaches 10MPa. And the stress value of lateral pressure is determined by λ. There are mainly two sets of joints distributing in the rock medium. For circular tunnel, there are 3612 blocks and the average area of the blocks is 0.09185m^2. For rectangular tunnel, there are 3744 blocks and the average area of the blacks is 0.091346m^2. For SWTA tunnel, there are 3827 blocks and the average area of the blocks is 0.091683m^2. The sample model is shown in Fig 2.

3.2 Simulation results analysis

The crack evolution of tunnels with three cross sections under different lateral pressures are shown in Fig.3~Fig.5.

Table 1: Material parameters of model (Yu Ya-lun et al, 2004)

Material	Density ρ / KN/m^3	Yong's Modulus E / GPa	Poisson's Ratio μ	Friction Angle θ /^{0}	Cohesion C / MPa	Tensile Strength σ_t / MPa	Fracture Toughness / MPa
Rock material	2550	40	0.22	35	35	9	1.1
Joint	/	/	/	20	3.5	0.9	/

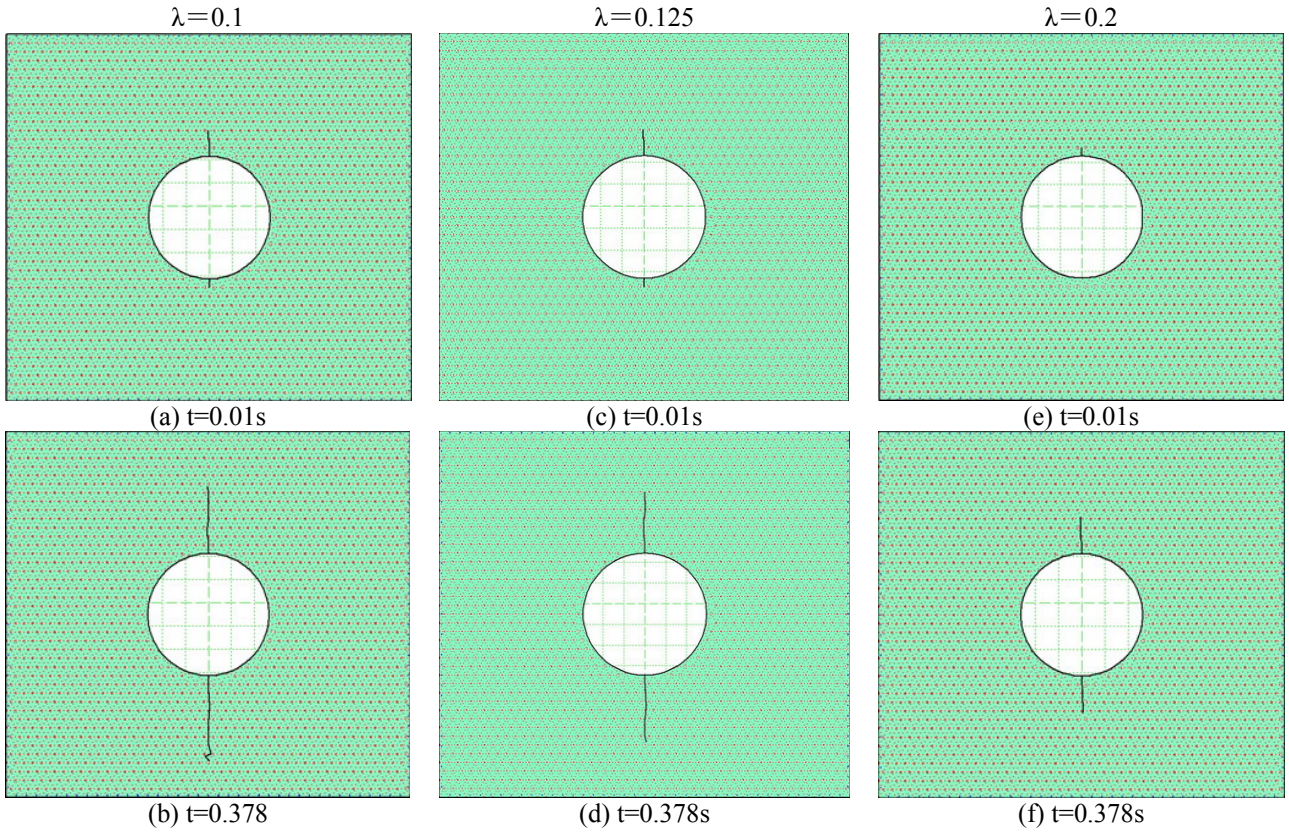

Fig. 3: The evolution of crack of circle tunnel

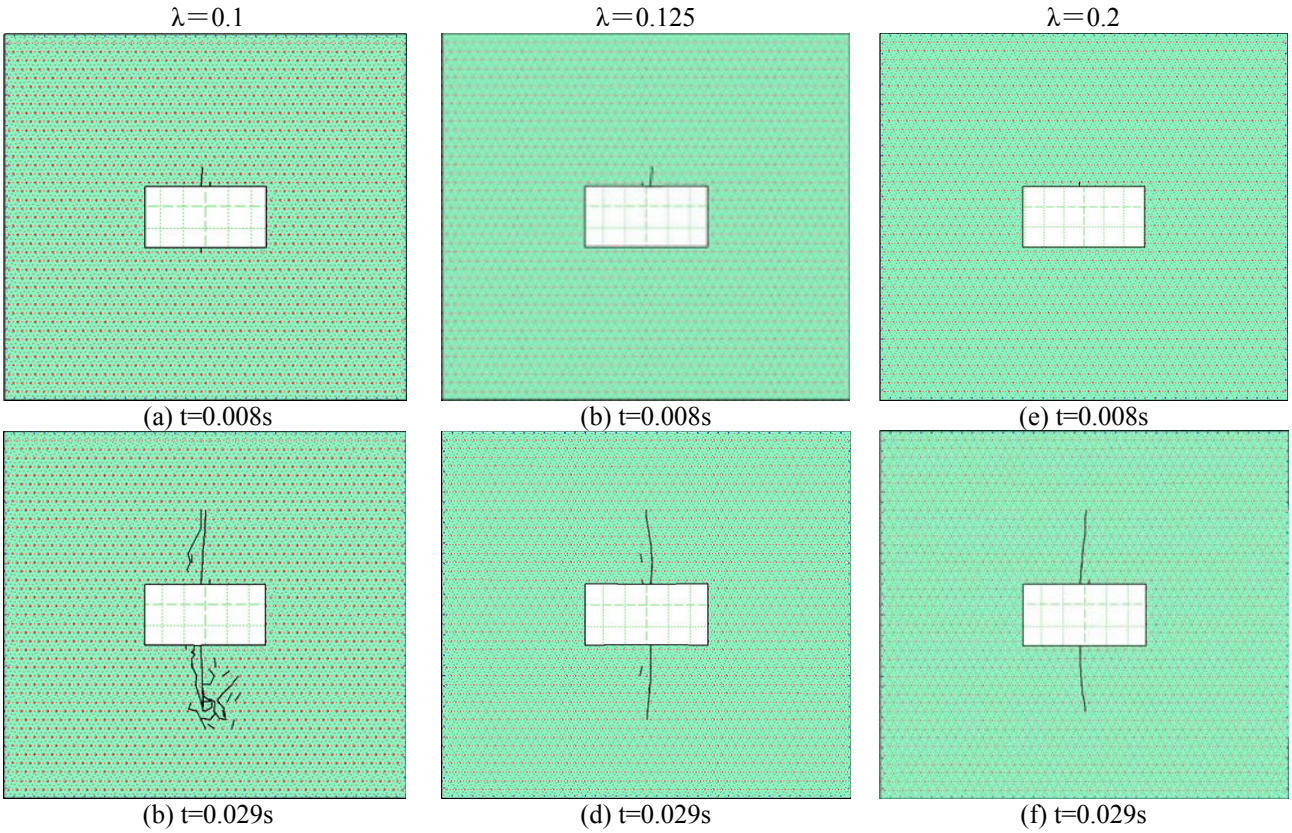

Fig. 4: The evolution of crack of rectangular tunnel

λ=0.1 λ=0.125 λ=2.8

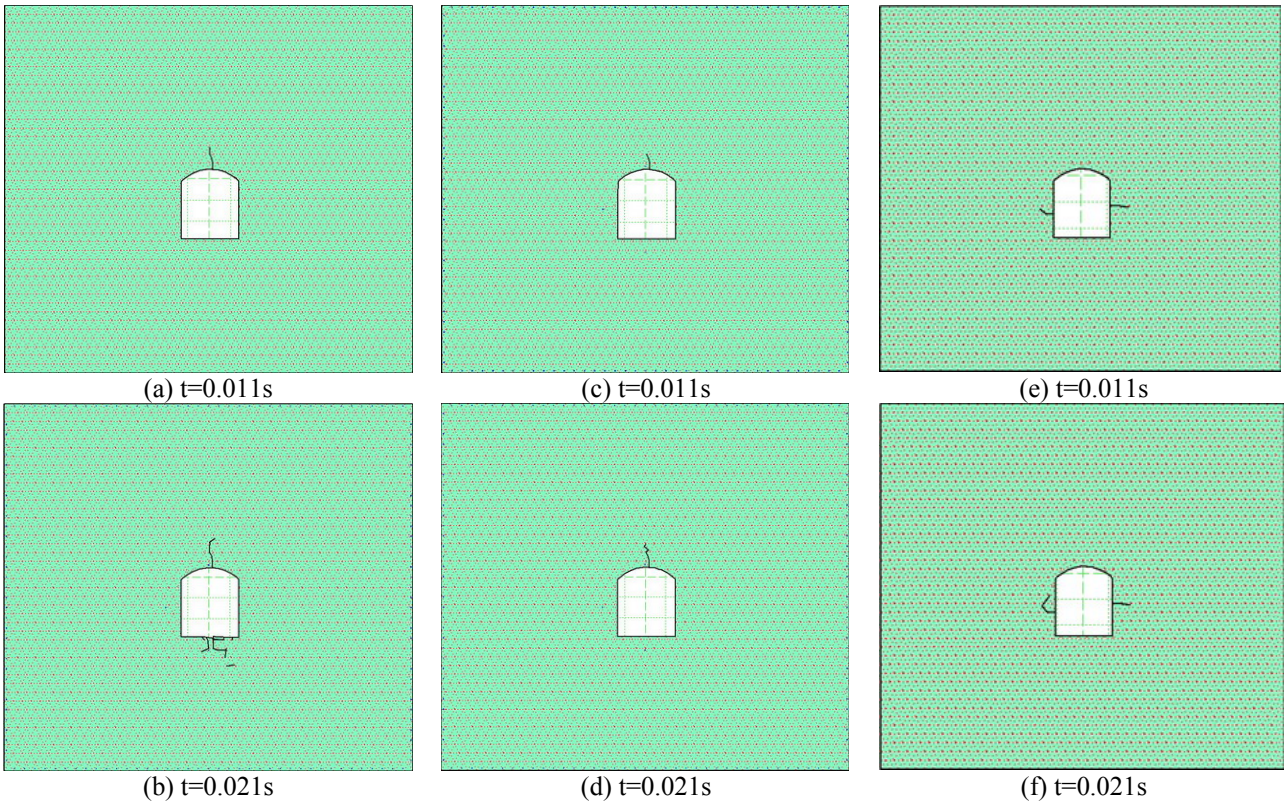

(a) t=0.011s (c) t=0.011s (e) t=0.011s

(b) t=0.021s (d) t=0.021s (f) t=0.021s

Fig. 5: The evolution of crack of SWTA tunnel

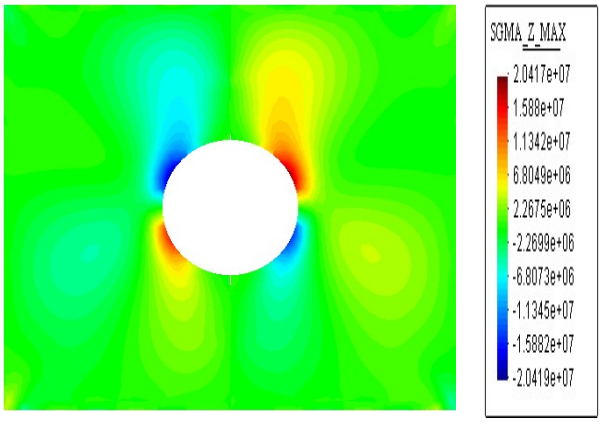

Fig. 6 Typical shear stress diagram

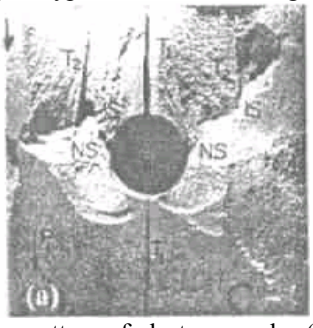

Fig. 7 Fracture pattern of plaster samples (Lajtai E Z et al, 1975)

For circular and rectangular tunnels, the author picked the time, when crack just began to initiate and λ=0.2, as the first line pictures. While SWTA tunnel, the author picked the same instance but λ=0.125. For three tunnels, author respectively adopted t=0.378s, 0.029s and 0.021s as the second line pictures. It can be found from the above simulation results:

(1) For every kind of tunnel, with λ increasing gradually, the time of crack initiation delays. Simultaneously, the velocity of crack propagation slows. And the length of crack shortens at same time. It is concluded that the harder tunnel is damaged, the more λ is.

(2) For the tunnel with different sections, when λ=0.125, the time of crack initiation is respectively 0.006s, 0.006s, 0.011s. It is indicated that the circular and rectangular tunnels fail more easily than SWAT tunnel. The failure of tunnel is related with tunnel's geometrical configuration.

(3) When λ<1, the lateral walls of tunnel sustain compressive stress and the top and roof of tunnel sustain tensile stress. In addition, compressive strength of the rock medium is far greater than its tensile strength. So the crack initiates from top and roof of tunnel firstly. This kind of crack is called primary crack (Fu et al, 2000). With stress concentration of tunnel's top and roof dying down, stress field transfers far from around of tunnel and new cracks are resulted. The new cracks are called remote cracks (Fu et al, 2000). It is shown in Fig. 4 (b) and (d) and Fig. 5 (b). When λ >1, the lateral walls of tunnel sustain tensile stress and the top

and roof of tunnel sustain compressive stress. So the crack initiates from lateral walls of tunnel firstly. It is shown in Fig. 5 (e) and (f).

(4) From the comparison of Fig. 6 with Fig. 7, shear stress distribution figured by diagram accords with the experiment results. The program is quite accurate in calculating stress, but there are some problems about criterion of shear crack initiation. So shear cracks is hardly found in the simulation results.

(5) Three issues need to be explained. Firstly, for rectangular and SWAT tunnels, when λ=0.1, the cracks propagate very severely. Secondly, for SWAT tunnel, if λ=0.2, the cracks do not form during the whole simulation process. So the author adopts λ=2.8 instead. The rock non-uniformity and the tunnel geometrical configuration maybe result in the above two problems. Thirdly, once the crack curves or curls, the direction of cracks growth was not calculated exactly. It is shown in Fig. 4 (b) and Fig. 5 (b). It is a problem of the present program. Improving on the crack propagation is one of directions in future works.

4. Conclusions

The crack evolutions of tunnels with three different sections under different lateral pressures were given in this paper. Simulation results indicated that the cracks initiation and propagation related with not only the lateral pressure coefficient (λ) but also the tunnel geometrical configuration. It was validated that there were two kinds of cracks during failure process of tunnel, which were primary cracks and remote cracks. In addition, the author found that the direction of cracks growth could not be calculated exactly by NMM. And there are some problems on the criterion of shear crack initiation. Nevertheless, NMM is still a valid numerical analysis method in calculating crack initiation and initial stages of crack growth. So the results of this research provide further insights and a new method in the research of the related issues.

References

Yang Zhi-fa, Ding Si-bao, Zhang San-qi. Elastical Atlas about Underground Engineering Plan Problem, Science Press, 1989.

Napier J A L, Hildyard M W. Simulation of Fracture Growth around Openings in Highly Stressed. *Brittle Rock*, 1992, 92(6), 159-168.

Fu Yu-fang, Huang Ming-li, Ren Feng-yu, Tang Chun'an. Numerical Analysis of Crack Evolution around Borehole in Rock Sample Subjected to Confining Pressures. *Chinese Journal of Rock Mechanics and Engineering*, 2000, 19(5), 577-583.

Zhao Xing-dong, Duan Jin-chao, Tang Chun'an, Zhu Wan-cheng. Study on Failure Mode of Tunnels with Different Sections. *Chinese Journal of Rock Mechanics and Engineering*, 2004, 23(s2), 4921-4925.

Shi Gen-hua. Numerical Manifold Method. Proceedings of ICADD-2, 1997, 1-3.

Shi Gen-hua. Numerical Manifold Method and Analysis of Discontinuous Deformation, Tsinghua University Press, 1997, 3-4.

G.X. Zhang, Y. Sugiura, H. Hasegawa, F.Q. Chen. Crack Propagation by Manifold and Singular Boundary Element Method. Proceedings of ICADD-3, 1999.

Yu Ya-lun et al. Engineering Blasting Theory and Technology. Metallurgical Industry Press, 2004, 156.

Lajtai E Z, Lajtai V N. The Collapse of Cavities. *Int. J. Rock, Min. Sci. & Geomech. Abst.*, 1975, 12(1), 81-86.

Applications of manifold method to geotechnical problems involving excavations

S. MIKI[1], T. SASAKI[2], Y. OHNISH[3], and S. NISHIYAMA[3]

[1] Kiso-Jiban Consultants Co., Ltd., JAPAN
[2] Suncoh Consultants Co., Ltd., JAPAN
[3] Kyoto University, JAPAN

Manifold method (MM) is a powerful numerical analysis method to simulate displacements and deformations of the ground including discontinuous planes such as joints and faults. However, MM lacks some practical functions in order to simulate geotechnical problems. We have equipped the MM with excavation process and material boundaries. The excavation is realized by releasing the contacts between surrounding area and excavation area which area bounded by joints. The material boundaries are formulated as a boundary between the elements, which share common cover mesh (mathematical mesh). Some example results indicate the MM will be applied to a simulation of geotechnical problems involving excavations.

Keywords: Manifold method; Excavation analysis; Material boundary

1. Introduction

The Manifold Method (MM)(Shi 1991), as well as Discontinuous Deformation Analysis (DDA)(Shi 1988), is a powerful numerical analysis method to simulate displacement and deformation of rock mass including discontinuous planes such as joint, faults and so on. MM also have an advantage that mathematical meshes (cover) are independent of physical meshes or block boundaries, and mesh making for the analysis became easy.

MM was originally developed by Shi, and various extensions have been proposed so far. For example, Chen et al (1997) have proposed the MM with high order displacement functions. Sasaki et al (1997) have equipped the MM with the rock bolt element and the elastic – plastic element. However, MM is insufficient to simulate geotechnical problems practically, because MM lacks some analysis functions such as excavation process, material property divisions, progressive analysis along construction processes, and so on. These are essential to the practical simulations.

In this study, we have equipped the MM with excavation process and material boundaries. Material boundaries, which are the boundary between different material property areas in the same block, have to set without losing easiness of mesh making. In realizing excavation process, it is essential that excavation surfaces work as free surfaces, and contacts and separations between blocks are enabled on the excavation surfaces. This report outlines the excavation process and the material boundary in the MM, and present analysis examples and applications.

2. Material boundary

2.1 Methodology to material boundary

The material boundary is a line divides different material properties. Fig. 1 is a schematic diagram of the material boundary, joint, mesh, and block in MM. Therefore, it is impossible to separate block along material boundary.

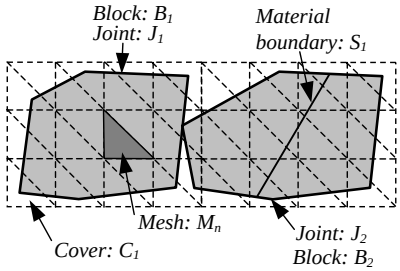

Fig. 1: Schematic diagram of material boundary, joint, mesh, block and cover.

In the Finite Element Method (FEM), a mesh making is generally done as material boundaries are fitted into mesh boundaries. In MM, it is also possible to make the mesh as material boundaries are fitted into mesh boundaries. However, this reduces a convenience that MM has in mesh making. In this study, the material boundary, which is realized without losing a convenience of mesh making, have been proposed.

In MM, displacements are solved for the nodes compose cover meshes, and an integration is done on the area material exist for each cover in the formulation. Therefore, the integration area is sometimes a part of the cover mesh. This relation is used for a formulation of the material boundary.

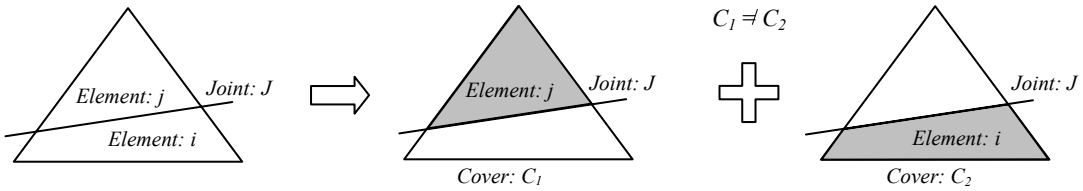

(a) Element divided by joint

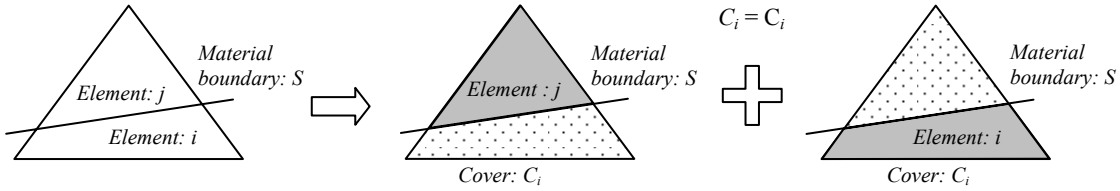

(b) Element divided by material boundary

Fig. 2: Schematic diagrams of joint boundary and material boundary

Assuming that the cover C_i is divided into two elements, an element i and j, by the material boundary S, as shown in Fig. 2(b).
The strain on the cover C_i can be represented by

$$[B_i][D_i] \tag{1}$$

where $[B_i]$ is displacement-strain matrix of the cover C_i, and $[D_i]$ is nodal displacement of the cover C_i. As two element i and j share common cover C_i, strain on the element i is equal to the strain on the element j. The potential energy due to elastic deformation Π_e is expressed by

$$\begin{aligned}\Pi_e &= \iint \frac{1}{2}[D_i]^T[B_i]^T[E_i][B_i][D_i] + \iint \frac{1}{2}[D_i]^T[B_i]^T[E_j][B_i][D_i] \\ &= \frac{1}{2}s_i[D_i]^T[B_i]^T[E_i][B_i][D_i] + \frac{1}{2}s_j[D_i]^T[B_i]^T[E_j][B_i][D_i]\end{aligned} \tag{2}$$

where $[E_i]$ and $[E_j]$ are stress-strain constitutive law matrices respectively, and s_i and s_j are area of element i and element j share cover C_i respectively. The stiffness matrix for cover C_i is obtained by minimizing the energy Π_e. Hence, stiffness of cover C_i is an average of stiffness of element i and element j weighted by its area. In Fig. 2, the difference between joint boundary and material boundary is illustrated. Along the joint boundary, contacts and separations between blocks are enabled, because the meshes in corresponding blocks have independent covers. On the other hand, separations between meshes are impossible along the material boundary, because corresponding meshes share common mathematical cover, and deformations of the meshes depend on area and material properties of each mesh.

2.2 Verification of material boundary

In order to verify the material boundary, the simple model, which is shown in Fig. 3, was served to an analysis. The model geometry is a rectangle 20m long and 10m wide. At the right and left sides of the model, lateral displacements were constrained as a boundary condition. At the bottom of the model, longitudinal displacements were also constrained. As shown Fig.3, the model was divided into two parts, material A and B, by the horizontal material boundary at level 10m. The material properties and analysis conditions are shown in Table 1. In the analysis, the Model 1 was a case where the numerical covers were divided by a material boundary. In the Model 2, the material boundary was fitted to the mathematical cover edges like a normal FEM. The calculated displacements and stresses due to material weight were compared for the verification.

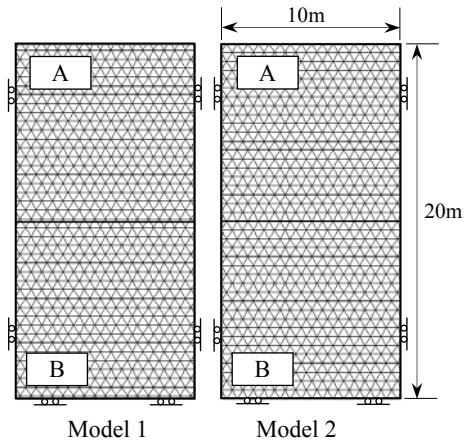

Fig. 3: Verification analysis model

Table 1: Material properties and analysis conditions

Material group	*A*	*B*
Young's modulus (MN/m^2)	10.0	100.0
Poisson's ratio	0.3	0.3
Density (kg/m^3)	2.0	2.0
Unit weight (kN/m^3)	20.0	20.0
Time step (s)	0.01	
Iteration (times)	500	
Maximum displacement ratio	0.0001	

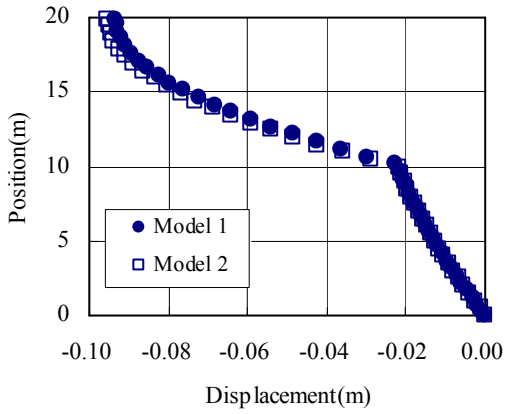

(a) Displacement

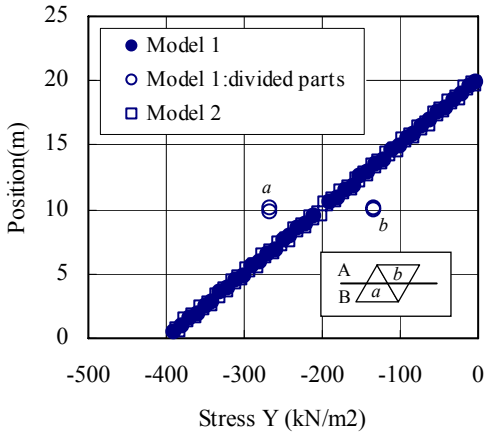

(b) Stress (over burden pressure)

Fig. 4: Displacements and stresses of Model 1 and 2

Fig. 4 shows the calculated displacements and stresses for the Model 1 and Model 2. The displacements (settlements) of the Model 1 were roughly consistent with that of Model 2, however displacements of the Model 2 were slightly larger than that of the Model 1. The stresses (over burden pressure) of the Model 1 agreed with that of the Model 2, and these values were consistent with analytical values, except for stresses at the boundary parts in Model 1. As shown Fig. 4, stresses along the material boundary shows alternately larger and smaller values than the exact value. However, average stresses along the boundary agreed with the exact value. It is consider that the material boundary in MM is applicable to practical use, although meshes along the material boundary have some errors in stress value.

3. Excavation analysis

Many geotechnical problems relate to excavations, and it is important to simulate along construction processes in estimating ground behavior. Many FEM codes are equipped with excavation process. It is easy to attach excavation processes to the MM.

3.1 Methodology to excavation process

In MM, there are two way to realize excavation processes.

One is a method that stresses of excavation meshes are released and stiffness of the meshes is weakened. The excavation meshes are bounded by material boundaries in advance, and the excavation is activated when time step iteration amounts to the specific step. This method is similar to the excavation processes in FEM.

The other is a method that contacts between excavation block and mother block are broken off. The excavation areas are bounded by the joints, and the excavation areas are modeled as a block in advance. Fig. 5 shows a concept of the excavation. This method is similar to the excavation processes in DDA (Therese et al. 2002). After the excavation, excavated blocks can move independently of mother block, and excavated surfaces act as free surfaces. Hence, contacts and separations between mother block and another block are enabled again.

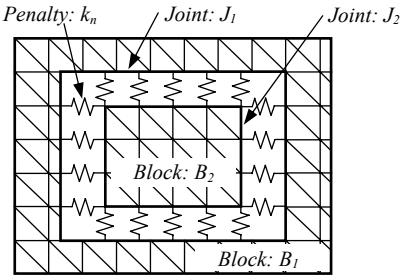

(a) Before excavation

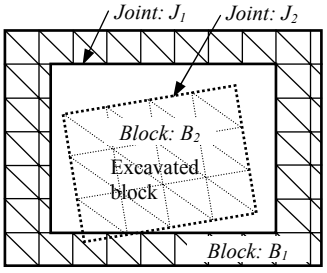

(b) After excavation

Fig. 5: Concept of the excavation

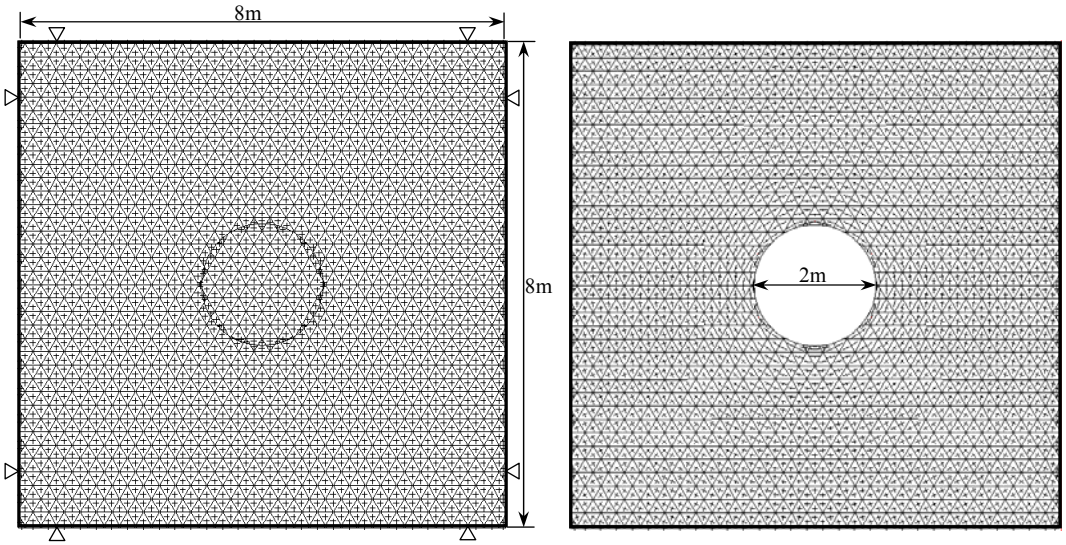

(a) Initial state (b) After excavation

Fig. 6: Stress distributions at initial state and after excavation by MM

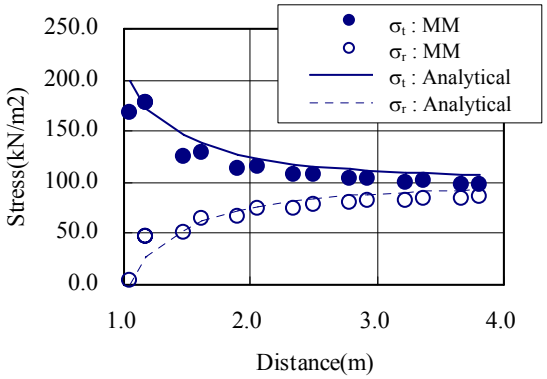

Fig. 7: Comparison of stress distributions along radial direction

3.2 Verification of excavation process

Verification analysis was done to demonstrate validity of the excavation. Fig. 6 shows the calculation model. The model geometry was a square 8m long and wide, and a circular tunnel, of which radius was 1m, was excavated at the center of the model. The tunnel was bounded by the joints in advance. The displacements of periphery of the model was constrained, and all meshes were subjected to a constant compressive stresses, $\sigma_x=\sigma_y=1000kN/m^2$, as a initial stress. Fig. 6(a) and Fig. 6(b) show stress distribution at the initial state and after excavation respectively. The material properties of a medium were assumed that the elastic modulus and Poisson's ratio were $1GN/m^2$ and 0.2 respectively.

In this problem, analytical stresses and displacements have been obtained for the case of a circular tunnel in an infinite elastic medium subjected to a constant stress. Fig. 7 shows analytical and calculated stresses along radial direction. The radial stresses and tangential stresses by MM were roughly consistent with the analytical solutions. The results show that excavation processes in MM work well.

4. Model analyses and applications

In order to examine the applicability of the proposed MM, two example models, excavation of the cavern and slope cut, were analyzed. These are familiar with practical geotechnical problems.

4.1 Excavation of underground cavern

Fig. 8 shows the underground cavern model with 4 joints and 1 material boundary. The model geometry was a square 300m long and wide, and the dimensions of the cavern, which was located at a center of the model, were 50m long and 40m wide. The material properties and analytical conditions are shown in Table 2.

Table 2: Material properties and analysis conditions

Material group		*A*	*B*
Young's modulus (MN/m^2)		5000.0	2000.0
Poisson's ratio		0.25	0.25
Density (kg/m^3)		2.7	2.7
Unit weight (kN/m^3)		27.0	27.0
Cohesion (MN/m^2)		4.0	2.0
Internal friction angle (deg)		55	45
Work hardening coefficient (MN/m^2)		50.0	20.0
Joint friction angle (deg)		45	
Time step (s)		0.01	
Iteration (times)	Stresses generation	500	
	Excavation	500	
Maximum displacement ratio		0.0001	

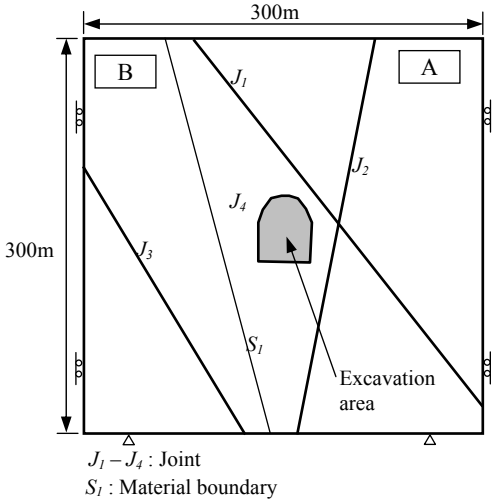

Fig. 8: Underground cavern model

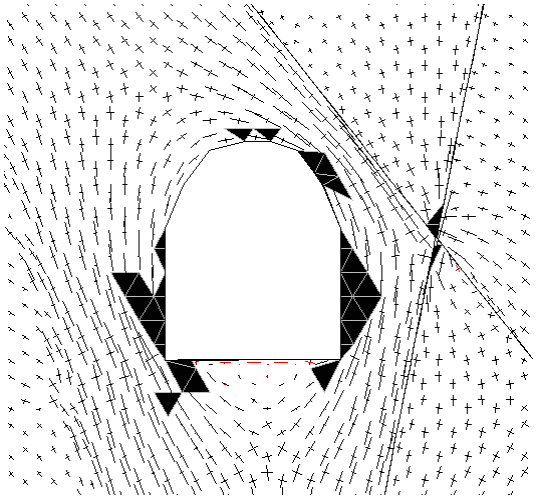

(a) Stress distribution and plastic regions after excavation

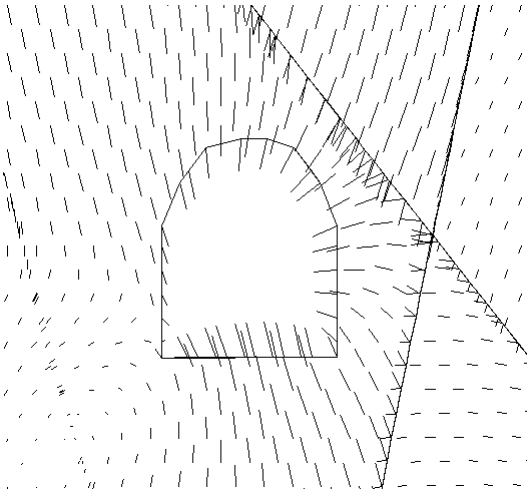

(b) Displacement vectors of the nodes after excavation (multiplied by 200)

Fig. 9: Stresses and displacements around the cavern

In the model, lateral displacements of both sides were constrained, and lateral and longitudinal displacements were constrained along the bottom line. The excavation area was bounded by the joint. The elastic-plastic constitutive law based on Drucker-Prager's yield criteria for an element, which have been introduced to the MM by Sasaki et al 1997, was applied.

In the analysis, the calculation was processed by two stages. At first stage, gravity was turned on, and initial stresses in the meshes and contact forces between blocks were generated. After first stage, the cavern was excavated.

Fig. 9 shows stress distribution and displacements around the cavern. The plastic regions appeared along the left and right walls, and at the crown. From the right wall to the crown, remarkable displacements were calculated. It was considered that the plastic regions and larger displacements along right wall were closely related to the existence of the two joints. These results agree with the physical phenomenon in rock masses. The discontinuity of the stress distribution and displacements along the joints were obvious. On the other hand, the stresses and displacements along the material boundary were continuously distributed.

4.2 Excavation of slope

Fig. 10 shows the slope cut model with 4 joints and 1 material boundary. The dimensions of the model were 80m long and 150m wide. The dimensions of the tunnel were 10m long and wide. In this model, the results were focused on stabilities of the slope and tunnel. The excavation areas were bounded by the joints beforehand. The material properties and analysis conditions are shown in Table 3. In the model, lateral displacements of both sides were constrained, and lateral and longitudinal displacements were constrained along the bottom line.

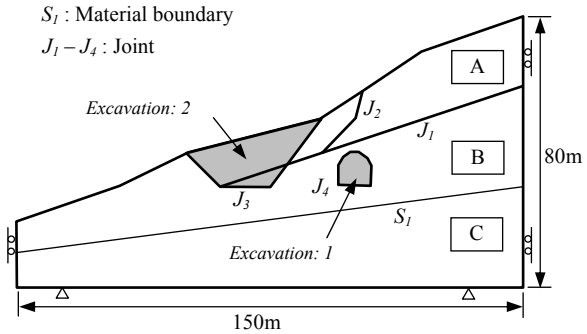

Fig. 10: Tunnel and slope cut models

In the analysis, the calculation was processed by three stages. At first, in order to generate initial stresses in the meshes, gravity was turn on. At second stage, the tunnel was excavated (Excavation: 1), and the slope cut was finally practiced.
In Fig. 11, the displacements, which caused by slope constructions, are shown. The displacements due to unloading followed by the slope cut were calculated. In this case, the displacements along the left side of the tunnel were about 1 cm. The displacement along the joint 1 and joint 2, which suggested the possibility of a sliding of the blocks, were also calculated. These results agree with a general tendency in slope excavations.

Table 3: Material properties and analysis conditions

Material group		*A*	*B*	*C*
Young's modulus (MN/m^2)		100.0	200.0	400.0
Poisson's ratio		0.40	0.35	0.30
Density (kg/m^3)		1.9	2.2	2.5
Unit weight (kN/m^3)		19.0	22.0	25.0
Joint friction angle (deg)			45	
Time step (s)			0.01	
Iteration (times)	Stresses generation		500	
	Tunnel excavation		500	
	Slope cut		500	
Maximum displacement ratio			0.0001	

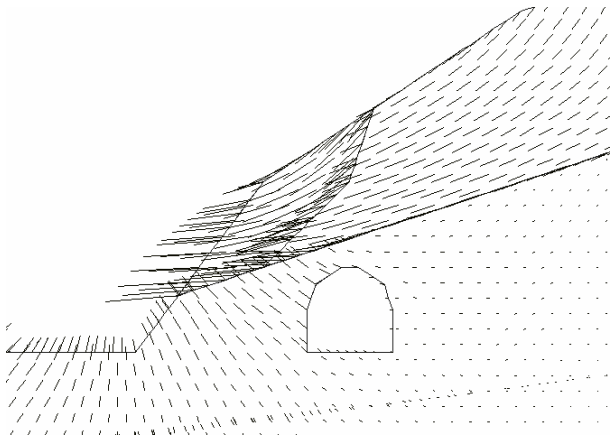

Fig. 11: Displacement vectors of the nodes after slope excavation (multiplied by 150)

5. Conclusions

We have introduced the material boundary and the excavation process to the MM, and examined the applicability of the MM for geotechnical problems involving excavations.
The following conclusions can be obtained;

(i) The material boundary is formulated as a boundary between the elements, which share common cover mesh.

(ii) The excavation is realized by releasing the contacts between surrounding area and excavation area which are bounded by joints.

The applicability of the MM has been confirmed by the simulation analyses. The results also present that the MM is suitable for the practical uses, and the MM will enable geotechnical engineers to perform a step-by-step analysis along the construction processes.

References

Chen, G., Ohnishi, Y. and Ito, T., Development of High Order Manifold Method, *Proc. Second International Congress on Analysis of Discontinuous Deformation (2nd ICADD)*, 1997, 132-154.

Sasaki, T., Morikawa, D., Ishii, D. and Ohnishi, Y., Elastic-Plastic Analysis of Jointed Rock Models by Manifold Method, *Proc. Second International Congress on Analysis of Discontinuous Deformation (2nd ICADD)*, 1997, 309-316.

Shi, G. H., Discontinuous Deformation Analysis – A New Numerical Model for the Statics and Dynamics of Block System, *Ph. D. Dissertation, Univ. of California Berkeley, Dept. of Civil Eng*., 1988.

Shi, G. H., Manifold Method of Material Analysis, *Transactions of the 9th Army Conference on Applied Mathematics and Computing, Report No.92-1, U.S. Army Research Office*, 1991.

Therese, S., Ming, L. and Arne, M., Numerical analysis of Gjovik Olympic cavern: a comparison of continuous and discontinuous results by using Phase^2 and DDA, *Proc. The Fifth International Congress on Analysis of Discontinuous Deformation (5th ICADD)*, 2002, 125-131.

Study on applications of Key Block Theory to rock engineering projects

O. Murakami[1], A.Yokoo[2], Y. OHNISHI[3] ,S. NISHIYAMA[3]

[1]1 Tsukuba Software Engineering Company Co. Ltd., Tokyo, 101-0041, JAPAN
[2] Kajima Corporation, Tokyo,107-8388, JAPAN
[3] School of Urban & Environment Engineering, Kyoto University, Kyoto, 615-8540, JAPAN

The behavior of the discontinuous rock masses affected by excavation is important indicators. This paper proposes an advanced method for analysis of the behavior of the discontinuous rock masses by using key block theory. We introduce practical problems in some Japanese projects of natural gas stockpiling base and the results of rock reinforcement and support design around underground cavern that was effectively performed from a reliable knowledge of the potential rock mass failure by using block theory analysis.

Keywords: Key-block theory; Natural gas stockpiling base; Support design

1. Introduction

Major underground natural gas storage facilities have been constructed in Japan. The advantage of underground gas storage facilities lies in their environmentally friendly and safe operation and economic construction. The Japanese government is proceeding with plans to achieve a LPG stockpile of 1.5 million tons by fiscal 2010. There are two kinds of method in stockpiling of LPG; above-ground aquifer refrigerated tank method, aquifer sealed underground cavern method. This aquifer sealed underground cavern is the method to store liquefied natural gas with the normal temperature and pressure by using water pressure. The measure to prevent leakage of liquid and gas phase is not concrete lining but the ground water pressure that keeps higher than the pressure of cavern. For example, because propane is liquefied at the temperature of 15°C and the pressure of 0.75MPa, the internal pressure is designed at 0.95MPa and the head of ground water is designed at more than 0.5 vertically for gas phase and more than 0 for liquid phase. It is necessary to supply underground cavern with water through some boring holes in order to keep water sealed function. Fig. 1 shows the water sealed underground cavern, and the inner wall are excavated rock mass that is not supported with concrete.

The way of storage of liquefied natural gas by water pressure through boring holes is shown in Fig.2. A method that can grasp the behavior of rock masses is necessary in order to design and construct based on a rational control for large-scale underground cavern. In the case of underground excavation of rock masses, sliding and opening of joints due to stress relaxation are considered to be the governing mechanisms of behaviors of the rock mass, so key block theory is very useful as an analytical method for jointed rock masses, and how to consider water pressure in key block analytical system is the important factor in the aquifer sealed underground cavern (Hatzor et al. 2002).

Fig.1: Aquifer sealed underground cavern.

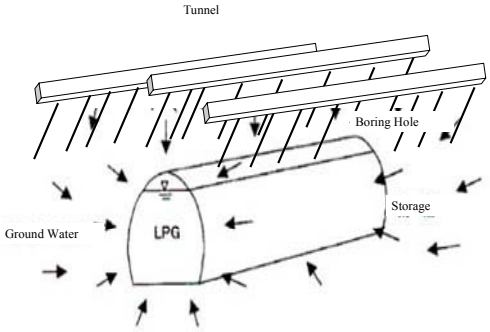

Fig.2: Concept of storage of liquefied natural gas.

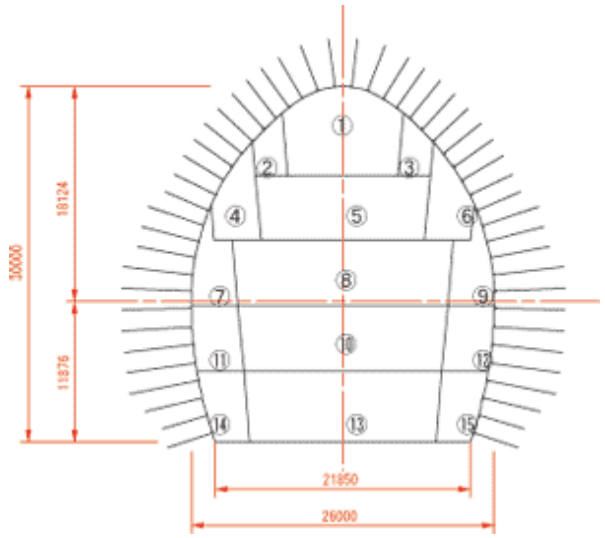

Fig.3: A typical example of cavern size and process of excavation

Fig.4: Tunnel for aquifer sealing

Excavation of underground cavern is generally performed by NATM. In Japan, a kind of rock is granite or diorite. Fig.3 shows a example of excavation process. In this excavation process, pore water pressure is always monitored in order to prevent unsaturated condition.

2. Developed key block analytical method

We introduce our developed key block analysis for aquifer sealed underground cavern with a calculation procedure.

First step shown in Fig.5;

1. Calculate the three dimensional coordinates of P0 intersection points of ridgelines of block planes and Pn0-PnX intersection points where the cavern cuts the block plane and intersection points of the ridgeline of block planes with the cavern.
2. Rotate block planes parallel to XY plane.

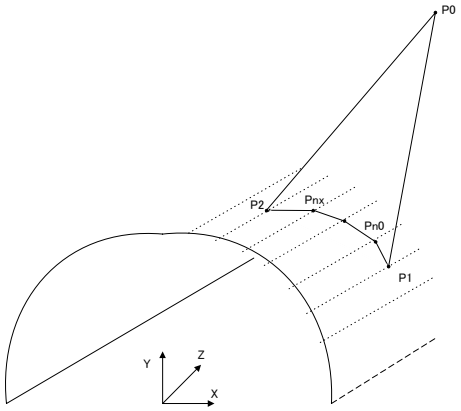

Fig.5 First step of key block analysis

Next step ;

3. Calculate a circumscribed quadrilateral of the block, and draw grids parallel to X-axis and Y-axis shown in Fig.6.
4. Extract grid points that are inside the block. Judgment of the positions of grids points is shown in Fig.7. Calculate original 3D coordinates of the extracted grid points that are ones before rotated coordinates by using inverse process shown in Fig.5.

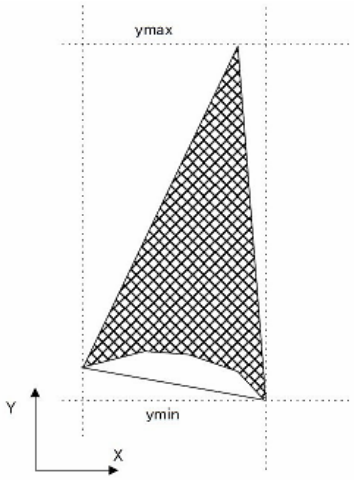

Fig.6 Second step of key block analysis

5. Calculate the distances between the grid points and plane of cavern.
6. Calculate the water pressures on the grid points using the distances.

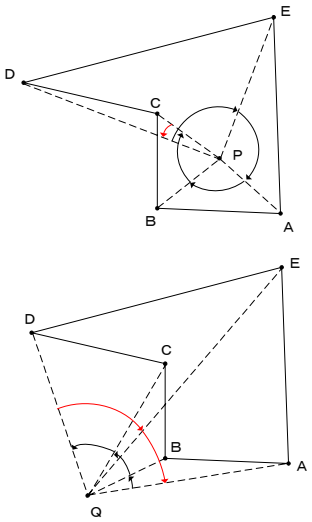

Fig.7: the method of judgment of a positional relationship between points and polygons.

Fig.7 shows the method of judgment of a positional relationship between points and polygons. In this figure, the angle between apexes of the polygon and the point A is 2π or -2π. In the case of point B, the angle shown in this figure is 0. The positional relationship between points and polygons can be judged by the angle.

3. Monitoring method of behaviors of key blocks

Rock masses in which excavations are constructed almost always contain discontinuities such as joints. These discontinuities intersect to create blocks of rock in the perimeter of an excavation. The behavior and stability of these relatively simple blocks is a problem of fundamental interest in the design and use of underground excavations. When a removable block has been identified, its stability must be evaluated so that the excavation design can include any ground support measures needed to maintain the stability of the underground cavern. In general, block behavior is influenced by the shear strength of the discontinuities, the initial stresses acting on the block faces, the changes in stresses that occur as the block forms, the block geometry and so on. Stress changes are a function of rock mass dilatancy, normal and shear stiffnesses, and block displacement. Key block geometry includes block height and width, block location in the excavation perimeter, displacement direction, and block size relative to the size of the underground cavern. Different approaches have been taken in evaluating keyblock behavior. However, it is difficult to judge whether detected keyblock is stable or unstable. Because there are errors in the data or the computations and the behavior of keyblock is affected by lots of factors, there are practical limits on prediction of the displacement that can be expected of a keyblock before either equilibrium is reached without support, or the keyblock completely fails.

We have developed the monitoring system of the behavior of keyblock by using photogrammetry (Nakai et al. 2003). This technique uses photographs of the object taken from multiple positions and orientations by a digital camera. The three-dimensional position of the point can be back-calculated by identifying the corresponding positions in the photographs. This is the basic principle of photogrammetry. An outline of procedure is shown in Fig.8. The object is photographed from various camera stations. Digital images for analysis are produced using targets attached to the object to specify measurement points in the underground cavern. The target on the image obtained by photography is processed to obtain the center of gravity. The center of gravity on the image is used as a basis for subsequent calculation. Calculations are made based on collinearity conditions. Collinearity means that the target as a measurement point, the image of the target, and the center of the camera lens are on the same line. In addition to the space coordinates of the target, exterior orientation parameters of camera such as camera position and orientation, and interior orientation parameters such as focal length c and the coefficients of lens distortion are unknown parameters. Observation equations are established from the collinearity condition. The observation equation with these unknown parameters is solved by the least square method. The method for solving all unknown numbers including camera parameters at once is known as self-calibration bundle adjustment. In the measurement in underground cavern, as is obvious from the photographing condition, the entire internal wall cannot be photographed at once, so connecting multiple photographs is required. To ensure the connection of photographs, numerous targets need to be photographed in respective photographs.

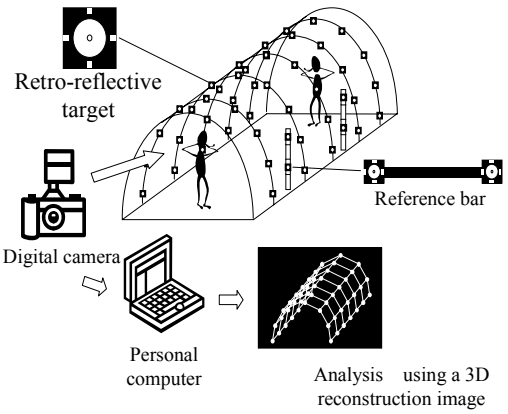

Fig.8: Outline of measurement using digital photogrammetry

Fig.9: Targets on the wall of tunnel and a measurement procedure (taking photos)

Measurements were taken in a 7-m-diameter tunnel for a length of 15 m. A total of 208 retro-reflective targets were positioned on the tunnel wall at intervals of about 1 m. For photographing, the object length of 15 m was hypothetically divided into three sections. Each section was further divided into five areas shown in Fig. 10. In each section, a total of 22 photographs were taken, 20 from either side in each area, and two in the front in Fig.11. A total of 66 images were obtained in three sections. Measurement accuracy was verified by comparing the image data with the measurements taken by Total Station instruments. Table 1 lists the results of the verification test. The standard deviations of the differences from the measurements by Total Station instruments are given in the table. It was assumed that the measurements by Total Station instruments contained an error of about 0.5 mm. The measurement results show that photogrammetry was considered as accurate as measurement by Total Station instruments. The photogrammetry technique is suitable for monitoring of keyblock under construction of underground cavern because displacements in a large area can be measured accurately. We have performed the measurement using photogrammetry only in tunnel construction. In the future, we plan to apply the photogrammetry to measurement of key block (Ohnishi et al. 2006).

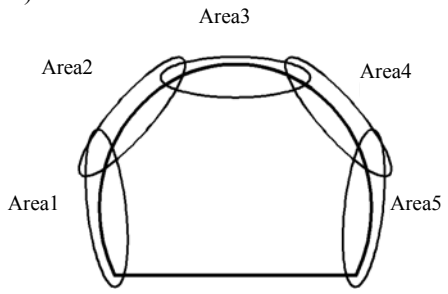

Fig.10: Divided area for exposure of photogrammetry

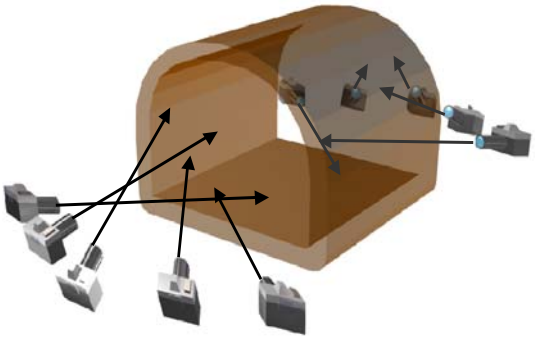

Fig.11: Digital camera configuration

Table 1: Accuracies of photogrammetry

X axis	0.6596 mm
Y axis	0.4541 mm
Z axis	0.5096 mm
3D coordinate	0.5480 mm

4. Conclusion

We present advanced key block analysis considering pore water pressure and photogarmmetry monitoring method for key blocks under construction of aquifer sealed underground cavern. The studies made so far show that key block analysis and photogrammetry are sufficiently applicable to rational and economical construction of civil engineering structures. We try to promote the spread of key block analysis with the new monitoring system.

References

Hatzor, Y.H., Talesnick, M. and Tsesarsky, M.,Continuous and discontinuous stability analysis of the bell-shaped caverns at Bet Guvrin, *Int J Rock Mech Min Sci.,* 2002, **39**(7), 867-886.

Nakai T., Ryu M., Ohnishi Y., Ohtsu H. and Nishiyama S., Keyblock Theory-Based Tunnel Support Design and its Validation through Digital Photogrammetry Monitoring of Field Application. The 2nd Southeast Asia Workshop on Rock Engineering, 2003.

Ohnishi,Y., Nishiyama, S., Yano, T., Matsuyama, H. and Amano, K, A study of the application of digital photogrammetry to slope monitoring systems, *Int J Rock Mech Min Sci.,* 2006, **43**(5), 756-766.

Application of DDA to Evaluate the Mechanism of Rock Slope Instability

G.C. MA[1], Y. OHNISHI[2], and K. MONMA[3]

[1] OYO Corporation, 1-5-1 Usaminami, Gifu-shi, 500-8367, JAPAN
[2] Kyoto University, 4, Kyoto Univ. Katsura, Saikyo-ku, Kyoto, 615-8540, JAPAN
[3] Toa Grout Kogyo Co. Ltd., 2-10-3 Yotsuya Shinjuku-ku, Tokyo, 160-0004, JAPAN

In order to analyze failure of rock slopes, numerical method will be extremely useful. However, it will be difficult to simulate collapse, considering difficulties of obtaining rock parameters, such as geological conditions into numerical calculation. In this paper, in order to clarify the rock mass failure process provided in rock mass monitoring, we applied a failure judgment standard for the existing discontinuities and the new discontinuities. From the application example to rock mass failure monitoring of Amatoribashi-Nishi site, it was clear that failure behavior such as a failure mode could be simulated well by DDA

Keywords: Numerical analysis; DDA; Rock mass; Rock mass failure monitoring

1. Introduction

Rock masses were generally accompanied with complex geological structure. There were various discontinuities such as fault, joint, crack and others. Therefore mechanical stability of a rock slope is in many cases influenced greatly by deformation and strength characteristic of the discontinuity existed in rock masses. Consequently, it was generally difficult to predict the outbreak and the scale of failure, and to evaluate the influence range for a rock mass failure phenomenon. Furthermore, it also is difficult to carry out effective stable countermeasures, because it progresses rapidly when the failure once begins. Besides, it could be thought that rock mass failure is affected not only by behavior of existing discontinuities but also by outbreak of new discontinuities due to reduction of rock mass strength caused by weathering or heavy rain.

It is a very important problem to take into account such peculiar property of rock masses in numerical analysis, and to study about the understanding of an omen phenomenon of rock mass failure, and to foresee or predict rock failure. As one of the research actions, rock mass failure monitoring at 13 places in Japan have been carried out. At each point, various measuring instruments have been installed to understand the behaviors just after or just before slope failure. And it was successful in measurement of rock mass failure behavior at Amatoribashi-Nishi site, which was one spot of 13 monitoring sites [1].

On the other hand, in the field of numerical analysis, some numerical analysis methods to directly model the discontinuity are suggested. Some analytical techniques can be tapped such as FEM (JFEM) [2] which uses joint element, rigid body spring model (RBSM), distinct element method (DEM) [3], discontinuous deformation analysis (DDA) [4, 5]. However, because it is extremely difficult in general to grasp all properties of a discontinuity firmly; for these numerical analysis, the following modeling technique were adopted in many cases; modeling the discontinuities as same probability distribution without sorting dynamically, or expressing a concrete as individual discontinuities in a model with the object of a geologic continuity. Even if such a method is effective to evaluate behavior of rock mass constituted by a uniform discontinuity, in many case they would not be suitable for evaluation of failure mechanism of the rock slope consisted by the discontinuities with different continuity and different cohesive degree. Therefore, we cannot but say that it is extremely difficult in technology of current numerical analysis to model all such surfaces of discontinuities and it was almost unable to extract the motive discontinuities of rock masses failure from a lot of discontinuities beforehand.

In this paper, we have applied DDA to rock masses failure behavior analysis, and shown that a device in analysis to simulate precisely the initial stress state in rock masses is necessary. And by examining relationship of a mechanical characteristics of the discontinuities occurred by new rock mass failure and to the existing data with the laboratory experiment, a rock mass failure process provided by rock mass failure monitoring has been simulated.

2. Applicability of DDA to rock mass failure behavior analysis

2.1 Fundamental

DDA, Discontinuous Deformation Analysis was developed by G. H. Shi [4, 5]. It is a method for dynamic and quasi-dynamic analysis for estimating elastic displacement and deformation of 2D cross

section consisted of polygon blocks (elements). Recently, DDA has been popularly applied to Rock-fall analysis [6, 7] and DDA can be applied to estimate mass movement of landslide, blasting [8] etc.

In addition, between contact blocks, penetration distance d_p is introduced. When apex of block i and edge line of block j contact, energy stored due to d_p is defined as equation (1) and is shown in the figure below.

$$\Pi_{Kp} = \frac{k_p}{2} d_p^{\ 2} \tag{1}$$

Here, k_p is stiffness of contact or constraint springs. Penetration d_p after contact is presented by apex coordinates of block and unknowns of blocks i and j.

By the way, k_p is designed not to penetrate between contact blocks, and plays a role of transferring forces between contact blocks. On the other hand, when a edge line of block contacts another block line, analysis is conducted as two sets of apex and edge contact.

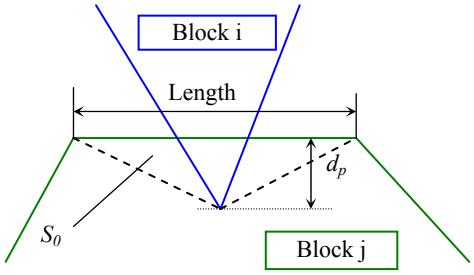

(a) Contact between apex and edge of blocks

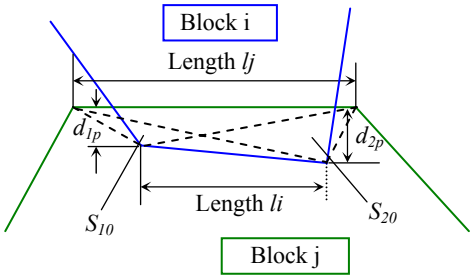

(b) Contact between edges of blocks

d_p,d_{1p}, d_{2p} :penetration distance from point to edge

S_0,S_{10}, S_{20} :Area of the penetration triangle

Fig. 1: Contact and penetration between blocks in DDA

2.2 Simulation of initial stress

In DDA, we can consider initial stress as input data, but in many cases in order to simulate the initial stress special technique is used because the initial stress changes with the position like a rock slope.

Conventionally, dynamic analysis is usually performed in this kind of analysis. In addition, both static and dynamic analyses can be conducted with the DDA method. For static analysis, the velocity of each block in the blocky system at the beginning of each time step is assumed to be zero. On the other hand, in the case of dynamic analysis, the velocity of the blocky system at the current time step is an accumulation of velocities in the previous time step.

In dynamic analysis, as the case that stress in a rock mass block or contact between blocks may become in an unstable state by its tare mass or deformation of itself at the first number step. In other words, even if it was being in stable state originally the rock mass, it may become unstable, and stable evaluation of rock mass in a limit state becomes difficult.

Therefore, in this study, we suggest a method of analysis that combined static analysis with dynamic analysis. In other words, we perform static analysis with number of steps at the beginning of analysis and carry out dynamic analysis afterwards. In the static analysis, an initial stress state by tare mass would be analyzed while reducing displacement velocity of a rock mass block to produce by the tare mass to the maximum. By this, to simulate a stable rock slope for the actual status is not to mention, a stress state of a rock slope just before failure can be simulated. By dynamic analysis of the next, calculate deformation of a rock mass block and dynamics relations at the time of contact between rock masses every step, and chase movement of each block, and analyze behavior at the time of failure and a trace or shape after failure.

2.3 Modeling of discontinuities

In DDA, discontinuities were handled as a boundary surface of a rock mass block. In other words, rock mass block is surrounded with the discontinuities, and blocks were deal with as homogeneous rock mass without discontinuities. Therefore, the strength evaluation of discontinuities expressed mechanical relations in contact or in separation between rock mass blocks, and it has to be using different mechanics model for the discontinuities existing or occurred newly with a failure. Both discontinuities would to obey Mohr-Coulomb criterion, but should to be supposed failure standards differently.

For modeling an existing discontinuity, many of analytical technique [2, 9] suggested till now, it is to evaluate the discontinuities uniformly as a constant condition from few laboratory experiments. Such methods would not very have problem in the case of property of a crack is simple, but it could cannot apply in the case of each crack has different strength

characteristic like the rock slope by weathering or deterioration. Besides, it is near to impossibility to examine the property of each crack by field or laboratory experiment entirely.

Therefore, the submission is that modeling of rock slope is to divide discontinuities into groups according to degree of cohesion and strength characteristic of the discontinuities not to sort by area, and to carry out the laboratory experiment for representative discontinuity in every group. Potential discontinuities exist in the actual rock mass, so it can be thought that the mechanical property of rock mass block to deal with here was different from the intact rock.

Next, we explain the new discontinuities occurring with rock mass failure. Generally, as the analysis method of outbreak or evolution of crack, there are the static methods by using a strength standard and the dynamic methods by using an energy standard as the outbreak condition of a crack. By suggestion technique, strength standard was used for an outbreak condition of the crack, and to deal with the problem of cracks occurring stability while maintaining static equilibrium. Therefore, dynamic or shocking load problem does not be intended. While just using the present DDA, at the first stage of modeling, the discontinuities that would occurs newly by the rock mass failure was defined beforehand as a boundary of rock block in various positions and directions, which should to be expected by considering the change of geologic and the distribution situation of the existing discontinuities. In this article, we name such boundary surface that becoming discontinuity from the middle stage of analysis as "potential surface". In other words as showing in Fig. 2, the potential surface can become discontinuity by a stress state, and defined as boundary surface (Fig. 2, *ab*) contacting with 2 adjacent rock block (Fig. 2, *A* and *B*). The potential surface would be given a strength equivalent for neighboring rock blocks and the continuity should be maintained till newly discontinuity was judged to outbreak by a given outbreak condition.

We suppose the failure criterion of new discontinuity obeys Mohr-Coulomb equation, to assume shear stress on the potential surface as τ, normal stress as σ, breaking mechanism of a discontinuity is expressed as equation (2).

$$\begin{aligned} &\text{Tension area (Tension failure)} && \sigma \geq \sigma_t \\ &\text{Compression area (Shear failure)} && \tau \geq \tau_t + \sigma \tan\phi \end{aligned} \tag{2}$$

Where, σ_t is tension strength of rock mass around the potential surface, τ_t is shear strength, ϕ is internal friction angle. Fig. 3 shows a general idea of Coulomb criterion, ϕ and τ_t can be expressed with tension strength σ_t and compressive strength σ_c as equation (3).

$$\begin{aligned} \sin\phi &= \frac{\sigma_c - \sigma_t}{\sigma_c + \sigma_t} \\ \tau_t &= \frac{\sigma_t}{2} \cdot \frac{1+\sin\phi}{\cos\phi} \end{aligned} \tag{3}$$

In DDA, creation of new discontinuities was judged by the contact condition of an apex and an edge. As showing in Fig. 2, apex *a* and *b* are contact points between rock block *A* and *B*. Potential surface *ab* is divided in half, and a failure condition is checked for contact point *a* and *b* respectively.

In addition, when a crack was judged to outbreak, the shear and tensile strengths of the potential surface would become zero at the same time, supposing the friction angle is not to change. And the potential surface would be haves as a new crack distinguished from an existing crack after failure.

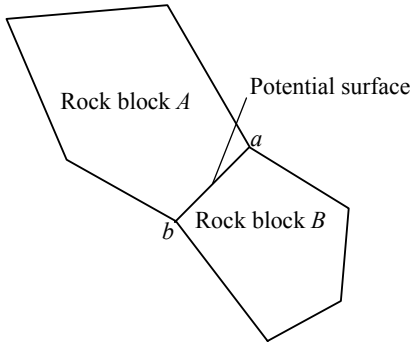

Fig. 2: Definition of potential surface

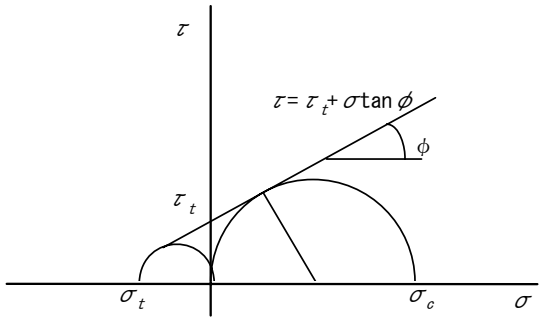

Fig. 3: Concept of Coulomb criterion of failure

2.4 Estimate of rock mass strength

By weathering, erosion and scale effect, the strength (σ_c, σ_t) of rock mass at the potential failure surface becomes smaller than the strength provided from the rock examination using the intact rock. A calculated strength for rock mass has been suggested by Ikeda [10], who said that the strength of rock mass would be calculated by taking advantage of rock material strength estimated by square of a crack index which is the ratio of the elastic wave speed of rock mass and the intact rock. In addition, Sezaki [11] evaluated the Young's modulus and compressive strength of the rock mass by evaluating statistically the relation between them with rock materials by using a rock mass database. Here, referring to the concept of Ikeda and Sezaki, we supposes that compressive strength (σ_c) and tension strength (σ_t) of a rock mass would fall off simply with a ratio from its of a rock materials (σ_c', σ_t'), and calls the coefficient k as "strength reduction rate". It can be expressed as equation (4).

$$\sigma_c = k \cdot \sigma_c' \qquad \sigma_t = k \cdot \sigma_t' \tag{4}$$

3. Examination of suggestion technique by a numerical experiment

To examine this suggestion technique to simulate a rock mass in a limit state, we carried out the numerical experiment that assumed rock mass there is a discontinuity on the back and did an overhang.

3.1 Analysis model and physical properties

Fig. 4 shows the analysis model assumed. In this rock slope, the crack would occur in the vicinity of the point showing in ○ mark in Fig. 4 in time by weathering or erosion, and it would be thought that the rock mass would cause failure. Here, strength of the discontinuities and the rock block were assumed using a rock test value obtained at Amatoribashi-Nishi site described later. The rock test results were as follows: compressive strength σ_c'=63.9MPa, tension strength σ_t'=10.6MPa, and friction angle ϕ =32. Table. 1 shows the rock properties and numerical experiment conditions.

3.2 Analytical procedure and the results

In DDA analysis, the case of static analysis carried out for ten first time steps (about 0.7 seconds), and the case of static analysis without ten step calculation have been compared. For strength reduction rate, three cases

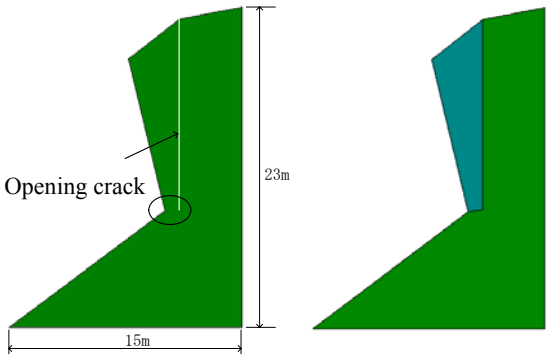

(a) Overhang rock mass assumed (b) Analysis model

Fig. 4: Analysis model assumed

Table. 1: Rock material properties and numerical experiment conditions

Item			Value
Analysis parameters	P (MN/m)		20000
	N*		300
	N_1*		10
Rock mass block	E* (GPa)		24.5
	ν *		0.2
The new crack occurred with failure	k=10%	ϕ(°)	45.7
		τ_t(MPa)	1.30
		σ_t(MPa)	1.06
	k=5%	ϕ(°)	45.7
		τ_t(MPa)	0.65
		σ_t(MPa)	0.53
	k=1%	ϕ(°)	45.7
		τ_t(MPa)	0.13
		σ_t(MPa)	0.11
Opening crack	ϕ(°)		32.0
	c* (MPa)		0

*N: Number of time steps, N1: Number of time steps for static analysis, E: Young's modulus, ν: Poisson's ratio, c: Cohesion

of k=1%, 5%, and 10% were examined.

Fig. 5 shows the deformation behavior of the rock block with k=5%, and Fig. 6 shows a time history for displacement increase and stress of the rock. By Fig. 5, It is cleared that a rock block shows deformation of toppling failure clearly when static analysis without first few step calculation. On the other hand, the rock block keeps a stable state without failure when static analysis and dynamic analysis were combined. And by Fig. 6, we understand that the minimum principal stress of the rock block changes with time when static analysis did not be performed in first few time steps. Such change arises from the variance of contact force between blocks and deformation of rock block caused by their tare mass. With the changes, the displacements of blocks were accumulated at every analysis time step. On the other hand, when analysis combines static analysis with dynamic analysis, the minimum principal

stress of blocks becomes almost constant, and there was not a change. Although it did not be shown in the figure, blocks were stable even if either analysis with a case of k=10% were carried out. Likewise, with a case of k=1%, the rock block falls down in both analyses.

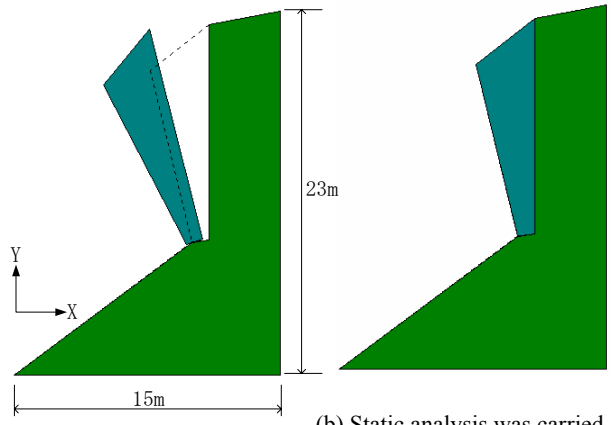

(a) Static analysis was not carried out

(b) Static analysis was carried out in t=0-0.7s, and the dynamic was carried out later

Fig. 5: Analysis results by DDA (k=5%)

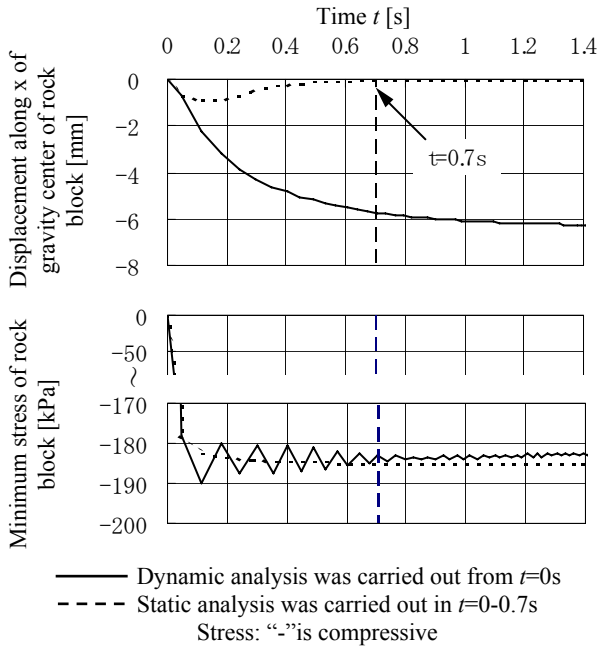

Fig. 6: History for displacement increase and stress of a rock block in turning by DDA (k=5%)

From these results, it is clear that the principal stress of a rock block changed periodically when dynamic analysis was carried out from first time steps. The rock slope that even if it has been stable originally would become to fail. It can be thought that such change would grow bigger in the case of a complicated model constituted with many blocks. Therefore, it can be thought, that if static analysis was carried out till changes between blocks by its tare mass was become to converge and the normal dynamic analysis was carried out after that, rock mass behavior from a stable state reaching failure can be analyzed.

4. Application for Amatoribashi-Nishi site rock mass failure

4.1 Rock mass failure of Amatoribashi-Nishi site

Fig. 7 shows a side photograph and a sketch of Amatoribashi-Nishi rock slope. In this figure, the dashed line shows the rock blocks recognized by the side sketch. And *a-d* block failed on February 27, 1999, approximately 2 weeks later *e* block was dropped on March 15. The rock slope collapsed twice in succession. A video image of the failure was recorded by ITV installed for the measurement of the rock slop.

According to the video, the failure process of toppling were seen, in the first failure, *d* block bent forward slowly and collapsed finally by destroying as to be stripped of *c* block which had became the support on the front. And in the second failure, *e* block bent forward slowly first and collapsed inclined to the plumb lower part all in one body afterwards for few five or six seconds. This time, simulation for twice failure of the rock mass was performed, and it was examined that the possibility to foresee or to predict a rock mass failure mode by a numerical analysis.

4.2 Analysis model and physical properties

Fig. 8 shows the analysis model. In the figure, *a-e* block supports the block showed in Fig. 7 respectively. These blocks have been divided into some small blocks beforehand and set the potential failure surface for each small block by assuming these blocks would to be destroyed to some small portions at the time of failure. But strength of the potential surface would use the rock mass strength to mention it later.

Fig. 9 shows a setting range of block material properties and discontinuity material properties in the analysis model. As shown in the figure, the block was assumed to be divided into 2 kinds and the discontinuities was into 3 kinds according to the difference of properties. Investigation before failure, we found that gaps were filled up with rubble whether they becomes hollow during blocks of *c* and *d*, *d* and *e*, and the backside of *e*. Such fillers could be recognized as discontinuous body in analysis, but they distinguished its properties from rock mass. As showing in Fig. 9(a), region *A* shows the rock lump part (rock lump), and *B* shows a partly filled up with rubble or hollow (filler).

In addition, by investigating failure behavior before and after, we classify the discontinuity roughly into two kinds of existing things and the things generated newly by failure. Furthermore, the existing discontinuity can be classified into two kinds of completely open thing and cohesive thing. The completely open discontinuities would be assumed they do not have cohesion, but the frictional resistance force would still stayed. From these prospects, the discontinuity can be assumed as three groups. As shown in Fig. 9(b), group Ⅰ points the completely open discontinuities, group Ⅱ points the cohesive discontinuities, and group Ⅲ points the discontinuities newly generated by failure.

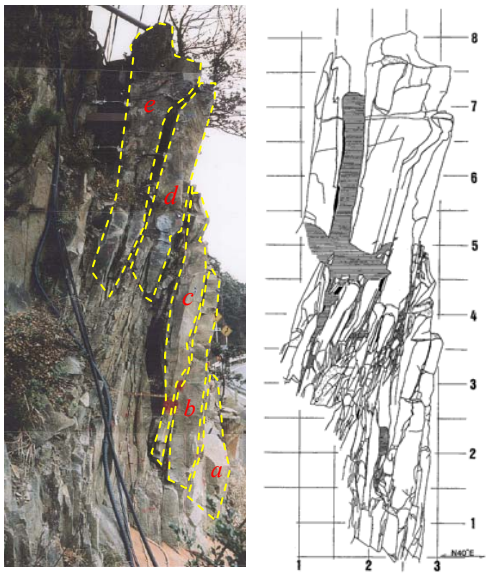

Unit of numeric: m

(a) A side photograph (b) A sketch

Fig. 7: Rock slope of Amatoribashi-Nishi site

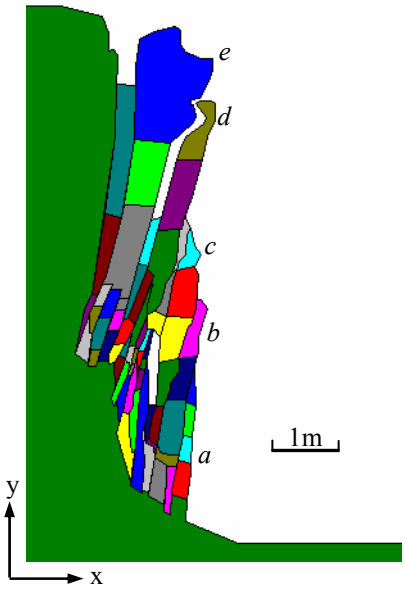

Fig. 8: Analysis model assumed

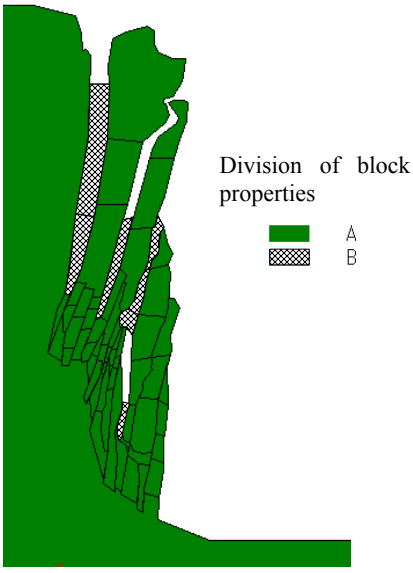

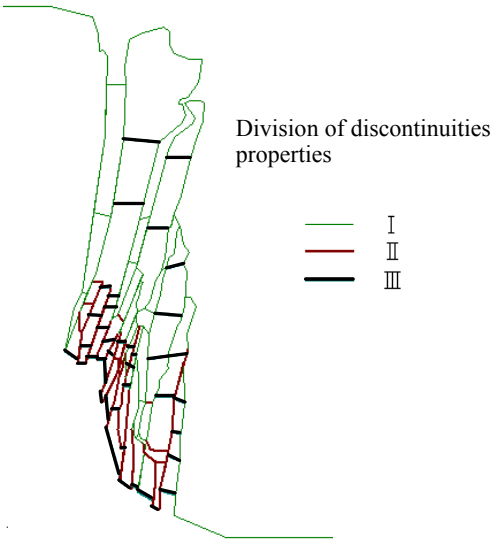

(a) Setting range of block properties (b) Setting range of discontinuity properties

Fig. 9: Setting range of the material properties

In order to obtain the material properties of the rock mass and the discontinuities, rock tests of uniaxial compression, Brizilian test, and multiple-stage direct shear test by using the specimen including existing discontinuity have been carried out. Table. 2 shows the results of the rock tests, and Table. 3 shows material properties and parameters used in the analyses. Where, rock block region *A* have adopted the rock test value, and for about region *B* the filler, the young's modulus were assumed to be 1/10 of the rock test value, the Poisson's ratio were to be 0.3. And about the discontinuities, for group Ⅰ, the fiction angle have adopted the rock test value, the cohesive strength were assumed to be zero; group Ⅱ have adopted the friction angle and cohesion of rock test value; and group Ⅲ were demanded from rock material strength (Table. 2) by using expression (3). In addition, as for the tensile strength of group Ⅲ, to take account of the weathering or deterioration of rock material itself, it were assumed to be smaller than provided by rock material tests. However, because there was not a method to set the value precisely, the tensile strength was assumed by performing the analysis repeatedly till the failure situation was reproduced.

4.3 Analysis results of rock mass failure behavior

Fig. 10 shows the rock mass failure situation of several time steps using k=30%. Fig. 11 shows rock mass collapse process at Amatoribashi-Nishi site. When compare the analysis results with the real failure video image showing in Fig. 11, it is clear that the failure mode of each block of the analysis results were good agreement with the real failure mode. The following are clear by examination in more detail.

As showing in Fig. 10(a), block *d* and *e* show similar movement at time 3.28s. This result agrees with the measurement results obtained in the rock mass monitoring about displacement before failure, in which the relative motion between block d and e was almost zero.

In Fig. 10(b), against the block *e* does not fall down, block *d* fall down greatly at 4.25s. When comparing this tendency with the first failure behavior of rock mass monitoring results, fall of block *d* agrees with the real failure at that block *d* was slowly bending forward at first. Fig. 10(c) showed a state of the failure that block *a* destroyed orderly from the upper part to the lower part at 4.99s till it does not support block *b*. In addition, block *b-d* is in simple fall failure mode. These were accord well with the real failure, the topping failure mode.

Fig. 10(d) and (e) showed the state of block *b-d* colliding at the ground front and back in 5.92s and 5.86s. Each block separated into 3-4 small rock lumps, but each block was not to separate into small rock lumps until arriving at the ground. This agrees well with the real failure mode. In addition, block *e* did not moved till now. This also agrees well with the real failure occurring twice.

Fig. 10(f) and (g) showed block *e* collapsing in 7.77s and 7.82s. Same as block *b-d*, separated into some small rock lumps at a moment to collide at the ground. In this way, two times of failure occurs, in addition, each failure range agrees with the real failure mode well. Fig. 10(h) showed the situation of failure before and after around 9.10s.

Table. 2: Results of rock material tests (Coarse sandstone)

Item		Value
Rock material	Uniaxial compressive strength σ_c' (MPa)	63.9
	Tensile strength σ_t' (MPa)	10.6
	Young' modulus E (GPa)	24.5
	Poisson's ratio ν	0.2
Discontinuities	Friction angle ϕ(°)	32.4
	Cohesion c (MPa)	0.056

Table. 3: Material properties and parameters used in analysis

Item			Value
Analysis parameters	P (MN/m)		200
	N		8000
	N_1		300
	Δt*		0.001
Rock block	Division *A*	E (GPa)	24.5
		ν (-)	0.2
	Division *B*	E (GPa)	2.45
		ν (-)	0.3
Discontinuities	Division Ⅰ	ϕ (°)	32.4
		c (MPa)	0
		σ_t (MPa)	0
	Division Ⅱ	ϕ(°)	32.4
		c (MPa)	0.056
		σ_t (MPa)	0
	Division Ⅲ	ϕ (°)	45.7
		τ_t (MPa)	3.90
		σ_t (MPa)	3.18

* Δt: Time interval in dynamic analysis.

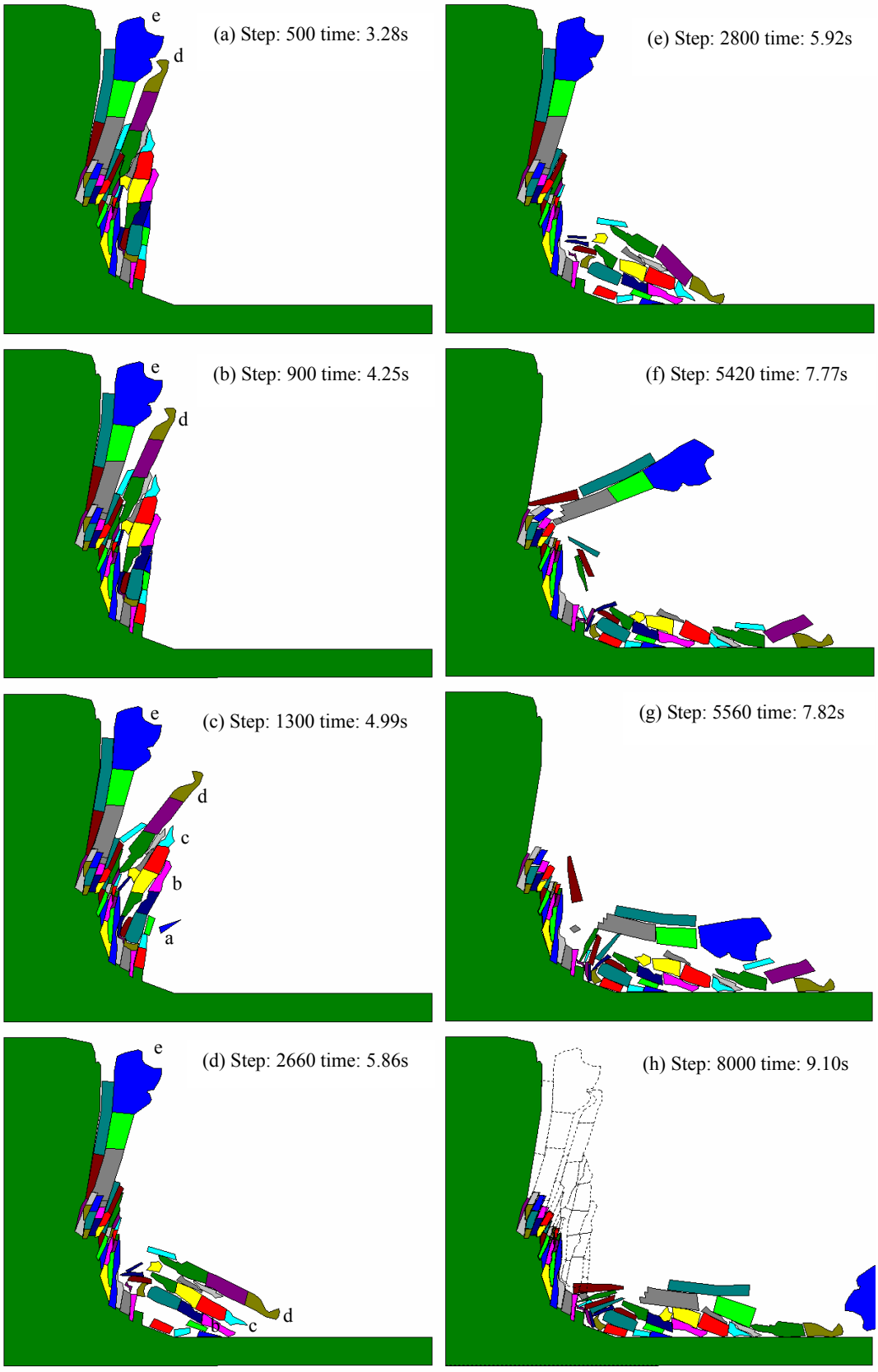

Fig. 10: Rock mass failure behavior by DDA (k=30%)

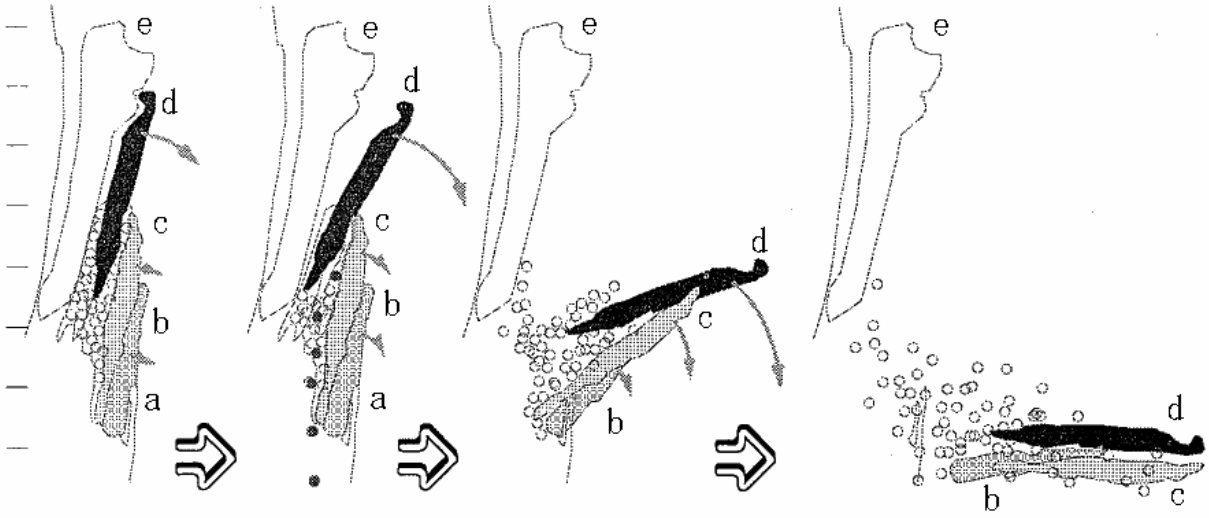

- ✧ Block d bends forward from the time before collapse 5 minute.
- ✧ AE events increase from this time, too.
- ✧ Some small rock-fall occurs from interval of block *b*, *c* and *d* on the time before collapse 1 minute 15 seconds.
- ✧ To be pushed by the fall block *d*, front block *c*, *b* and part of exfoliate and fall down.

(a) Block *a*-*d*

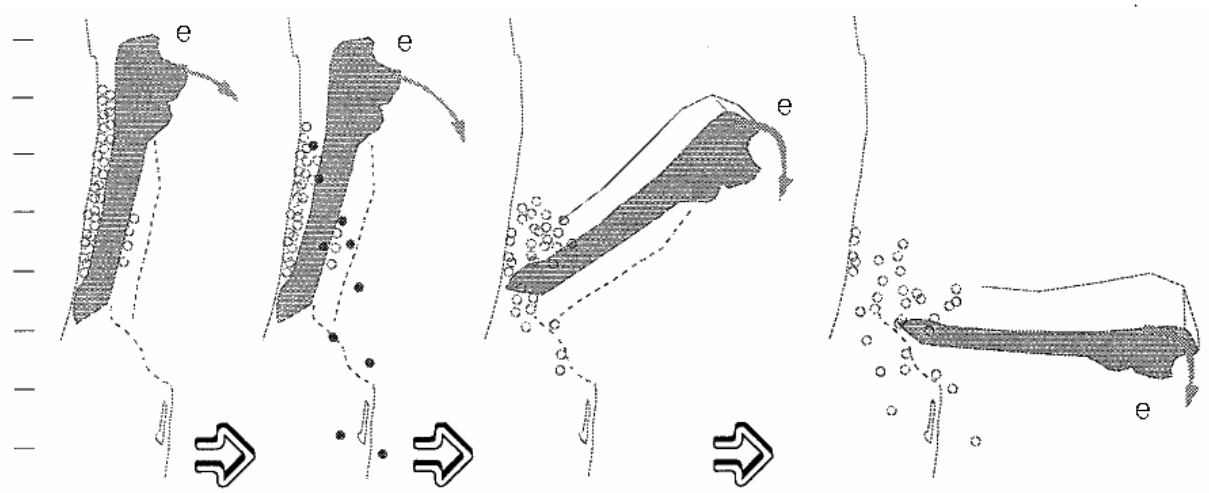

- ✧ Fall speed grows big from the time before collapse 4 hours.
- ✧ There are rock-falls before collapse 1 hour, and speed accelerates after this again.
- ✧ There become much AE events from the time before collapse 10 minute.
- ✧ Rock-fall occurs frequently from the time before collapse 5minute.
- ✧ Block begins to collapse to fall down straight forward as the fulcrum in block bottom end.

(b) Block *e*

Fig. 11: Rock mass collapse process at Amatoribashi-Nishi site [1]

4.4 Speculation

The analysis results by the application of numerical analysis suggested in this paper showed a good agreement with the real failure process. By these, it was clear that if modeling was carried out well by referring to the results of laboratory experiment and by using this technique, the rock mass failure process could be predicted. Following, we made a try to evaluate the strength reduction rate (k) quantitatively, examining how much of reduction of the strength of discontinuities and rock mass would cause failure.
Here, we performed two analyses in assuming strength reduction rate k to 100% and 50% without change other analysis conditions.

We show the last situation of the rock mass in case of k=100% for Fig. 12 and in case of k=50% for Fig. 13. By checking Fig. 12, block *a* - *d* showed big displacement, but was not to fail. In addition, by Fig. 13, rock mass reached to failure, but, for the block surrounded with circles ○, they are not separate into small rock lump blocks that were divided beforehand though the collision with ground. On the other hand, by the results of real failure (Fig. 11), block *a* - *d* did not separated into small blocks until its arriving at the ground, but each block had broke to 3 or 4 small blocks after arrival at the ground. By these results, it can be estimated that the average strength of the rock mass should be 50 - 30% of the laboratory experiment value which used for the intact rock material, so that failure showing in Fig. 11 occurred as for this district rock mass. However, as an application of DDA in this article, we tried different approach to express outbreak of a new crack with failure as the potential surface. In future, development of analytical method for the rock failure that can express crack promotion is expected by doing a device to divide the rock block into many more small blocks.

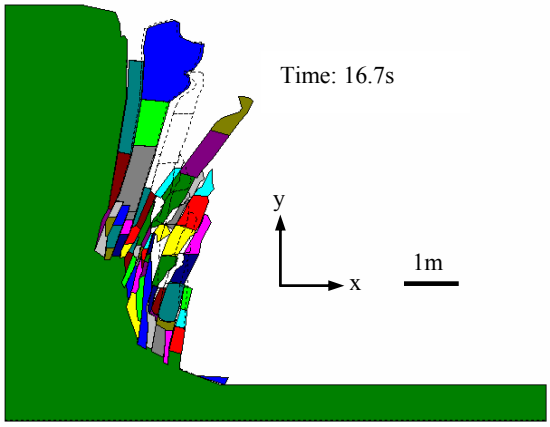

Fig. 12: Analysis results by DDA (k=100%)

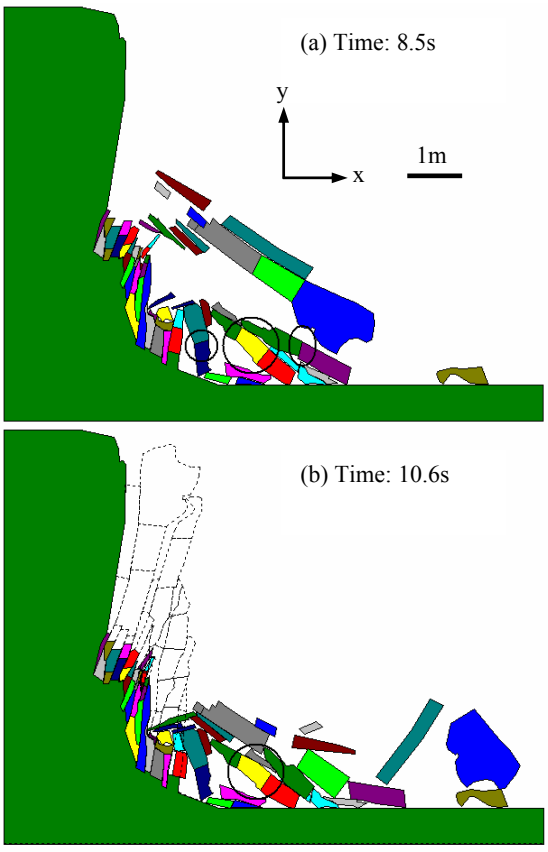

Fig. 13: Analysis results by DDA (k=50%)

5. Conclusions

In this article, in order to clarify the rock mass failure process provided in rock mass monitoring, we have applied a failure judgment standard based on Mohr-Coulomb criterion for the existing discontinuities and the discontinuities newly occurred with failure. And we have made the discontinuity model that grouped the discontinuity by this standard. In addition, it has been clarified by performing a numerical experiment that a fluctuation of initial stress by its tare of rock mass occurs when carrying out the analysis by DDA, and that this fluctuation would give the analysis results big influence when we reproduce an extreme stable state like a rock slope. Moreover, we devised an application of analytical technique to avoid it. By the numerical experiment, initial stress distribution by tare mass has been simulated well as occurring smoothly, and confirmed that it was possible to analyze rock mass behavior from a stability state to reaching fall failure by reduction of rock mass strength.

In addition, from the application example to rock mass failure monitoring of Amatoribashi-Nishi site, it was clear that failure behavior such as a failure mode and a failure rang could be simulated well by DDA if we assume the strength of discontinuities about around 30% of the laboratory experiment value. Furthermore, it was clear too that failure behavior of rock mass was

dependent widely on not only the existing discontinuities but also setting of the position and strength characteristic of the discontinuities which would occurred with failure. However, it was nothing but absolutely that we have tried an application in a failure example provided alone this time. Therefore, it is indispensability in order to foresee or expect slope failure that collect a rock mass failure example and a mechanics test result, and collection of fundamental data of how much we assume the strength reduction.

References

1. Momm, K., Onoda, S., Ochiai, T., Arai, K., Tsunaki, R. and Asai, K., 2002. A monitoring example of displacement behavior proceeding to failure at the toppling rock slope, *J. of the Jpn. Landslide Soc*., Vol.39, No.1, 62-69.
2. Goodman, R.E. 1976. "Methods of Geological Engineering in Discontinuous Rocks", *West Publish. Co.*
3. Cundall, P.A, 1971. A Computer Model for Simulating Progressive, Large Scale Blocky Rock System, *ISRM Symposium, Nacy, France,* 11-18.
4. Shi, G.H., 1989. Block system modeling by Discontinuous Deformation Analysis, *Univ. of California*, *Berkeley*, *Dept. of Civil Eng.*
5. Goodman, R.E. and Shi, G.H., 1987. The application of block theory to the design of rock bolt support for tunnels, *Felsbau 5*.
6. Shinji, M., Ohno, H., Otsuka, Y. and Ma, G.C., 1997. Viscosity coefficient of the rock-fall simulation, *Proc. of ICADD-2, Kyoto,* 201-210.
7. Ma, G.C., Nakanishi, A., Ueno, S., Mishima, S., Nishiyama, S. and Ohnishi, Y., 2004. Study on the applicability of rock fall simulation by using DDA, *In Proc. of the ISRM Symp. 3rd Asia Rock Mechanics Symp., Kyoto, 1-3 December 2004,* eds. Y. Ohnishi and K. Aoki, 1233-1238.
8. Ma, G.C., Miyake, A., Ogawa, T., Wada, Y., Ogata, Y. and Katsuyama, K., 1995. Numerical simulations on the blasting demolition by DDA method, *Proc. of 2nd International Conference on Engineering Blasting Technique (ICEBT), Kunming*, 79-84.
9. Bhasin, R.K. and H~~o~~eg, K., 1998. Parametric study for a large cavern in jointed rock using a distinct element model (UDEC-BB), *Int. J. Rock Mech. Min. Sci*. Vol. 35, No.1, 17-29.
10. Ikeda, K., 1979. The property and the strength of fissured rock masses, *Journal of Japan Society of Engineering Geology*, Vol.20, No.4, 20-32 (in Japanese).
11. Sezaki, M., Aydan, Ö., Ichikawa, Y. and Kawamoto, T., 1990. Properties for initial design of tunnels by NATM using rock mass data-base system, *Journals of the Japan Society of Civil Engineers*, No.421/VI-13, 125-133 (in Japanese).

Redevelopment of DDA program and its application

C.Y. HE, G. DENG and Yu-Jie WANG

Department of Geotechnical Engineering, China Institute of Water Resources and Hydropower Research, P. R. CHINA

The Dos-based DDA program originally developed by Shi has been upgraded into the Windows-based version by China Institute of Water Resources and Hydropower Research (IWHR) recently. In this new version of DDA program, user-friendly pre-procession and post-procession were developed and dynamic slope excavation can be simulated. An application of the new program to deep seated sliding analysis of Xiangjiaba gravity dam was presented in this paper.

*Keywords:*Re-development; DDA; Windows-based program

1. Introduction

Discontinuous Deformation Analysis (DDA), which is a new numerical method, has been widely used in practice. Based on the theoretical aspect of the DDA, a Dos-based program has been developed by Dr Shi. Three programs, named DC, DF and DG have been written by Dr Shi to accomplish the Pre-procession, post-procession and result visualization function respectively. The user interface of these programs is similar to UI of DOS system. Interaction between user and program is not available. However, when the geometry, boundary conditions and loading of practical problems are quite complex, an application of those programs is difficult. For DC program particularly, when block is generated, the number of block is determined by the material number of "Joint". If there is more than one "Joint", the number of block can not be determined. If there are many blocks, the block materials generated by DC are difficult to check. To apply DDA to hydropower engineering successfully, redevelopment of DDA program seems to be necessary.

Based on the source code of DDA provided by Dr Shi, a Windows-based DDA program has been developed by combining DC, DF and DG programs into one program named DDA-IWHR by using Microsoft Visual C++. This development mainly includes:

(1) to obtain the geometrical data for the DDA program by direct use of DXF files generated by AutoCAD;

(2) to develop a new mutual-interactive file named "bl*" to automatically generate the block material number, joint material number, loading information and others geometrical information needed in the late DDA analysis;

(3) to add multi-step excavation function to simulate stability status in slope excavation procedure.

(4) to enrich the post-procession function by taking advantage of the commercial program to dynamically display the color flood of displacement and stress.

2. Pre-procession program

2.1 Generation of diagram

The generation of diagram is fully accomplished by the "Pre" Menu as shown in Fig. 1.

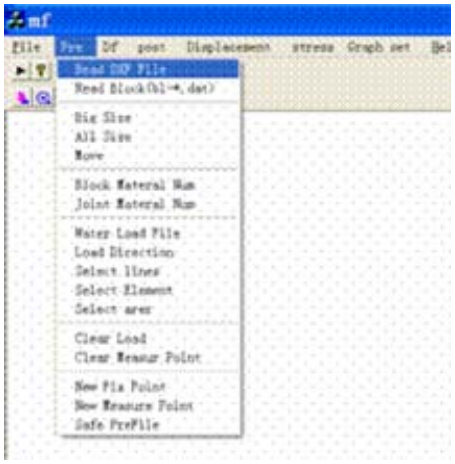

Fig. 1: Pre Menu designed for generation of diagram

The menu is designed for generating the geometrical information automatically, the procedure generally includes: (1) to click "Read DXF File" to choose the AUTOCAD DXF file; (2) to generate the needed geometry data by executing MC.exe; (3) to use the Menus "Big Size", "All Size" and "Move" to zoom in or out and to check the generated figure.

2.2 Edition of block and joint material number

For block material numbering, the Menu of "Block Material Num" is selected firstly to input the designed

number of block in the dialog box for material numbering; then to set the specified color to the corresponding block in the figure window by left clicking the mouse.

Similarly, the joint material numbering is also set by using the Menu of "Joint Material Num".

2.3 Load

There are two methods for inputting the load. The first way is to read the load data file directly, such as uplifting pressure of dam foundation. This method is suitable for those with bulk data. For those problems with small loading information, the interactive input is a much simple way.

For this way, just simply selecting "Water Load file" Menu to pop up the standard IO dialog box. There are three ways for the load edition:

(1) to choose "Select lines" Menu to select a line and apply load. Move cursor to lines to be dealt with. When these lines are highlighted, click left button. Load value and position is calculated automatically and marked in the figure.

(2) to choose "Select element" Menu to calculate automatically and to mark load values and application points of lines in block elements.

(3) The "Select area" Menu that is designed for selecting a zone is to calculate automatically and to mark the load magnitude and application points of lines in this selected zone.

The other interactive input way is to use "Load direction" Menu. In this Menu, There are five choices, namely "left", "right", "up", "down" and "water", which stand for the direction of load. By selecting one of these five options, the load magnitudes and application point of lines can be determined and marked automatically.

2.4 Setting up fixed measuring points

Since the block file generated by directly reading DXF files, the necessary information on fixed and measuring points are not included in the generated file. This task may be finished by using the "New Fix point" Menu. By moving cursor to a point that will be set a fixed one, requiring fixing, a color circle indicating a fixed point has been set up will be displayed by clicking the left button of mouse.
Following a similar procedure, the measuring point may be set up by selecting the "New Measure point" Menu.

2.5 Saving data

When all the necessary geometrical and loading information have been processed following the procedures mentioned above, a file named "bl-*.dat" will be saved by choosing "Save profile" Menu, "*"standing for the prefix of DXF file.

2.6 Block data re-reading

If edition of bl-*.dat file has been completed and the file was saved already, you can choose "Readblock (bl-*.dat)" and edit data directly when re-edition is needed.

3. DDA computation

After the data file named "b1-*.dat" that is designed for the geometrical information was obtained, the DDA computation can be advanced by combining the other data file named 'df*" specifying the other governing parameters. We can use "Df" Menu as shown in Fig. 2 to adjust the values of rigidity of spring, load step, and minimum error tolerance.

The "Calculate" Menu is used to control DDA analysis without excavation, however, the "Step df" Menu is for excavation case. The multi-step excavations of slope can be simulated by using the "Step df" Menu.

Fig. 2: DDA Computation Menu

4 Post-Procession Function Of DDA

Based on the program DG originally developed Dr. Shi, a new Windows-based post-procession program has been developed, the main Menu "post" dealing with the post-procession function is illustrated in Fig.3, which includes:

(1) The "Read dgdt file" Menu is used to input the post-procession file.
(2) The "Begin_step_plot" Menu is designed for reading the multi-stage excavation file. Using this Menu, we may display the movement status of blocks at step N.

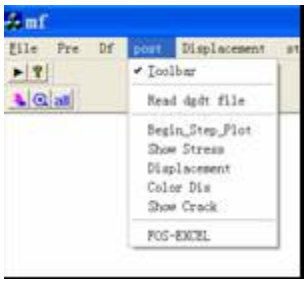

Fig. 3: Post-procession Menu

The Menu of "Color Dis" deals with color display mode for displacement vector. Currently, only four color modes are developed, that is

(1) R-B transient color mode. This mode changes the color from blue to red. Blue stands for minimum displacement, and the red the maximum displacement.
(2) RGB transient color mode.
(3) RYB transient color mode.
(4) BGY transient color mode.

The Menu of "FOS-EXCEL" is used to display the factor of safety at each computation step. Firstly, the Menu reads out the factor of safety at each step from the DGDT file, saving these information to a FS.txt file. Secondly, the plot of safety against the iteration step can be drew by using EXCEL.

The main Menu of "Displacement" is used to display the horizontal and vertical displacement, as shown in Fig. 4.

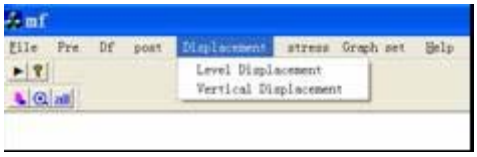

Fig. 4: Displacement Menu

The main Menu "Stress" provides four modes for stress display, as shown in Fig. 5. The "Small principle stress" is used to display minimum main stress; the "Big principle stress" maximum main stress; the "X string" the horizontal stress; and the "Y string" the vertical stress.

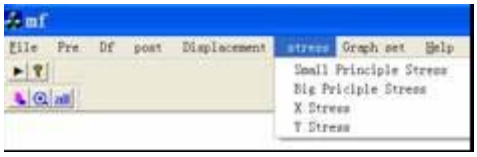

Fig. 5: Stress Menu

For each mode of stress display, four color modes are also available. similar to displacement. The displacement of a slope displayed by the R-B transient color mode is illustrated in Fig. 6.

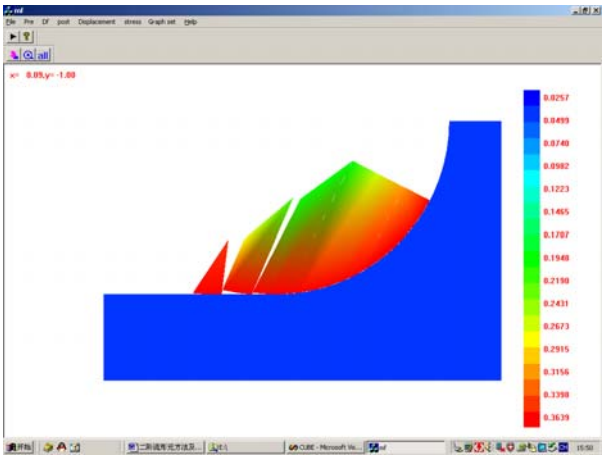
Fig. 6: Slope displacement displayed by the R-B transient color mode

5. Application

After re-development of Windows-based DDA program was completer, the deep-seated stability analysis of Xiangjiaba gravity dam was performed by using the new version of program.

5.1 Background

The Xiangjiaba hydropower project is the last stage hydropower station in the cascade exploitation of hydropower resource of Jinsha river. Xiangjiaba dam is a concrete gravity dam with a length of 897m, a height of 161m. This dam is built on Triassic sandy rock. As a main feature of engineering geology of the dam site, Limeiwan knee-like deflection zone with a width of 100m stretches into the dam site from Limeiwan chase at North West corner and extends to South East corner of the dam site. Due to this deflection zone, the bedrock condition at the dam site becomes quite complicated and poor. In addition, 2 first-level and 10 second-level seams dipping at a intermediate angle were also found at the dam site. From failure mode analysis, these geological discontinuities probably form one part of slip surface. in addition, the rock mass at the downstream side displays considerable discontinuities dipping upstream. Therefore, at the Xiangjiaba dam site, a potential deep seated sliding of the dam exists, a stability analysis is necessary to perform. A typical cross section of Xiangjiaba dam along the foundation conditions is illustrated in Fig. 7.

The DDA method is applied to investigate the deep seated stability analysis problem.

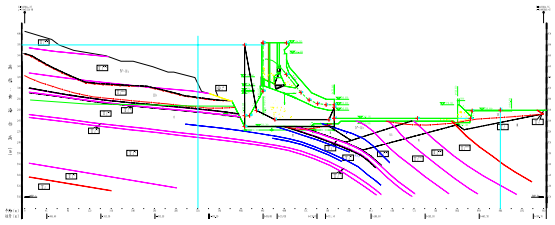

Fig. 7: typical cross section of Xiangjiaba dam

5.2 DDA numerical modeling

It is very easy to generate computation model using new pre-procession program, the main procedures for modeling are as follows: (1) to establish a new layer in CAD, and to re-plot the figure by lines or multi-lines, using different line color to specify different joint materials. (2) to close another layers when re-plotting was completed, and to copy the new figure to a new file, saving as a DXF file. (3) to open a new DDA program, inputting the DXF file to generate automatically all geometry data needed by MS.exe. (4) to execute MC.exe to generate a block file bl*.dat. The DDA numerical model of No. 12 monolith generated automatically by the redeveloped DDA program is shown in Fig. 8.

For complex geology model, numbering of block material is not sure to be right, because MC.exe will generate number of block according to number of joint material. Number of block and joint material can be edited in an interactive way. Different block materials and different lines will be shown using different colors. Since a geometry point in DDA program will stand for multi points, we can move the curse to verify whether or not this case was occurred. When the curse is moved, the coordinate, element number, element material, adjacent joint, and joint number will be displayed at the up-left corner of screen. By careful checking whether the values appeared are correct, the validation of numerical model and accuracy of result can be achieved by careful check.

Since the geometrical information was obtained automatically from the CAD file, the fixed and measuring points should still be set by using mouse.

According to design criteria of hydraulic structure (DL5077-1997), uplift pressure used in analysis is illustrated in Fig. 7. The load case is normal impounded level with upstream water level 380.0m and downstream water level 265.8m. Water loads in many points are set by giving controlling point coordinates and load value in order.

Load value and position on lines in block elements are calculated automatically and illustrated in figure as concentrate forcse. A DDA format load file is generated. The total procession of DDA model generation is in an automatic and interactive way. It is very fast and convenient. A typical DDA model generated is shown in Fig. 8.

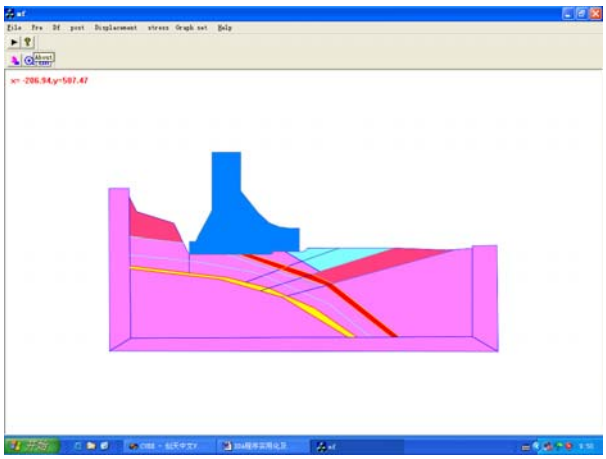

Fig. 8: A DDA numerical model for the Xiajiaba Project

The strength parameters of Xiang Jia Ba gravity dam in DDA is listed in Table 1.

Table 1 strength parameters of Xiangjiaba gravity dam

Rock and structure type	Defor-mation modulus (Gpa)	Poisson's ratio	Internal friction angle (°)	Cohesion force (Mpa)	Tensile strength (Mpa)	Bulk density (kN/m^3)
Rock Ⅱ	20	0.22	43.2	0.53	3	26
RockⅢ_1	11.75	0.25	37.4	0.38	2.35	26
RockⅢ_2	9.25	0.28	34.2	0.305	1.65	26
Rock Ⅳ	4	0.3	27.2	0.17	1	26
JC2	0.72	0.4	15.4	0.045	0	23
Fault	1.28	0.4	16.7	0.06	0	23
Concrete	20	0.167	56.3	2	1.85	24
Interface between rock and concrete			38.7	0.38	2.35	

5.3 Engineering computation

Many weak zones, such as JC2, JC3 and JC4, exist in No. 12 section. Geological conditions are much complex. There are many potential sliding surfaces. How to determine the true minimum FOS and its corresponding slice surface is the key point of engineering analysis. It is advantageous that DDA method not only satisfies Newton's Law, but also movement equation. In DDA, both load increment

method and reduced strength method may be applied to make the structure be a limit state, showing where the structure begins to damage, damage process and failure state. In the DDA analysis of Xiangjiaba dam, the load increment method is used, and having the horizontal load be increased several times to make the dam in a limit state, as shown in Fig 9.

Besides gravity load, the loads in gravity dam include horizontal load at the upstream face of dam, and seepage forces in the bed rock. According to design criteria, uplifting pressure at bed rock is assumed to be distributed in fold lines. Seepage force at any point of bed rock is calculated based on the vertical height between the point and the seepage line.

In order to explore the influence of seepage force on the dam stability, two load modes of water load in bed rock are introduced. One is that the water load was applied directly on specified sliding surface with same load value and inverse load direction. The factor of safety calculated is 2.390. The other load method is to apply water load on all joints in bed rock with the same load value and inverse load direction. The factor of safety calculated for this water load module is 2.419. It can be found from comparison that the factors of safety calculated water load modules are very close and both reasonable.

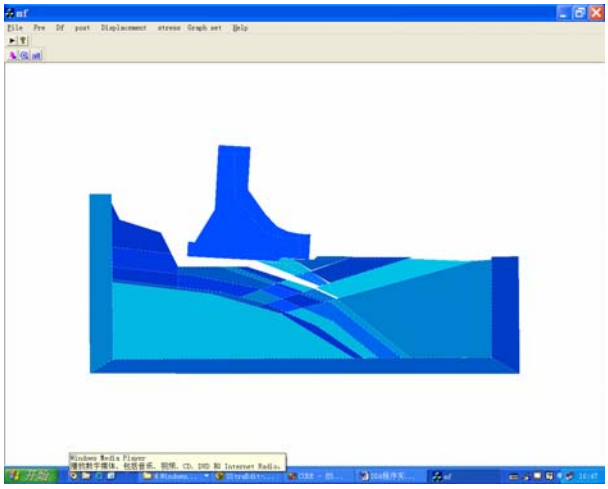

Fig. 9:

The values of the factor of safety during the iteration are recorded and saved to a single file named FS.txt. by the new DDA post-procession program. Convergence curve can be plotted by using EXCEL. By carefully checking whether this convergence curve displays a general relationship, whether the principal parameters used in DF program are reasonable can be analyzed. A typical convergence curve of the factor of safety is illustrated in Fig. 10.

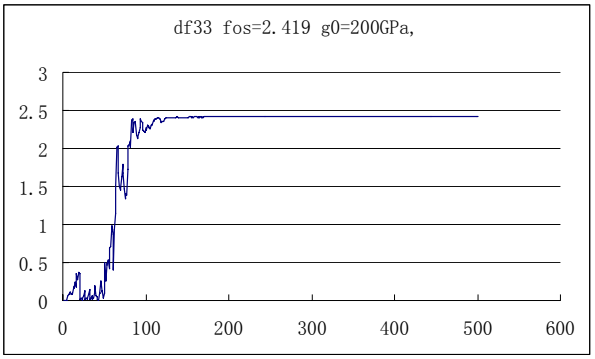

Fig. 10: Convergence curve of the factor of safety

6. Conclusions

Based on the Dos-based DDA program developed by Dr. shi, DC, DF and DF programs have been combined into a Windows-based program. The new-version of DDA program has been applied into deep seated stability analysis of Xiangjiaba gravity dam successfully.

Acknowledgement

Thanks a lot for Dr. Shi Genhua and his DDA program. It's grateful to have a chance to listen to Dr. Shi.

References

Shi, G-H. (1988). Discontinuous Deformation Analysis: A New Numerical Model for the Statics and Dynamics of Block Systems. Ph.D. Thesis, Department of Civil Engineering, University of California, Berkeley, 378 pp.

Shi, G-H. (1990). Forward and Backward Discontinuous Deformation Analyses of Rock Systems. Proceedings of the International Conference on Rock Joints, Loen, Norway. Balkema, pp. 731-743.

Shi, G-H. and Goodman, R.E. (1984).Discontinuous Deformation Analysis. Proceedings of the 25th U.S. Symposium on Rock Mechanics, pp. 269-277.

Shi, G-H. and Goodman, R.E. (1985). Two Dimensional Discontinuous Deformation Analysis. International Journal for Numerical and Analytical Methods in Geomechanics, vol. 9, pp. 541-556.

On seismic dynamic stability of No.Ⅱ deformation body by Newmark Method for Laxiwa Hydropower Project

SHI LI

Northwest Hydro Consulting Engineers, CHECC, Xi'an, P. R. CHINA

No.Ⅱ deformation body is located downstream to the left abutment for Laxiwa hydropower project, and its stability mainly affects the safety of left abutment and the zone of flood energy dissipation. The analysis of dynamic stability was made for No.Ⅱ deformation body by Newmark method and the process safety coefficient and its displacement were obtained. The comparative analytic computations of the above results were carried out between conventional pseudo-static method and 3-D finite element method, and the feasibility and reliability in the analysis of earthquake dynamic stability of the slope by Newmark method was discussed. It is concluded that it can basically satisfy design standards of No.Ⅱ deformation body under earthquake condition.

Keywords: No.Ⅱ deformation body; Newmark method; Stability analysis; Permanent deformation

1. Introduction

The pseudo-static method is often used in the earthquake stability of the slope. The earthquake action is assumed to be applied on the slope as constant static load, and its magnitude will be determined by the earthquake intensity where it is located. In fact, the magnitude and direction of earthquake action will vary with time. So, the pseudo-static method does not objectively and truly reflect dynamic stability under earthquake condition. In virtue of latest NM (Newmark) analytic procedure provided by Dr. Shi Genhua (an international famous math dynamics and a rock engineering expert) and using process curve of seismic acceleration at Laxiwa dam site. Under the guidance of Dr. Shi Genhua, the earthquake dynamic stability of No.Ⅱ deformation body for Laxiwa project was analyzed by Newmark method, and the process safety coefficient and its displacement were obtained. The comparative analytic computations of process results were carried out between conventional pseudo-static method and 3-D finite element method, and the stability of No.Ⅱ deformation body under earthquake action was comprehensively assessed while the feasibility in the analysis of earthquake dynamic stability of large rock slope by Newmark method was verified.

2. Geologic description of No.Ⅱ deformation body

Laxiwa hydropower project is situated on the main stream of Yellow River at the boundary of Guide and Guinan Counties. The project is composed of double curvature arch dam with log spiral, surface, deep and bottom outlets for discharging flood, plunge pool behind the dam, right-bank intake, and power intake system. The concrete double curvature arch dam is 250m high in maximum, with a total reservoir capacity of 1.079 billion m3, and an installed capacity of 4200MW that is the largest on the Yellow River.

No.Ⅱ deformation body is located at the downstream of left abutment for Laxiwa hydropower project, with the minimum leading-edge elevation of 2395m and trailing-edge pull crack crest elevation of 2650m. The elevation of 2395m is 90m away from arch abutment and the crest elevation is 50m from arch abutment. The width is about 150m along the river and the length inward from the river-bank is about 200m, with an elevation difference of 255m and a total of excavated quantity of 181m3. The boundary is strictly controlled by soft structural plane (Table 1). The upstream tends to be mid-dip angle fault F29, the bottom slide plane is of low-angle fault Hf4, and the trailing-edge pull crack plane is of high dip-angle pull crack; the downstream is of steep dip-angle fissure L145 in SN direction, and its stability mainly affects the safety of left abutment and energy dissipation zone for flood discharge.

In view of external features, the gentle slope is located at El.2395m~2450m, which the surface layer is collapsed, accumulated and covered, with structural loosening of rock mass. The steep slope is located at 2450m~2650m with a dip of 50°~65°, and the rock mass of top slope is pulled along structural plane. The hanging wall rock mass at upstream side of fault F29 indicates that the rock is obvious loose and broken. Besides the occurrence of main cracks (10~30cm wide) at trailing edge of pull crack, there still exists bunching in parallel with unloading tensile fissures, which will be spit into 20~30cm slate rock, and slate crushed rock has an evident outward slope tilting bending phenomenon. The deep rock mass has no distinct pullout phenomenon

Table 1 Boundary conditions and features of No.Ⅱ deformation body

Structural plane	Overall occurrence	Features of structural plane
F29	Strike NE34°、Dip SE、Dip angle 36°	Extending about 400m, the width of fracture zone is about 20~50cm at El. 2400~2680m. There are obvious staggered faults at both sides of rock mass, with its staggered fault Hf4 of 15~20cm.
Hf4	Strike NW290°、Dip SW、Dip angle 14°	The shallow fracture zone is about 25~50cm wide, and is 85cm wide at the intersection of fracture zone F29. It is 15~30cm wide at deep fracture zone, with interacted thickness of 8~10cm. There still exists red-reddish brown interlayer soil of 2~3cm besides broken rock and crushed zone, etc.
LF1	Strike NE65~80°、Dip SE、Dip angle 70~80°	Pull crack joints filled with clay and broken stone are 10~20cm wide, 100~150m deep.
L145	Strike NW355°~NE4°、Dip NE or SE、Dip angle 80~88°	The fracture plane is flatten, intermittent extension, bunching, filling kalk, and somewhat weathered.

at the downstream L145, and this group of fissures is developed in parallel, with an intermittent extension.

In view of internal features, the top is merely loose and pull crack, and the bottom is pull crack and shear crushing. The deformation of rock mass attenuates inward river-bank from the slope, and the local scratch (plunge direction of 205° and plunging angle of 21°) occurs at El.2395 platform (Hf4 lying wall plane). The loose deformation is gradually reduced from upstream to downstream, with many pull cracks upstream in a large scale. The pull-crack joints are decreased, diminished and disappeared from upstream to downstream boundary L145.

The basic earthquake intensity is 7 degrees at Laxiwa dam site, with earthquake inertia force coefficient of F=0.14. The ground water line in the dam region is around El.2300m, and no effect will be formed to No.Ⅱ deformation body. Moreover, the top of No.Ⅱ deformation body has already been loosened and distorted and drainage effect itself is quite good. Therefore, the effect will not be considered in the analysis of earthquake dynamic stability.

By geologic investigation and relevant research, it shows that No.Ⅱ deformation body has the creep and pull crack, and is presently in a stable condition by means of many monitoring. Moreover, owing to its important location, the study on the stability of No.Ⅱ deformation body has turned into the most key engineering geologic issue of high slope for Laxiwa hydropower project.

3. Basic Principle of Newmark Method

The essential philosophy of Newmark method will result in double integration of rock mass movement and acceleration at corresponding time interval, in order to solve the total displacement of the rock mass.

3.1Fundamental assumption

1. Effect of vertical earthquake force will be ignored, merely considering the displacement at result of horizontal earthquake force;
2. Reduction of material strength under live load will not be considered;
3. Earthquake acceleration will be uniformly distributed within the landslide.

3.2Basic principle

The fundamental principle of Newmark method is to perform double integration to obtain permanent deformation on the basis of the landslide of acceleration (a) movement at the time interval (t，t+△t). Moreover, this integration will be calculated when the safety factor of the slope is less than one at that time interval. The integrations of all the time intervals being less than one shall be accumulated to acquire permanent deformation at result of the earthquake in the slope.

In the time zone (t~t+△t), the integration by Newmark method will be assumed as below:

$$\{\dot{u}_{t+\Delta t}\} = \{\dot{u}_t\} + [(1-\delta)\cdot\{\ddot{u}_t\} + \delta\cdot\{\ddot{u}_{t+\Delta t}\}]\cdot\Delta t \quad (1)$$

$$\{u_{t+\Delta t}\} = \{u_t\} + \{\dot{u}_t\}\cdot\Delta t + \left[(1/2-\alpha)\cdot\{\ddot{u}_t\} + \alpha\cdot\{\ddot{u}_{t+\Delta t}\}\right]\cdot\Delta t^2 \quad (2)$$

Where,

A and δ—— integral parameters;

{ut}、{ut+△t}—— displacement vector;

$\{\dot{u}_t\}$、$\{\dot{u}_{t+\Delta t}\}$—— velocity vector;

$\{\ddot{u}_t\}$、$\{\ddot{u}_{t+\Delta t}\}$—— acceleration vector.

The solution of displacement at time (t+△t) in Newmark method is achieved by satisfying the time (t+△t) movement equation, that is,

$$[M]\cdot\{\ddot{u}\} + [C]\cdot\{\dot{u}\} + [K]\cdot\{u\} = \{F\} \quad (3)$$

Where,

[M] —— structural mass matrix;

[C] —— structural damping matrix;

[K] —— structural rigidity matrix;

{F} —— joint load vector.

Thus, it is solved firstly from Equation (1):

$$\{\ddot{u}_{t+\Delta t}\} = \frac{1}{\alpha \Delta t^2} \cdot \{\{u_{t+\Delta t}\} - \{u_t\}\} - \frac{1}{\alpha \Delta t} \cdot \{\dot{u}_t\} - (\frac{1}{2\alpha} - 1) \cdot \{\ddot{u}_t\}$$

(4)

When the above equation is substituted into Equations (1) and (3), two-step recurrence formulae will be obtained from the calculation of $\{u_t\}$、$\{\dot{u}_t\}$、$\{\ddot{u}_t\}$:

$$\left\{\frac{1}{\alpha \Delta t^2}[M] + \frac{\delta}{\alpha \Delta t}[C] + [K]\right\}\{u_{t+\Delta t}\} = \{F\} + [M]\left\{\frac{1}{\alpha \Delta t^2}\{u_t\} + \frac{1}{\alpha \Delta t}\{\dot{u}_t\} + (\frac{1}{2\alpha} - 1)\{\ddot{u}_t\}\right\} + [C]\left\{\frac{\delta}{\alpha \Delta t}\{u_t\} + (\frac{\delta}{\alpha} - 1)\{\dot{u}_t\} + (\frac{\delta}{2\alpha} - 1)\Delta t\{\ddot{u}_t\}\right\}$$

(5)

（Here, δ ≥0.50，α ≥0.25（0.5+ δ ）^{2} are required）

4. Analyses by Newmark Method

4.1 Analytical model

In light of boundary control structural plane of No.Ⅱ deformation body, groups of F29, Hf4, LF1 and L145 are generated via NB as shown in Fig.1.

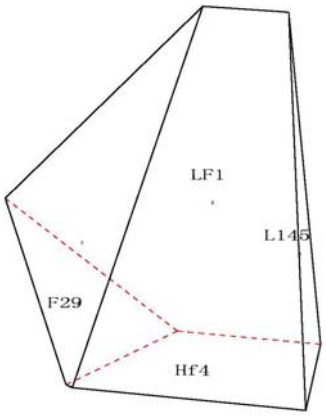

Fig.1 No.Ⅱ deformation body model

4.2 Calculating results

The stability analysis was made to the above model under earthquake action by adopting latest NM (Newmark) analytic procedure provided by Dr. Shi Genhua, and its calculating results are as follows:

（1）Safety factors at time interval of 0～10s、10～20s and 20～30s are shown in Figs. 2～4.

（2）Displacements at time interval of 0～10s、10～20s and 20～30s are shown in Figs. 5～7, of which abscissa is time (s), and ordinate is displacement.

It can be known from the above calculating results:

1) Between 13s and 16s, the safety factor is less than 1.0, and is 1.05 lower than design value. At other time interval, it is larger than 1.0, and is generally around 1.5.

2) There has no obvious displacement for No.Ⅱ deformation body under earth load action.

5 .Analysis of Limit Equilibrium Method for rigid body

5.1 Analytical model

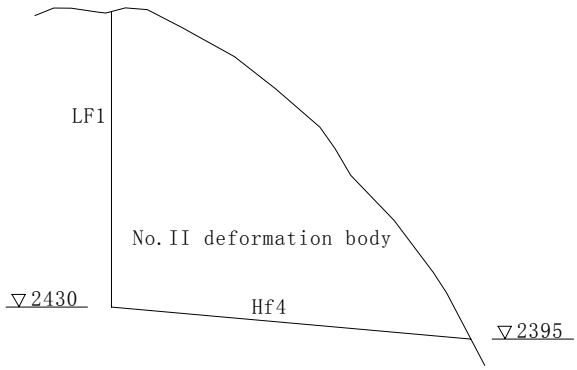

Fig.8 Calculating model for single-face sliding

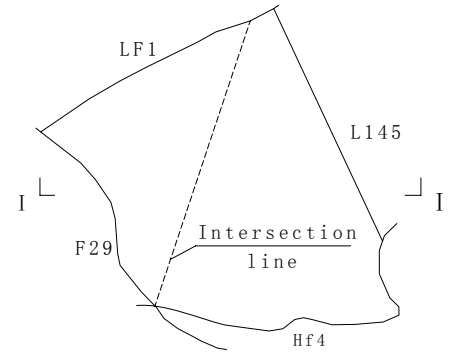

（a）Ichnography

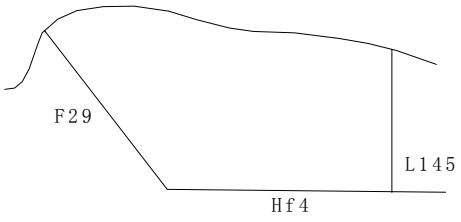

（b） Profile chart of Ⅰ－Ⅰ

Fig.9 Calculating model for double-face sliding

5.2 Standard for stability against sliding

The design standard for slope engineering is not available in China for the time being. With reference to the existing hydropower projects (such as Lijiaxia, Longyangxia, etc.), the standard of stability against sliding is determined for No.Ⅱ deformation body, which is shown in Table 2.

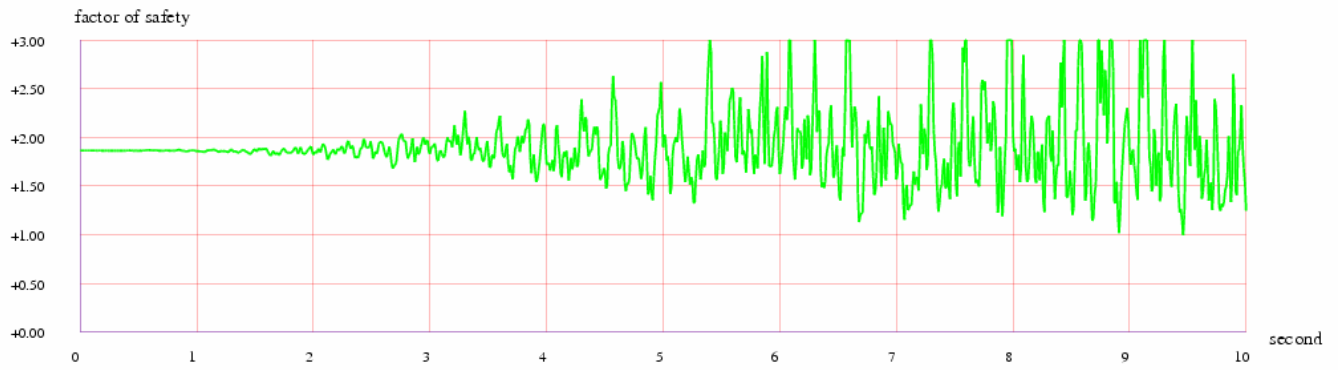

Fig.2 Safety factors at time interval of 0～10s

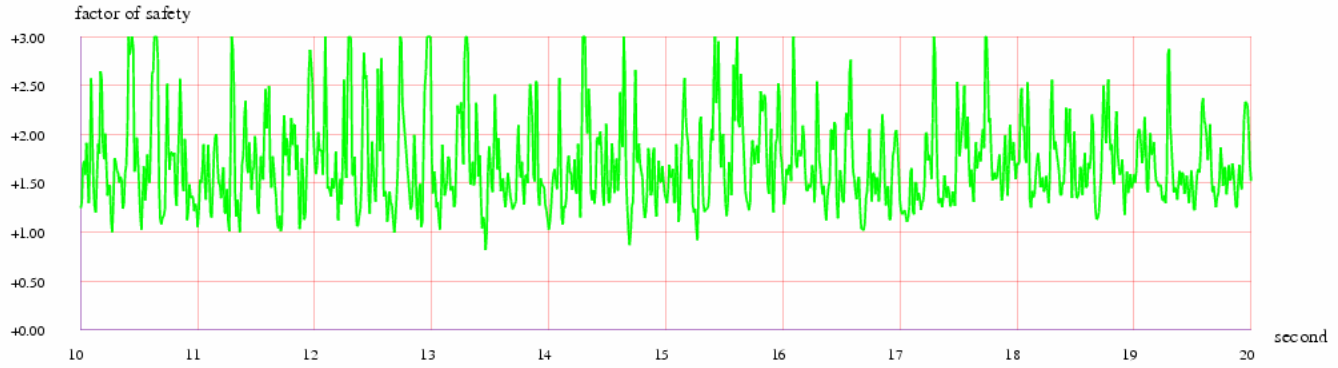

Fig.3 Safety factors at time interval of 10～20s

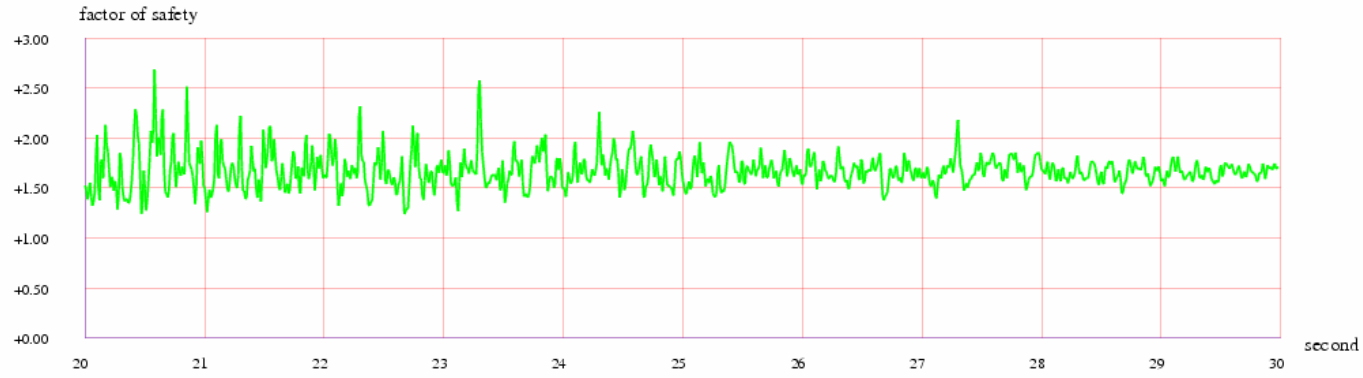

Fig.4 Safety factors at time interval of 20～30s

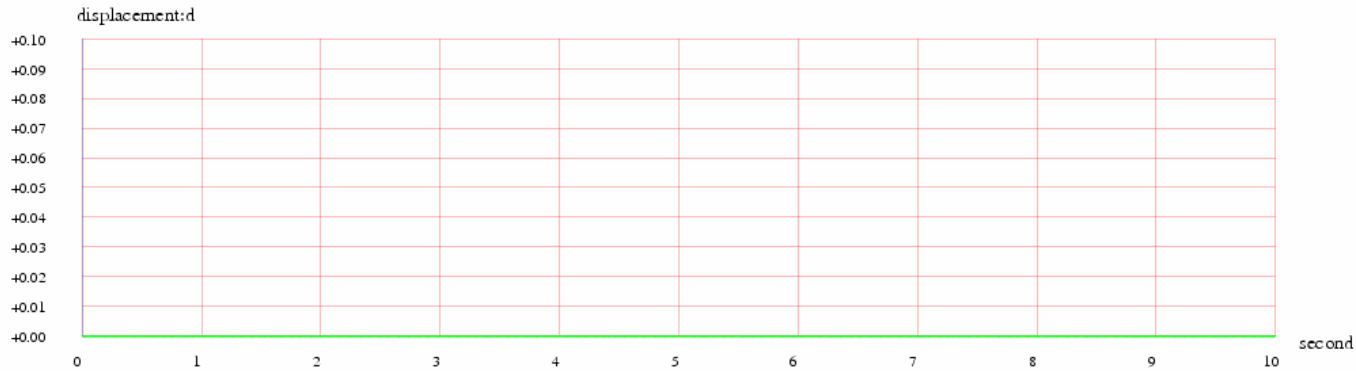

Fig.5 Displacement at time interval of 0～10s

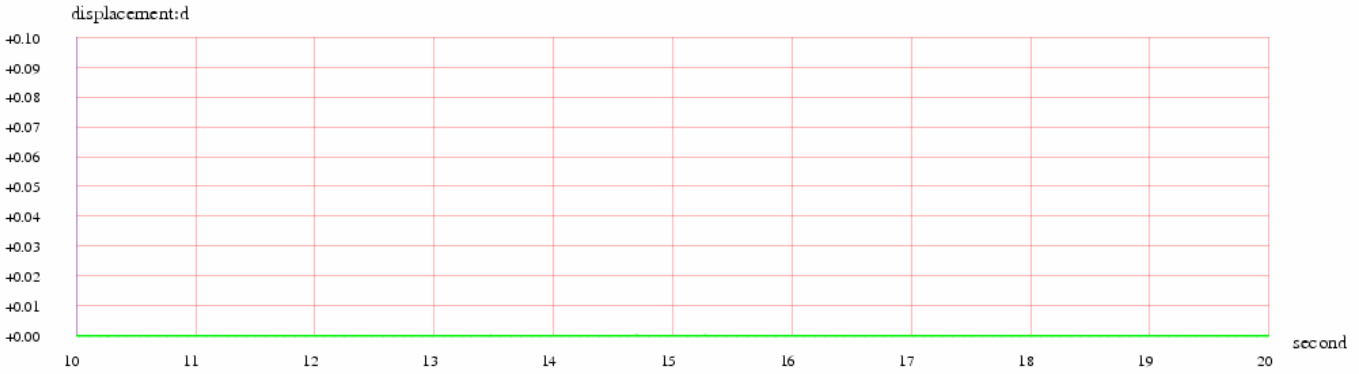

Fig.6 Displacement at time interval of 10～10s

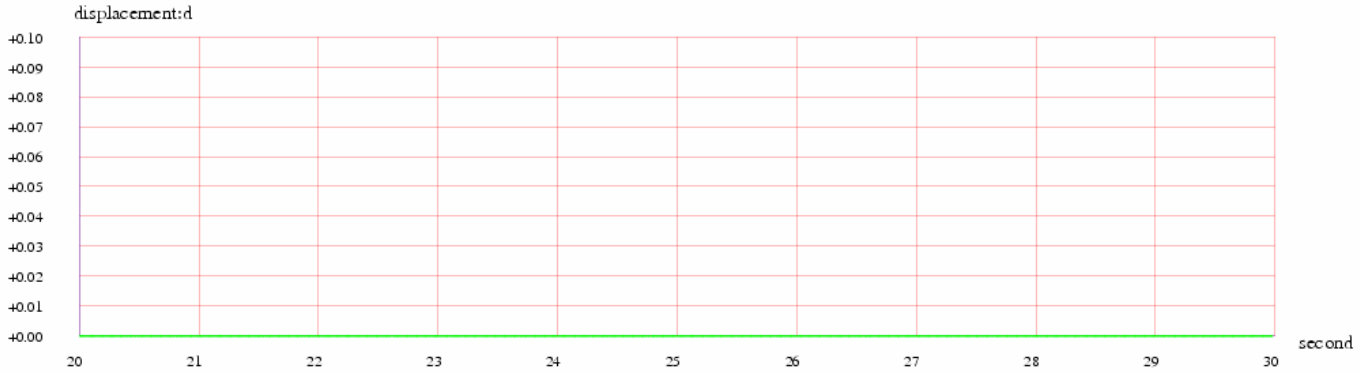

Fig.7 Displacement at time interval of 20～30s

Table 2 Design standard of stability against sliding for No. Ⅱ deformation body

Load combination	Shearing Kc
Basic combination (dead weight)	1.5
Special combination (dead weight +earthquake)	1.05

Table 3 Safety factor of stability against sliding for No. Ⅱ deformation body

Load combination		Shearing Kc	Remarks
Basic combination (dead weight)		1.82	Calculating model for double-face sliding
Special combination (dead weight + earthquake)		1.61	
Basic combination (dead weight)		1.58	Calculating model for single-face sliding
Special combination	Intersecting earthquake	0.94	
（dead weight + earthquake）	Transverse earthquake	1.00	

5.3 Calculating results

The results checked by the limit equilibrium method for rigid body is indicated in Table 3. It can be seen from Table 3 that the calculating results of double-face sliding can meet design requirements under various operating conditions, and the above results can meet operating conditions under basic combinations. However, the shearing is respectively 0.94 and 1.00 under earthquake condition, less than design standard.

6. 3-D finite element calculation

The 3-D finite element calculation will be made by applying TFINE and FLAC3D procedures.

The 3-D finite element calculation is made in the scope of nearly one time of dam height upstream, nearly two times of dam height downstream and 1.5 times of dam height at both sides of banks. In addition to simulating

main faults at dam site, it shall still simulate structural planes (F29, Hf4, L145, etc.) of No.Ⅱ deformation body. The simulating depth of dam foundation is one time of dam height (500m), i.e. simulating elevation from the crest (El. 2460m) to the foundation (El. 1960m) below. The simulating calculation of thick joint unit is performed, and the result of 3-D finite element analysis is concluded as follows:

1. Faults F29，Hf4 are in a transpression condition, and point safety degree is greater than 1.2 under normal load.

2. Under normal load, No.Ⅱ deformation body has a little effect subject to dam thrust. As a whole, No.Ⅱ deformation body is deformed toward downstream and river bed, less than 20mm. Water load has little influence, thus it is deemed that No.Ⅱ deformation body is of self-stable structure.

3. The safety degree of each structural plane is mostly above 1.2, and Faults F29，Hf4 close to upstream and leading edge are less than 1.2 without any yield. The safety degree of L145 is adequate.

7. Analyses

By calculation results of Newmark method in contrast to those of the limit equilibrium method for rigid body and 3-D finite element, it can be found that：

1. Safety factors of Newmark method and limit equilibrium method for rigid body are consistent under earthquake action, i.e. safety factors are less than design standard values under this earthquake action.

2. The displacement of No.Ⅱ deformation body under earthquake action is very small calculated by Newmark method, which is in conformity with simulating calculated results of 3-D finite element, that is, No.Ⅱ deformation body is deformed toward downstream and riverbed and its displacement is less than 20mm.

3. The dynamic simulation of earthquake action is achieved by Newmark method, reflecting comparatively and truly the stable state of slope under earthquake action. This has advantages compared to the limit equilibrium method for rigid body.

4. The permanent displacement value of the slope can be computed by Newmark method. However, there is no provision about maximum allowable displacement specified in Hydraulic Aseismic Code in China. Therefore, it is unable to balance the stable condition of slope by means of permanent displacement value, which is stipulated in the Cost Estimation Criteria of Hydropower Engineering prepared by the Hydropower Department of American Federal Energy Regulatory Commission. This clause is stated like this "Deformation calculation is only applicable to non-liquefied stable disruption. Provided that the embankment is compacted densely with good construction quality, the peak acceleration is not larger than 0.2g, and the deformation will not be considered. Otherwise, the permanent deformation analysis must be executed. The analysis shall be made by Newmark permanent deformation method and simplified Newmark permanent deformation method. Generally, the maximum displacement value along the potential slip crack plane shall not exceed 2 inches (61cm) calculated by the above method. The greater deformation value may be accepted, which depends on freeboard, dam cracking healing capacity, etc."

This provision provides a reference for stable dynamic analysis of slope.

8.Conclusion

Based upon calculations of Newmark method, limit equilibrium method for rigid body and 3-D finite element, it will be known as below:

1. The variation of safety factor in the time-interval of earthquake can be well simulated by Newmark method under earthquake action. Meantime, the permanent deformation value is also obtained, which can be utilized in the analysis of important slope.

2. No.Ⅱ deformation body has met design standard, but the safety factor is less than one in local time interval under earthquake action. In consideration of its location importance, proper engineering treatment measures shall be conducted to ensure adequate safety margin.

Reference

Gen-hua Shi. *User's Manual for Keyblock Codes of Dynamic Newmark Method* [M].U.S.A.: DDA Company, 1999.

Gen-hua Shi. *Technical Manual for Keyblock Codes of Dynamic Newmark Method* [M].U.S.A.: DDA Company, 1999.

Xu-cheng Wang. *Finite Element Method* [M]. Beijing: Tsinghua University Press, 2003.

Zu-yu Chen. *Rock Stability of Rock Slope-Principle, Method and Procedure* [M]. Beijing: China Waterpower Press, 2005.

American Federal Energy Regulatory Commission. Office of Hydropower Licensing. *Engineering Guidelines for the Evaluation of Hydropower Projects*.